STATE OF CALIFORNIA • DEPARTMENT OF TRANSPORTATION

TECHNICAL REPORT DOCUMENTATION PAGE

TR0003 (REV 10/98)

ADA Notice

For individuals with sensory disabilities, this document is available in alternate formats. For alternate format information, contact the Forms Management Unit at (916) 445-1233, TTY 711, or write to Records and Forms Management, 1120 N Street, MS-89, Sacramento, CA 95814.

1. REPORT NUMBER	2. GOVERNMENT ASSOCIATION NUMBER	3. RECIPIENT'S CATALOG NUMBER
CA15-2420		

4. TITLE AND SUBTITLE	5. REPORT DATE
Racking Response of Reinforced Concrete Cut and Cover Tunnel	January 2016
	6. PERFORMING ORGANIZATION CODE

7. AUTHOR	8. PERFORMING ORGANIZATION REPORT NO.
Kyungtae Kim, Christopher Giacalone, Ahmed Elgamal, and P. Benson Shing	UCSD / SSRP-15-03

9. PERFORMING ORGANIZATION NAME AND ADDRESS	10. WORK UNIT NUMBER
Department of Structural Engineering School of Engineering 10. Work Unit No. (TRAIS) University of California, San Diego La Jolla, California 92093-0085	11. CONTRACT OR GRANT NUMBER 65A0458
12. SPONSORING AGENCY AND ADDRESS	13. TYPE OF REPORT AND PERIOD COVERED
California Department of Transportation 13. Type of Report and Period Covered Final Report Division of Engineering Services	Final Report 14. SPONSORING AGENCY CODE

15. SUPPLEMENTARY NOTES

Prepared in cooperation with the State of California Department of Transportation.

16. ABSTRACT

Currently, the knowledge base and quantitative data sets concerning cut and cover tunnel seismic response are scarce. In this report, a large-scale experimental program is conducted to assess: i) stiffness, capacity, and potential seismically-induced nonlinear deformation mechanisms of a representative reinforced concrete tunnel liner, and ii) seismic demand as dictated by the surrounding soil and the tunnel-ground interaction mechanisms. In this regard, the conducted testing efforts allow for more accurate representation of the tunnel reinforced concrete liner configuration, and for use of field soil materials and construction procedures. Based on the recorded experimental data sets, computational studies are performed to further assess the involved soil-structure-interaction mechanisms. Overall, these studies constitute an initial important step towards ultimately providing experimentally validated engineering procedures for use in the development of cut and cover tunnel seismic assessments and design guidelines.

17. KEY WORDS	18. DISTRIBUTION STATEMENT
Cut-and-Cover Tunnel, Reinforced Concrete, Laminar Soil Container, Centrifuge, Finite Element, FHWA	Unlimited

19. SECURITY CLASSIFICATION *(of this report)*	20. NUMBER OF PAGES	21. COST OF REPORT CHARGED
Unclassified	349	

DISCLAIMER

This document is disseminated in the interest of information exchange. The contents of this report reflect the views of the authors who are responsible for the facts and accuracy of the data presented herein. The contents do not necessarily reflect the official views or policies of the State of California or the Federal Highway Administration. This publication does not constitute a standard, specification or regulation. This report does not constitute an endorsement by the California Department of Transportation of any product described herein.

For individuals with sensory disabilities, this document is available in Braille, large print, audiocassette, or compact disk. To obtain a copy of this document in one of these alternate formats, please contact: The Division of Research and Innovation, MS-83, California Department of Transportation, P.O. Box 942873, Sacramento, CA 94273-0001

STRUCTURAL SYSTEMS

RESEARCH PROJECT

Report No.
SSRP-15-03

RACKING RESPONSE OF REINFORCED CONCRETE CUT AND COVER TUNNEL

by

KYUNGTAE KIM

CHRISTOPHER GIACALONE

AHMED ELGAMAL

P. BENSON SHING

Final Report Submitted to the California Department of Transportation (Caltrans) under Contract No. 65A0458

January 2016

Department of Structural Engineering
University of California, San Diego
La Jolla, California 92093-0085

University of California, San Diego
Department of Structural Engineering
Structural Systems Research Project

Report No. SSRP-15-03

Racking Response of Reinforced Concrete Cut and Cover Tunnel

by

Kyungtae Kim
Postdoctoral Scholar, UC San Diego

Christopher Giacalone
Graduate Student Researcher

Ahmed Elgamal
Professor of Structural Engineering, UC San Diego

P. Benson Shing
Professor of Structural Engineering, UC San Diego

Final Report Submitted to the California Department of Transportation under Contract No. 65A0458

Department of Structural Engineering
University of California, San Diego
La Jolla, California 92093-0085

January 2016

ACKNOWLEDGEMENTS

Funding for the investigations presented in this report was provided by the California Department of Transportation (Caltrans) under Contract No. 65A0458. The authors are most grateful to Caltrans engineers, and in particular, the General Earthquake Committee, for their continuous technical input and advice. Dr. Charles Sikorsky of Caltrans was the project manager, providing unfailing support and guidance throughout the project.

ABSTRACT

Currently, the knowledge base and quantitative data sets concerning cut and cover tunnel seismic response are scarce. In this report, a large-scale experimental program is conducted to assess: i) stiffness, capacity, and potential seismically-induced nonlinear deformation mechanisms of a representative reinforced concrete tunnel liner, and ii) seismic demand as dictated by the surrounding soil and the tunnel-ground interaction mechanisms. In this regard, the conducted testing efforts allow for more accurate representation of the tunnel reinforced concrete liner configuration, and for use of field soil materials and construction procedures. Based on the recorded experimental data sets, computational studies are performed to further assess the involved soil-structure-interaction mechanisms. Overall, these studies constitute an initial important step towards ultimately providing experimentally validated engineering procedures for use in the development of cut and cover tunnel seismic assessments and design guidelines.

TABLE OF CONTENTS

LIST OF FIGURES

LIST OF TABLES

1. Introduction

1.1 Cut and cover tunnels: brief general background

Worldwide, a significant increase in traffic and the scarcity of open space have contributed to the proliferation of sub-surface shallow tunnels. Essentially, cut-and-cover tunnels are often of rectangular shape, constructed with relatively shallow earth cover to improve the environmental impact of roads and railway lines (including noise reduction and continuity of the ground surface layout).

(FHWA 2009) reports two types of construction, bottom-up and top-down, as shown in Figure 1-1. The construction sequences presented in Section 5 of the Technical Manual for Design and Construction of Road Tunnels – Civil Elements are as follows (FHWA 2009):

- "Bottom-up construction (Figure 1-1a): a trench is excavated from the surface within which the tunnel is constructed. The trench is backfilled and the surface restored afterward and it can be formed using open cut (sides sloped back and unsupported) or with vertical faces using an excavation support system. In this construction, the tunnel is completed before it is covered up and the surface reinstated.
- Top-down construction (Figure 1-1b): the tunnel walls are constructed first, usually using slurry walls (although secant pile walls are used). The support of excavation is often the final structural tunnel walls. Secondary finishing walls are provided upon completion of the construction. Next the roof is constructed and tied into the support of excavation walls. The surface is then reinstated before the completion of the construction. The remainder of the excavation is completed and tied into the walls. The tunnel finishes are installed within the completed structure. For wider tunnels, temporary or permanent piles or walls elements are sometimes installed along the center of the proposed tunnel to reduce the span of the roof and floors of the tunnel."

Further details concerning construction type, such as advantage/disadvantage and selection decision are summarized in Table 1-1 and can be found in Section 5 of FHWA (2009).

Highway cut-and-cover tunnels in California (CA) span over a number of different geometric configurations, age groups, and construction styles. Typical sections of cut-and-cover tunnels in-service in CA are shown in Figure 1-2 and Figure 1-3. At the highway interchange of interstates 105 and 405 (Los Angeles, CA), the Southeast connector tunnel (Figure 1-2) was

designed as an inverted U-shape supported by piled footings (cast-in-place concrete structure). At the interchange of the interstates 15 and 215 (San Bernardino, CA), the southbound ramp connector (Figure 1-3) was recently designed as a box structure (cast-in-place concrete structure). The Doyle Drive Battery Tunnel (http://www.presidioparkway.org), which passes below Presidio Park in San Francisco, CA, is one such more recent example using the cut-and-cover construction method (Figure 1-4).

Seismic response of the underground structure is governed by deformation and inertial responses of surrounding soil in view of (Wang 1993): (1) low stiffness of the surrounding soil due to the relatively small overburden pressure, and (2) site amplification effects. Moreover, soil backfill may consist of compacted material with properties that are different with those of the in-situ soil, resulting in some added complexity of the overall system response (Wang 1993). Thus, the seismic design of such a structure is dictated by considerations that differ from those of above ground structures.

1.2 Research objectives and scope

Much research has been done on bored deep tunnels, mainly in rock, in comparison to the available literature on shallow tunnels embedded in relatively softer soils (Wang, 1993). The current effort aims ultimately to provide experimentally validated engineering procedures for use in the development of cut and cover tunnel seismic assessments and design guidelines. To achieve the objectives, studies presented in this report are comprised of the following three main experimental modeling exercises:

1. Quasi-static cycling loading test on a 1/3 scale model idealization of the Doyle Drive Battery Tunnel (http://www.presidioparkway.org)

The motivation behind preforming this is twofold. The first reason is to more accurately determine elastic stiffness of the structure in order to accurately create a representative scaled model for subsequent soil-structure testing. The second reason is to document the large deformation response characteristics, and the permanent deformation patterns, for calibration of the numerical techniques to be used for seismic ground-tunnel analyses.

2. Pushover tests on a 1/9 scale ground-tunnel model in a laminar soil container

A soil-tunnel model was tested by push-over loading on the outer boundary of a large laminar container. The purpose of this testing phase is to assess the ground-structure system response, and influence of the soil deformation on the tunnel loading demands.

On the basis of the test results, calibration of a Finite Element (FE) model is undertaken. This model is then used to assess the system dynamic response during earthquake simulations with varying key parameters such as soil properties, embedment depth of the tunnel, and characteristics of the earthquake input.

3. Centrifuge modeling tests

Preliminary Centrifuge tests were conducted to document salient aspects of the involved seismic wave propagation characteristics. Changes in the response due to presence of the structure are of interest.

1.3 Outline of the report

- Chapter 2 presents a literature review related design guidelines and seismic modeling of cut and cover tunnels.

- Chapter 3 presents the experimental study of a 1/3 scale reinforced concrete tunnel model idealized based on the San Francisco Doyle Drive Battery Tunnel Cross-sectional configuration (Caltrans 2012). The specimen design, test setup, and experimental results are presented in detail.

- Chapter 4 describes details of the large ground-tunnel laminar container testing phase. Configuration of the test, employed tunnel model, soil properties, and loading protocol are discussed.

- Chapter 5 presents results of the laminar container tunnel-ground experiment.

- Chapter 6 presents a FE model calibration effort based on the test results presented in Chapter 5.

- Chapter 7 presents a representative numerical study conducted to evaluate dynamic earth pressures on the tunnel under earthquake excitation with linear and nonlinear soil properties.

- Chapter 8 presents the experimental configuration and results of the preliminary centrifuge testing phase.

- Chapter 9 presents a summary of the study and the major observations and conclusions. Recommendations for future research are included.

Table 1-1: Advantage/disadvantage and required conditions of bottom-up and top-down cut-and-cover construction (FHWA, 2009)

Construction Type	Bottom-up	Top-down
Advantage	• Conventional construction method well understood by contractors • Waterproofing able to be applied to the outside surface of the structure • Easy access to the inside of the excavation for the construction equipment and the delivery storage and placement of materials • Drainage systems able to be installed outside the structure to channel water or divert it way from the structure	• Early restoration of the ground surface above the tunnel • Usage of temporary support of excavation walls as the permanent structural walls • Internal bracing effect of the structural slabs, thus reducing the amount of tie backs required • Somewhat less width for the construction area • Easier construction of roof • Possible lower cost for the tunnel by eliminating the separate, cast-in-place concrete walls within the excavation and reducing the need for tie backs and internal bracing • Possible shorter construction duration by overlapping construction activities
Disadvantage	• Somewhat larger footprint required for construction than for top-down construction • Difficulty to restore the ground surface to its final condition until construction is complete • Temporary support or relocation of utilities required • Possible dewatering that could have adverse effects on surrounding infrastructure	• Inability to install external waterproofing outside the tunnel walls • More complicated connections for the roof, floor, and base slabs • Potential water leakage at the joints between the slabs and the walls • Risks that the exterior walls will exceed specified installation tolerances and extend within the neat line of the interior space • Limited access to the excavation to portals • Limited spaces for excavation and construction of the bottom slab
Selection condition	• No right-of way restrictions • No requirement to limit sidewall deflections • No requirement for permanent restoration of surface	• Limited width of right-of way • Necessary for sidewall deflections to be limited to protect adjacent features • Requirement for surface to be restored to permanent usable condition as soon as possible

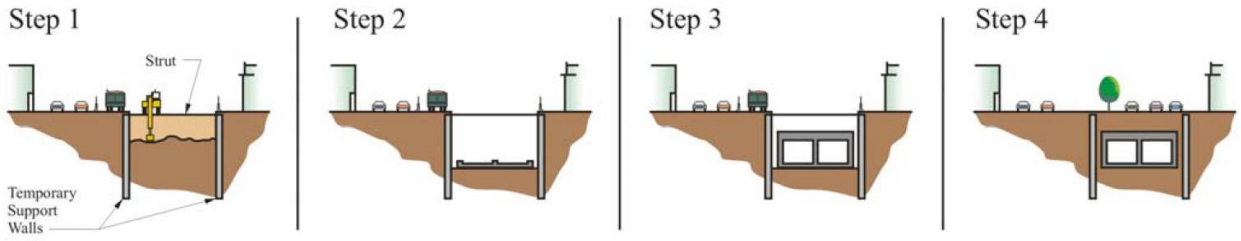

(a)

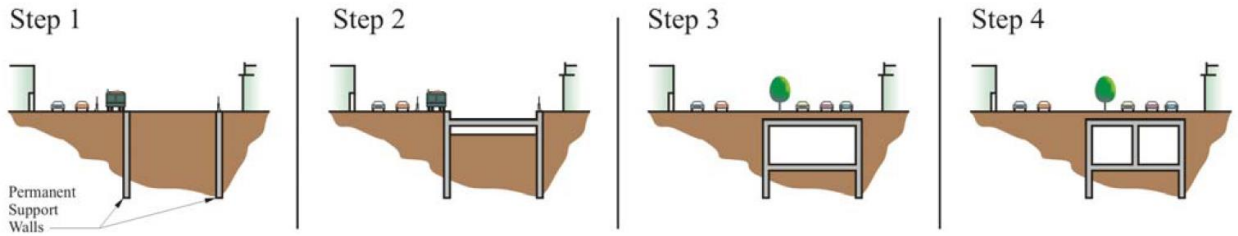

(b)

Figure 1-1: Cut and cover tunnel construction sequence; (a) Bottom-up and (b) Top-down (FHWA 2009)

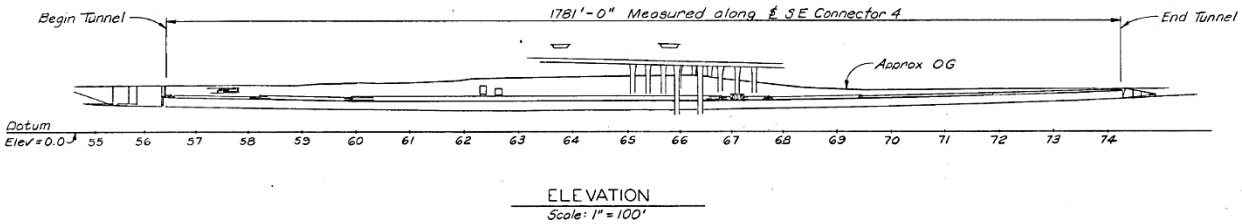

(a) Elevation view

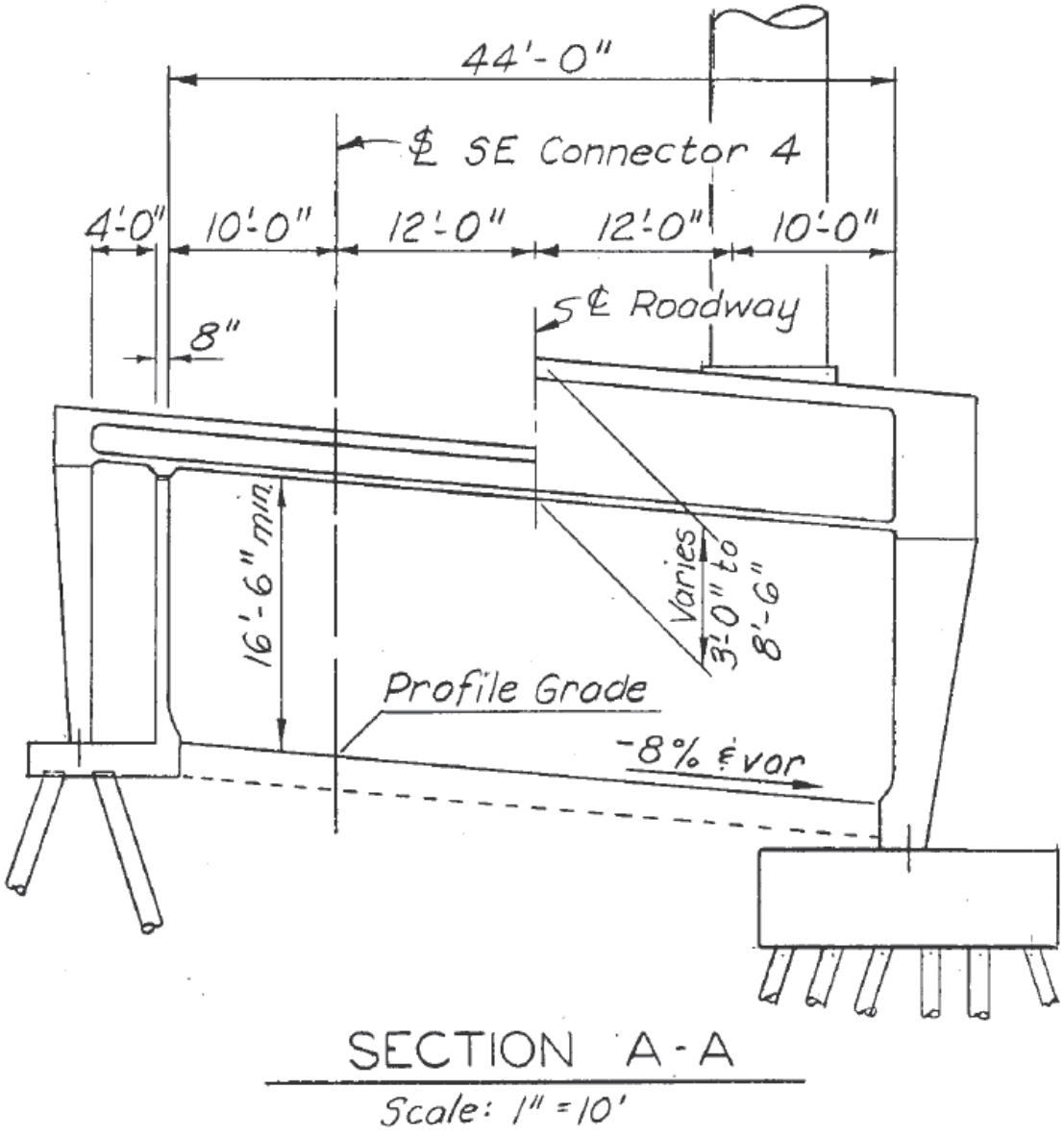

(b) Typical section view

Figure 1-2: As-built drawing of I-105/I-405 Southeast connector tunnel

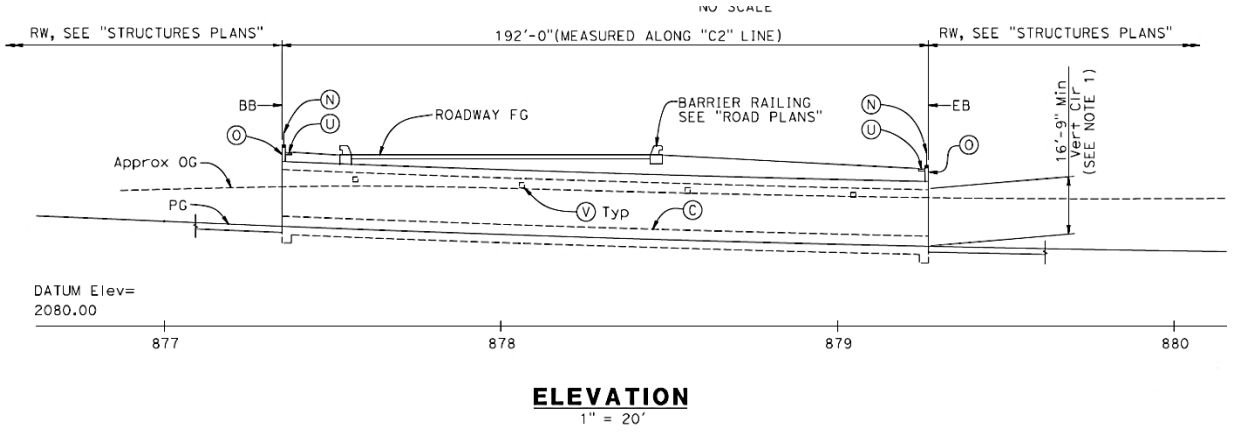

(a) Elevation view

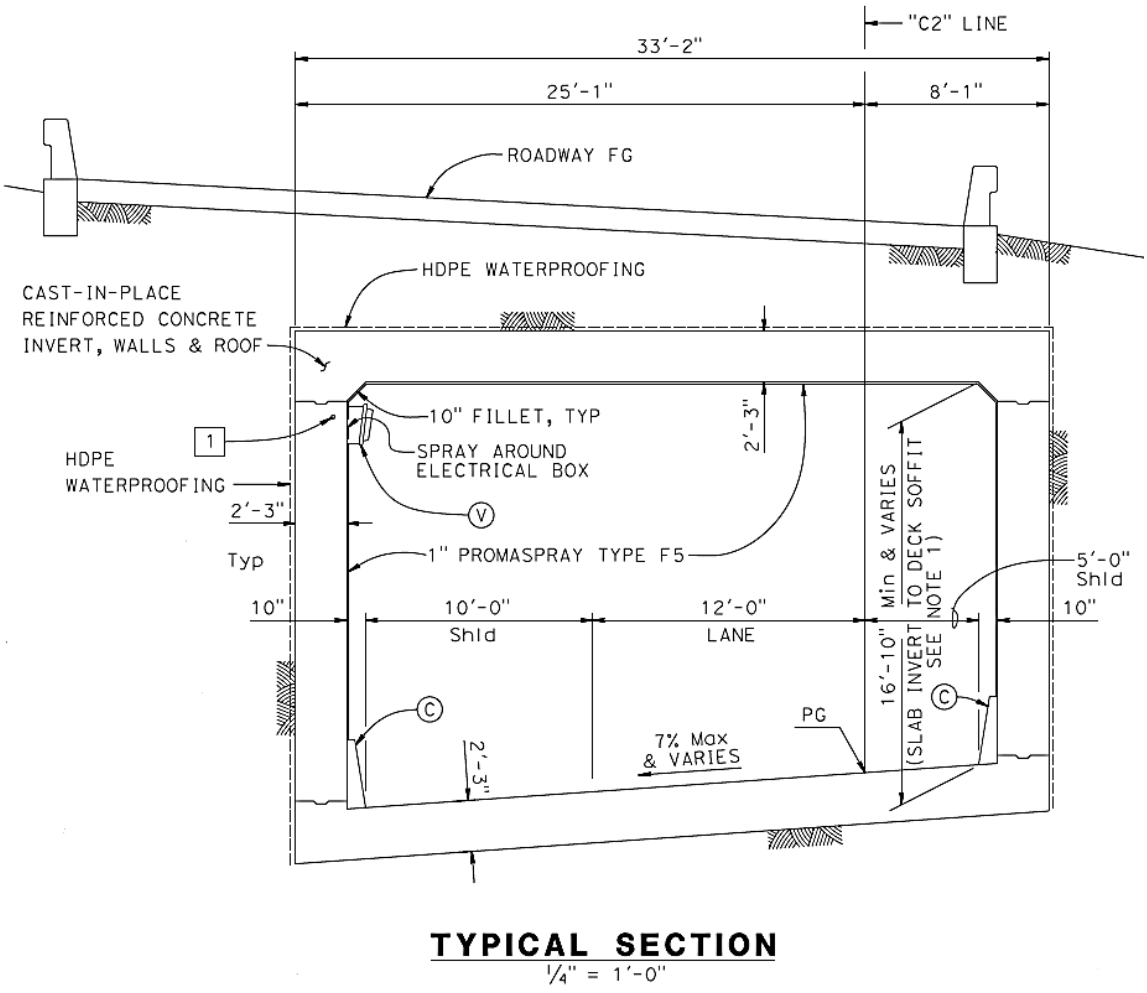

(b) Typical section view

Figure 1-3: As-built drawing of I-15 ramp connector tunnel

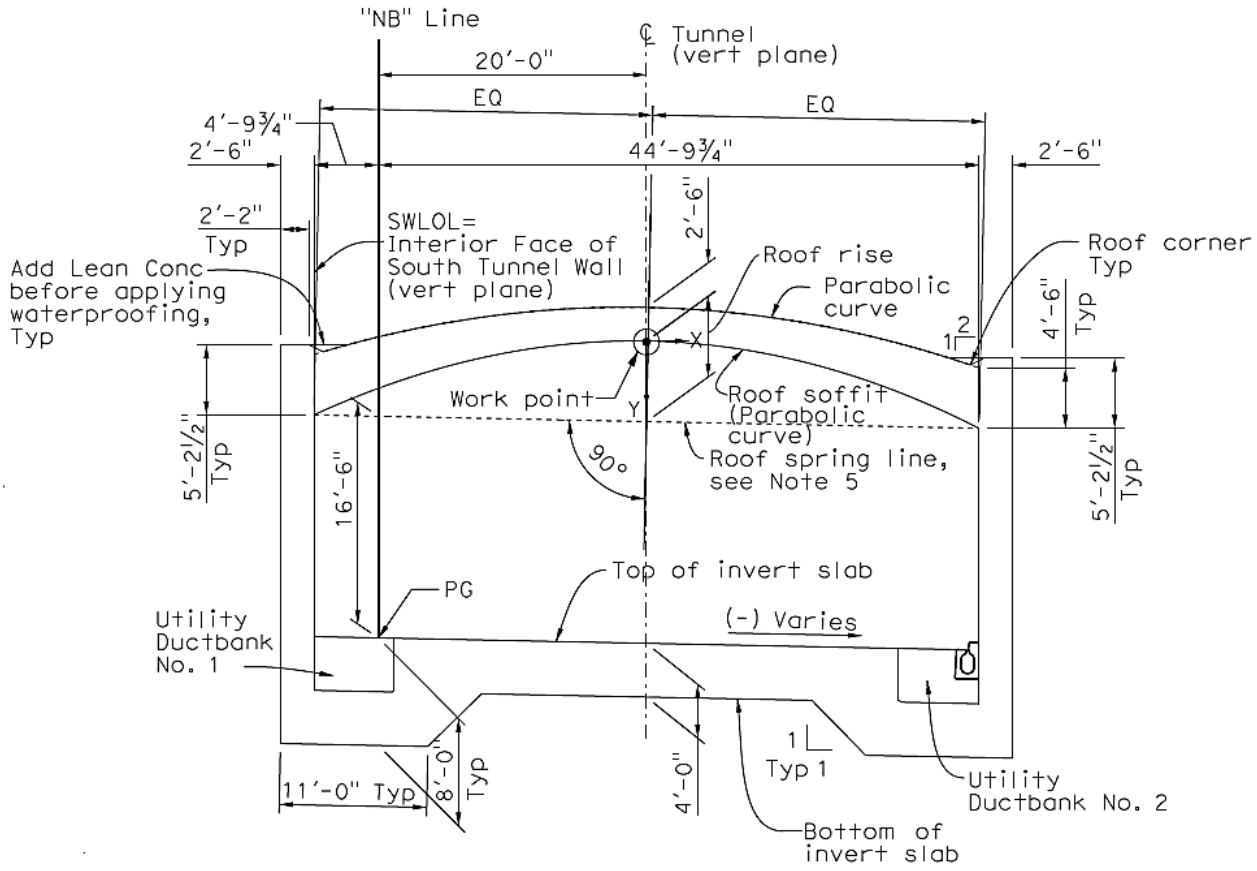

Figure 1-4: Configuration of the Doyle Drive Battery Tunnel cross-section

2. Brief Literature Review

2.1 Introduction

As discussed earlier in Section 1.1, cut-and-cover tunnels may assume a rectangular cross-section for shallow depth transportation. In such cases, the tunnel is essentially designed as a rigid frame box structure. In terms of seismic design, this box tunnel has different characteristics from that of a bored circular tunnel as discussed in FHWA (2009):

1) "Seismic ground deformation and shaking intensity tend to increase at the associated relatively shallow depth due to lower soil stiffness and site amplification effects.
2) Since a box frame does not generally transmit static loads as efficiently as a circular lining, the box frame is required to have much thicker walls and slabs. Consequently, a rectangular tunnel is usually stiffer than a circular tunnel in the transverse direction. Subjected to potentially large seismic ground deformation due to the shallow depth, this characteristic makes the soil-structure interaction (SSI) effect important from the earthquake resistance point of view.
3) Soil is typically backfilled above the cut-and-cover tunnel (between the in-situ soil and the structure). In general, the backfill soil consists of compacted material that has different properties from that of the in-situ soil. The properties of the backfill should be properly represented in the design and analysis. However, this aspect is not often adequately accounted in analytical solution. Thus, if the properties of the backfill play a critical role in evaluating seismic response, a more elaborate numerical analysis should be performed."

As such, this chapter first reviews seismic design approaches for rectangular tunnels as presented in FHWA (2009). Thereafter, efforts related to numerical simulation and analysis of tunnel structures are discussed. A brief review on effects of the tunnel-soil interface and the dynamic earth pressure on the tunnel structure is presented. Finally, typical design guidelines are included (load combinations and limit states) based on the AASHTO LRFD Bridge Design Specifications (AASHTO 2010) as presented in FHWA (2009).

2.2 Seismic design approaches

During seismic shaking, tunnels undergo three primary modes of deformation (Owen and Scholl 1981):

1) "Axial compression and extension (Figure 2-1a, b):
   - Axial deformations in tunnels are induced by components of seismic waves generating motions parallel to the axis of the tunnel and cause alternating compression and tension.
2) Longitudinal bending (Figure 2-1c, d):
   - Bending deformations are caused by the components of the seismic waves that produce particle motions perpendicular to the longitudinal axis.
   - Those deformations are controlled by the extent of ground motion incoherency along the tunnel axis.
3) Ovaling for circular tunnels or racking for rectangular tunnels (Figure 2-1e, f)
   - The ovaling or racking deformations are developed by shear waves propagating normal to the tunnel axis and cause a distortion of the tunnel cross-section.
   - The extent of ovaling/racking deformations generally depends on shear stiffness of the tunnel relative to that of the surrounding soil."

Among these representative deformation modes, for the purpose of this study, focus is placed below on the racking response of rectangular (cut-and-cover) tunnels.

2.2.1 Evaluation of transverse racking response of rectangular tunnel structures

To evaluate transverse response (racking deformation) of rectangular tunnels, FHWA (2009) recommends either: (1) a simplified analytical method, or (2) a more elaborate numerical modeling approach. FHWA (2009) states that the numerical modeling can be employed on the basis of the degree of complexity of the soil-structure system, subsurface conditions, seismic hazard level, and importance of the structures. Particularly, numerical modeling should be considered in cases where simplified analysis methods are less applicable, more uncertain, or inconclusive. This analysis is also to be considered where a very important structure is in a severe seismic environment (FHWA, 2009).

Table 2-1 provides four different approaches to analyze the seismically induced cut-and-cover tunnel racking deformation (Wang, 1993). For the racking deformation method, the amount of racking imposed on a rectangular tunnel is equal to the free-field shear distortion of

the surrounding soil (Figure 2-2). This method was adopted earlier for the San Francisco Bart subway station project (Kuesel 1969) and the LA Metro project (Monsees and Merritt 1991). This free-field deformation method provides a simple and effective design tool when the shaking intensity is relatively low or the ground is very stiff (Wang, 1993). However, this method leads to conservative design of the tunnel, particularly in soft soil (Wang, 1993).

Wang (1993) suggested a simplified analytical procedure to account for Soil Structure Interaction (SSI) in evaluating the racking response of rectangular tunnels. This simplified analytical procedure is adopted in FHWA (2009). Details of the procedure are presented in the following sub-sections. Wang (1993) also conducted comprehensive finite element analyses (Figure 2-3) using five types of the structure geometry (elastic structure; Figure 2-4). The numerical results are compared with the analytical solution as shown in Figure 2-5.

2.2.2 Analytical solution for racking response of rectangular tunnels

While closed form solutions for SSI are developed for a circular tunnel, such solutions are not available for rectangular tunnels due to their significantly variable geometric characteristics (Wang, 1993). However, simple and practical procedures accounting for dynamic SSI effects were developed by Wang (1993). In evaluating the SSI effects, a number of factors are considered such as relative stiffness between the surrounding soil and the tunnel, structure geometry, earthquake input motion, and variation of the tunnel embedment depth (Wang, 1993). The most important factor is the relative stiffness of soil in pure shear relative to the structure (Figure 2-6), defined as the flexibility ratio (F_{rec}) by the following expression (Wang, 1993):

$$F_{rec} = \frac{G_m}{K_s}\frac{W}{H} \tag{2.1}$$

where G_m is the average strain-compatible shear modulus of the surround grounding, W is width of the structure, H is height of the structure, and K_s is racking stiffness of the tunnel.

The rectangular tunnel racking stiffness can be obtained (Wang, 1993) by applying a unit lateral force at the roof level (without soil), while the base of the structure is restrained against translation, but with the joints free to rotate (Figure 2-6b). The structural racking stiffness is defined as the ratio of the applied force to the resulting lateral displacement. In performing this

analysis, it is important to use an appropriate moment of inertia taking into account the potential development of "cracked section", particularly for the vertical walls (Wang, 1993).

The value of the flexibility ratio dictates (Wang, 1993):

- $F \rightarrow 0.0$: The structure is rigid, so it will not rack regardless of the distortion of the ground (i.e. the structure must take the entire load)
- $F < 1.0$: The structure is considered stiff relative to the surrounding soil medium and will therefore exhibit lower deformation.
- $F = 1.0$: The structure and surrounding soil medium have equal stiffness, so that the structure will undergo approximately the same free-field distortions.
- $F > 1.0$: The racking distortion of the structure is amplified relative to the free field, though not because of dynamic amplification. Instead, the distortion is amplified because the soil medium now has a cavity, providing lower shear stiffness than the non-perforated ground in the free field.
- $F \rightarrow \infty$: The structure has no stiffness, so it will undergo deformations identical to the perforated ground.

On the basis of the flexibility ratio, a step by step procedure was developed by Wang (1993). This procedure is adopted in Section of 13.5.1.3 of FHWA (2009) and replicated below (also summarized in Table 2-2).

- Step 1: Estimate the free-field ground strain (γ_{max}) at the structure elevation caused by the design-level vertically propagating shear waves (see Table 2-2 for deriving the ground strain). Determine free-field relative displacement ($\Delta_{free\text{-}field}$) corresponding to the top and the bottom elevation of the tunnel (Figure 2-2):

$$\Delta_{free\text{-}field} = H\,\gamma_{max} \tag{2.2}$$

- Step 2: Determine the racking stiffness (K_s) of the tunnel from a structural frame analysis (Figure 2-6b). The racking stiffness should be computed using the displacement of the roof subjected to a unit lateral force applied at the roof level, while the base of the structure is restrained against translation, but with the joints free to rotate. The ratio of the applied force to

the resulting lateral displacement yields K_s. In performing the structural frame analysis, appropriate moment of inertia values, taking into account the potential development of cracked section, should be used.

- Step 3: Determine the flexibility ratio, F_{rec} (see Eq. 2.1)

- Step 4: Determine the racking coefficient, R_r (ratio of tunnel racking relative to the free-field displacement, $\Delta_{free\text{-}field}$)

For no-slip interaction condition (Wang, 1993; Penzien, 2000)

$$R_r = \frac{4(1-\nu_m)F_{rec}}{3-4\nu_m+F_{rec}} \tag{2.3}$$

where ν_m is Poisson's ratio of the surrounding soil. For full-slip interface condition (Penzien, 2000)

$$R_r = \frac{4(1-\nu_m)F_{rec}}{2.5-3\nu_m+F_{rec}} \tag{2.4}$$

- Step 5: Determine the racking deformation of the tunnel, Δ_s.

$$\Delta_s = R_r \, \Delta_{free\text{-}field} \tag{2.5}$$

- Step 6: Obtain the seismic demand in terms of internal forces (and material strains) by imposing Δ_s in a frame analysis. As shown in Figure 2-7, two pseudo-static lateral forces configurations are recommended. From these considerations, the more critical response should be used for design (FHWA, 2009).

- Step 7: For effects of vertical seismic motion, apply a vertical pseudo-static loading equivalent to the product of the vertical seismic coefficient and the combined dead and design overburden loads (based on the involved vertical seismic motion). The vertical seismic coefficient can be reasonably assumed to be 2/3 of the design peak horizontal acceleration divided by the gravity.

- Step 8: Combine seismic demands due to the racking deformation and vertical seismic motion with non-seismic loads using appropriate load combinations (recommended load factor of 1.0 for the seismic demands).

2.2.3 Numerical modeling approach

The analytical solution above (Section 2.2.2) is developed based on the following ideal conditions and assumptions (FHWA, 2009):

- The tunnel is of rectangular shape
- The material of the surrounding soil is uniform and isotropic.
- The tunnel is relatively deep so that there is no reflection and refraction of seismic wave from ground surface.
- There is only one single tunnel considered (i.e. no interaction from other tunnels or structures in the soil of interest).

However, the actual soil-tunnel system encountered in the field may be of a more complex configuration. As a consequence, the use of numerical methods may be required. In addition, numerical methods may be necessary for very important tunnel structures located in severe seismic conditions.

FHWA (2009) also provides the numerical modeling approach details. There are three types of two-dimensional analysis methods. A summary of these methods is presented below as and details can be found in Section 13.5.1.5 of FHWA (2009):

1. Pseudo-Static Seismic Coefficient Deformation Method

   The seismic load is generated in a pseudo-static manner as equivalent inertial load throughout the numerical domain corresponding to the ground free-field acceleration amplification profile along the lateral boundaries (Figure 2-8). The ground acceleration profile is derived as a function of depth from a separate one-dimensional free-field site response analysis.

2. Pseudo-Dynamic Time-History Analysis

   This procedure is similar to that of the pseudo-static seismic coefficient deformation method, except for the derivation of ground displacements imposed on the lateral boundary of the numerical domain (Figure 2-9). Figure 2-10 shows an example of this method. Alternatively,

the model in Figure 2-10 can be performed in a "de-coupled" manner in which the tunnel model is analyzed separately from the surrounding soil. The tunnel model subjected to the free-field displacement along the perimeter of the tunnel cavity (from the free-field site response analysis) through interaction soil springs to evaluate its seismic response.

3. Dynamic Time History Analysis

   In general, the inertia of the tunnel is relatively small with respect to that of the surrounding soil. Thus, the pseudo-static or pseudo-dynamic analysis is suitable for evaluating the tunnel deformation. As the inertial effect of the tunnel is considered to be significant and a further refined analysis is necessary, a dynamic time history analysis approach can be adopted.

   in this situation, the entire soil-structure system (Figure 2-11) is subjected to dynamic excitation using ground motion time histories as input at the base of the system. The input ground motions (representative of the seismic environment of the site and its conditions) should be developed to match the target design response spectra (FHWA 2009).

2.2.4 Seismic design loads and criteria

In general, "the design of tunnel structures (including non-standard retaining walls) shall be consistent with Caltrans Bridge Design Specifications (Caltrans 2008) and AASHTO LRFD bridge design specifications. The structures shall be designed to resist load effects induced by construction staging, dead weight, superimposed dead load, live load, earth pressure/surcharge, hydrostatic water pressure, thermal gradients, creep/shrinkage, wind load, and earthquake load" (Doyle Drive Replacement Project, 2009). In this subsection, the earthquake loads are presented.

The following sub-sections summarize seismic design philosophy for tunnel structures as presented in Wang (1993). "The seismic design of a tunnel shall be based on two level design criteria that are recommended to ensure that transportation tunnels constructed in moderate to high seismic areas represent functional adequacy and economy while reducing lift-threatening failure." The two design criteria are as follows (Wang, 1993):

- "The Operating Design Earthquake (ODE) is defined as the earthquake event that can reasonably be expected to occur during the design life of the facility (e.g., at least once). The ODE design goal is that the overall system shall continue operating during and after an ODE. If the members experience little to no damage, the inelastic deformations in the members should be kept low."

- "The Maximum Design Earthquake (MDE) is defined as an event that has a small probability of exceedance during the facility life (e.g., 5 percent). The MDE design goal is that public safety shall be maintained during and after an MDE."

From the MDE, the tunnel must provide sufficient capacity in the structural members. The potential instability modes due to the development of plastic hinges should be prevented" (Wang, 1993).

2.2.4.1 Loading criteria for MDE

According to Wang (1993): "For a cut-and-cover tunnel, the recommended seismic loading combination for the MDE is as follows:

$$U = D + L + E1 + E2 + EQ \tag{2.6}$$

where U = required structural strength capacity

D = effects due to dead loads of structural components

L = effects due to live loads

$E1$ = effects due to vertical loads of earth and water

$E2$ = effects due to horizontal loads of earth and water

EQ = effects due to design earthquake (MDE)"

Comments on the loading combinations for MDE (Eq. 2.6) are stated in Wang (1993) as follows:

- "The structure should first be designed with adequate strength capacity under static loading conditions.
- The structure should then be checked in terms of ductility (its allowable deformation vs. maximum deformation imposed by earthquake) as well as strength when earthquake effects, *EQ*, are considered. The '*EQ*' term for conventional surface structure design reflects primarily the inertial effect on the structures. For tunnel structures, the earthquake effect is governed not so much by a force or stress, but rather by the deformation imposed by the ground.
- In checking the strength capacity, the effects of earthquake loading should be expressed in terms of internal moments and forces, which can be calculated according to the lining deformations imposed by the surrounding ground. If the 'strength' criteria expressed by Eq.

2.6 can be satisfied based on elastic structural analysis, no further provisions under the MDE are required. Generally, the strength criteria can easily be met when the earthquake loading intensity is low (i.e. in low seismic risk areas. and/or the ground is very stiff.

- If the flexural strength of the structure lining, using elastic analysis and Eq. 2.6 is found to be exceeded (e.g. at certain joints of a cut-and-cover tunnel frame., one of the following two design procedures should be followed:

  1. Provide sufficient ductility (using appropriate detailing procedure) at the critical locations of the structure to accommodate the deformations imposed by the ground in addition to those caused by other loading effects (see Eq. 2.6). The intent is to ensure that the structural strength does not degrade as a result of inelastic deformations and the damage can be controlled at an acceptable level.

     In general, the more ductility that is provided, the more reduction in earthquake forces (the '*EQ*' term) can be made in evaluating the required strength, *U*. As a rule of thumb, the force reduction factor can be assumed equal to the ductility (factor) provided. This reduction factor is similar with definition to the response modification factor used in the LRFD specification (AASHTO, 2010).

     Note that, since an inelastic 'shear' deformation may result in strength degradation, it should always be prevented by providing sufficient shear strengths in structure members, particularly in the cut-and-cover rectangular frame. The use of ductility factors for shear forces may not be appropriate.

  2. Re-analyze the structure response by assuming the formation of plastic hinges at the joints that are strained into inelastic action. Based on the plastic hinge analysis, a redistribution of moments and internal forces will result.

     If new plastic hinges are developed based on the results, the analysis is re-run by incorporating the new hinges (i.e. an iterative procedure) until all potential plastic hinges are properly accounted for. Proper detailing at the hinges is then carried out to provide adequate ductility. The structural design in terms of required strength (Eq. 2.6) can then be based on the results from the plastic-hinge analysis.

     As discussed earlier, the overall stability of the structure during and after the MDE must be maintained. Realizing that the structures also must have sufficient capacity (besides the earthquake effect) to carry static loads (e.g. *D*, *L*, *E1*, *E2*, and *H* terms), the potential

modes of instability due to the development of plastic hinges (or regions of inelastic deformation) should be identified and prevented (Monsees and Merritt 1991).

- For cut-and-cover tunnels, the evaluation of capacity using Eq. 2.6 should consider the uncertainties associated with the loads *E1* and *E2*, and their worst combination.

In many cases, the absence of live load, *L*, may present a more critical condition than when a full live load is considered. Therefore, a live load equal to zero should also be used in checking the structural strength capacity using Eq. 2.6."

2.2.4.2 Loading criteria for ODE

According to Wang (1993): "For a cut-and-cover tunnel, the recommended seismic loading combination for the ODE is as follows:

$$U = 1.05D + 1.3L + \beta_1(E1 + E2) + 1.3EQ \tag{2.7}$$

where *D*, *L*, *E*1, *E*2, *EQ* and *U* are as defined in Eq. 2.6, $\beta_1 = 1.05$ if extreme loads are assumed for *E1* and *E2* with little uncertainty. Otherwise, use $\beta_1 = 1.3$. Comments on the loading combinations for ODE (Eq. 2.7) are stated in Wang (1993) as follows:

- The structure should first be designed with adequate strength capacity under static loading conditions.
- For cut-and-cover tunnels, the evaluation of capacity using Eq. 2.7 should consider the uncertainties associated with the loads *E1* and *E2*, and their worst combination.
- When the extreme loads are used for design, a smaller load factor is recommended to avoid unnecessary conservatism. Note that an extreme load may be a maximum load or a minimum load, depending on the most critical case of the loading combinations. For a cut-and-cover tunnel, the most critical seismic condition may often be found when the maximum lateral earth pressure, *E2*, is combined with the minimum vertical earth load, *E1*. If a very conservative lateral earth pressure coefficient is assumed in calculating the *E2*, the smaller load factor $\beta_1 = 1.05$ should be used.
- Redistribution of moments (e.g. ACI 318-08) for cut-and-cover concrete frames is recommended to achieve a more efficient design.

- If the 'strength' criteria expressed by Eq. 2.7 can be satisfied based on elastic structural analysis, no further provisions under the ODE are required.
- If the flexural strength of the structure, using elastic analysis and Eq. 2.7, is found to be exceeded, the structure should be checked (for its ductility) to ensure that the resulting inelastic deformations, if any, are small. If necessary, the structure should be redesigned to ensure the intended performance goals during the ODE.
- Zero live load condition (i.e. L =0) should also be evaluated in Eq. 2.7."

2.3 Numerical modeling for seismic analysis of tunnel structures

Shamsabadi et al. (2014) presented "innovative" numerical analyses of the Caldecott and Devil's slide tunnel structures (bored through variable rock formations) located in the California (CA) San Francisco Bay area. They used a two-step analysis procedure to evaluate the performance of the tunnel liner subjected to spectrum-compatible earthquake input motions. In the first step, seismic induced deformations of the tunnel are computed without the presence of the liner due to seismic wave propagation through the rock and or soil medium (i.e. free-field deformation from wave scattering analysis (Figure 2-12a). In the second step, the free-field deformation is imposed on the tunnel liner through springs accounting for interaction between the liner and the surrounding medium (Figure 2-12b). Similarly, this two-step analysis procedure was applied to analyze the Yerba Buena Island Tunnel (Figure 2-13), located between the cities of San Francisco and Oakland, CA (Law and Lam 2003; Shamsabadi and Law 2012).

For seismic analyses of the Caldecott Tunnel fourth bore (Yang et al. 2008), wave scattering analyses was conducted using spectrum-compatible time histories to account for localized geologic characteristics including site specific topography and corresponding soil properties (Figure 2-14a). The results from the wave scattering analyses provided estimates of the tunnel liner distortion (fourth bore; Figure 2-14b). For design analyses of the Caldecott tunnel (fourth bore), the wave scattering analysis assisted in providing multiple-support displacement time history inputs to beam-spring and beam-continuum models (Thapa et al. 2008).

Shamsabadi et al. (2001) conducted soil-tunnel-structure interaction analysis for seismic retrofit of the Posey and Webster Street Tunnels located in the San Francisco Bay area,

California (Shamsabadi et al. 2001). A three-dimensional global soil-tunnel structure interaction model was employed using soil springs at the centerline of the tunnel (linear elastic model for the tunnel model; linear elastic model for vertical and horizontal soil springs but non-linear elastic spring in the longitudinal direction; Figure 2-15a). A set of three component-response-spectrum-compatible rock motion time histories was used. In addition, to evaluate capacity of the tunnel (nonlinear non-homogeneous soil and nonlinear concrete), a two-dimensional quasi-static pushover local racking analysis was performed (Figure 2-15b). This local analysis method is also presented as "Pseudo-Dynamic Time-History Analysis" in FHWA (2009) and further discussed earlier in this chapter (Section 2.2.3).

Wang (1993) performed tunnel-ground interaction analyses (Figure 2-3) using five types of geometry (Figure 2-4) as a parametric study to study effect of the relative stiffness between the tunnel and the surrounding soil. The structural members were modeled by linear elastic beam element. Soil material properties were also linear elastic. No-slip condition along the soil/tunnel interface was assumed. From these comprehensive analyses, the numerical results were compared with the simplified analytical racking solution developed by Wang (1993). This analytical solution is further discussed earlier in this chapter (Section 2.2.2).

2.4 Interface effects between tunnel and soil

Huo et al. (2006) describes the potential to impose seismically induced displacements to the tunnel based on: 1) relative stiffness between the tunnel and the surrounding soil and 2) friction developed along the interface. These two factors are not only correlated, but also have opposite effects (Huo et al. 2006). For a stiff tunnel relative to the soil (i.e. the free-filed/surrounding soil undergoes a large deformation), high friction at the interface constrains that displacement. Consequently, it can be expected that soil deformation and degradation around the tunnel will be limited (Huo et al. 2006). On the other hand, if friction is low, smaller shear stresses are transmitted to the tunnel (i.e., limited deformations in the tunnel). However, the potential for developing considerable soil displacement is increased, resulting in degradation of soil shear modulus. As such, it might be expected that the surround soil tends to induce large deformations, resulting in high normal stresses at the interface.

From the seismic analyses of circular tunnels (Sedarat et al. 2009), it was observed that a realistic representation of the soil-tunnel interface prevented development of unrealistic normal tensile stresses and provided control of the tangential tractions at the interface (Sedarat et al.

2009). As a consequence, the lining thrust increments induced by ovaling deformation (for circular tunnels) was considerably different from those from the analytical solution in the studied case (Sedarat et al. 2009). Meanwhile, it was shown that bending moments were less sensitive to the soil-tunnel interface conditions (Sedarat et al. 2009).

2.5 Dynamic earth pressure

This section was thoroughly discussed in Hashash et al. (2001). A summary of the discussion is presented here. Based on the Mononobe-Okabe theory (Seed and Whitman 1970) and the Japanese Society of Civil Engineers (JSCE 1998), earthquake loads caused by inertia forces of the surrounding soil are quantified for dynamic earth pressure by a determined seismic coefficient and the soil properties. The Mononobe-Okabe method was originally developed for above-ground earth retaining walls. This method assumes sufficiently moving and/or tilting wall structures to have a yielding active earth wedge forming behind the wall (Hashash et al., 2001). However, the yielding active earth edge is unlikely to be achieved for a buried rectangular structural frame moving together with the ground (Hashash et al., 2001).

The Mononobe-Okabe method may lead to unrealistic results for a rectangular tunnel structure racked by an amount greater than the deformation of the surrounding ground (Hashash et al., 2001). This unrealistic result tends to be amplified with increasing burial depth due to the inertia force of the thick soil cover acting as a surcharge (Hashash et al., 2001). In spite of this drawback (Hashash et al., 2001), this method has been reported (Wang, 1993) to provide a reasonable safety measure against dynamic earth thrust for shallow tunnels.

2.6 Load combinations and limit states (AASHTO LRFD Bridge Design Specifications)

Design and construction considerations of cut-and-cover tunnels are presented in Section 5 of the Technical Manual for Design and Construction of Road Tunnels – Civil Elements (FHWA 2009). This section reports the load combination approach, essentially exactly as presented in the AASHTO LRFD Bridge Design Specifications (AASHTO 2010).

2.6.1 Loads

Paragraph 3.3.2 “Load and Load Designation” of the AASHTO LRFD specifications defines permanent loads and transient loads used for the design of the tunnel. These loads are summarized in Table 2-3.

2.6.2 Limit states, load factors, and combinations

The loads defined in Table 2-3 should be factored and combined in accordance with the LRFD specifications as shown in the following:

$$\sum \eta_i \gamma_i Q_i \leq \varphi R_n = R_r \tag{2.8}$$

where:

η_i = load modifier relating to the ductility, redundancy, and operation importance of the feature being designed ($\eta_i = \eta_D \eta_R \eta_I$). For typical cut-and-cover tunnels, η_D = 1.0 (relating to ductility); η_R = 1.0 (relating to redundancy); η_I = 1.05 (relating to the importance of the structure).

γ_i = load factor. Values for γ can be found in Table 2-4.

Q_i = force effect acting on the tunnel member being designed

R_n = nominal resistance

R_r = calculated resistance of the member or connection

φ = resistance factor; the AASHTO LRFD specifications provides the resistance factors for each material used in the member section; Section 5 for the concrete design; Section 6 for the steel design. For buried structures and tunnel liners, Section 12 can be consulted.

The tunnel as a buried structure shall be designed for force effects resulting from horizontal and vertical earth pressure, pavement load, live load, and vehicular dynamic load allowance. Earth surcharge, live load surcharge, down-drag loads, and external hydrostatic pressure shall be evaluated where construction or site conditions warrant. Water buoyancy loads shall be evaluated for buried structures with inverts below the water table to control floatation, as necessary.

2.6.2.1 Service and strength limit states

The cut-and-cover tunnel as a type of buried structure is designed in accordance with Section 12 of the AASHTO LRFD specifications. The tunnel structure shall be evaluated for Service Limit State Load Combination I and Strength Limit State Load Combinations I and II (Paragraph 12.5.1 of the AASHTO LRFD specifications), defined as follows:

- Service Limit State Load Combination I: Load combination relating to the normal operational use of the bridge with a 90 km/hr wind and all loads taken at their nominal values. Also

related to deflection control in buried metal structures, tunnel liner plate, and thermoplastic pipe, to control crack width in reinforced concrete structures, and for transverse analysis relating to tension in concrete segmental girders. This load combination should also be used for the investigation of slope stability.

- Strength Limit State Load Combination I: Basic load combination relating to the normal vehicular use of the bridge without wind.
- Strength Limit State Load Combination II: Load combination relating to the use of the bridge by owner-specified special design vehicles, evaluation permit vehicles, or both without wind.

It is stated in FHWA (2009) that, in some cases, the absence of live load can create a governing case (e.g., live load can reduce the effects of buoyancy). Thus, in addition to the limit states (Service I and Strength I and II), Service Limit State Load Combination IV and Strength Limit State Load Combination III (that do not include live loads) are recommended to be evaluated and their definitions are as follow:

- Service Limit State Load Combination IV: Load combination relating only to tension in prestressed concrete columns with the objective of crack control.
- Strength Limit State Load Combination III: Load combination relating to the bridge exposed to wind velocity exceeding 90 km/hr.

Extreme event loading is not required for buried structures in the AASHTO LRFD specification. However, cut-and-cover tunnels can be subjected to extreme event loading such as earthquakes, fires, and explosions. The FHWA (2009) recommends that, during the planning phase of a tunnel, a risk analysis shall be performed to identify the probability of the extreme loads occurring, the level (at which they may occur), and the need for designing the tunnel to resist these loads. For earthquakes, the Extreme Event Limit State Load Combination I is evaluated. The earthquake load should be applied to the tunnel lining as appropriate for the seismic zone for the tunnel (FHWA, 2009). To take into consideration this load, Chapter 13 of the FHWA (2009) provides recommendations, as discussed earlier in Section 2.3. For cut-and-cover tunnels below the water table, the effect of buoyancy should be evaluated using Service Limit State Load Combination IVA as presented in Section 5.5.2 of the FHWA (2009).

2.6.2.2 Load combinations

Table 2-4 summarizes the load combinations associated with the limit states defined above in Section 2.6.2.1. Using the load combinations, a typical loading diagram for a cut-and-cover tunnel (associated with the bottom-up construction) is shown in Figure 2-16. Subjected to those loading considerations, components such as walls, roof, and base are designed.

Table 2-1: Seismic racking design approaches (Wang, 1993)

Approaches	Advantages	Disadvantages	Applicability
Dynamic earth pressure methods	▪ Used with reasonable results in the past ▪ Require minimal parameters and computation error ▪ Serve as additional safety measures against seismic loading	▪ Lack of rigorous theoretical basis ▪ Resulting in excessive racking deformations for tunnels with significant burial ▪ Use limited to certain types of ground properties	For tunnels with minimal soil cover thickness
Free-field racking deformation method	▪ Conservative for tunnel structure stiffer than ground ▪ Comparatively easy to formulate	▪ Non-conservative for tunnel structure more flexible than ground ▪ Overly conservative for tunnel structures significantly stiffer than ground ▪ Less precisions with highly variable ground conditions	For tunnel structures with equal stiffness to ground
Soil-structure interaction finite element analysis	▪ Best presentation of soil-structure system ▪ Best accuracy in determining structure response ▪ Capable of solving problems with complicated tunnel geometry and ground conditions	▪ Requires complex and time consuming computer analysis ▪ Uncertainty of design seismic input parameters may be several times the uncertainty of the analysis	All conditions
Simplified frame analysis model	▪ Good approximation of soil-structure interaction ▪ Comparatively easy to formulate ▪ Reasonable accuracy in determining structure response	Less precision with highly variable ground	All conditions except for compacted subsurface ground profiles

Table 2-2: Summary of the step by step procedure for the racking analysis of rectangular tunnels (FHWA, 2009)

Step 1*	Estimate the free-field ground strains, γ_{max} (at the structure elevation); determine free-field relative displacement ($\Delta_{free\text{-}field}$) corresponding to the top and the bottom elevation of the tunnel $\Delta_{free\text{-}field} = H\ \gamma_{max}$,where, on the basis of i) *PGA*, $\gamma_{max} = \tau_{max} / G_m$, $\tau_{max} = (PGA/g)\sigma_v R_d$, $\sigma_v = \gamma_t (h+D)$; ii) *PGV*, $\gamma_{max} = V_S / C_{se}$
Step 2	Determine the racking stiffness (K_s) of the box structure from a structural frame
Step 3	Determine the flexibility ratio $F_{rec} = (G_m/K)(W/H)$ where W = width of the box structure
Step 4	Determine the racking coefficient, $R_r = \Delta_s/\Delta_{free\text{-}field}$ $R_r = \frac{4(1-\nu_m)F_{rec}}{3-4\nu_m+F_{rec}}$ for no-slip interface condition (Wang, 1993; Penzien, 2000) $= \frac{4(1-\nu_m)F_{rec}}{2.5-3\nu_m+F_{rec}}$ for full-slip interface condition (Penzien, 2000)
Step 5	Determine the racking deformation of the tunnel, $\Delta_s = R_r\ \Delta_{free\text{-}field}$
Step 6	Obtain the seismic demand in terms of internal forces (and material strains) by imposing Δ_s in a frame analysis
Step 7**	For effects of vertical seismic motions, apply a vertical pseudo-static loading equivalent to the product of the vertical seismic coefficient and the combined dead and design overburden loads for the effects of vertical seismic motions.
Step 8	Combine seismic demands due to racking deformations and vertical seismic motions with non-seismic loads using appropriate load combinations (recommended load factor of 1.0)

* H = height of the box structure
G_m = Effective strain-compatible shear modulus of ground surrounding tunnel (ksf)
τ_{max} = Maximum earthquake-induced shear stress (ksf)
σ_v = Total vertical soil overburden pressure at invert elevation of tunnel (ksf)
γ_t = Total soil unit weight (kcf)
h = Soil cover thickness measured from ground surface to tunnel crown (ft)
D = Height of tunnel (ft)
R_d = Depth dependent stress reduction factor; Rd = 1.0 – 0.00233z for z < 30 ft, 1.174-0.00814z for 30 ft < z < 75 ft; z = depth (ft) from ground surface to the invert elevation of the tunnel and is represented by z = $(h+D)$
V_S = peak particle velocity
C_{se} = effective shear wave propagation velocity

** The vertical seismic coefficient can be reasonably assumed to 2/3 of the design peak horizontal acceleration divided by the gravity

Table 2-3: Load and load designation for the design of cut-and-cover tunnels (AASHTO 2010)

Symbol	Definition
• Permanent Loads	
DD	Downdrag
DC	Dead load of structural components and nonstructural attachments
DW	Dead load of wearing surfaces and utilities
EH	Horizontal earth pressure load
EL	Accumulated locked-in force effects resulting from the construction process, including the secondary forces from post-tensioning
ES	Earth surcharge load
EV	Vertical pressure from dead load of earth fill
• Transient loads	
BR	Vehicular braking force
CE	Vehicular centrifugal force
CR	Creep
CT	Vehicular collision force
CV	Vessel collision force
EQ*	Earthquake
FR	Friction
IC	Ice load
IM	Vehicular dynamic load allowance
LL	Vehicular live load
LS	Live load surcharge
PL	Pedestrian live load
SE	Settlement
SH	Shrinkage
TG	Temperature gradient
TU	Uniform temperature
WA	Water load and stream pressure
WL	Wind on live load
WS	Wind load on structure

* This load should be applied to the tunnel lining as appropriate for the seismic zone for the tunnel. Chapter 12 of the FHWA (2009) provides recommendations.

Table 2-4: Cut-and-cover tunnel LRFD load combinations (FHWA 2009)

Load Comb. Limit State	DC		DW		EH* EV#		ES		EL	LL IM	WA	TU CR SH		TG
	Max	Min	Max	Min	Max	Min	Max	Min				Max	Min	
Strength I	1.25	0.90	1.50	0.65	1.35	0.90	1.50	0.75	1.00	1.75	1.00	1.20	0.50	0.00
Strength II	1.25	0.90	1.50	0.65	1.35	0.90	1.50	0.75	1.00	1.35	1.00	1.20	0.50	0.00
Strength III	1.25	0.90	1.50	0.65	1.35	0.90	1.50	0.75	1.00	0.00	1.00	1.20	0.50	0.00
Service I	1.00		1.00		1.00		1.00		1.00	1.00	1.00	1.20	1.00	0.50
Service IV	1.00		1.00		1.00		1.00		1.00	0.00	1.00	1.20	1.00	1.00
Service IVA**	0.00		0.90		0.90		0.90		0.00	0.00	1.00	0.00	0.00	0.00
Extreme Event I	1.25	0.90	1.50	0.65	1.35	0.90	1.50	0.75	γEQ^{+}	1.00	N/A	N/A	N/A	N/A

*The load factors shown are for at-rest earth pressure. At-rest earth pressure should be used for all conditions of design of cut-and-cover tunnel structure. Horizontal earth pressure is not used for Load Combination Service IVA.
The load factors shown are for rigid frames. All cut-and-cover tunnel structures are considered rigid frames.
+ This load factor is determined on a project specific basis and is not in the scope of the FHWA.
** This load case used to check buoyancy for tunnel structures below the permanent groundwater table.

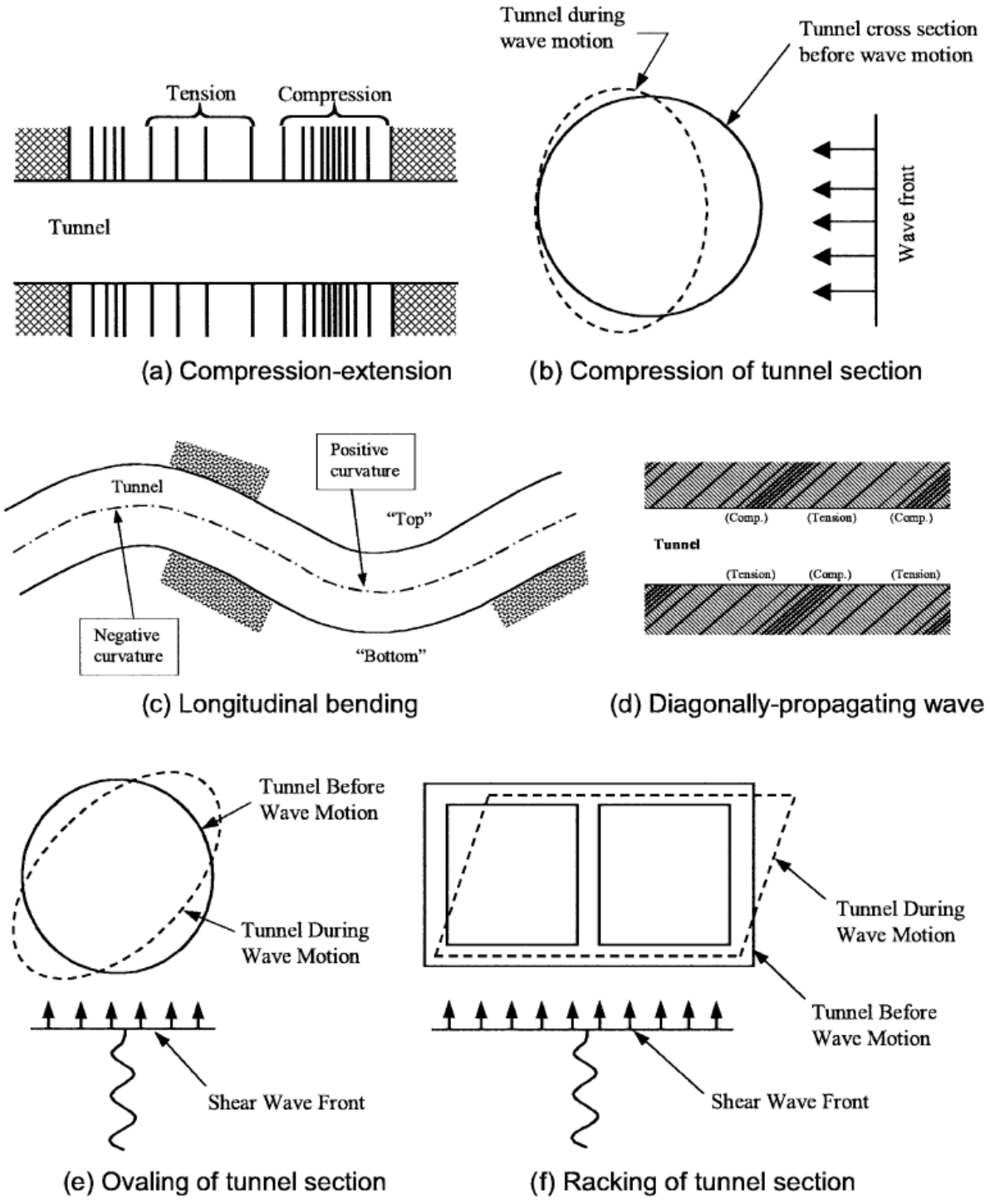

Figure 2-1: Deformation modes of tunnels due to seismic waves (after Owen and Scholl, 1981)

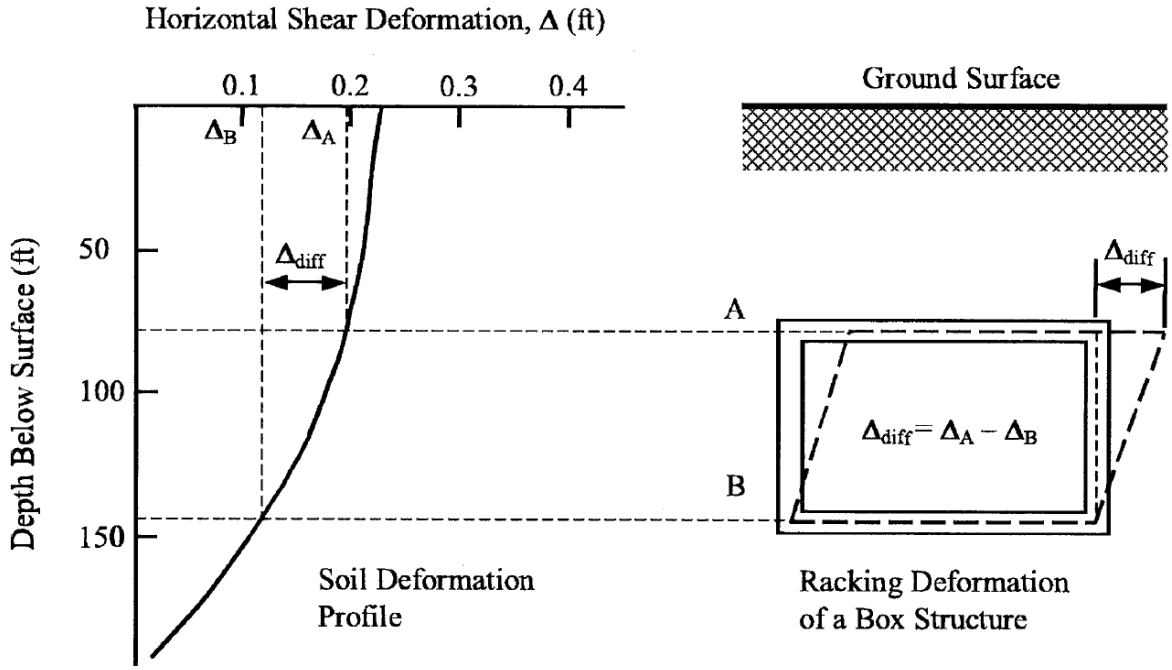

Figure 2-2: Typical free-field racking deformation imposed on a buried rectangular frame (after Wang, 1993)

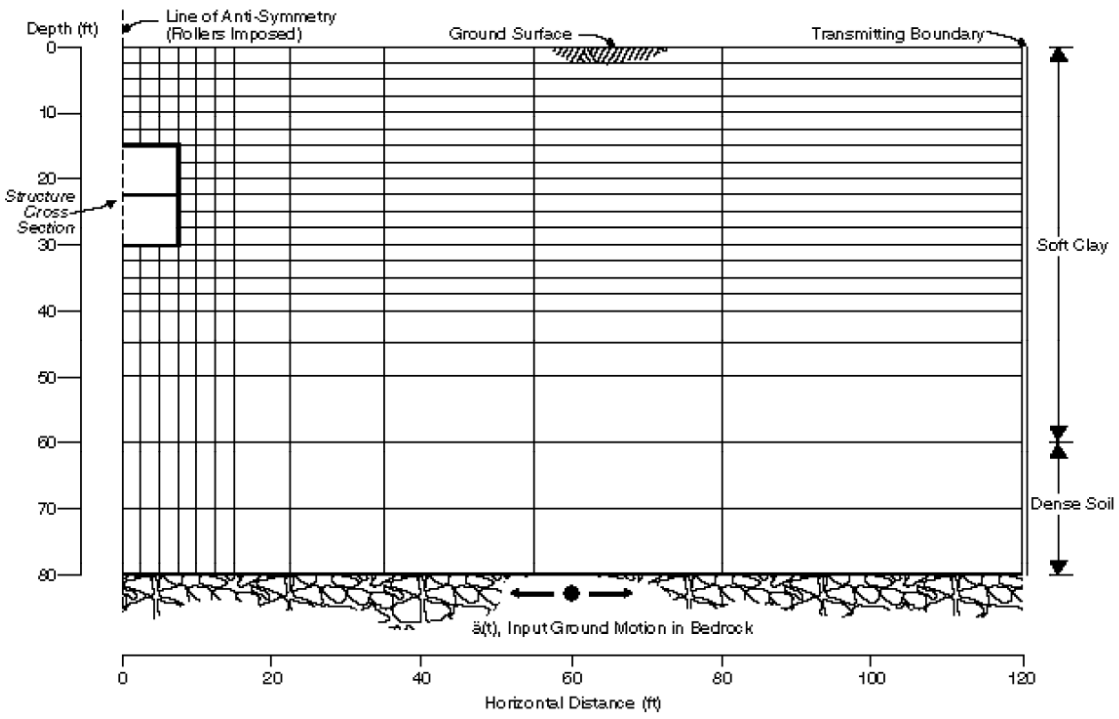

Figure 2-3: Typical Finite Element Model conducted by Wang (1993)

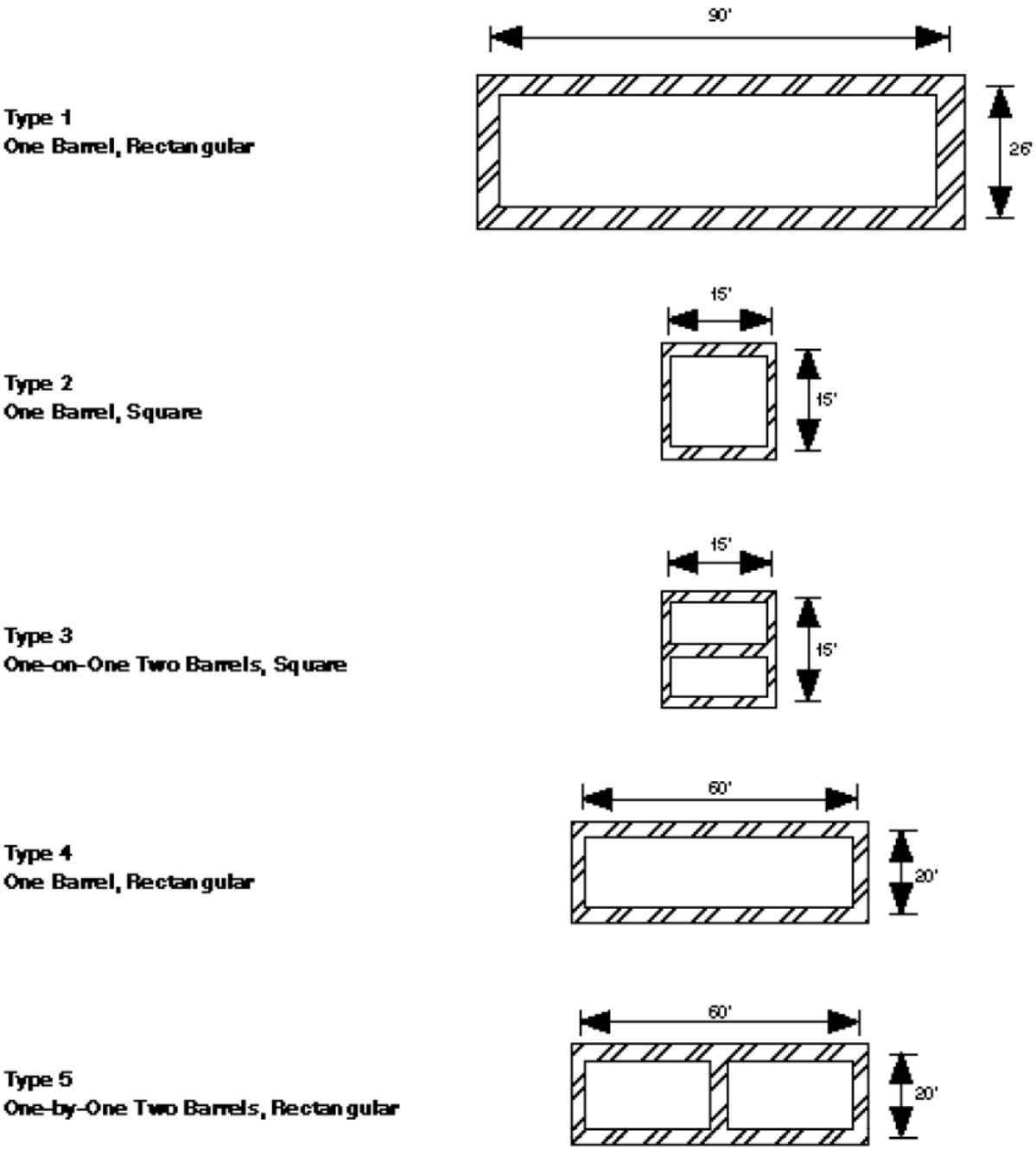

Figure 2-4: Types of structure geometry used in the Finite Element study conducted by Wang (1993)

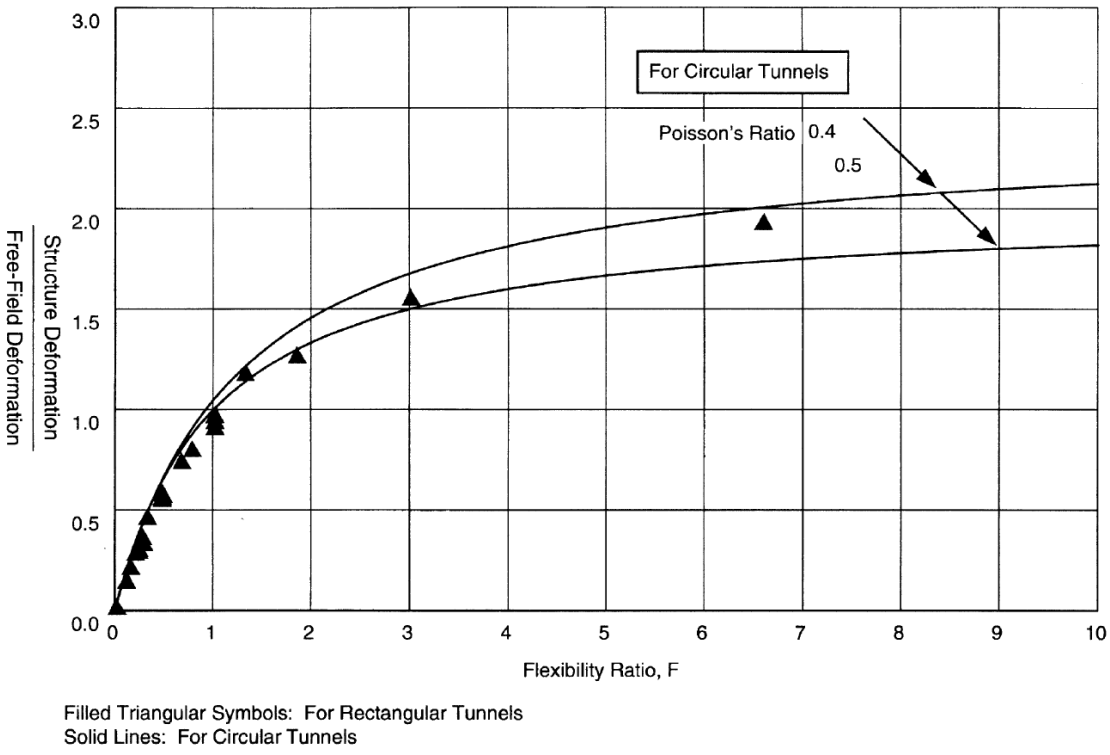

Figure 2-5: Normalized structure deflections from Finite Element analyses compared with closed form solution for a circular tunnel (Wang 1993)

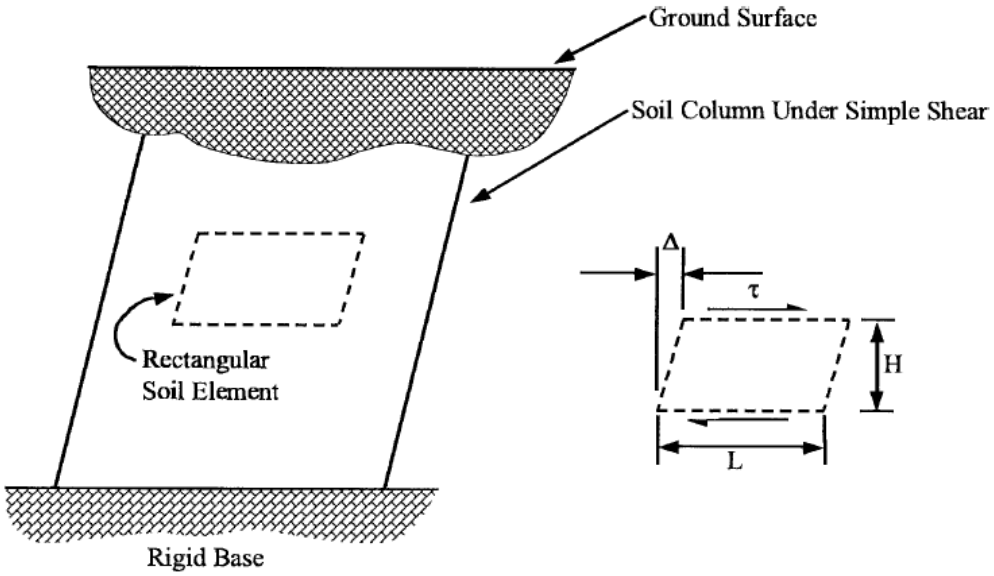

(a)

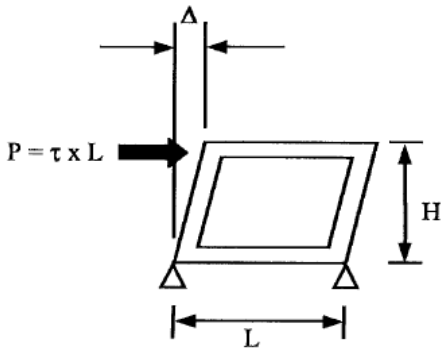

(b)

Figure 2-6: Relative stiffness between soil and a rectangular frame (after Wang, 1993): (a) flexural (shear) distortion of free-field soil medium; (b) flexural (racking) distortion of a rectangular frame

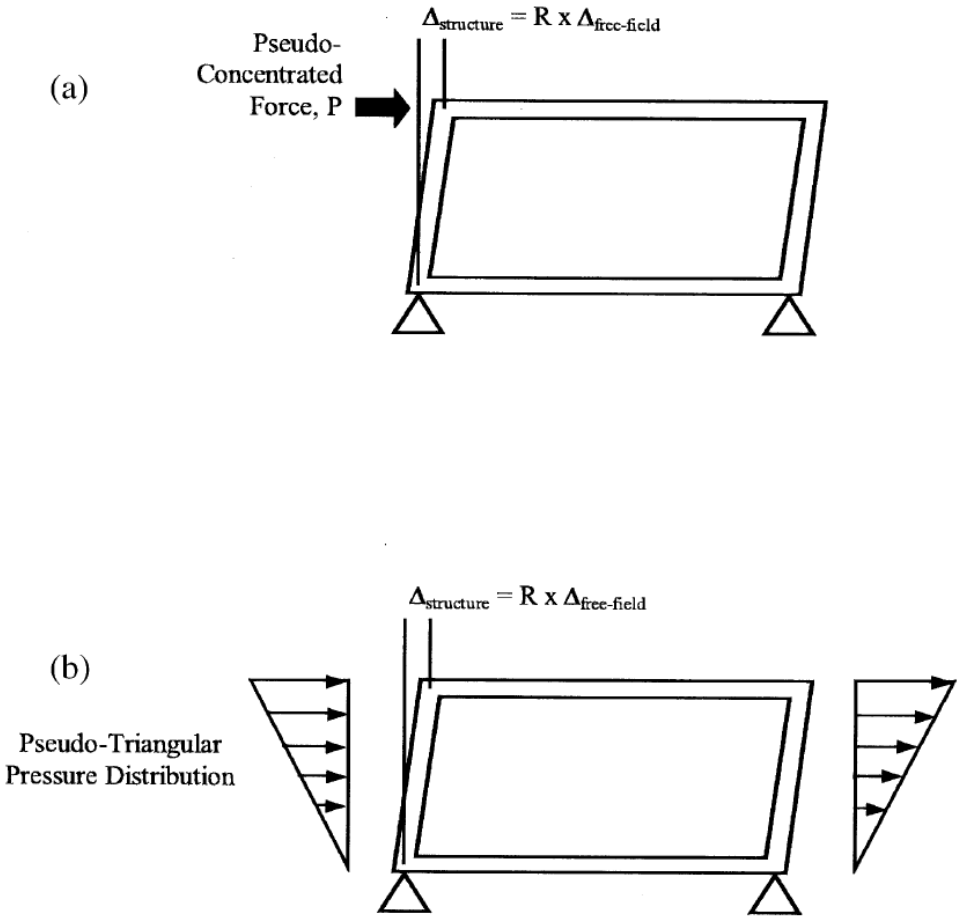

Figure 2-7: Simplified racking frame analysis (after Wang, 1993): (a) pseudo-concentrated force for deep tunnels; (b) pseudo-triangular pressure distribution for shallow tunnels

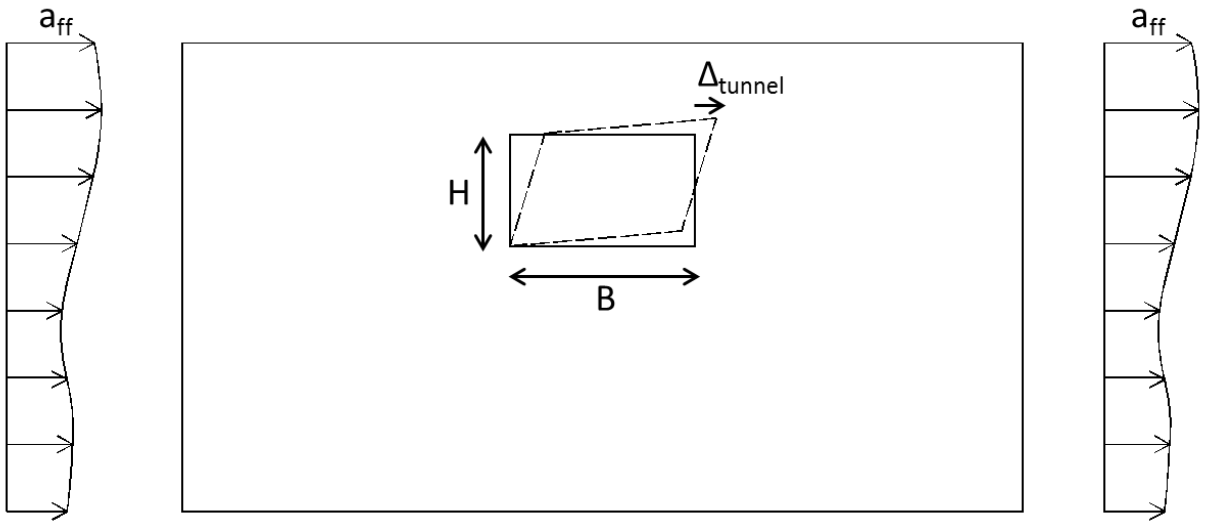

Figure 2-8: Schematic of the pseudo-static seismic coefficient deformation method (FHWA, 2009)

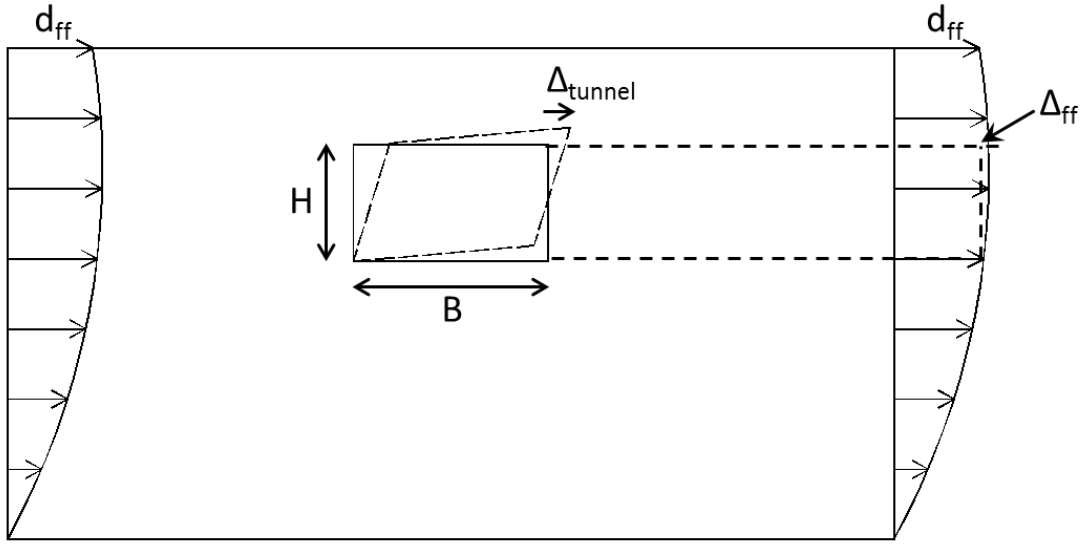

Figure 2-9: Schematic of the pseudo-dynamic time history analysis method (FHWA, 2009)

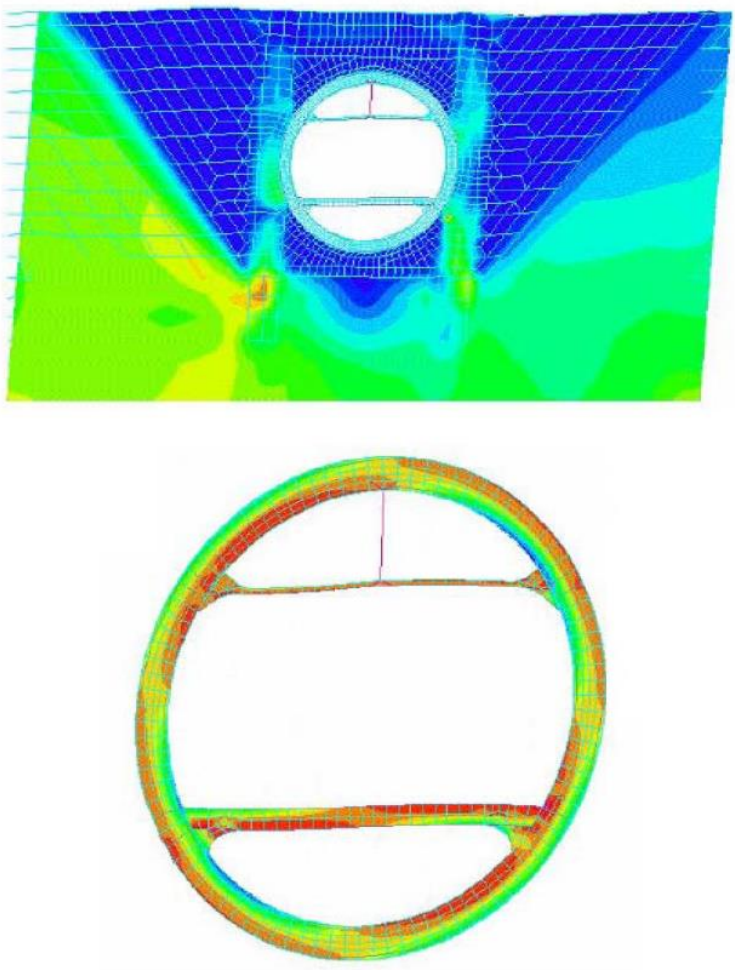

Figure 2-10: Example of the pseudo-dynamic displacement time history method (Shamsabadi et al. 2001; FHWA 2009)

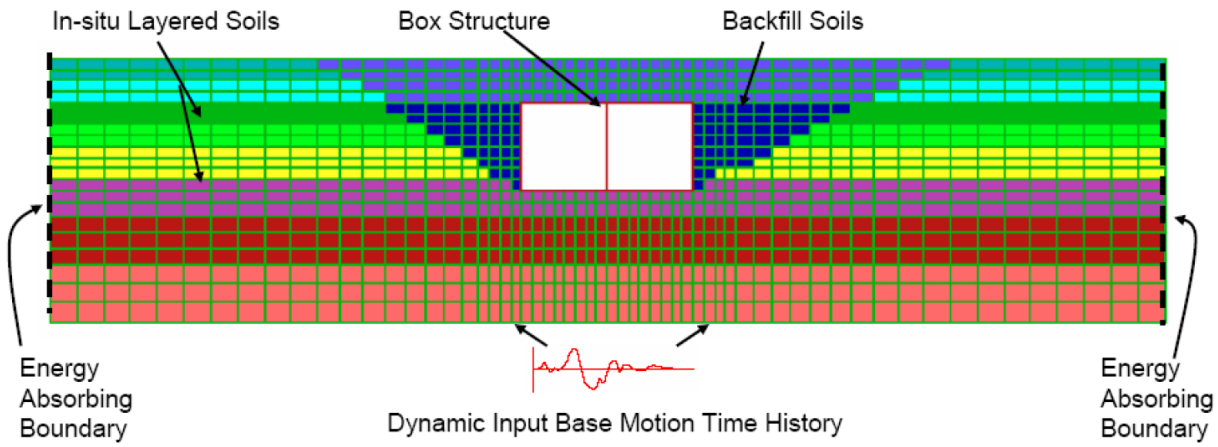

Figure 2-11: Sample of the dynamic time history analysis model (FHWA, 2009)

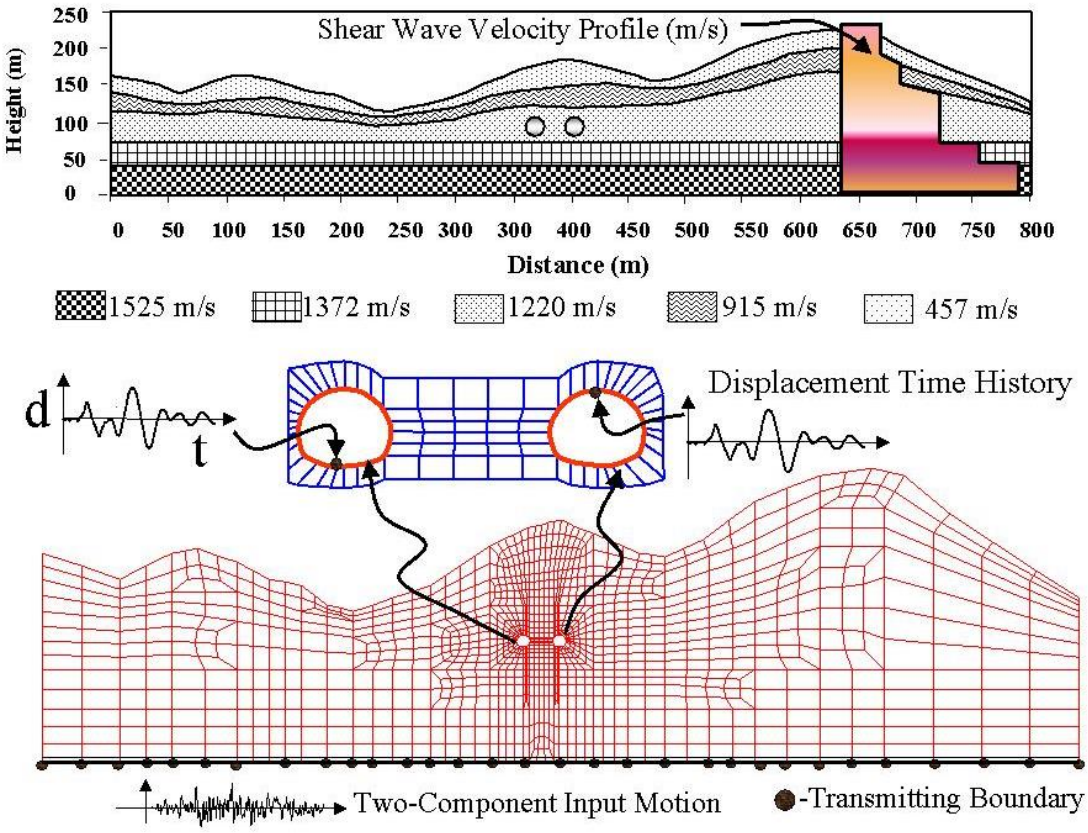

(a)

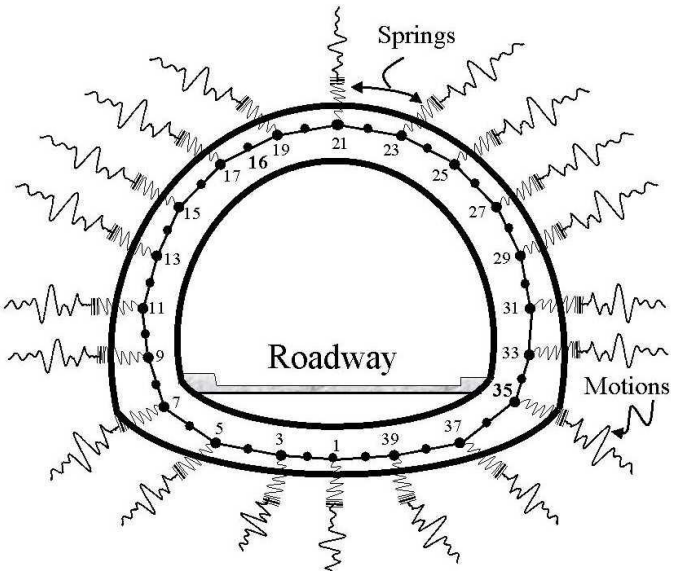

(b)

Figure 2-12: Numerical model of the two-step procedure; (a) mesh for wave scattering analysis and (b) structural analysis through springs for interaction between tunnel liner and surrounding medium (Shamsabadi et al. 2014)

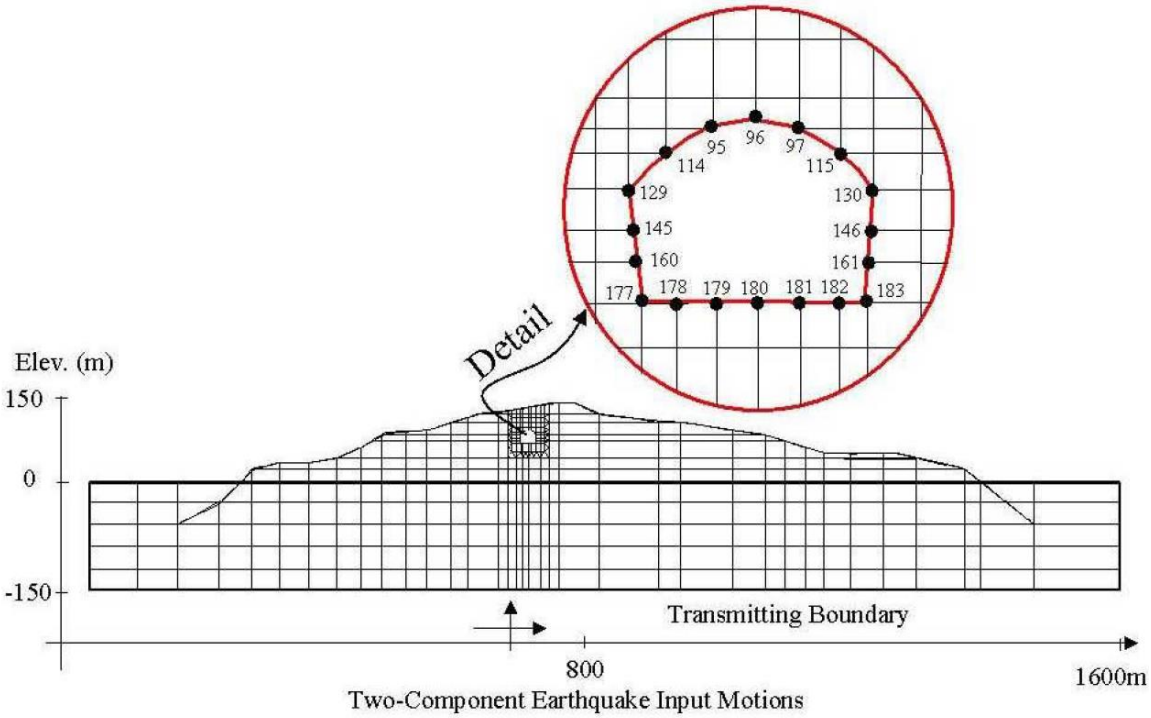

(a)

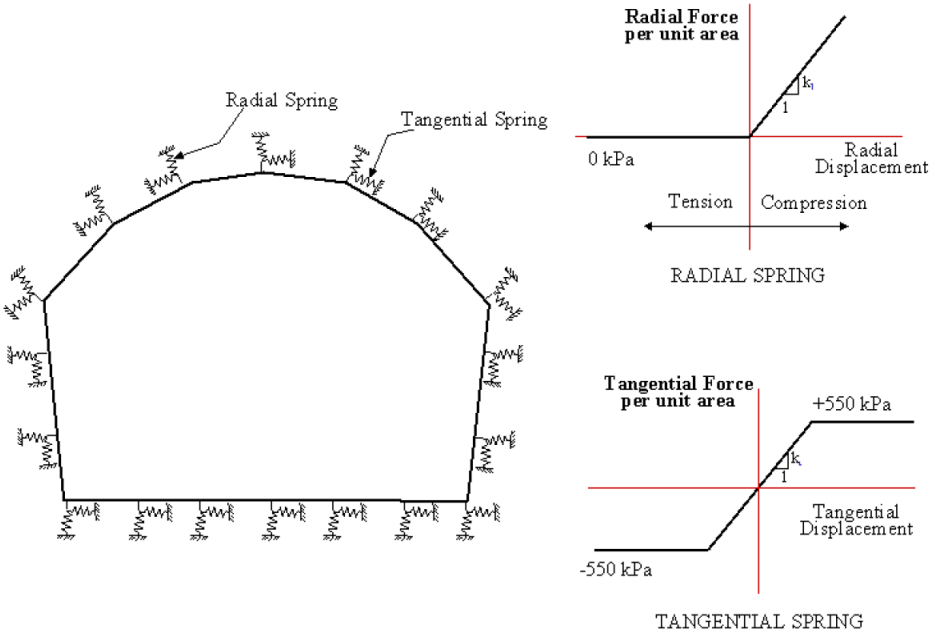

(b)

Figure 2-13: Numerical model of the two-step procedure for the Yerba Buena Island Tunnel; (a) mesh for wave scattering analysis and (b) structural analysis through springs for interaction between tunnel liner and surrounding medium (Shamsabadi et al. 2014)

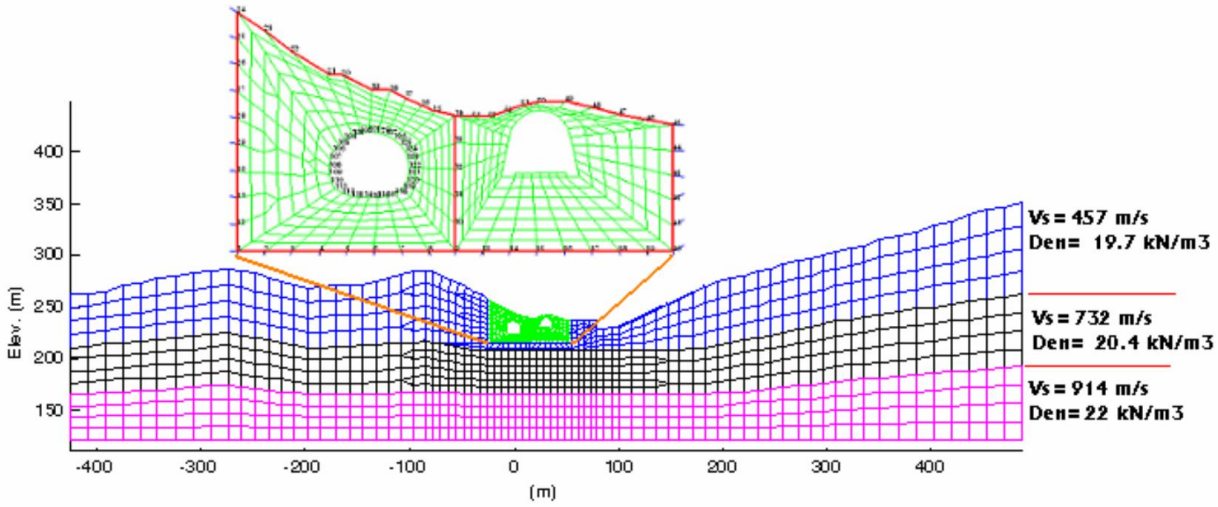

(a)

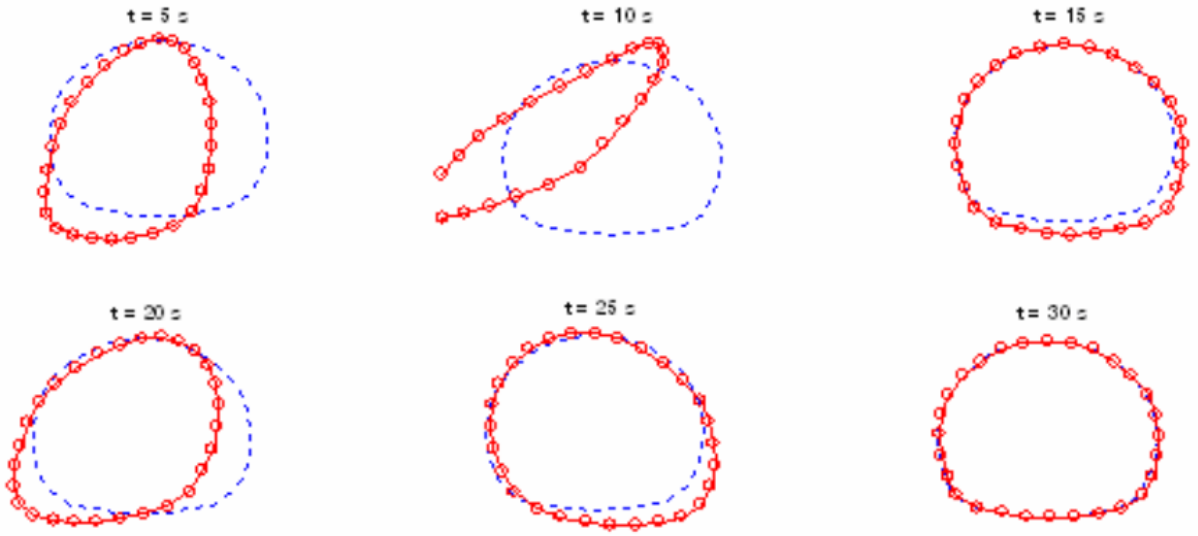

(b)

Figure 2-14: Numerical model of the Caldecott Tunnel; (a) Finite Element mesh for transverse cross-section and (b) snapshot deformation of bored tunnel liner (Yang et al. 2008)

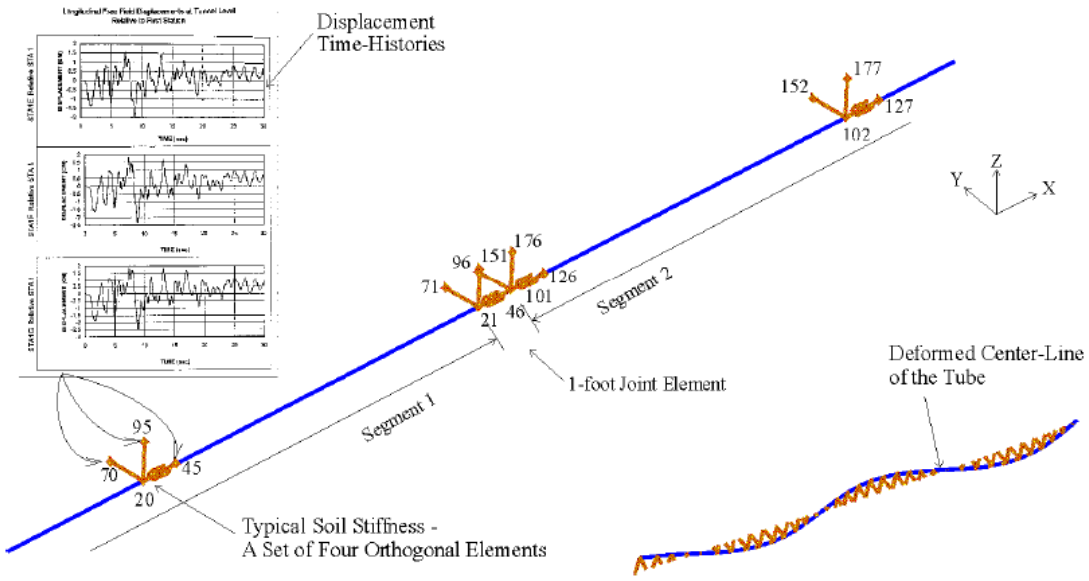

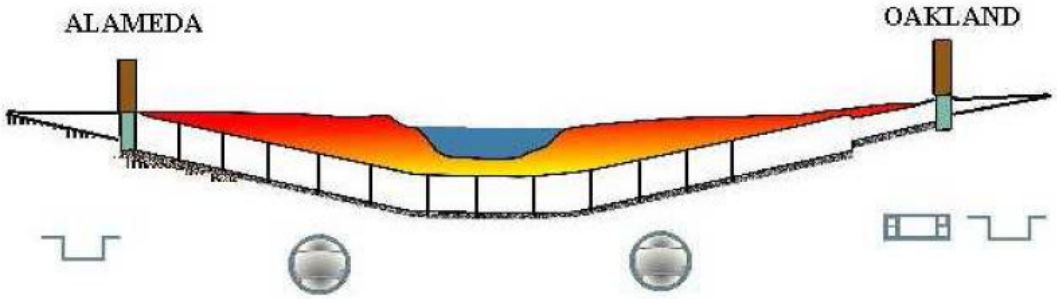

(a)

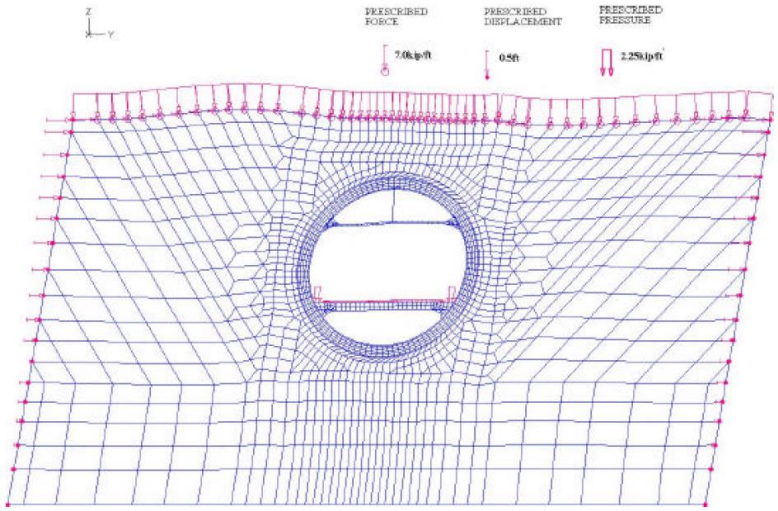

(b)

Figure 2-15: Numerical model for seismic retrofit of the Posey-Webster Tunnels; (a) three dimensional global modeling of soil-structure interaction and (b) two-dimensional local racking analysis model (Shamsabadi et al. 2001)

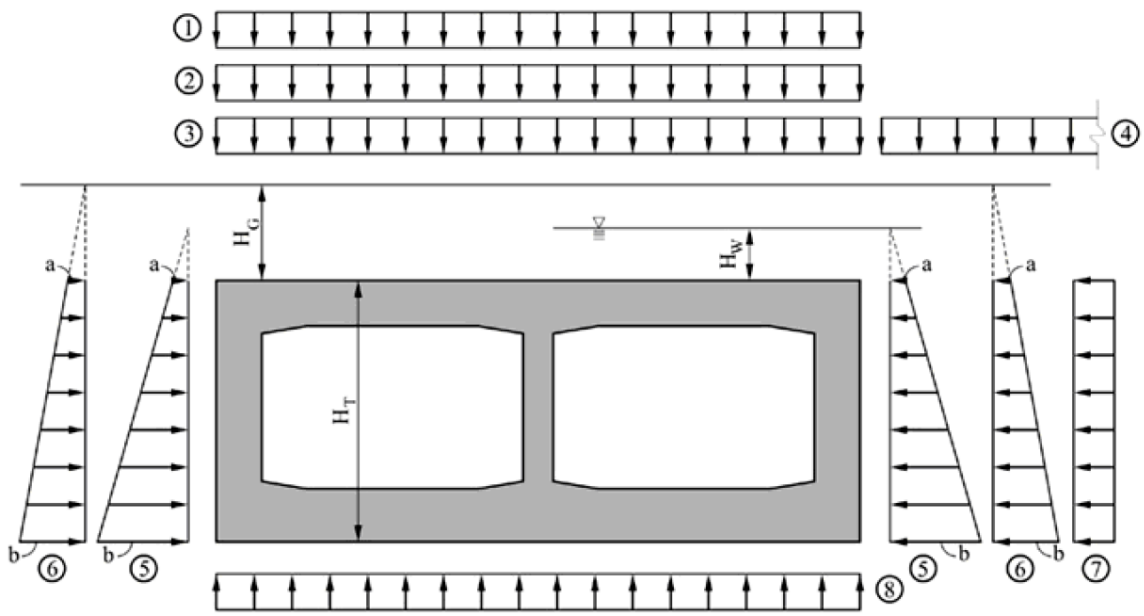

① - Live Load – determined as per site conditions & AASHTO LRFD specifications
② - Vertical Earth Load = $\gamma_S(H_G-H_W) + \gamma_{Sb}(H_W)$
③ - Vertical Hydrostatic Pressure = $\gamma_W H_W$
④ - Vertical Surcharge Load – determined as per site conditions (F_S)
⑤ - Horizontal Hydrostatic Load: a = $\gamma_W H_W$ b = $\gamma_W(H_W+H_T)$
⑥ - Horizontal Earth Load: a = $\gamma_S R_O(H_G-H_W) + \gamma_{Sb} R_O H_W$ b = a + $\gamma_{Sb} R_O H_T$
⑦ - Horizontal Surcharge Load = $F_S R_O$
⑧ - Vertical Hydrostatic Load (Buoyancy) = $\gamma_W(H_W+H_T)$

where: γ_S = dry unit weight of soil
γ_{Sb} = buoyant unit weight of soil
H_G = height of backfill over the tunnel
H_W = height of water table over the tunnel
H_T = height of the tunnel structure
R_O = at rest lateral earth pressure coefficient
F_S = magnitude of surcharge in units of Force/Area

Figure 2-16: Cut and cover tunnel loading diagram – Bottom up construction in soil (FHWA 2009)

3. Experimental study: cyclic response of 1/3 scale RC tunnel model

3.1 Scope of study

Documentation of the actual stiffness and strength response characteristics of an actual tunnel liner segment is of value for future soil-structure experimental and computational studies. For that purpose, it was feasible to build and test a 1/3 scale reinforced concrete (RC) tunnel segment under quasi-static cyclic lateral loading in the Powell Structural Systems Laboratory at UCSD. Details of this effort included below.

3.1.1 Prototype structure

The tunnel model configuration was based on the as-built drawings of the Doyle Drive Battery Tunnel (Caltrans 2012). The tunnel cross-sectional shape was in the form of box or frame with a slightly arched roof as opposed to a typical cut-and-cover tunnel (Figure 3-1b).

The idealized section of the prototype Doyle Drive tunnel section is approximately 55 feet wide by 33 feet tall at the peak, sloping down to 30 feet at the side walls. Figure 3-2 shows the geometry of a representative section of the original tunnel. The corresponding idealized model was created for this test (Figure 3-3). The as-built drawings are presented in Appendix A.

3.1.2 Determination of specimen scaled geometry

The model was chosen to be built at 1/3rd scale. There were several considerations that went into that decision. First, physical space for the test was available in the south Powell laboratory. This meant that the maximum tunnel model width could be as much as twenty five feet. This constraint set the largest scale factor that could be used at 1/3rd. The second consideration was that the smallest readily available reinforcing bar was #3 rebar. Since, it was not possible to locate any ribbed rebar smaller than the #3 bar; it would not have been possible to build a scale reinforced concrete model any smaller. This is why it was deemed necessary to build and test the 1/3rd scale model. On this basis, the actual elastic stiffness and ultimate capacity of the structure can be determined.

Table 3-1 summarizes the scaling laws applied to the tunnel model. The overall dimensions of the model were scaled down to the 1/3rd size of the prototype with a cross sectional width of 18.2 ft and height of 9.9 ft at the wall (Figure 3-4). The effective story height

(measurement between roof/wall and slab/wall) was 6.8 ft. After scaling, the geometry of the structure was evaluated to determine cost and feasibility of construction. It is noted that the geometry of the original tunnel base (slab) would be difficult and expensive to construct while also not adding much significance to the structural response. Thus, the inverted tunnel base was slightly modified to be straight (Figure 3-5). The dimension determined to be critical, the effective story height, wall thicknesses, width, height, and arch radii, were all maintained.

3.1.3 Determination of reinforcement scaling

The rebar layout and spacing was designed to follow as closely as possible the rebar layout of the typical tunnel cross-section of the Doyle Drive tunnel specified on the as-built drawings provided by Caltrans (Figure 3-2). All efforts were made to maintain an equivalent steel to concrete ratio and keep the rebar spacing as equivalent as possible. Due to the scaling by 1/3rd, bar sizes were not able to be exactly scaled. For example, a #5 bar (spaced at 6 in with a diameter of 0.625 in) would ideally be scaled to a bar of diameter 0.208 in spaced at 2 in. Due to limitations in possible rebar sizes, the smallest bar that could be acquired was a #2 unribbed bar with a diameter of 0.250 in. The lack of ribbing posed several issues but the ability of the concrete to appropriately adhere to the steel ensured that the full strength of the steel can be developed, instead of the bond failing before the steel yields. This problem prevented the use of the unribbed bars in any fashion other than as ties. Table 3-2 shows the conversions from full scale to $1/3^{rd}$ scale for all the rebar sizes in the specimen.

3.2 Specimen dimensions, reinforcement details, and materials

3.2.1 Specimen dimensions

Figure 3-6 shows overall dimensions of the 1/3 scale model cross section. The wall thickness was 10 in and the slab thickness was 16 in. For the arched roof, thickness ranged from 10 in at the center to 16 in at the wall interfaces. The model length of 5 ft was determined by the available size and number of actuators producing the total force applied to the structure less than or equal to 150 kips. A full set of design plans can be seen in Appendix B.

3.2.2 Reinforcement details

The final reinforcement layout consisted of 18 layers of the rebar along length of the tunnel (Figure 3-7). For the primary longitudinal reinforcement in the walls, #4 bars spaced at 3.25 in were used. The #4 bars were also used in the reinforcement of the roof, and although not necessary, the lap splice detail in the roof of the prototype was maintained in the model. The #3 bars were used for the transverse reinforcement (Figure 3-6). A smooth 0.25 in bar was used to simulate the #2 bar and was only used as ties throughout the structure.

3.2.3 Material properties

Concrete with a specified compressive strength of 4.0 ksi at 28 days, a slump of 3.5 inches, and a maximum aggregate size of 3/8 in was used for the tunnel base. For the walls and the roof, concrete with a specified compressive strength of 4.0 ksi at 28 days, a slump of 5 inches, and a maximum aggregate size of 3/8 in was used. The specimens were tested after the concrete strength in the base, walls and roof had reached 4.0 ksi. Table 3-3 presents the actual strengths of the concrete measured on the days of the structural tests. All the deformed reinforcing bars (to improve bonding) were Grade 60 complying with the ASTM A706 standards. The smooth reinforcing bar (due to the limitation in possible rebar sizes) was A36 steel (ASTM A36 standards).

Table 3-4 presents results from material tests on the steel reinforcement.

3.3 Construction

Pictures of construction of the specimen are presented in Appendix C. The specimen was built by RTD Construction (RTD) with the aid of a steel work subcontractor, O.M. Reinforcing, and under the general supervision of the lab staff. A total of 120 strain gauges were installed on the rebar. Once all the strain gauges were applied and tested, O.M. Reinforcing tied together the rebar cage for the base of the structure and the vertical members in the walls. Minor spacing adjustments were made in the center of the base due to the addition of PVC pipes that needed to be in place in order to later connect the structure to the laboratory strong floor.

The specimen was casted in two stages. The first stage was the pour of the 16 in thick base. The upper inner surface (what would have been the roadway) was finished smooth. Then the walls and roof were poured two weeks later. Special attention was also given to the location

of the cold joint. After the first pour, some roughness was introduced to the cold joint by raking the wet concrete. Before the final pour, steel brushing was applied to the joint to partially expose the aggregates. The joint was cleaned of debris and dust, and wetted immediately before receiving the fresh concrete.

Erection of the form work to define the inner geometry of the tunnel was then performed by RTD. During this process, the proper radius for the inner roof arch was set. O.M. Reinforcing then returned to finish tying together the complete rebar cage. This operation proceeded slowly due to the small bar spacing and the high quantity of ties.

During construction of the rebar cage along the roof, the following issue arose; the geometry of the inside arch was well defined by the form work, but the problem stems from the fact that the same was not true for the top radius. Due to limitations in tie lengths, a smooth even curve was not possible to achieve for the rebar cage. When finally completed and adjusted, to the best of the abilities of the iron workers and the lab staff, large discrepancies where observed in the thickness of the potential concrete cover. A standard 1 in cover should have been produced if the rebar cage was built exactly to the design drawings. However, this was not achievable so that a cover ranging from 1 in at the center of the arch to up to 2.5 in at the intersection of the arch and walls was observed.

In the second stage, the concrete was poured in both walls and the roof at the same time. Before the final pour, steel brushing was applied to the joint to partially expose the aggregates. The joint was cleaned of debris/dust and wetted immediately before receiving the fresh concrete. A significant amount of water was added (but within manufacturers specifications) to increase the flow ability of the concrete. The structure was left to cure for one week before the form work was removed.

In order for the cyclic loading application, a loading frame was attached at a level of the top of the wall (Figure 3-8). Three actuators (total 150 kips loading capacity) were attached to the South fixture (Figure 3-8c). Four thread rods were added along the tunnel width (Figure 3-8a). These rods were intended to provide only compressional forces on the wall during the cyclic loading.

3.4 Instrumentation

The specimen was internally and externally instrumented to monitor the deformation during testing (see Appendix B for the instrumentation layout). The internal instrumentation consisted of electrical resistance strain gages attached to the longitudinal and transverse reinforcement. External instrumentation consisted of displacement transducers and inclinometers attached to the specimen to measure the lateral displacements and different deformations such as flexure deformation, shear deformation, base rotation, joint rotation, and sliding at the interfaces. Pictures of the instrumentation are shown in Appendix C.

The strain gages were placed at different elevations. In selected layers of longitudinal bars near the faces and centerline of the specimen, the strain gages monitored the strain distribution along these bars. The location of the strain gauges was also determined to measure the strains in the estimated plastic hinge regions (Appendix B).

The lateral displacement along the height of each wall was measured with horizontal displacement transducers mounted along two parallel lines on each of the North and South faces of specimen. These transducers primarily measured not only the horizontal displacement but also potential out of plane twisting of the structure. Vertical displacement transducers were mounted at the base of the walls to measure the base rotation uplift. In addition, transducers were mounted to measure potential sliding between the tunnel base with respect to the strong floor. Drawings on the exact locations of the displacement transducers are shown in Appendix B.

Inclinometers were placed at all member intersection (i.e. wall to roof, wall to slab). The gauges were mounted at the specified locations to measure rotation at the joints of the structure. Drawings on the exact locations of the inclinometers are shown in Appendix B.

3.5 Test setup and loading protocol

Simplified calculations were performed using a standard Whitney stress block procedure to determine the estimated maximum load that the structure would take before failing. The calculations were later verified using finite element software. From the calculations, it was determined that approximately a maximum of 120 kip of force would be necessary to fail the structure. As a consequence, three 50 kip actuators were chosen.

A loading frame was constructed using high strength steel I-beams and high strength rods. Drawings of the loading frame are shown in Appendix B. This system allowed the

actuators to load the structure only in a compressive manner, never directly placing a tension force onto the concrete. The specimen was fixed to the lab floor at 7 points using rods post-tensioned to a force of 100 kips each. It was estimated that the friction force created by the self-weight of the structure and the pretension force to exceed 150 kip. Figure 3-9 shows the layout of the experiment in the Lab.

The loading protocol can be seen in Figure 3-10 and Table 3-5. Since a critical objective of the test was to accurately capture the elastic stiffness of the structure, the protocol focused heavily on small incremental displacements at the beginning of the test and once the structure was likely in the inelastic region the displacement increments increased.

The structure was initially pushed by the actuators which defined North as the positive direction for the test. During the testing process, the specimen would be deformed by the actuator, as per the testing protocol instructed, and then the research team would mark the cracks in the concrete. Black marker was used when the specimen was deformed in the positive (North) direction and red marker was used when the specimen was deformed in the negative direction (South).

3.6 Experimental results

3.6.1 Load-displacement response

Figure 3-11 shows a relationship between the applied force and the lateral displacement measured at top of the walls (1/3 scale). At the top locations (North and South), an average of two measurements (e.g., L009 and L010 on the South wall shown in Appendix C) was plotted. The average displacement indicated that the north and south wall deflection varied slightly due to the flexure of the roof.

Figure 3-12 shows the corresponding relationship at prototype scale. The tunnel reached the peak displacement of 19.7 in. This peak displacement corresponded to a drift ratio of 8% (using the wall height of 20.5 ft). It was observed from strain gauge data that first yield of the rebar occurred at approximately 1% drift (see Appendix D). At this drift, the secant stiffness of the tunnel was determined to be 194 kip/ft per unit width of 1ft in the model scale (Figure 3-12). After the 7% drift ratio with the lateral load capacity of 65 kip/ft/ft, the tunnel exhibited slight load degradation under cyclic loading.

3.6.2 Lateral deformation of the wall

Figure 3-13 shows the measured lateral displacement from the transducers along the South wall at the peak displacements of the different cycles. Compared to the response along the North wall (Figure 3-14), the tunnel exhibited relatively symmetric behavior. Due to the most damage occurring at the roof/wall and base/wall, the lateral deformation essentially remained linear along the wall up to the peak drift ratio.

3.6.3 Flexural curvature

For curvature of the wall, roof, and base, Figure 3-15 shows the sign and naming conventions. At the interfaces (roof/wall and base/wall), Figure 3-16 and Figure 3-17 show the measured curvature from the strain gauge data. First, some of the noisy strain gauge data sets were removed from consideration. Then the data average over the maximum of 6 possible gauges at joints of the roof/wall and slab/wall where measurements were taken. The curvature was calculated by combining the strain average from each side of the rebar and dividing by the diameter of the rebar.

3.6.4 Damage evolution

During the test, a damage evolution is shown in Figure 3-18 through Figure 3-30. It can be seen from the force-displacement and the strain gauge data that first yield of the rebar occurred at approximately 1% drift (precisely 0.75%). At this drift ratio, the tunnel was mainly experiencing hairline cracks across the width of the walls (Figure 3-19). At the same time, the tunnel was starting to uplift. At 2% drift, the edges were uplifting about 1/8 in. Figure 3-20 shows the uplift at the southeast corner of the structure. At the drift ratio of approximately 3%, the force-displacement curve began to plateau. Figure 3-21 shows that the cracks had reached the full width of the tunnel specimen. Figure 3-23 shows significant flexural cracks of up to ¼ in at the 4% drift ratio. After one cycle at the 6% drift ratio, the concrete began to bulge, but did not yet spall (Figure 3-24). At the same drift ratio, the joint, the North wall, and the base cracked completely through the thickness of the wall (Figure 3-25 and Figure 3-26). At the 7% drift ratio, the structure began to decrease in capacity. The concrete spalled at both roof wall joints and the bars appeared to be buckled. Figure 3-27 shows the damage at the South wall. The last cycle went to the 8% drift ratio, during this cycle bars began to rupture (Figure 3-28).

3.7 Finite element analysis of the 1/3 scale tunnel

3.7.1 Finite element modeling of the 1/3 scale tunnel test

3.7.1.1 Structural model

A finite element (FE) model to simulate the lateral force-displacement behavior of the 1/3 scale RC tunnel is presented. A static FE analysis was performed using the OpenSees platform (McKenna 1997). Two different types of elements were employed (Figure 3-31). For the wall/roof connection and the wall/slab connection, elastic beam-column elements with rigid material properties were employed. For wall, slab, and roof, the nonlinear-force-based beam-column element was used (distributed plasticity with 5 Gauss-Lobatto integration points).

Based on original cross-sections and material properties of the tested tunnel specimen, fiber sections were assigned to the nonlinear (force-based) beam-column elements (Figure 3-32). In the fiber sections, constitutive relations for the concrete and steel reinforcement fibers were employed. Table 3-6 and Table 3-7 summarize the employed constitutive model parameters. For the concrete material, the uniaxial Kent-Scott-Park model with degraded linear unloading/reloading stiffness was used (i.e. Concrete02 in OpenSees). The reinforcing steel (longitudinal bars) was represented by a uniaxial Giuffre-Menegotto-Pinto model with isotropic strain hardening of 2% (i.e. Steel02 in OpenSees).

3.7.1.2 Boundary conditions

Zero length elements with a uniaxial material of "elastic-no-tension" were lined along the slab only in the normal direction. This uniaxial material (Figure 3-33) was to be allowed an uplift of the slab with a rigid material property for elasticity modulus in compression. Three locations in the middle (at the same locations in the test as shown in Figure 3-9) were fixed for all translations. As a consequence, no slip was allowed in the tangential direction.

3.7.2 Simulation results

3.7.2.1 Load-displacement response

As conducted in the test, the FE model was subjected to the same gravity load and displacement demands (Figure 3-10) at the top of the wall (south) as the test specimen. The FE

results provided a good match with the experimental load-displacement response (Figure 3-34). Table 3-8 summarizes the lateral load capacities obtained from the test and FE analysis. It was observed that the FE analysis overestimated the capacity by 6% (except of the last cycle) and by 9% (including the last cycle).

3.7.2.2 Strain in wall longitudinal reinforcement

Figure 3-35 shows a comparison of experimental and numerical strains versus the lateral loads for the longitudinal reinforcement in the south wall (see Appendix B for the locations). The FE model provided a good prediction for yielding in these bars. However, this model underestimated or overestimated the post-yield strain in the particular locations. This discrepancy could be contributed to the concrete model with no-tensile strength and modeling limitations such as simulating closing/opening of tensile cracks and bond-slip behavior in this model.

3.8 Summary

The behavior of the 1/3 scale reinforced concrete tunnel segment subjected to quasi-static cyclic loading was studied. This test was conducted to evaluate the lateral load capacity of the cut-and-cover tunnel adopted from the Doyle Drive Battery Tunnel. In addition, the large deformation response characteristics and permanent deformation patterns were addressed. During the application of the cyclic loading, the tunnel exhibited a maximum drift ratio of 8% (lateral displacement divided by the wall height). The first yield occurred at about 1% drift ratio with the secant stiffness of 582 kip/ft per unit length (1ft) in prototype scale. The load capacity increased as the drift ratio reached 7% with 200 kip per unit length (1 ft in prototype scale). After that, load degradation was observed and the longitudinal reinforcement began to rupture at 8% drift.

Based on the employed boundary condition, the middle of the slab was fixed to the strong floor (i.e. both ends can move upwards), most damage essentially evolved at the interface between the roof/wall and base (slab)/wall. Minor cracks were observed in the roof/slab. On the basis of the lateral displacement measured at the top of both walls, slight deformation developed in the roof (relatively minor and negligible).

Upon testing, the OpenSees FE model was calibrated. The model results matched well with the experimental force-displacement relationship. Thus, the employed cut-and-cover tunnel numerical model can be used to study soil-structure interaction (e.g., to investigate important

aspects of the tunnel layout/configuration such as embedment, overburden pressure, dynamic earth pressure, and so forth).

Table 3-1: Scaling factors for 1/3 scale model (Harris and Sabnis 2010)

Quantities	**Dimensions**	**Scale Factor**	**Value**
Geometry			
Linear dimension	L	S_l	3
Linear displacement	L	S_l	3
Area	L^2	S_l^2	9
Moment of inertia	L^4	S_l^4	81
Loading			
Concentrated load	F	S_l^2	9
Moment or Toque	FL	S_l^3	27
Shear force	F	S_l^2	9
Material-related properties			
Stress	FL^{-2}	S_E	1
Modulus of elasticity	FL^{-2}	S_E	1
Poisson's ratio	-	1	1
Specific weight	FL^{-3}	S_E/S_l	1/3
Strain	-	1	1

Table 3-2: Reinforcement Conversion Chart

Full Scale	**1/3 Scale**	**Type of Reinforcement**
#4 @ 8"	#2 @ 3.75"	Ties
#5 @ 6"	#3 @ 2.5"	Longitudinal
#5 @ 8"	#3 @ 3.75"	Longitudinal
#5 @ 6"	#2 @ 2.5"	Ties
#5 @ 8"	#2 @ 3.75"	Ties
#6 @ 12"	#3 @ 5"	Transverse
#9 @ 8"	#3 @ 2.75"	Longitudinal
#10 @ 8"	#4 @ 3.25"	Longitudinal

Table 3-3: Compressive Strength of Concrete

Test Time	**Region**	**Compressive Strength of Concrete (ksi)**
28 day	Base	4.513
28 day	Walls & Roof	4.325
Day of Test	Base	5.006
Day of Test	Walls & Roof	4.545

Table 3-4: Yield and Tensile Strength of Longitudinal Reinforcement

Bar Size	Yield Strength (ksi)	Tensile Strength (ksi)
#2	62.991	70.912
#3	62.085	69.856
#4	64.433	95.539

Table 3-5: Loading Protocol

Cycle Number	Drift ratio (%)	Displacement (inch)
1 – 2	0.25	0.21
3 – 4	0.50	0.41
5 - 6	0.75	0.62
7 – 8	1.0	0.82
9 – 10	1.5	1.23
11 – 12	2.0	1.64
13 - 14	2.5	2.05
15 – 16	3.0	2.46
17 – 18	3.5	2.87
19 – 20	4.0	3.28
21 – 22	5.0	4.10
23 - 24	6.0	4.92
25- 26	7.0	5.74
27 – 28	8.0	6.56

Table 3-6: Constitute model paramters for concrete material

Parameters	Walls	Roof/slab
Compressive strength, f_c'	4.55 ksi	5.01 ksi
Strain at compressive strength, ε_c	0.002	0.002
Crushing strength, f_{cu}	1.74 ksi	1.74 ksi
Strain at crushing strength, ε_{cu}	0.004	0.004

Table 3-7: Constitutive model paramters for reinforcement material

Parameters	Description	No. 3 bar	No. 4 bar
Fy	Yield strength	63.7 ksi	64.8 ksi
E	Initial elastic modulus	29000 ksi	29000 ksi
b	Strain-hardening ratio	0.02	0.02
R0	Coefficients for transition between elastic to plastic branches	18	18
cR1		0.925	0.925
cR2		0.1	0.1

Table 3-8: Maximum lateral load resistance

Experimental result (kips)	FE analysis result (kips)	FE prediction error
110.5	117.3	6% (excluding for the last cycle)
	120.3	9% (including the last cycle)

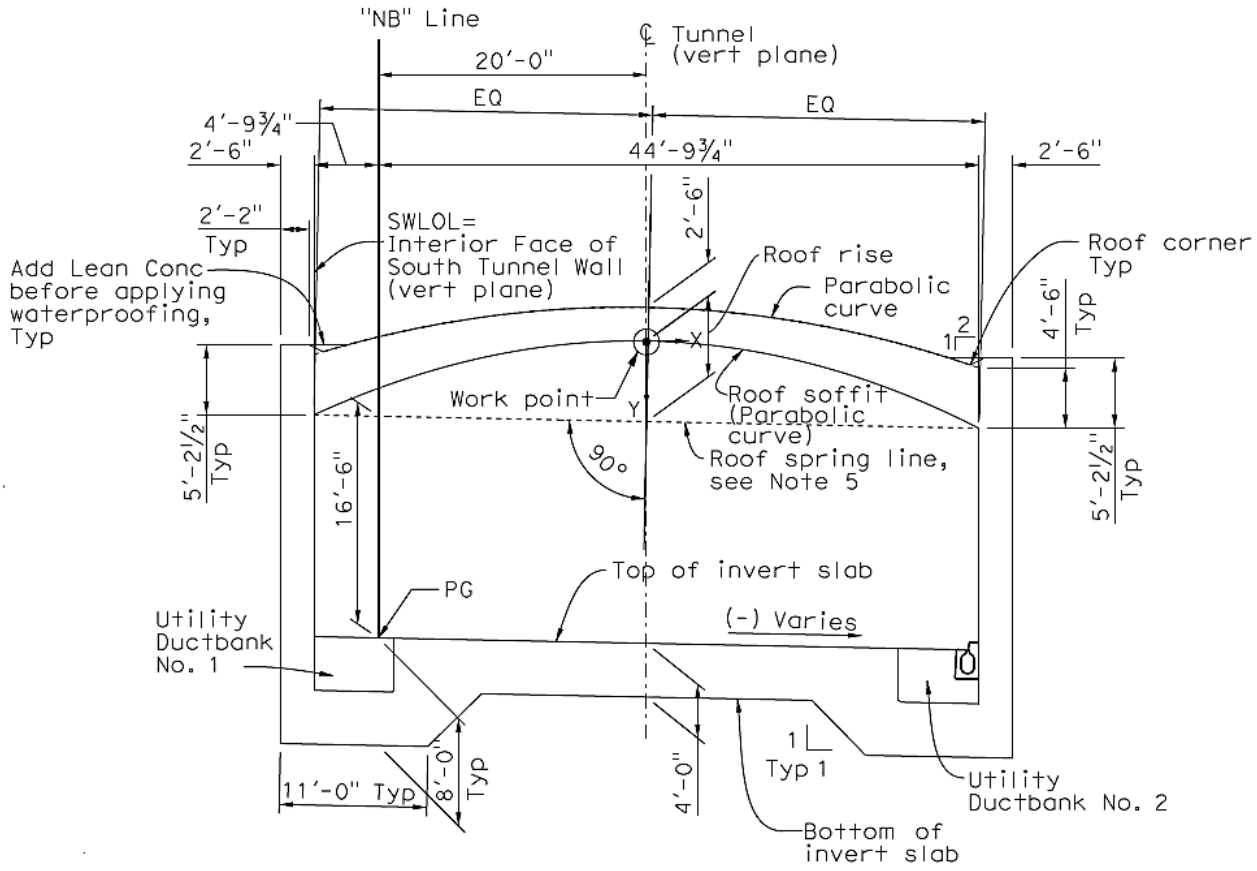

Figure 3-1: Configuration of the Doyle Drive Battery Tunnel cross-section

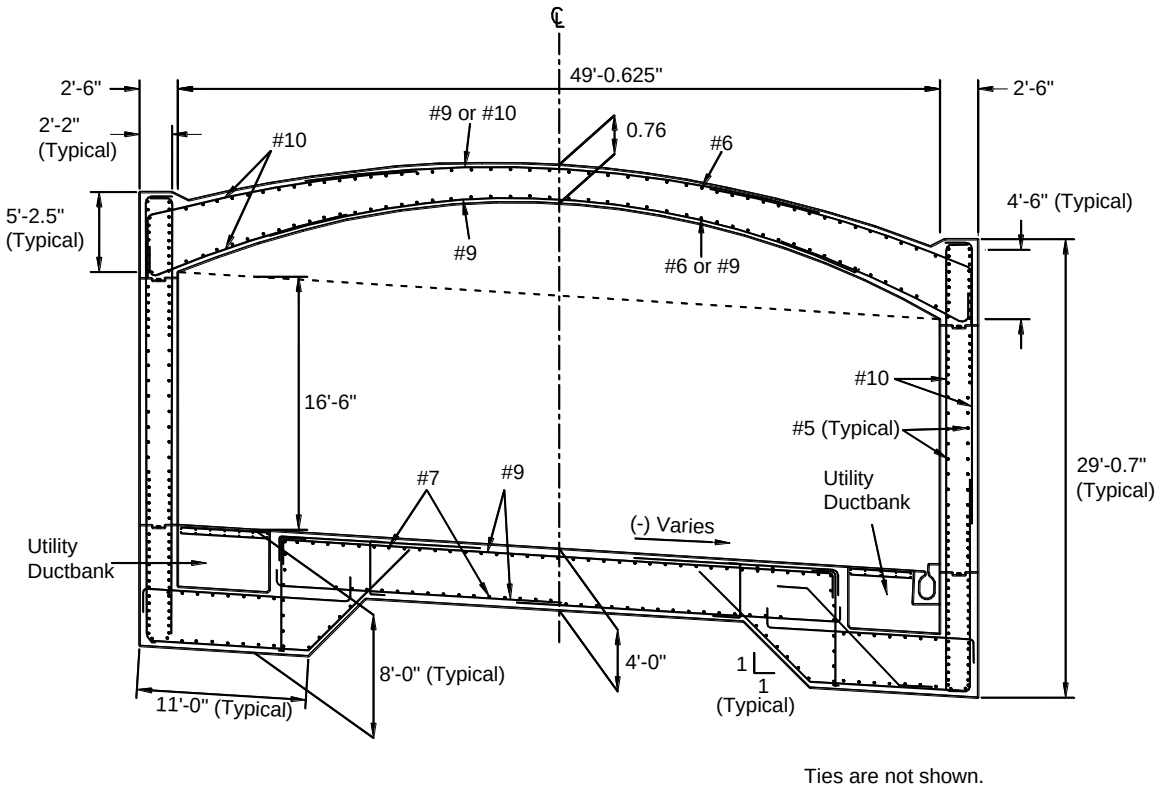

Figure 3-2: Typical cross-section of the Doyle Drive Battery Tunnel (Caltrans, 2012)

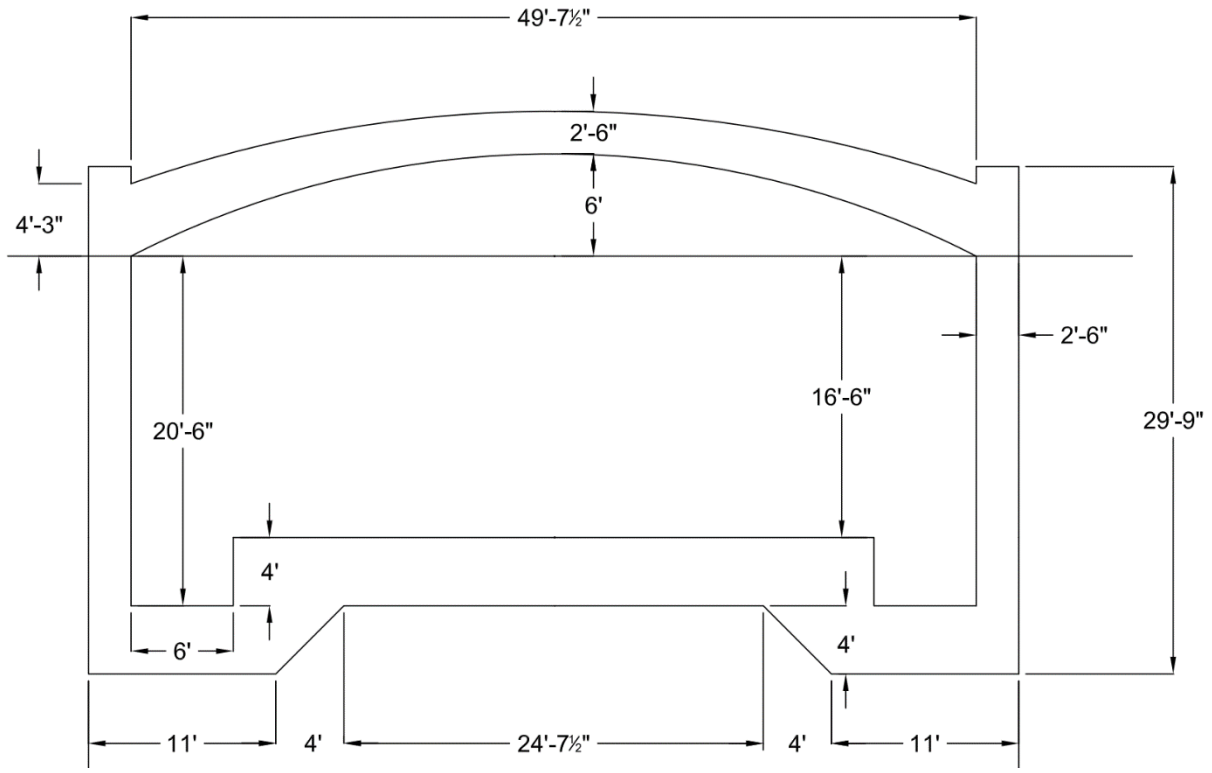

Figure 3-3: Equivalent unbanked full scale typical tunnel cross section

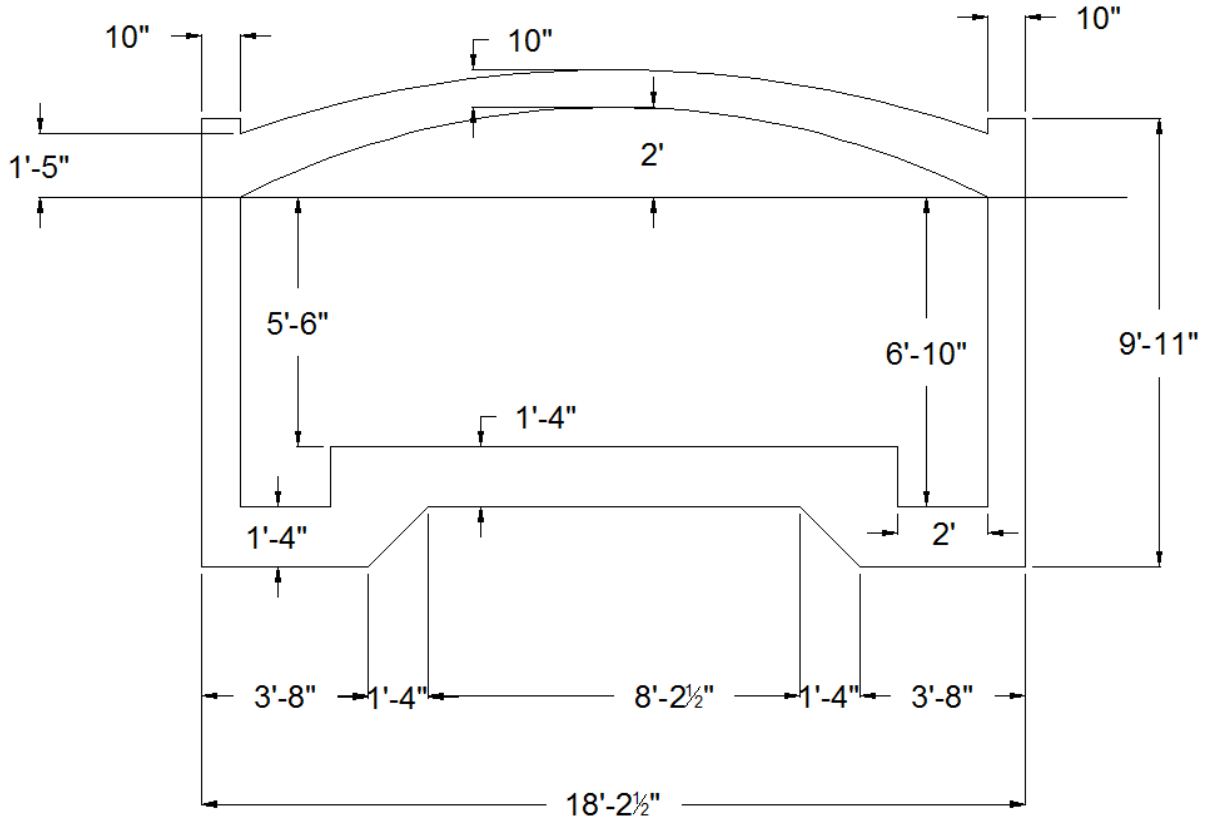

Figure 3-4: Scaled (1/3rd) cross section of the equivalent unbanked full scale tunnel

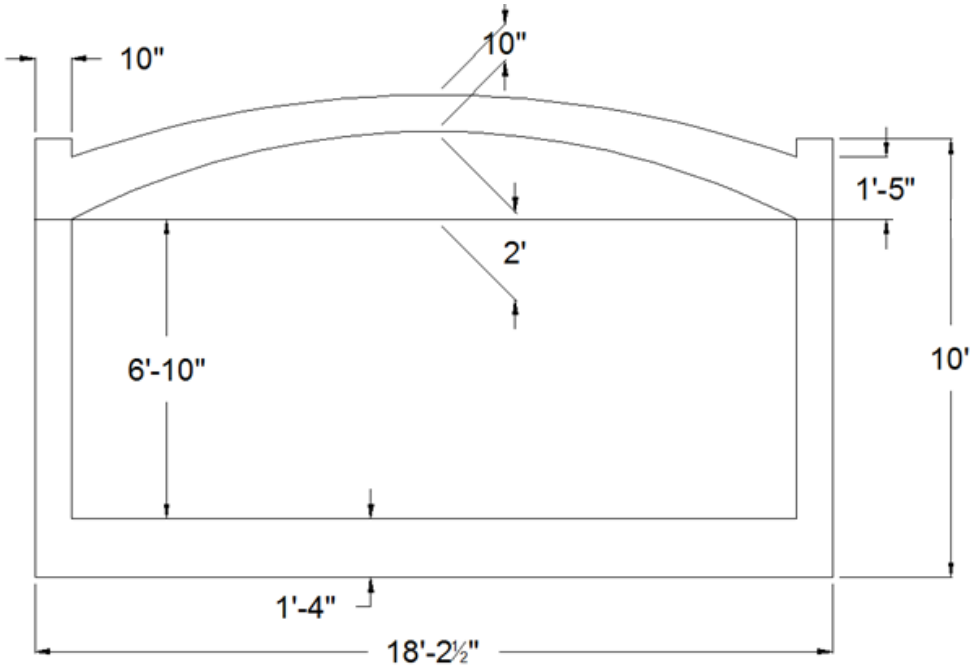

Figure 3-5: Cross section of the final specimen design (1/3 scale)

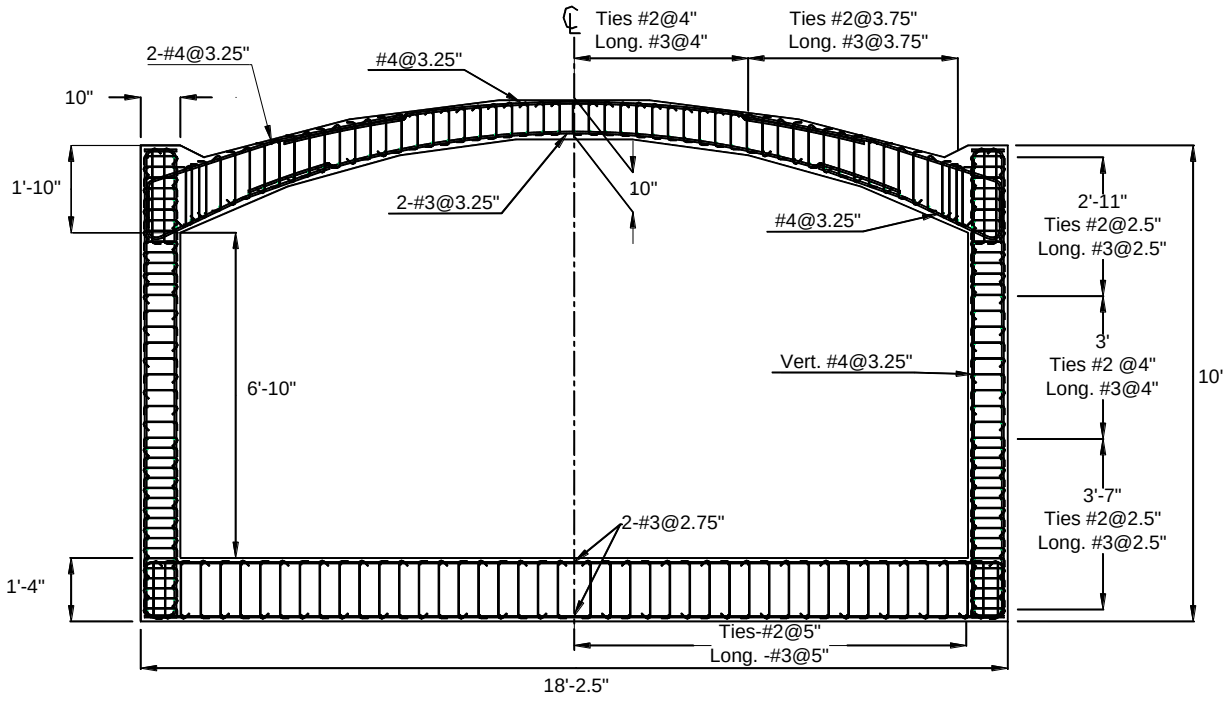

Figure 3-6: Typical reinforcement layout in the model specimen

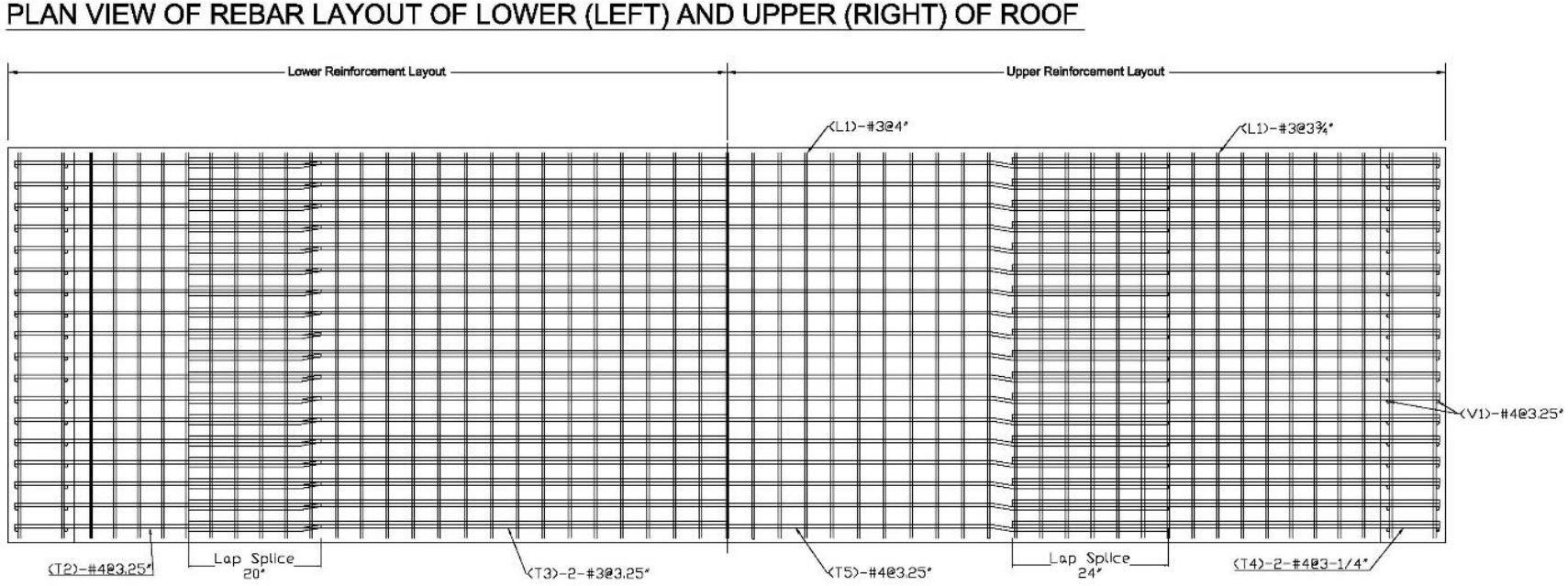

Figure 3-7: Plan view of rebar layout of lower (left) and upper

(a) Test setup

(b) Loading frame North-Top connection

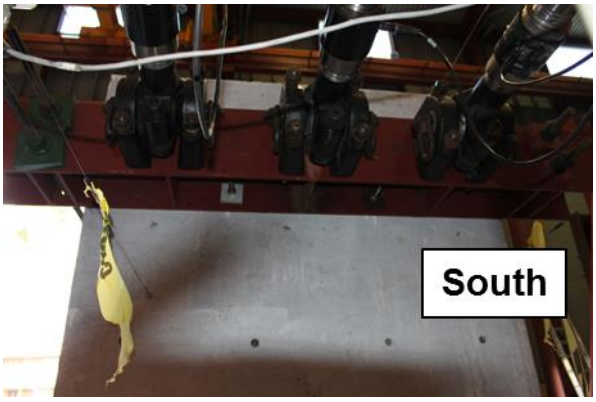

(c) Location of the actuators (South-Top)

Figure 3-8: Photograph of the test setup

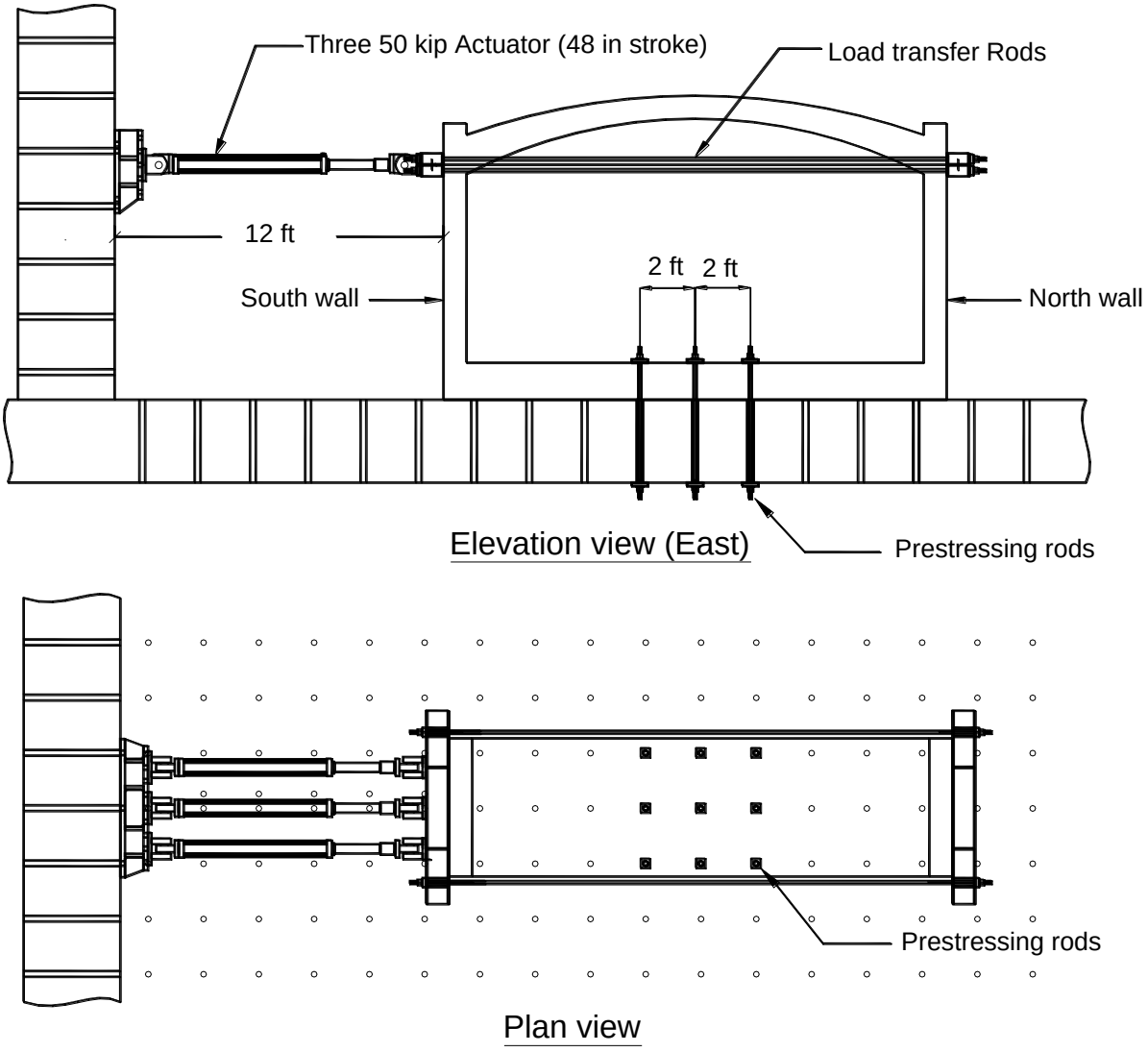

Figure 3-9: Elevation and plan view of test setup in the South Powell Lab

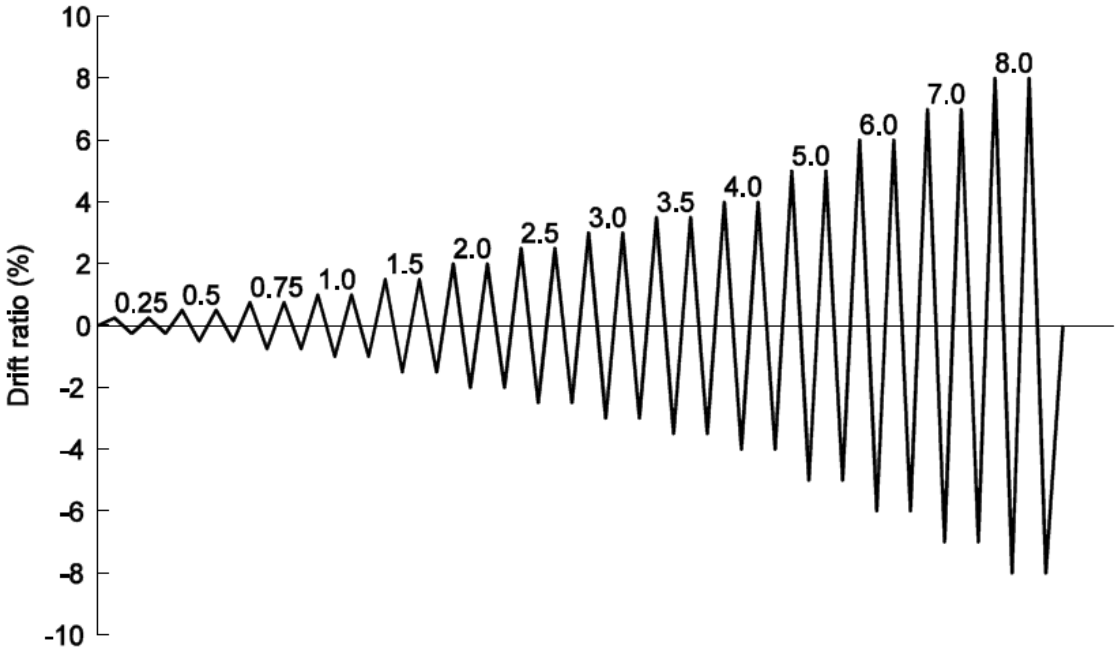

Figure 3-10: Graphical representation of loading protocol

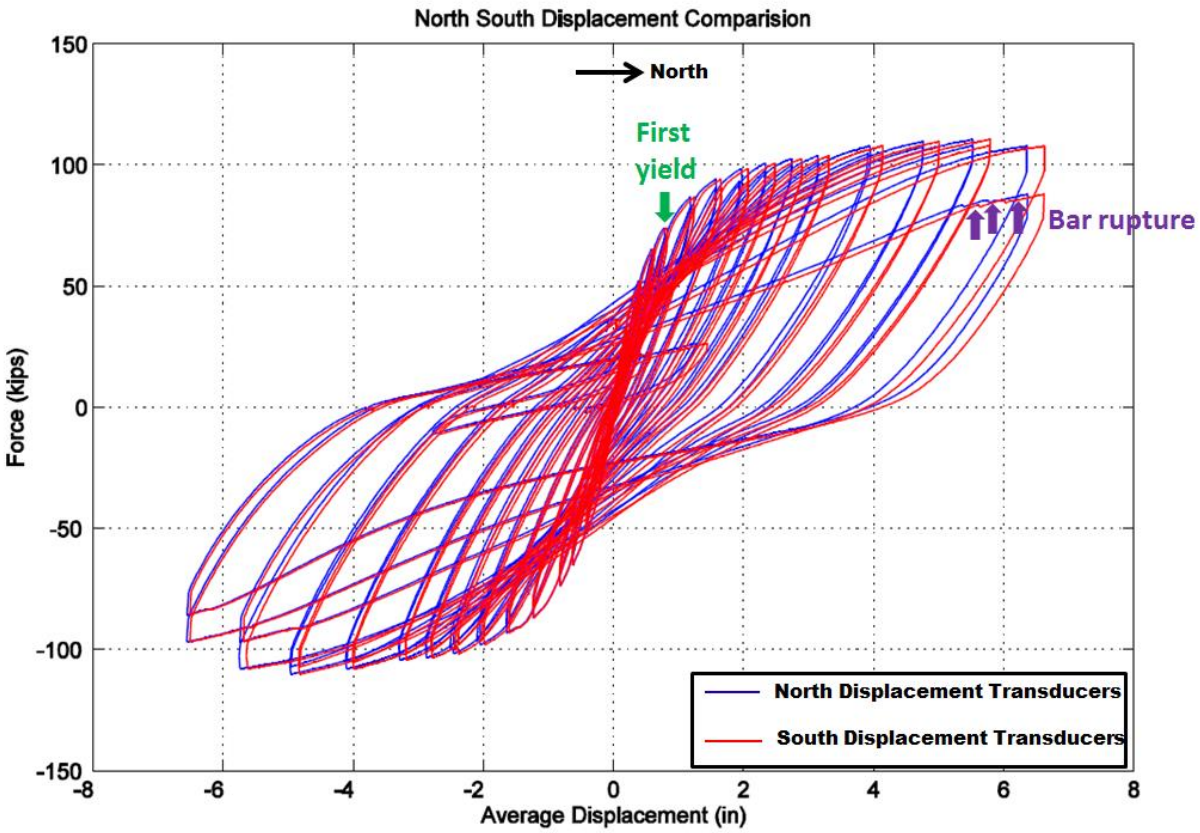

Figure 3-11: Force versus displacement diagram for both North and South walls

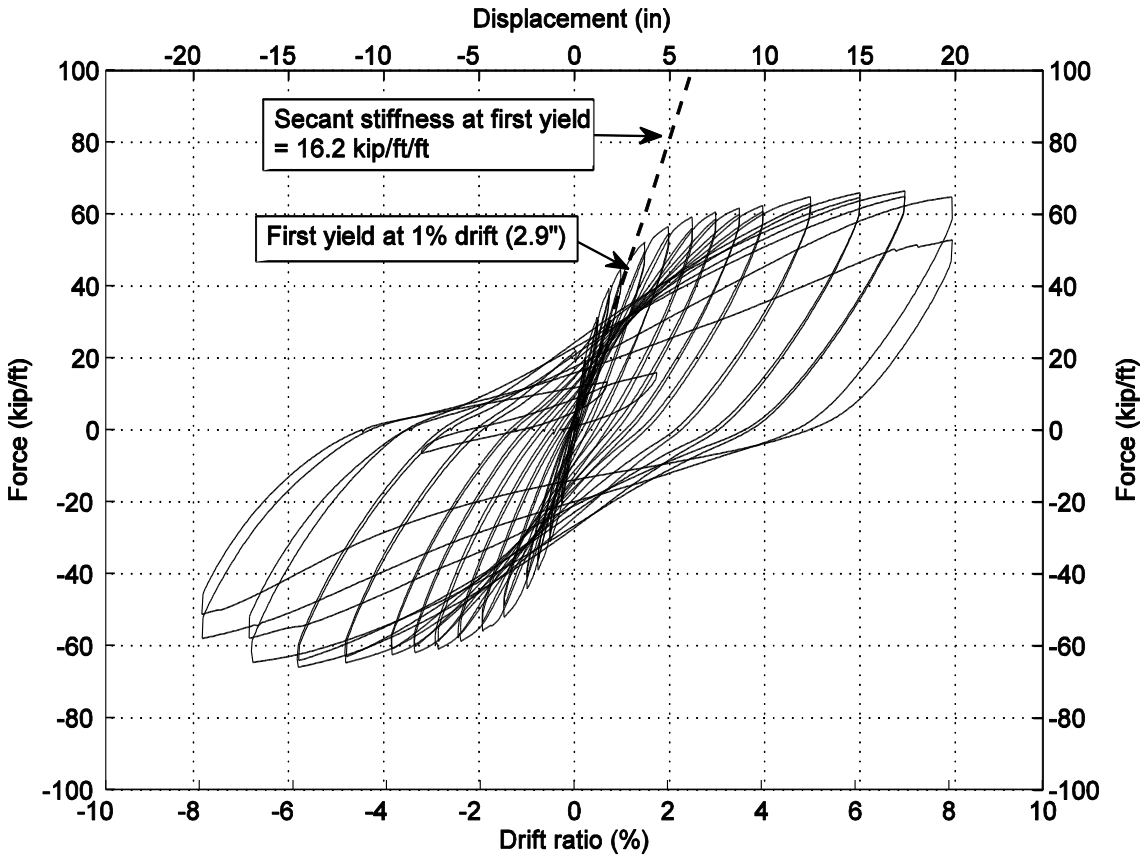

Figure 3-12: Force displacement graph showing secant stiffness at the first yield

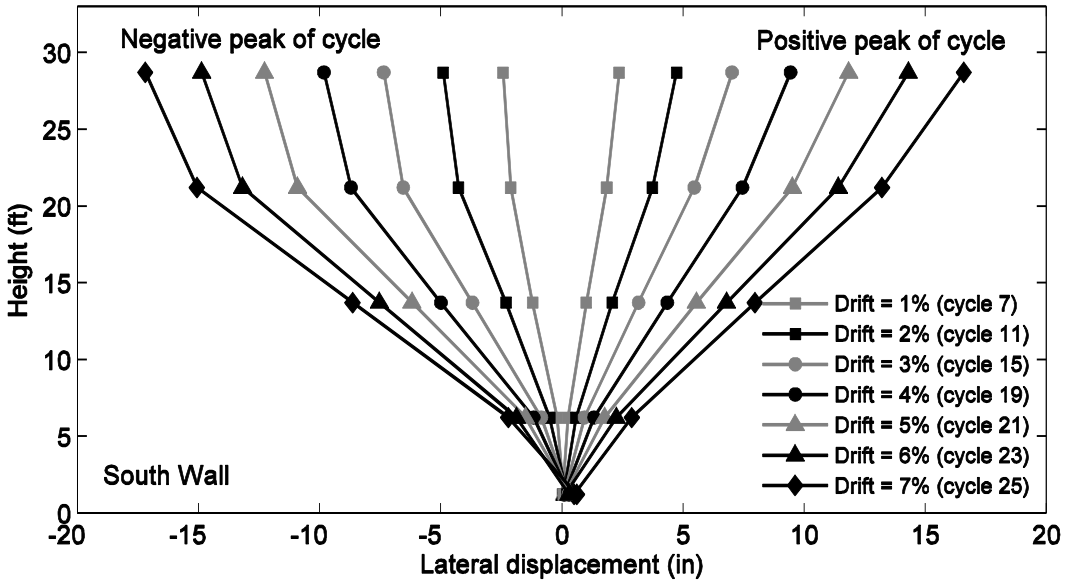

Figure 3-13: Lateral displacement along the South wall

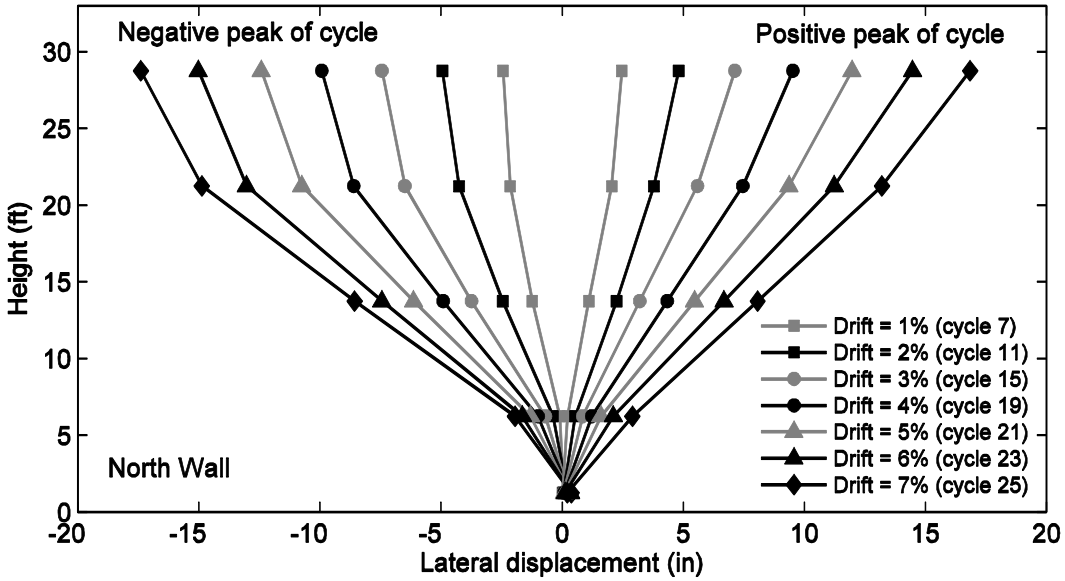

Figure 3-14: Lateral displacement along the North wall

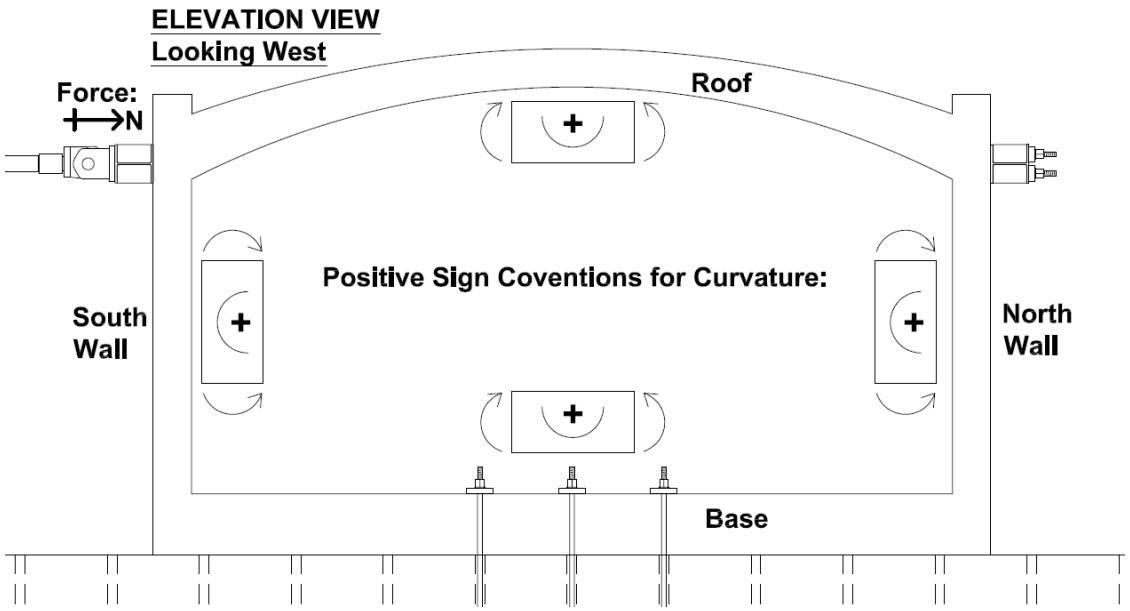

Figure 3-15: Sign convention and layout of curvature data

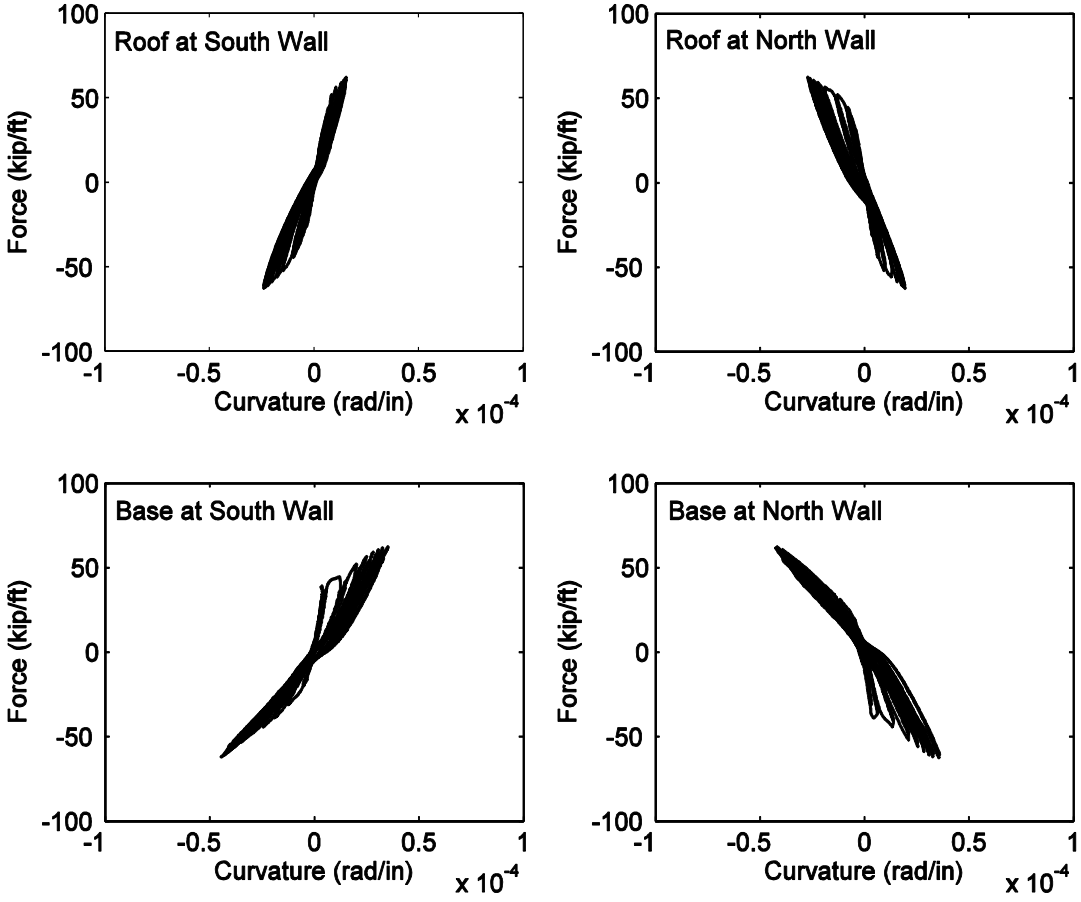

Figure 3-16: Comparison of curvature in the roof and the base at the joints

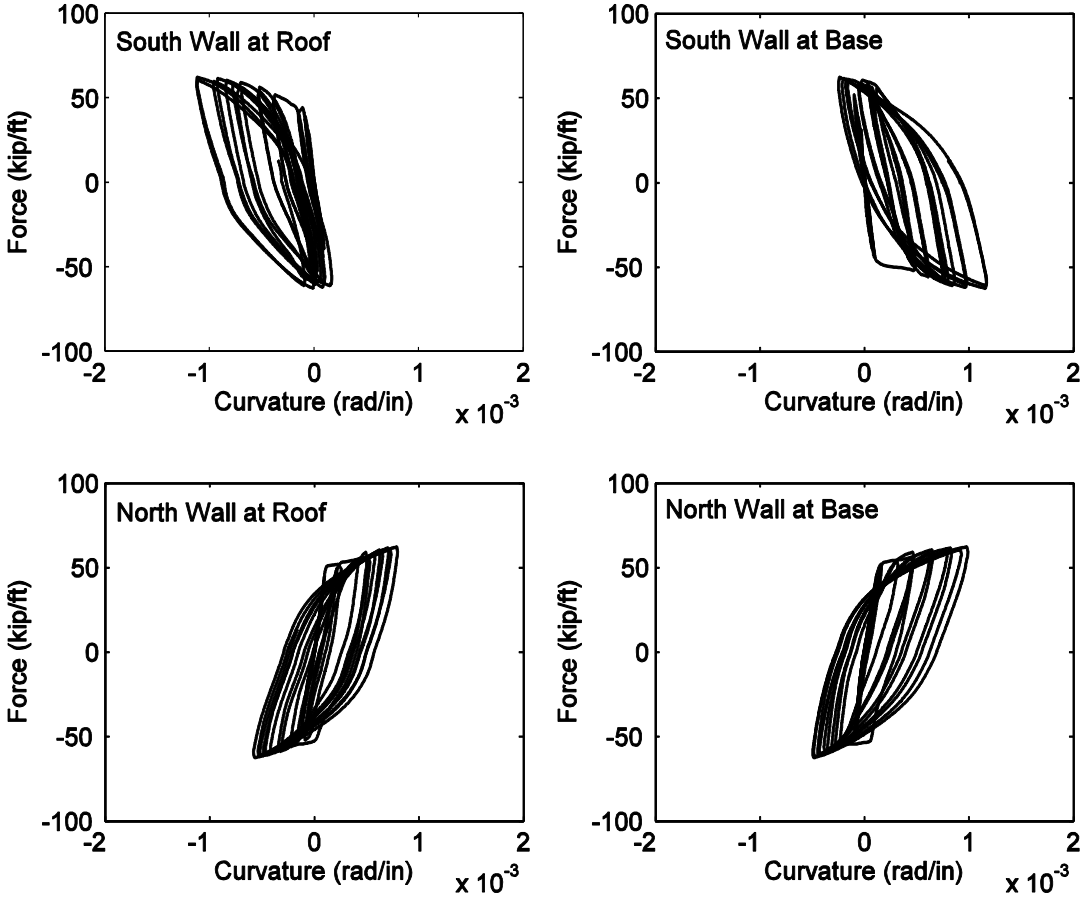

Figure 3-17: Comparison of the curvature in the north and south walls at the joints

Figure 3-18: Tunnel Elevation at start of test looking North-East.

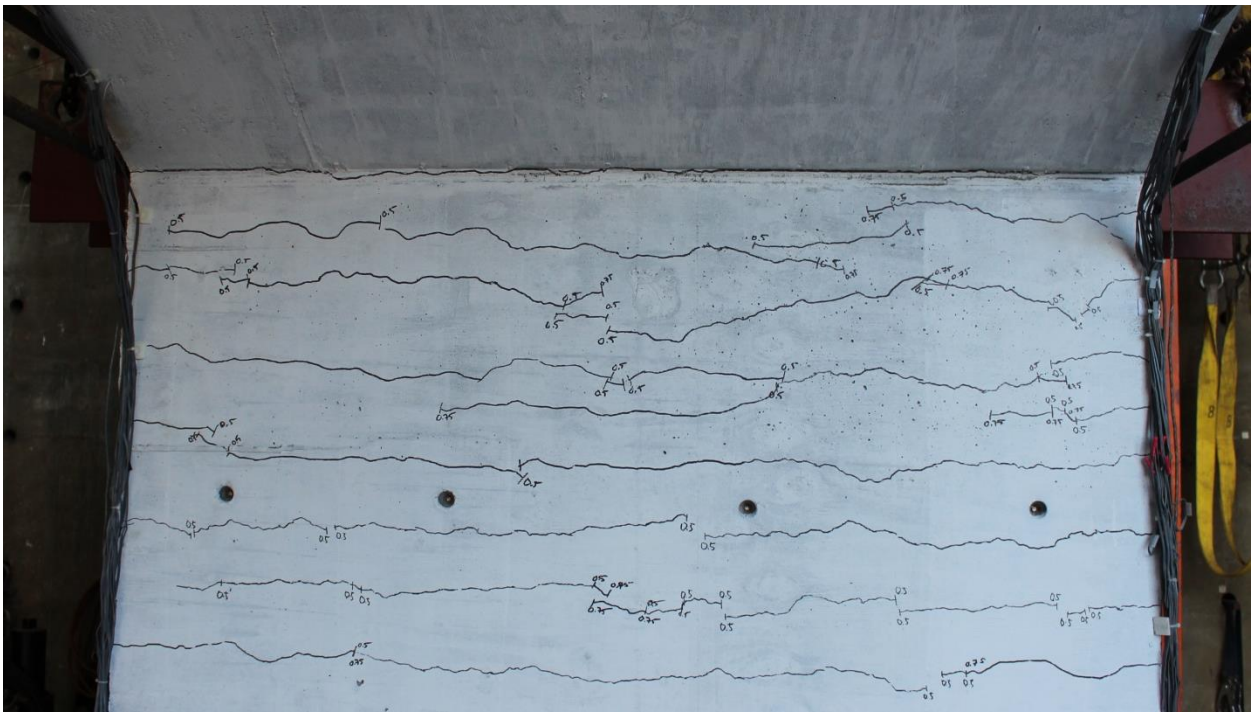

Figure 3-19: First yield at 0.75% drift ratio (Cycle 5-6). Picture of inside South wall at roof looking South

Figure 3-20: Uplift lift occurring at 2.0% drift ratio (Cycle 11-12). Picture of East face at Southeast corner at base/lab floor intersection looking South-West.

Figure 3-21: Flexural cracks occurring in the base at 2.0% drift ratio (Cycle 11-12). Picture of Southeast corner at base/lab floor intersection looking South-West.

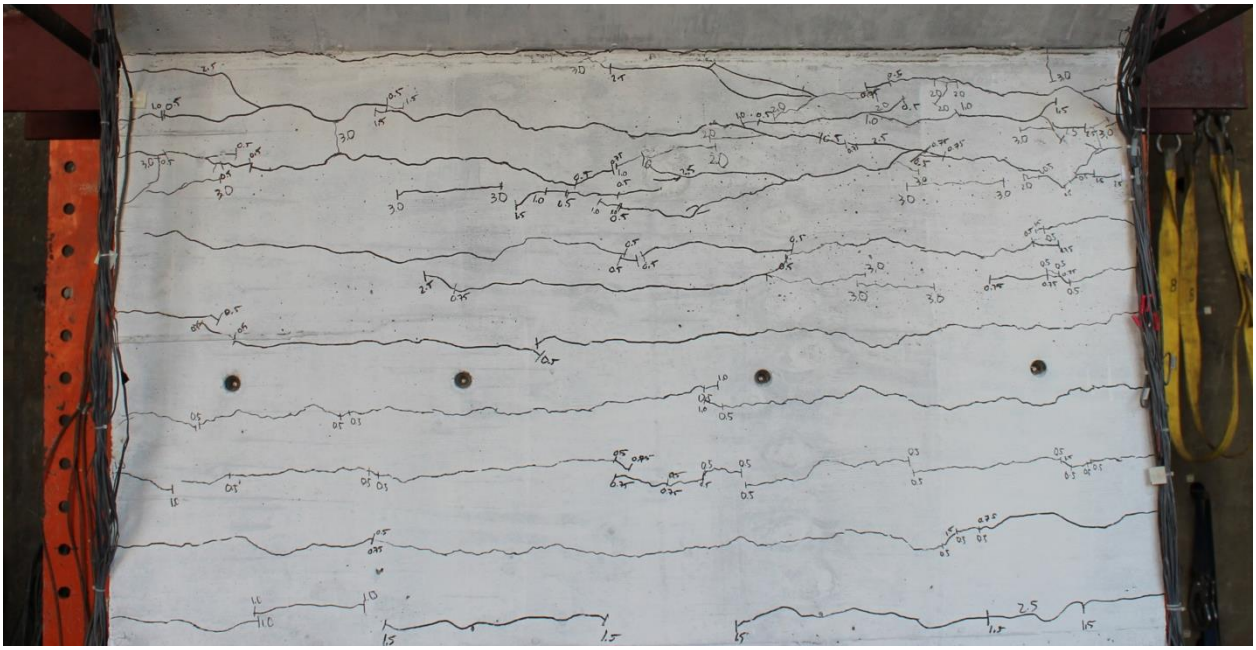

Figure 3-22: Extension of flexural cracking, cracks span width of tunnel at roof/south wall interface during positive extension at 3.0% drift ratio (Cycle 15-16). Picture of inside South wall at roof looking South

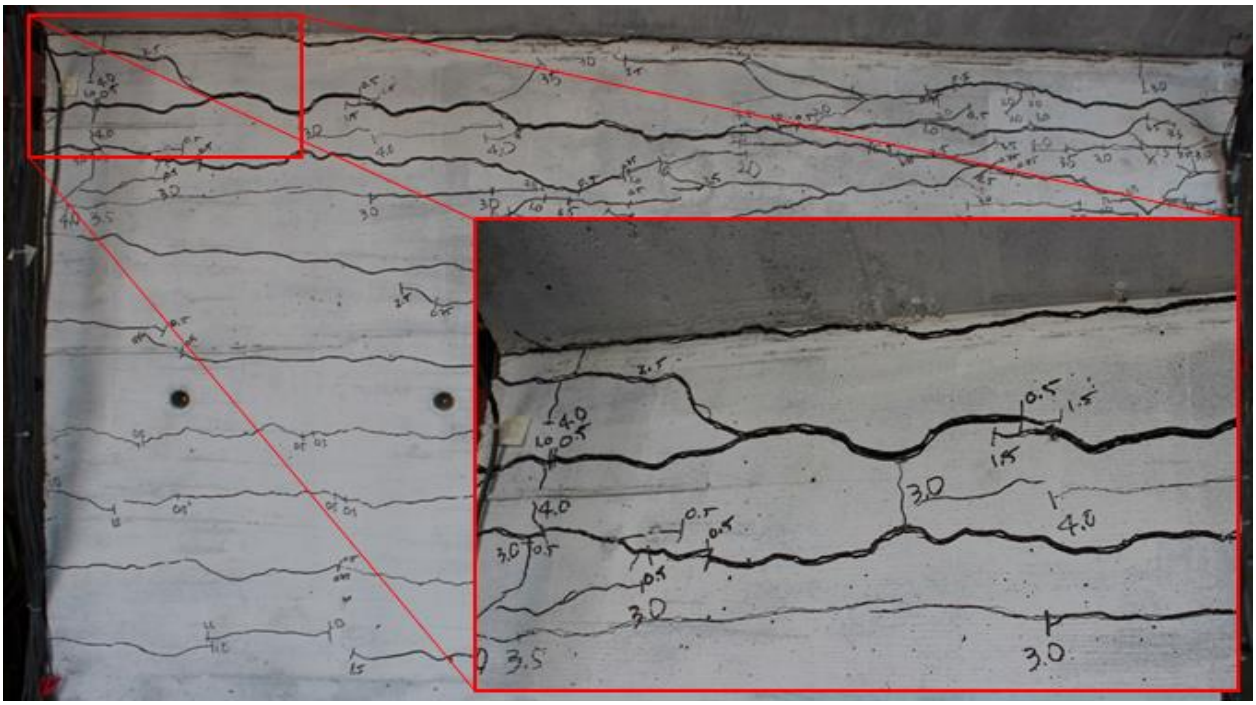

Figure 3-23: Significant flexural cracking, 0.25” maximum crack width at roof/south wall interface during positive extension at 4.0% drift ratio (Cycle 19-20). Picture of inside South wall at roof looking South

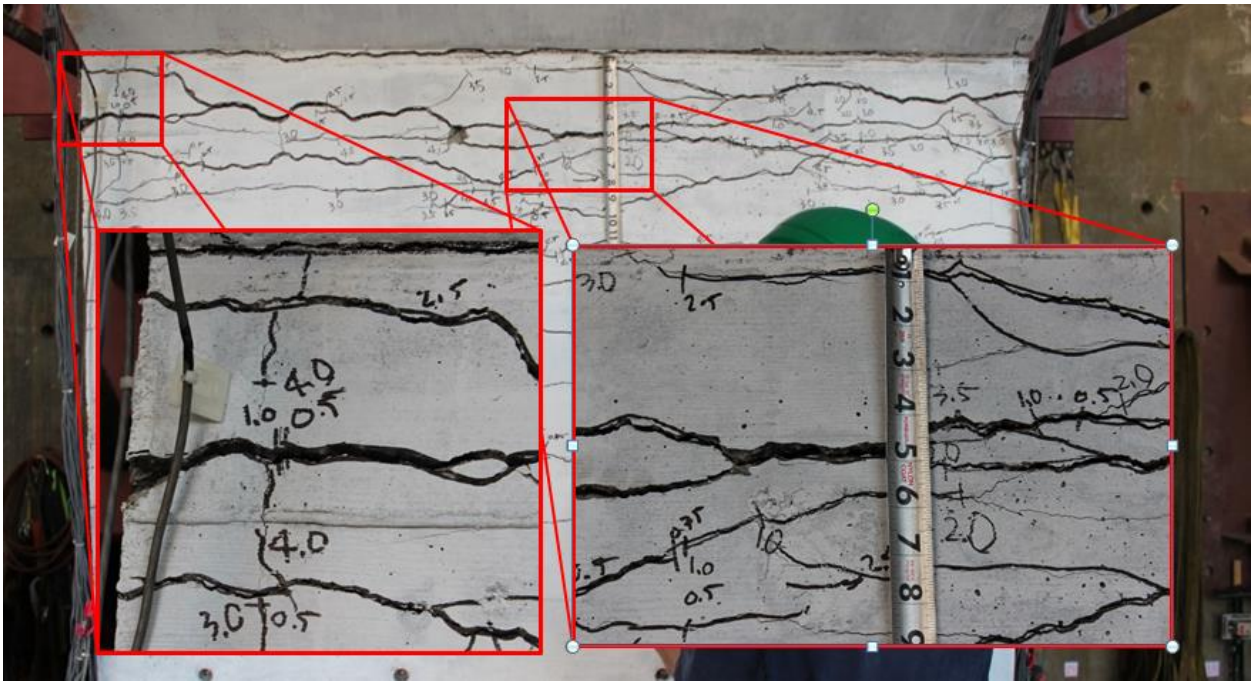

Figure 3-24: Flexural cracks at roof/south wall interface during positive extension at 6.0% drift ratio (Cycle 23-24). Picture of inside South wall at roof looking South.

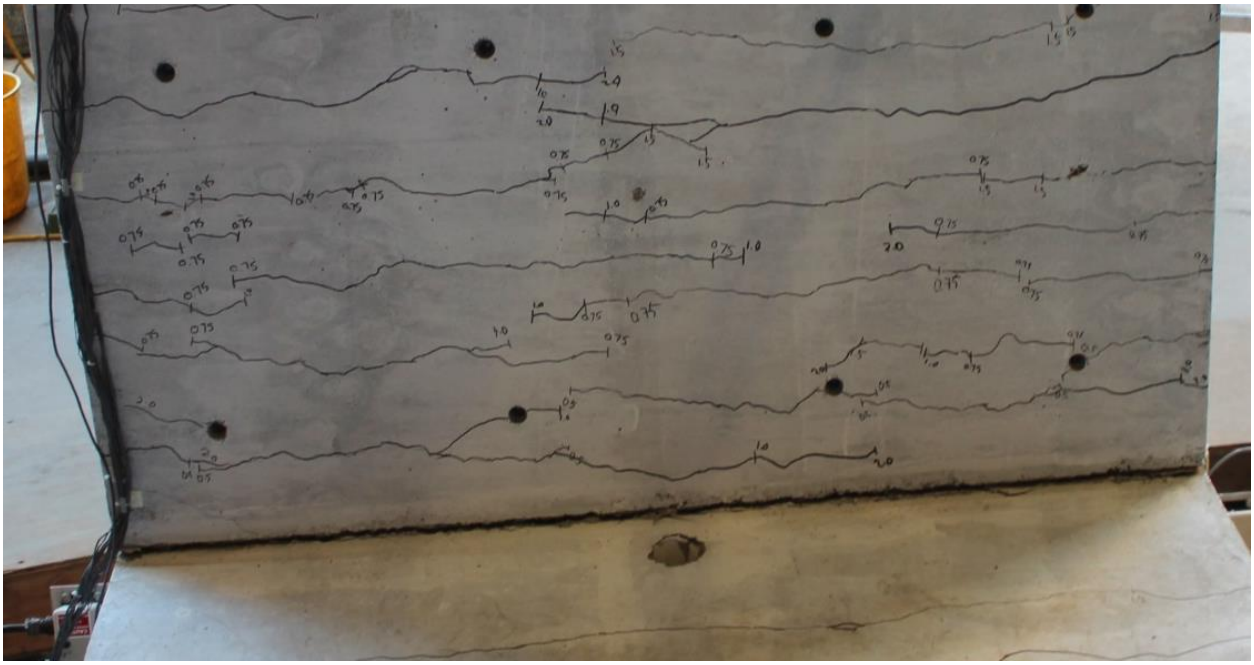

Figure 3-25: Flexural cracks at base/north wall interface during positive extension at 6.0% drift ratio (Cycle 23-24). Picture of inside North wall at base looking North.

Figure 3-26: Flexural cracks at base/north wall interface during positive extension at 6.0% drift ratio (Cycle 23-24). Picture of East face at North wall slab interface looking West.

Figure 3-27. Significant concrete spalling at roof/south wall interface during negative extension at 7.0% drift ratio (Cycle 25-26). Picture of inside South wall at roof looking South-West.

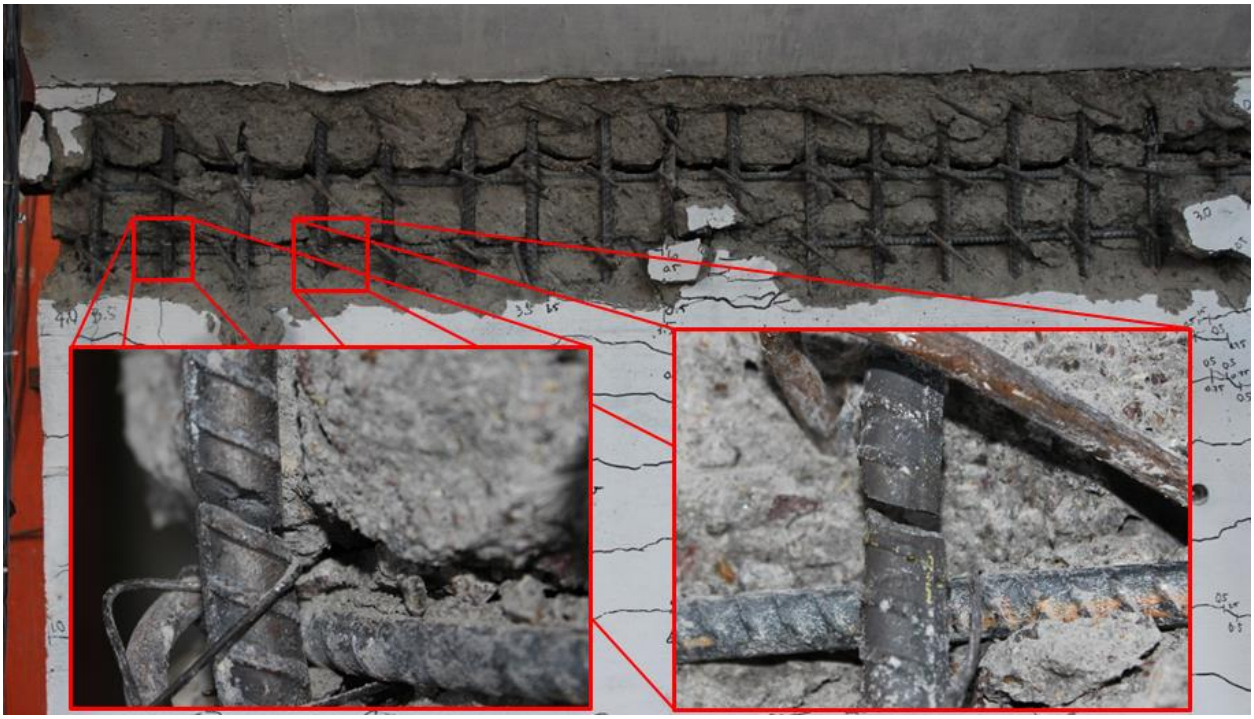

Figure 3-28: Bar Ruptures and significant concrete spalling at roof/south wall interface during positive extension at 8.0% drift ratio (Cycle 27-28). Picture of inside South wall at roof looking South.

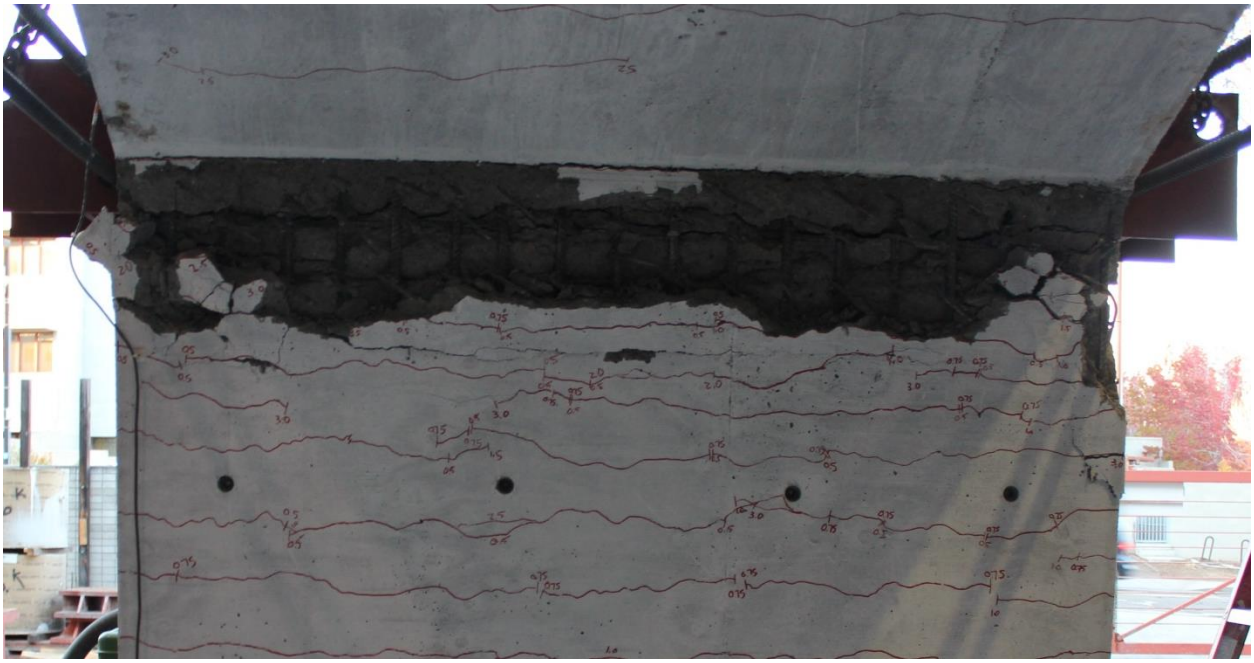

Figure 3-29: North wall roof interface during negative extension at 8.0% drift ratio (Cycle 27-28). Picture of inside South wall at roof looking South.

Figure 3-30: North wall roof interface during negative extension at 8.0% drift ratio (Cycle 27-28). Picture of West face at North wall roof interface looking East.

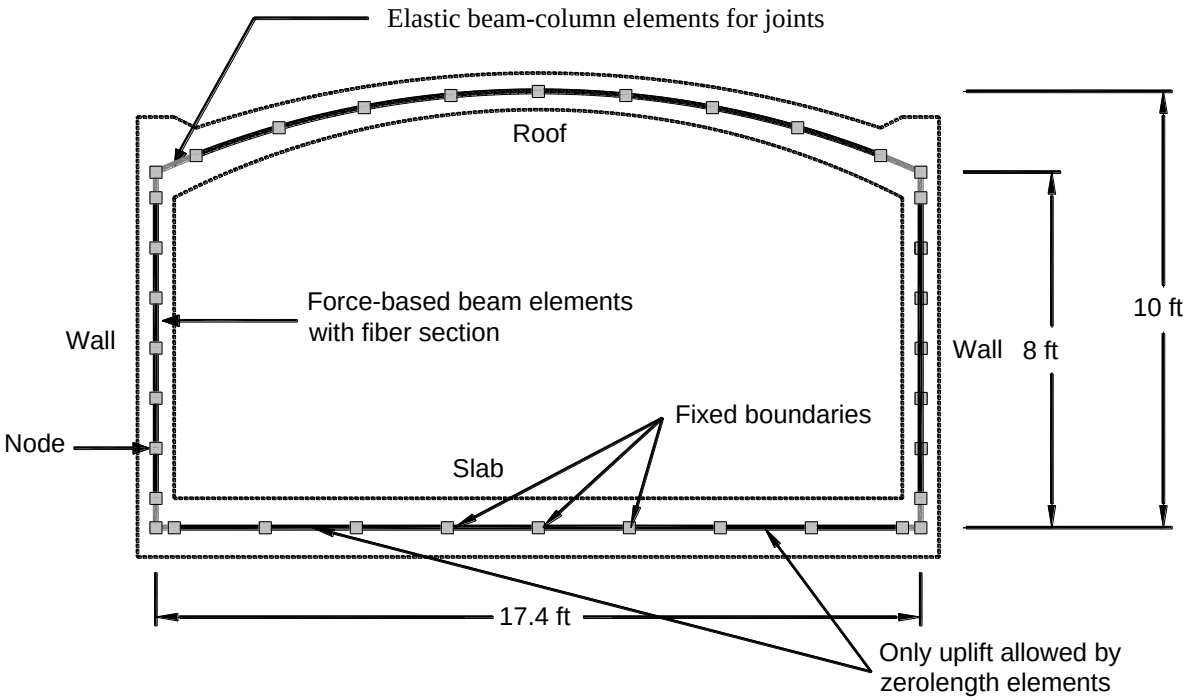

Figure 3-31: FE mesh for the 1/3 scale tunnel specimen in the OpenSees platform

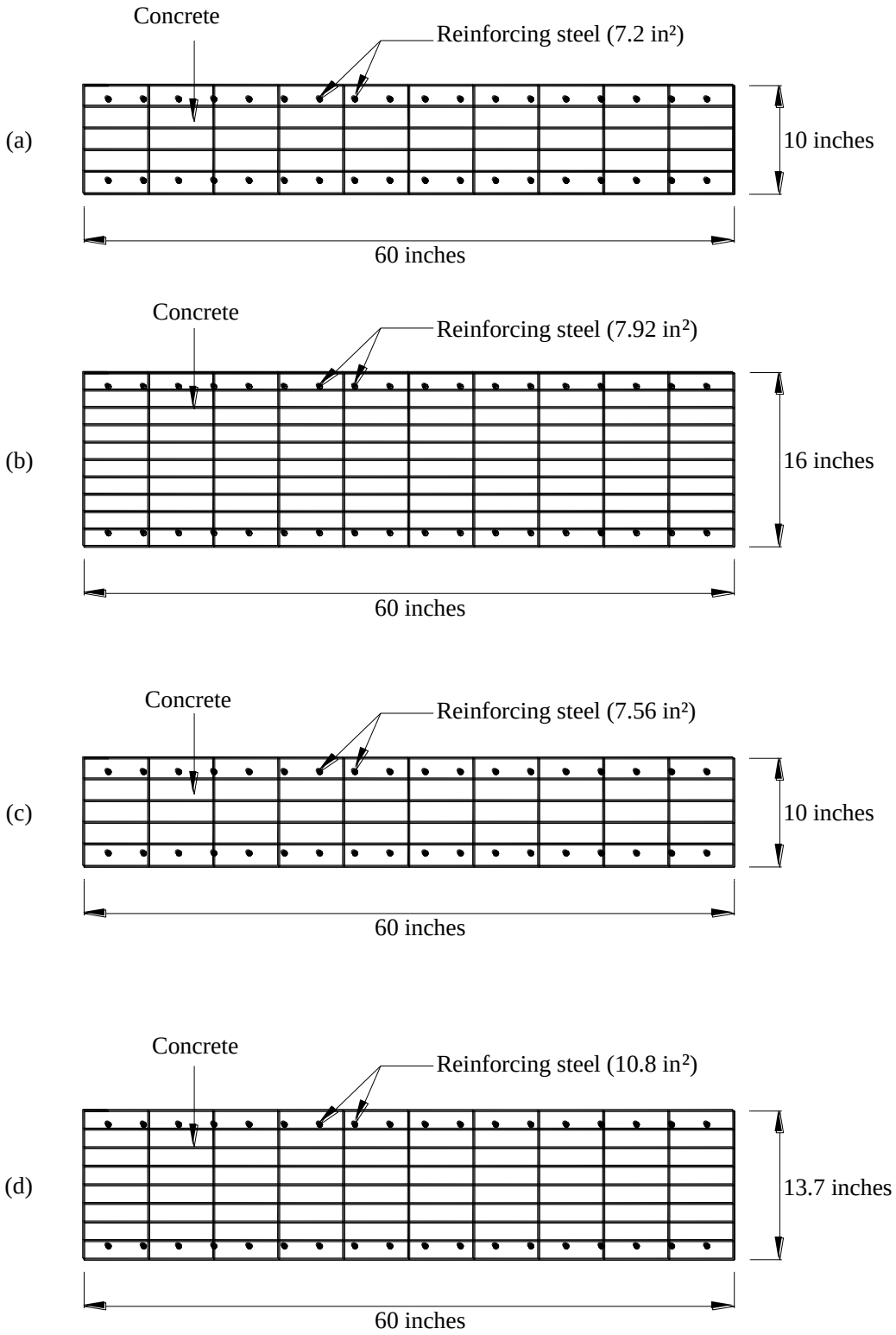

Figure 3-32: Fiber discretization of cross-sections in (a) walls; (b) slab; (c) middle of roof; (d) roof close to the wall

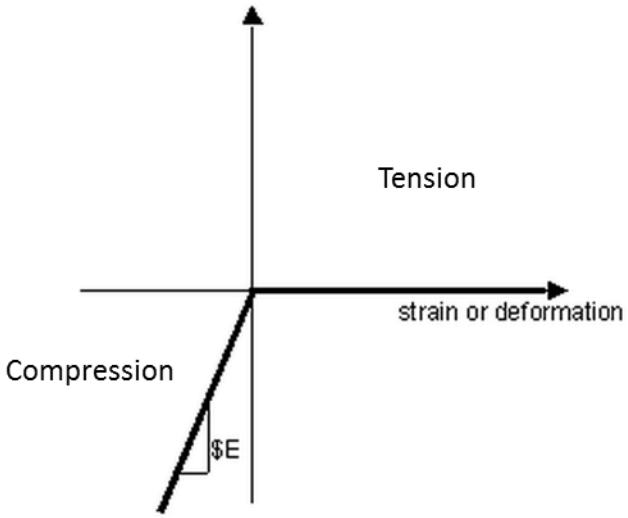

Figure 3-33: Behavior for the elastic-no tension material

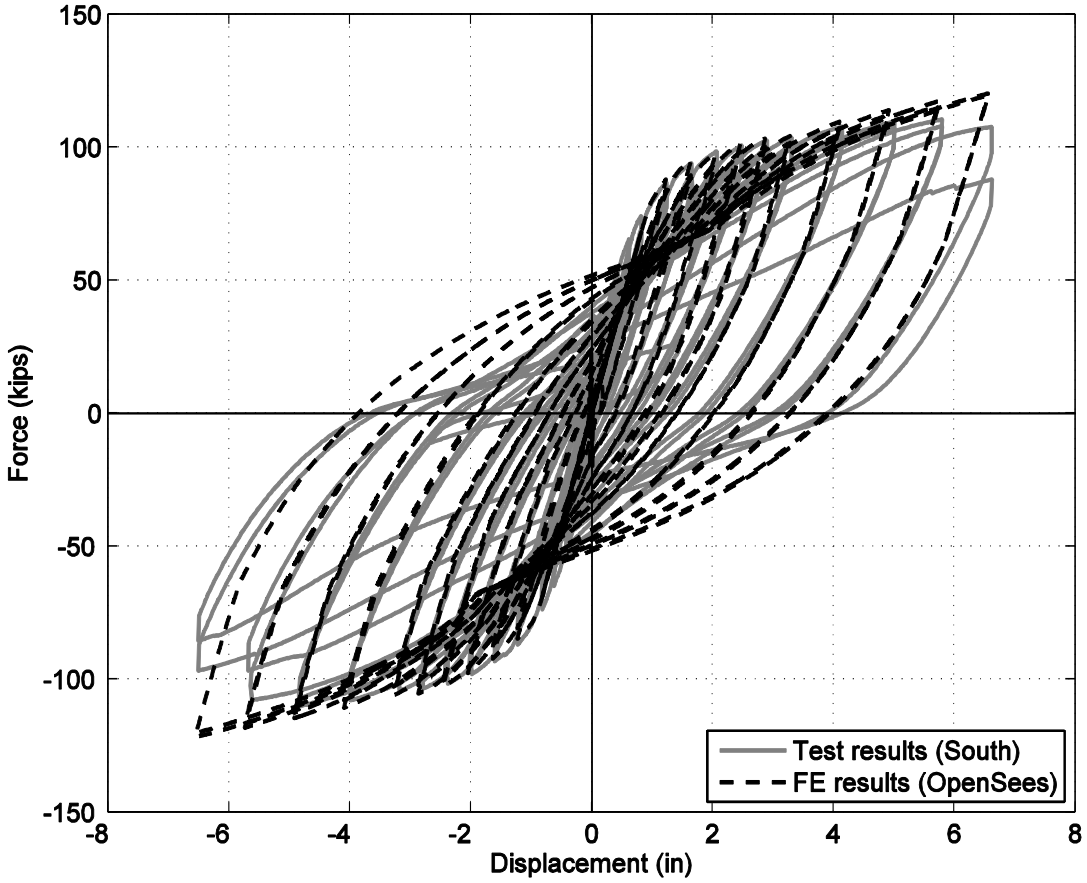

Figure 3-34: Comparison of lateral load vs. displacement from the test and the FE analysis

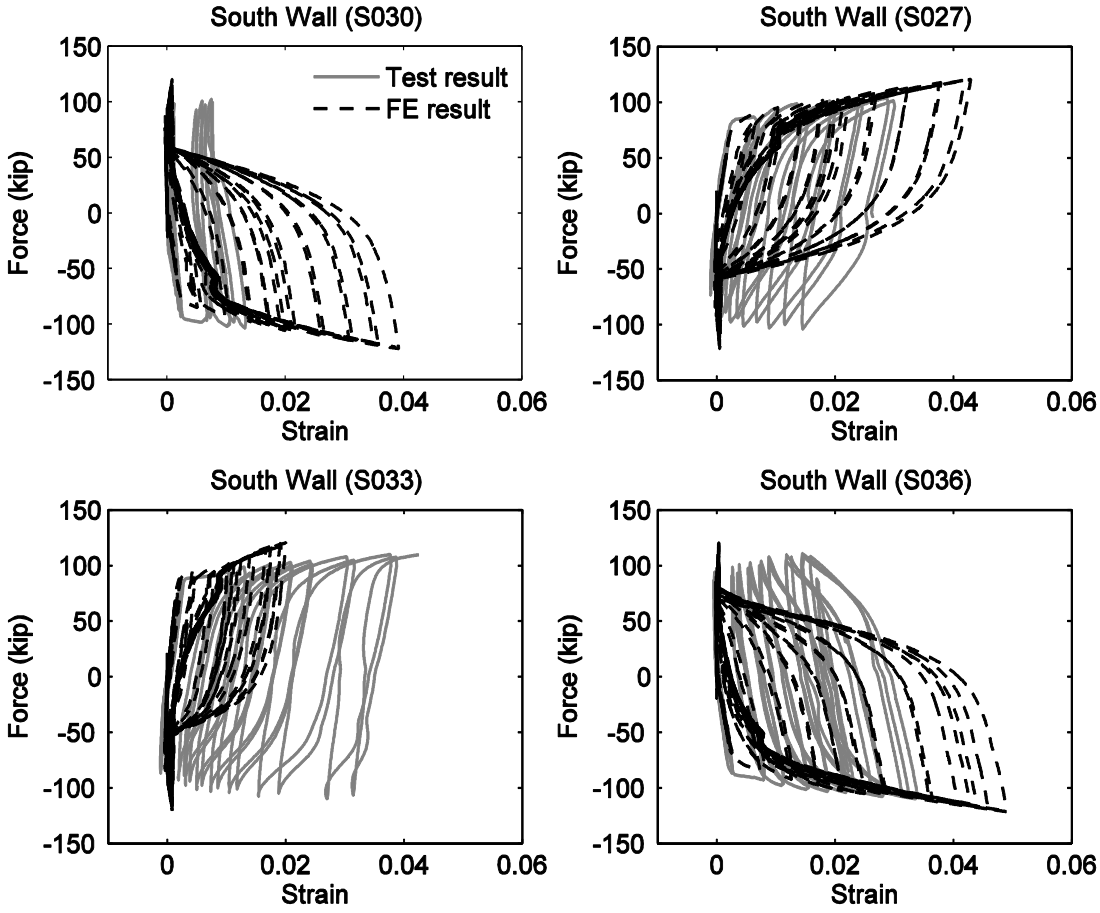

Figure 3-35: Comparison of lateral load vs. axial strain in the reinforcement on the south wall from the test and the FE analysis

4. Laminar Container Tunnel-Ground Testing Phase

4.1 Introduction

As a main element of the research scope, an experimental effort is conducted to obtain insights related to the mechanisms of interaction between the tunnel liner and the surrounding ground. For that purpose, a 1/9th scale model of the tunnel is embedded in large soil container, with an applied external push-over lateral displacement profile. This chapter presents the experimental configuration, and the characteristics of the employed soil and tunnel models are presented.

4.2 Description of laminar container

Figure 4-1 shows the employed laminar soil shear container at the UCSD Englekirk center. This soil box, funded by the California Department of Transportation (Caltrans), has a length of 22 ft (6.7 m), a width of 9.6 ft (3 m) and a height of 15.2 ft (4.7 m). The container consists of 31 steel laminar frames, each separated by a steel roller system on stainless steel lined webs, to allow for uni-directional movement. Movement of the laminar frames, when subjected to uni-directional dynamic loading, results ideally in a predominantly shear loading scenario.

The laminar container consists of: i) nine frames of a W8x35 steel section in the lower region of the box, ii) sixteen frames of a W8x15 steel section in the mid height region, and iii) six frames of the W8x10 steel section in the uppermost region. This variation in steel frame section sizes reduced the container construction cost and results in ratio of laminar frame weight to soil is in the range of 8 to 10%; a common range in similar full-scale laminar soil boxes in Japan.

4.3 Scaling relations in one-g model test

For 1g model tests in soil-structure systems, scaling relationships between a model (similitude) and the corresponding prototype are discussed. Since soil is a stress-dependent material, its stress-strain behavior should be appropriately presented by the model as illustrated in Figure 4-2. Fundamental laws of mechanics such as equilibrium and mass balance of soil skeleton (dry soil) also need to be satisfied in the similitude through the scaling factors. From governing equations for these principles, the following relations are derived by Iai (1989):

$$\lambda_\sigma/\lambda = \lambda_\rho = \lambda_\rho \lambda_u/\lambda_t^2 \text{ (from equilibrium)} \quad (4\text{-}1)$$

$$\lambda_\varepsilon = \lambda_u/\lambda \text{ (from strain definition)} \quad (4\text{-}2)$$

$$\lambda_\sigma = \lambda_D \lambda_\varepsilon \text{ (from constitutive law)} \quad (4\text{-}3)$$

where λ = geometrical scaling factor (prototype/model)

λ_σ = stress scaling factor (prototype/model)

λ_ε = strain scaling factor (prototype/model)

λ_D = modulus of soil scaling factor (prototype/model)

λ_ρ = density scaling factor (prototype/model)

λ_u = displacement scaling factor (prototype/model)

λ_t = time scaling factor (prototype/model)

Iai (1989) derived the strain scaling factor (λ_ε) from shear wave velocity tests in the model and prototype such as:

$$\lambda_\varepsilon = \lambda \left[\frac{(V_s)_m}{(V_s)_p}\right]^2 \quad (4\text{-}4)$$

where $(V_s)_m$ and $(V_s)_p$ denote shear wave velocities of soil deposits in the model and prototype, respectively. If the preliminary data for stress-dependent behavior of soil in the model are not available, it is assumed that the shear modulus at small strain of 10^{-6} is proportional to the square roof of the confining pressures. Consequently, this assumption leads to the following relation:

$$\lambda_\varepsilon = \lambda^{0.5} \quad (4\text{-}5)$$

In practice, as the density of the soil in the model is the same as that in the prototype, the density scaling factor is unity ($\lambda_\rho = 1$). Table 4-1 summarizes the main scaling factors derived by Iai (1989). The scaling factors for structures as a beam (e.g. a sheet pile) are also shown in Table 4-1. For such a structure in two dimensions (2D), its dimensions and cross-sections are generally specified per unit length (i.e. an axis out-of plane in Figure 4-2). Thus, the scaling factors shown in Table 4-1 are specified per unit length.

4.4 Tunnel model: design, construction, and stiffness testing

4.4.1 Specimen Dimensions

Figure 4-3 shows a schematic view of the soil-tunnel model in prototype scale. To allow for a singnificant extent of the soil domain on both sides of the tunnel, a scaling factor of 1/9 was adopted (as compared to the original Doyle Drive tunnel idealization). Table 4-2 summarizes the employed geometric dimensions of the tunnel specimen. Figure 4-4 shows the tunnel model, with a width of 6 ft. Based on the aspect ratio (0.55) of height to width of the 1/3rd scale reinforced concrete (RC) specimen, height of the tunnel was 3.3 ft. Length of the tunnel (9.25 ft) perpendicular to its cross-section was essentially equal to that of the container width (i.e., resulting in a plane strain model configuration). In prototype scale, the equivalent dimensions are 30 ft, 53 ft, and 83 ft for height, width, and length, respectively

4.4.2 Design

Due to model detail challenges in construction of an RC specimen at 1/9 scale, the model tunnel was built using steel (Figure 4-4). An added advantage of using steel is that this model will remain in the linear range during the testing phase and will be available to use in future experiments. A wooden frame was mounted above the steel roof simply to produce its curved roof geometry of the prototype.

Based on the behavior of the tested 1/3 scale RC tunnel specimen (Figure 4-5) as discussed earlier in Section 3.6, deformation was mainly observed along the walls. Deformation of the roof and the floor slab was comparatively negligible. As such, the model roof and slab were constructed of relatively rigid thin-walled hollow structural steel (HSS) sections for simplicity (Figure 4-4b). The desired tunnel wall lateral stiffness was achieved by using steel plates of appropriate thickness (0.75 in) as discussed further in the following sections.

4.4.3 Lateral stiffness of the 1/9 scale tunnel specimen

Figure 4-6 shows the relationship between the applied force and the lateral displacement measured at top of the wall during the 1/3 scale RC tunnel test. To determine thickness of the steel plate representing the wall, secant stiffness in this relationship is adapted based on the scale laws (Iai 1989) to go from the 1/3 scale to the 1/9 scale.

4.4.3.1 Determination of lateral stiffness

The relationship between the force and the displacement from the RC tunnel test was modified to evaluate stiffness per unit length (1ft). First, the applied force was divided by length of the tunnel wall (5 ft). Based on scaling laws for a test at ambient gravity (1 g) derived by Iai (1989), Figure 4-7 shows the lateral force and displacement scaled from 1/3 scale to 1/9 scale.

Figure 4-8 shows initial stiffness and secant stiffness at first yield for the 1/3 scale RC model and 1/9 scale model. To determine lateral stiffness of the 1/9 scale model, a target drift ratio of 1% in prototype scale was assumed. For this drift ratio, a corresponding displacement of 2.5 in was computed. Using the displacement scaling factor of 27 (= $9^{1.5}$ from prototype to 1/9 scale; Table 4-1), the target displacement at 1/9 scale was 0.1 in. As such, secant stiffness of 13.3 kip/in per unit length (1ft) was obtained from the target displacement in Figure 4-8b. Consequently, the stiffness of the 1/9 scale steel specimen with length of 9.3 ft was 123 kip/in.

In determining lateral stiffness of the tunnel, the stress-dependent behavior of soil was taken into account. If the tunnel specimen was tested using clay/looser sand or without consideration of soil-structure interaction, the defined lateral stiffness of the tunnel would differ from that used in the current test phase. As such, Table 4-3 summarizes a comparison of the tunnel lateral stiffness (1/9 scale) with and without stress-dependent behavior (i.e. using strain scaling factor, $\lambda_\varepsilon = 1$ or $= \lambda^{0.5}$, respectively; Table 4-1**)**. It was observed that the 1/9 scale tunnel model relatively behaved stiffer in consideration of stress-dependent behavior of the soil (Table 4-3a).

4.4.3.2 Lateral stiffness testing

Figure 4-9 shows a test setup to measure lateral stiffness of the 1/9 scale tunnel specimen (without the wooden frame affixed to the roof) under a fixed base condition. Figure 4-10 shows the measured displacement upon application of point loads at top of the wall. Table 4-4 summarizes the test results. Elastic response was observed up to the lateral displacement of 0.21 in corresponding to a 0.8% drift ratio with an effective height of 27.25 in. The measured lateral stiffness was 123 kip/in (= 25.7 kip/0.21 in). In prototype scale, lateral displacement was 5.67 in (scale factor of 27, $\lambda 1.5$ where $\lambda = 9$) and drift ratio corresponds was 2.4% based on the scale factor of 3 (= $\lambda^{0.5}$, where $\lambda = 9$). The corresponding lateral stiffness was 3,321 kip/in (39.9 kip/in per unit length of 1 ft) by using a scale factor of 27 (= $\lambda^{1.5}$ where $\lambda = 9$).

4.5 Engineering properties of Employed Soil

The employed Carroll Canyon Type II Washed Concrete Sand aggregate was supplied by Hanson Aggregates. This aggregate was produced at the Carroll Canyon Plant, San Diego, CA. Table 4-5 provides specific information about this soil as reported by the supplier. To investigate properties of the employed sand, sieve analysis and direct shear tests were conducted. Figure 4-11 shows the grain distribution curve determined by sieve analysis (ASTM C136) as conducted by Hanson Aggregates.

For the direct shear test, samples from a stockpile on site were tested. Direct shear tests were performed to failure at three different normal stresses (Figure 4-12). On the basis of peak strength, the samples overall showed a friction angle of about 40 degrees and cohesion of about 300 psf. At ultimate strength, the sample showed a friction angle of about 39 degrees and cohesion of about 150 psf (Figure 4-13).

Group Delta Consultant, Inc. conducted nuclear gauge measurement to verify dry density, moisture content, and relative compaction of the soil. Prior the test date (June 19th, 2014), the measurement (12 locations on soil surface) was performed as follows:

1) April 29th (51 days before; elevation of compacted soil at 2 ft)
2) April 30th (50 days before; elevation of compacted soil at 4 ft)
3) May 1st (49 days before; elevation of compacted soil at 6 ft)
4) June 11th (8 days before; elevation of compacted soil at 8 ft)

After the container was completely filled (elevation of compacted soil at 13 ft), additional measurements were conducted on June 16th (2 days before the test). Figure 4-14 shows approximate locations of the measurement (at this final elevation, three locations were added for a total of 15 locations). Table 4-6 summarizes measured dry density, moisture content, and relative compaction. Table 4-7 summarizes averages of the test results conducted on the different dates (i.e. at the different compacted soil surface elevations).

4.6 Instrumentation types and layout

Figure 4-15 shows an overall view of instrumentation layout used for the test. The employed instruments are summarized in Table 4-8. Details of each instrumentation layout can be found in Appendix G.

4.7 External loading system and Loading Protocol

Figure 4-16 shows a schematic view of the employed loading system. The loading frame with a hinged connection at its base was pulled by loading rods attached a reaction strong wall. As such, the loading frame attempted to provide a linearly prescribed displacement loading along height of the container in one direction (from the loading frame to the reaction wall). The maximum target displacement to be achieved was 5 in at the level of the soil surface (associated with 3% average shear strain = target displacement / height of the soil). During the test, the loading was applied and stopped at every 1 in to measure lateral soil deformation at the various inclinometers located within soil container and to investigate an unstable test setup configuration (Figure 4-15).

Table 4-1: Main scaling factors for 1g model tests (Iai 1989)

Quantity	**Scaling factor (1/3 scale to 1/9 scale)**		
	Generalized scaling factors	**$\lambda_\varepsilon = \lambda^{0.5}$, λ_ρ=1**	**CASE of λ = 3**
Length	λ	λ	3
Density	λ_ρ	1	1
Time	$(\lambda\lambda_\varepsilon)^{0.5}$	$\lambda^{0.75}$	2.3
Acceleration	1	1	1
Velocity	$(\lambda\lambda_\varepsilon)^{0.5}$	$\lambda^{0.75}$	2.3
Displacement	$\lambda\lambda_\varepsilon$	$\lambda^{1.5}$	5.2
Stress	$\lambda\lambda_\rho$	λ	3
Strain	λ_ε	$\lambda^{0.5}$	1.73
Stiffness	$\lambda\lambda_\rho/\lambda_\varepsilon$	$\lambda^{0.5}$	1.73
EI*	$\lambda^4\lambda_\rho/\lambda_\varepsilon$	$\lambda^{3.5}$	46.8
EA*	$\lambda^2\lambda_\rho/\lambda_\varepsilon$	$\lambda^{1.5}$	5.2
Moment*	$\lambda^3\lambda_\rho$	λ^3	27
Shear*	$\lambda^2\lambda_\rho$	λ^2	9
Axial Force*	$\lambda^2\lambda_\rho$	λ^2	9

*specified per unit breadth of the tunnel along its longitudinal axis (based on 2D Plane Strain)

Table 4-2: Geometric dimension of the tunnel specimen

Dimension	1/9 Scale	Prototype Scale
Width (ft)	6	54
Height (ft)	3.3	53
Length (ft)	9.25	83

Table 4-3: Lateral stiffness per unit length (ft) in the 1/9 scale tunnel model with and without stress-dependent behavior of soil

a) Stiffness scale factor ($model_{1/3\ scale}$ / $model_{1/9\ scale}$) = 1.73 (= $\lambda^{0.5}$)

	1/3 model	**1/9 model**
Lateral stiffness	23.0kip/in/ft	13.3 kip/in/ft

b) Stiffness scale factor ($model_{1/3\ scale}$ / $model_{1/9\ scale}$) = 3 (= λ); no strain effect

	1/3 model	**1/9 model**
Lateral stiffness	23.0 kip/in/ft	7.7 kip/in/ft

Table 4-4: Lateral stiffness test results of the 1/9 scale steel tunnel specimen

Quantity	1/9 Scale	Prototype scale
Target lateral displacement (in)	0.21	5.67
Drift (%)	0.8	2.4
Lateral stiffness (kip/in)	123	3,321 (40 kip/in per unit length of 1ft)

Table 4-5: Specification from sand supplier

Supplier's Data

Supplier	Hanson Aggregates
Plant	Carroll Canyon, San Diego
Material name	Carroll Canyon Type II Washed Concrete Sand
Date	January 14th, 2011

Sieve Analysis

Sieve size	% passing
9.50 mm (3/8")	100
4.75 mm (#4)	100
2.36 mm (#8)	91
1.18 mm (#16)	66
600 μm (#30)	43
300 μm (#50)	19
150 μm (#100)	6
75 μm (#200)	2.8

Additional Data

Specific gravity (bulk)	2.66
Absorption (%)	1.3
Sand equivalent	84
Durability index	86
Sodium soundness (%)	5
Potential reactivity	Innocuous

Table 4-6: Summary of conducted nuclear gauge density test measurement on June 16th, 2014 (final configuration of filled sand)

Location	Dry Density (pcf)	Moisture Content (%)	Relative Compaction (%)
1	110.2	2.5	93
2	109.7	2.6	92
3	111.4	2.4	94
4	114.5	2.7	96
5	112.8	2.1	95
6	112.7	2.2	95
7	115.9	2.1	97
8	114.3	2.4	94
9	113.4	2.8	95
10	111.6	2.1	94
11	115.8	2.2	97
12	111.1	2.0	93
13	113.2	1.7	95
14	112.2	2.1	94
15	113.3	2.9	95

Table 4-7: Average results from nuclear gauge density test measurements

Date	Dry Density (pcf)	Moisture Content (%)	Relative Compaction (%)
04/29/2014	112	4.4	99
04/30/2014	114	5.1	101
05/01/2014	112	5.1	99
06/11/2014	111	7.7	98
06/16/2014	113	2.3	95

Table 4-8: Summary of instrumentation

Laminar container box and backfill			
Instrument	Purpose	Location	Output
String potentiometer (SP)	Measure lateral displacement near base and top of the laminar box	Laminar container – reaction wall	Displacement (inches)
Linear variable displacement transducer (LVDT)	Measure vertical displacement of backfill (heave/settlement)	Backfill	Displacement (inches)
Accelerometer (A)	Measure P and S-wave propagation	Backfill	Acceleration (g)
Inclinometer (IncS)	Measure bi-direction horizontal displacement along the depth of backfill	Backfill	Displacement (inches)
AfB soil pressure sensor (AfB)	Measure lateral soil pressure applied by a loading frame along the height of the laminar container	Backfill – laminar container	Pressure (psi)
Tunnel specimen			
Instrument	Purpose	Location	Output
Strain gauge (S)	Measure strain along the walls and the slab to calculate curvature and bending moment	Wall, Slab	Strain
Linear variable displacement transducer (LVDT)	Measure racking and vertical deformation	Wall, Slab	Displacement (inches)
String potentiometer (SP)	Measure horizontal translation of the tunnel relative	Laminar container – base and top of the walls	Displacement (inches)
Inclinometer (Inc)	Measure rotation of the tunnel	Slab, Roof	Rotation (degrees)
Tactilus sensor (TS)	Measure soil pressure along the tunnel	Wall, Slab, Roof	Pressure (psi)
Tekscan sensor	Measure soil pressure on the wall (active earth pressure)	Wall	Pressure (psi)

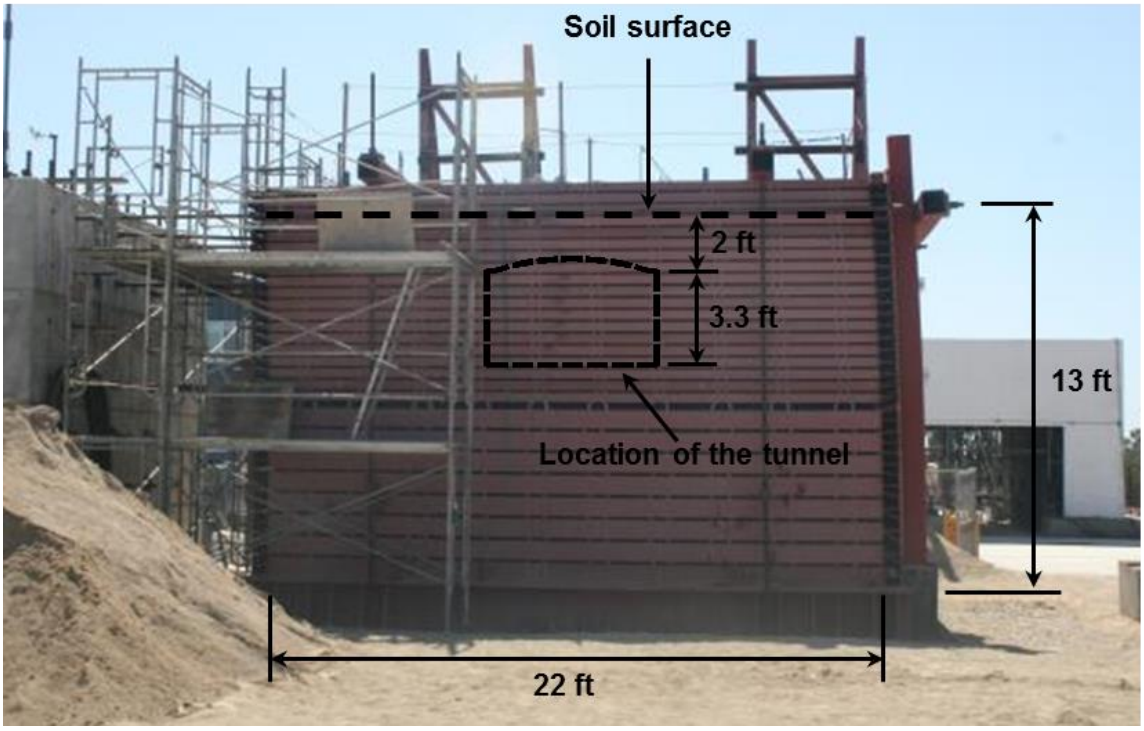

Figure 4-1: Photograph of UCSD laminar soil shear box under quasi-static loading

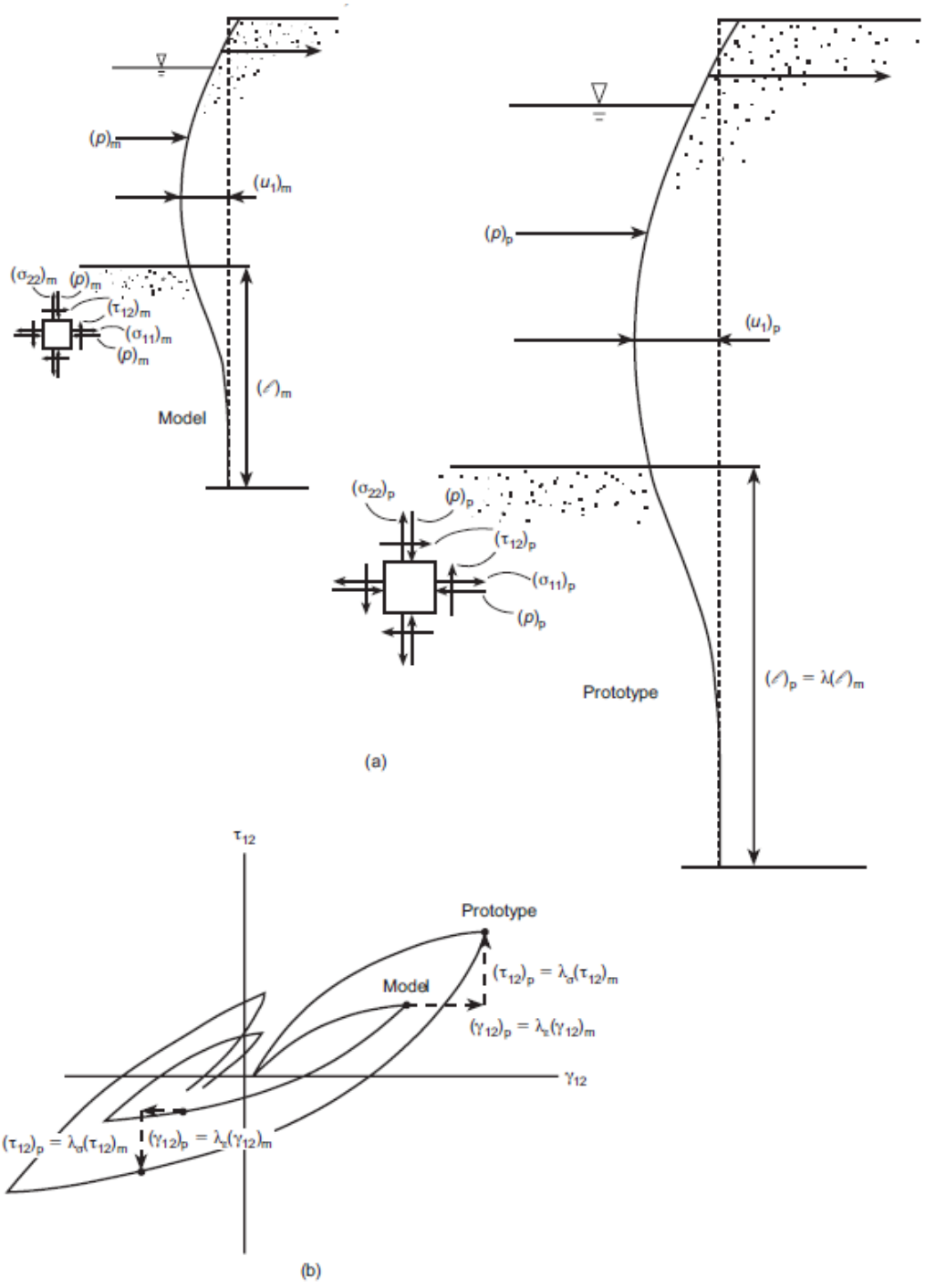

Figure 4-2: Illustrative example of model and prototype (Iai, 1989): (a) relevant quantities of prototype and model and (b) stress-strain relations of soils in prototype and model

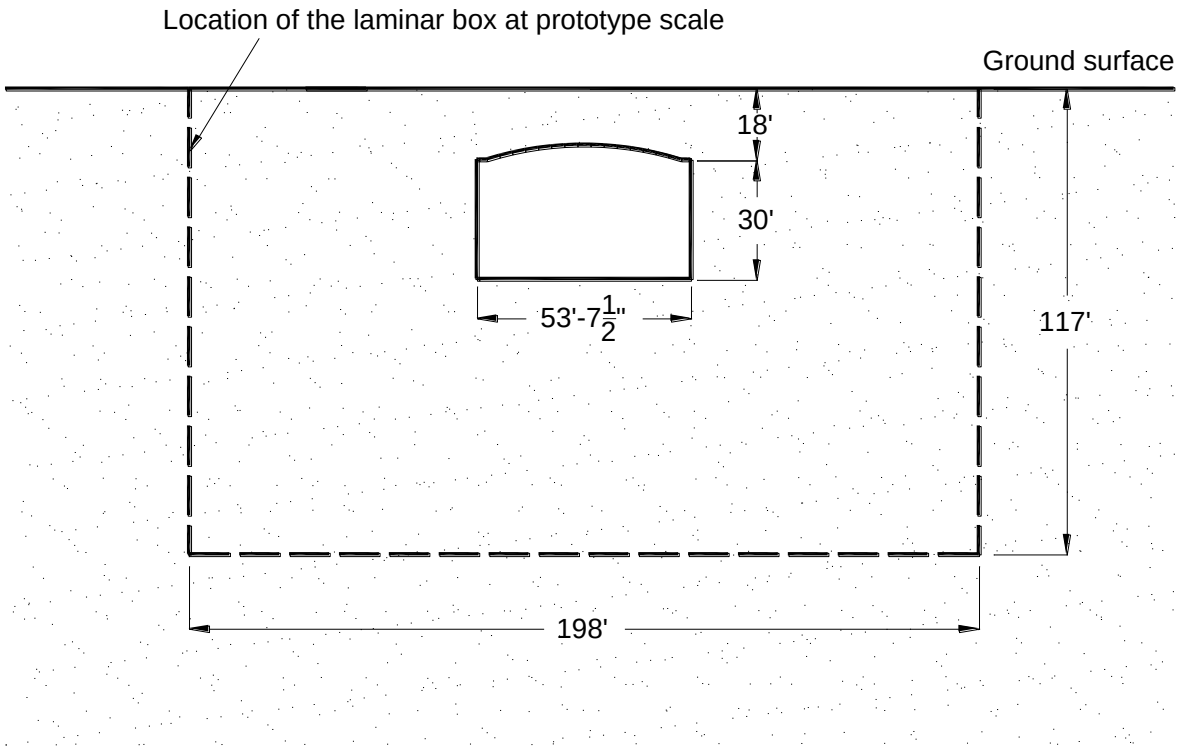

Figure 4-3: Schematic view of the soil-tunnel system in prototype scale

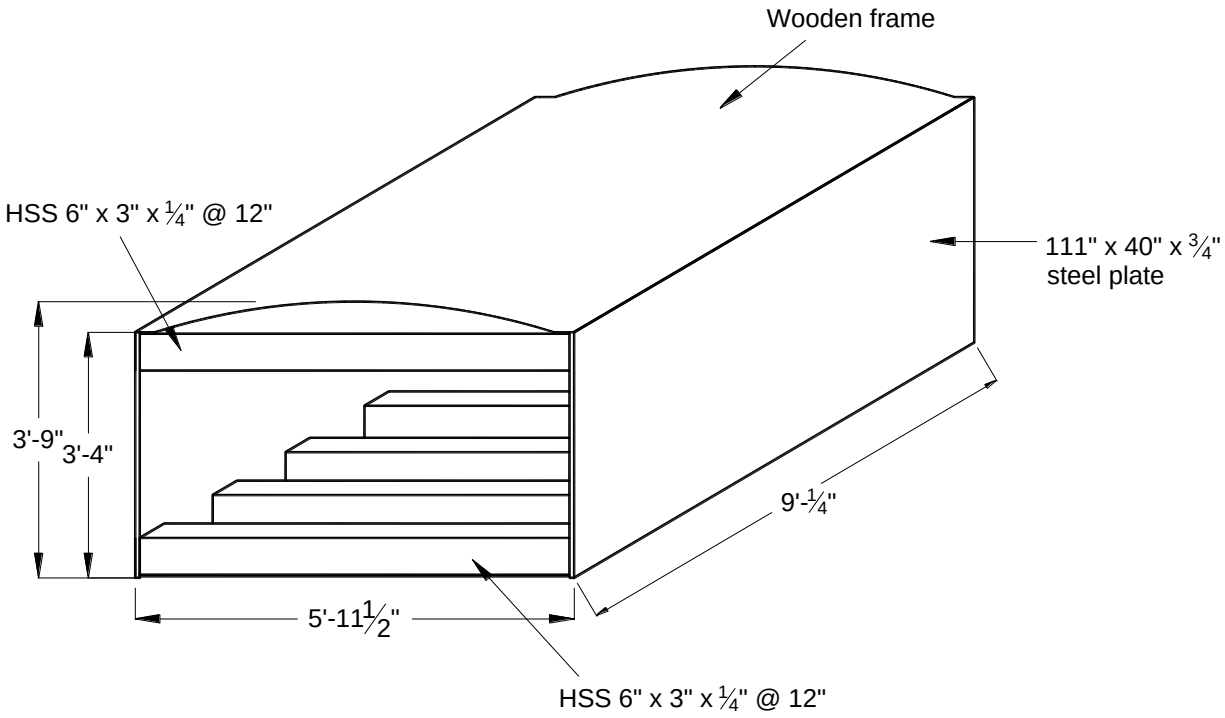

(a) Overall drawing of the 1/9 scale tunnel specimen

(b) Photograph of the 1/9th scale tunnel specimen (cross-sectional view)

Figure 4-4: 1/9th scale tunnel specimen used for the laminar container test

\

Figure 4-5: Test setup for the 1/3 scale RC tunnel subjected to cyclic loadings

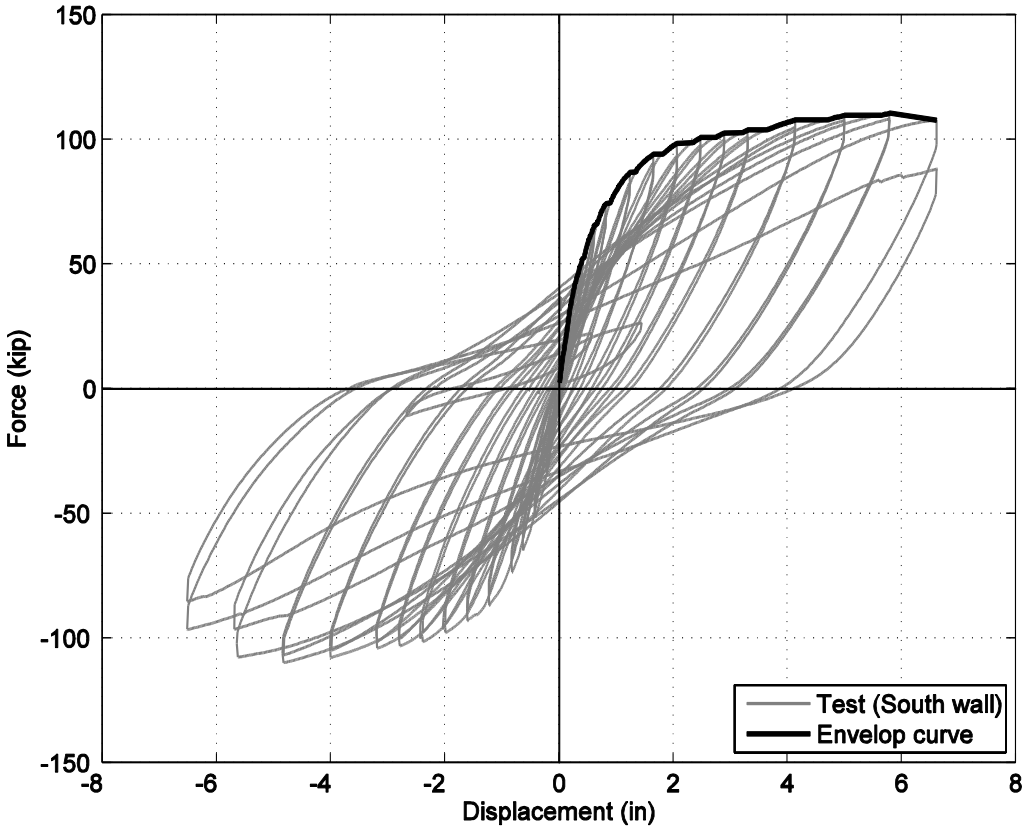

Figure 4-6: Lateral load vs. displacement measured in the 1/3 scale reinforced concrete tunnel test

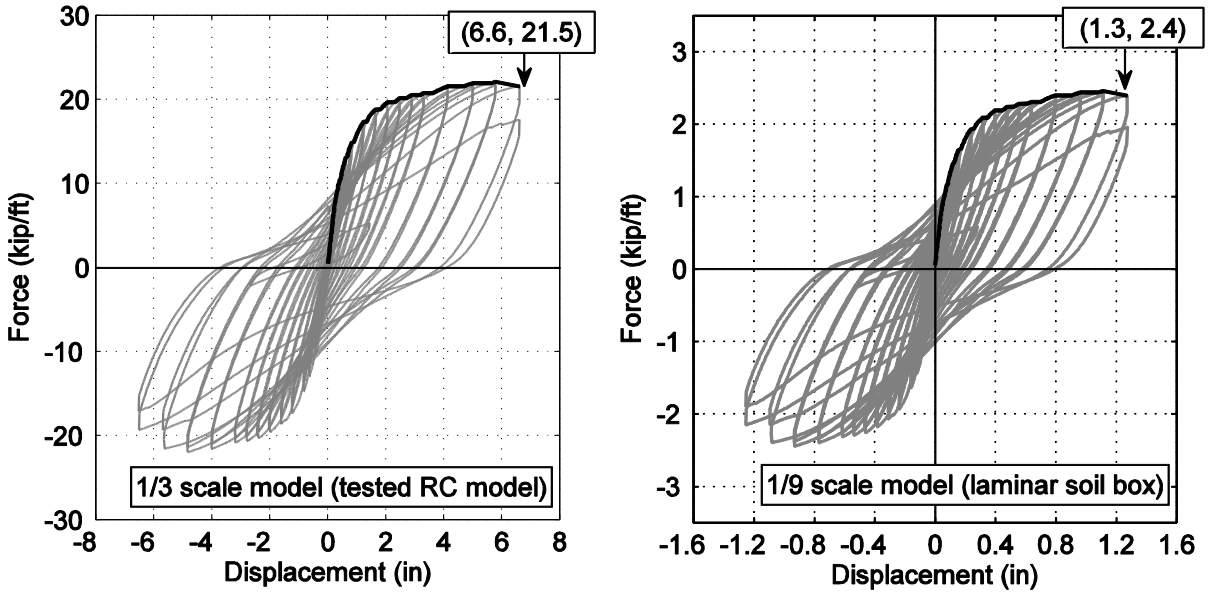

(a) 1/3 scale RC tunnel specimen (b) 1/9 scale tunnel model

Figure 4-7: Lateral load vs. displacement (per unit width of 1 ft) (a) measured in the 1/3 RC model and (b) converted for the 1/9 scale tunnel specimen

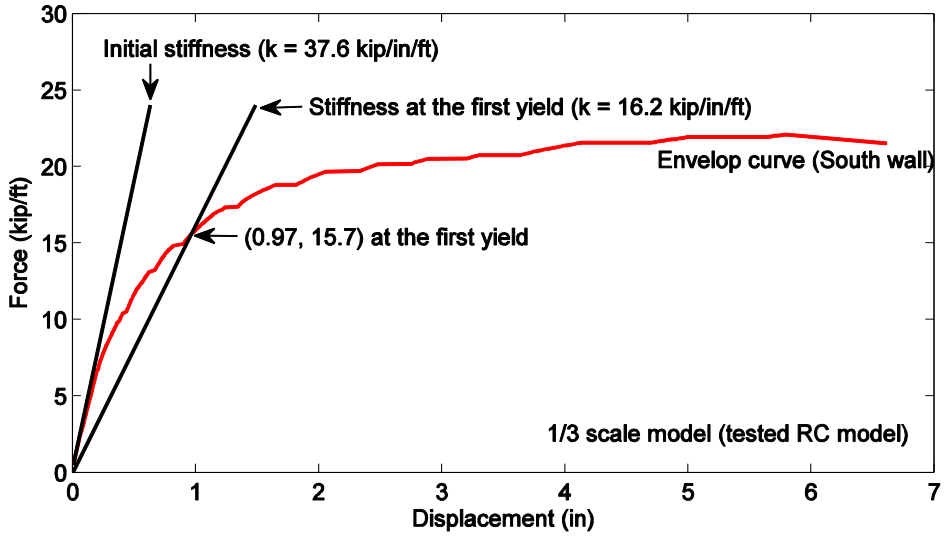

(a) 1/3 scale RC tunnel model

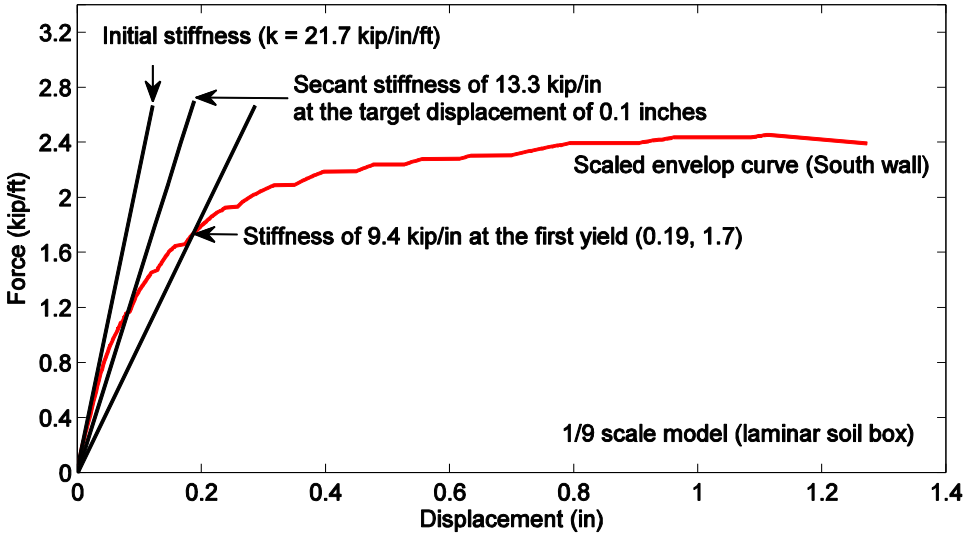

(b) 1/9 scale tunnel model

Figure 4-8: Lateral stiffness per unit length (1ft) of (a) 1/3 scale RC tunnel specimen and (b) 1/9 scale tunnel specimen

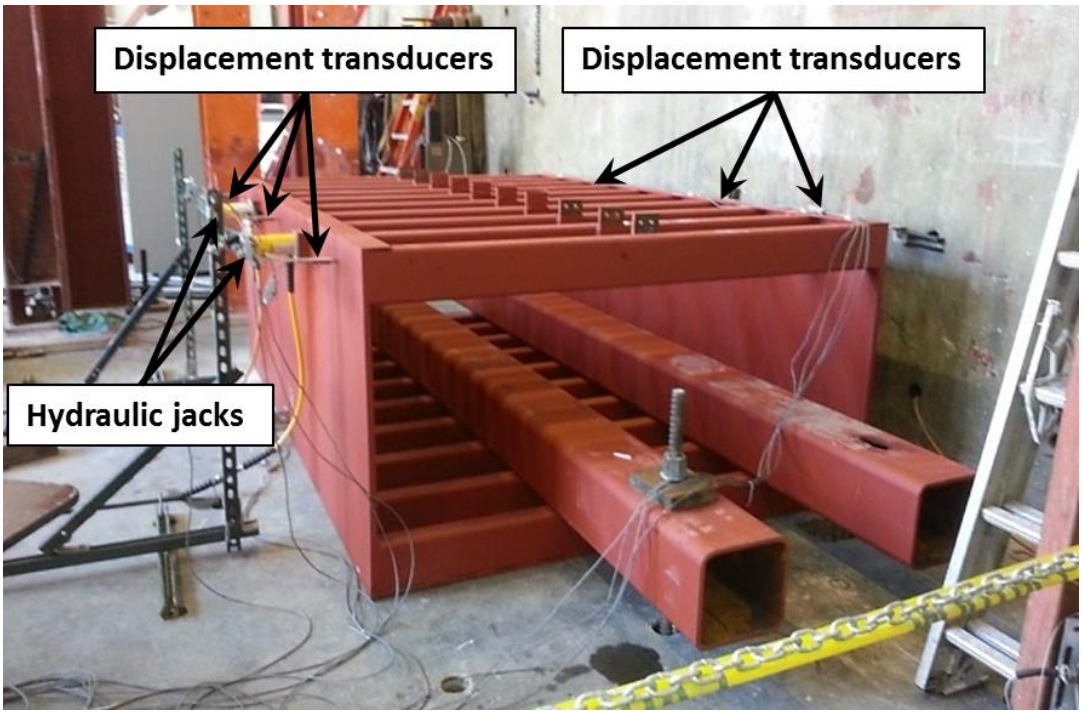

Figure 4-9: Photographs of test setup to measure lateral stiffness of the 1/9 scale steel tunnel specimen

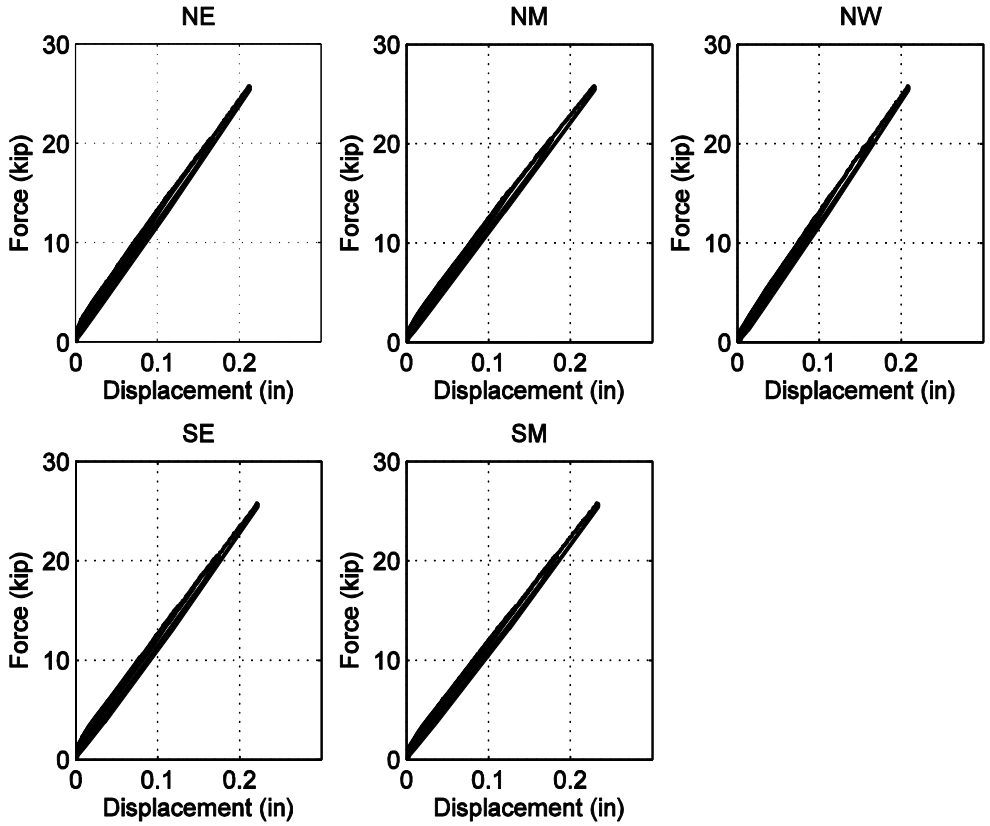

Figure 4-10: Lateral load vs. displacement measured from the physical test

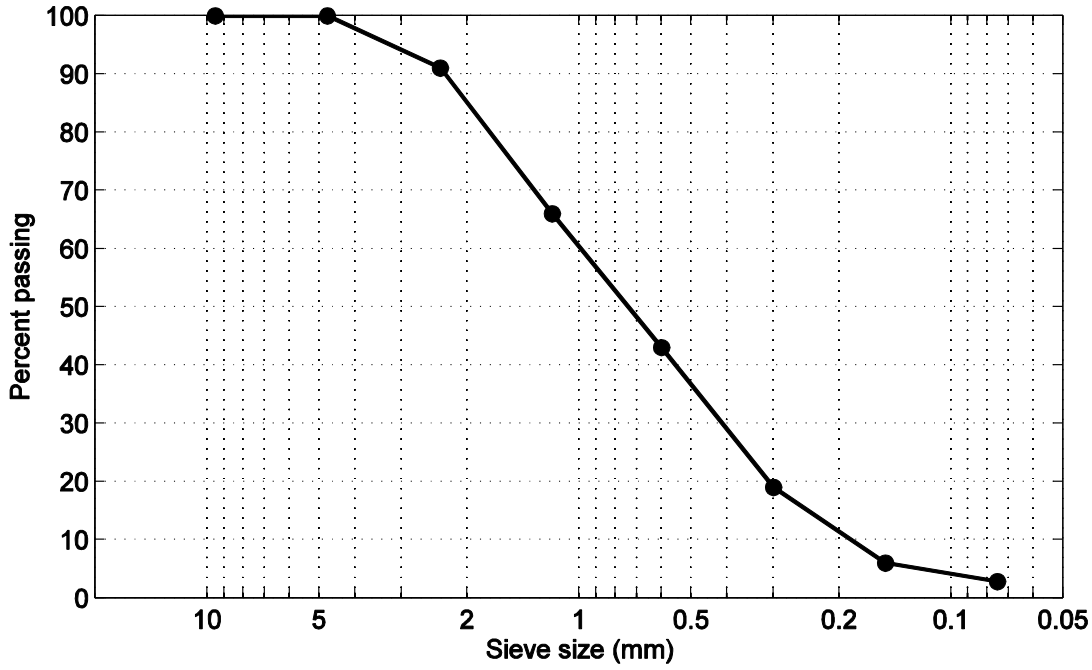

Figure 4-11: Grain size distribution from sieve analysis (ASTM C136) conducted by Hanson Aggregates.

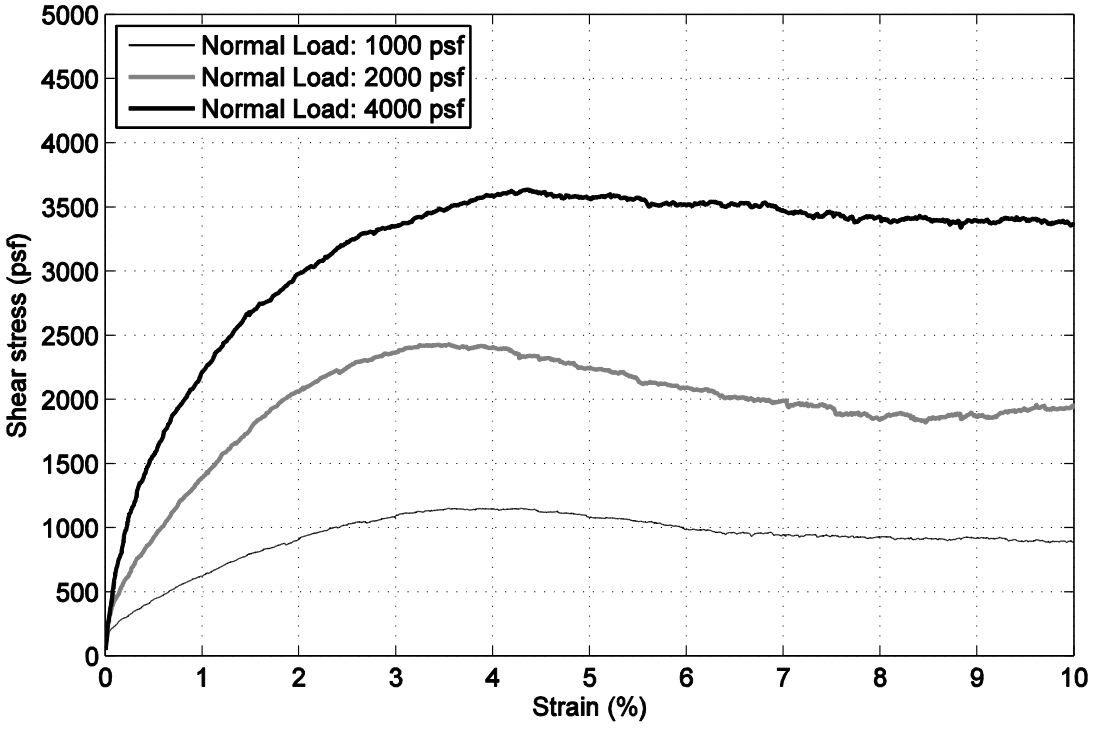

Figure 4-12: Shear strain vs. stress from direct shear tests conducted by Hanson Aggregates.

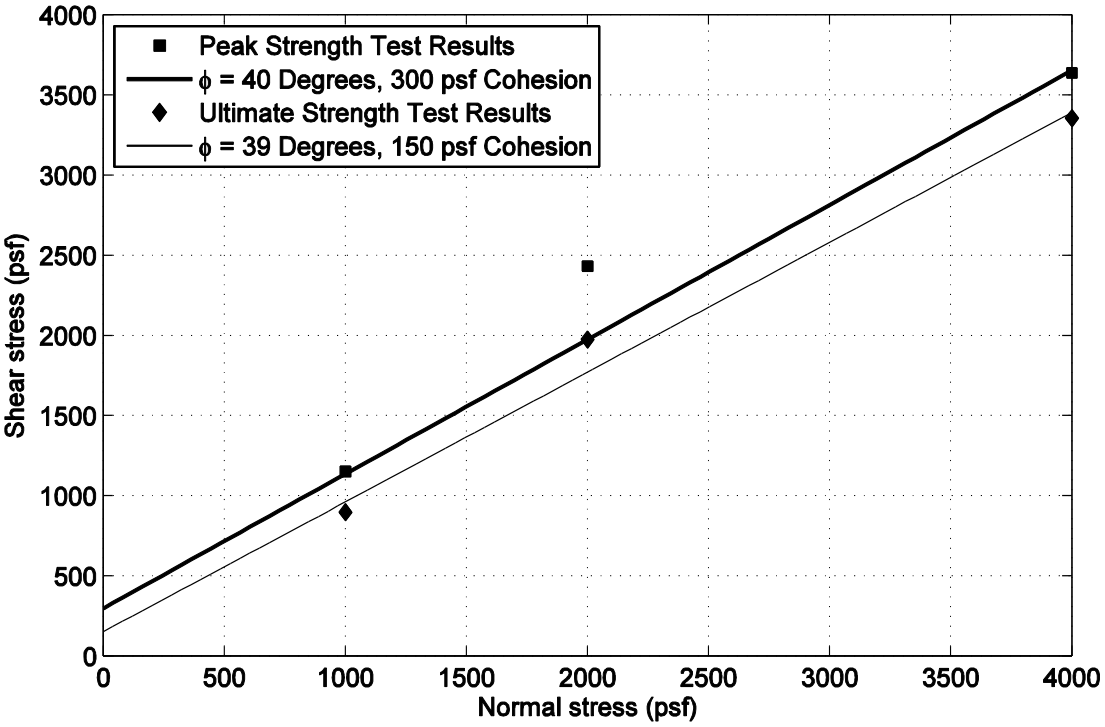

Figure 4-13: Normal stress vs. shear stress from direct shear test

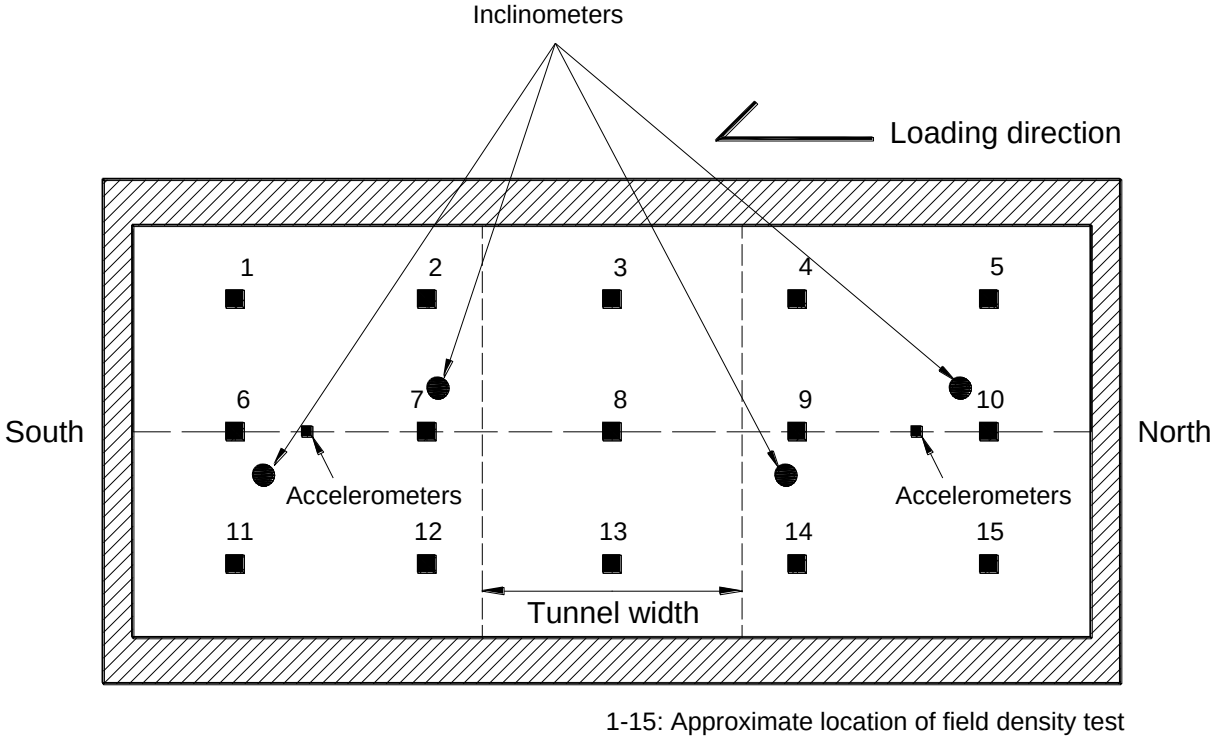

Figure 4-14: Field density test location map (plan view)

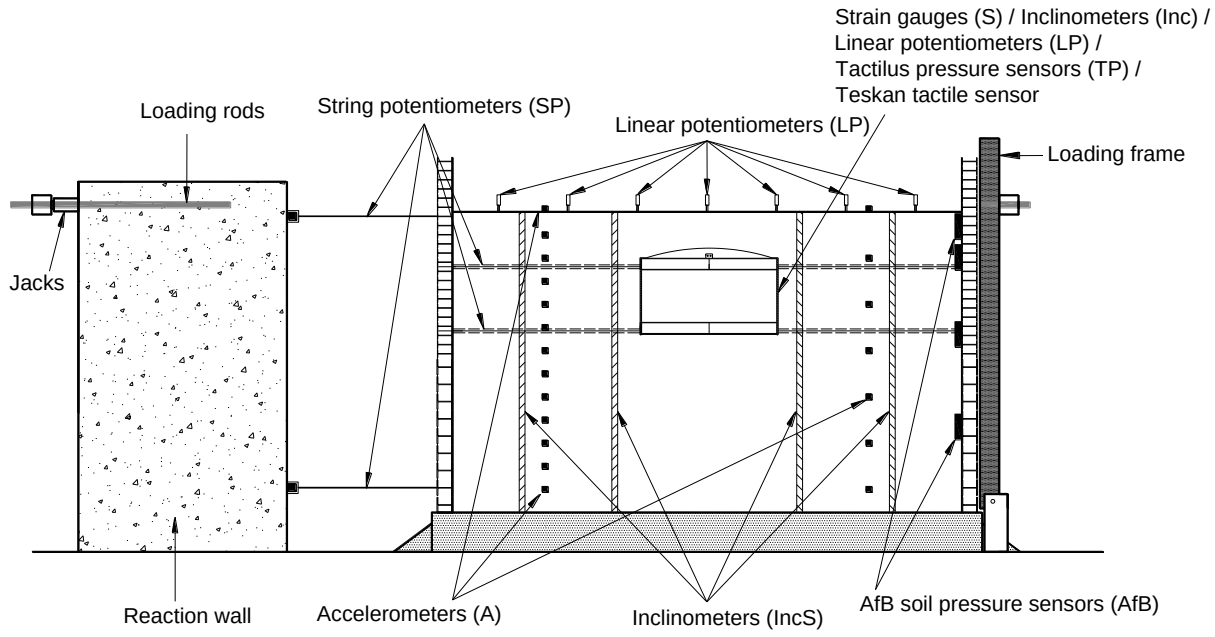

Figure 4-15: Schematic view of instrumentation layout

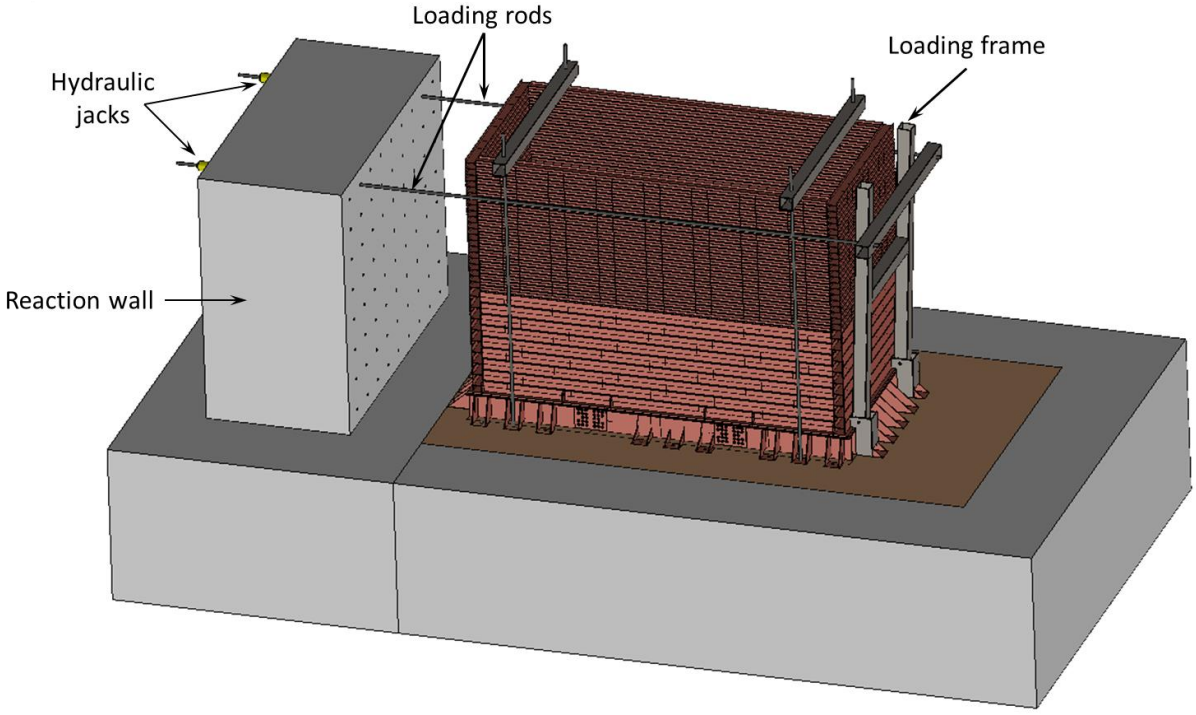

Figure 4-16: Loading system configuration

5. Laminar Container Tunnel-Ground Testing: Test Results

5.1 Introduction

As described earlier in Chapter 4, the 1/9 scale idealized model of the tunnel was embedded in the large laminar soil container, with an applied external push-over lateral displacement profile. Two push-over loading scenarios were applied. In the first, the virgin soil model with a fully embedded tunnel was tested. In the second, the same model was used, with the soil excavated up to the level of the roof (as further described below). The following experimental results derived from the employed instrumentation are presented in this chapter:

1. Shear wave velocity
2. Relationship of lateral load versus displacement
3. Soil deformation along depth
4. Tunnel deformation (racking and bending moments)
5. Soil pressure

5.2 Scaling laws from 1/9 scale to prototype scale

As discussed earlier in Section 4.3, for 1-g model tests in the soil-structure system, the stress-dependent behavior of soil is necessary to be taken into account. Assuming that shear modulus at small strain (e.g. 10^{-6}) is proportional to the square root of the confining pressure, the relationship of the strain from the model scale (1/9 scale) to the prototype scale is (Iai, 1989):

$$\lambda_\varepsilon = \lambda^{0.5} \tag{5-1}$$

where λ = geometrical (length) scaling factor (prototype/model) and λ_ε = strain scaling factor (prototype/model). As such, λ_ε has a value of 9 in this study. Displacement is the product of strain and length, and accordingly scaled by $\lambda\lambda_\varepsilon$ (9 x 3 = 27 in this study). Table 5-1 summarizes the main scaling laws from the employed 1/9 scale to the full-scale original prototype scale that was adopted from the Doyle Drive Battery Tunnel (Figure 5-1). In this chapter, all results are presented in prototype scale unless noted otherwise.

5.3 Laminar container tunnel-ground original testing configuration

In the following sections, all results from the 1/9 scale model are presented in prototype scale unless notes otherwise.

5.3.1 Measurement of shear wave velocity

Figure 5-2 shows the layout of the accelerometers deployed to measure shear wave (V_s) and P-wave (V_p) velocities propagated through soil deposit (based on time of peak arrivals or peak cross correlation between recorded accelerations at the different sensors). At two locations designated as south and north, hammer impacts were applied at the ground surface to trigger the waves (Figure 5-2).

To remove redundant noise in the measured acceleration, a high-pass filter with a frequency of 20 Hz and a low-pass filter with a frequency of 80 Hz were employed. Figure 5-3 and Figure 5-4 show the filtered acceleration time histories for V_s and V_p, respectively, in the narrow time window showing the wave propagation.

The arrival time difference of first peaks for V_s and V_p was computed at four different depths;

1) level of the tunnel roof
2) level of the tunnel slab
3) depth of 54 ft (27 ft below the tunnel)
4) depth of 108 ft (near the container base)

Table 5-2 summarizes the estimates of the measured velocities and corresponding shear modulus and Poisson's ratio at these locations. Figure 5-5 shows the measured V_s and V_p profiles along depth. Specifically, the measured V_s and V_p in the soil adjacent to the tunnel (between roof and slab) were about 1040 ft/sec and 2820 ft/sec. Using dry unit weight (113 pcf) measured from the nuclear gauge (see Section 4.4), the maximum shear modulus, G_{max}, is computed as 26.5 ksi. Using this shear modulus and V_p of 2820 ft/sec, Poisson's ratio of 0.421 was obtained. It is noted that, in the layer 1 (from soil surface to the tunnel roof level), the estimated velocities appeared to be very high (partially due to time step size resolution) and are this roughly assumed to be the same as those in the underlying layer (Table 5-2)

5.3.2 Load-displacement response

Figure 5-6 shows the relationship between lateral load and measured displacement at the soil surface (per 1 ft of the tunnel length; Figure 5-2). In this 1/9 scale model, the loading was stopped at container top lateral displacement of 1 in, 3 in, 4 in, and 5 (model scale) in order to investigate soil deformation along the depth (using the deployed inclinometers). Before the loading was reapplied, some stress-relaxation and creep behavior was observed (Figure 5-6). For this 1/9 scale model, the maximum lateral load reached 224 kips (1890 kips/ft in prototype scale as shown in Figure 5-6) and the test was stopped after the container top (soil surface) had attained a displacement of 5 in (11.3 ft in prototype scale).

5.3.3 Loading displacement profile

During the test, it was observed that the loading frame started bending particularly after the lateral displacement reached about 3 in (model scale). As such, measurement by hand was conducted to determine the actual displacement profile along the outer laminar container side (Figure 5-7).

5.3.4 Soil deformation

5.3.4.1 Lateral soil deformation from inclinometers

During the test, lateral deformation of the soil deposit was measured by four inclinometers along depth (see Figure 5-8 for plan view of installation and Figure 5-9 for photographs of measurement). The measurement was repeated at the applied ground surface displacements of sequentially 0 in, 1 in, 3 in, 4 in, and 5 in in model scale (0 ft, 2.3 ft, 6.8 ft, 9 ft, and 11.3 ft in prototype scale, respectively). Figure 5-10 shows the measured profile change along the depth (prototype scale). At two measuring locations (Inclinometers 2 and 3; with the tunnel placed in between), it was also observed that lateral deformation from soil surface to the tunnel slab level was relatively lower and exhibited a linear profile. Related to the soil deformation profile, Figure 5-11 shows photographs of separation of the soil from the laminar container boundary (South side) and cracks on the soil surface as the applied displacement reached the target displacement of 5 in (in model scale).

5.3.4.2 Vertical deformation on the soil surface

During the testing, vertical deformation on soil surface was measured using LVDTs (Figure 5-12). In this model, soil heave was observed near north side of the soil (being pushed). Near the south side settlement was noticeable as the applied displacement reached 2 in (model scale). After this displacement, the south side was pushed by the tunnel specimen. Consequently, soil heave was observed (Figure 5-13).

5.3.5 Response of tunnel specimen

5.3.5.1 Racking

Figure 5-14 shows linear potentiometers mounted inside the tunnel to measure its lateral deformation. No deformation was observed in the vertical direction (Figure 5-15; no data from LP 19). Consequently, the lateral displacement (racking) of the tunnel at the roof relative to the base was measured from the diagonal potentiometers (Figure 5-16). During the testing, the racking increased linearly (up to the drift ratio of about 1.5% in prototype scale) as the applied lateral displacement reached about 1.8 in model scale) at the soil surface (about 4 ft in prototype scale). The maximum drift ratio reached 2.5 % (prototype scale) for the wall height of 20 ft (corresponding to 0.8 % in model scale).

The racking displacement was compared to the relative soil displacement at the levels of the roof and the slab (measured by the inclinometers in the free-field). As shown in Figure 5-16, for lower drift ratios, the tunnel racking response falls within the band measured in the free-field from the nearby inclinometers (2 and 3). The ground response from inclinometer 3 was very similar to the racking up to a drift ratio of 1.5% (Figure 5-16). Ground surface displacement beyond about 5 ft did not appear to cause any additional racking which reached a maximum of about 2.5 %.

Table 5-3 summarizes the ratio of the tunnel racking to the ground relative displacement from inclinometers 1–3. As expected, the ratio tended to decrease with distance away from the tunnel. In addition, the ratio was relatively higher in the south region than that in north region.

5.3.5.2 Tunnel translation inside the container

Figure 5-17 shows the instrumentation layout of the string potentiometers to measure horizontal translations of the tunnel inside the container. Figure 5-18 shows the measurement from the string potentiometers. The results will be used to infer overall deformed configuration of the model as will be discussed in Section 5.6.4.

5.3.5.3 Bending moment in tunnel walls

Figure 5-19 shows bending moment profiles developed along the tunnel walls per unit length (1ft) specified at different drift ratios (in prototype scale). The bending moments were calculated based on curvature measured from the strain gauges mounted on both sides of the walls (designated as south and north; see Appendix G for the instrumentation layout). On the north side (being pushed during the test), the maximum bending moment of about 990 kip-ft/ft was developed near bottom of the wall (Figure 5-19). On the other side (south), a maximum bending moment of about 990 kip-ft/ft was also developed near top of the wall (Figure 5-19).

With the increase in drift ratio (particularly beyond 1% - 1.5%), the bending moment profile along the wall height was observed to develop an increasingly nonlinear shape (Figure 5-19). This possibly is a consequence of the changing profile of the lateral soil displacements as documented by the inclinometers (section 5.3.4.1). The full data set of curvature estimates as deduced from the strain gages and the corresponding bending moment is presented in Appendix H.

5.3.5.4 Deformed configuration

Figure 5-20 shows a schematic deformed configuration of the soil and the tunnel at the end of the test (reaching the lateral displacement of 5 in at soil surface in model scale) on the basis of the following data sources:

1. Inclinometers along depth of the soil
2. LVDTs on soil surface and inside the tunnel
3. String potentiometers inside the tunnel

5.3.6 Earth pressure response

During the test, earth pressure response was measured from three sets of the pressure sensors (see Appendix G for the instrumentation layout) as follows:

1. Pressure cell sensor (AfB sensor): a total 8 sensors were installed along north side of the laminar container to measure lateral pressures developed on the container boundary from the applied pushover loading (Figure G-9 in Appendix G)
2. Tactilus pressure sensor: total 32 sensors were installed along the perimeter of the tunnel to measure normal earth pressures (Figure G-13 in Appendix G)
3. Tekscan pressure sheet: one 16 in by 19 in sensor was installed on the north face of the tunnel (active earth pressure region; Figure G-13 in Appendix G)

Preliminary analyses of the recorded pressures are presented in Appendix I.

5.4 Laminar Container Tunnel-Ground Second Testing Phase

5.4.1 Test configuration

Figure 5-21 shows a schematic test configuration of an additional quasi-static test two weeks after the original test was conducted. Figure 5-22 shows the schematic view in prototype scale. Soil cover of 2 ft (18 ft at prototype scale) was excavated down to a level of the tunnel roof (Figure 5-23). From the previous test, a residual (lateral) displacement was 2 in (4.5 ft at prototype scale) at the elevation where the force was applied. As conducted in the previous test, the loading frame placed in the north was pulled by two hydraulic jacks up to a lateral displacement of 2.5 in (5.6 ft at prototype scale). During the test, the applied force stopped at every 0.5 in to measure soil deformation from inclinometers, V_s, V_p, and actual loading displacement profile along height of the laminar box (due to the bending of the loading frame in the previous test). Results from the test are presented as follows:

1. Relationship of lateral load versus displacement
2. Applied displacement profile along wall of the laminar container
3. Soil deformation
4. Tunnel deformation

All results are presented at prototype scale using the scaling laws as summarized in Table 5-1, otherwise noted.

5.4.2 Load-displacement response

Figure 5-24 shows the relation between applied lateral load (per unit length of 1 ft) and displacement at top of the laminar container, along with that measured from the previous test. Measured displacement was added to the residual displacement of 4.5 ft from the original test. The lateral loading was interrupted briefly every 1.1 ft (0.5 in in model scale) to measure the corresponding soil deformation profile. The maximum lateral load reached 1370 kip per unit length (160 kips in model scale).

5.4.3 Displacement profile

As discussed earlier in Section 5.3.3, the hand measurement was conducted to document the displacement profile along the side of the laminar container. The results are shown in Figure 5-25 (values presented in model scale).

5.4.4 Soil deformation from inclinometers

During the test, deformation of the soil along the depth was measured by four inclinometers (Figure 5-8 for plan view of installation and Figure 5-9 for photographs of measurement). Figure 5-26 shows the displacement profile change along the soil depth relative to the initial measurement (prototype scale).

5.4.5 Tunnel translation

Figure 5-27 shows measurements (in model scale) from the string potentiometers that are connected from the tunnel and the laminar frames at levels of the roof and the slab. As such, the displacements shown are actually relative values between the tunnel and the corresponding laminates at the same level.

5.4.6 Tunnel racking

As discussed earlier in Section 4.6.1, lateral deformation (racking) of the tunnel at the roof relative to the base was measured from the diagonal potentiometers (Figure 5-16). Figure 5-28 shows the measurement from the potentiometers. During the testing, the displacement increased more or less linearly (Figure 5-29). The maximum drift ratio of 0.9 % (effective height

of 20 ft) was developed at the target displacement of 5.6 ft (at this displacement, the drift ratio was about 2.2% in the previous test).

Table 5-4 summarizes the ratio of the tunnel racking to the relative ground displacement (between levels of the roof and the slab) at the locations of the inclinometers 1-3. As shown in Figure 5-29, the measured response of the tunnel and the surrounding soil remained essentially linear. Thus, the ratio was relatively constant, regardless of the distance of the free-field from the tunnel and its drift ratio.

5.4.7 Bending moment in tunnel walls

Curvature measured from strain gauges mounted on both side of the walls were used to estimate the bending moment profile along the wall (Figure 5-30). On the north side of the wall (being pushed during the test), a maximum bending moment of 251 kip-ft per ft (per unit length) was developed near the roof (height of 21 ft). On the other side (south), a maximum bending moment of 240 kip-ft per ft was developed near the roof (height of 6 ft). The bending moment constantly increased as the drift ratio increased.

5.5 Summary

A 1/9 scale tunnel-ground model in a laminar container was tested by lateral push-over loading. A prescribed lateral displacement was applied to the laminar container outer boundary. In addition to the original test, a second phase of load application was performed, without soil above the tunnel roof (basically to provide additional data for numerical model calibration).

Shear wave velocity of the ground stratum was estimated. Using inclinometers, response of the soil and the tunnel was documented at various locations within the stratum. Racking and displacement of the tunnel was documented throughout. With the aid of strain gages on the tunnel walls, bending moments were evaluated at various levels of the applied ground displacement profile. This data provides valuable quantitative response characteristics that form a basis for calibration of numerical analysis frameworks.

Table 5-1: Main scaling factors for 1g model tests (Iai 1989)

Quantity	**Scaling factor (1/9 scale to prototype scale)**		
	Generalized scaling factors	**$\lambda_\varepsilon = \lambda^{0.5}$, λ_ρ=1**	**CASE of λ = 9**
Length	λ	λ	9
Density	λ_ρ	1	1
Time	$(\lambda\lambda_\varepsilon)^{0.5}$	$\lambda^{0.75}$	5.2
Acceleration	1	1	1
Velocity	$(\lambda\lambda_\varepsilon)^{0.5}$	$\lambda^{0.75}$	5.2
Displacement	$\lambda\lambda_\varepsilon$	$\lambda^{1.5}$	27
Stress	$\lambda\lambda_\rho$	λ	9
Strain	λ_ε	$\lambda^{0.5}$	3
Stiffness	$\lambda\lambda_\rho/\lambda_\varepsilon$	$\lambda^{0.5}$	3
EI*	$\lambda^4\lambda_\rho/\lambda_\varepsilon$	$\lambda^{3.5}$	2187
EA*	$\lambda^2\lambda_\rho/\lambda_\varepsilon$	$\lambda^{1.5}$	27
Moment*	$\lambda^3\lambda_\rho$	λ^3	27
Shear*	$\lambda^2\lambda_\rho$	λ^2	729
Axial Force*	$\lambda^2\lambda_\rho$	λ^2	81

*specified per unit length of the tunnel along its longitudinal axis (based on 2D Plane Strain)

Table 5-2: Measured soil material properties prior the test

Layer	Depth (ft)	V_s (ft/sec)	V_p (ft/sec)	Shear modulus (ksi)	Poisson's ratio
1	0 – 18	1044	2823	26.562	0.421
2	18 – 54	1044	2823	26.562	0.421
3	54 – 81	1131	3750	31.173	0.450
4	81 - 108	2223	4500	120.431	0.339

Table 5-3: Ratio of the racking of the tunnel to the free-field displacement during the 1st test

Tunnel	Ground		Ratio of the racking to the free-field
Drift ratio (racking) of the tunnel	Relative displacement at levels of the roof to the slab (in)	Distance from the tunnel wall (ft)	
1% (2.5 in)	2.4	9 (south side)	1.0
	3.7	9 (north side))	0.7
	5.6	45 (north side)	0.4
1.5% (3.7 in)	4.2	9 (south side)	0.9
	6.4	9 (north side))	0.6
	9.4	45 (north side)	0.4
2% (4.9 in)	7.0	9 (south side)	0.7
	10.4	9 (north side))	0.5
	14.7	45 (north side)	0.3

Table 5-4: Ratio of the racking of the tunnel to the free-field displacement during the 2nd test

Tunnel	Ground		Ratio of the racking to the free-field
Drift ratio (racking displacement) of the tunnel	Relative displacement at levels of the roof to the slab (in)	Distance from the tunnel wall (ft)	
0.3% (0.7 in)	1.3	9 (south side)	0.5
	1.6	9 (north side))	0.4
	2.7	45 (north side)	0.3
0.6% (1.5 in)	3.3	9 (south side)	0.5
	4.1	9 (north side))	0.4
	6.6	45 (north side)	0.2
0.9% (2.2 in)	6.8	9 (south side)	0.3
	7.6	9 (north side))	0.3
	11.2	45 (north side)	0.2

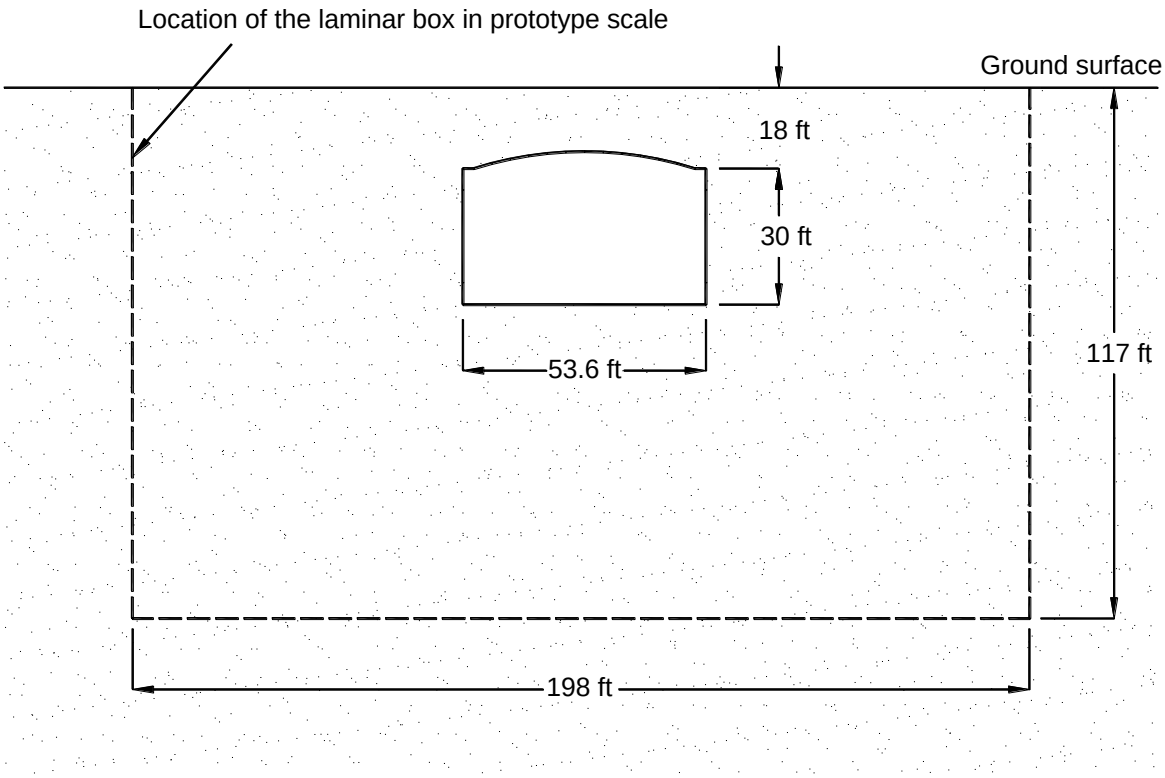

Figure 5-1: Schematic view of the soil-tunnel system in the original test (in prototype scale).

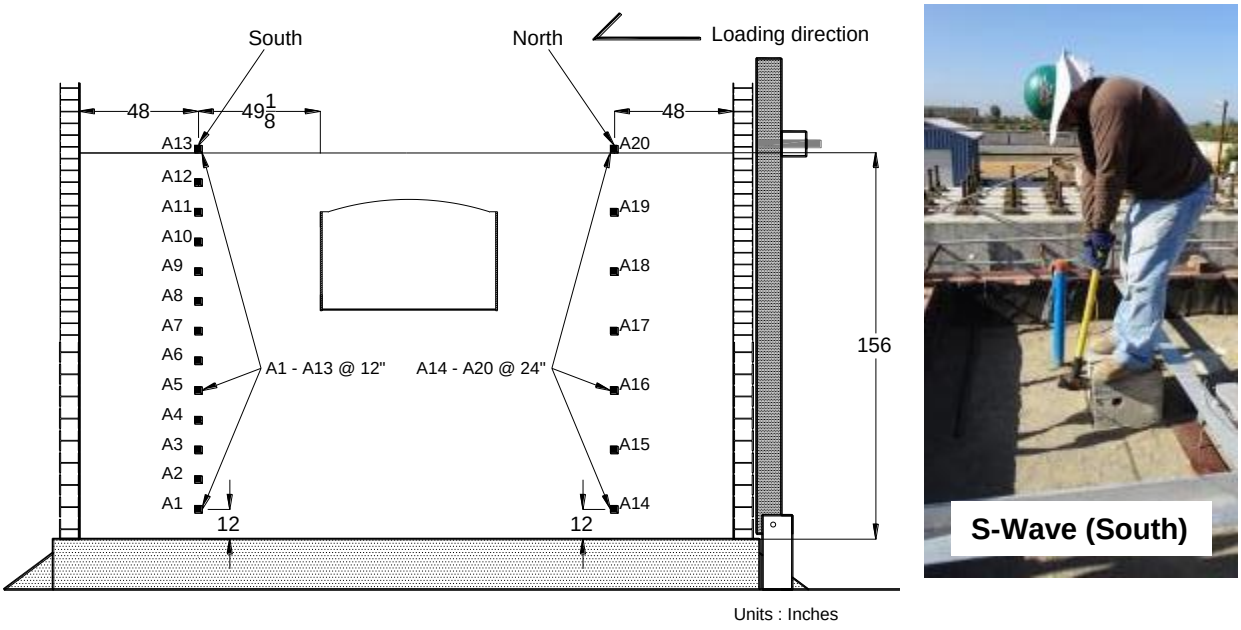

Figure 5-2: Schematic of model and accelerometers to measure shear wave velocity propagation (triggered by a hammer impact on the soil surface as shown in the photograph)

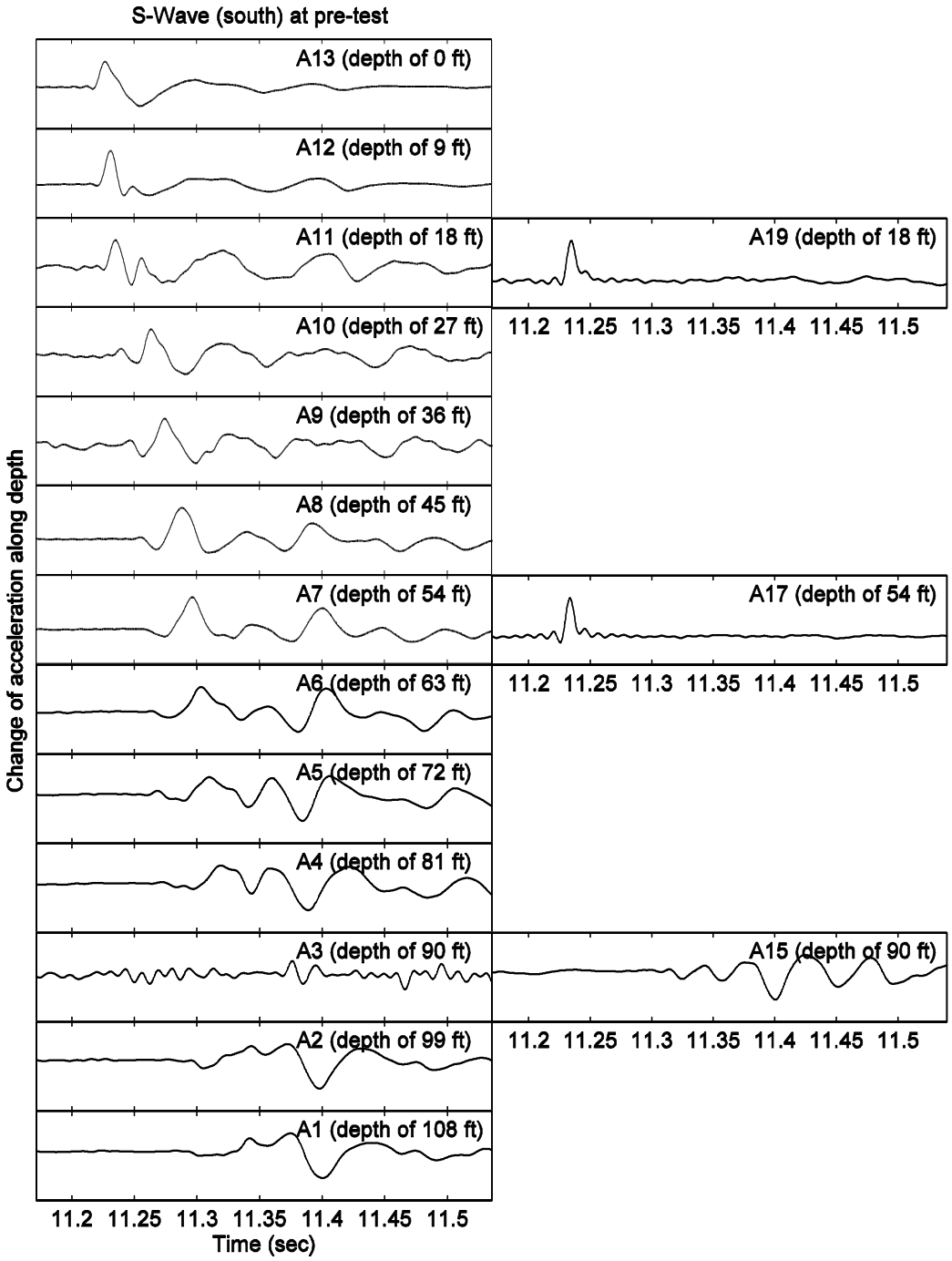

Figure 5-3: Acceleration time history for measurement of shear wave velocity (wave triggered at South array prior to testing)

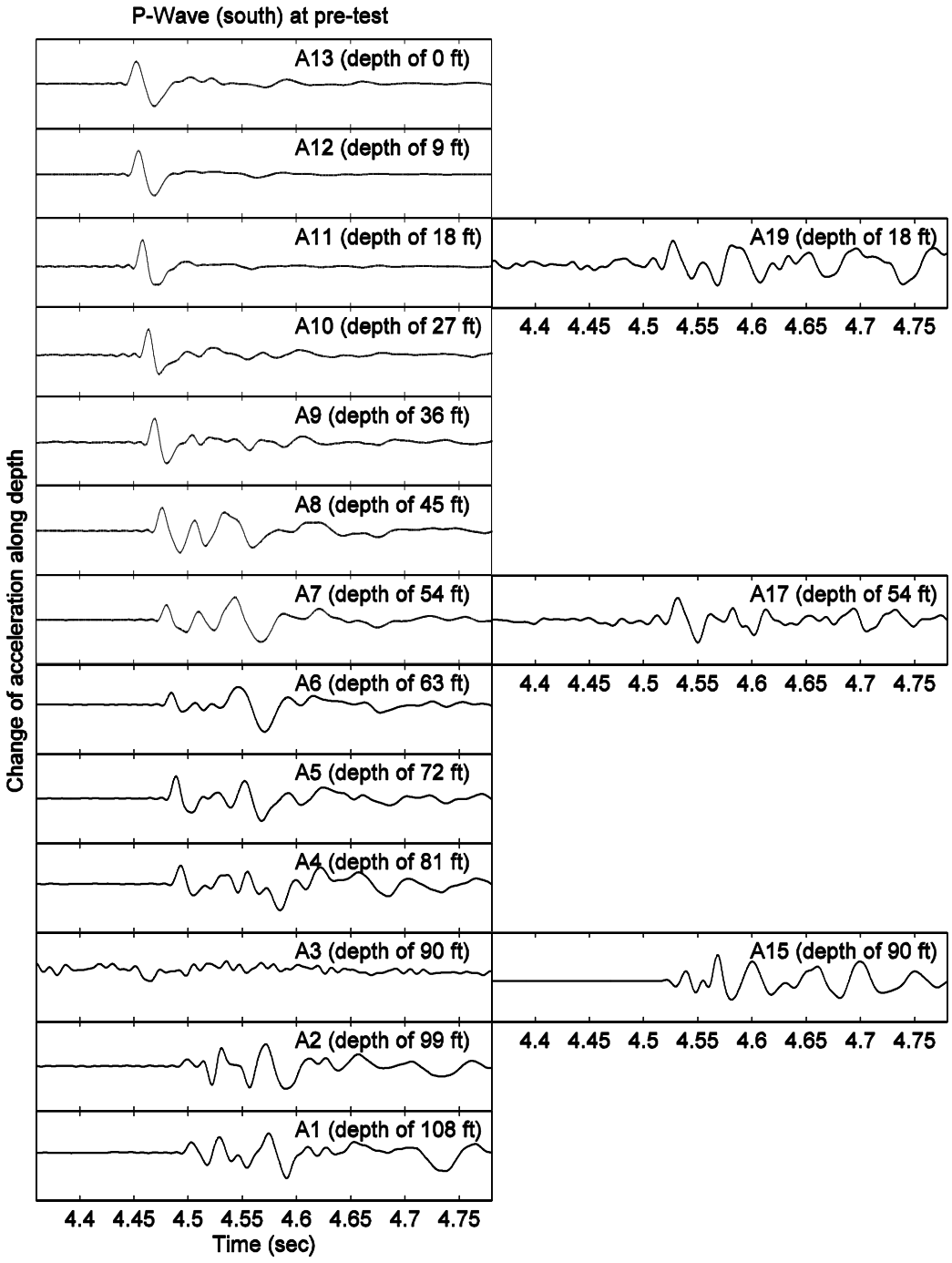

Figure 5-4: Acceleration time history for measurement of P-wave velocity (wave triggered at South array prior to testing)

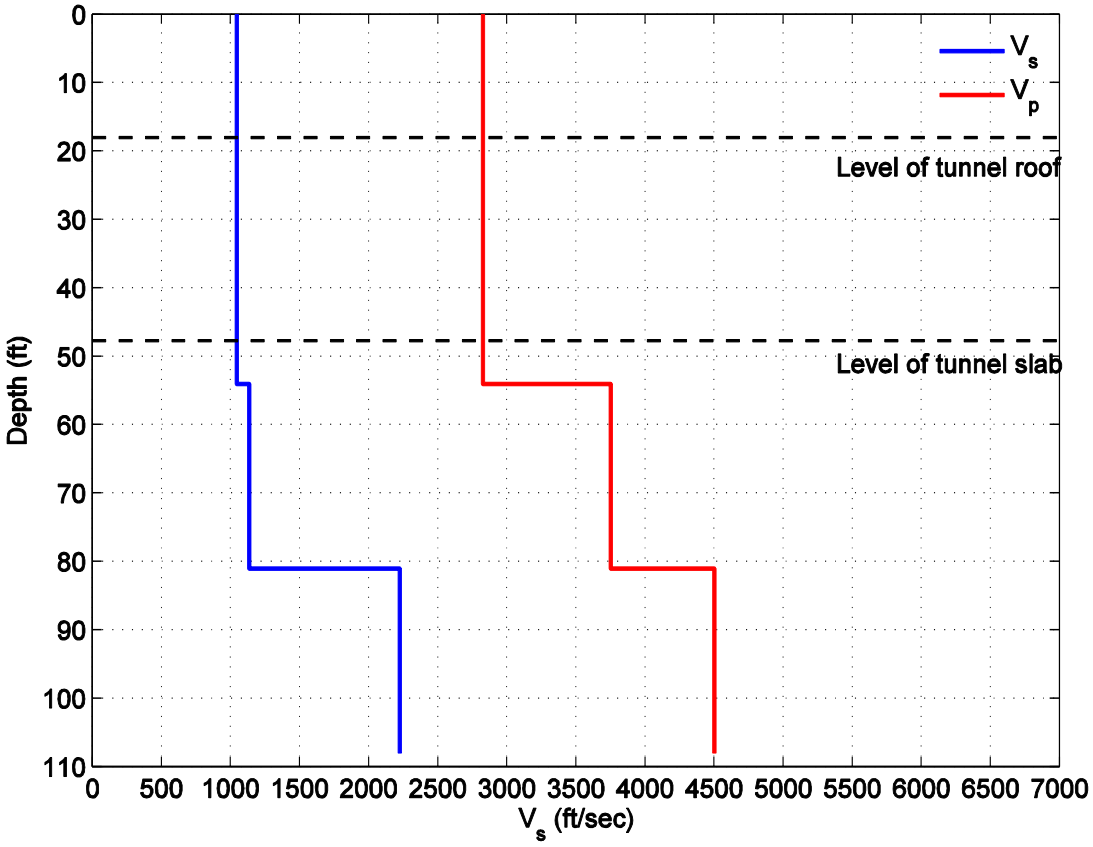

Figure 5-5: Estimated S-wave and P-wave profile along the depth of the soil prior the testing

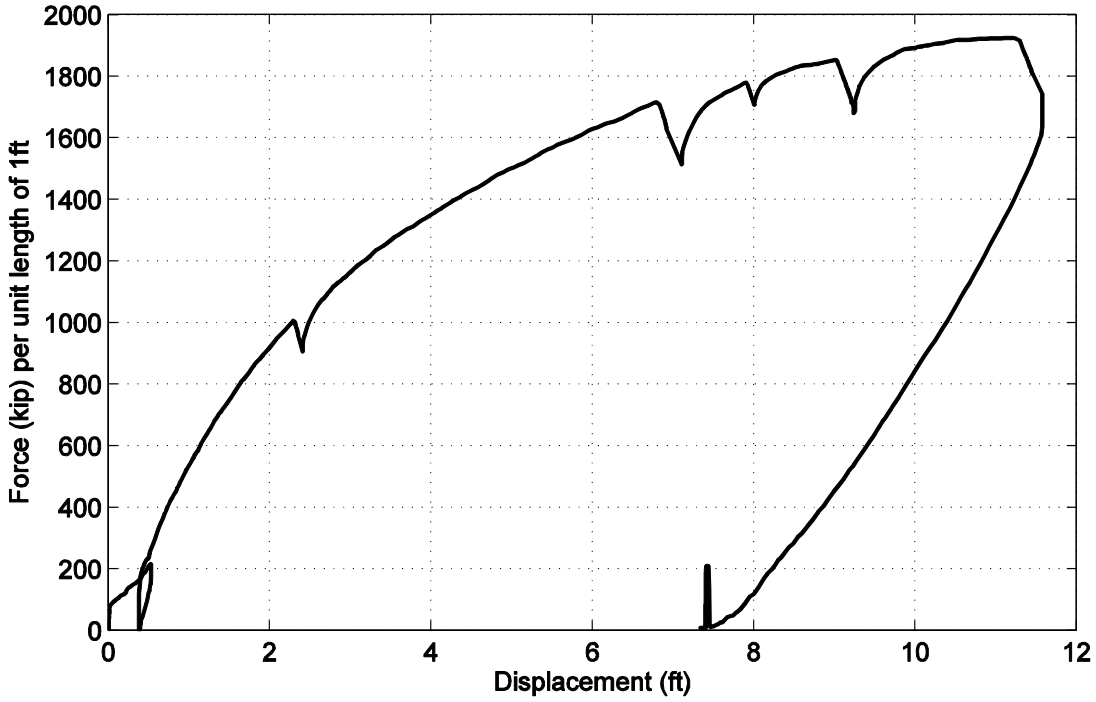

Figure 5-6: Lateral force vs. displacement measured at soil surface in the laminar container (tunnel buried)

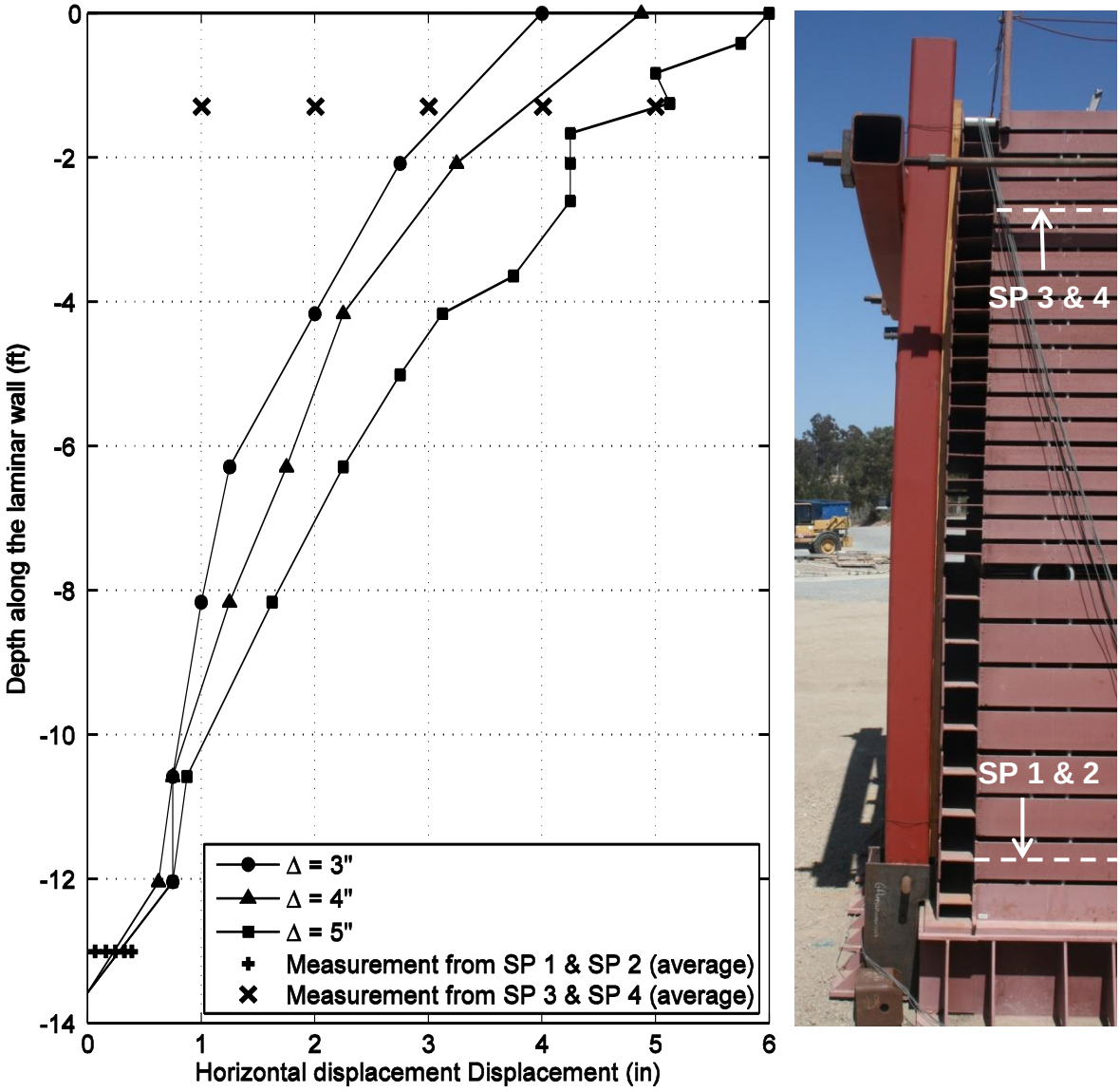

Figure 5-7: Measured lateral loading displacement profile along height of the laminar container (south side, shown in model scale)

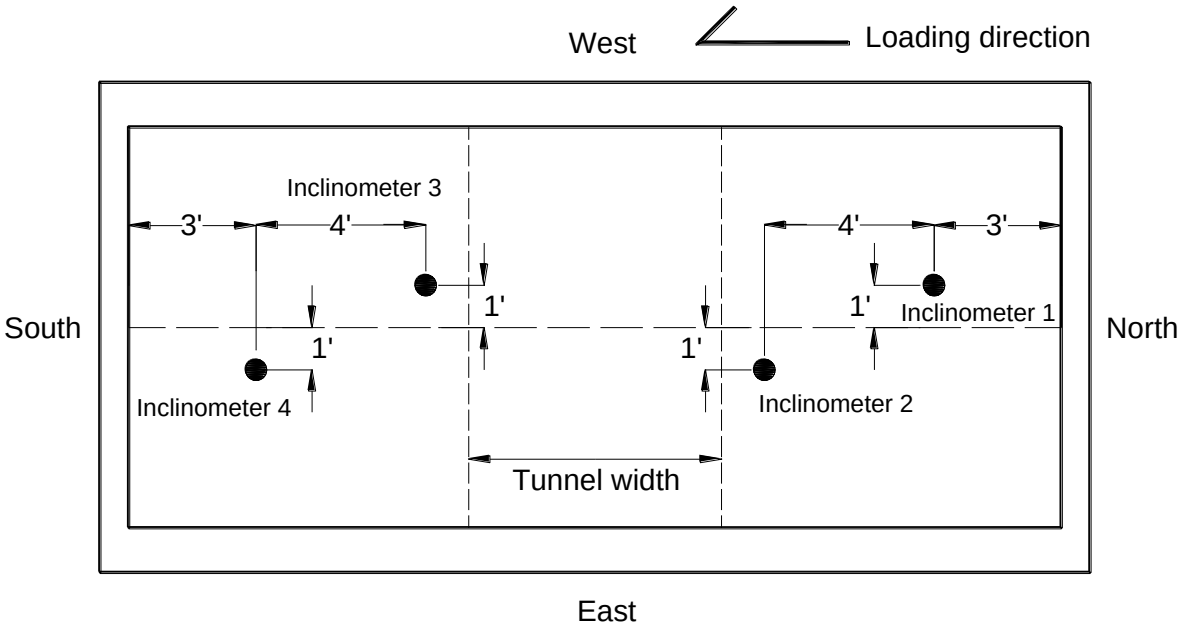

Figure 5-8: Location of inclinometers in plan view

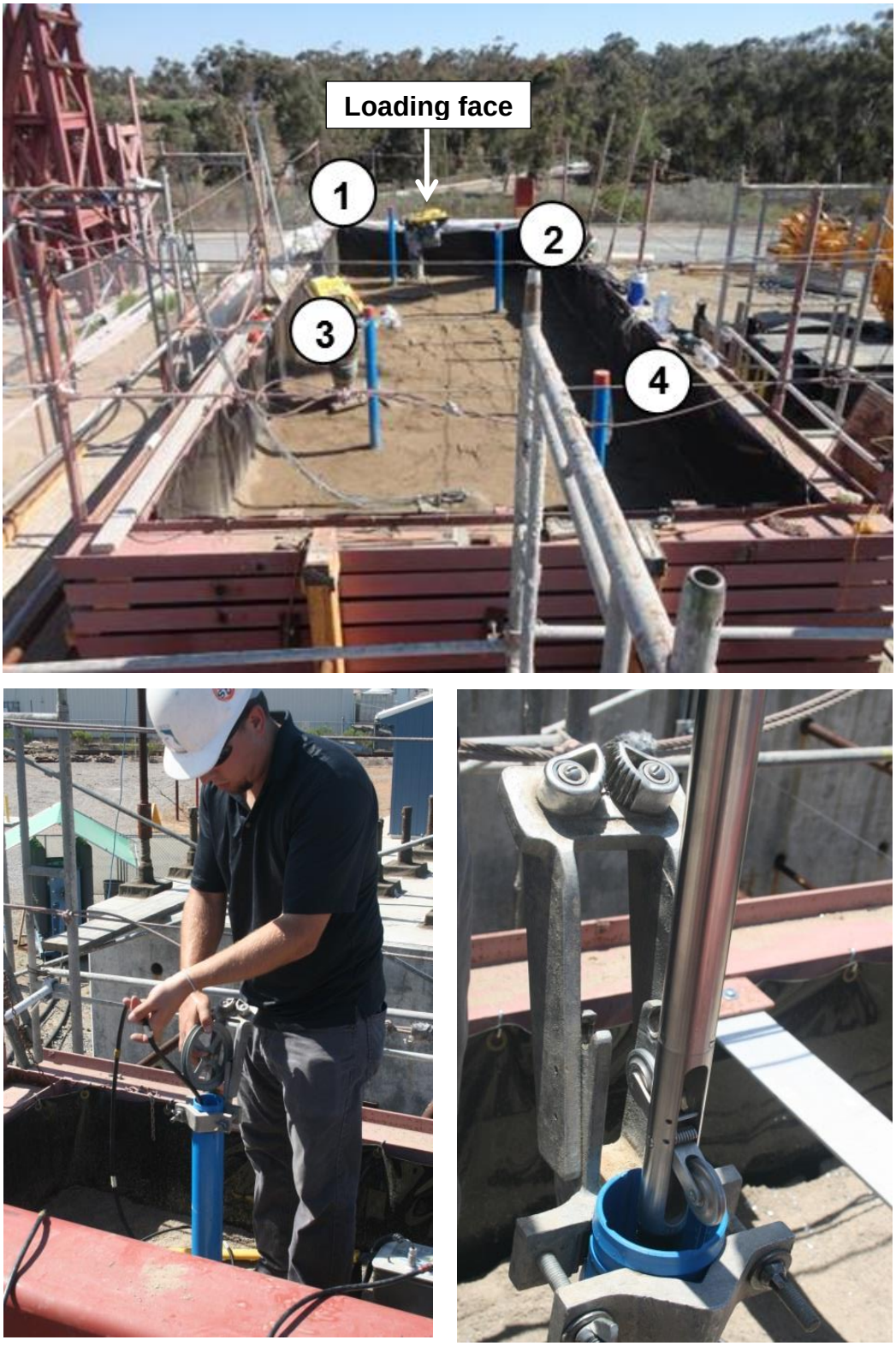

Figure 5-9: Inclinometer measurement during the test

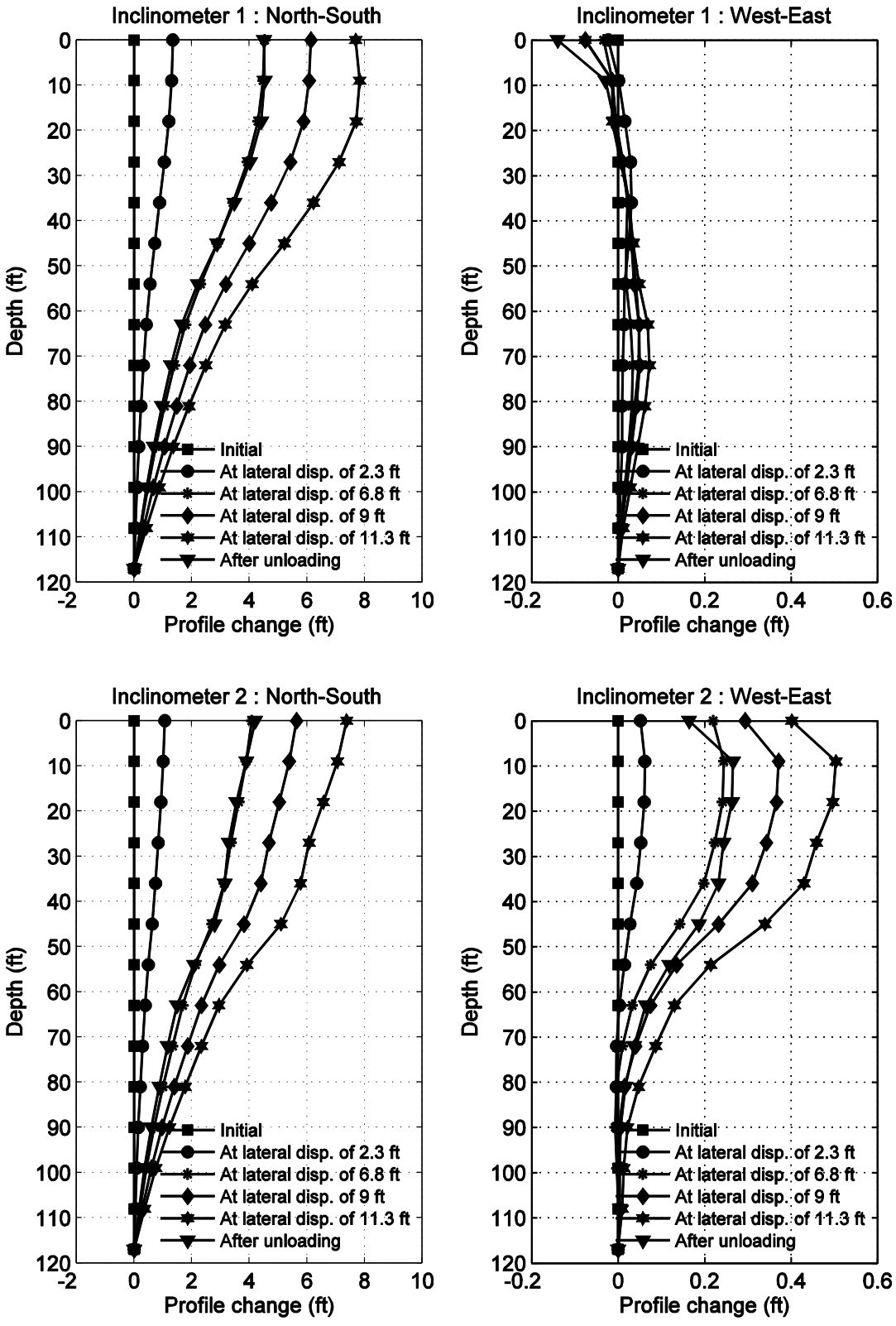

Figure 5-10: Soil deformation measured from inclinometers in North-South (loading) and West-East directions (cont.)

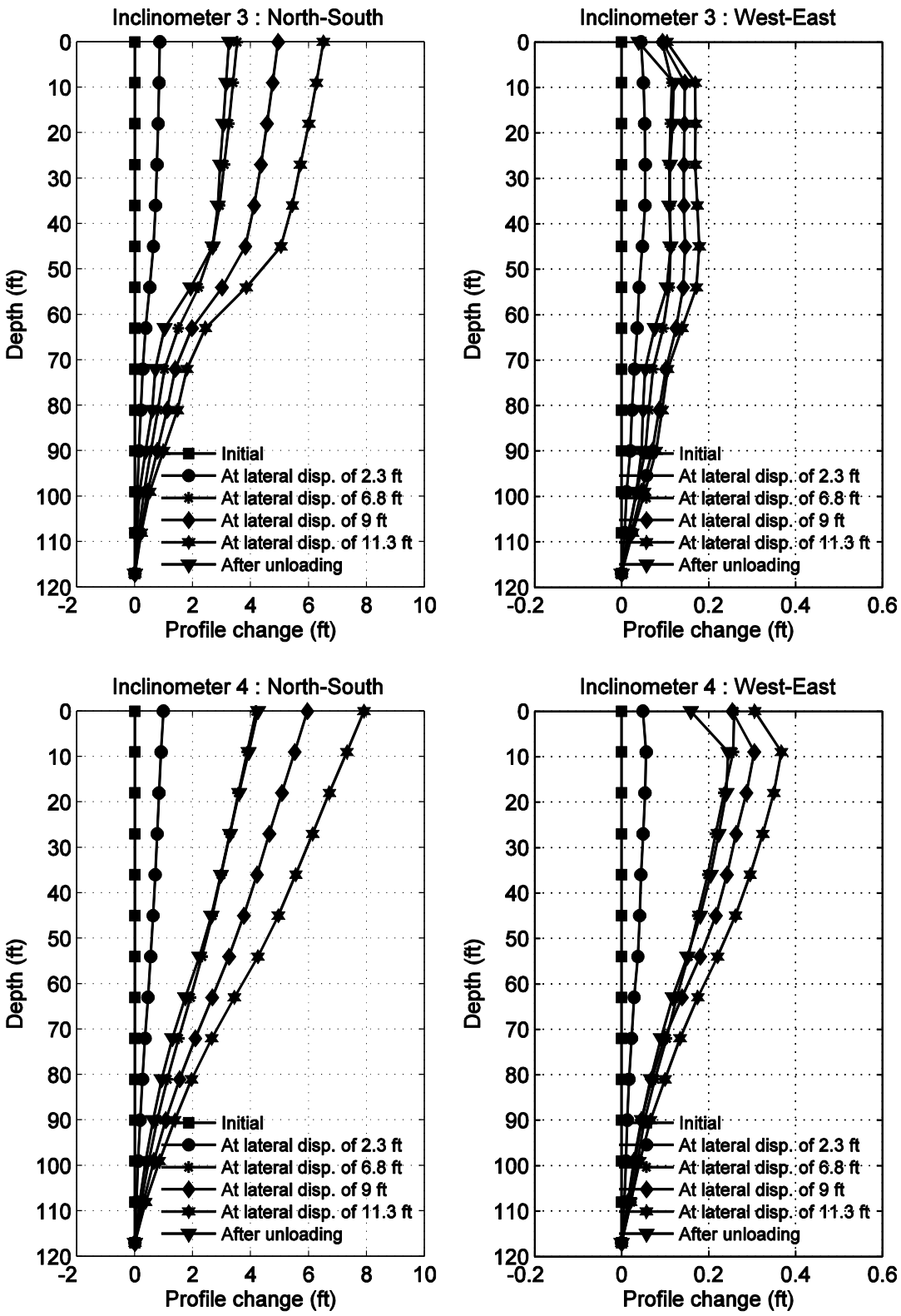

Figure 5-10 (continued): Soil deformation measured from inclinometers in North-South (loading) and West-East directions

Figure 5-11: Soil separation on south side of laminar container

Figure 5-12: Photographs of linear potentiometers on soil surface

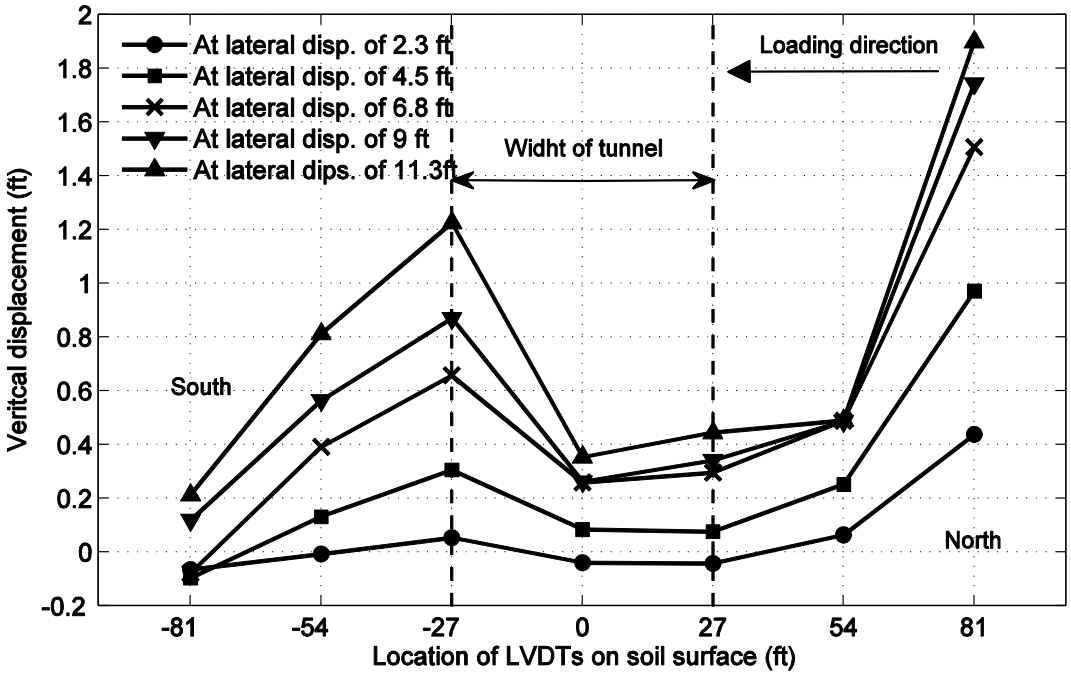

Figure 5-13: Vertical deformation on soil surface measured from linear potentiometers (prototype scale)

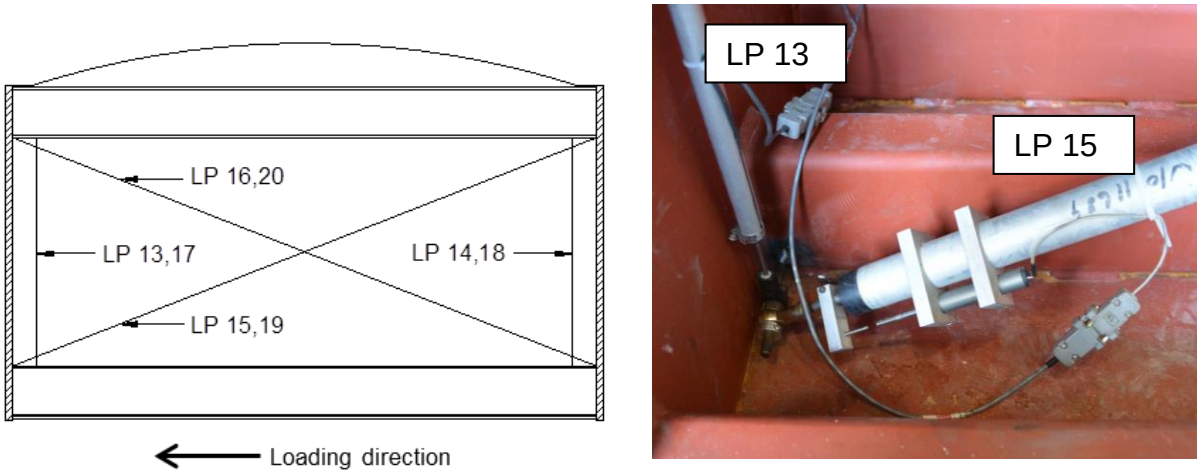

Figure 5-14: Location of linear potentiometers inside the tunnel specimen

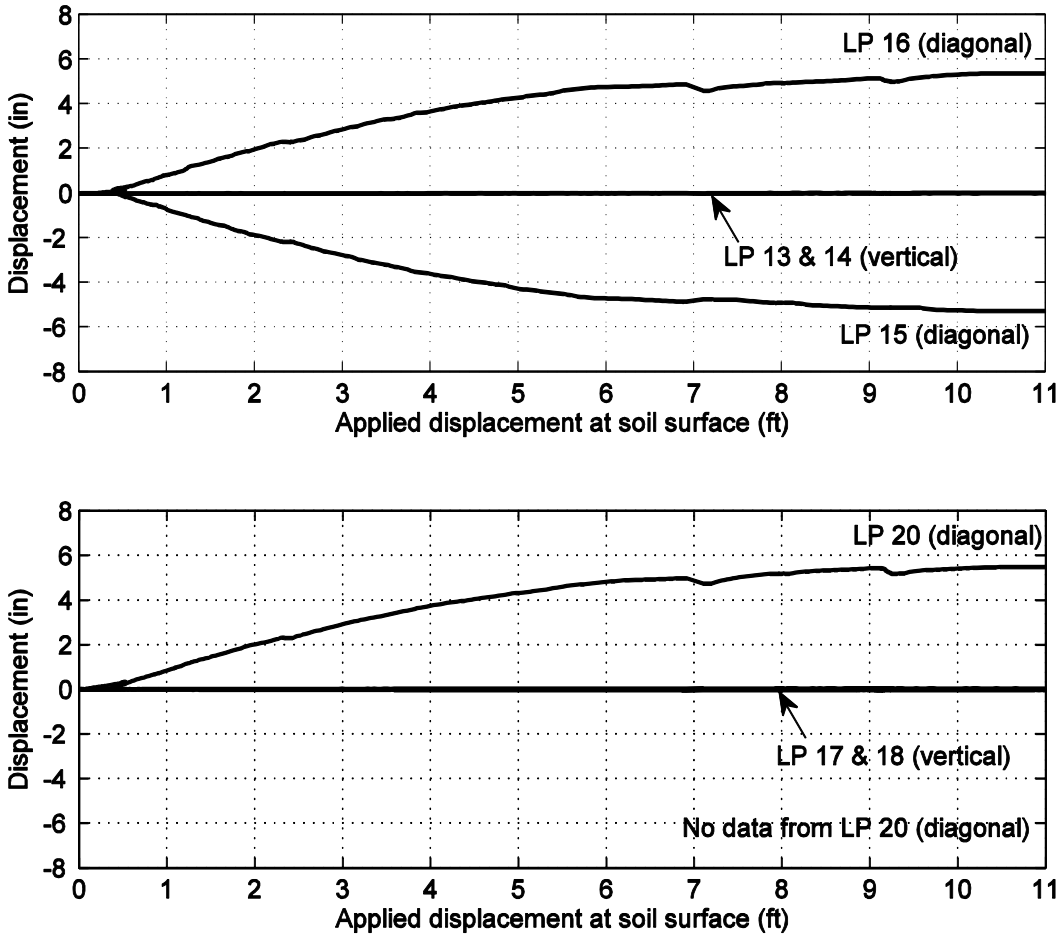

Figure 5-15: Displacement measured from linear potentiometers installed inside tunnel

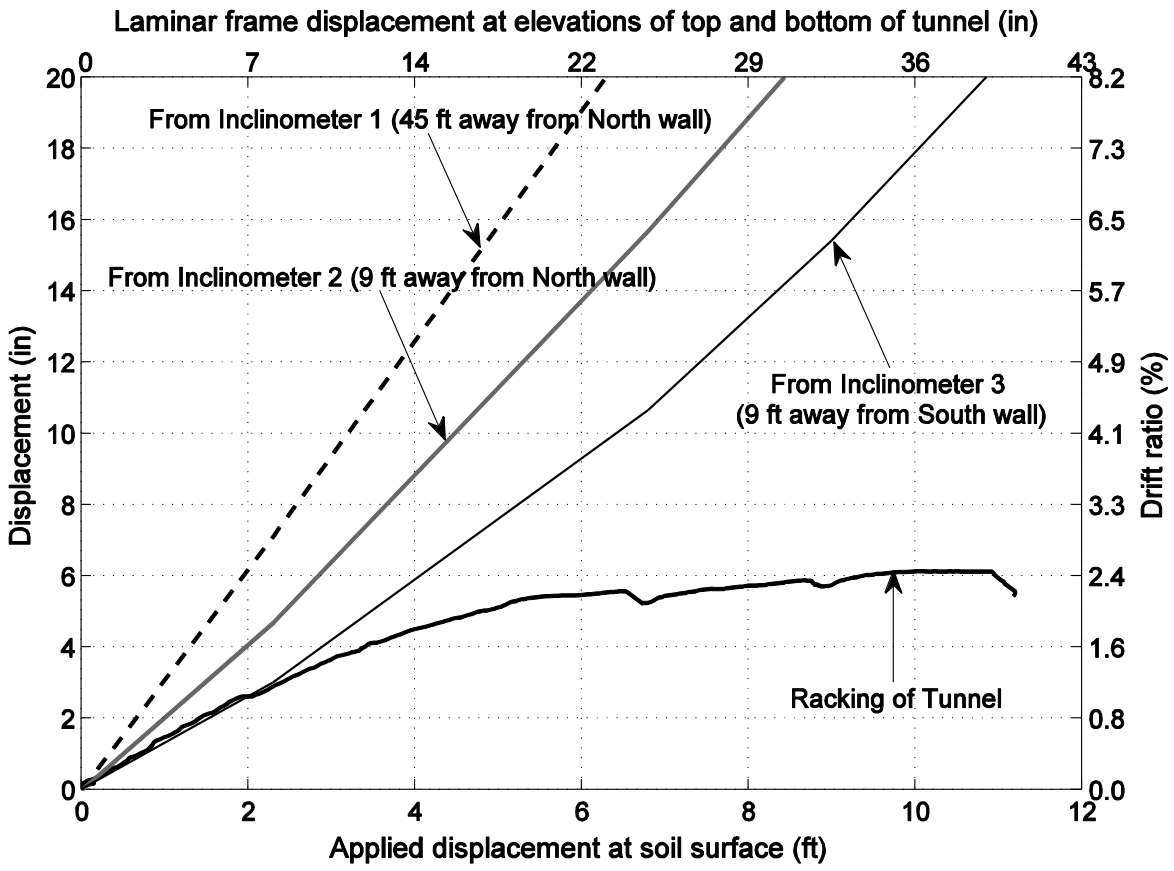

Figure 5-16: Comparison of lateral deformation (racking) of the tunnel with the soil relative displacement (levels of the tunnel roof relative to the tunnel slab), measured from inclinometers

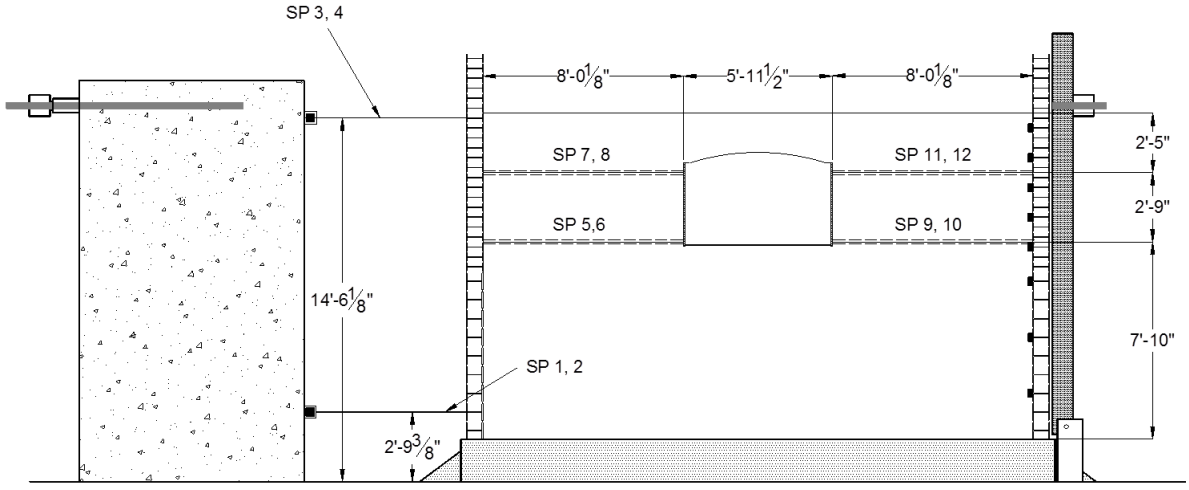

(a) Elevation view

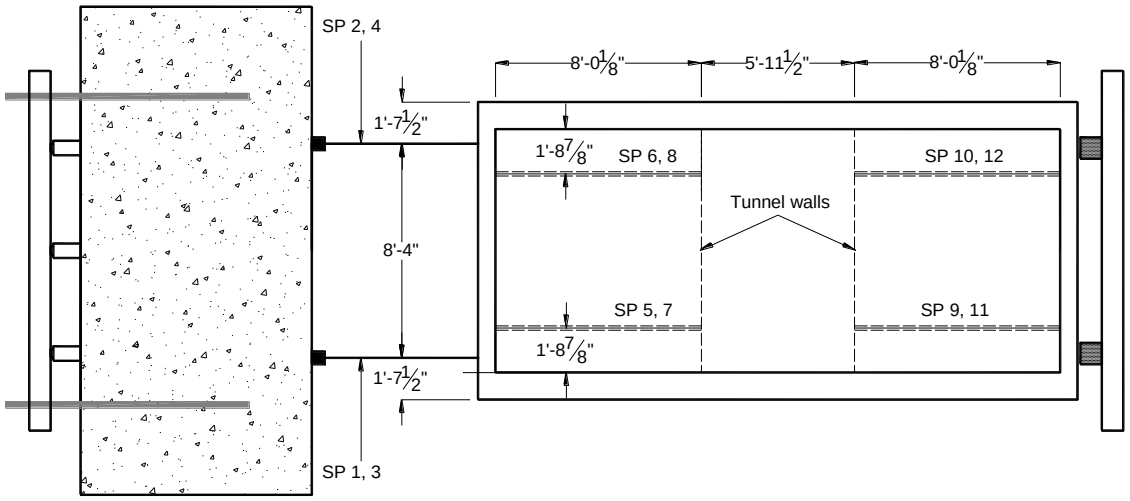

(b) Plan view

Figure 5-17: Instrumentation layout of string potentiometers to measure translations of the tunnel inside the container

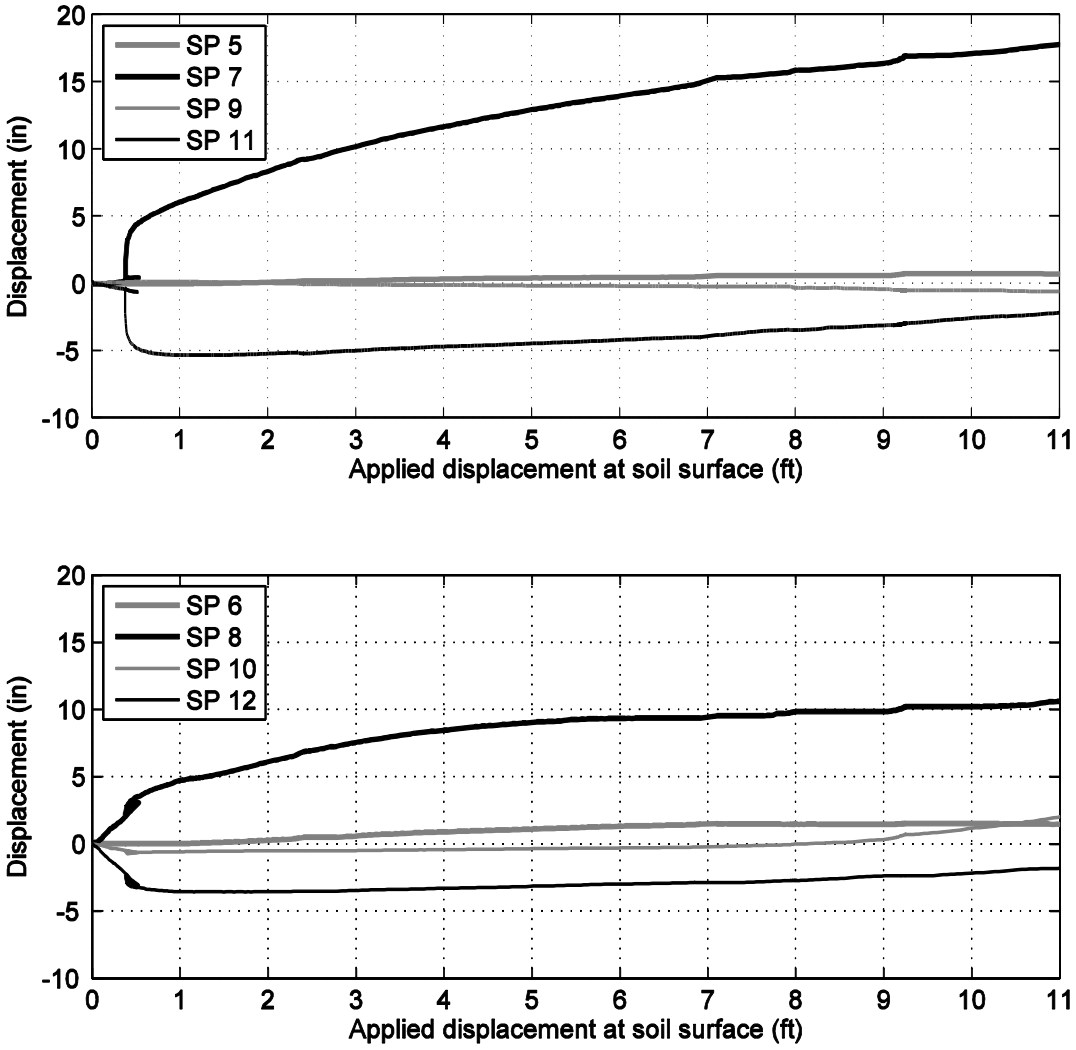

Figure 5-18: Lateral displacement measured from string potentiometers at levels of top and bottom of tunnel walls inside laminar container

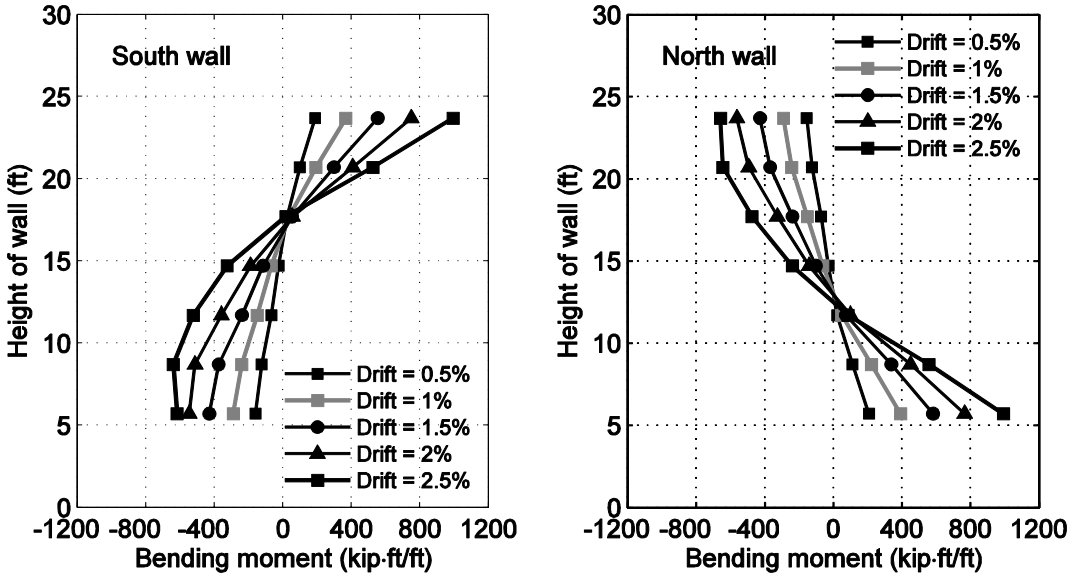

Figure 5-19: Variation of bending moment profile along tunnel walls

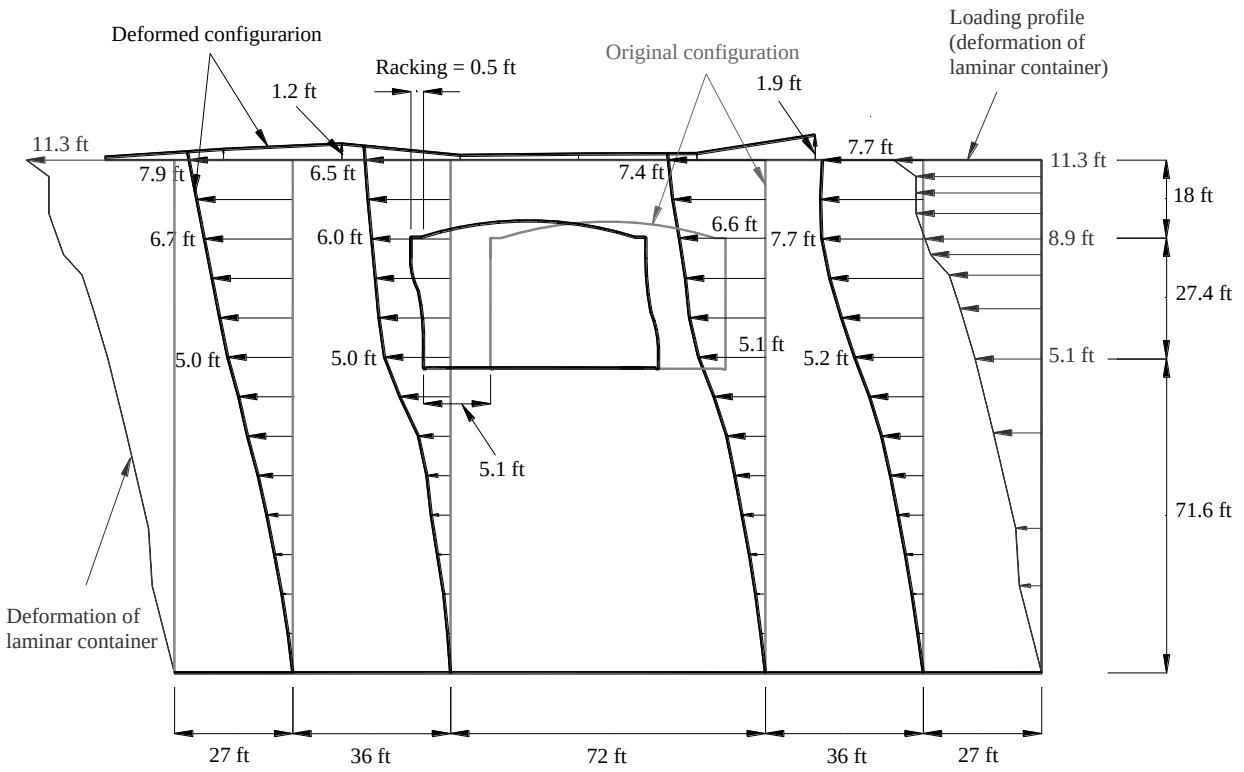

Figure 5-20: Lateral displacement measured from string potentiometers at levels of top and bottom of tunnel walls inside laminar container

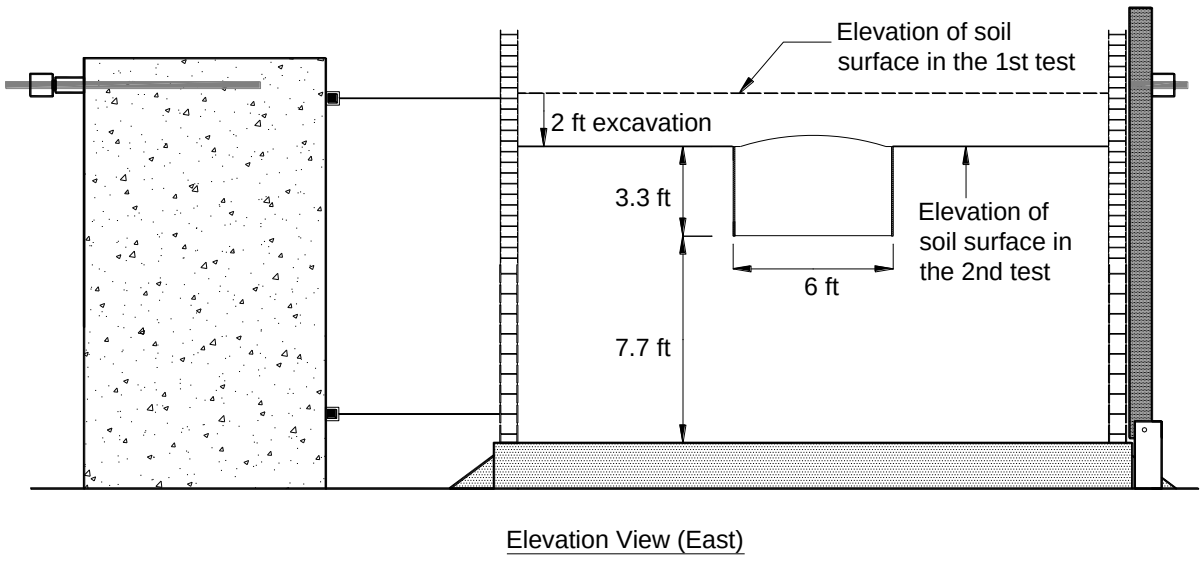

Figure 5-21: Schematic elevation view of soil configuration for 2nd test

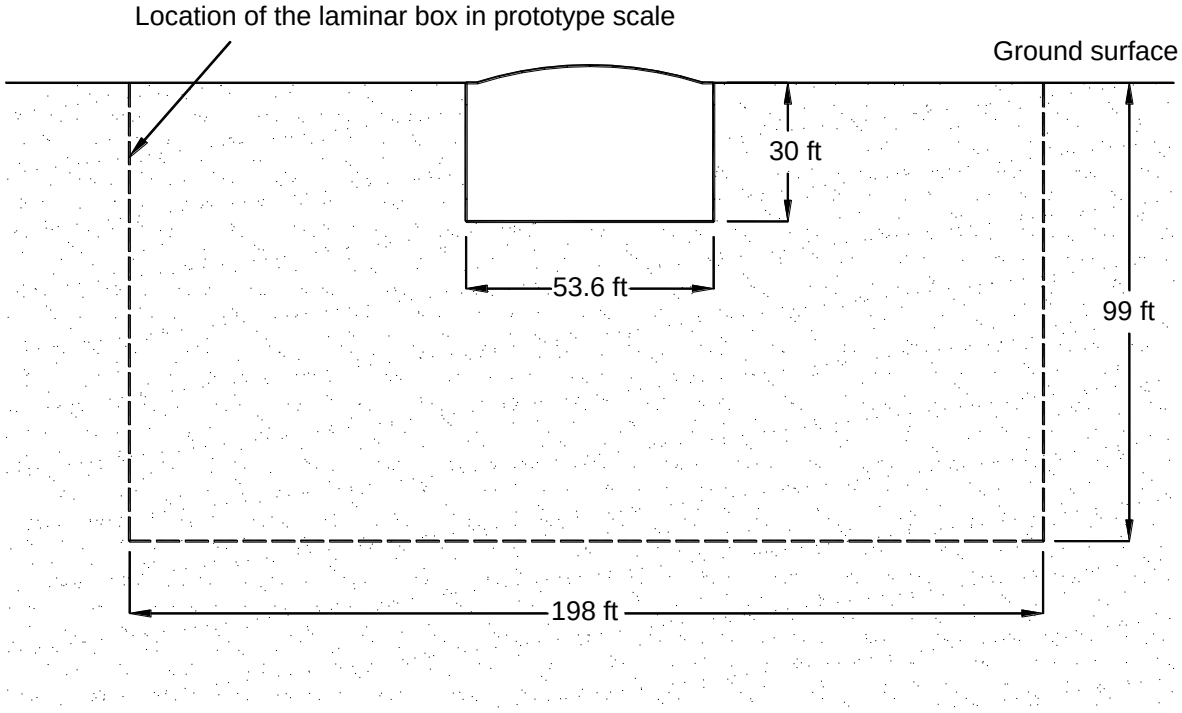

Figure 5-22: Schematic view of the soil-tunnel system in the 2nd test (in prototype scale)

Figure 5-23: Photograph of soil surface configuration for 2nd test

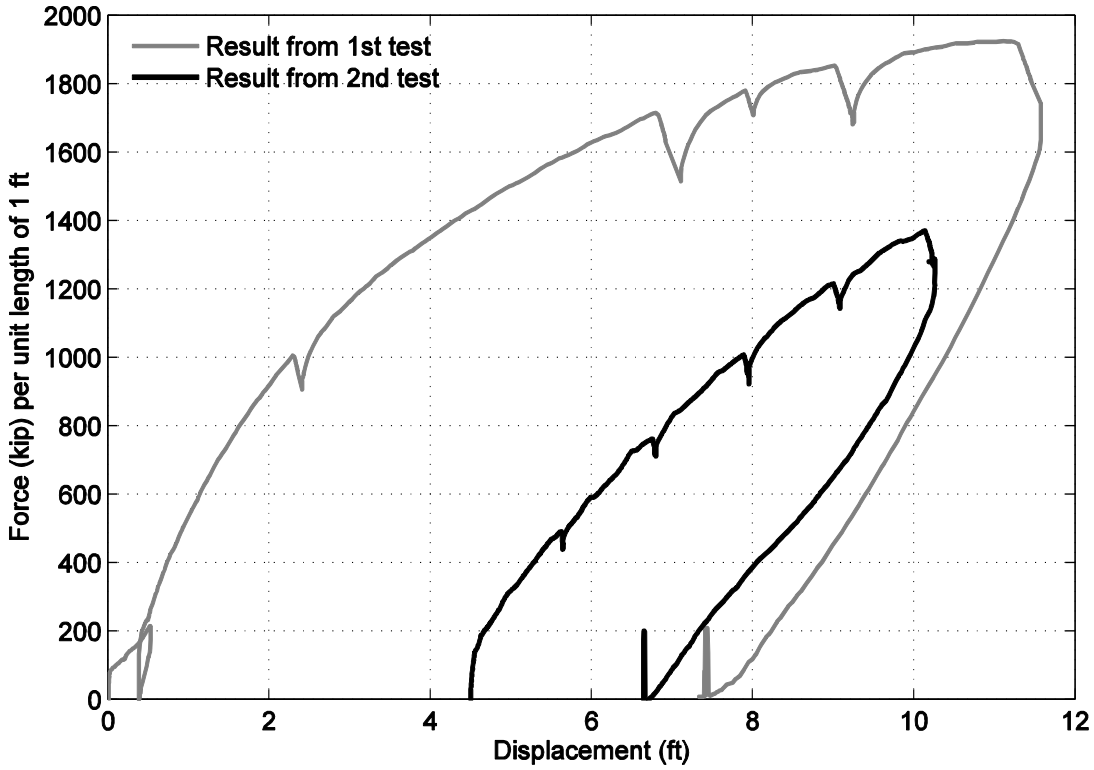

Figure 5-24: Lateral force vs. displacement at top of the laminar container in the 2nd test with residual displacement from the 1st test in prototype scale

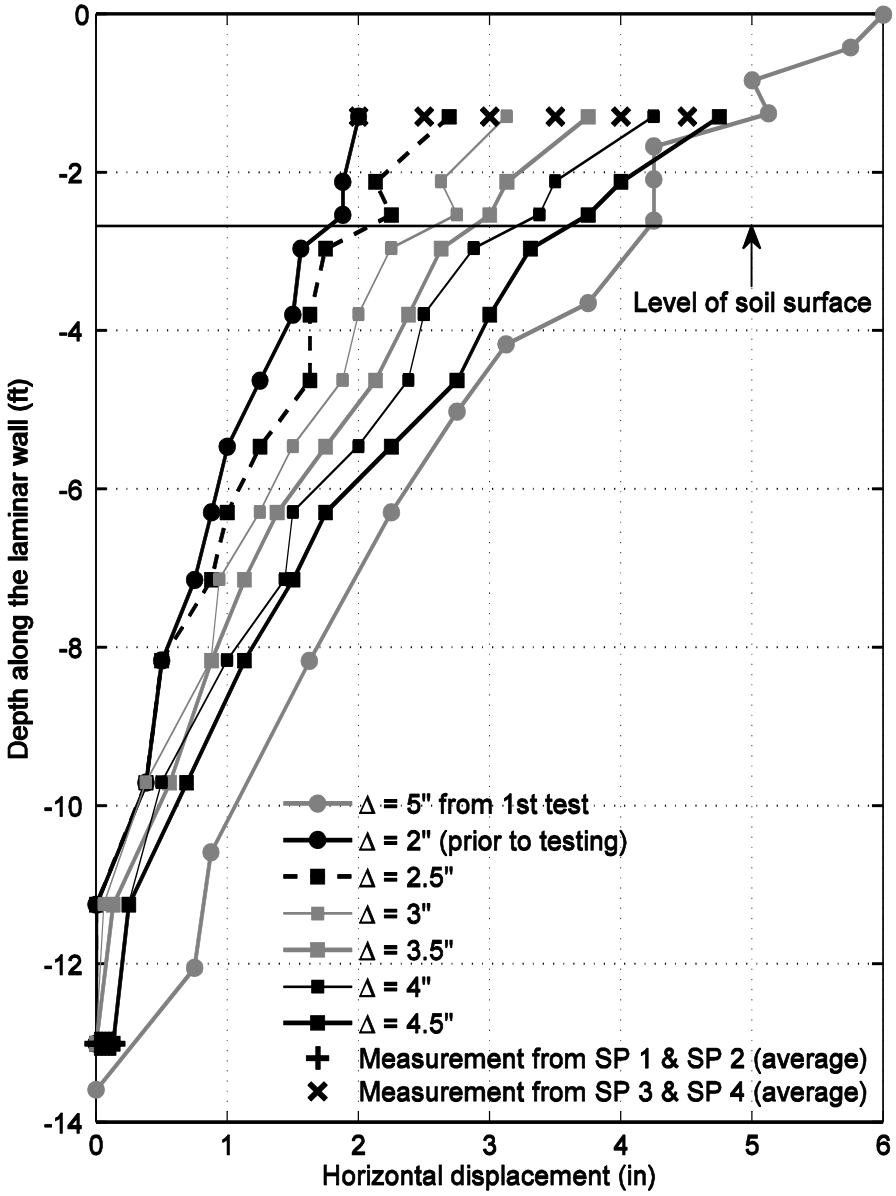

Figure 5-25: Measured vertical displacement profile in the 2nd test (south side, shown in model scale)

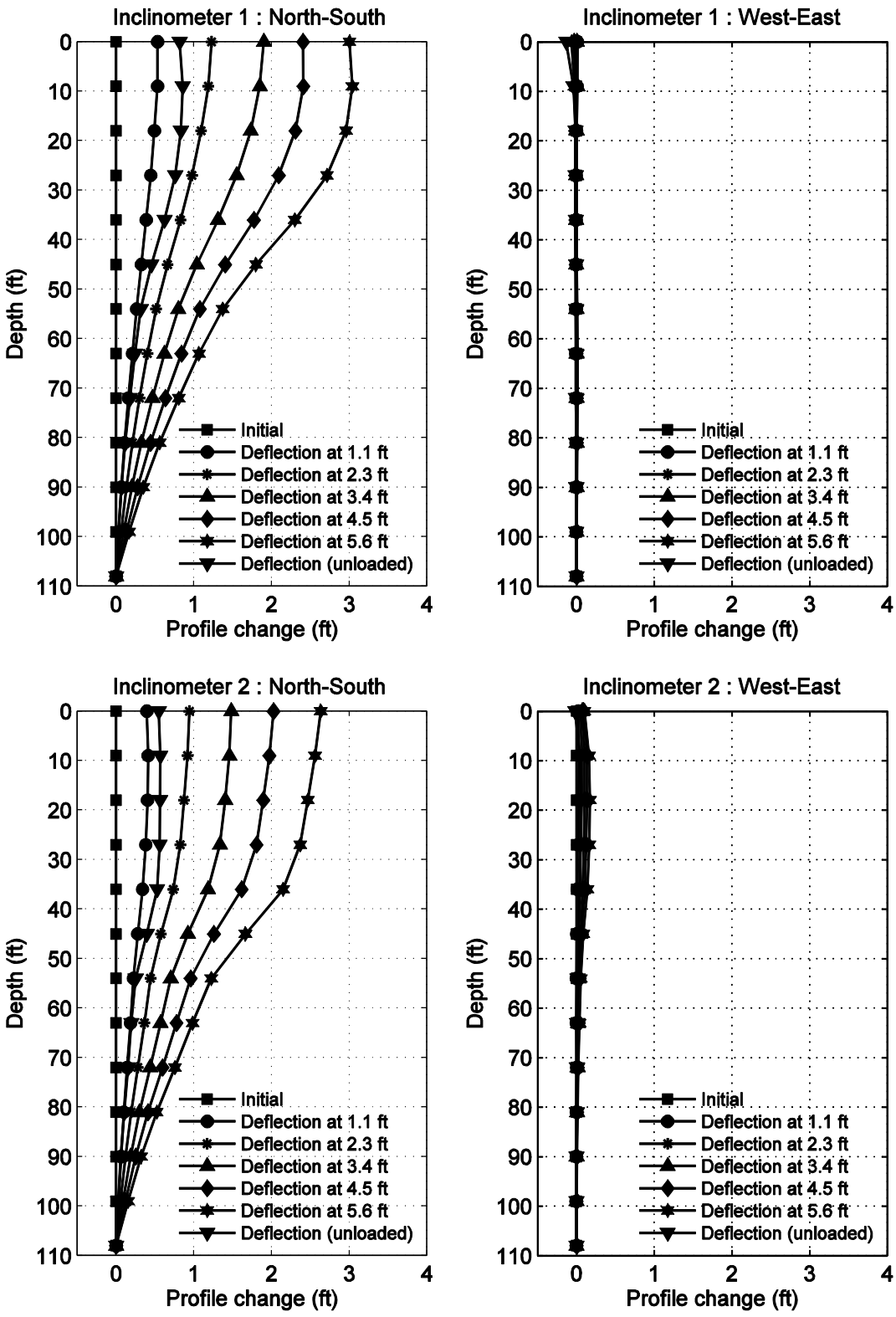

Figure 5-26: Soil deformation measured from inclinometers in the 2nd test

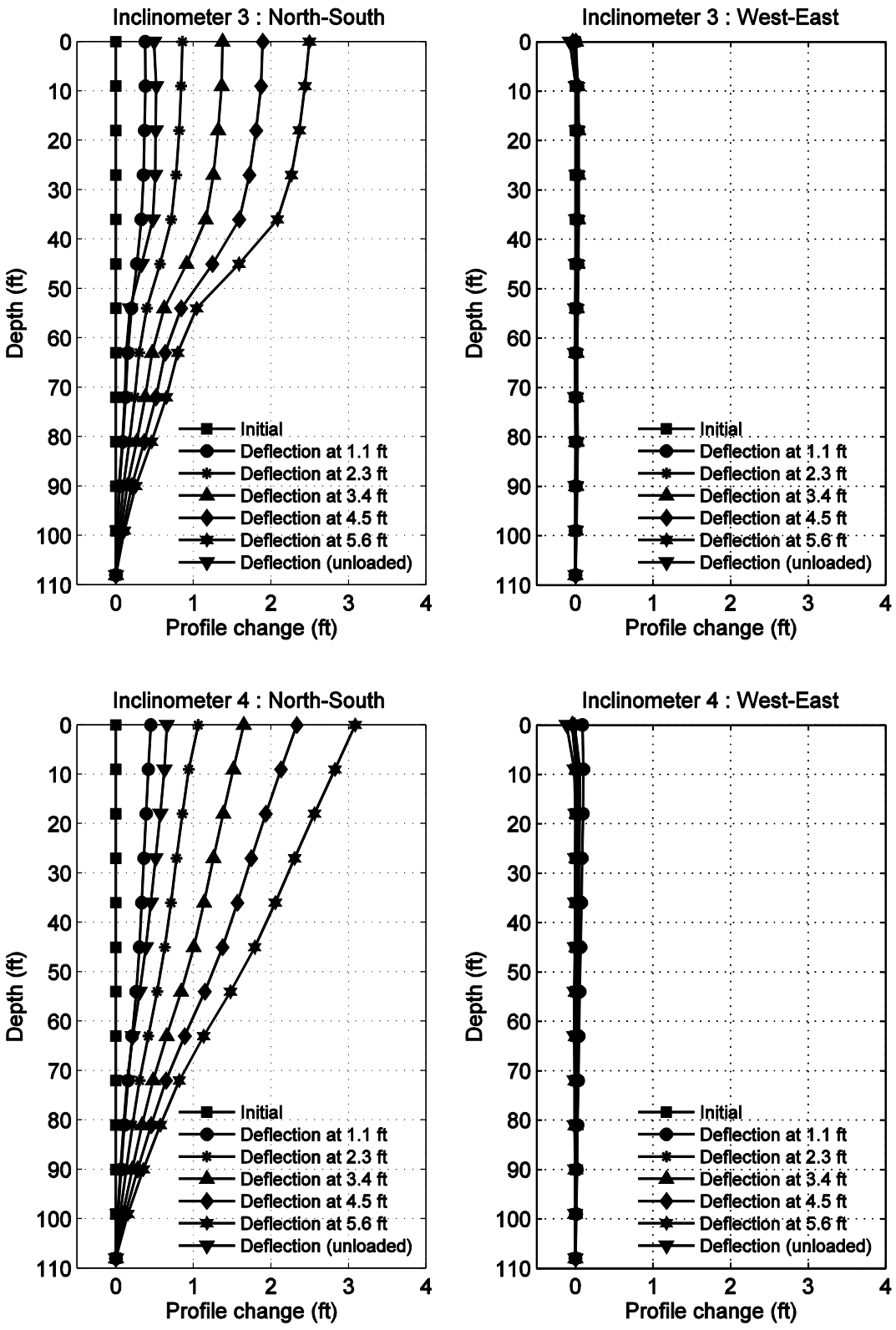

Figure 5-26: (continued) Soil deformation measured from inclinometers in the 2nd test

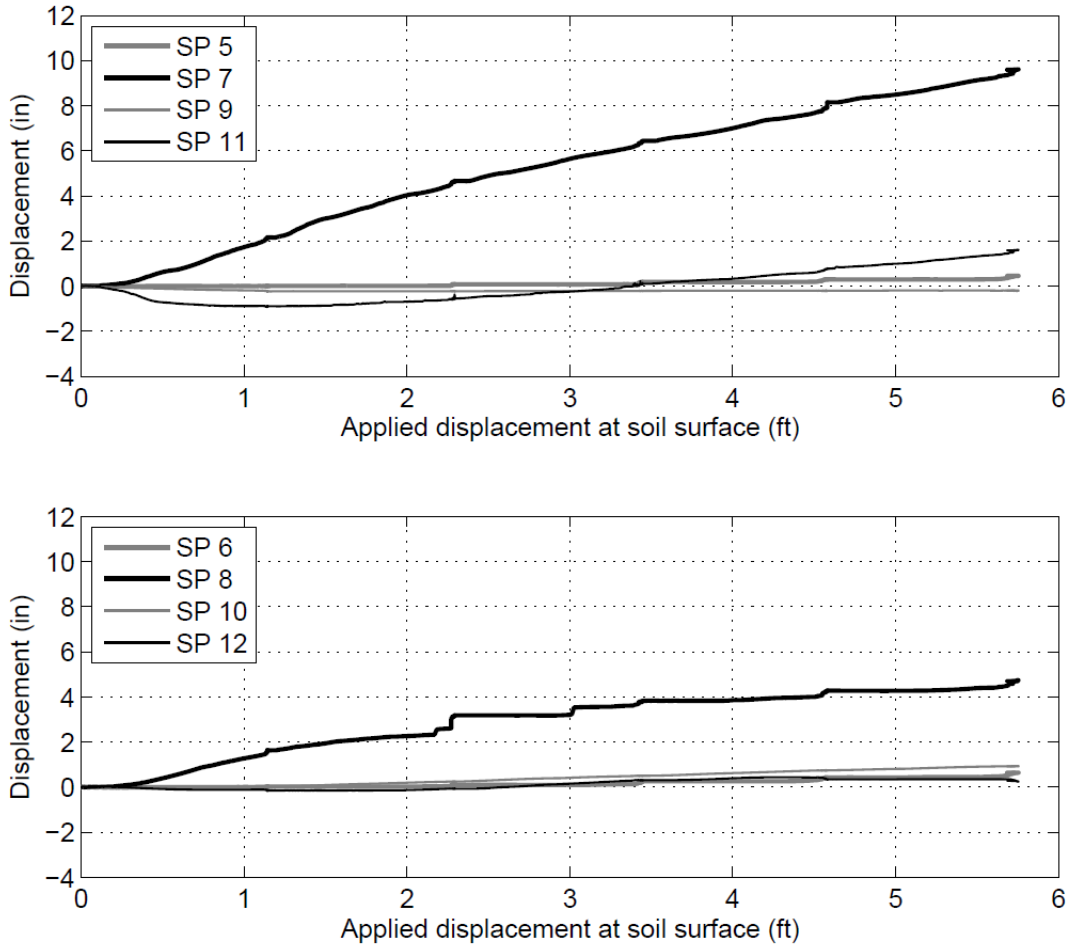

Figure 5-27: Lateral displacement measured from string potentiometers at levels of top and bottom of tunnel walls inside laminar container in the 2nd test

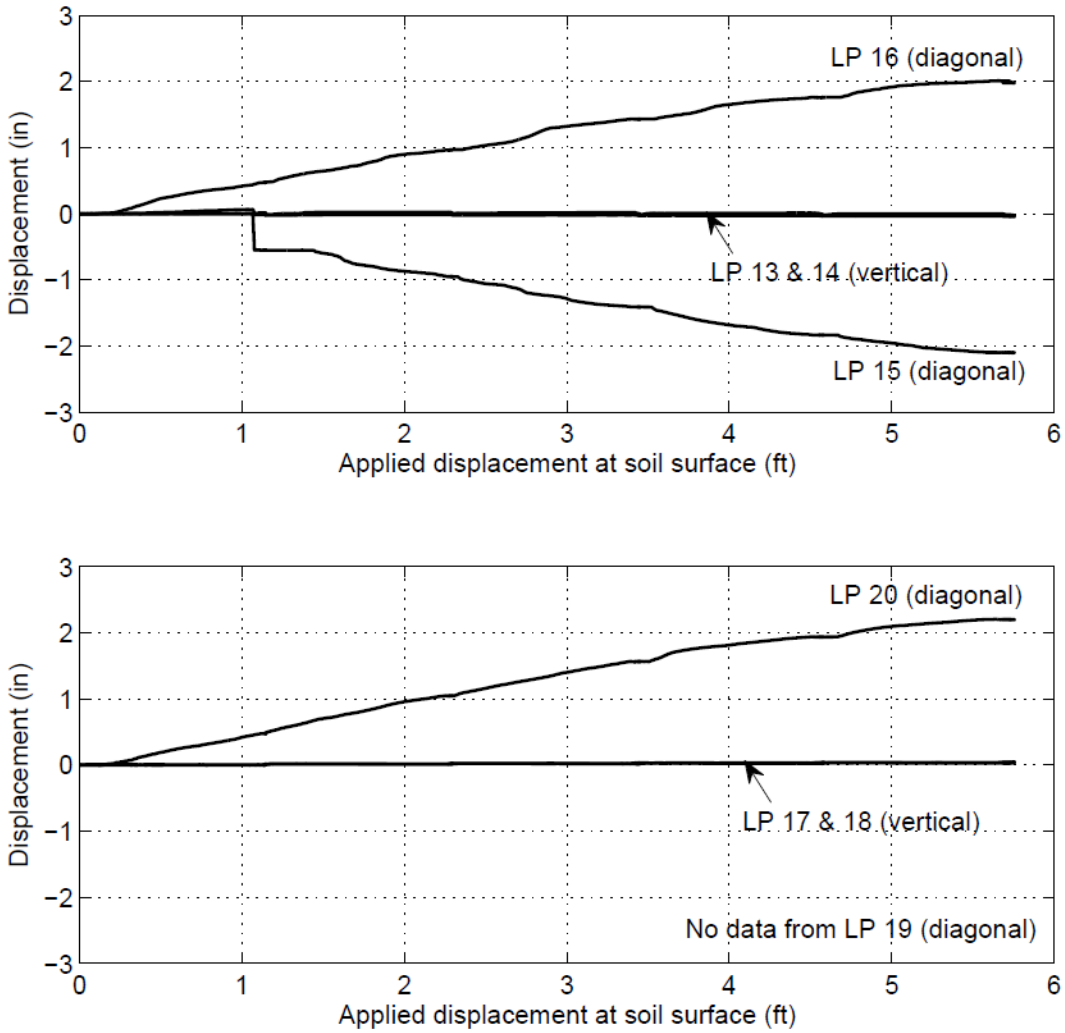

Figure 5-28: Displacement measured from linear potentiometers installed inside tunnel in the 2nd test

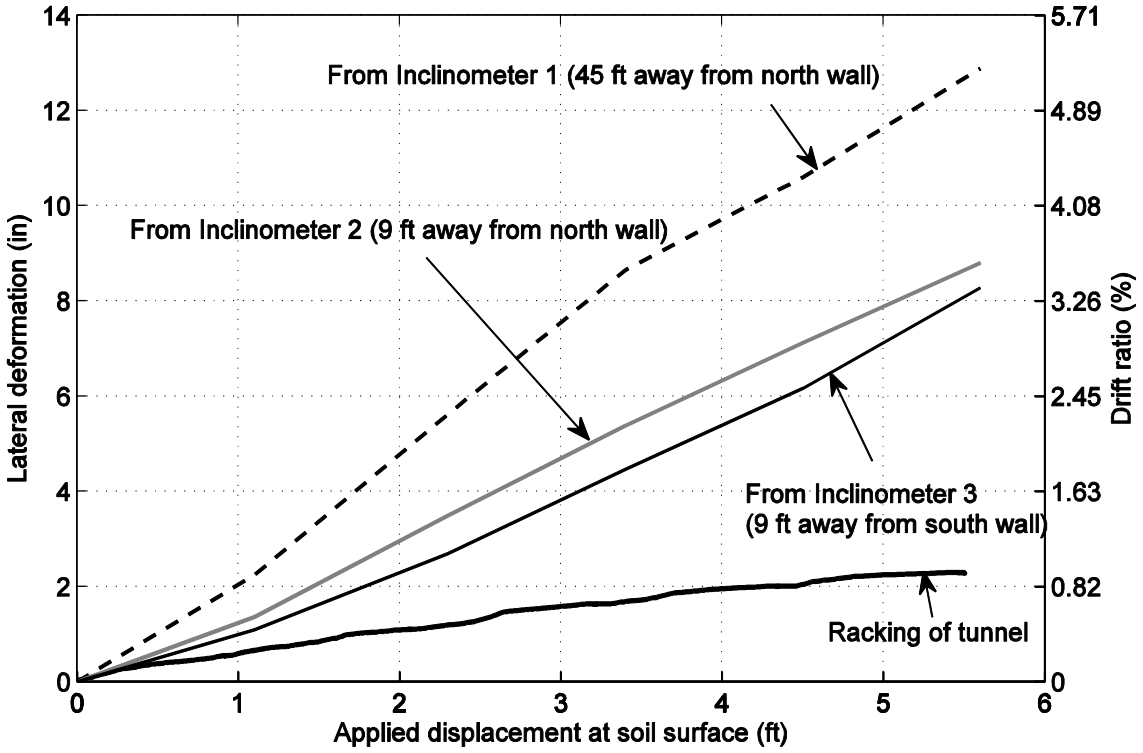

Figure 5-29: Comparison of drift ratio (%; effective height of 20 ft in prototype scale) and lateral deformation of tunnel from the 2nd test

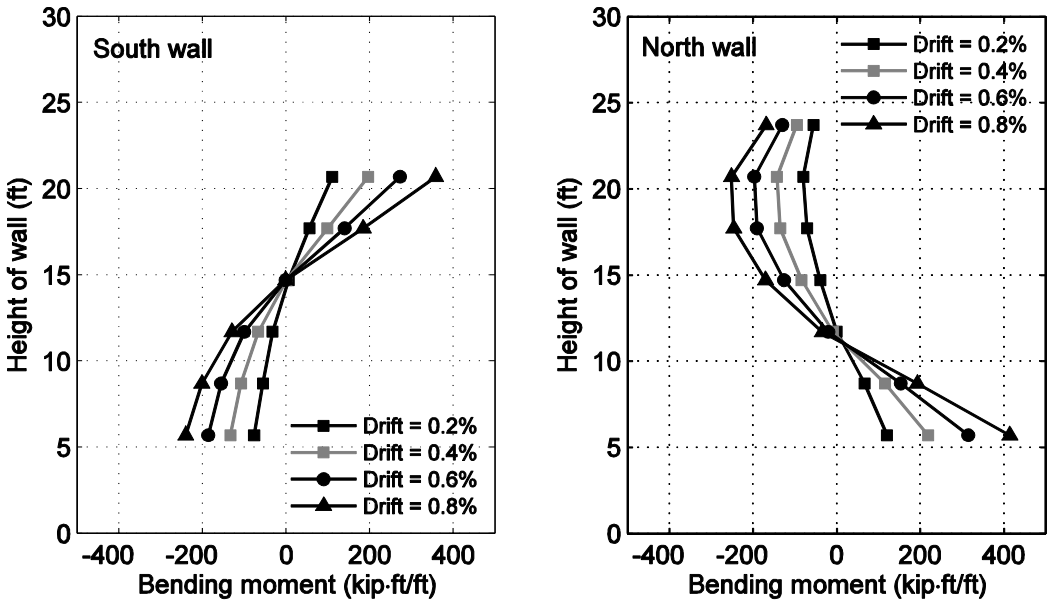

Figure 5-30: Variation of bending moment profile along tunnel walls in the 2nd test

6. Finite element analysis of laminar container tunnel-ground testing

This chapter presents the calibration effort of a FE model based on the 1/9 scale laminar soil container experiment (original test as discussed earlier in Chapter 5). This effort is made in the model scale. The following issues are addressed:

1. Calibration of soil material properties based on the estimated shear wave velocity profile
2. Relation between applied load and measured displacements on soil surface
3. Lateral soil deformation from the inclinometer readings
4. Vertical deformation along the soil surface from the linear variable displacement transducers (LVDTs)
5. Racking of the tunnel
6. Bending moments along the tunnel walls
7. Normal earth pressures on the tunnel walls

6.1 FE model configuration

6.1.1 Soil mesh and boundary conditions

System modeling and response computations were performed using the OpenSees platform, an object-oriented, open-source FE analysis framework (Mazzoni et al. 2006). In a two dimensional (2D) plane strain configuration, four-node quadrilateral elements represented the backfill soil as shown in Figure 6-1.

Along both sides of the soil mesh, additional quadrilateral elements were included to represent the steel laminates using essentially rigid material properties (Table 6-1). Between the mesh elements on the lateral boundaries and the main soil domain, spring elements were deployed with uniaxial materials (normal direction) as shown in Figure 6-2. Along the depth on the left hand side (where the wall moves away from the soil), an elastic-no tension material property (Young's modulus of 1×10^9 ksi) was employed (Figure 6-3a). Along the right hand side (where the wall pushes on the soil), elastic material property both in compression and tension was used (Figure 6-3b). Along the left and right walls, vertical relative translation was allowed (i.e. no friction).

6.1.2 Soil material property

The low strain shear modulus of 2.95 ksi (model scale) from the shear wave velocity measurements was specified for the soil. From the direct shear tests (see Section 4.5), a friction angle of 40 degrees at a peak shear strain of 3% were used. Dry unit weight of that soil was 113 pcf.

For the soil, the OpenSees PressureDependMultiYield (PDMY) material is used for the soil (Yang 2000). Table 6-2 summarizes the employed soil material properties based on test results.

6.1.3 Tunnel model

Elastic beam-column elements were employed for the tunnel model. Table 6-3 summarizes the employed linear material properties. This model consisted of the components walls, roof, and slab (Figure 6-4). Based on the steel tunnel specimen in the laminar container test (in model scale), dimensions of each component were determined. Essentially rigid material property in terms of moment of inertia was employed for the slab and the roof. For the wall, the actual material properties employed in the test were used.

6.1.4 Interface model between soil and tunnel

Zero length elements (in OpenSees) were included along the interface between the soil and the tunnel. An elastic uniaxial material was assigned in the normal and tangential directions. A fully tied condition, via an essentially rigid material property was prescribed in both compression and tension (no separation/slip allowed). As such, soil forces transmitted into the tunnel were dictated by these elements. In this configuration, the interface elements are merely acting as a mechanism to allow for convenient documentation of the forces acting along the tunnel wall.

6.1.5 Loading for pushover analysis

The actual loading displacement profile along the laminar soil box height (see Section 5.4) was applied to the FE model. Figure 6-5 shows the applied displacement profile to the right side of the FE model (absolute displacement shown; the applied displacement direction was from right to left as shown in Figure 6-6).

6.2 Simulation results

Prior to applying the displacement profile (pushover analysis), Figure 6-7 shows contour plots of vertical displacement (settlement), horizontal stress (σ_{xx}), and shear stress (τ_{xy}) obtained from the gravity analysis. Compared to at-rest pressure, the resulting stresses showed a good agreement.

For the pushover analysis, the lateral displacement profile along the right hand side of the soil (from right to left) was applied up to 5 in (in model scale). Due to the lateral boundary condition (no friction specified), it was observed that heave was developed at the right hand side (pushing) and settlement was induced at the left hand side (moving away) of the soil domain (Figure 6-8).

6.2.1 Load-displacement response of the soil

Figure 6-9 shows a comparison of the relationship between lateral force and displacement at soil surface from the test and the FE analysis. The FE model captured the maximum load up to 4 in, but initial stiffness was overestimated.

6.2.2 Soil shear stress

As the applied displacement reached 5 in at the soil surface, Figure 6-10 shows the contour of the shear stress and ratio of the current shear stress relative to the peak shear strength.

6.2.3 Soil lateral deformation

Figure 6-11 shows a comparison of the lateral soil deformation along depth from the inclinometers in the test (Section 5.5.1) with that from the FE analysis. As the applied displacement reached up to 5 in at the soil surface, the results from the FE model generally matched the test results. After the applied displacement of 3 in, the deformation from the test was underestimated slightly.

6.2.4 Vertical deformation along soil surface

Figure 6-12 shows a comparison of vertical deformation on the soil surface measured from LVDTs (see Section 5.3.4.2) during the test with that from the FE analysis. On the right hand side of the tunnel (soil being pushed), vertical deformation showed a reasonable agreement

with that during the test (up to the applied lateral displacement of 3 in). Meanwhile, response of the soil (from the FE analysis) on the left hand side of the tunnel (laminates were moving away) showed relatively higher settlement with respect to the test results.

6.2.5 Racking of tunnel

Figure 6-13 shows a comparison of the drift ratio (racking) of the tunnel from the test and the FE analysis (in which lateral displacement difference between the top and the base of the tunnel is shown). The initial racking response was represented well by the FE model up to 0.4% drift ratio (about 0.1 in relative displacement at the roof to the slab). After this drift ratio, it was observed that the FE results included a noticeable component of essentially rigid body rotation. In the end, deviation between the rigid body motion and the pure deformation (i.e. excluding the rigid body motion) became about 0.2% drift ratio (corresponding to the racking of 0.1 in).

6.2.6 Earth pressure along wall of the tunnel

As discussed earlier in Section 5.3.6, preliminary assessment of the recorded pressures (Figure 6-14) was made, and a more comprehensive analysis is continuing. The earth pressure from the preliminary analyses presented in Appendix I is now compared with that from the FE analysis. In the numeral model, normal earth pressures were recorded by the zerolength elements along the tunnel. Along the right hand side of the wall (Figure 6-1), the earth pressure was compared to that of the sensor data (Figure 6-15). Despite the scatter, there appears to be a level of agreement between the two (Figure 6-15).

6.2.7 Bending moment in tunnel walls

From the FE analysis, the bending moment profile along the tunnel wall was compared to that from the test. As shown in Figure 6-16 (left hand side; south in the test) and Figure 6-17 (right hand side; north in the test), the computed bending moments matched to data to a noticeable degree. Partially due to the numerical modeling simplifications and idealizations (e.g., the employed boundary condition between the tunnel and the soil of no friction/separation), the FE model appears to overestimate the bending moment near the bottom of the walls.

6.3 Summary

The FE model was calibrated on the basis of the laminar soil container test (the original test) in model scale. The FE results were compared to the test results in the following aspects:

1) Relation of load versus displacement applied to top of the laminar box
2) Lateral soil deformation compared to results from the inclinometers
3) Vertical deformation along soil surface compared to results from linear variable displacement transducers (LVDT)
4) Racking of tunnel compared to results from the LVDTs and Sting Pots.
5) Bending moment along the tunnel walls
6) Normal earth pressure on the tunnel walls

In general, the FE model matched some of the significant salient aspects of the overall response. Potentially useful insights can be gleaned from further parametric studies to evaluate effects such as burial depth, shape of the tunnel cross-section, tunnel-soil relative stiffness, input shaking characteristics, and so forth.

Table 6-1: Linear material properties for the laminar frames

Property	Laminar frames
Young's modulus, E (ksi)	1×10^{8}
Poisson's ratio (ν)	0.316
Mass density ($lb \cdot s^2/in^4$)	1.692×10^{-4}

Table 6-2: Model parameters for the PDMY material (http://soilquake.net/opensees)

Parameters	Description	Value (for dry dense sand)
ρ	Soil total mass density	1.692×10^{-4} $lb \cdot s^2/in^4$
G_r	Reference low-strain shear modulus	8.83 ksi
B_r	Reference bulk modulus	21.5 ksi
ϕ	Friction angle at peak shear strength	40°
γ_{max}	Octahedral shear strain at which the peak shear strength is reached	0.03
p_r'	Reference mean confining pressure at which G_r, B_r, and γ_{max} are defined	7.452 psi
d	A positive constant defining variations of G and B as a function of effective confinement p_r'	0.5
PTAng	Phase transformation angle	27°
contrac	A non-negative constant defining the rate of shear-induced volume decrease	0.03
dilat1	A non-negative constant defining the rate of shear-induced volume increase	0
dilat2		0
liquefac1	Parameter controlling the mechanism of liquefaction-induced perfectly shear strain accumulation	0
liquefac2		0
liquefac3		0
NoYieldSurf	Number of yield surfaces	20
e	Initial void ratio	0.45

Table 6-3: Linear material properties for the tunnel

Property	Components of tunnel			
	Wall	Wall joint	Slab	Roof
Young's modulus, E (ksi)	29000	29000	29000	29000
Area of cross-section, A (in^2)	0.75	0.75	0.59	0.59
Moment of inertia, I (in^4)	0.035	3,515	1×10^{6}	1×10^{6}

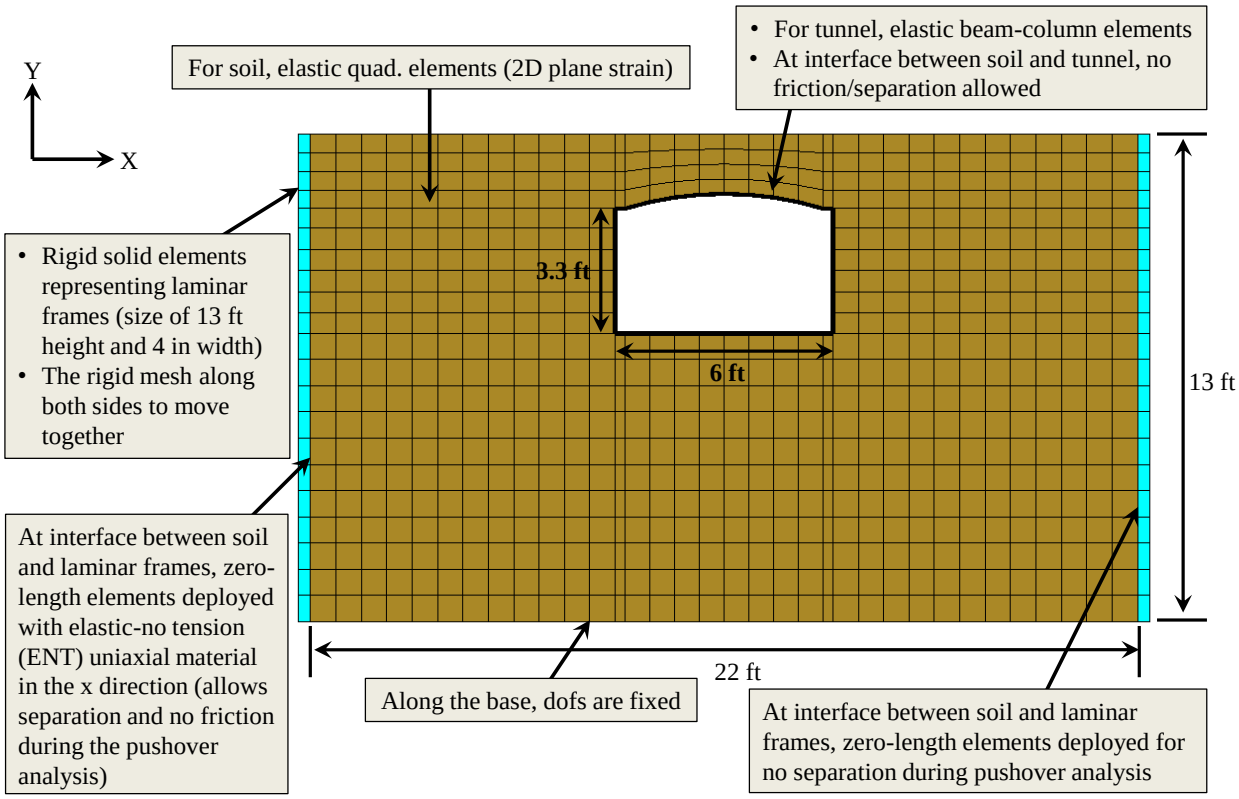

Figure 6-1: FE mesh for the soil in the laminar soil box

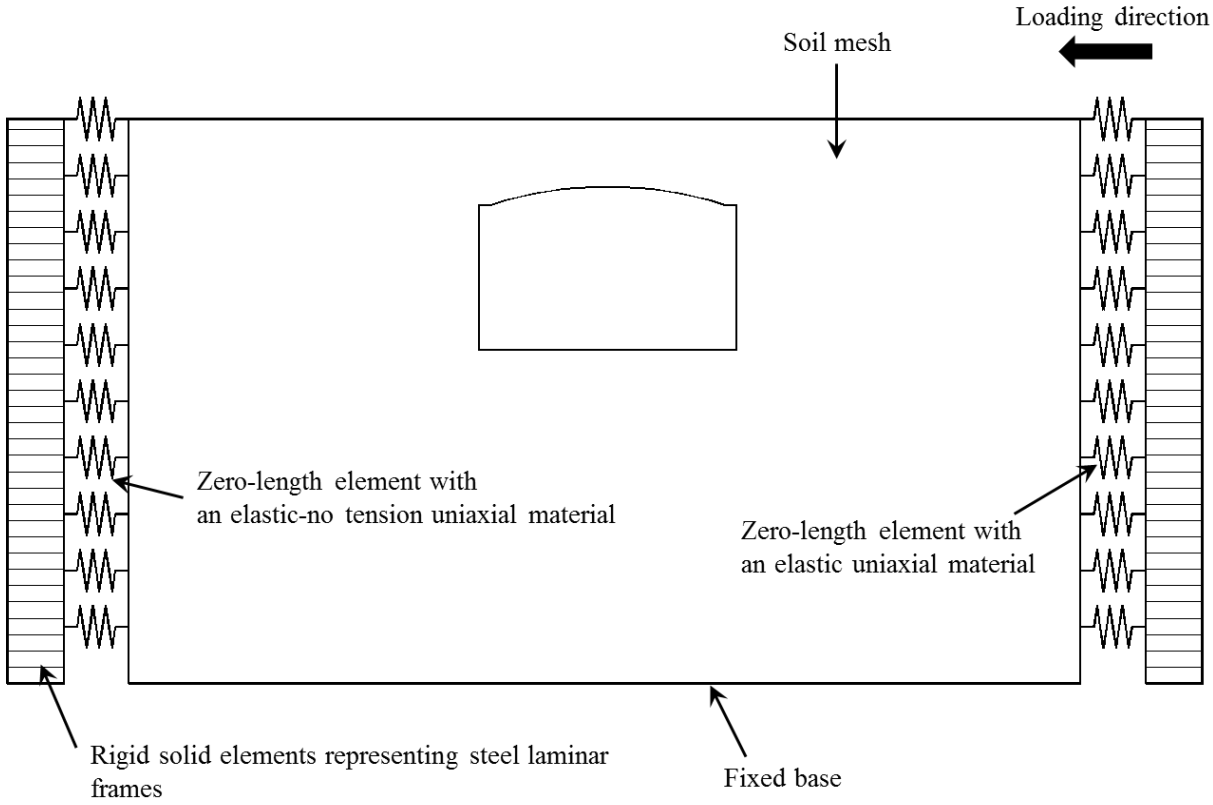

Figure 6-2: Schematic view of boundary conditions between laminar frames and soil

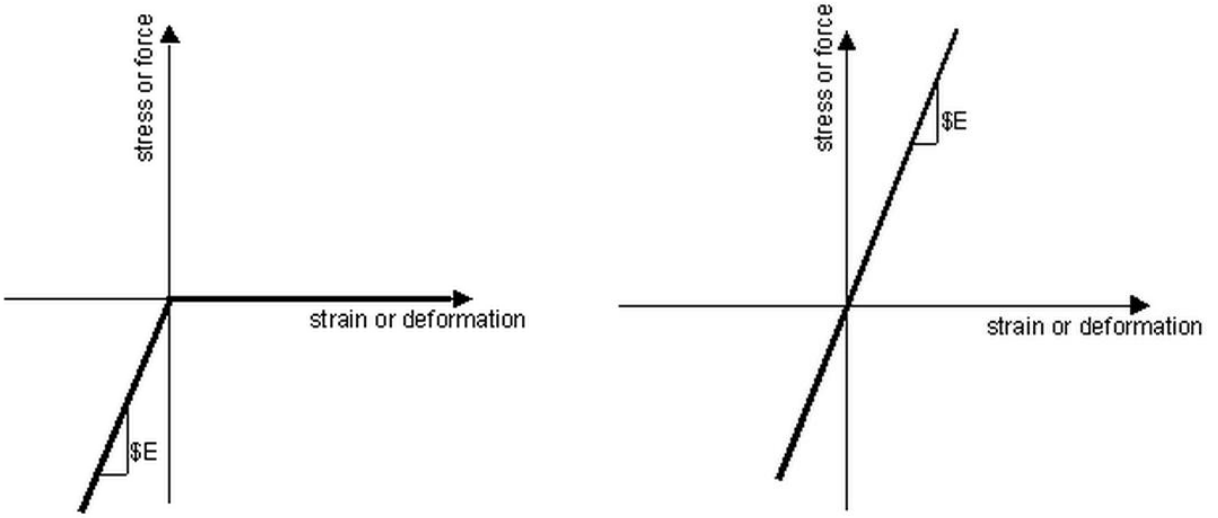

(a) Elastic-no tension material (pulled; left hand side)

(b) Elastic material (pushed; right hand side)

Figure 6-3: Relation of force and deformation in elastic materials for spring elements along lateral boundaries between laminar frames and soil

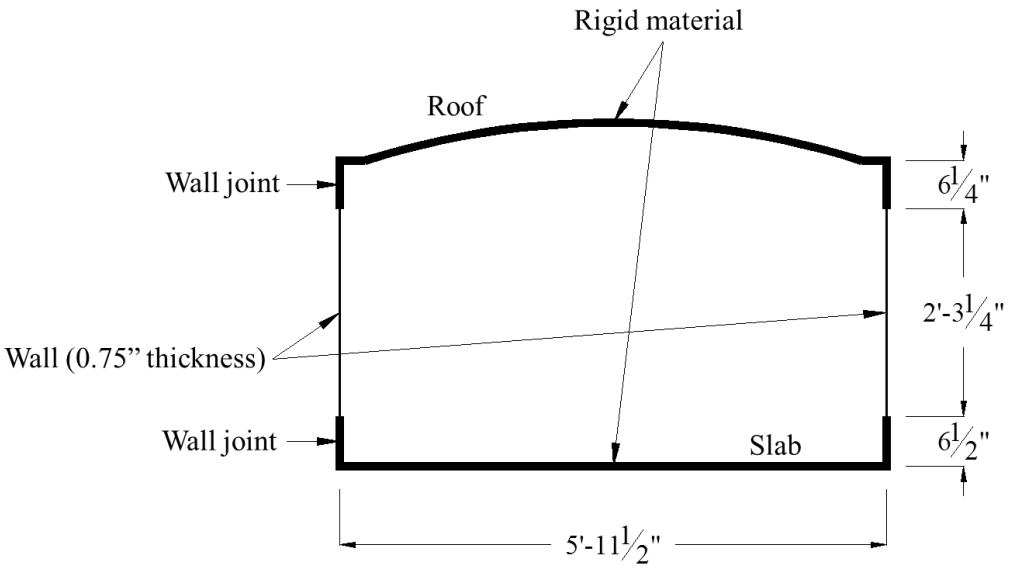

Figure 6-4: Schematic view of the tunnel

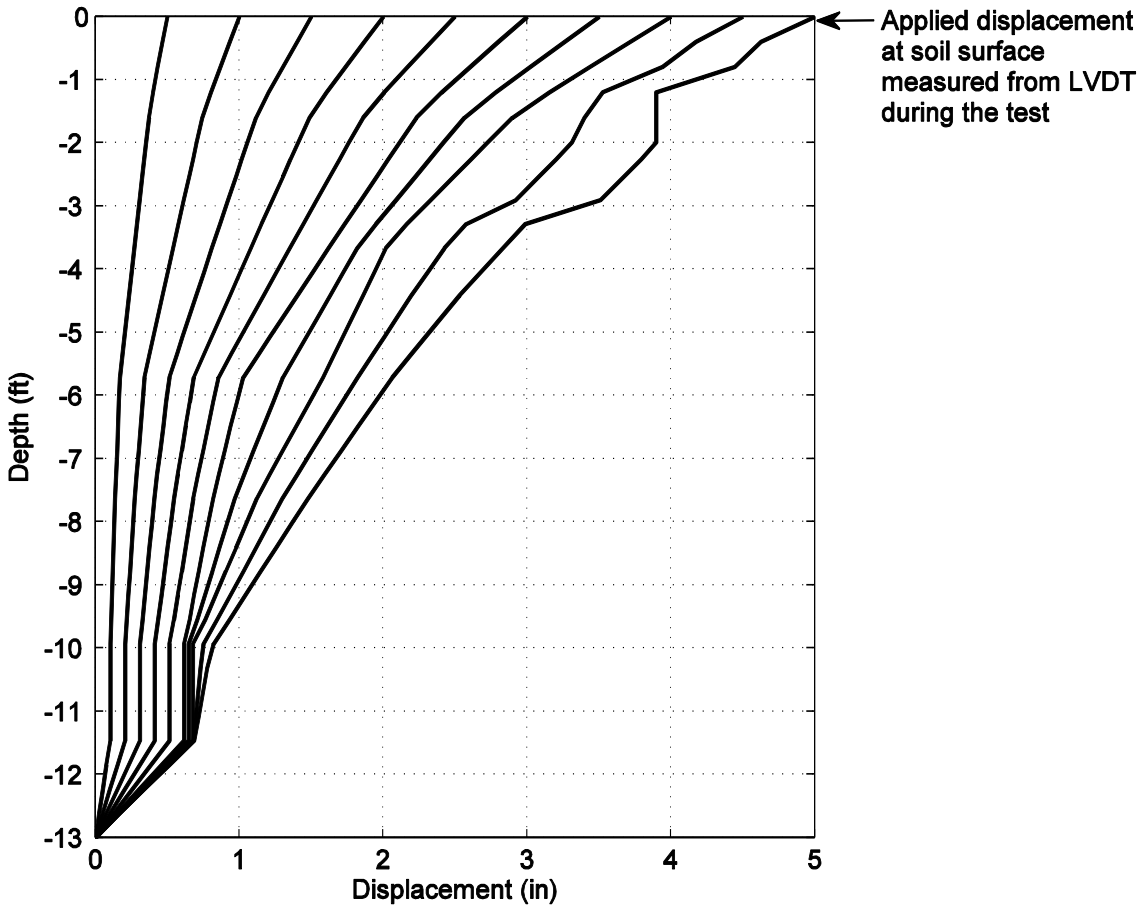

Figure 6-5: Applied displacement profile along laminar soil box (absolute displacement shown)

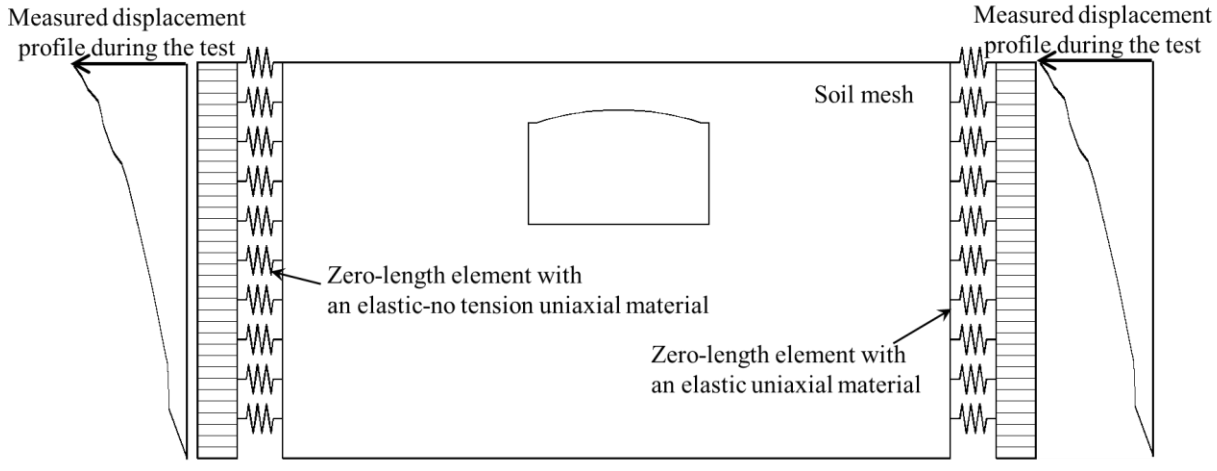

Figure 6-6: Applied displacement profile along laminar frames

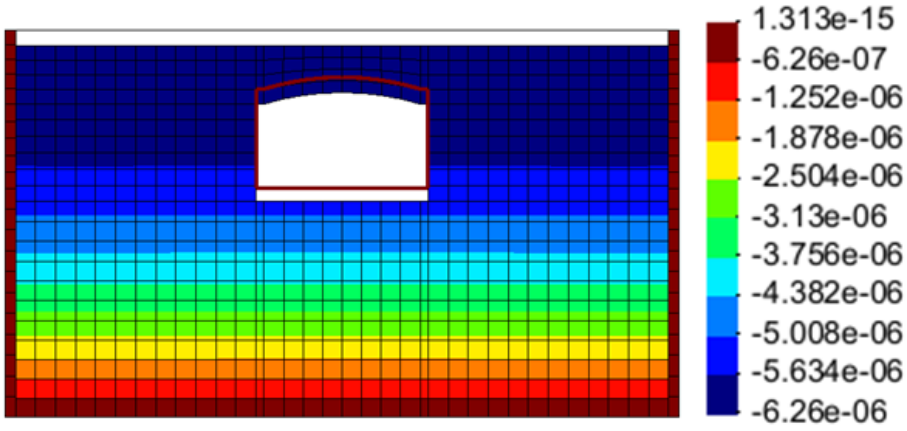

(a) Vertical displacement (in inch)

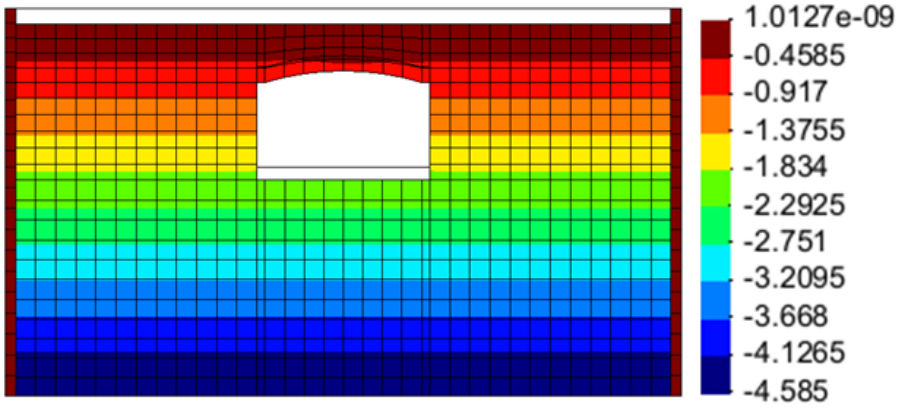

(b) Horizontal stress (σ_{XX} in psi)

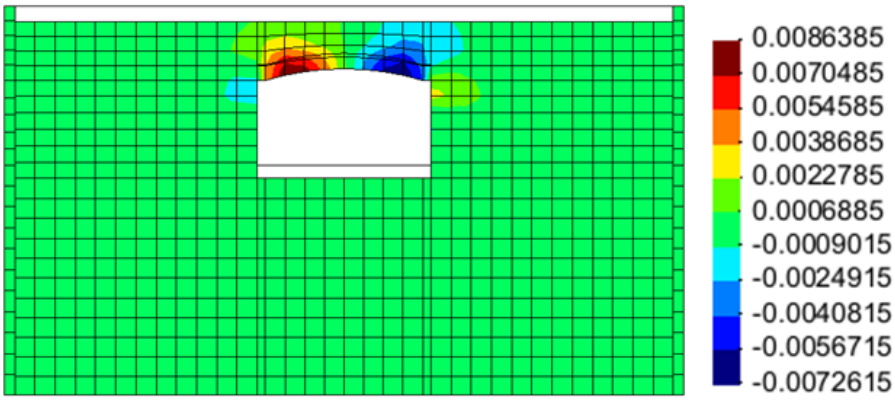

(c) Shear stress (τ_{XY} in psi)

Figure 6-7: Results from gravity analysis prior to applying lateral loads

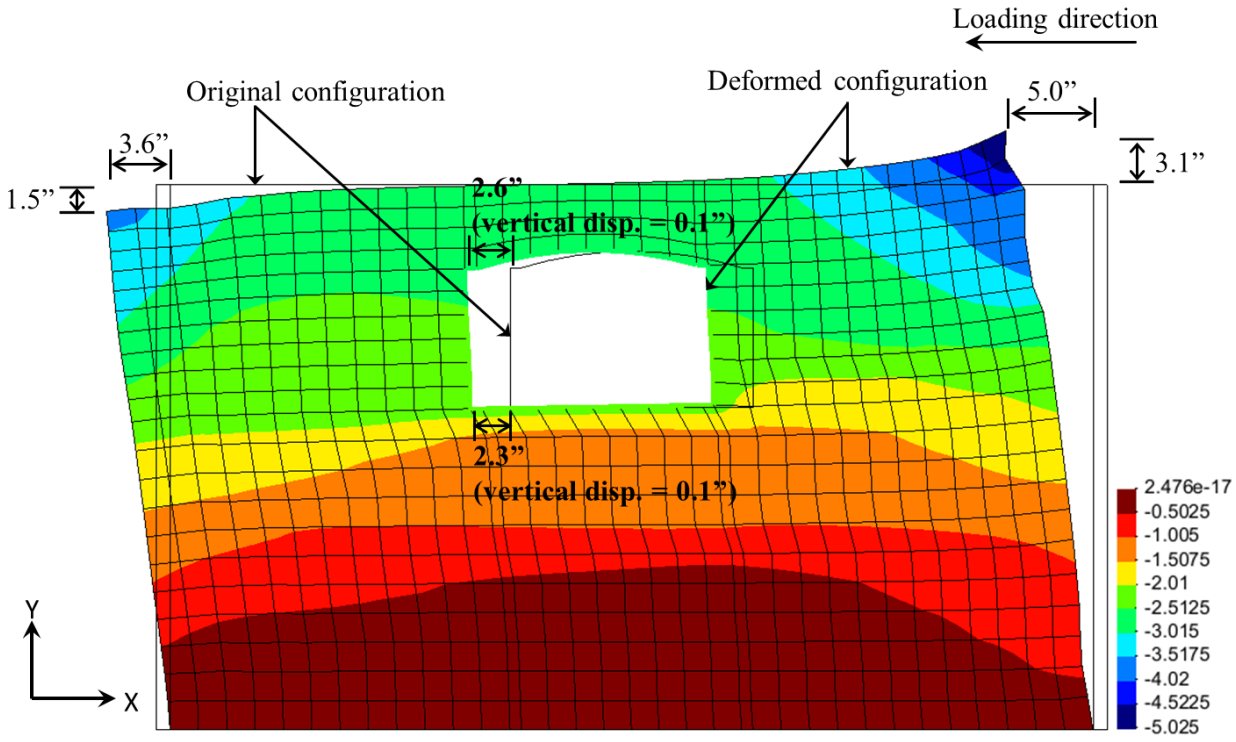

Figure 6-8: Deformed shape (scale factor of 5) and lateral displacement contour (in)

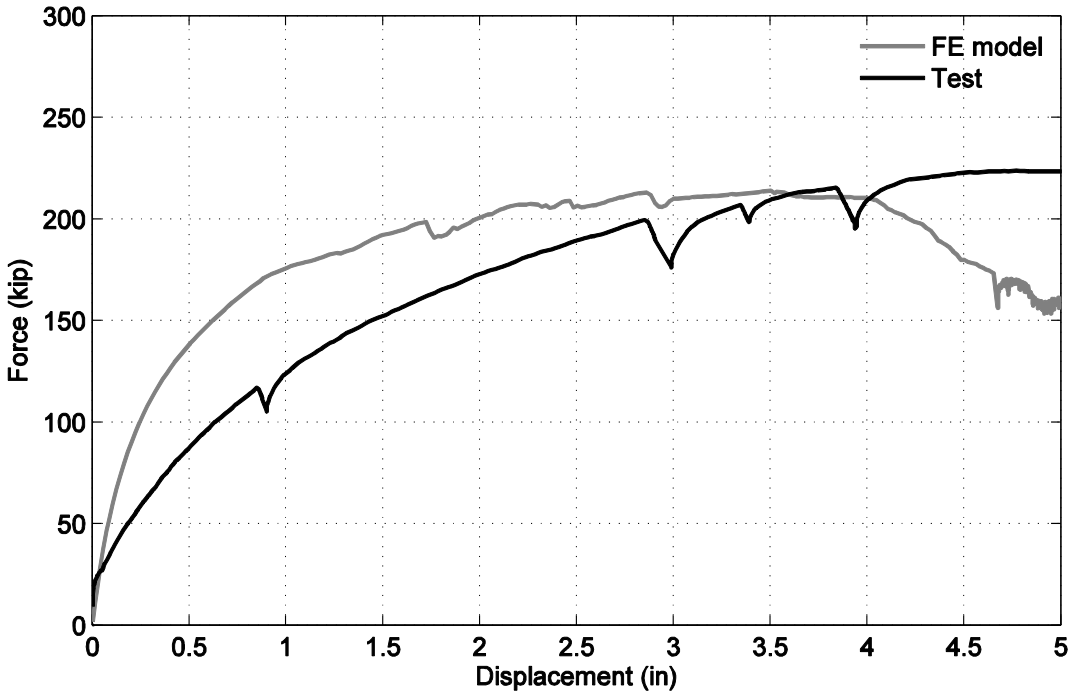

Figure 6-9: Comparison of the applied force and the lateral displacement at soil surface from the test and the FE analysis

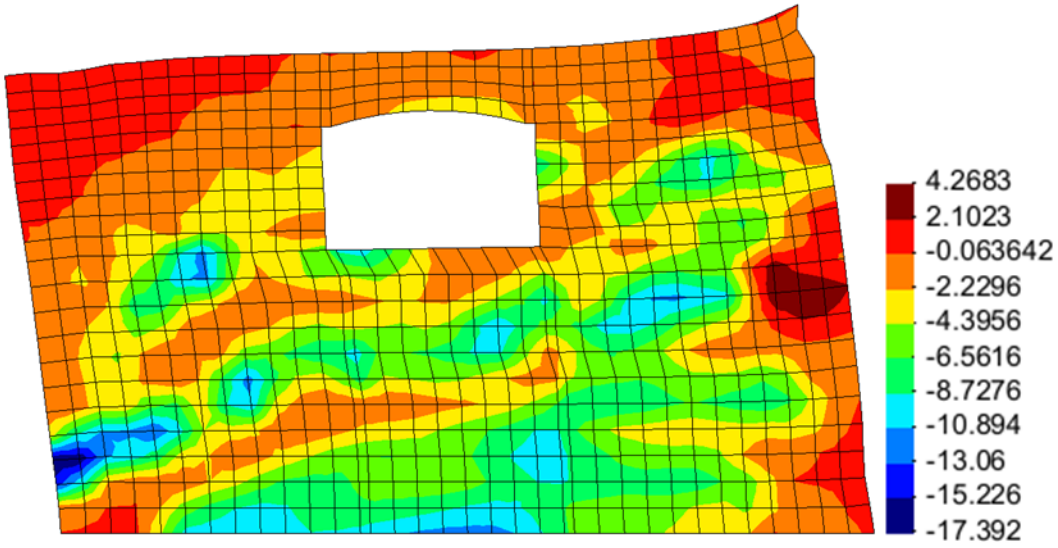

(a) Shear stress (units in psi)

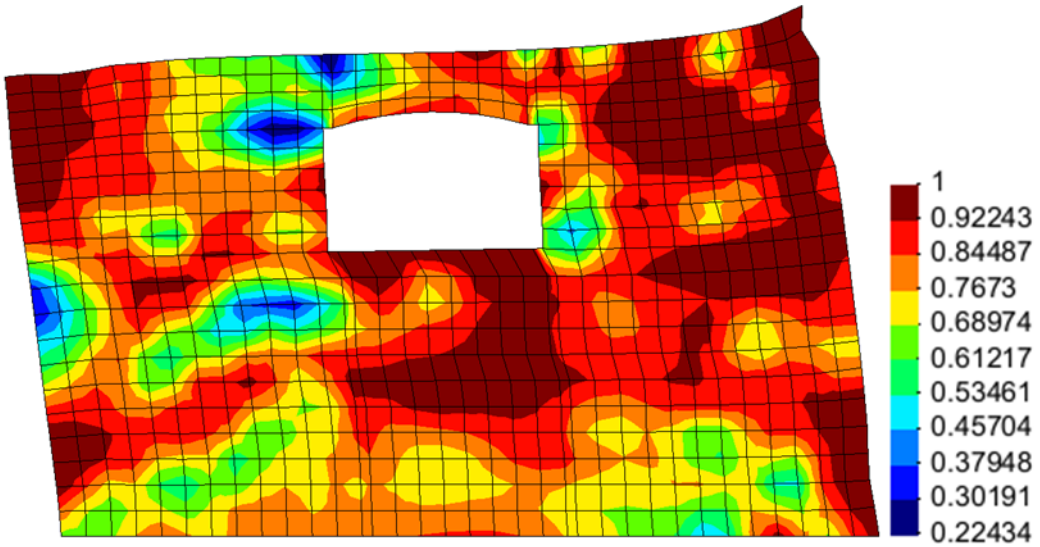

(b) Ratio between shear stress and peak shear strength

Figure 6-10: Stress contour of soil elements as the applied lateral displacement reaches 5 inches

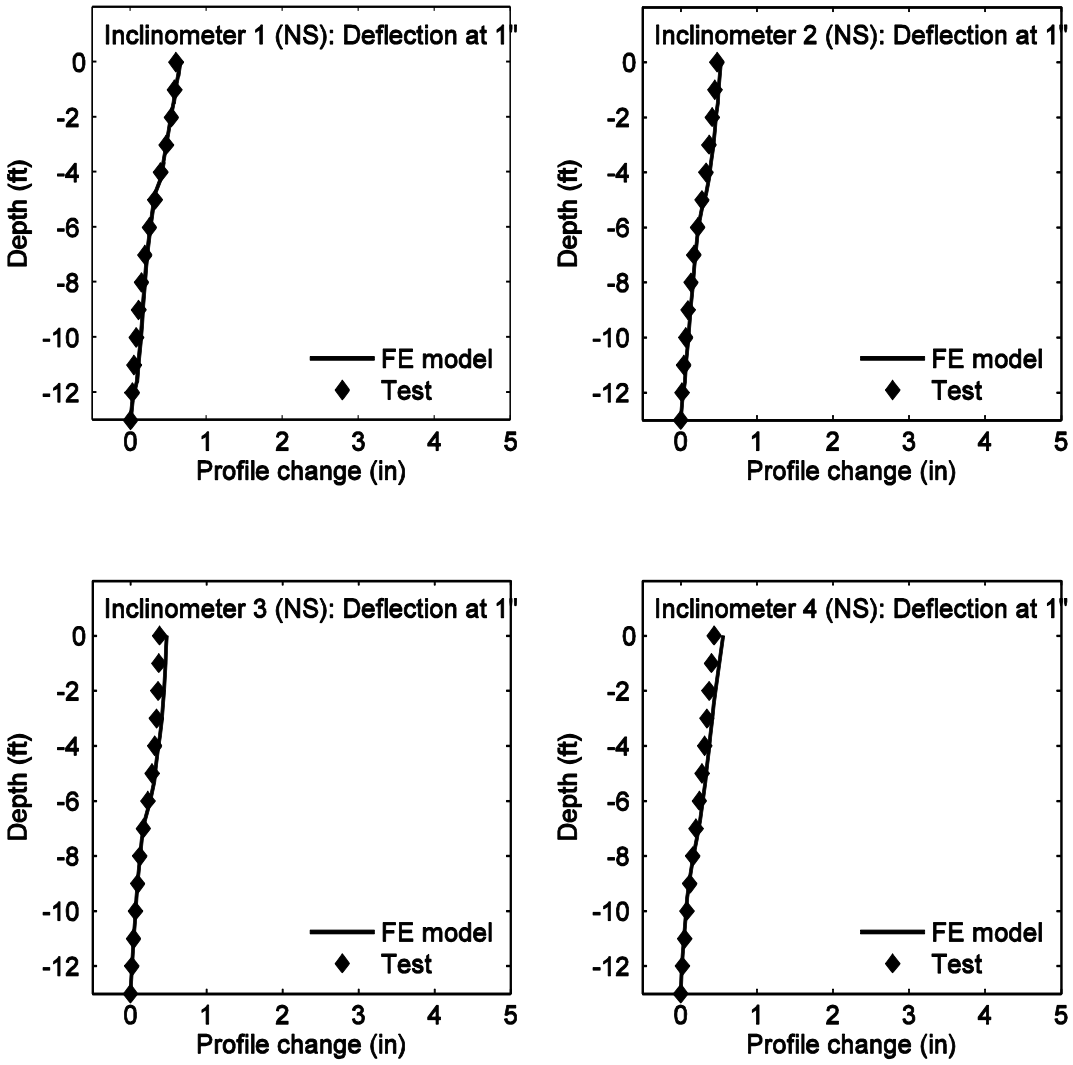

Figure 6-11: Lateral deformation from FE model and inclinometers during the test (cont.)

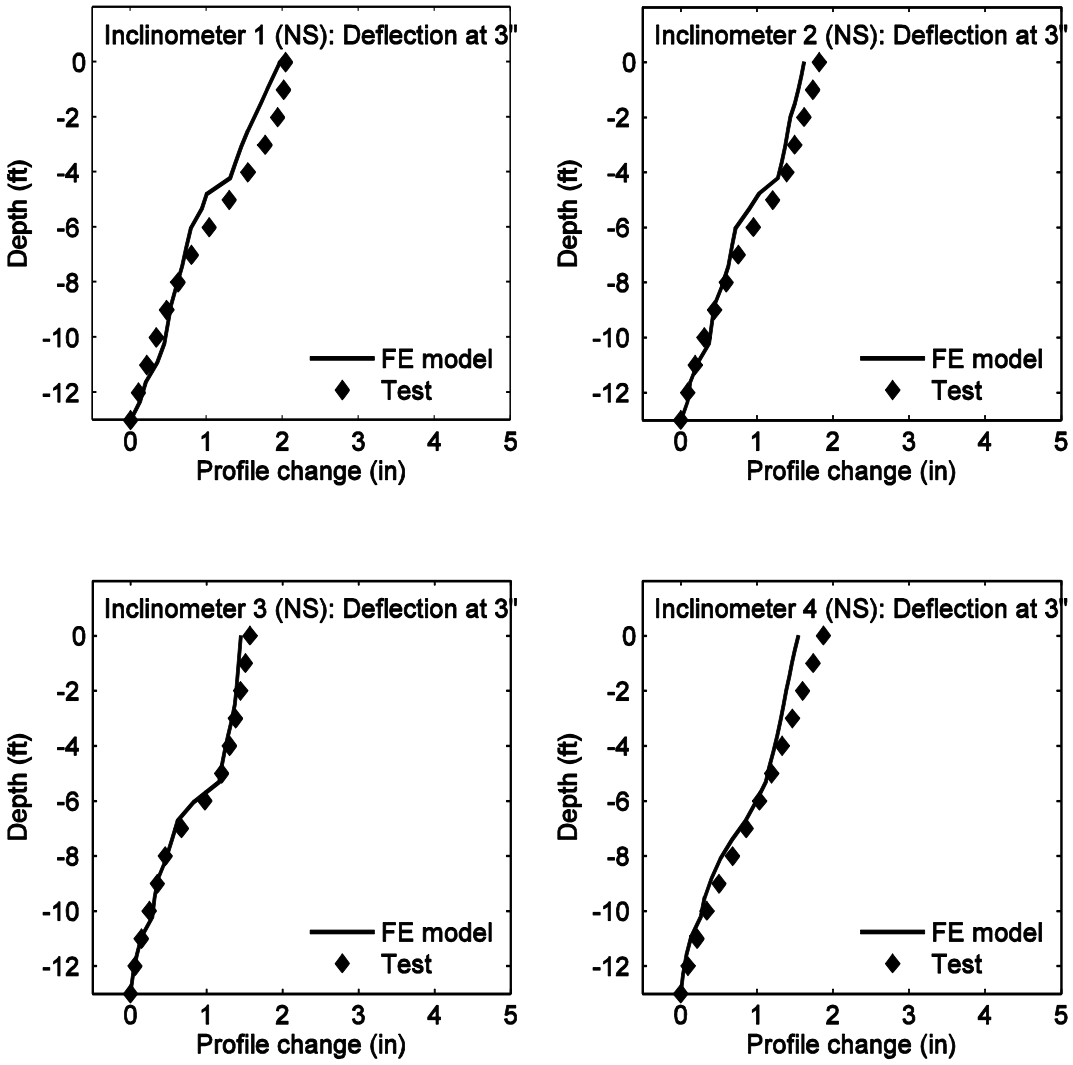

Figure 6-11: (continued) Lateral deformation from FE model and inclinometers during the test (cont.)

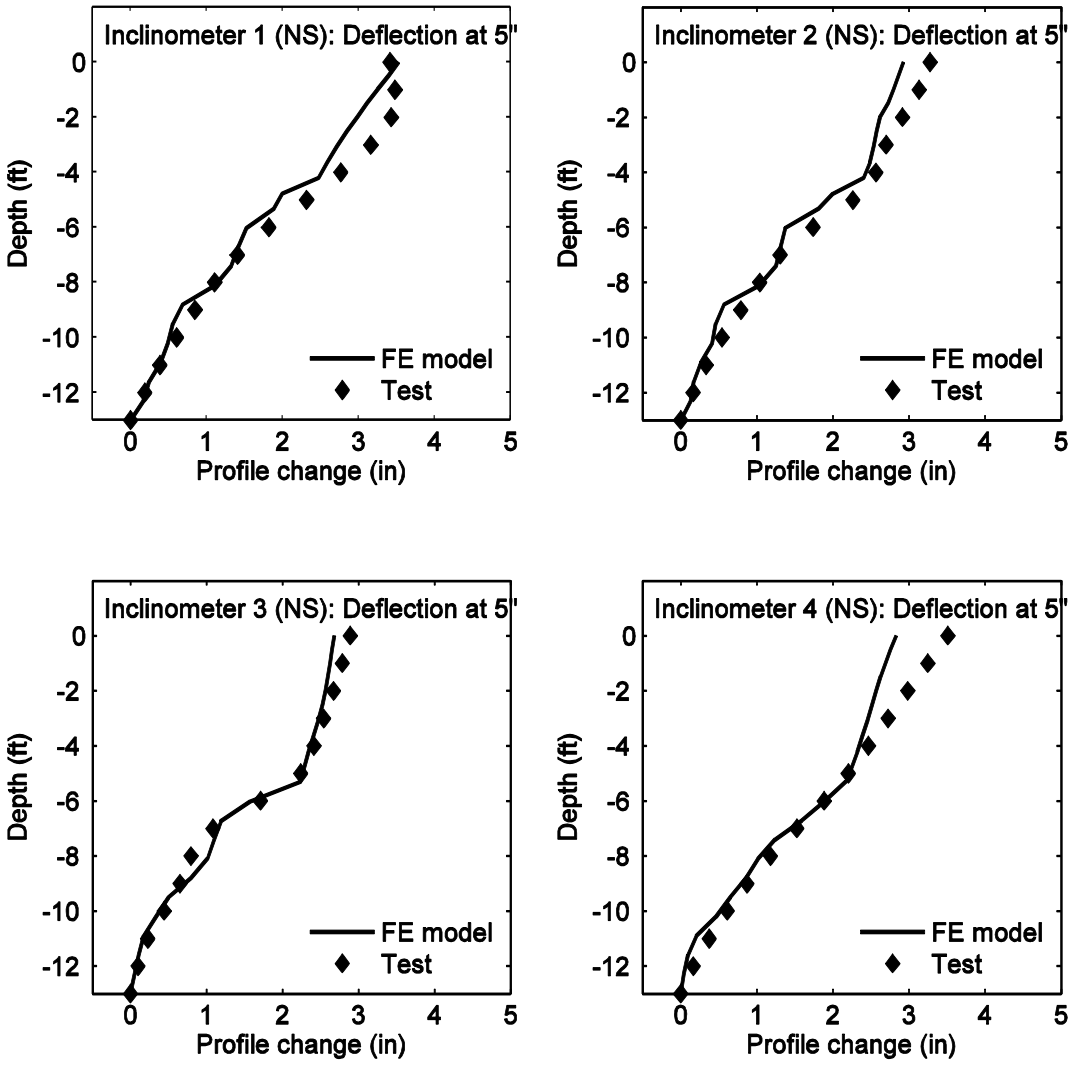

Figure 6-11: (continued) Lateral deformation from FE model and inclinometers during the test

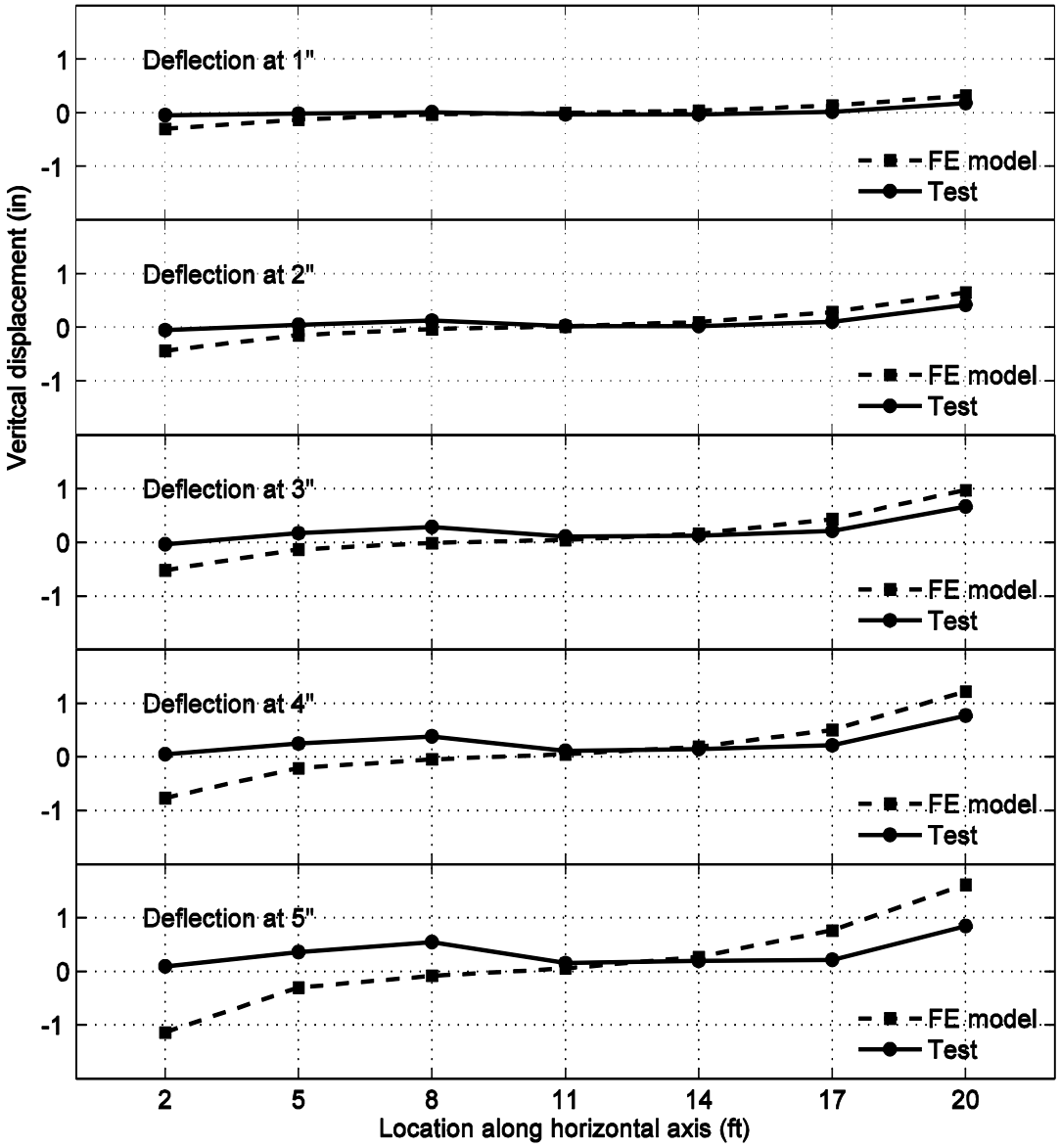

Figure 6-12: vertical deformation along soil surface from the test and the FE analysis

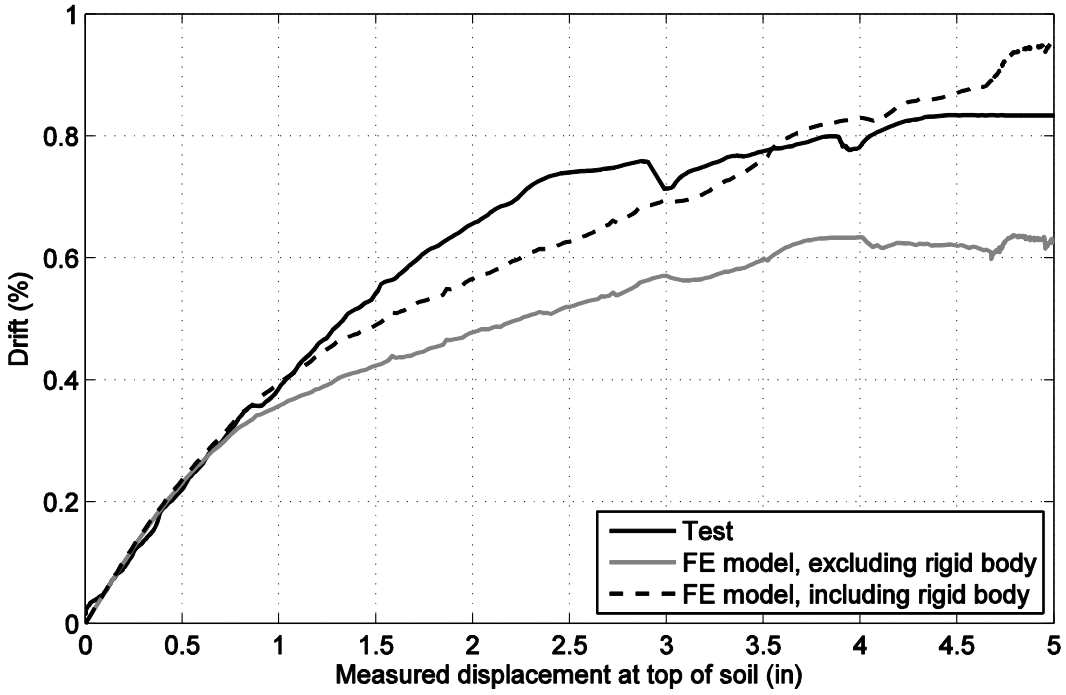

Figure 6-13: Drift ratio (racking of tunnel) from FE model and test

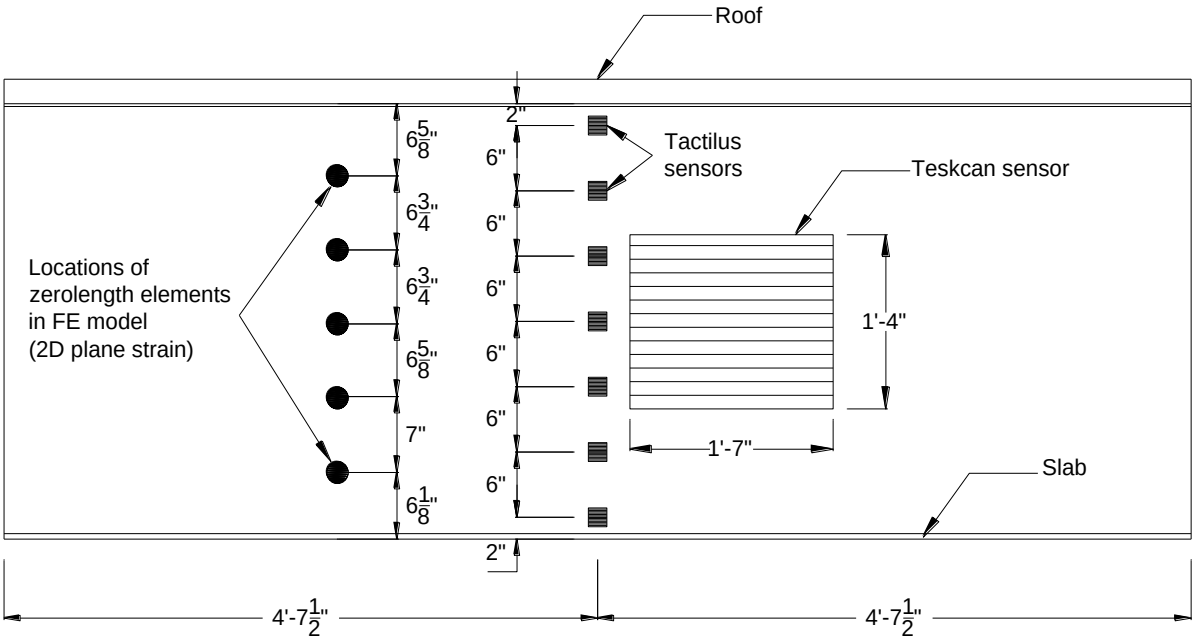

Figure 6-14: Location of pressures sensors used for laminar soil box test

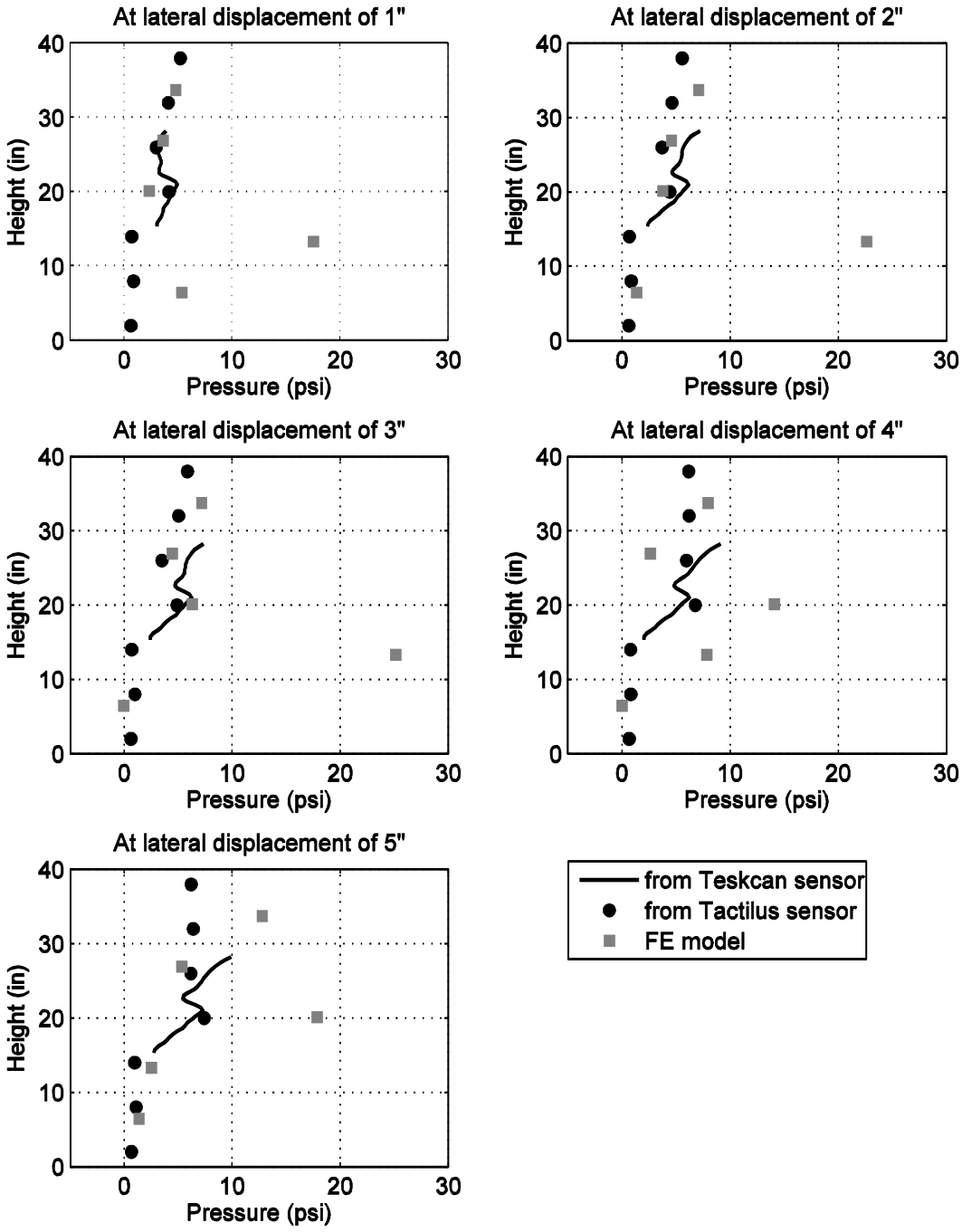

Figure 6-15: Comparison of earth pressure along the North wall (right hand side) of the tunnel

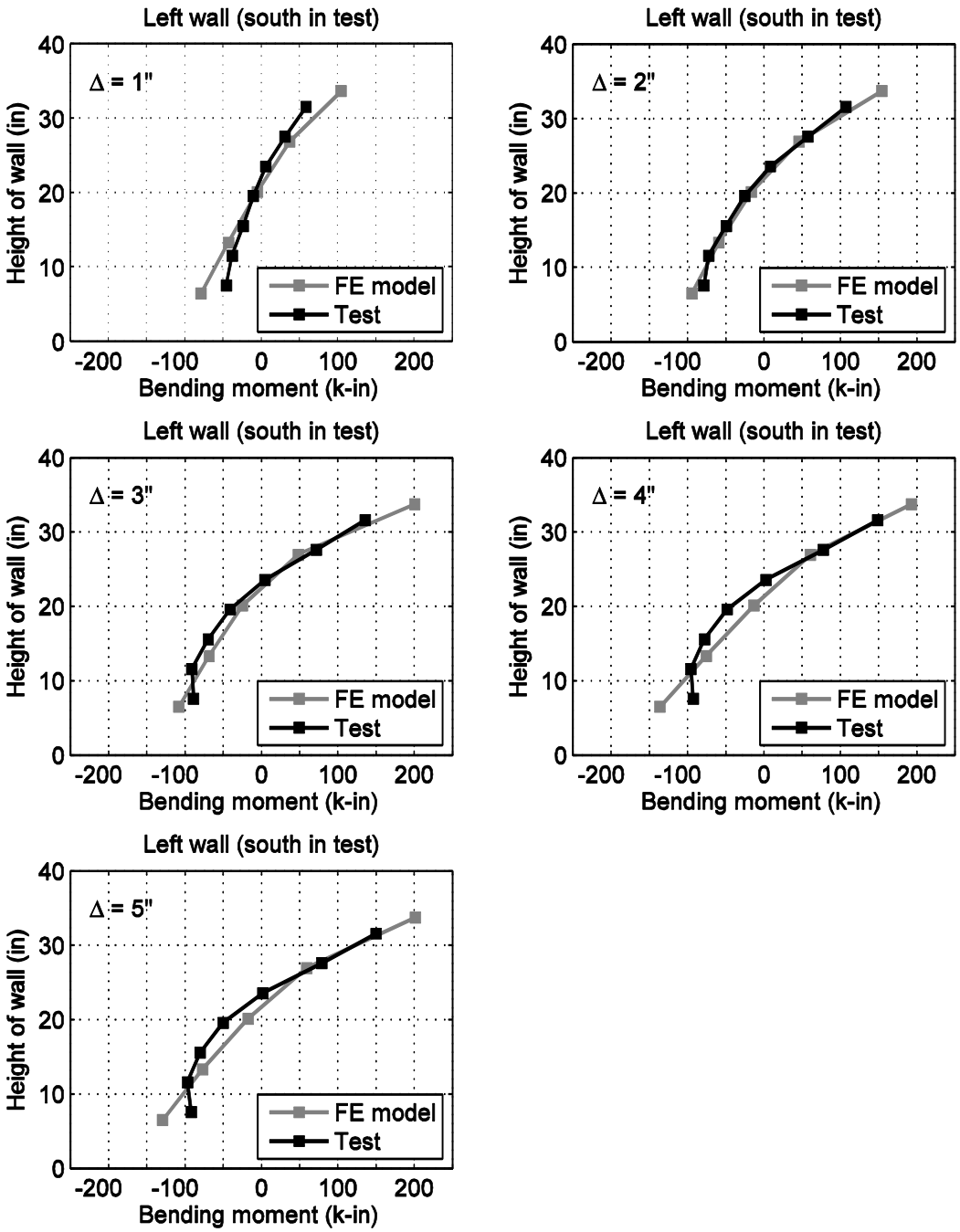

Figure 6-16: Comparison of bending moments along the South wall (left hand side) of the tunnel

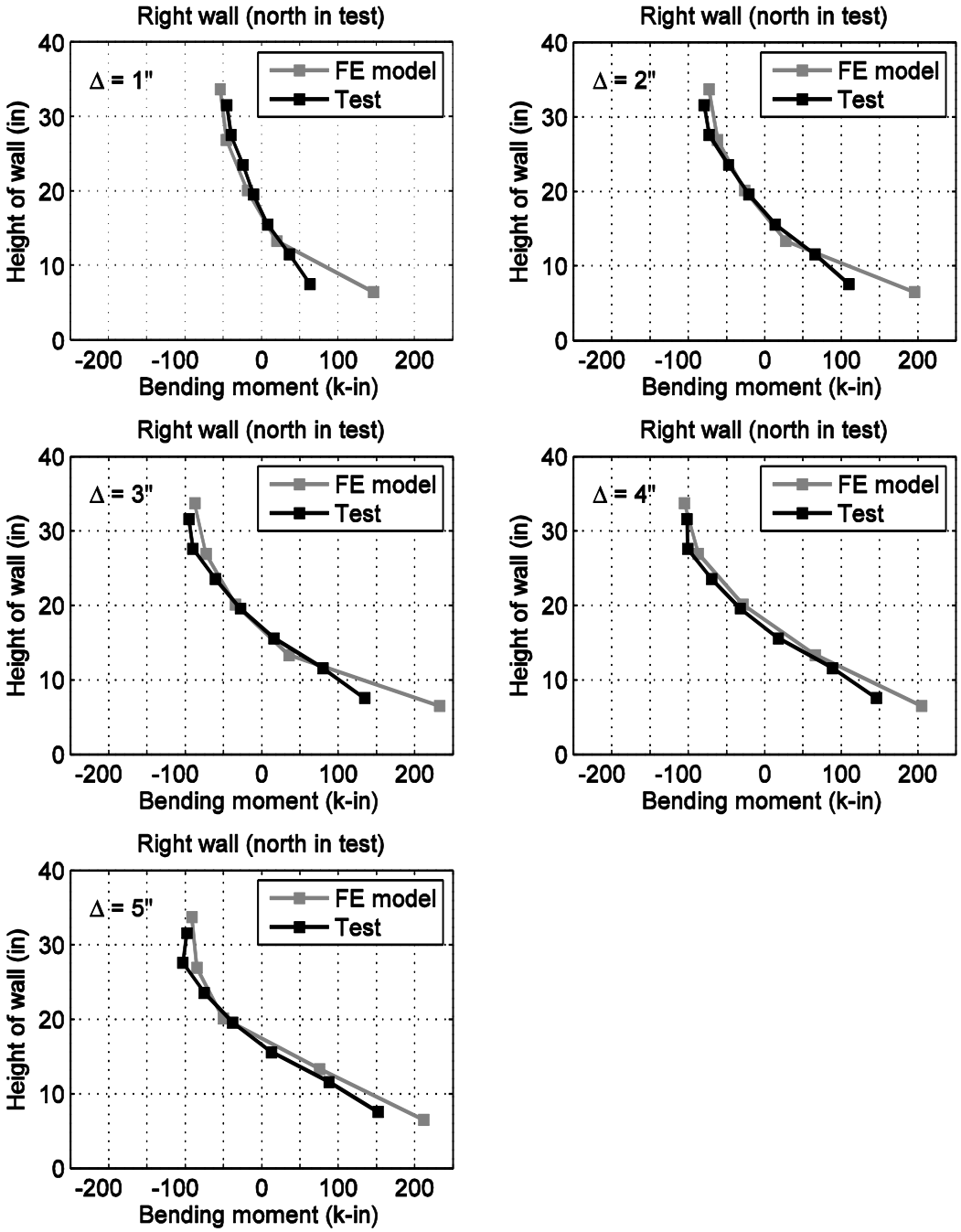

Figure 6-17: Comparison of bending moments along the North wall (right hand side) of the tunnel

7. Dynamic FE analysis of a cut-and-cover tunnel

7.1 Introduction

Building on the conducted FE model calibration effort, this chapter presents a representative numerical analysis of an actual tunnel-ground earthquake excitation scenario. For that purpose, normal earth pressure distribution along the tunnel walls is evaluated in linear and nonlinear simulations. As a benchmark for comparison, the case of linear soil properties is analyzed, followed by soil modeling that allows nonlinear hysteretic behavior, with and without a simple no tension-logic, as detailed below.

7.2 Finite Element model configuration

Figure 7-1 shows the 2D plane strain Finite Element (FE) model using the OpenSees framework (Mazzoni et al. 2006). Employed dimensions and material properties of the tunnel were based on the calibrated model as discussed earlier in Chapter 3 (elastic beam-column elements). For the tunnel model, the total number of nodes and elements were 32 and 32, respectively. Table 7-1 summarizes the employed material properties. Along the slab and the roof, essentially rigid material properties were used. Consequently, the overall lateral stiffness was dictated by the walls. As such, the corresponding lateral stiffness of the tunnel model was 3.6 kip/in per unit length (1 in) under simply supported boundaries at both ends of the slab.

To model the soil domain (Figure 7-1), 4-node quadrilateral elements were used. A total of 21 layers were specified along the depth (117 ft). A fixed boundary along the soil base was used. Along both sides of the soil mesh, lateral and vertical translations were constrained to be identical (i.e. shear beam assumption). For the soil mesh, the total number of nodes and elements were 770 and 714, respectively.

For inclusion of soil nonlinearity, the ground was modeled as a nonlinear hysteretic material (Prevost 1978; Elgamal et al. 2008) with a Von Mises (J_2) multi-surface kinematic plasticity model (Pressure IndependMultiYield model in OpenSees). This material reproduces the soil hysteretic elasto-plastic shear response and the accumulation of any permanent deformation. The nonlinear shear stress-strain backbone curve is represented by the hyperbolic relation (Kondner 1963) defined by two material constants in terms of low strain shear modulus and ultimate shear strength. In the FE model, the shear modulus is defined to increase with

confinement following by a parabolic relationship (Table 7-2) and the peak shear strength (attained at a shear strain of 3%) increases with depth (to mimic the strength of a cohesionless soil with friction angle of 40 degrees). For all layers, Poisson's ratio of 0.32 and unit weight of 113 pcf were specified. Rayleigh damping was included at a value of 2 % for the soil and the tunnel (at the frequencies of 2 Hz and 6 Hz).

7.2.1 Relative stiffness between the soil and the tunnel

As discussed earlier in Chapter 2, tunnel racking response can be estimated by the flexibility ratio (relative stiffness between tunnel and the surrounding soil). The flexibility ratio is computed as (Wang, 1993):

$$F_{rec} = \frac{G_m}{K_s}\frac{W}{H} = \frac{14.7\ k/in^2 \times 52\ ft}{3.6\ k/in/in \times 30\ ft} = 7 \qquad (7.1)$$

where G_m is average strain-compatible shear modulus of the surrounding soil (For the F_{rec} in this study, shear modulus at very low strain, G_{max}, was used for in-situ soil), W is width of the tunnel, H is height of the tunnel, and K_s is the reciprocal of the lateral racking deflection caused by a unit concentrated force. Thus, the tunnel was expected to behave in a relatively flexible mode compared to the ground, with larger racking compared to shear distortion of the soil in free-field (i.e., away from the tunnel location).

7.2.2 Earthquake motion

For the dynamic analysis (after gravity loading was applied), the 1994 Northridge earthquake ground motion recorded at CSMIP Station 24279 (Newhall, Fire station) was selected. Figure 7-2 shows the 90 degree component motion recorded at the station (20 sec window shown out of 60 sec with time step of 0.02 sec). From deconvolution using SHAKE 91 (Idriss and Sun 1992), the outcrop motion at depth of 117 ft was computed and applied to the soil base. Figure 7-3 shows 5% damped spectral acceleration of the outcrop motion (with a predominant frequency is about 0.3 sec).

7.2.3 Computational procedures

Prior to the earthquake excitation, gravity loads were statically applied. In the dynamic analysis phase, 3000 times steps ($\Delta t = 0.02$ sec., providing accuracy up to 12.5 Hz) of transient nonlinear analysis were executed during 60 sec of earthquake excitation. The Newmark-β time-stepping method was employed to integrate the equation of motion with the integration parameters $\gamma = 0.5$ and $\beta = 0.25$.

7.3 Numerical results

Prior to the dynamic analysis phase, the static horizontal and vertical soil stresses were inspected. From the dynamic analysis phase, acceleration response at ground surface and at levels of the tunnel roof and slab were recorded. As the maximum soil stress was developed, the horizontal and vertical soil stresses were evaluated (dynamic part, as well as the total including the own weight static component). Consequently, the peak earth pressure distribution along the perimeter of the tunnel can be displayed and assessed.

7.3.1 Stress state under the static own weight

Figure 7-4 shows contour of the horizontal and vertical soil stresses under gravity loading. Along the depth, the horizontal and vertical stress profiles essentially complied with the at-rest pressure $K_o\gamma H$, where K_o is the coefficient of lateral earth pressure, $K_o = \nu/(1-\nu)$, ν is Poisson's ratio, γ is the unit weight of the soil, and H is depth.

7.3.2 Linear analysis

Figure 7-5 and Figure 7-6 show acceleration time histories at the soil surface and levels of the roof and the slab in the free-field (located about 120 ft away from the tunnel) and above/on the tunnel, respectively. In this studied case, the difference between the free-field and the tunnel location was relatively minor. Figure 7-7 shows the peak ground acceleration (PGA) in free-field and above/below and along the tunnel wall (left). Although the Peak acceleration was similar at the roof and the slab, higher and lower accelerations of the tunnel along the wall were observed due to its flexibility.

7.3.2.1 Deformed configuration

Figure 7-8 shows the deformed shape of the FE model as the PGA occurred at 5.44 sec. Figure 7-9 shows a comparison of the tunnel racking (lateral displacement at the roof relative to the slab) with a differential free-field displacement corresponding to those locations. Due to the relative flexibility of the tunnel with respect to the surrounding soil (flexibility ratio of 7 using the Eq. 8.1), the racking response was magnified by about 230%. This racking response is similar to the racking ratio of 2.2, as would be predicted by Wang (1993) procedure.

7.3.2.2 Stress state during shaking

As the PGA occurred (the FE model swung from right to left), Figure 7-10 and Figure 7-11 show contour plots of the total horizontal and vertical soil stresses, respectively. Along the side of the walls, the total horizontal pressure varied significantly. Excluding the static response, the pressure of the dynamic part only are shown in Figure 7-12 (horizontal) and Figure 7-13 (vertical). While the dynamic effect was negligible in the vertical response, the horizontal response was quite significant.

7.3.2.3 Normal pressure on the tunnel

Figure 7-14 shows the normal pressure time history developed at bottom of the left wall. The maximum normal pressure was about 39 psi at the instant when the PGA occurred (at 5.44 sec). At this time instant, Figure 7-15a shows the normal earth pressure distribution along the perimeter of the tunnel. As shown in the contour of the soil stresses (Figure 7-10), significant variation of the earth pressure occurs along the walls.

Figure 7-15b shows the normal earth pressure distribution resulting from the dynamic response only (excluding the static pressure). The maximum pressure was about 21 psi (120% of the at-rest horizontal stress). Meanwhile, due to the shallow overburden soil above the tunnel and the employed horizontal shaking, the normal earth pressure along the roof was relatively low.

7.3.3 Nonlinear analysis

Results from the nonlinear analyses using a nonlinear hysteretic material with and without tension-cutoff will be presented.

7.3.3.1 Undrained clay without tension-cutoff

7.3.3.1.1 Response time histories from shaking

As shown earlier in Section 7.3.2, Figure 7-16 and Figure 7-17 show the acceleration response in the free-field (about 120 ft away from the tunnel) and above/on the tunnel, respectively. The difference between the free-field and the tunnel responses was relatively small. However, higher and lower deviations were observed along the tunnel wall (Figure 7-18).

7.3.3.1.2 Deformation

Figure 7-19 shows the deformed shape of the FE model as the PGA occurred at 5.52 sec. Due to the relatively flexible tunnel model (flexibility ratio of 7), the racking response was about 210% (230% in the linear analysis) compared to the shear distortion in free field (Figure 7-20).

7.3.3.1.3 Stress state during shaking

As the PGA occurred (the FE model swung from right to left), Figure 7-21 and Figure 7-22 show contour of total horizontal and vertical soil stresses, respectively. Excluding the static response, the pressures from the dynamic part only are shown in Figure 7-23 (horizontal) and Figure 7-24 (vertical).

7.3.3.1.4 Normal pressure on the tunnel

Figure 7-25 shows the normal earth pressure time history developed at bottom of the left wall. It was observed that residual earth pressure was about 15 psi. As the maximum normal pressure was developed at the bottom of the wall, Figure 7-26a shows the normal pressure profile along the perimeter of the tunnel. Figure 7-26b shows the normal earth pressure from the dynamic part only (excluding the static own weight pressures). The total pressure profile shows a maximum of 34 psi at bottom of the left wall (as much as twice the at-rest pressure).

7.3.3.2 Hysteretic soil model with tension-cutoff

In this case, effects of the tension-cutoff were negligible in terms of acceleration in the free-field/near the tunnel and earth pressure distribution exerted on the tunnel. In other words, the results were essentially those reported above for the nonlinear soil case.

7.4 Summary

Dynamic response of a tunnel-ground system was studied under earthquake excitation (the 1994 Northridge earthquake ground motion recorded at the Newhall, Fire station). In this study, the lateral (racking) stiffness of the tunnel was relatively low compared to the surrounding soil (flexibility ratio of 7). From the linear and the nonlinear analyses, the main observations are:

1. Differences in acceleration response between the free-field and near the tunnel were generally small.
2. Racking ratio of the tunnel was high (2.1 nonlinear case and 2.3 linear case), in comparison to the free-field shear distortion in at levels of the roof and the slab. As such, the deviation was as much as twice the free-field response in both cases (linear and nonlinear). For the linear case, this deviation matched closely with the racking ratio of 2.2 as derived by the Wang (1993) procedure.
3. In the nonlinear soil cases, ground yielding with some permanent deformation resulted in larger earth pressures. Pressure from the dynamic effects only was as much as twice that of the original own weight static state.
4. The effect of tension-cutoff for the soil nonlinear material was negligible in the case studied herein.
5. While, a single soil-tunnel study is conducted in this Chapter, Appendix J discusses the results of further parametric studies in which soil stiffness properties are varied within a wide range. Comparison of these numerical parametric study outcomes to the FHWA (2009) design procedure are included in this Appendix.

Table 7-1: Tunnel material properties (beam-column elements) for linear analysis

Property	Components of the tunnel			
	Wall	Slab	Roof	Wall Joints
Young's modulus, E (ksi)	87000	87000	87000	87000
Area of cross-section, A (in^2)	6.75	5.34	5.34	6.75
Moment of inertia, I (in^4)	25.6	1×10^9	1×10^9	3×10^9

Table 7-2: Soil material properties

Layer	Thickness (ft)	Shear modulus (psi)	Shear strength (psi)	Poisson's ratio	Unit weight (pcf)
1	3.92	3641	21	0.316	113
2	3.92	6306	25	0.316	113
3	3.92	8141	29	0.316	113
4	6.06	10001	33	0.316	113
5	4.69	11678	37	0.316	113
6	5.11	13020	42	0.316	113
7	5.11	14286	46	0.316	113
8	5.11	15449	50	0.316	113
9	5.11	16530	54	0.316	113
10	4.88	17522	58	0.316	113
11	6.29	18568	62	0.316	113
12	6.29	19681	66	0.316	113
13	6.29	20734	69	0.316	113
14	6.29	21736	73	0.316	113
15	6.29	22694	76	0.316	113
16	6.29	23613	79	0.316	113
17	6.29	24497	83	0.316	113
18	6.29	25351	86	0.316	113
19	6.29	26177	89	0.316	113
20	6.29	26978	92	0.316	113
21	6.29	27755	94	0.316	113

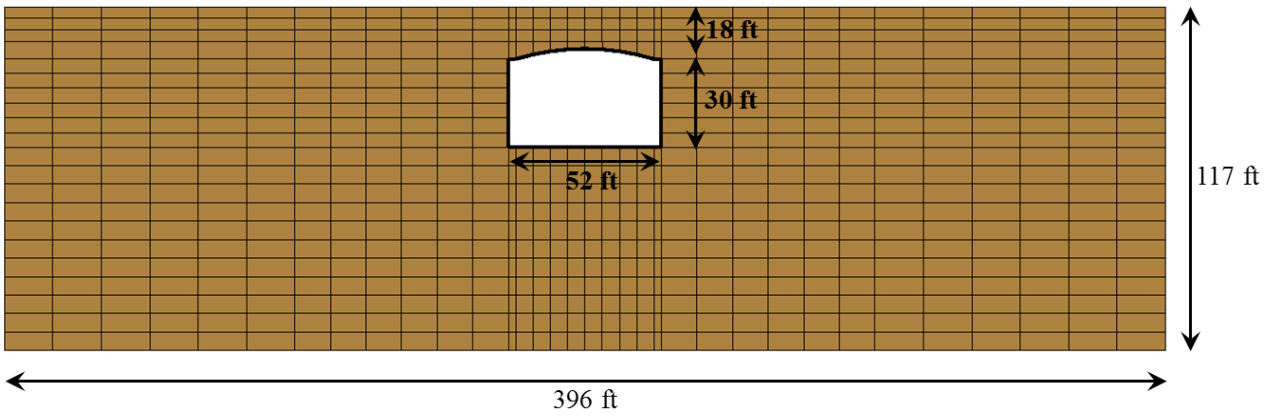

Figure 7-1: FE mesh for the tunnel-ground model in 2D plane strain

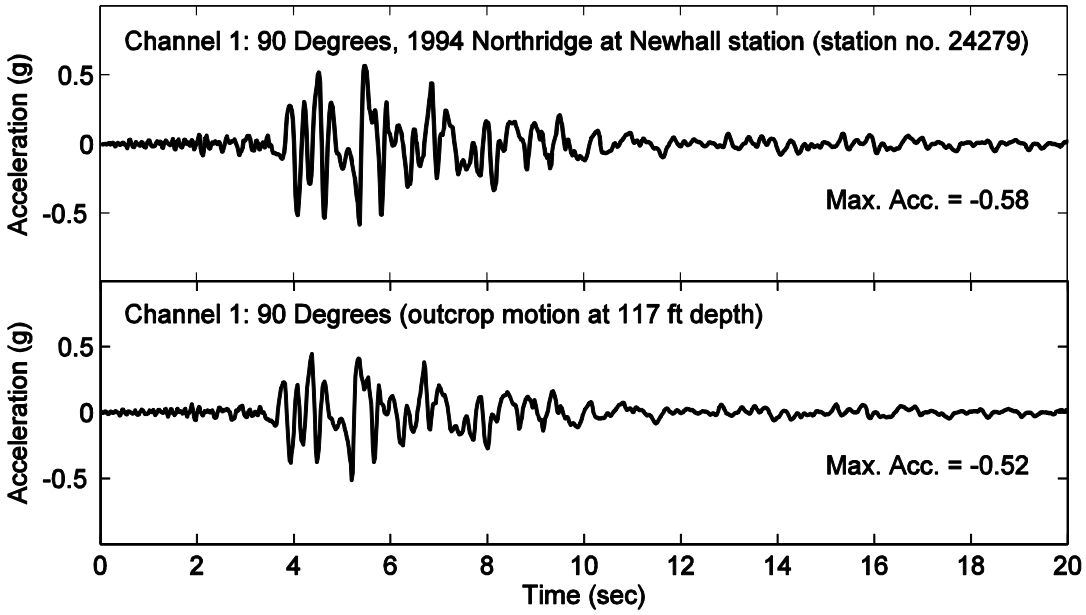

Figure 7-2: Northridge earthquake record (Newhall station, CSMIP station No. 24279) and outcrop motion at depth of 117 ft from deconvolution (base of the soil domain)

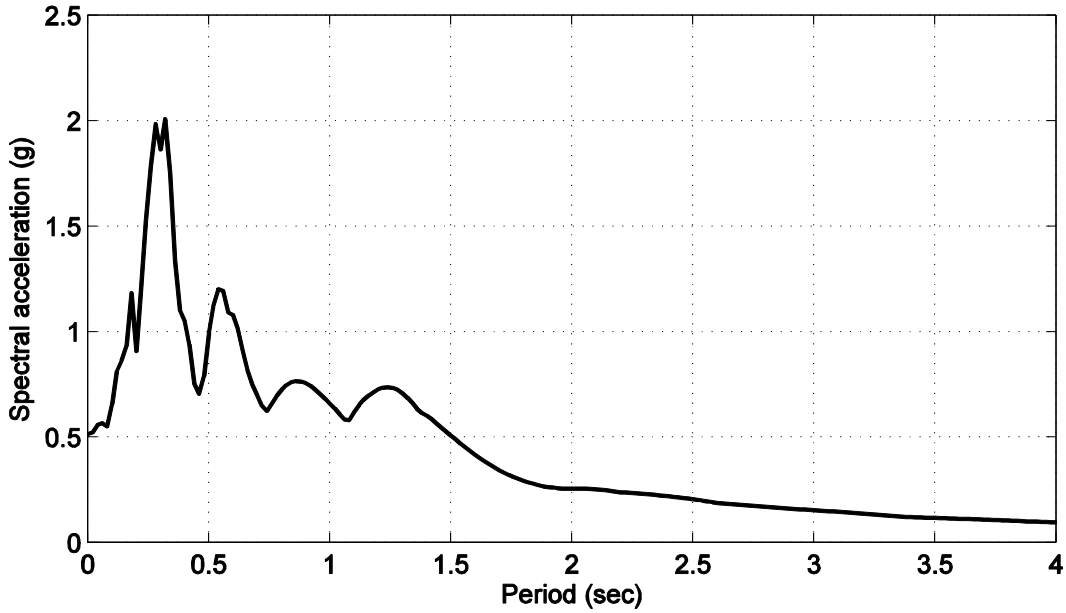

Figure 7-3: Spectral acceleration (5% damped) of the outcrop motion at depth of 117 ft from deconvolution of the Northridge earthquake record (Newhall station, CSMIP station No. 24279)

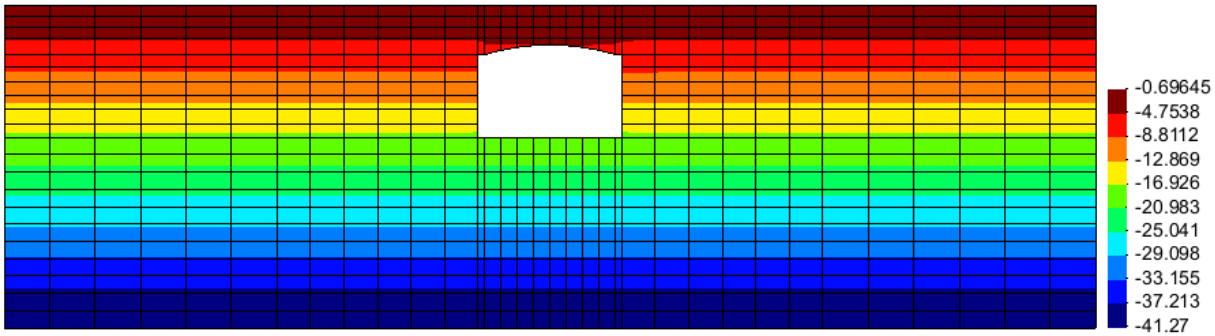

(a)

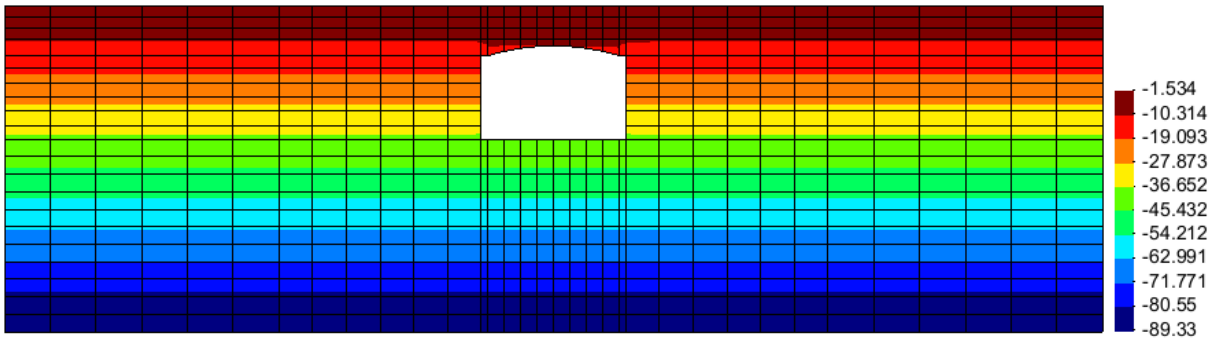

(b)

Figure 7-4: Contour of horizontal (a) and vertical (b) stresses under gravity (shown in psi)

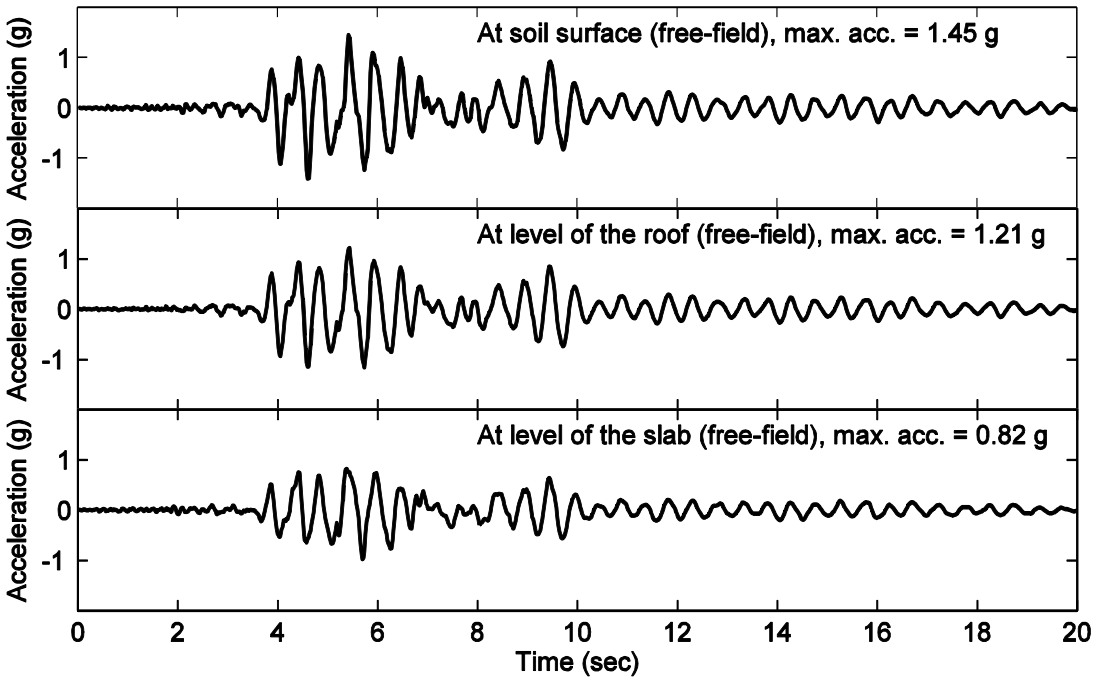

Figure 7-5: Acceleration time histories in free-field at levels of soil surface, the roof, and the slab

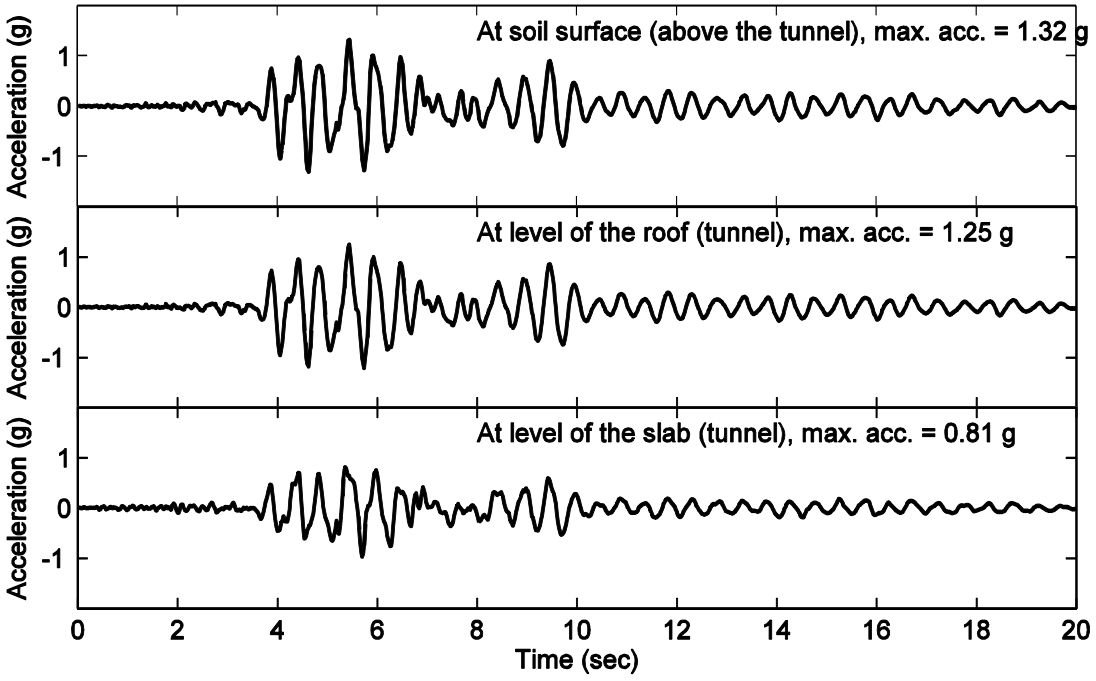

Figure 7-6: Acceleration time histories at levels of soil surface above the tunnel, the roof, and the slab

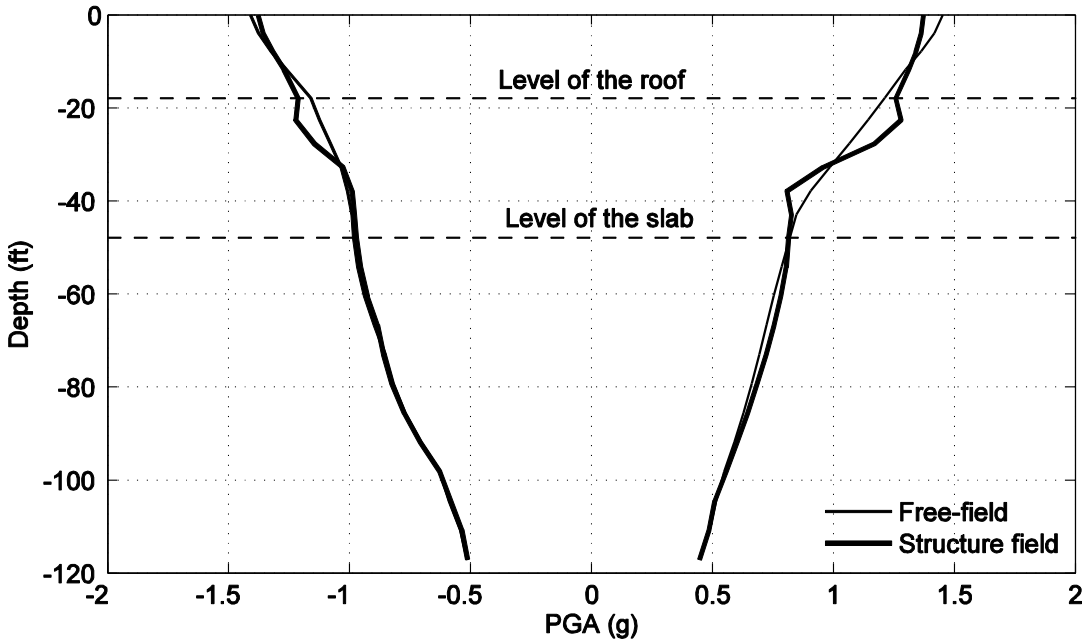

Figure 7-7: Profile of peak ground acceleration (PGA) in free-field and structure field

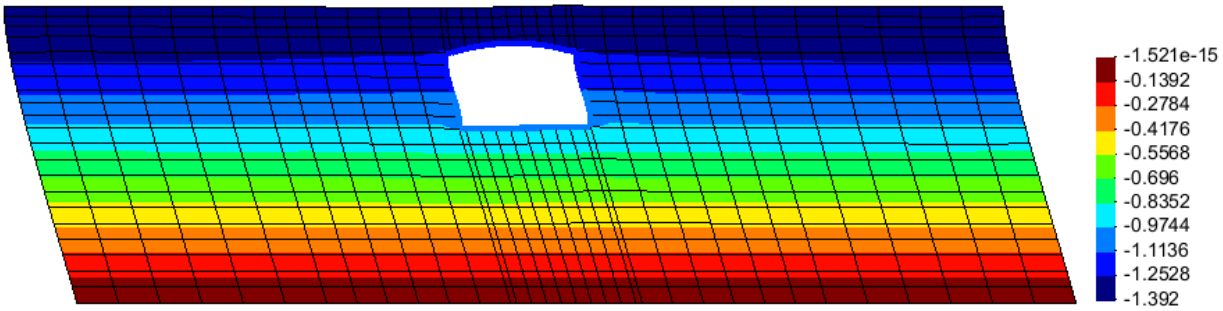

Figure 7-8: Deformed mesh at 5.44 seconds of base excitation (contour indicates horizontal displacement in inches)

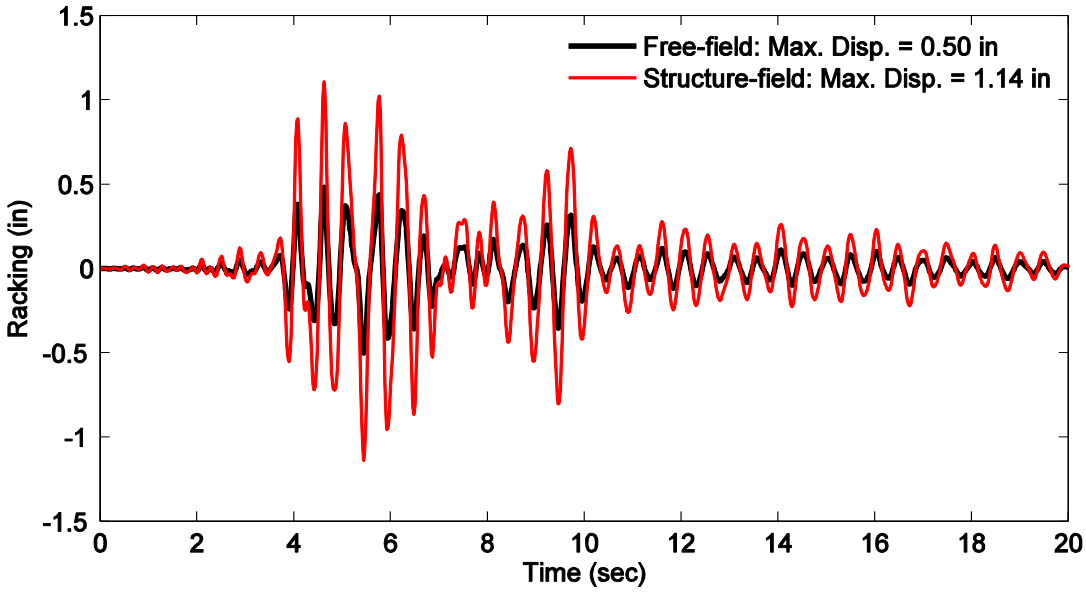

Figure 7-9: Racking response time histories in the free-field and the structure field (left wall)

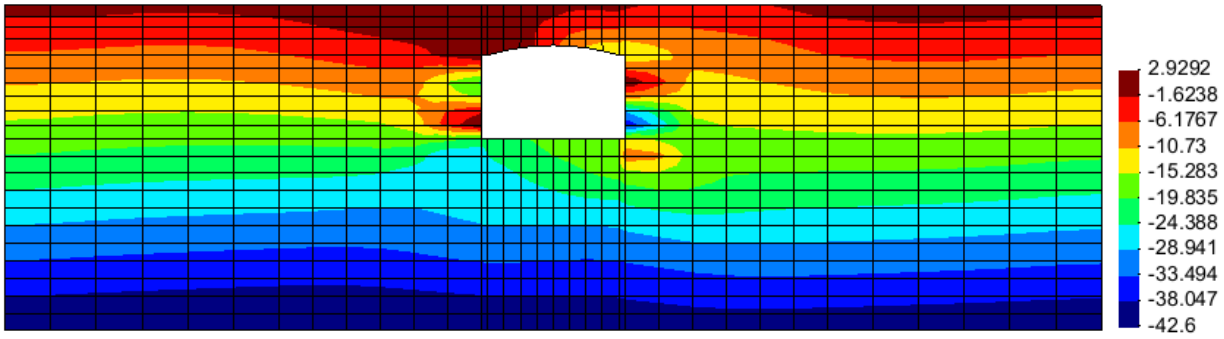

(a)

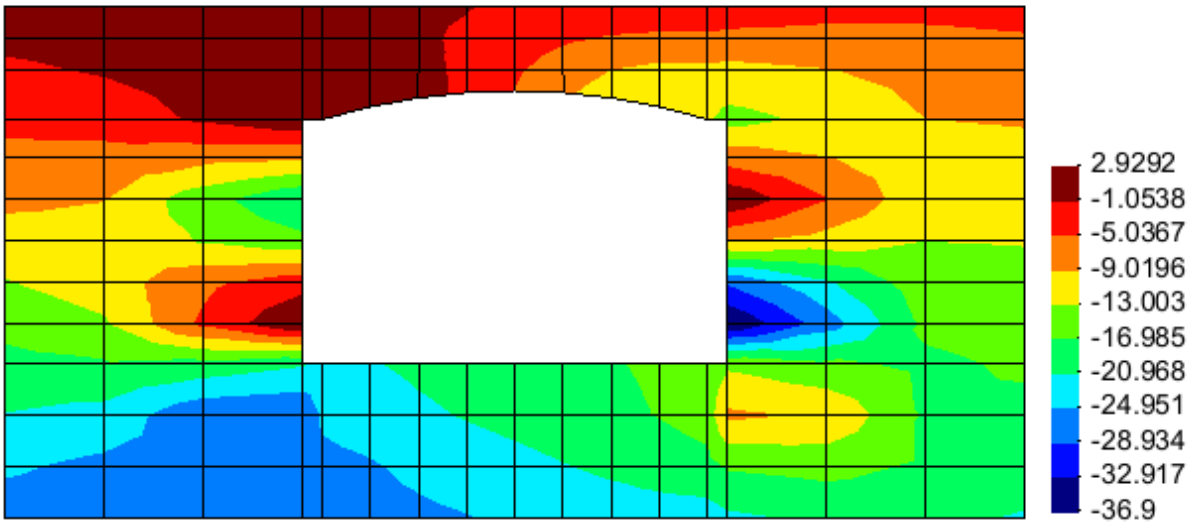

(b)

Figure 7-10: Contour of horizontal stress at 5.44 seconds of base excitation (units in psi): (a) along depth of the soil; (b) close-up

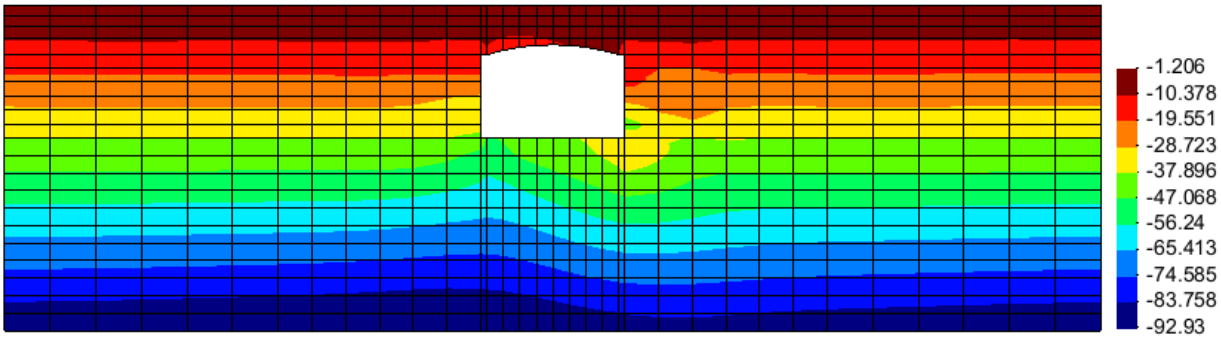

(a)

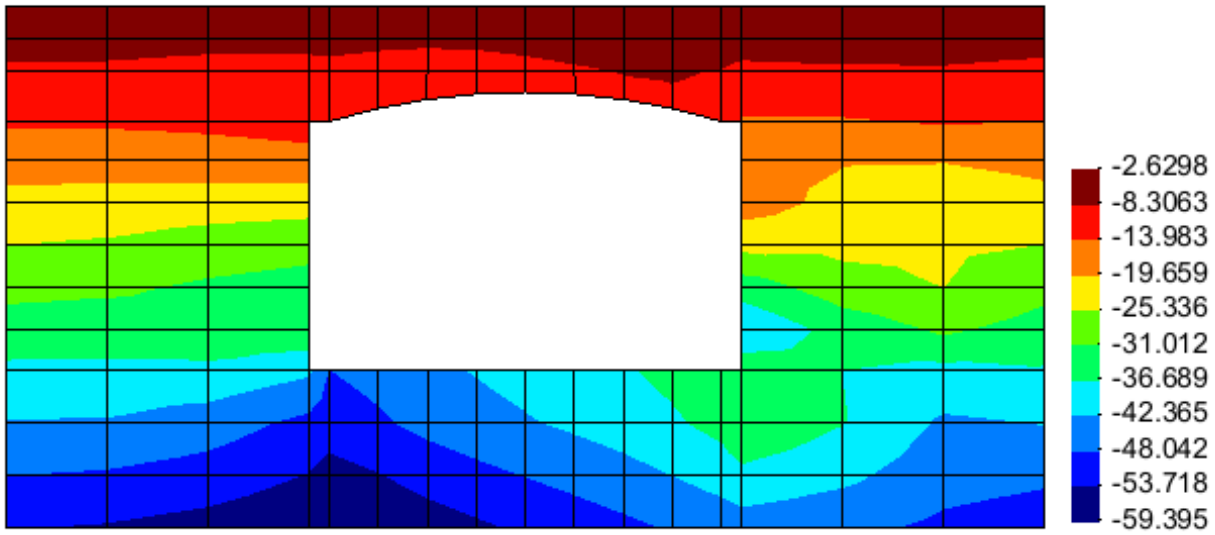

(b)

Figure 7-11: Contour of horizontal vertical stress at 5.44 seconds of base excitation (units in psi): (a) along depth of the soil; (b) close-up

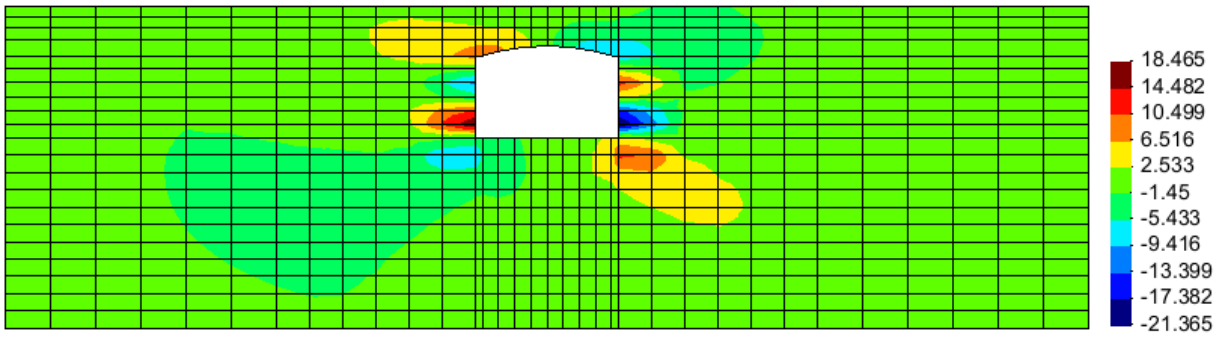

(a)

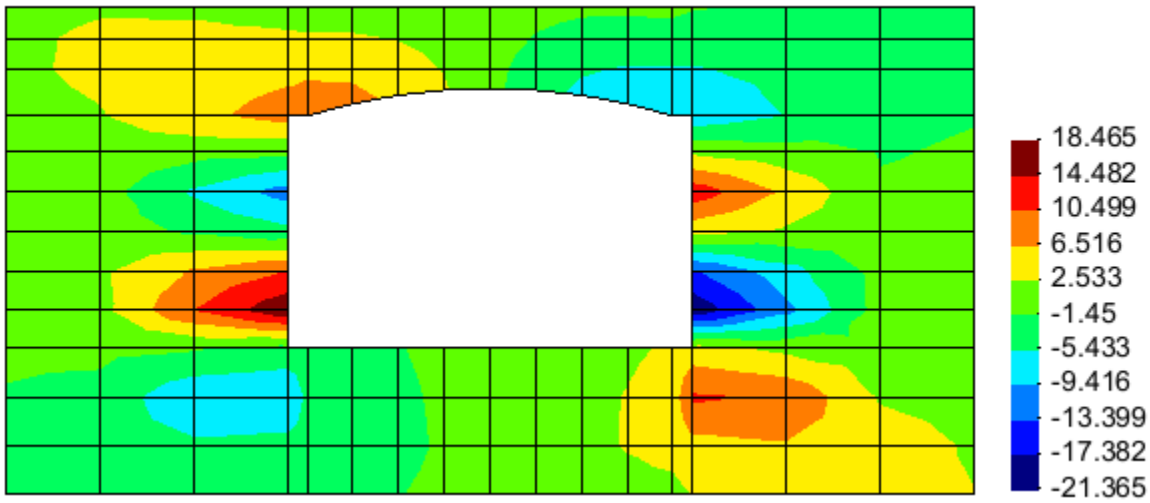

(b)

Figure 7-12: Dynamic part only; contour of horizontal stress at 5.44 seconds of base excitation (units in psi): (a) along depth of the soil; (b) close-up

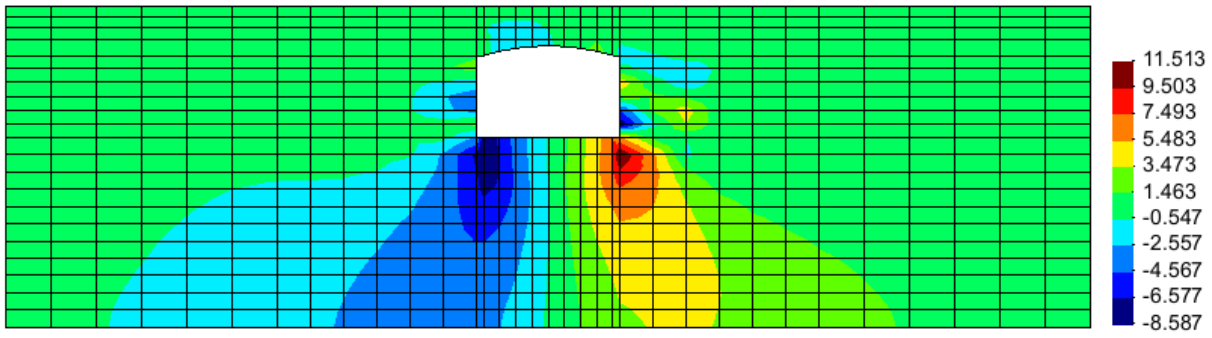

(a)

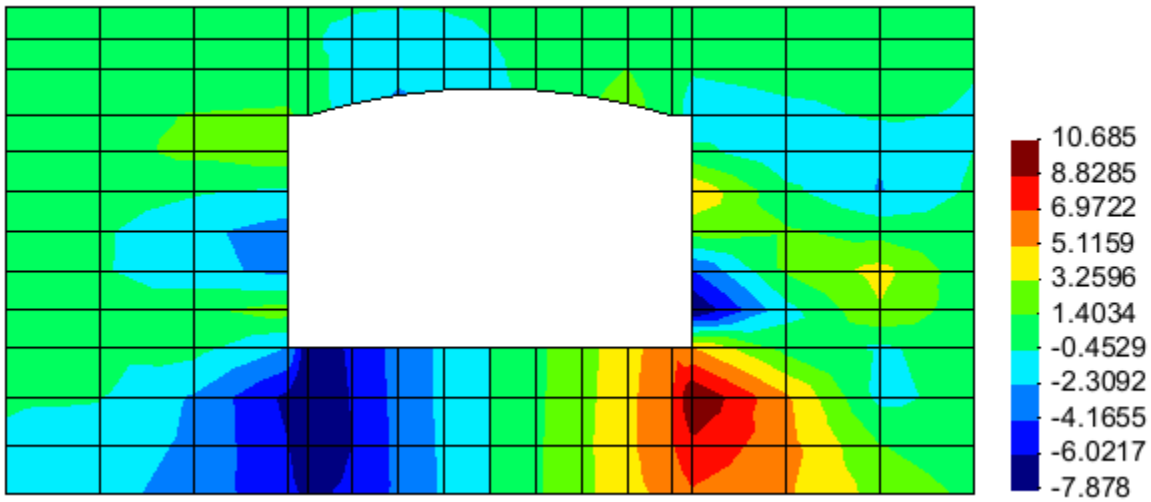

(b)

Figure 7-13: Dynamic part only; contour of vertical (bottom) stress at 5.44 seconds of base excitation (units in psi): (a) along depth of the soil; (b) close-up

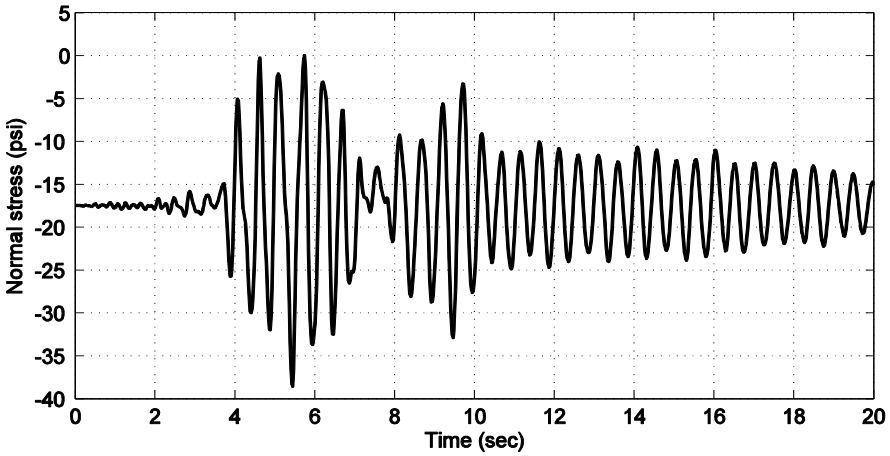

Figure 7-14: Normal (lateral) stress history at left bottom of the tunnel

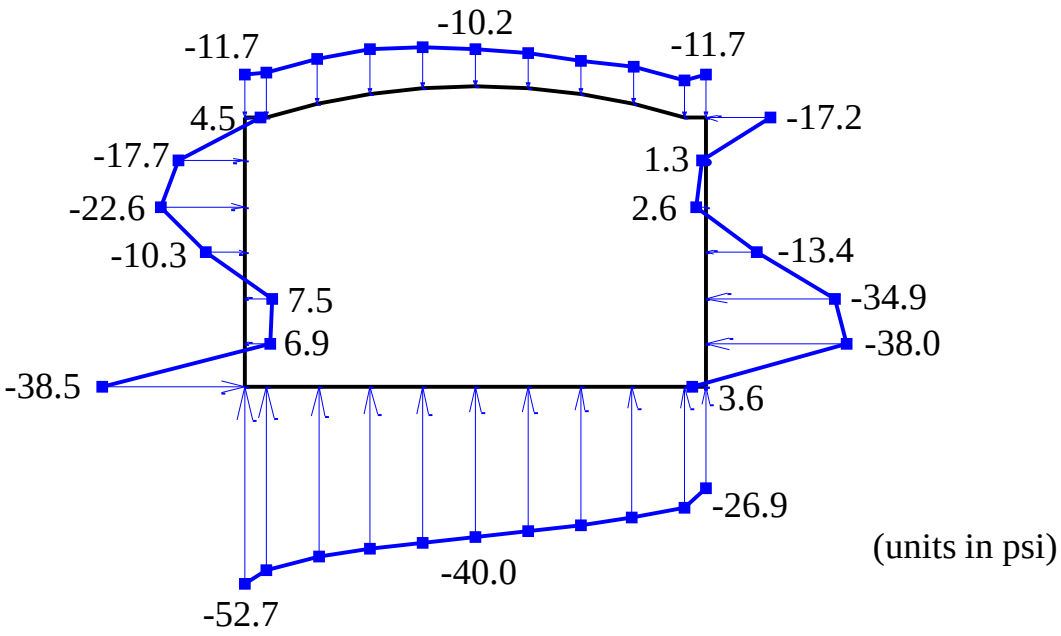

(a) Total earth pressure

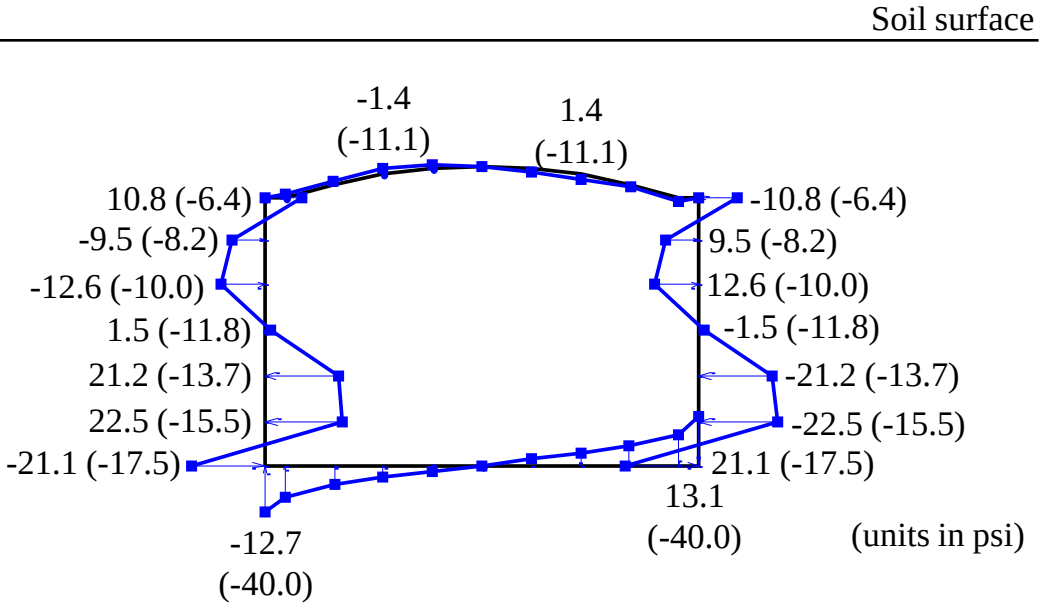

(b) Dynamic part only earth pressure (static pressure shown in the parenthesis)

Figure 7-15: Normal earth pressure profile along the tunnel as the maximum pressure developed at bottom of the left wall at 5.44 seconds

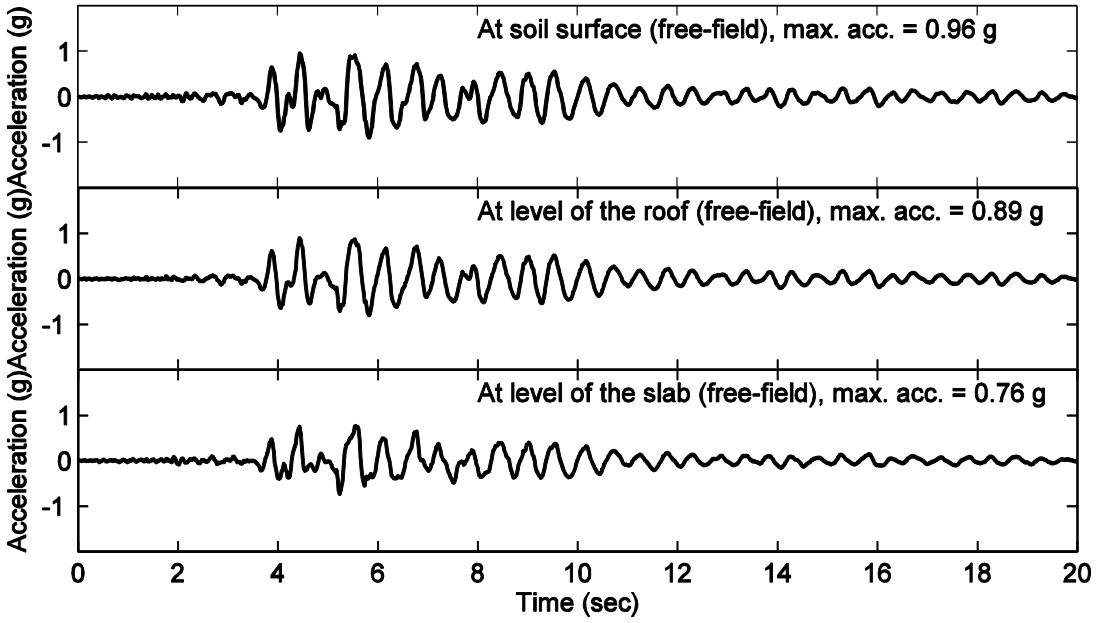

Figure 7-16: Acceleration time histories in free-field at levels of soil surface, the roof, and the slab

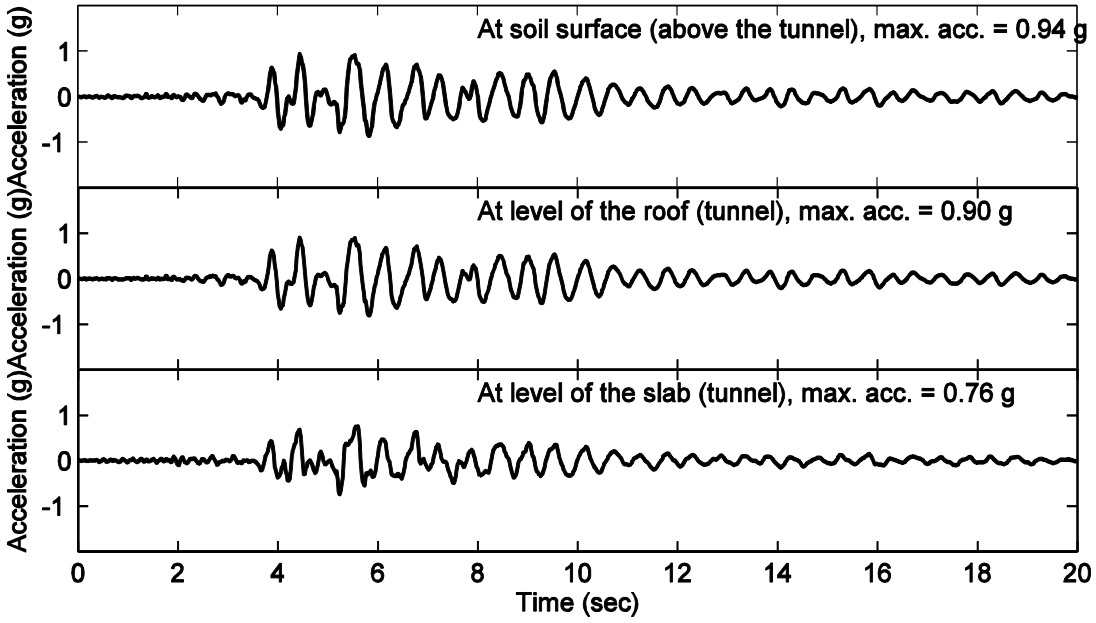

Figure 7-17: Acceleration time histories at levels of soil surface above the tunnel, the roof, and the slab

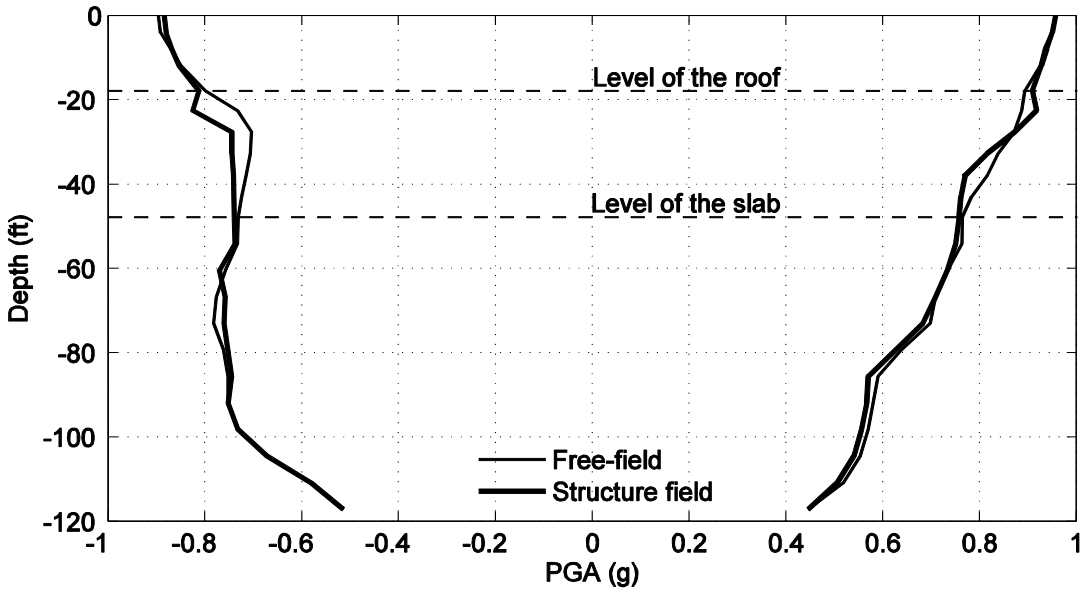

Figure 7-18: Profile of peak ground acceleration (PGA) in free-field and structure field

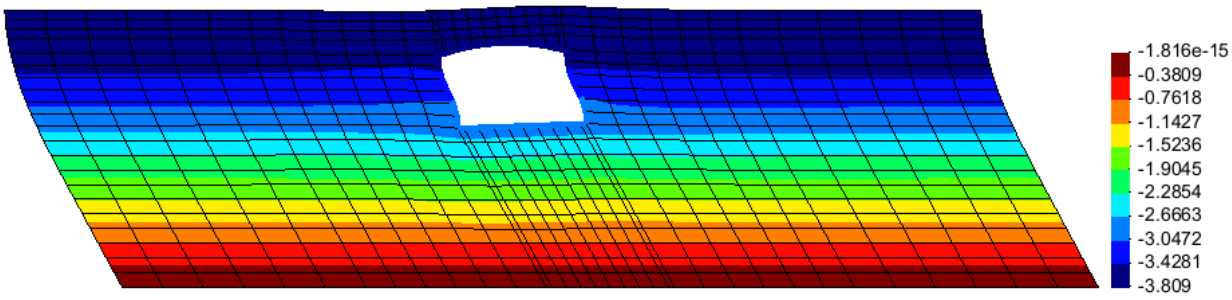

Figure 7-19: Deformed mesh at 5.52 seconds of base excitation (contour indicates horizontal displacement)

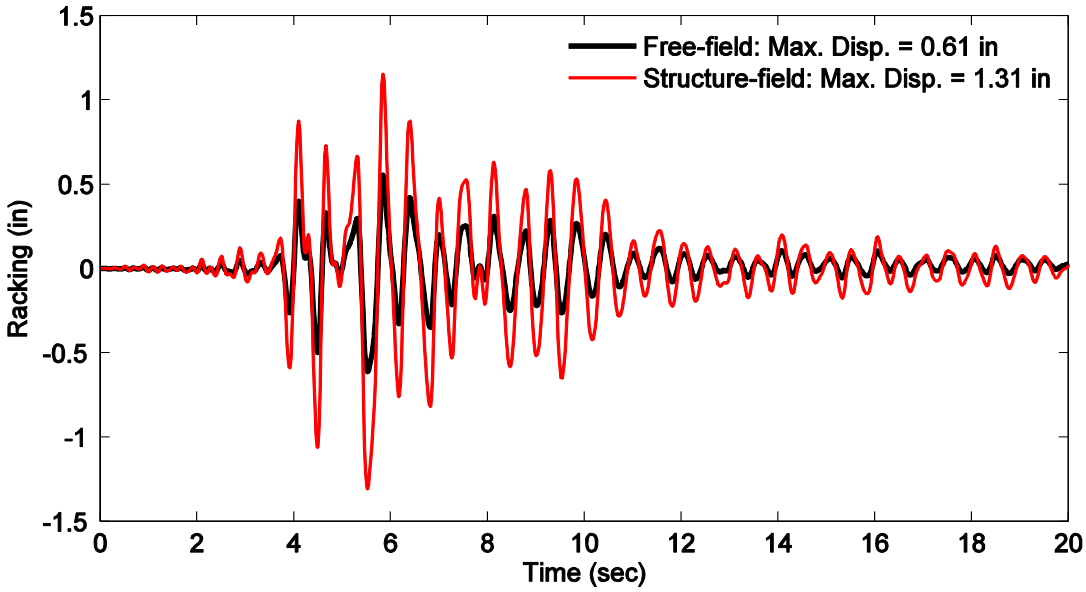

Figure 7-20: Racking response time histories in the free-field and the structure field (left wall)

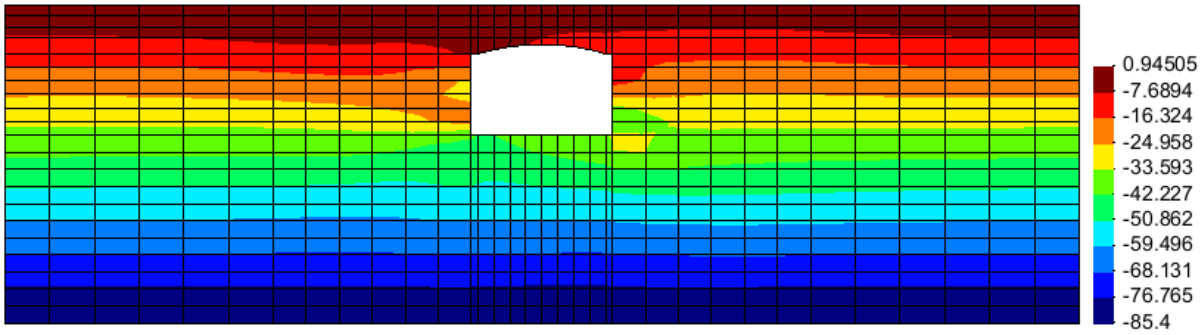

(a)

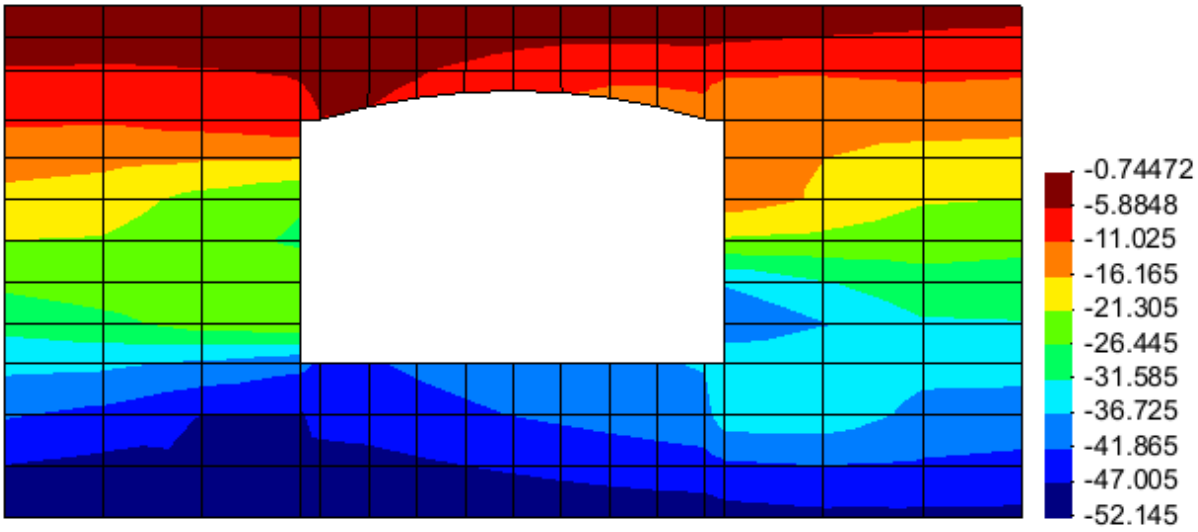

(b)

Figure 7-21: Contour of horizontal stress at 5.52 seconds of base excitation (units in psi): (a) along depth of the soil; (b) close-up

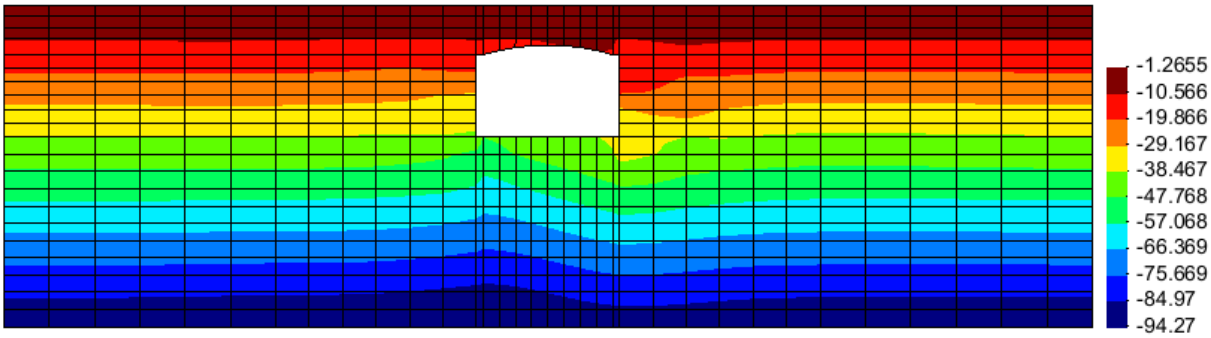

(a)

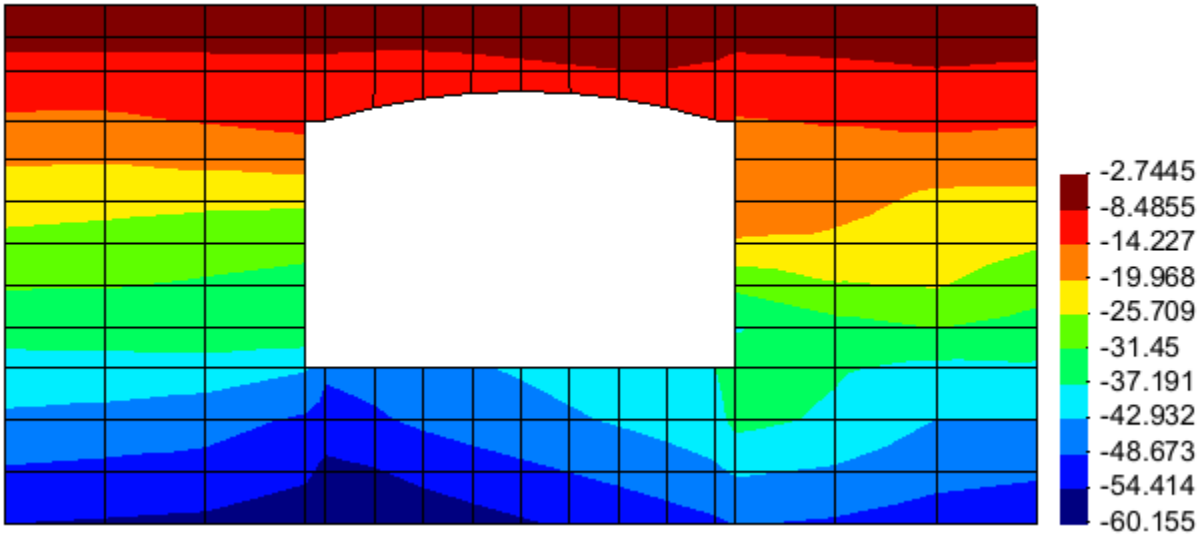

(b)

Figure 7-22: Contour of vertical stress at 5.52 seconds of base excitation (units in psi): (a) along depth of the soil; (b) close-up

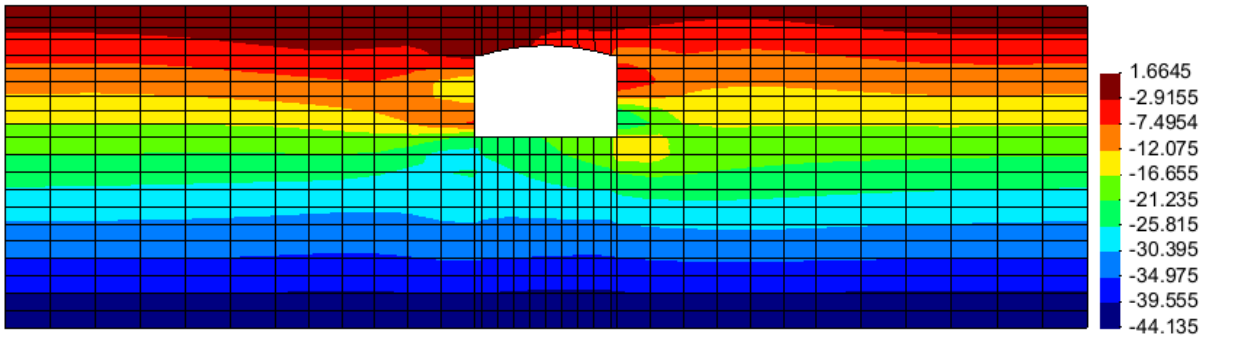

(a)

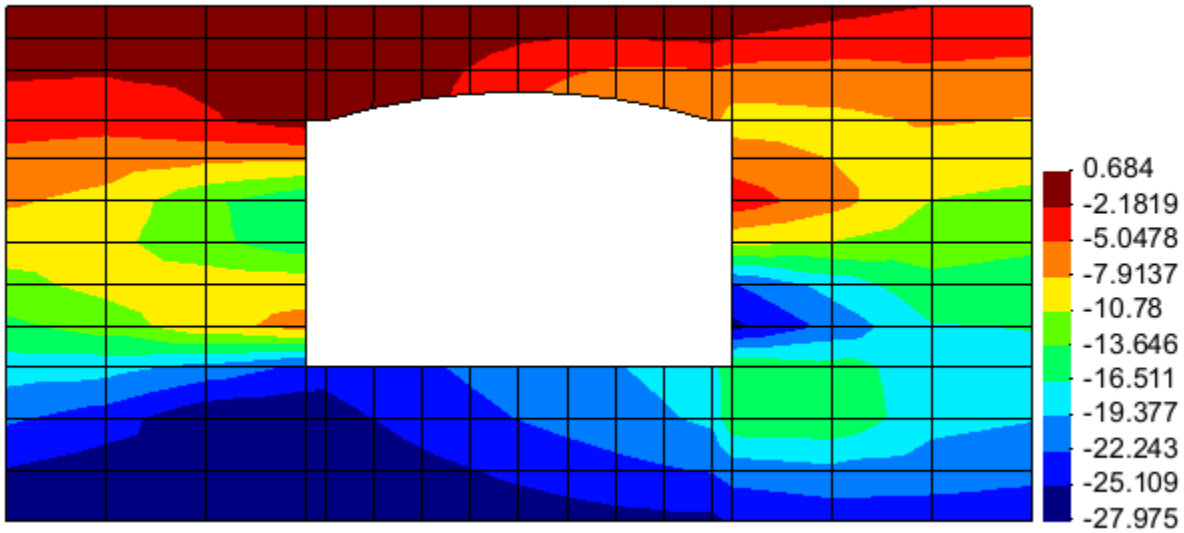

(b)

Figure 7-23: Dynamic part only; contour of horizontal stress at 5.52 seconds of base excitation (units in psi): (a) along depth of the soil; (b) close-up

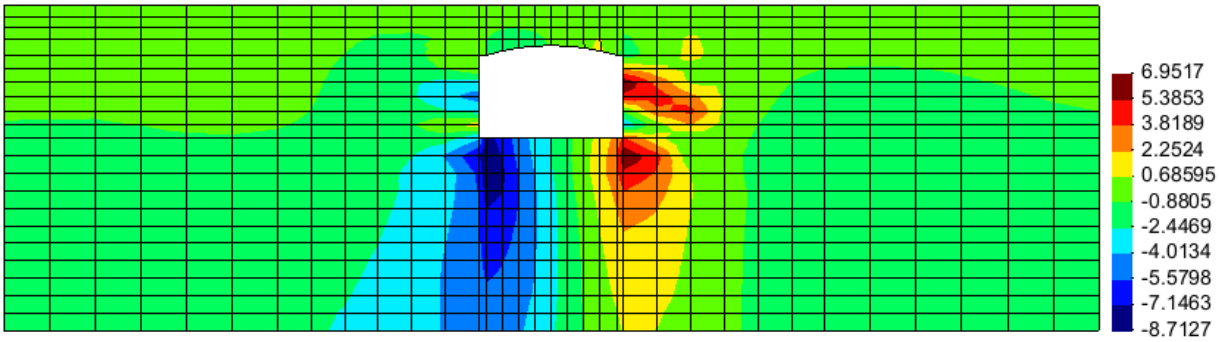

(a)

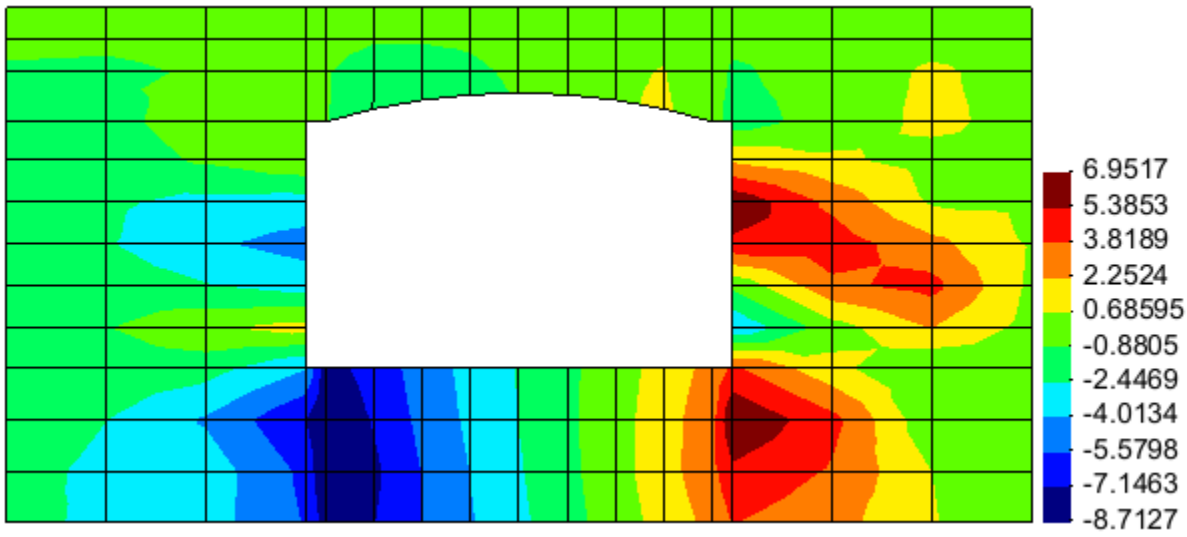

(b)

Figure 7-24: Dynamic part only; contour of vertical stress at 5.52 seconds of base excitation (units in psi): (a) along depth of the soil; (b) close-up

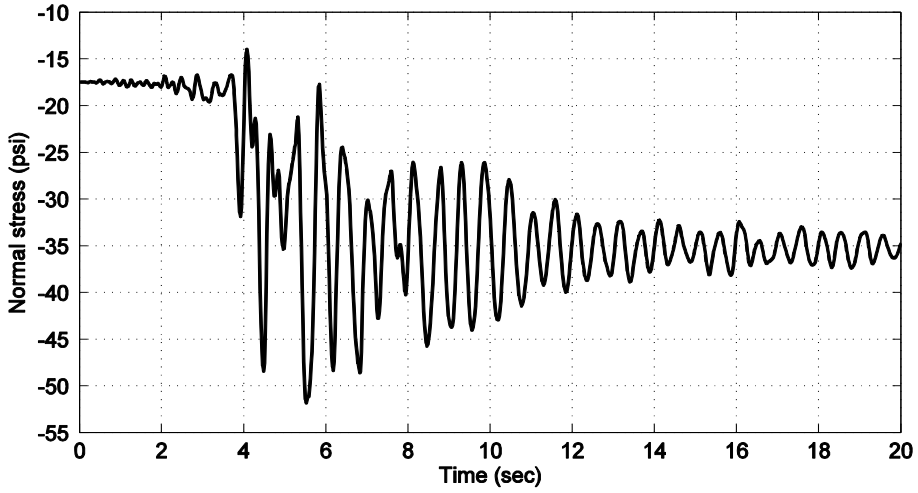

Figure 7-25: Normal (lateral) stress history at left bottom of the tunnel (using the nonlinear soil properties)

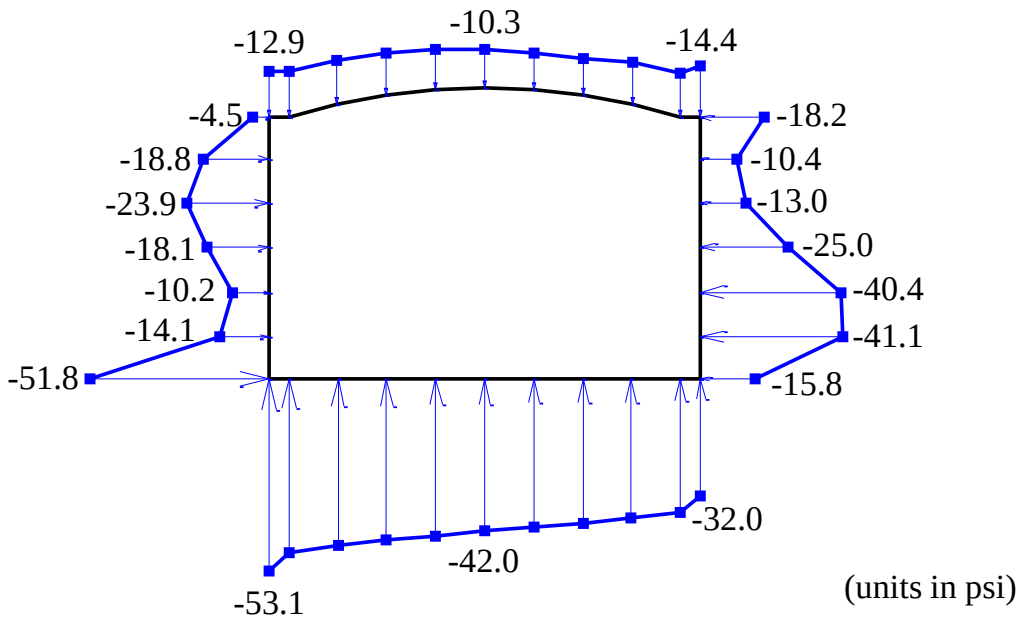

(a) Total earth pressure

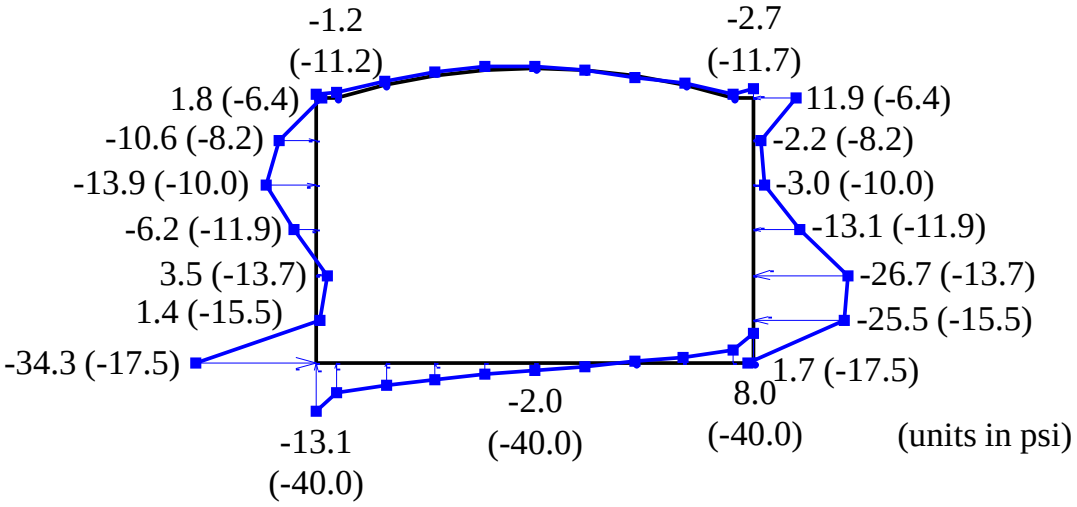

(b) Dynamic part only earth pressure (static)

Figure 7-26: Normal earth pressure profile along the tunnel as the maximum pressure developed at bottom of the left wall at 5.44 seconds

8. Centrifuge Tunnel-Ground Testing Phase

8.1 Introduction

This chapter presents a simple experimental effort conducted on the centrifuge (modeling at 30g, where g is the gravity acceleration). Effects due to the wave preparation mechanism are of interest in this test (for further calibration of the numerical models). Acceleration response at levels of soil surface and within the ground is recorded. Before the shaking phase, shear wave velocity measurements were done to evaluate the soil profile stiffness characteristics.

8.2 Centrifuge modeling

Figure 8-1 shows the UCSD centrifuge (model C61-3) manufactured by Actidyn. Table 8-1 summarizes the main characteristics of this centrifuge. Figure 8-2 illustrates a comparison of vertical stress values in prototype scale and centrifuge model scale. Table 8-2 summarizes the scaling factors. As shown in Figure 8-2, the stresses are identical in both scales. The same concept also applies to strain, which leads to a 1:1 scale for relationship of soil stress-strain mobilized in the centrifuge model.

8.3 Model configuration

8.3.1 Soil material

Sieve analysis will be conducted to determine the sand grain size distribution. As mentioned earlier, shear wave velocity along the profile depth was also measured.

8.3.2 Model container

Figure 8-3 shows the rigid box container used in the test. Inner dimensions of the box were 14 in (length) x 14 in (width) x 9.5 in (height). This box is made of aluminum.

8.3.3 Tunnel model (for future testing)

Figure 8-4 shows the tunnel model, a hollow square box aluminum tube. Two different thicknesses (3/16 in and 1/4 in) were chosen to allow for further studies into the effect of relative stiffness between the tunnel and the surrounding soil. Table 8-3 summarizes properties of the tunnel specimens in model scale. The dimension of the aluminum tube was 3 in (width) x 4 in

(height) x 13.75 in (length). In prototype scale (30g testing environment), these dimensions correspond to 7.5 ft (width) x 10 ft (height) x 34.4 ft (length) with two different thicknesses of 5.6 in and 7.5 in. Under the simply supported boundary condition (Wang 1993), computed lateral stiffness (in prototype scale) per unit length of 1 ft was 302 kip/ft (5.6 in thickness) and 720 kip/ft (7.5 in thickness).

8.3.4 Model sand preparation

To achieve a target sand relative density of 90%, the dry pluviation technique (raining of sand through air) was used as shown in Figure 8-5. The centrifuge rigid box height was divided into layers of 1 in thickness. After the pluviation, each sand layer was tamped additionally (Figure 8-5).

8.4 Instrumentation: accelerometers

Due to ongoing developments in the data acquisition system, the instrumentation used in the tests included only accelerometers. Six accelerometers were placed inside the rigid soil box. One accelerometer was mounted at the container base to compare the target acceleration input with the input shaker signal. Figure 8-6 shows two types of miniature accelerometers manufactured by PCB Piezotronics (Model 355M69 and Model 352M54, which differ in the mounting mechanism). The range of acceleration that can be recorded is ±100g. The sensitivity of the accelerometers is ±10% (50 mV/g). The actual weight of the accelerometers is 10 gm (Model 355M60) and 1.8 gm (Model 352M54).

8.5 Test configuration

Tests were conducted according to the following scenario:

- Free-field test: The soil container was filled without the tunnel model to evaluate response of the sand stratum. Figure 8-8 shows the accelerometer instrumentation layout in this test. To examine the boundary effect of the rigid soil box, two sets of the accelerometers were placed near the side of the box and in the center. It is noted here that plans are underway to include in tunnel models in future tests.

8.6 Earthquake simulation

Figure 8-7 shows the servo-hydraulic centrifuge shaker manufactured by PVL Technologies, Inc. to produce one dimensional horizontal shaking. Table 8-4 summarizes specifications of the shake table. This shaker produces earthquake signals based on the provided input voltage. The response of the shaker to this signal is in the form of displacement that is measured using an LVDT attached to the shaker moving base plate.

8.6.1 Pulse input motion

Prior to the earthquake shaking phase, a pulse-type input motion was used to evaluate shear wave velocity in the soil model. Figure 8-10 shows the pulse input that was a half sinusoidal wave with a frequency of 75 Hz and amplitude of 6 g in model scale.

8.6.2 Earthquakes input motions

The earthquake motion used in the test was derived from the 1989 Loma Prieta earthquake (CDMG 58235 Saratoga, W. Valley Coll.) specified in the reference (Mason et al. 2010). A process of bandpass filtering was applied to produce the voltage signal for the shaker. A low frequency of 0.4 Hz (12 Hz at 30g-level) in the bandpass was used to limit maximum displacements (to about 0.2 in) for the shaker. A high frequency of 5 Hz (150 Hz at 30g-level) was used to remove extraneous high frequency motions (around 200 Hz) beyond the capacity of the shaker. Figure 8-11 and Figure 8-12 show the original records and the filtered earthquake motions. The predominant frequencies were in the range of 0.83 Hz (24.9 Hz at 30g).

8.7 Test results

8.7.1 Results from the free-field test

Prior the earthquake shaking, the pulse wave (Figure 8-10) was applied to the model base to measure the shear wave velocity with depth. The measured acceleration was filtered with a range of 0.1 Hz to 10 Hz. Figure 8-13 shows measured acceleration time histories from the accelerometers. On the basis of the arrival time differences of the first peak, the shear wave velocity (average) of 1823 ft/sec was evaluated in the center of the soil (from A2-A4 in Figure 8-8) as summarized in Table 8-6.

8.7.1.1 Acceleration time histories

From the Loma Prieta earthquake shaking (Saratoga W V Coll 270), Figure 8-14 shows measured acceleration time histories with a filter of 0.2 Hz to 3 Hz along depth. Figure 8-15 shows the peak ground acceleration (PGA). The PGA of 0.322g at soil surface increased by about 10%, compared to 0.295 g at the depth of 15 ft (location of the tunnel slab if the tunnel is present).

8.7.1.2 Evaluation of shear stress-strain history

Shear stress and strain time histories can be roughly evaluated (Zeghal et al. 1995). On the basis of a one-dimensional shear beam idealization, shear stress at any level z may be expresses as:

$$\tau(z,t) = \int_0^z \rho \ddot{u}\, dz \tag{8.1}$$

where z = depth coordinator, t = time, $\tau(z,t)$ is horizontal shear stress, and $\ddot{u}$ is absolute horizontal acceleration. Utilizing linear interpolation between downhole accelerations (Figure 8-16), the shear stress at level z_i can be computed as:

$$\tau_t(t) = \sum_{k=1}^{i-1} \rho \frac{\ddot{u}_k + \ddot{u}_{k+1}}{2} \Delta z_k, i = 2, 3, \ldots \tag{8.2}$$

where subscript i refers to level z_i and Δz_k is the spacing interval as shown in Figure 8-16. The estimated stress is second-order accurate. A corresponding second-order accurate shear strain γ_i can be expresses as:

$$\gamma_i(t) = \frac{1}{\Delta z_{i-1} + \Delta z_i} \left[(u_{i+1} - u_i) \frac{\Delta z_{i-1}}{\Delta z_i} + (u_i - u_{i-1}) \frac{\Delta z_i}{\Delta z_{i-1}} \right] \tag{8.3}$$

where $u_i = u(z,t)$ is absolute displacement derived by double integrating the acceleration time history.

Resulting from the above equations (8.2) and (8.3), shear stress and strain time histories at the depth of 7.5 ft are shown in Figure 8-17 (in the center) and Figure 8-18 (near the side boundary).

8.8 Summary

A description of the centrifuge modeling test to document the mechanisms of dynamic wave propagation within a soil stratum soil-stratum was presented. This effort is a first step towards testing that includes the tunnel model. Further studies are underway, along with related numerical model calibration efforts.

Table 8-1: Characteristics of the UCSD centrifuge (model C61-3)

Force (g x ton)	50
Radius (m)	2.0
Basket Width (m)	0.6
*Basket Length (m)	1.0
Basket Depth (m)	0.60
Maximum Acceleration (g)	130
Maximum Load Under Maximum Acceleration (kg)	230
Maximum Load (kg)	500
Maximum Acceleration Under Maximum Load (g)	100
Maximum Power Consumption under Maximum Acceleration (kW)	25

* Measured in the shaking direction

Table 8-2: Scaling relationships for the centrifuge modeling (Taylor 1995)

Quantity	Prototype	Centrifuge Model (Ng)
Length	l	l/N
Density	ρ	ρ
Dynamic time	t	t/N
Frequency	f	Nf
Acceleration	a	Na
Velocity	v	v
Displacement	d	d/N
Stress	σ	σ
Strain	ε	ε

Table 8-3: Properties of the aluminum tunnel specimens at model scale

Specimen	Thickness (in)	Width (in)	Height (in)	Length (in)	Volume (in^3)	Density (lb/ft^3)	Mass (lb)
1	0.1875	3	4	13.75	34.16	167	3.3
2	0.25	3	4	13.75	44.69	167	4.3

Table 8-4: Specifications of the servo-hydraulic shaker

Method	Servo-hydraulic single-actuator system
Shaking type	Periodic or random, determined by input signal
Shaking direction	One direction
Nominal shaking force	4,800 lb (21 kN)
Maximum shaking velocity	15 in/sec (0.4 m/sec)
Maximum table displacement	±0.25 in (±6.35 mm)
Maximum payload dimension (L x W x H)	20 in x 17.5 in x 17 in (500 mm x 445 mm x 400 mm)
Maximum payload weight	350 lb (160 kg)
Nominal shaking frequency range	0 – 200 Hz
Maximum centrifugal acceleration	80 g

Table 8-5: Earthquake input motions used in the centrifugal acceleration of 30 g

Earthquake	**Prototype**		**Centrifuge test (30g-level)**	
	PGA (g)	**Predominant frequency (Hz)**	**PGA (g)**	**Predominant frequency (Hz)**
Loma Prieta Saratoga W V Coll 270	0.29	0.83	8.7	24.9

Table 8-6: Shear wave velocity profile before the Loma Prieta Earthquake excitation

Accelerometer	Depth (ft)	Arrival time of the first peak (sec)	Time difference in the adjacent layers (sec)	Shear wave velocity (ft/sec)	Average shear wave velocty between A2 and A4 (ft/sec)
A2	15	1.5120	-	-	1823
A3	7.5	1.5156	0.0036	2083.3	
A4	0	1.5404	0.0084	1562.5	

Figure 8-1: Photograph of the UCSD centrifuge

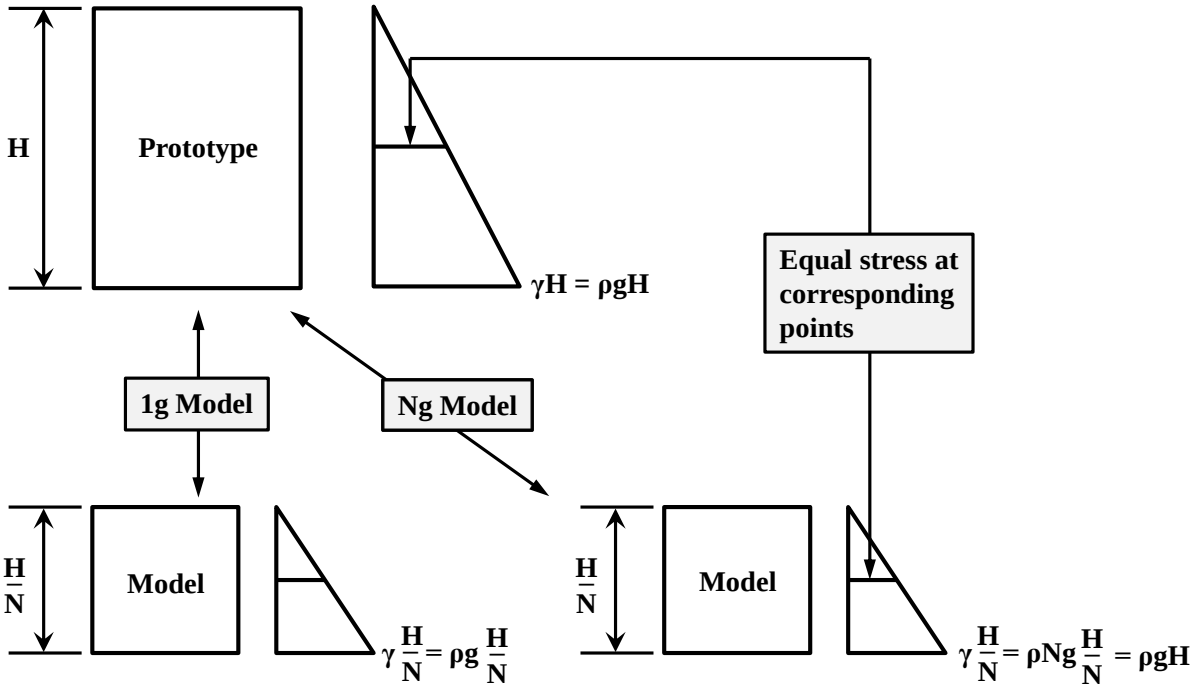

Figure 8-2: Stresses in centrifuge modeling (after Taylor, 1995)

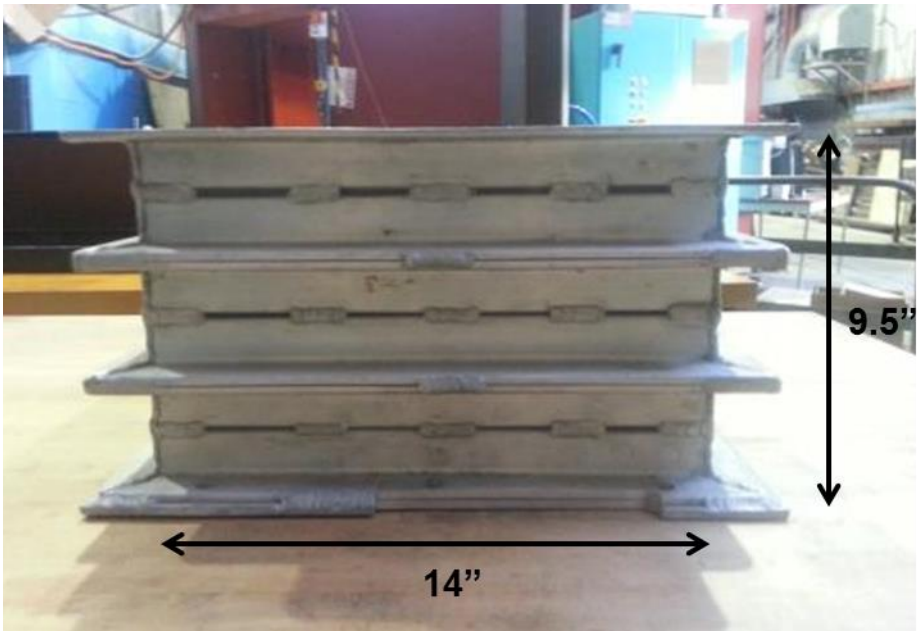

(a) Elevation view

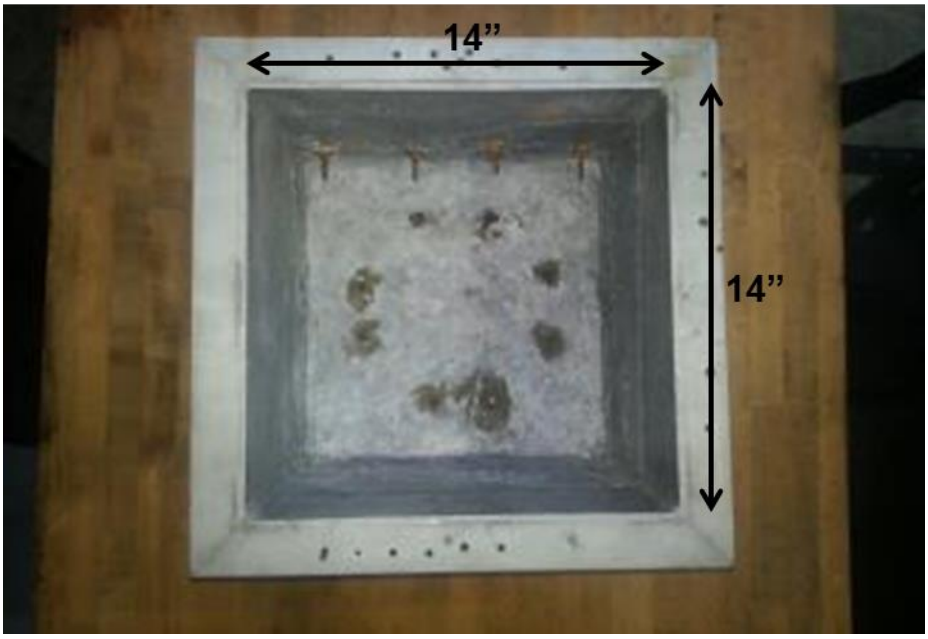

(b) Plan view

Figure 8-3: Rigid centrifuge soil box

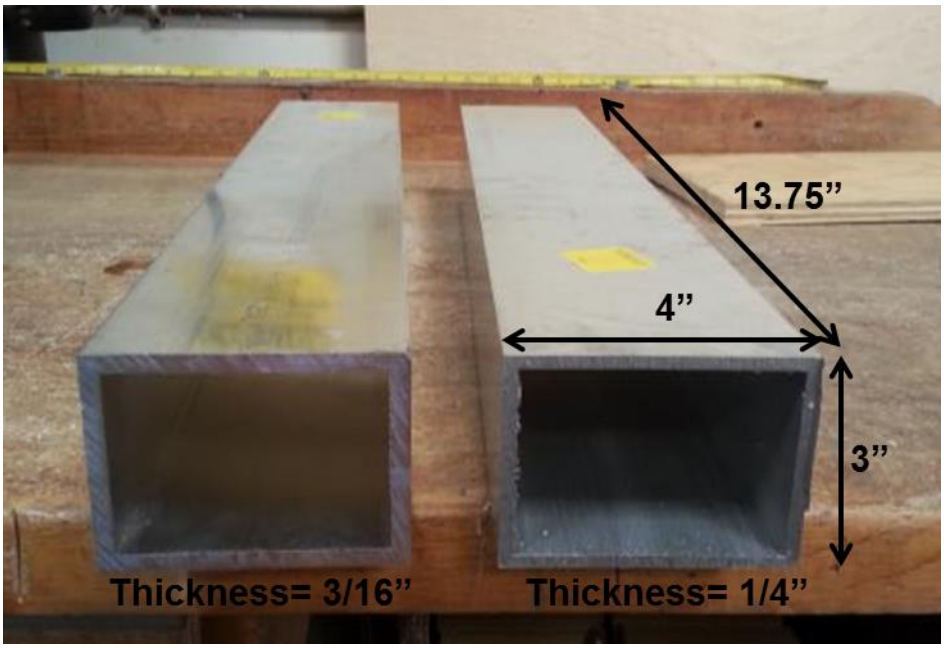

Figure 8-4: Photograph of the aluminum tunnel specimens with two different thickness

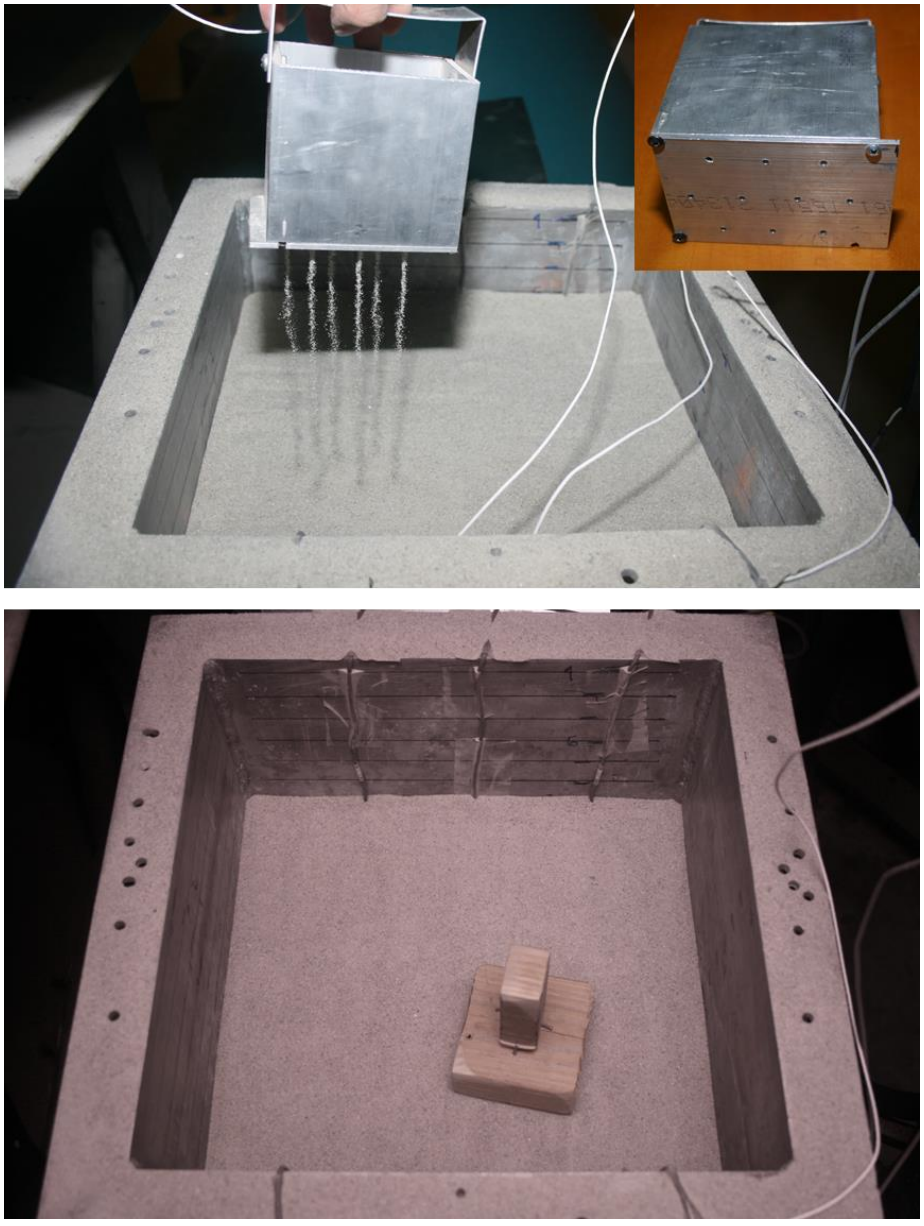

Figure 8-5: Sand model preparation using raining and tamping techniques

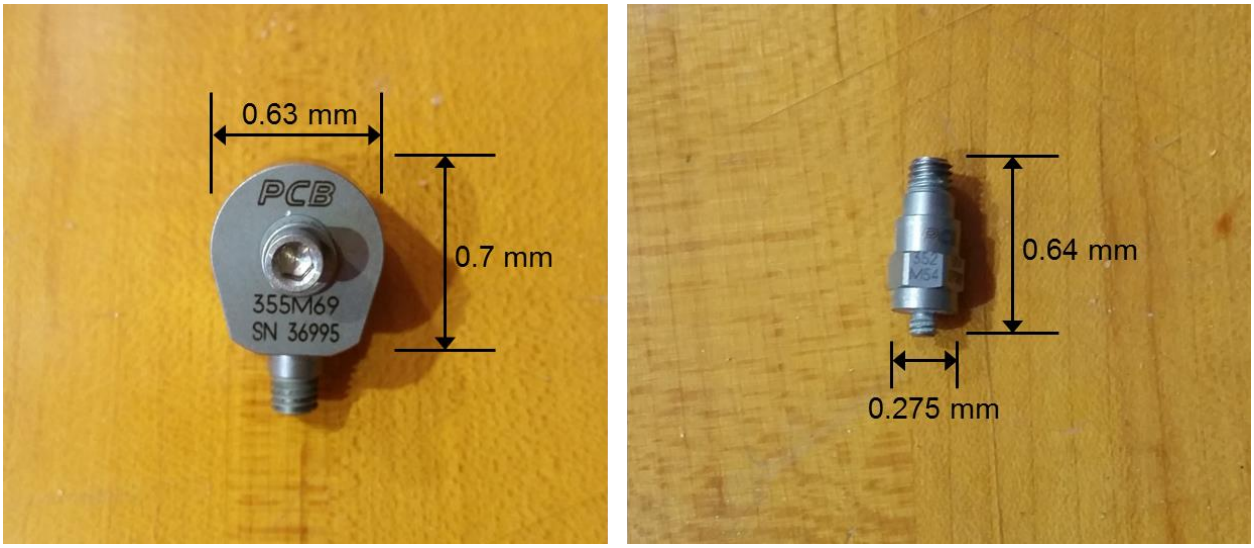

(a) Model 355M69 (b) Model 342M54

Figure 8-6: Accelerometers used in the centrifuge testing

Figure 8-7: One directional servo-hydraulic centrifuge shaker

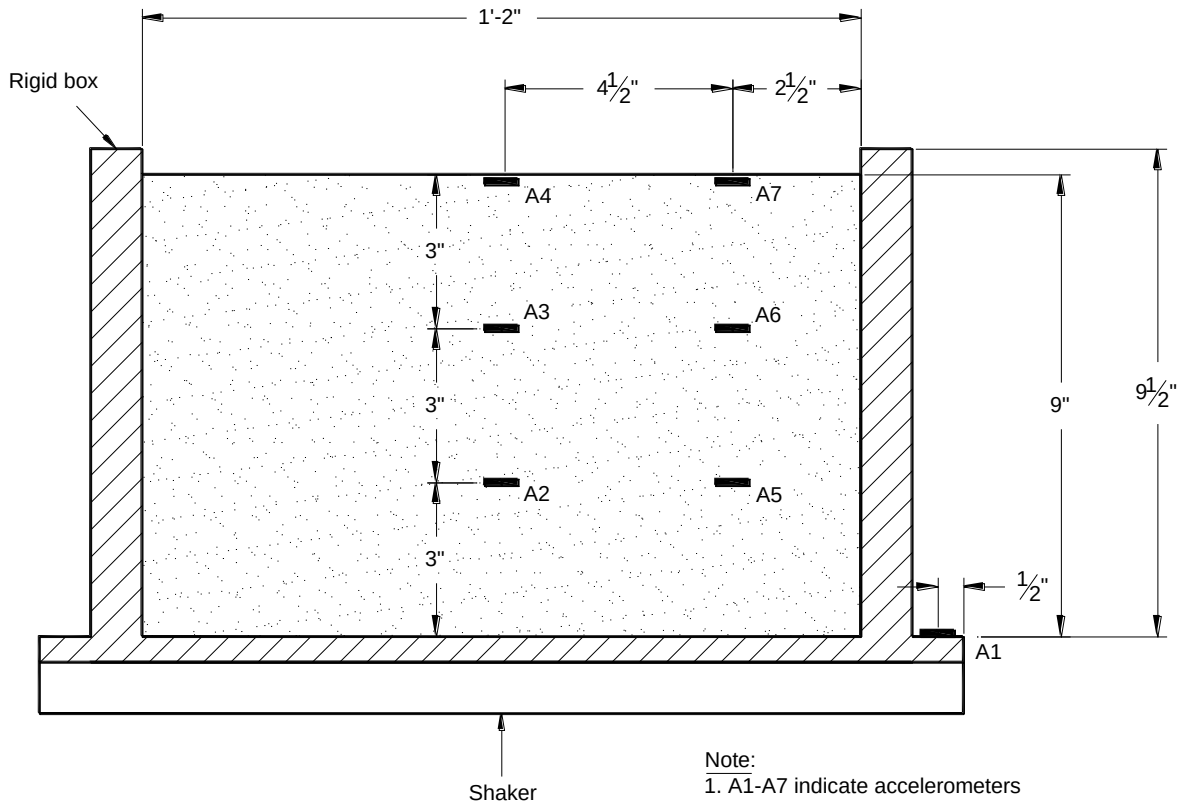

Figure 8-8: Instrumentation layout for the free-field test

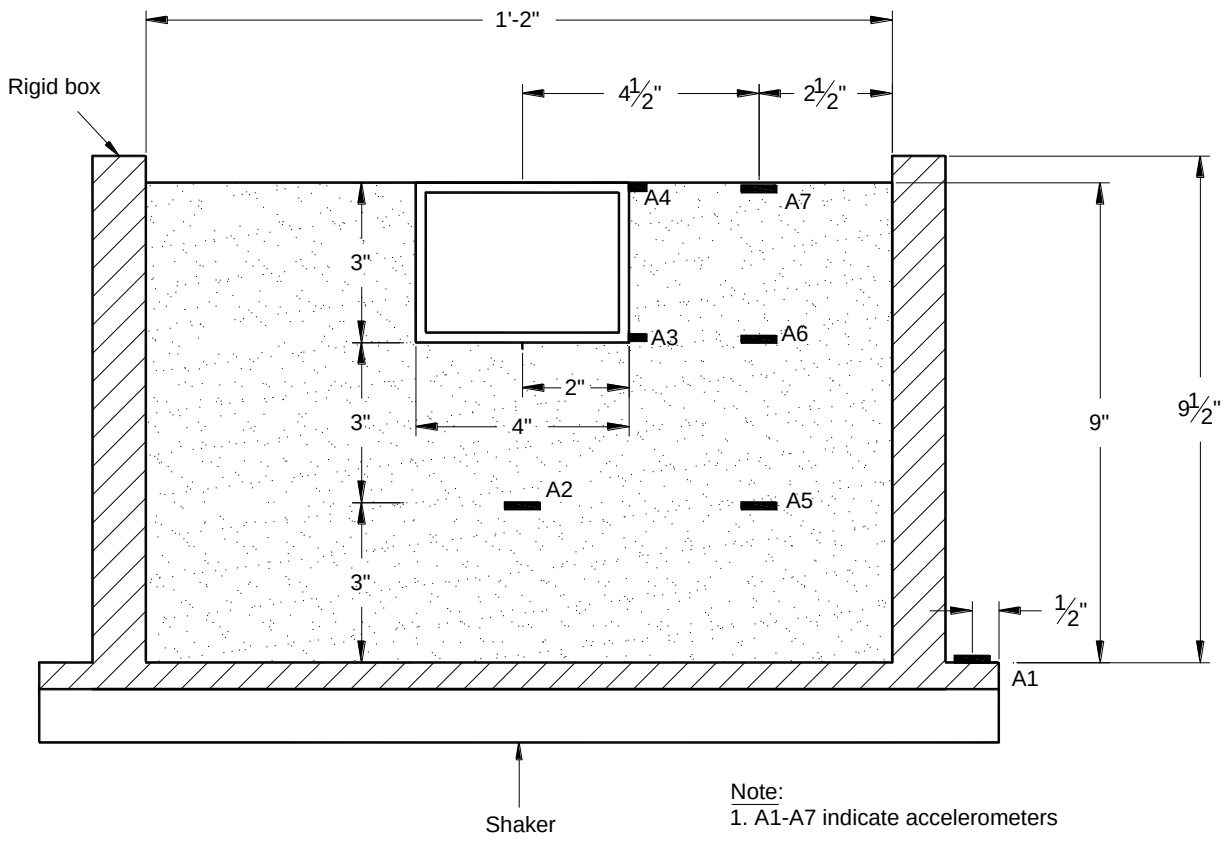

Figure 8-9: Instrumentation layout for the tunnel-ground system with a burial depth of 0 inch

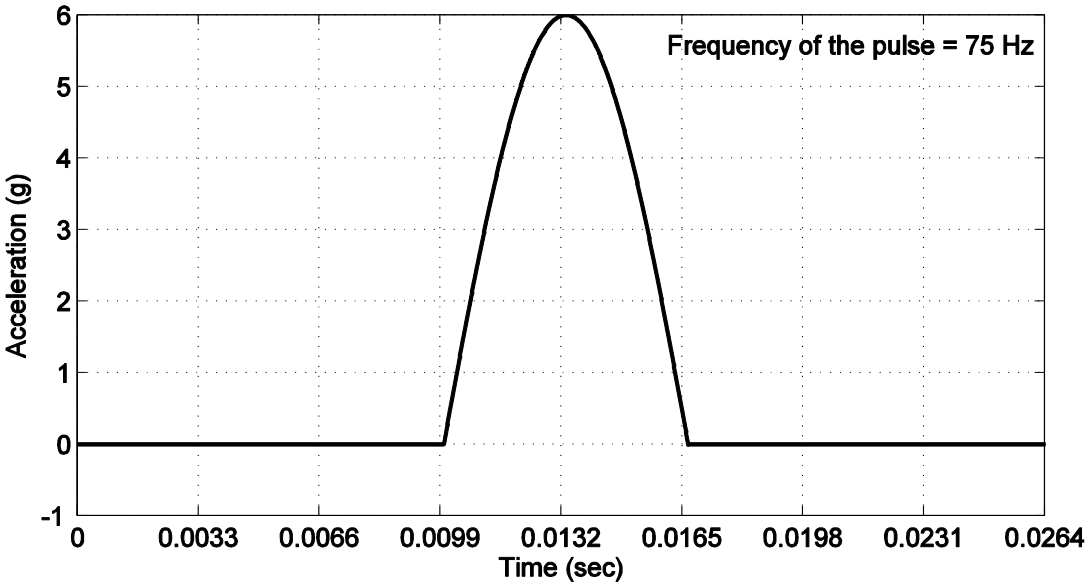

Figure 8-10: Pulse input for the shear wave velocity measurement

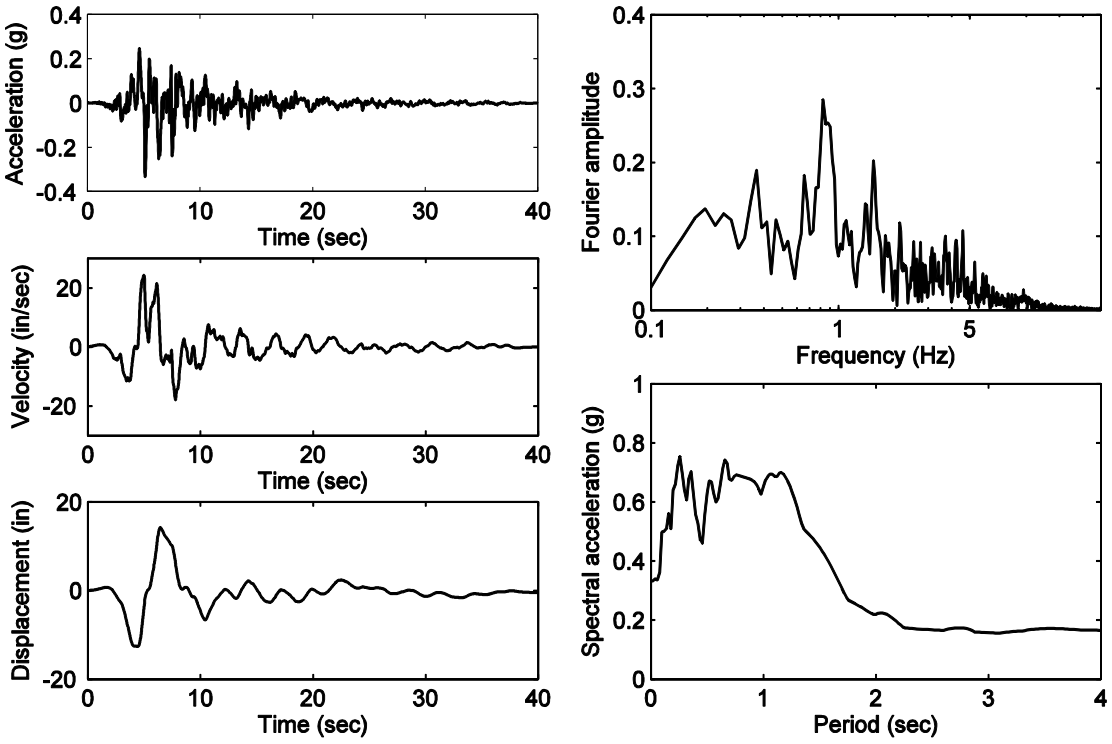

Figure 8-11: Time histories and frequency content for the actual Loma Prieta (Saratoga W C Coll 270) earthquake

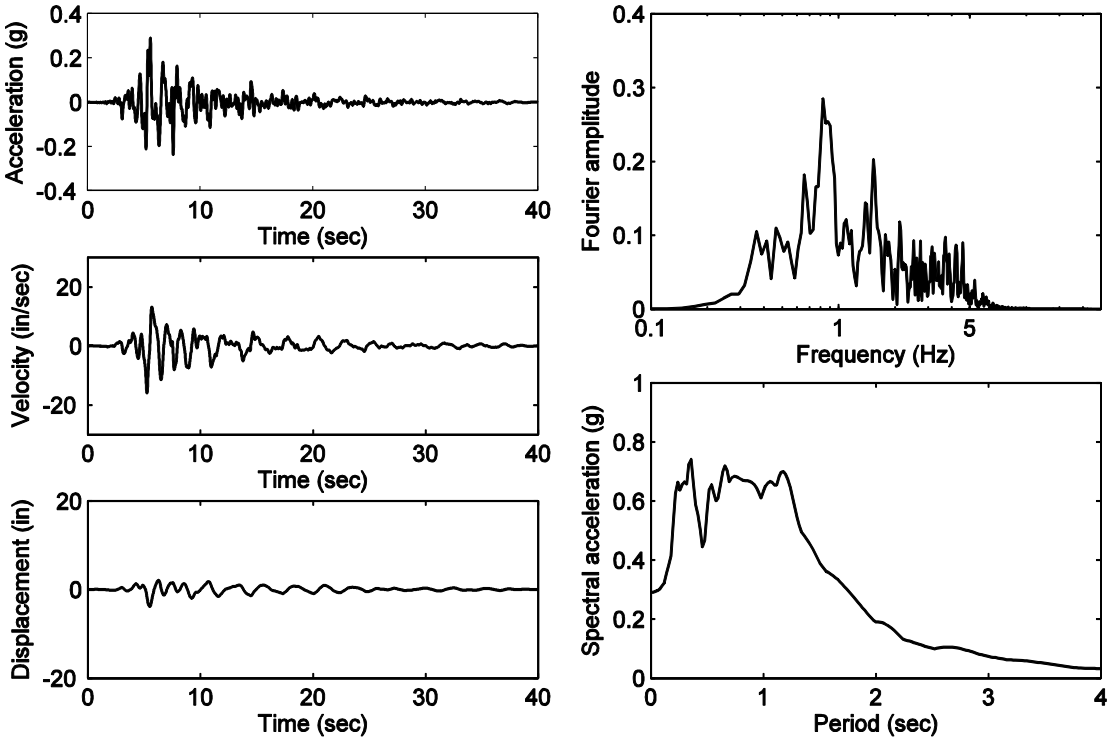

Figure 8-12: Time histories and frequency content for the filtered Loma Prieta (Saratoga W C Coll 270) earthquake

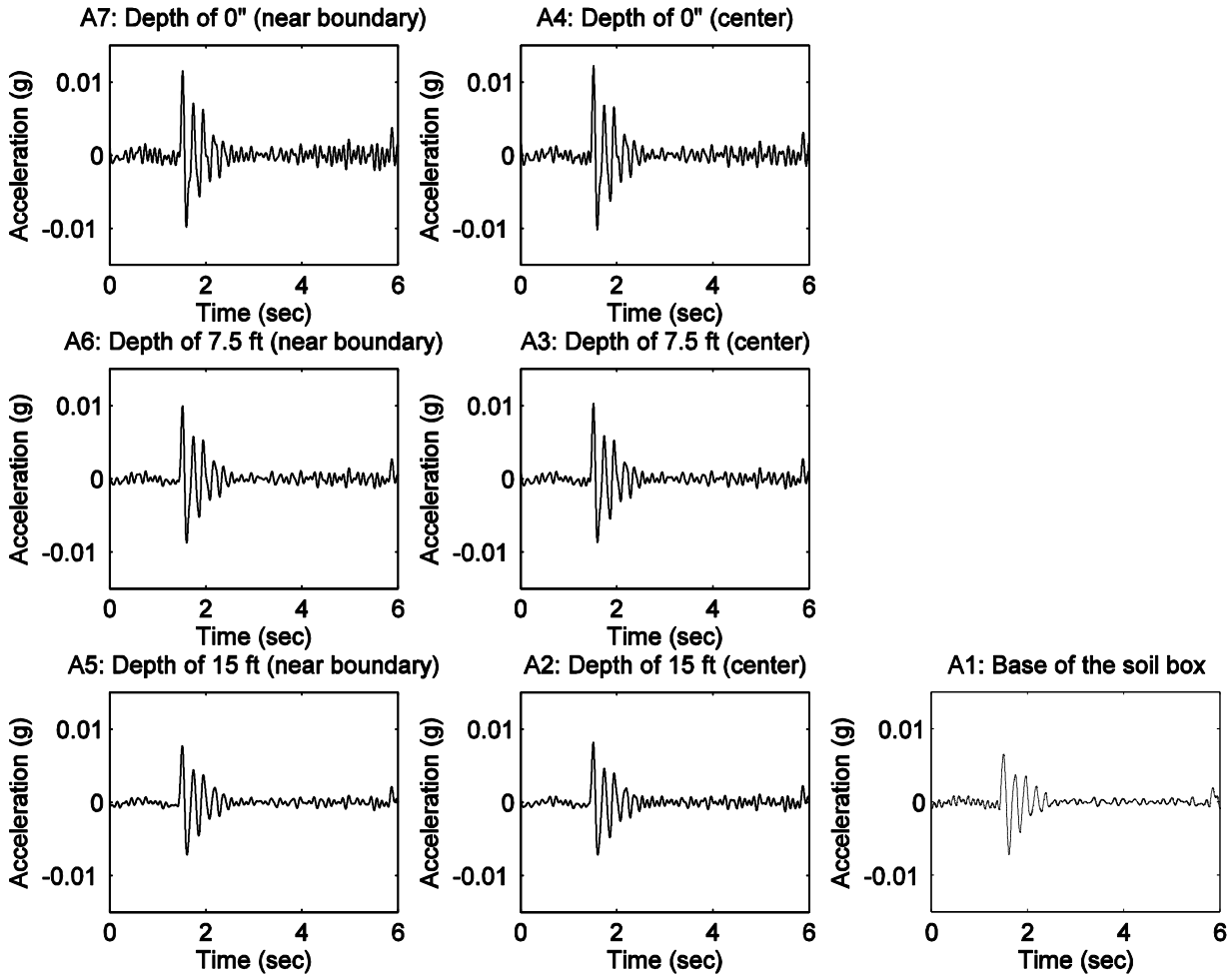

Figure 8-13: Measured acceleration time histories from the accelerometers in the free-field test by applying the pulse input to the model base prior to the Loma Prieta earthquake shaking

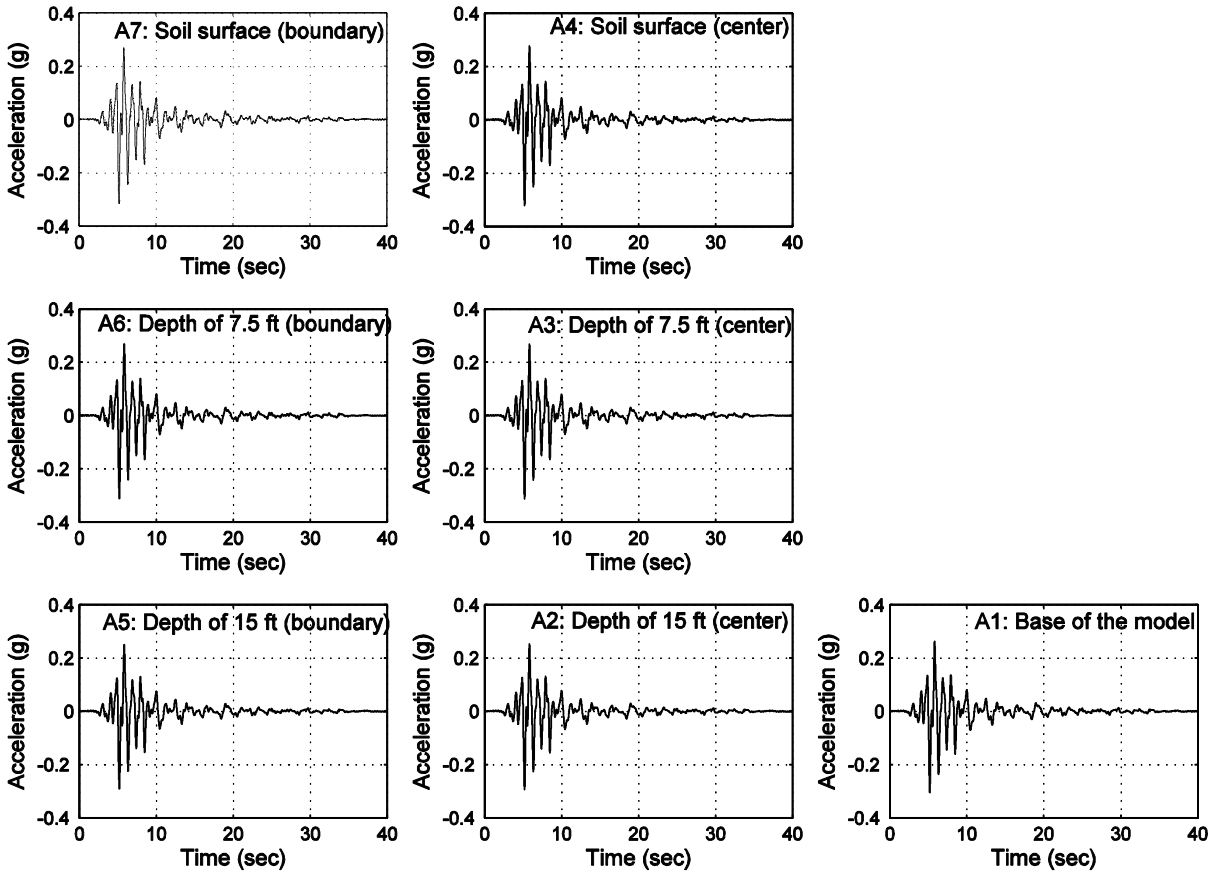

Figure 8-14: Measured acceleration time histories from the accelerometers in the free-field test under Loma Prieta earthquake shaking

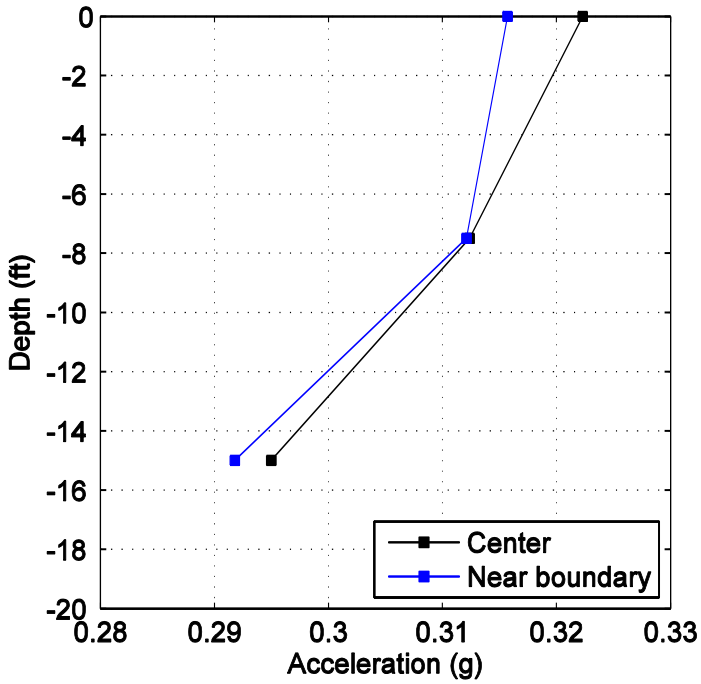

Figure 8-15: Peak ground acceleration along depth in the free-field test under the Loma Prieta (Saratoga W V Coll 270) earthquake excitation

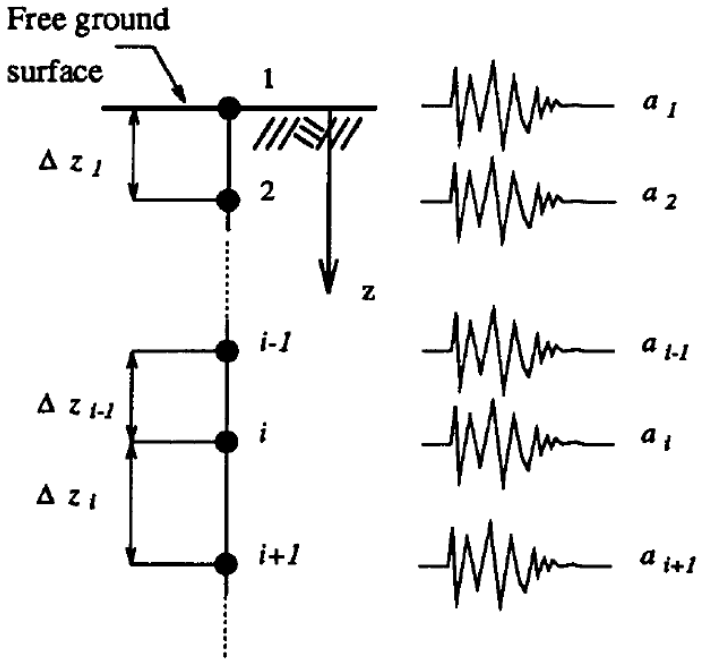

Figure 8-16: Downhole accelerometer array (Zeghal et al. 1995)

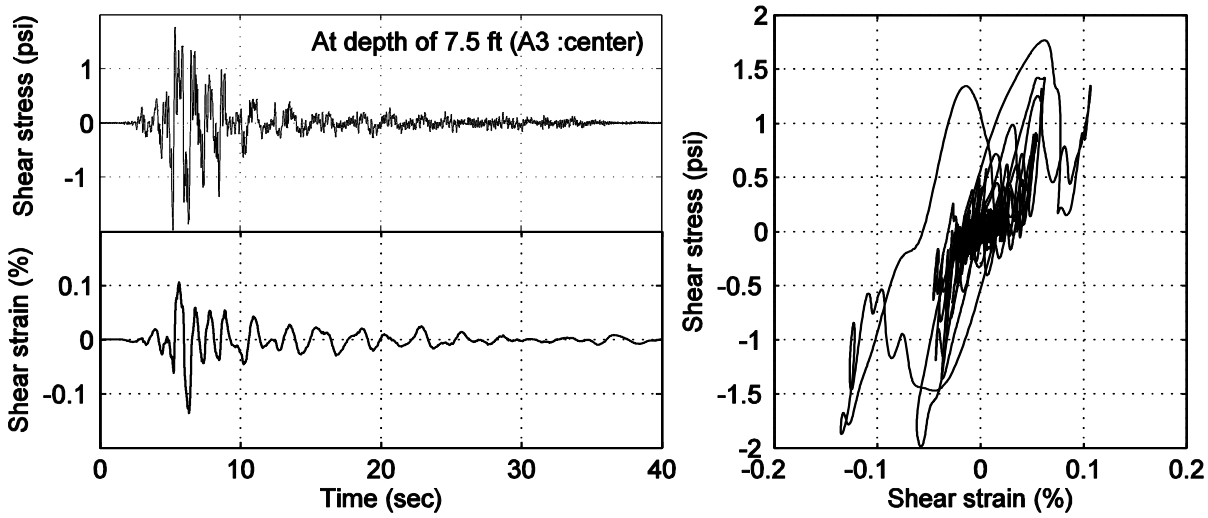

Figure 8-17: Shear stress and strain time histories and their hysteretic loop at depth of 7.5 ft (A3 in the center) in the free-field test

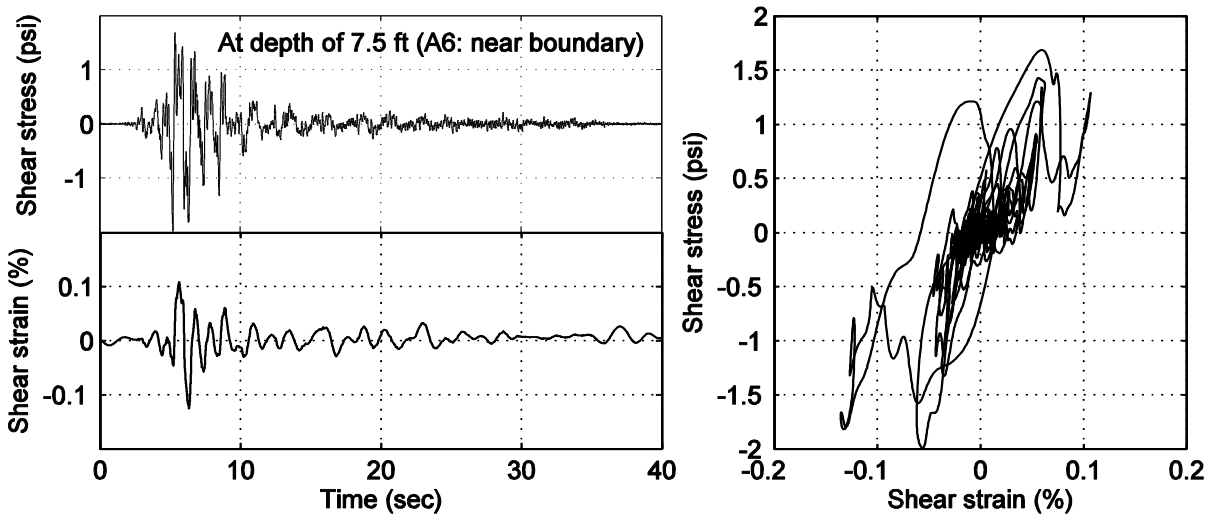

Figure 8-18: Shear stress and strain time histories and their hysteretic loop at depth of 7.5 ft (A6 near boundary) in the free-field test

9. Summary and conclusions

This study reported herein presents new data from conducted cut-and-cover tunnel experiments. In particular, the following investigations were undertaken:

1. A 1/3 scale reinforced concrete (RC) tunnel test under quasi-static cyclic loading.
2. A 1/9 scale tunnel-ground laminar soil container test, through application of shear push-over loading on the outer boundary of the laminar container.
3. Preliminary centrifuge test to document related wave propagation characteristics.

The experimental data is used to calibrate Finite Element (FE) models, to be used for conducting a wide range of parametric studies. On the basis of the experimental and numerical results, current design guidelines can be assessed and recommendations for any updates can be made.

The 1/3 scale RC tunnel model was idealized based on the Doyle Drive Battery Tunnel Liner configuration. The test aimed to document the tunnel lateral stiffness and large deformation response characteristics. This assessment provided elastic stiffness of the subsequent experimental tunnel models to investigate the associated soil-structure response. Validation of a tunnel finite element (FE) model was conducted, for use in the subsequent FE soil-structure interaction analyses.

The 1/9 scale laminar container experimental soil-structure model was conducted to obtain insights related to the mechanisms of interaction between the tunnel liner and the surrounding ground. For that purpose, the tunnel was embedded in the large laminar soil container, with an applied external push-over lateral displacement profile.

Preliminary centrifuge tests were conducted to furnish additional data concerning the aspects of dynamic wave propagation effects. Acceleration response at various locations within the soil model (free-field without the tunnel model) was documented.

Calibration of FE models was conducted on the basis of the test results. Using these calibrated models, additional representative numerical parametric investigations were undertaken to assess seismic earth pressure on the tunnel walls.

On the basis of the above studies, a pilot comparison between FE simulation results and the current simplified analytical analysis guidelines (FHWA, 2009) was performed. The results shed light on ranges of applicability and potential under-/over-estimation when using the simplified analysis procedure (please see Appendix J). Overall, this effort partially constitutes a basis for further recommendations and updates.

References

"American Concrete Institute (ACI)." Building Code Requirements for Structural Concrete (ACI-318-08) and Commentary ACI Committe 318, Farmington Hills, MI, 2008.

AASHTO (2010). LRFD Bridge Design Specifications, 5th Edition, Washington DC.

Caltrans (2008). "Bridge Design Specifications " California Department of Transportation, Divison of Structures, Sacramento, CA.

Caltrans (2012). "Personal communication."

Elgamal, A., L. Yan, Z. Yang and J. P. Conte (2008). "Three-dimensional seismic response of Humboldt Bay bridge-foundation-ground system." Journal of Structural Engineering 134(7): 1165-1176.

FHWA (2009). Technical manual for design and construction of road tunnels - civil elements, U.S. Department of transportation. Federal Highway Administration. Publication No. FHWA-NHI-10-034, 702 p.

Harris, H. G. and G. Sabnis (2010). Structural modeling and experimental techniques, CRC press.

Huo, H., A. Bobet, G. Fernández and J. Ramírez (2006). "Analytical solution for deep rectangular structures subjected to far-field shear stresses." Tunnelling and underground space technology 21(6): 613-625.

Iai, S. (1989). "Similitude for shaking table tests on soil-structure-fluid model in 1g gravitational field." Soils and Foundations 29(1): 105-118.

Idriss, I. and J. I. Sun (1992). "User's Manual for SHAKE91." Center for Geotechnical Modeling, Department of Civil Engineering, University of California, Davis.

JSCE (1998). Earthquake resistant design for civil engineering structures in Japan. Japanese Society of Civil Engineers, Tokyo.

Kondner, R. L. (1963). "Hyperbolic stress-strain response: cohesive soils." Journal of the soil mechanics and foundations division, ASCE 89(1): 115-143.

Kuesel, T. R. (1969). "Earthquake design criteria for subways." Journal of the structural division.

Law, H. K. and I. P. Lam (2003). "Evaluation of seismic performance for tunnel retrofit project." Journal of Geotechnical and Geoenvironmental Engineering 129(7): 575-589.

Mason, H., B. Kutter, J. Bray, D. Wilson and B. Choy (2010). Earthquake motion selection and calibration for use in a geotechnical centrifuge. Proceedings of the 7 th International Conference on Physical Modelling in Geotechnics.

Mazzoni, S., F. McKenna, M. H. Scott and G. L. Fenves (2006). "OpenSees command language manual." Pacific Earthquake Engineering Research (PEER) Center.

Monsees, J. and J. Merritt (1991). Earthquake considerations in design of the Los Angeles Metro. Lifeline Earthquake Engineering, M.A. Cassuro, ed., ASCE, New York, NY.

Owen, G. N. and R. E. Scholl (1981). Earthquake engineering of large underground structures, Federal Highway Administration and National Science Foundation.

Prevost, J.-H. (1978). "Plasticity theory for soil stress-strain behavior." Journal of the Engineering Mechanics Division 104(5): 1177-1194.

Sabatini, P., R. Bachus, P. Mayne, J. A. Schneider and T. Zettler (2002). Geotechnical Engineering Circular No. 5: Evaluation of soil and rock properties.

Sedarat, H., A. Kozak, Y. M. Hashash, A. Shamsabadi and A. Krimotat (2009). "Contact interface in seismic analysis of circular tunnels." Tunnelling and underground space technology 24(4): 482-490.

Seed, H. B. and R. V. Whitman (1970). Design of earth retaining structures for dynamic loads. Lateral Stresses in the Ground and Design of Earth-Retaining Structures, ASCE.

Seed, H. B., R. T. Wong, I. Idriss and K. Tokimatsu (1986). "Moduli and damping factors for dynamic analyses of cohesionless soils." Journal of geotechnical engineering 112(11): 1016-1032.

Shamsabadi, A. and H. K. Law (2012). "Personal communication."

Shamsabadi, A., T. Marcher, M. Kapuskar and E. Saurer (2014). "Numerical methods for innovative seismic design and analysis of tunnel structures located in highly active seismic zones." Numerical Methods in Geotechnical Engineering, Taylor & Fracnis Group, London, pp. 1175-1180.

Shamsabadi, A., H. Sedarat and A. Kozak (2001). "Seismic soil-tunnel-structure interaction analysis and retrofit of the Posey-Webster Street Tunnels." presented at The 2nd UJNR (United States and Japan Cooperative Program in Natural Resources) Workshop on Soil-Structure Interaction, Tsukuba, Japan.

Taylor, R. N. (1995). Geotechnical centrifuge technology, Blackie Academic and Professional, London.

Thapa, B. B., J. Van Greunen, Y. Sun, M. T. McRae and H. K. Law (2008). "Design analyses for a large-span tunnel in weak rock subject to strong seismic shaking." North American Tunneling 2008 Proceedings: 417.

Wang, J.-N. (1993). "Seismic design of tunnels." Parsons Brinckerhoff Monograph 7.

Yang, C. T., H. K. Law and A. Shamsabadi (2008). Seismic Analyses for the Fourth Bore of Caldecott Tunnel. Geotechnical Earthquake Engineering and Soil Dynamics IV, ASCE.

Yang, Z. (2000). Numerical modeling of earthquake site response including dilation and liquefaction, University of California at San Diego, Dept. of Structural Engineering.

Zeghal, M., A.-W. Elgamal, H. Tang and J. Stepp (1995). "Lotung downhole array. II: Evaluation of soil nonlinear properties." Journal of geotechnical engineering 121(4): 363-378.

APPENDIX A: General Plan of Doyle Drive Battery Tunnel

The as-built drawings of the Doyle Drive Battery Tunnel, as earlier discussed in Section 3.1, are presented in Figure A-1 through Figure A-3.

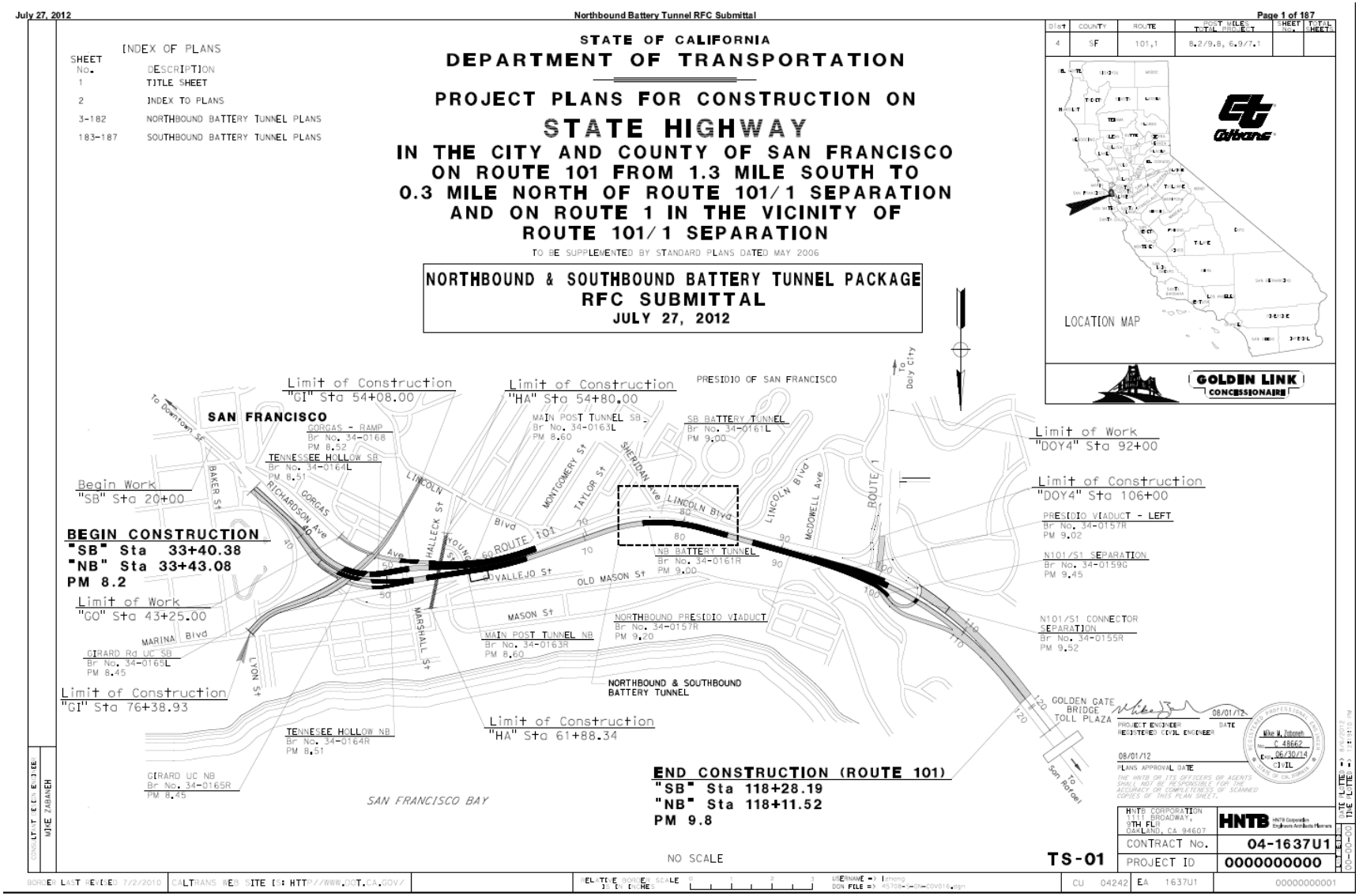

Figure A-1: Project plans for construction

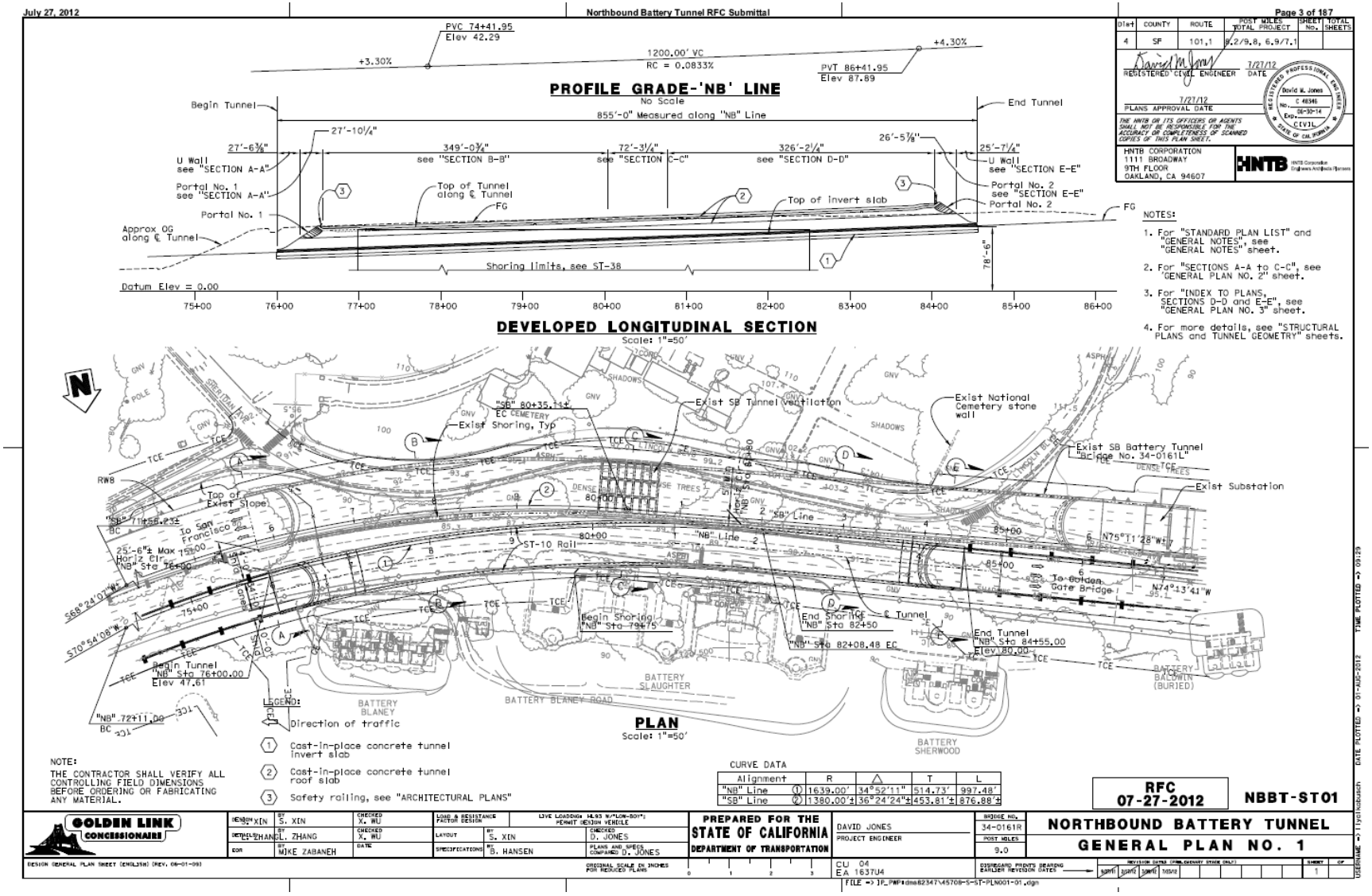

Figure A-2: Northbound battery tunnel (general plan 1)

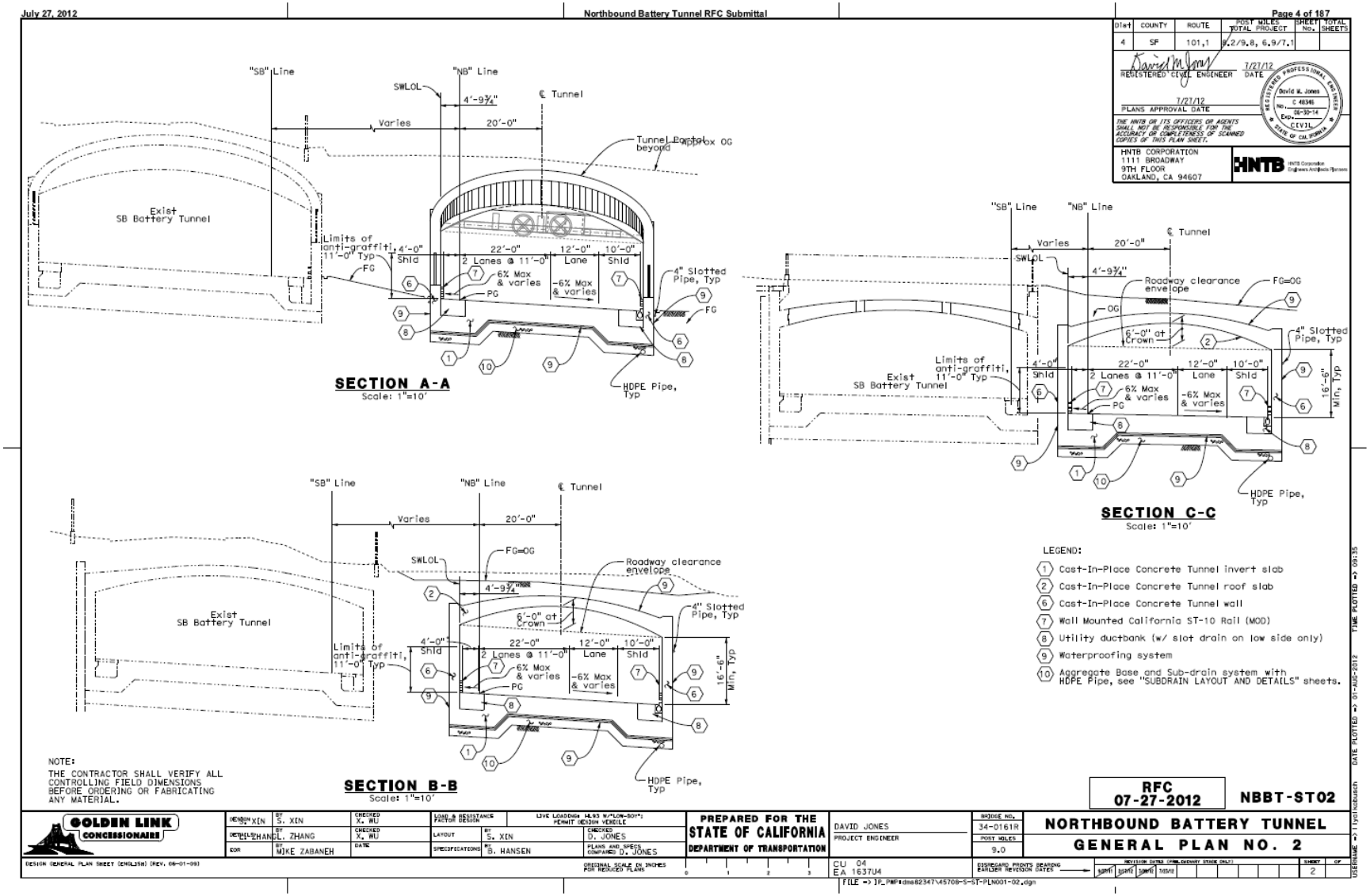

Figure A-3: Northbound battery tunnel (general plan 2)

APPENDIX B: Construction Drawings of the Model

The construction drawings and instrumentation layouts of the 1/3 scale reinforced concrete tunnel specimen presented in Chapter 3 are presented.

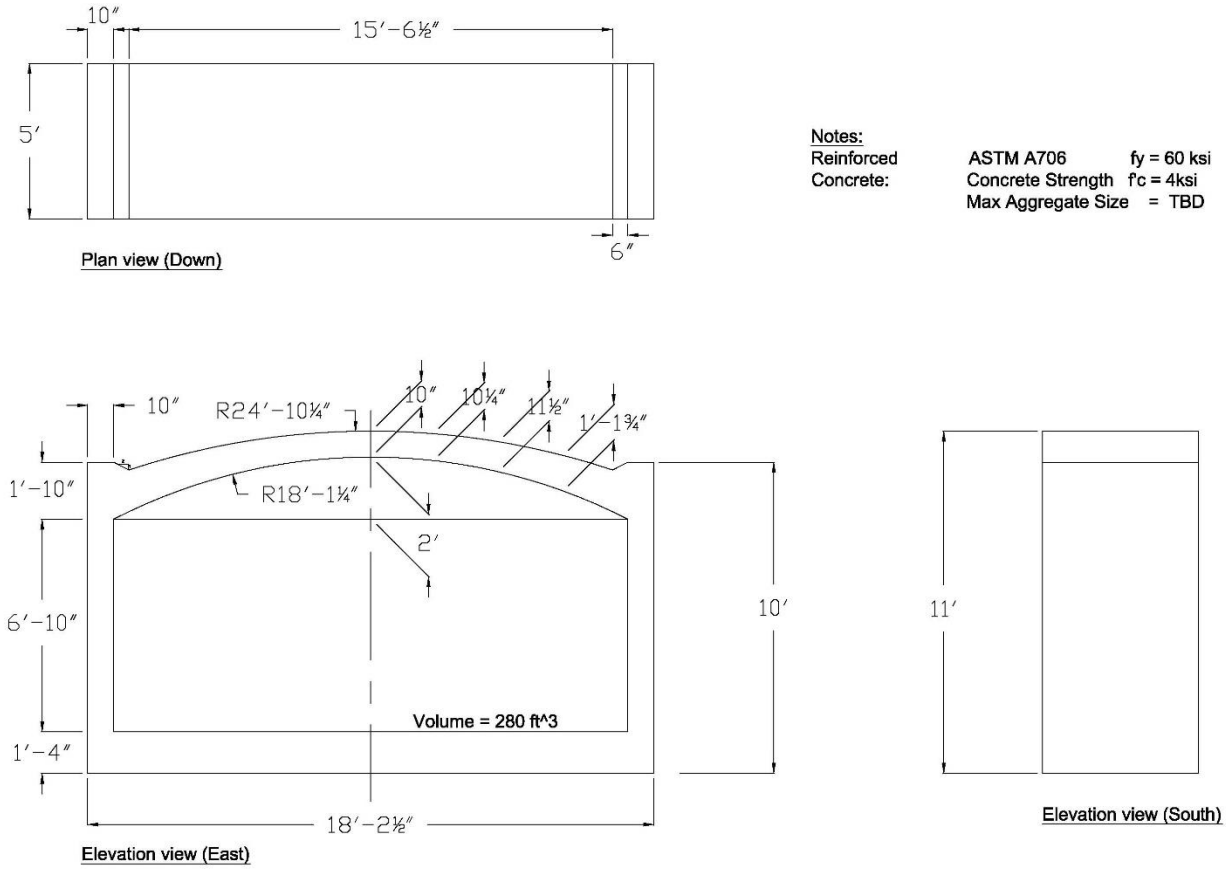

Figure B-1: Geometric configuration drawing of the 1/3 scale reinforced concrete tunnel specimen

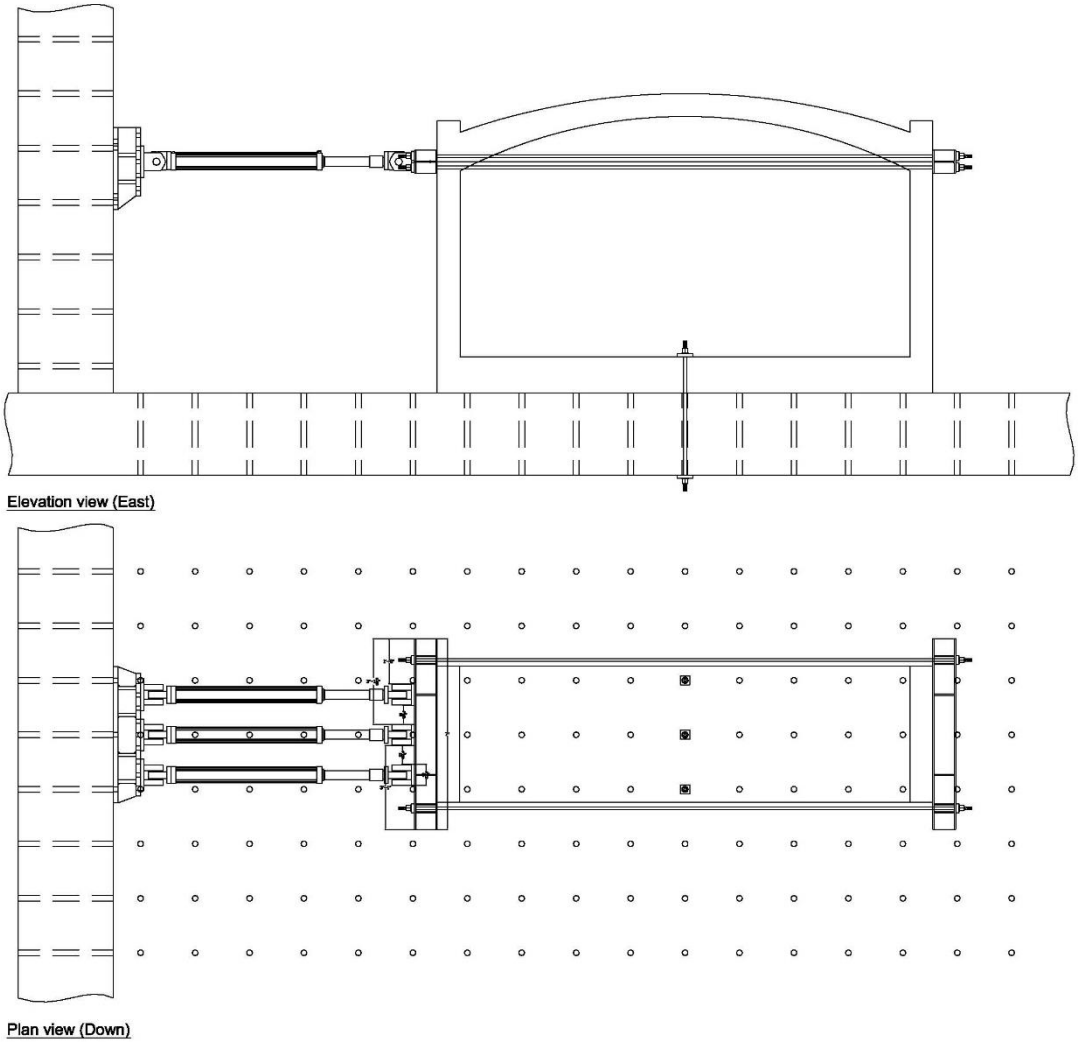

Figure B-2: Drawing of the loading configuration

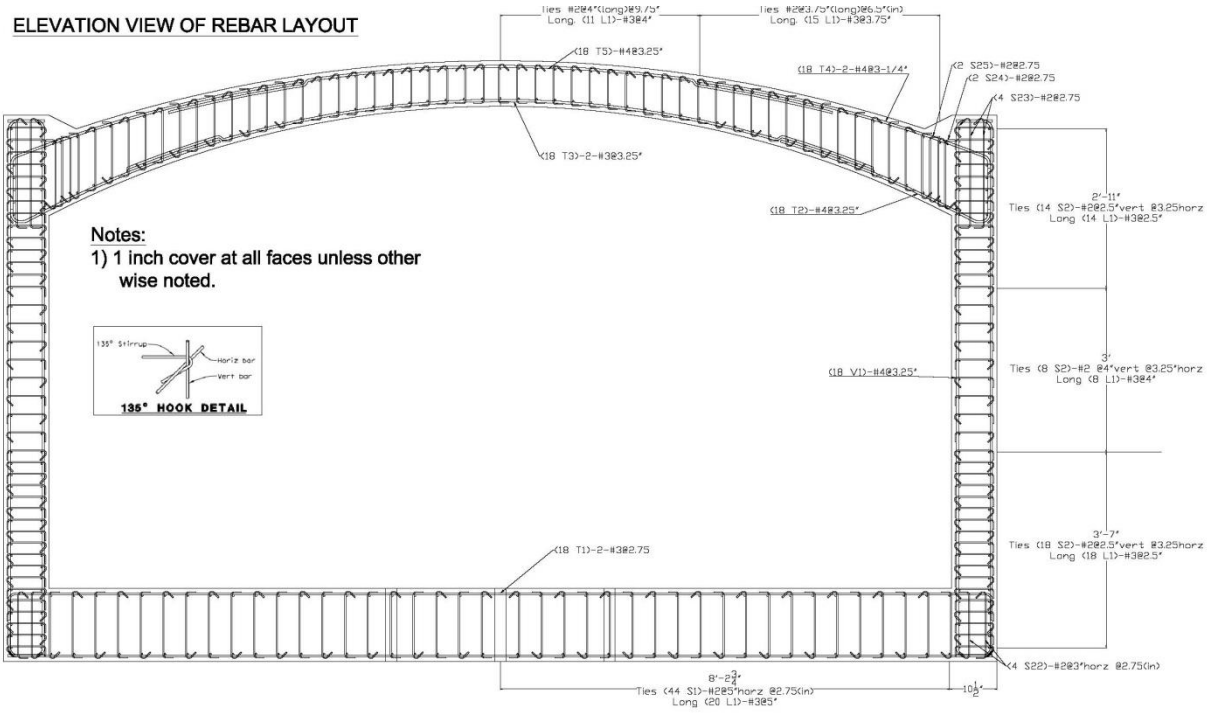

Figure B-3: Elevation view of rebar layout

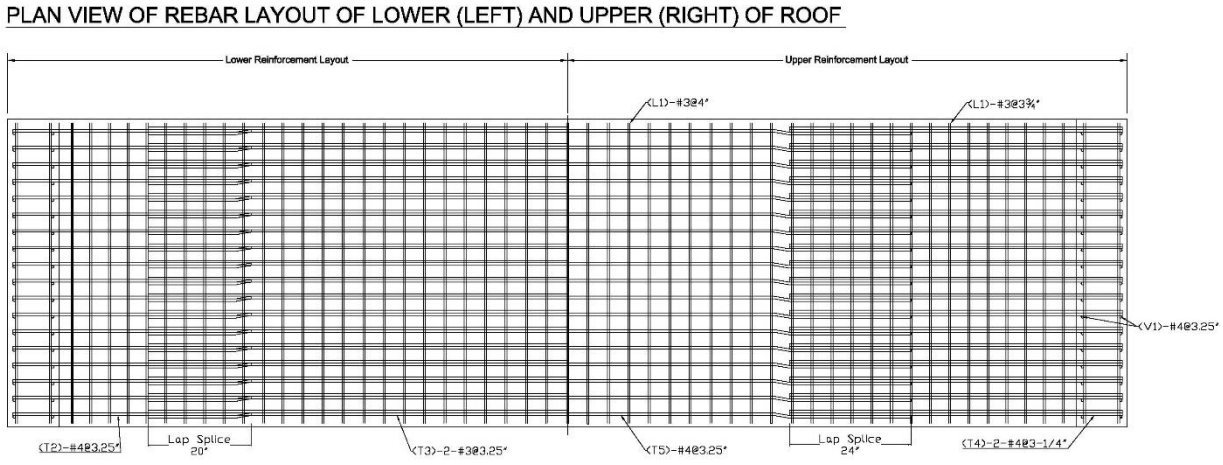

Figure B-4: Plan view of rebar layout of lower (left) and upper (right) of roof

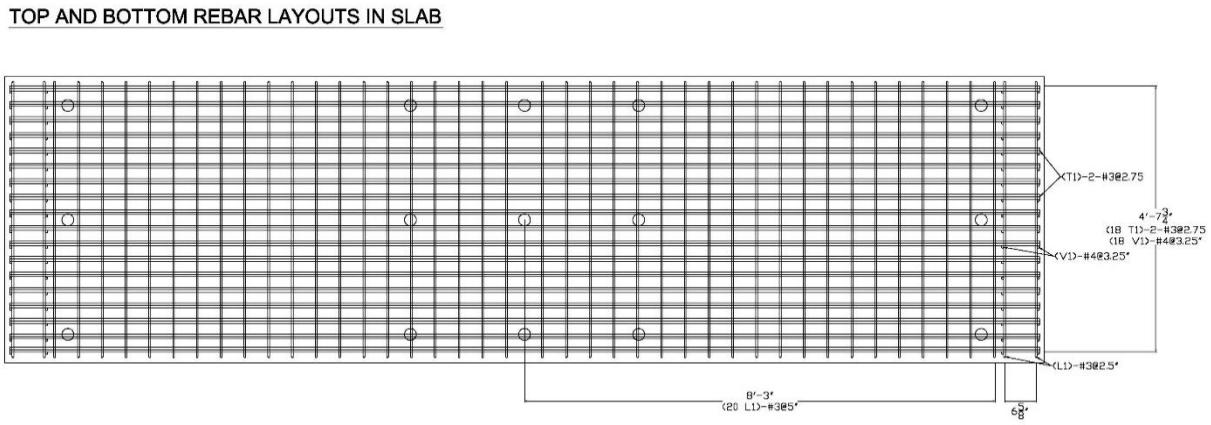

Figure B-5: Top and bottom rebar layouts in slab

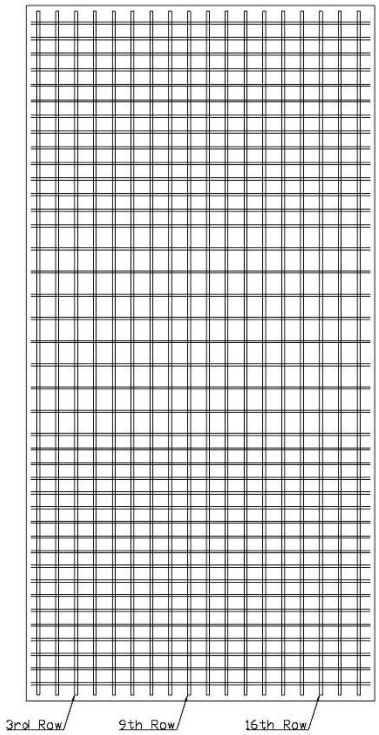

Figure B-6: Elevation view of rebar layout in North wall (looking south)

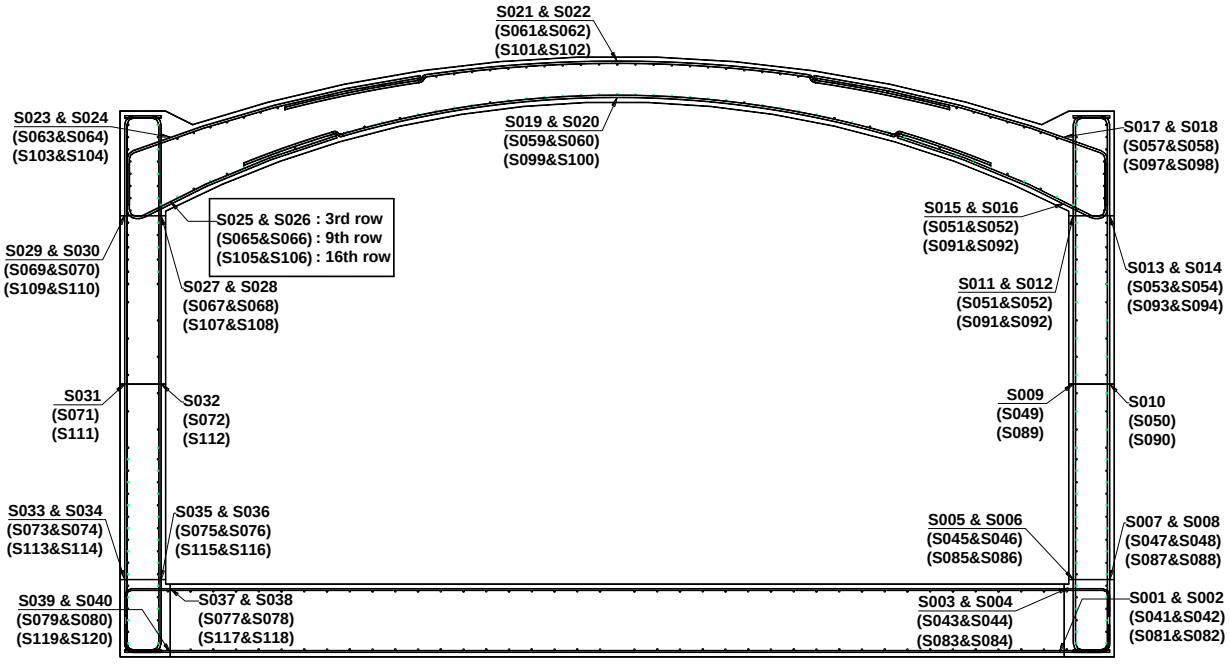

Figure B-7: Instrumentation layout of strain gauges

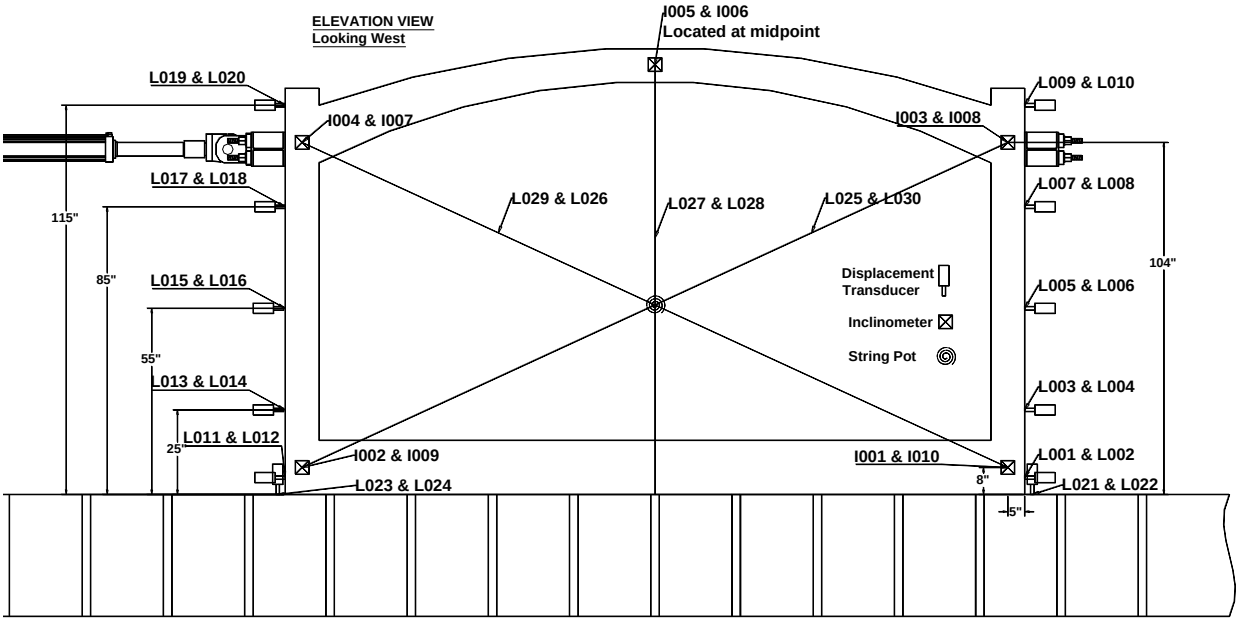

(a)

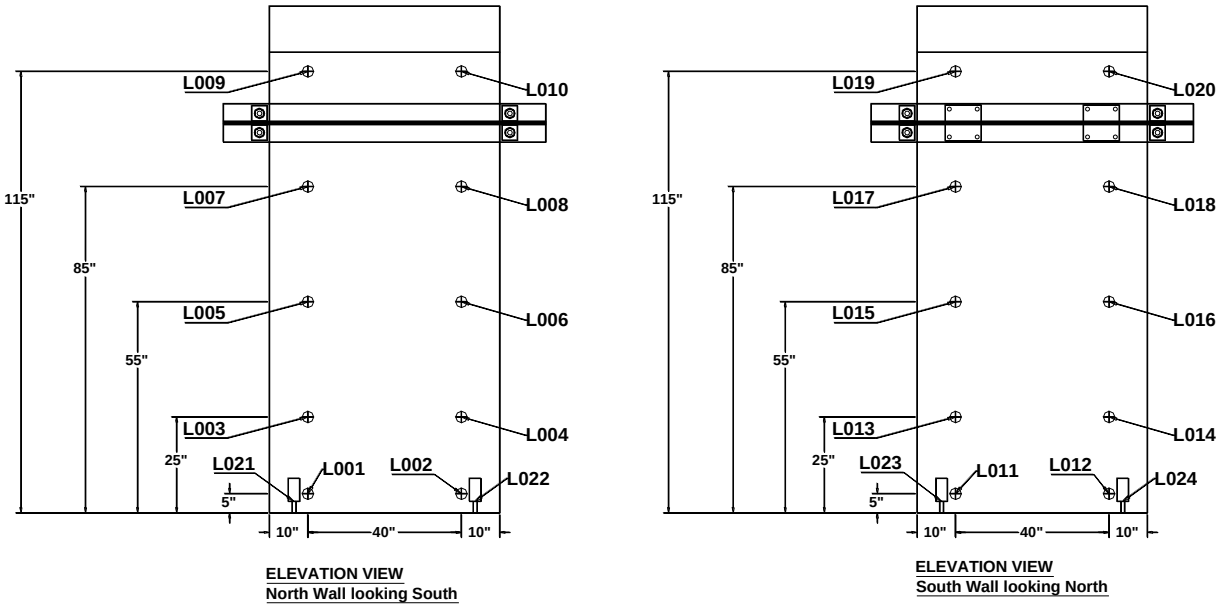

(b)

Figure B-8: Instrumentation layout of displacement transducers, inclinometers, and string potentiometers;(a) looking West and (b) looking South and North

APPENDIX C: Construction Photos

The construction sequence for the 1/3 scale reinforced concrete tunnel specimen presented in Chapter 3 is presented.

Figure C-1: Strain gages on longitudinal reinforcing bar in the slab

Figure C-2: Formation of reinforcing in the slab

Figure C-3: Form for concrete pour in the slab

Figure C-4: Concrete pour for the slab

Figure C-5: Smoothing surface on concrete for the slab

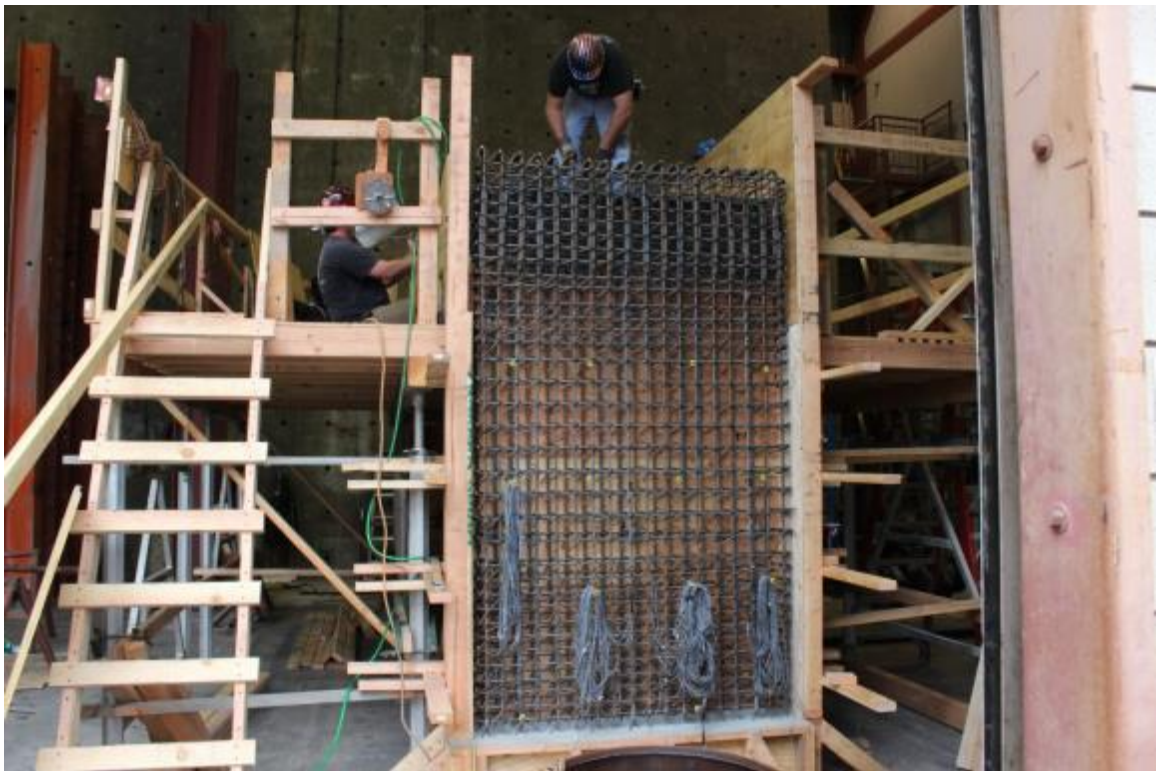

Figure C-6: Reinforcing and form for the wall

Figure C-7: Installation of strain gauge on the longitudinal reinforcement in the wall

Figure C-8: Reinforcing and form for the roof

Figure C-9: Concrete pour for the wall

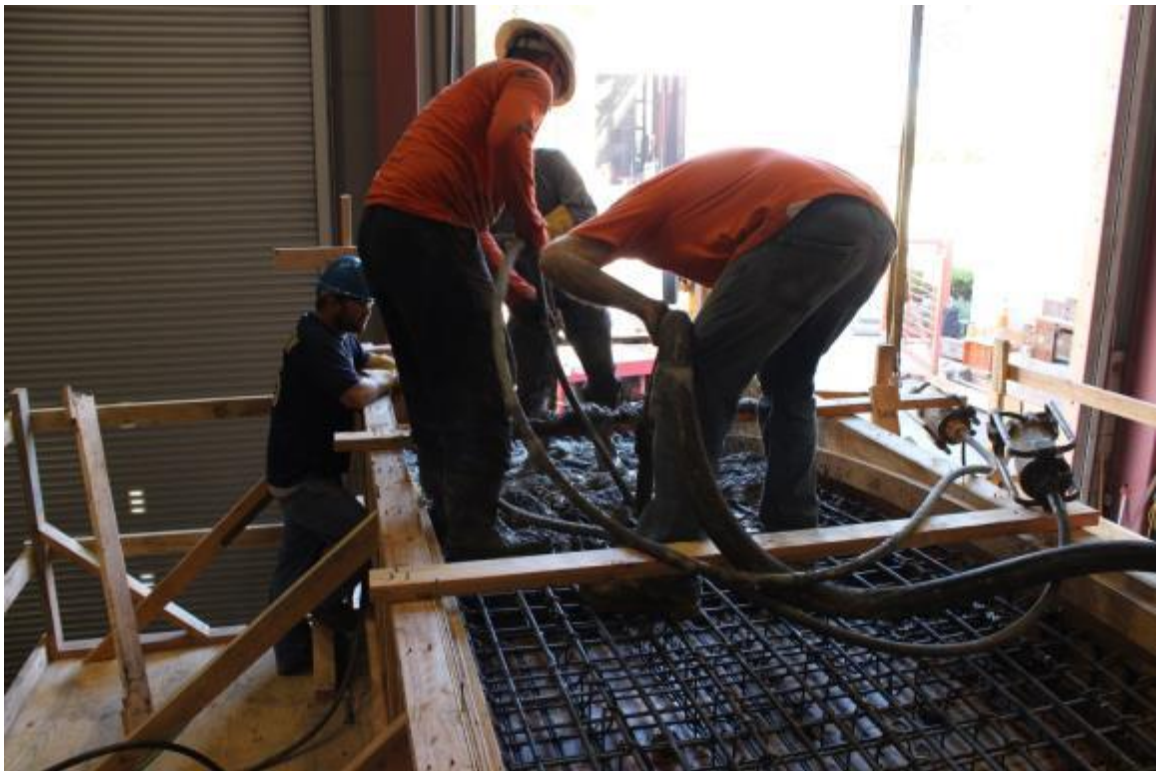

Figure C-10: Concrete pour for the roof

Figure C-11: Smoothing surface on concrete for the roof

Figure C-12: After removal of the form

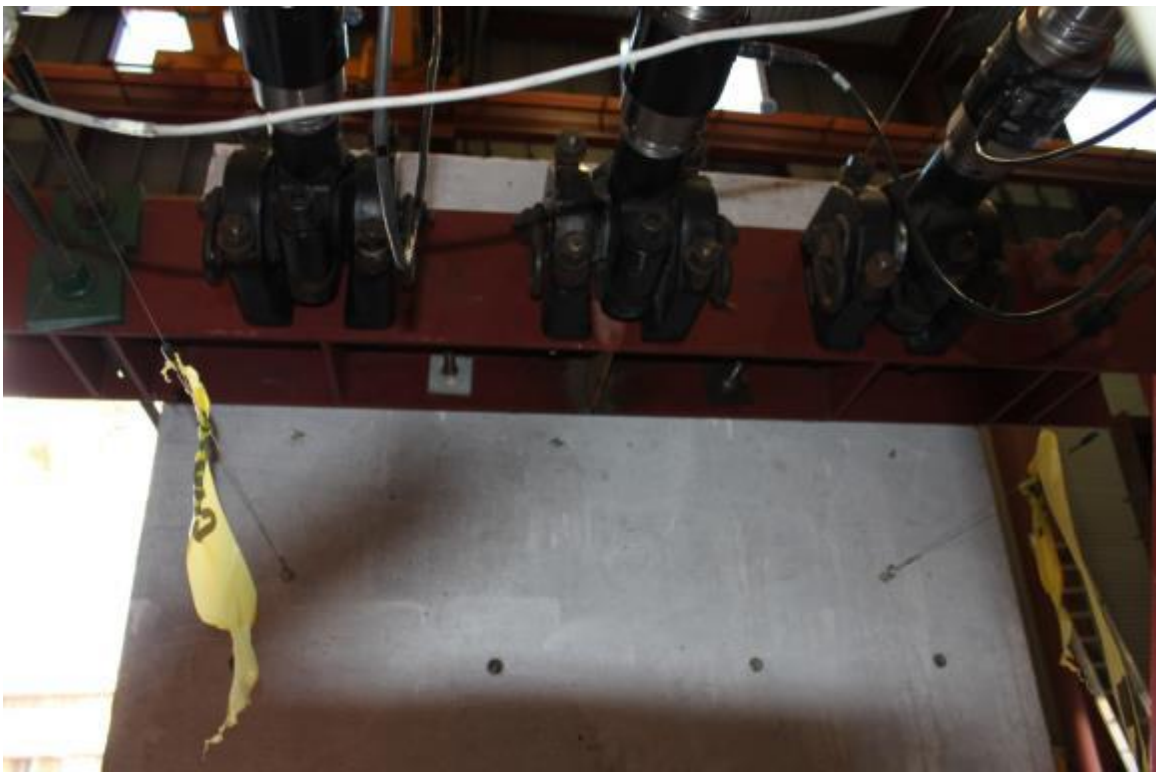

Figure C-13: Installation of the actuators on the South wall

Figure C-14: Installation of loading frame attached to the North wall with 12” long threaded rods

Figure C-15: Installation of the displacement transducers along the South wall

Figure C-16: Final configuration of the 1/3 reinforced concrete tunnel specimen

APPENDIX D: Strain Gauge Output

Strains were measured from the gauges on the longitudinal reinforcement (Figure D-1) during the quasi-static cyclic test presented in Chapter 3. The relationship of the strain and the applied force is shown in Figure D-2 through Figure D-21.

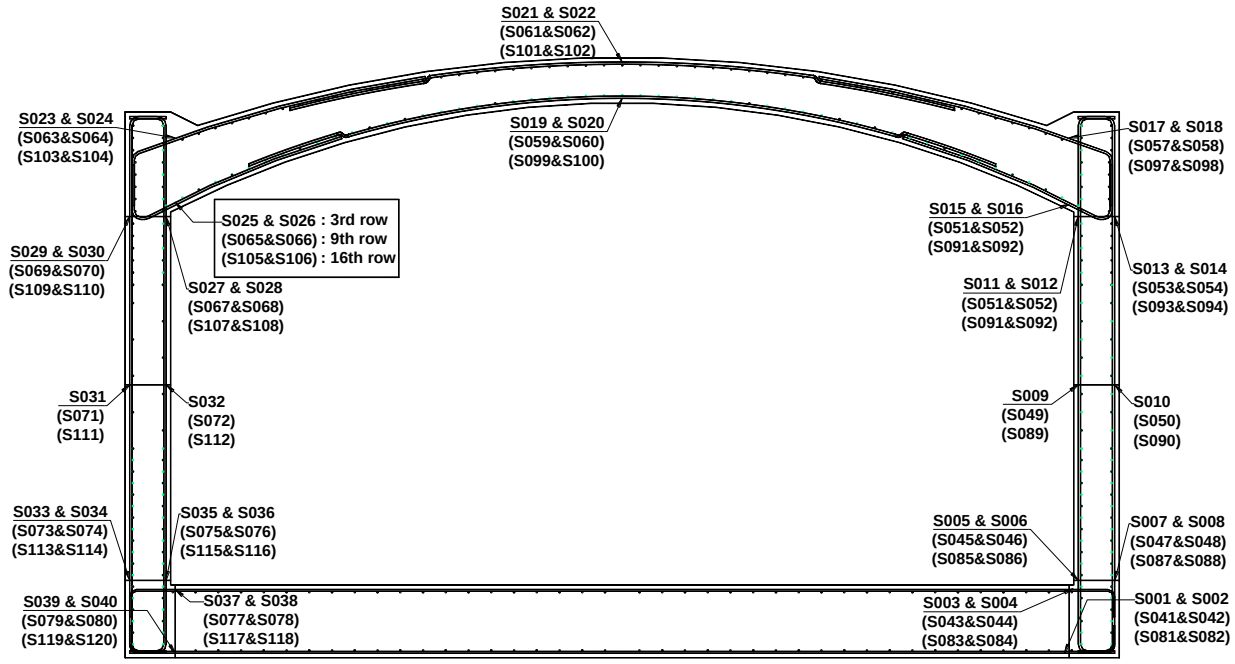

Figure D-1: Instrumentation layout of strain gauges

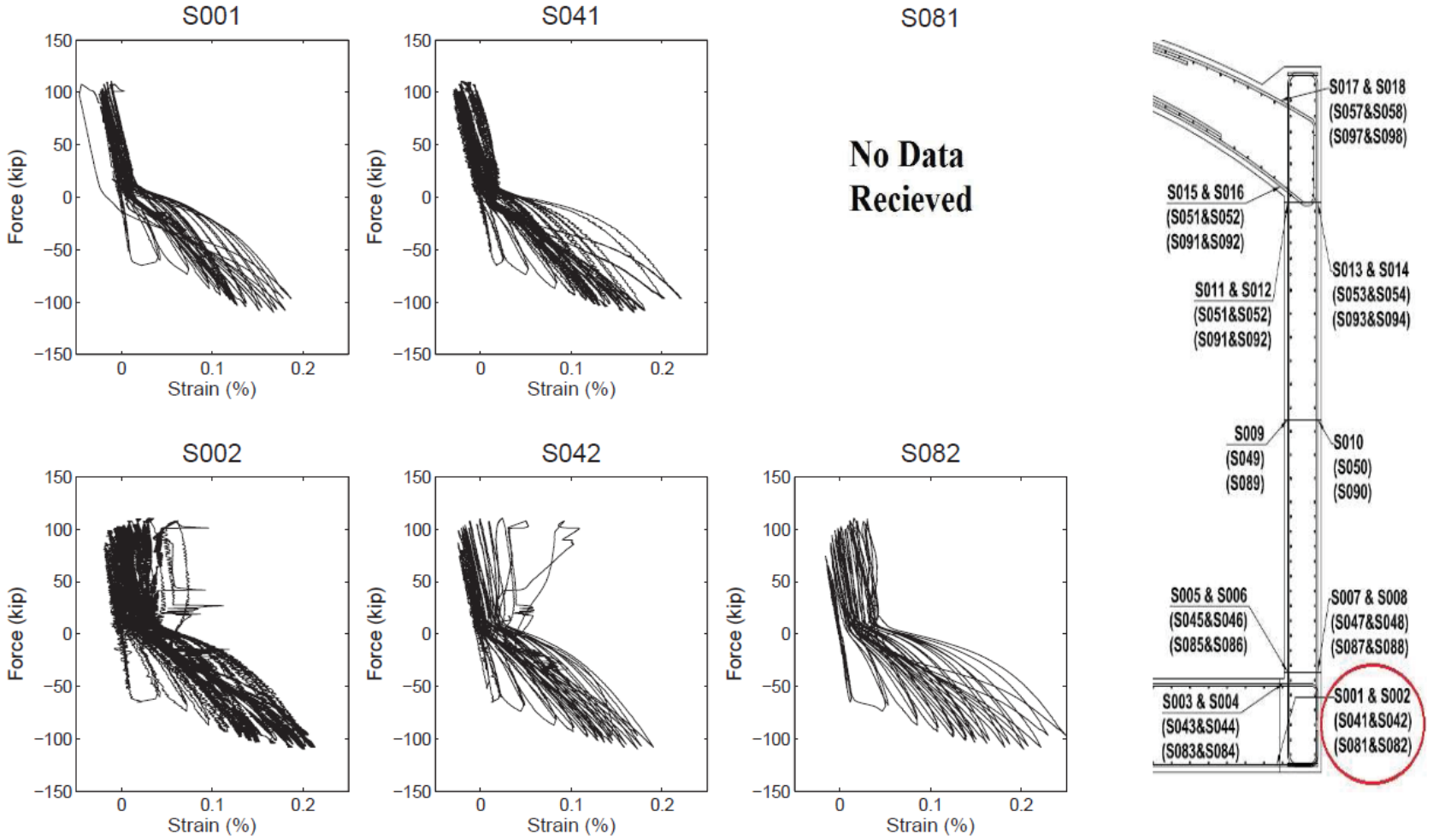

Figure D-2: Strains measured at the bottom slab (North Wall)

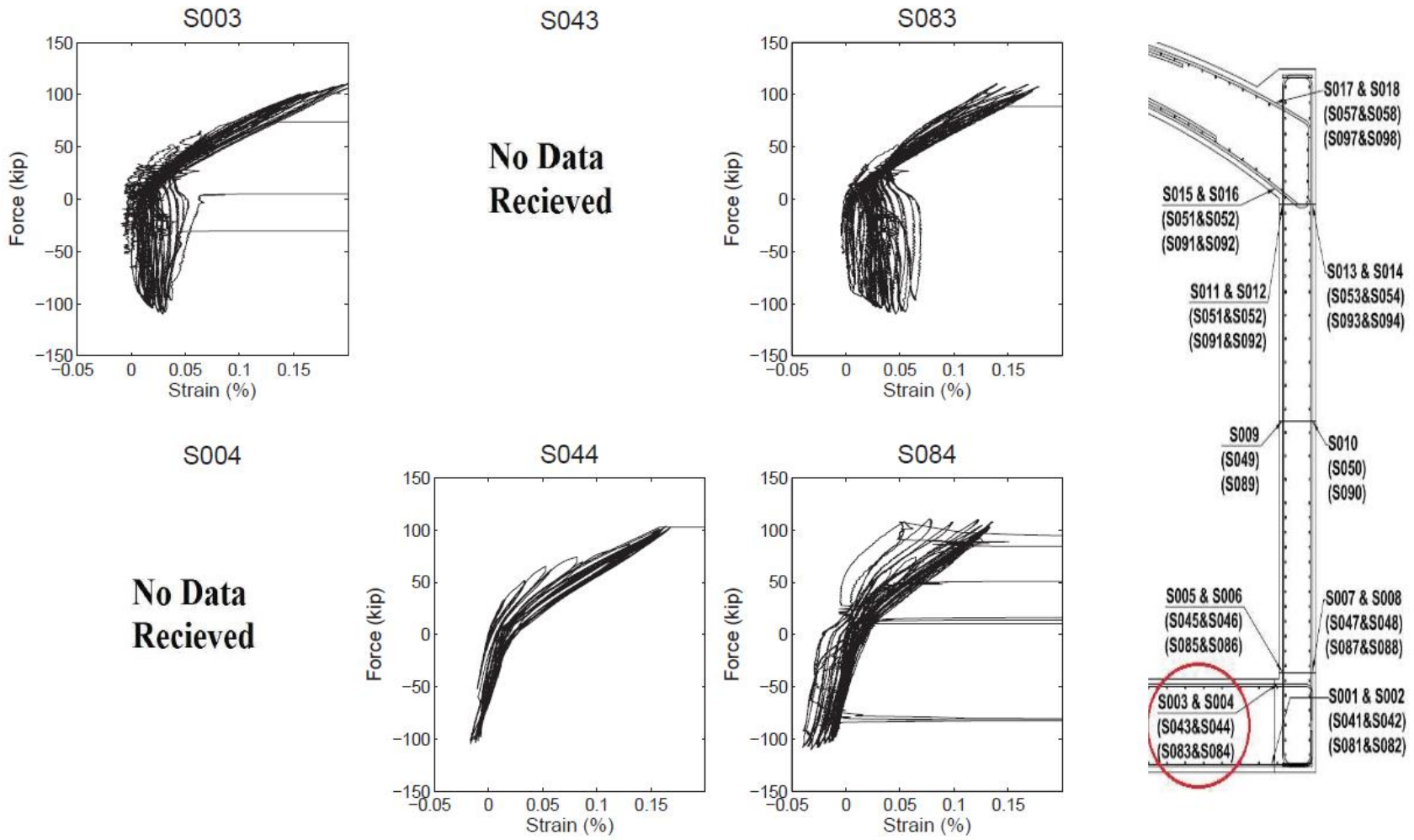

Figure D-3: Strains measured at the top slab (North Wall)

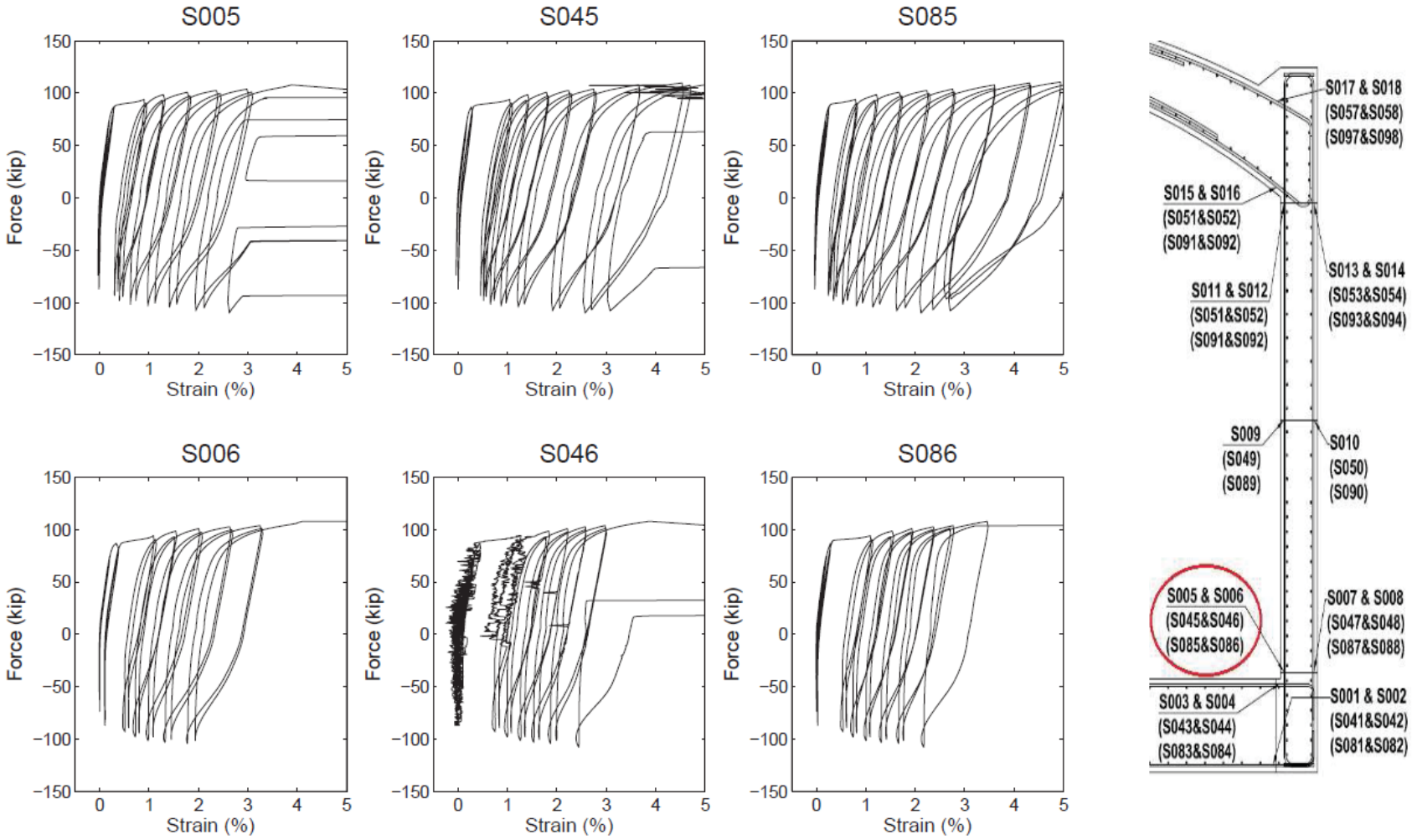

Figure D-4: Strains measured at base of the North Wall (inside)

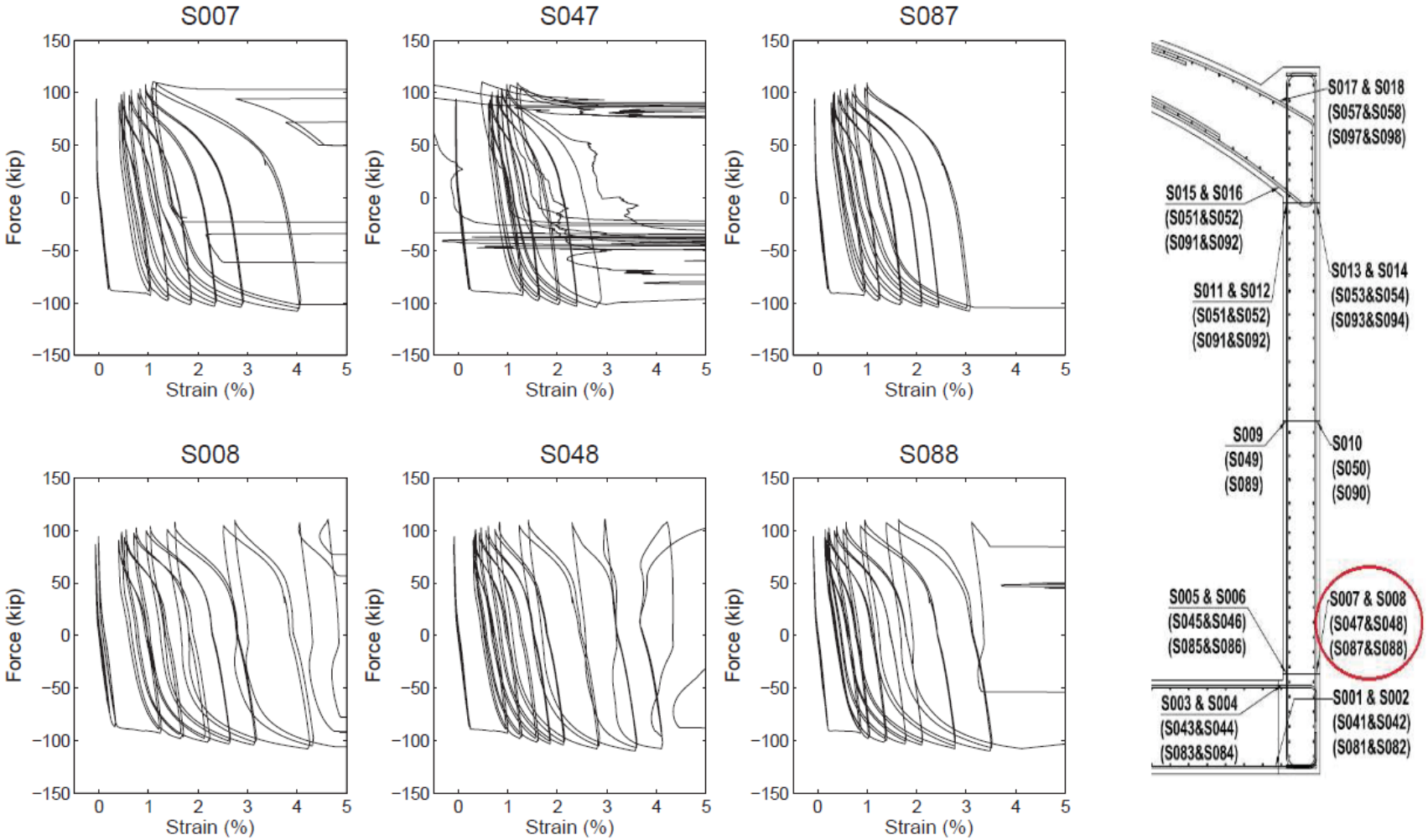

Figure D-5: Strains measured at base of the North Wall (outside)

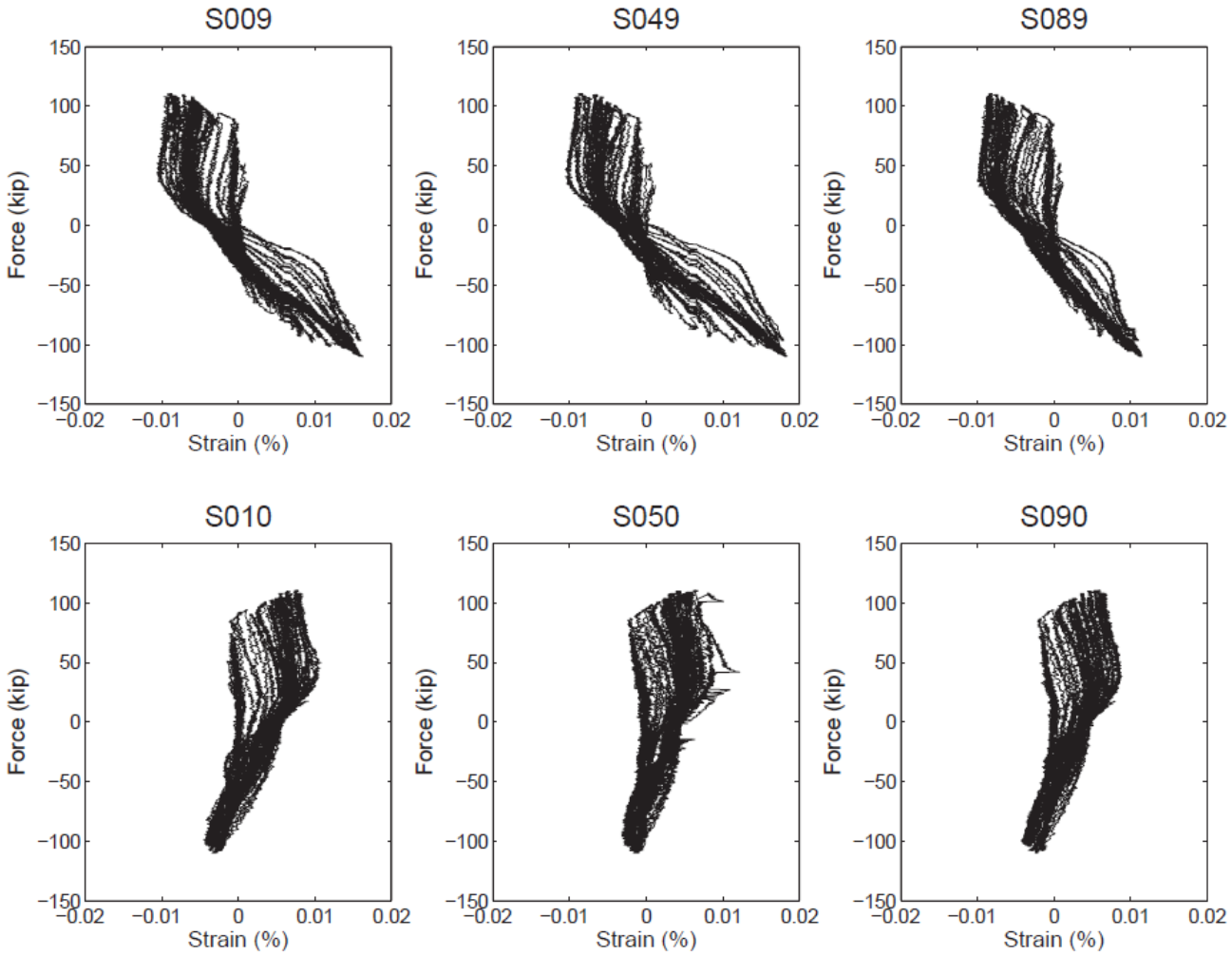

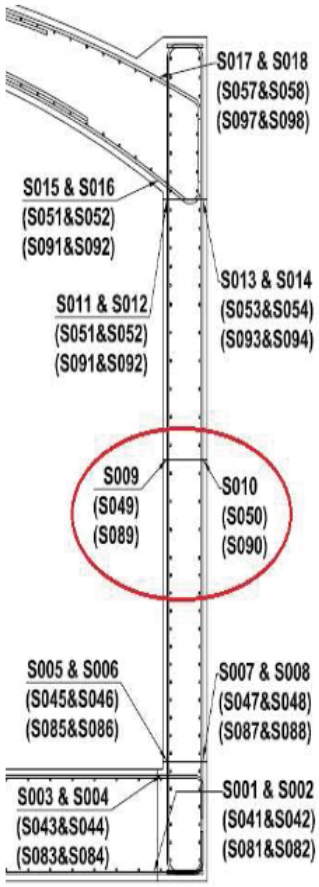

Figure D-6: Strains measured at middle of the North Wall

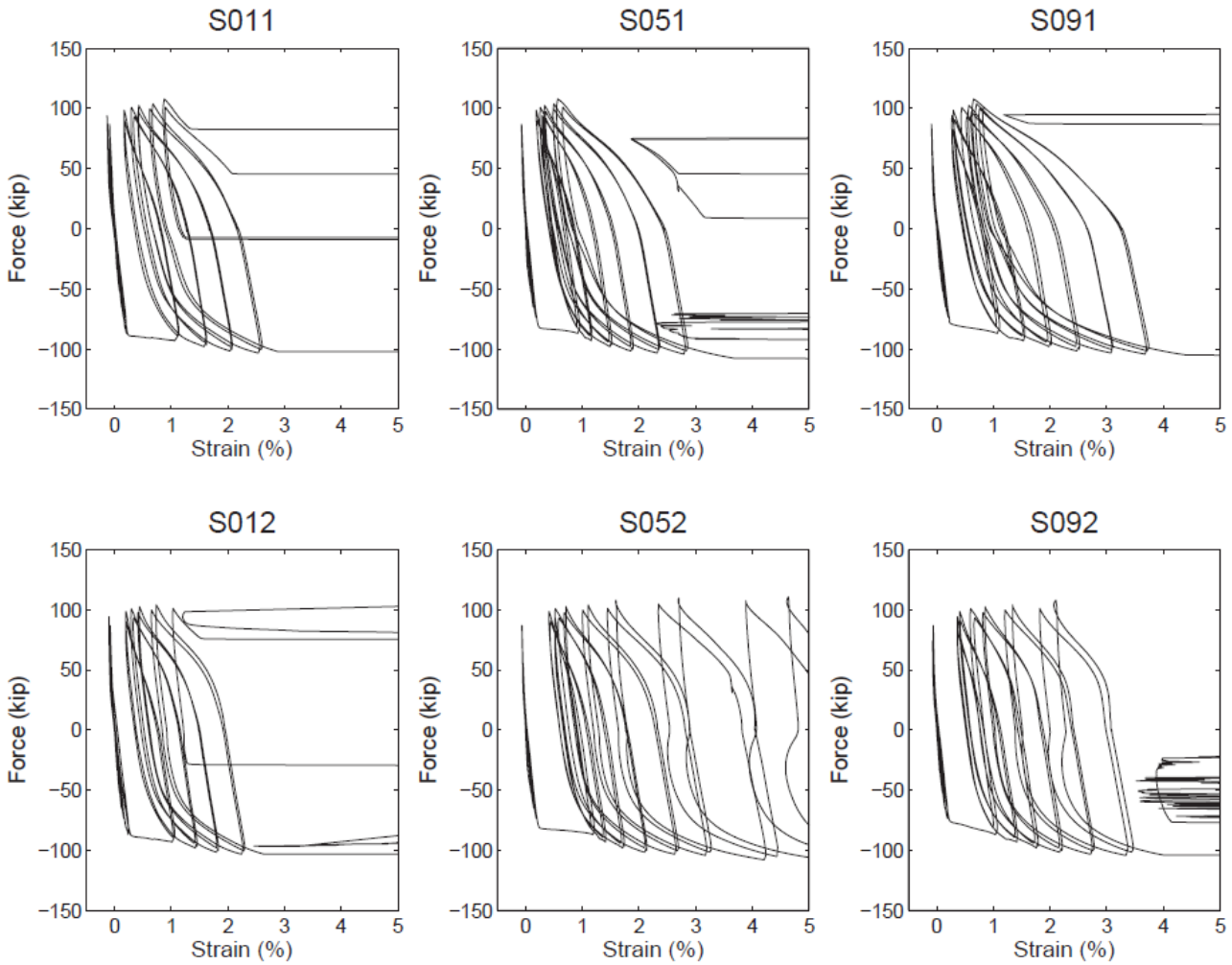

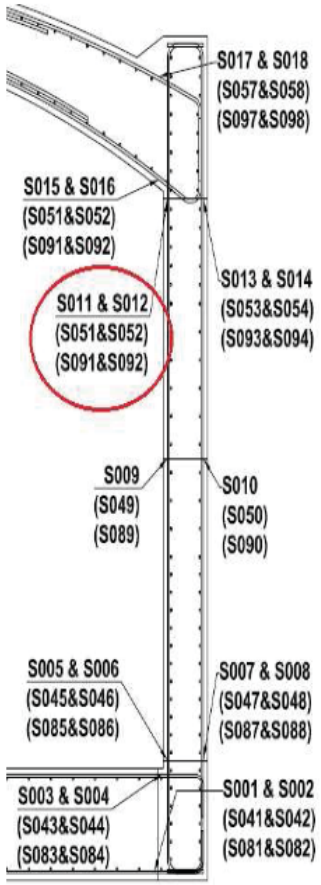

Figure D-7: Strains measured at top of the North Wall (inside)

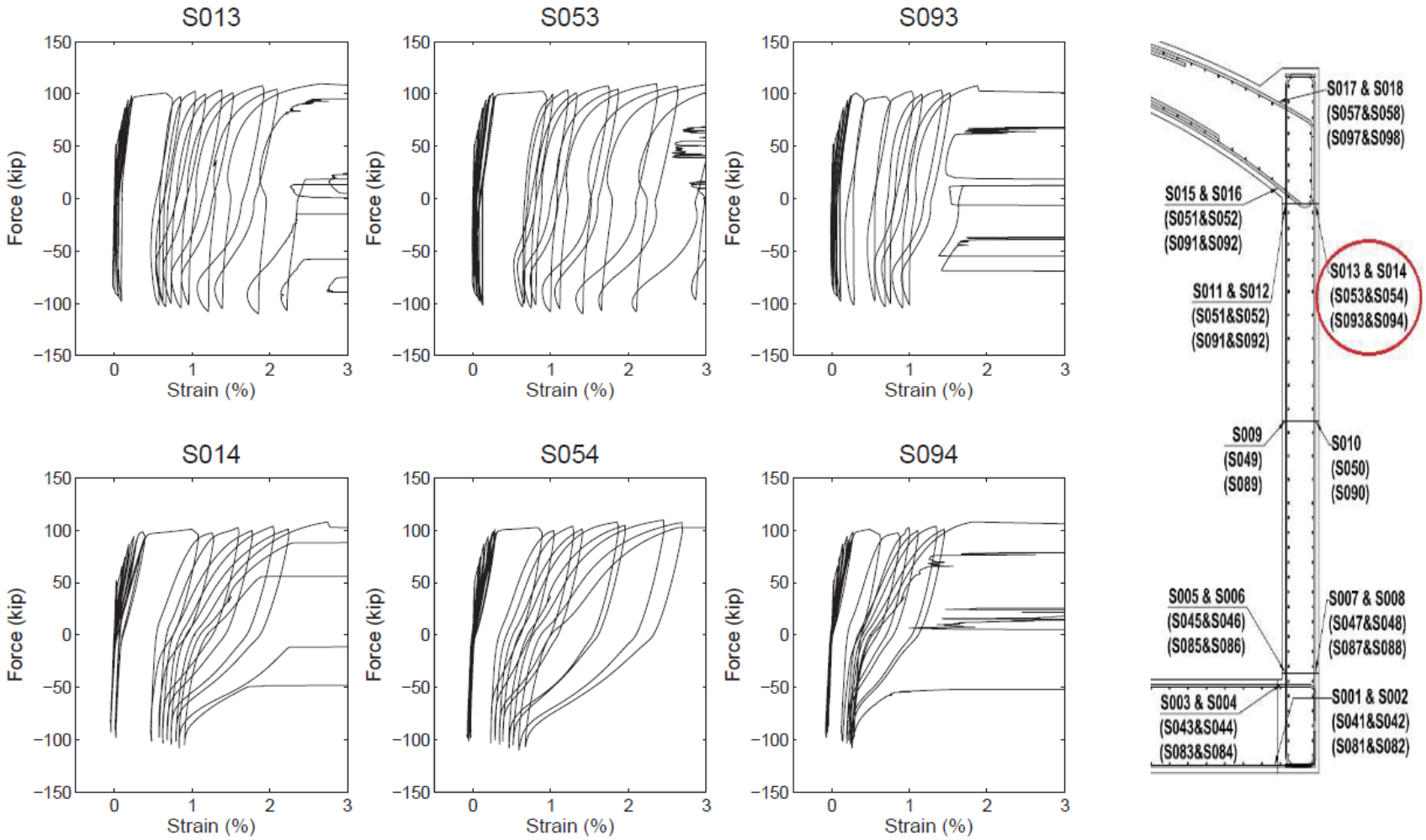

Figure D-8: Strains measured at top of the North Wall (outside)

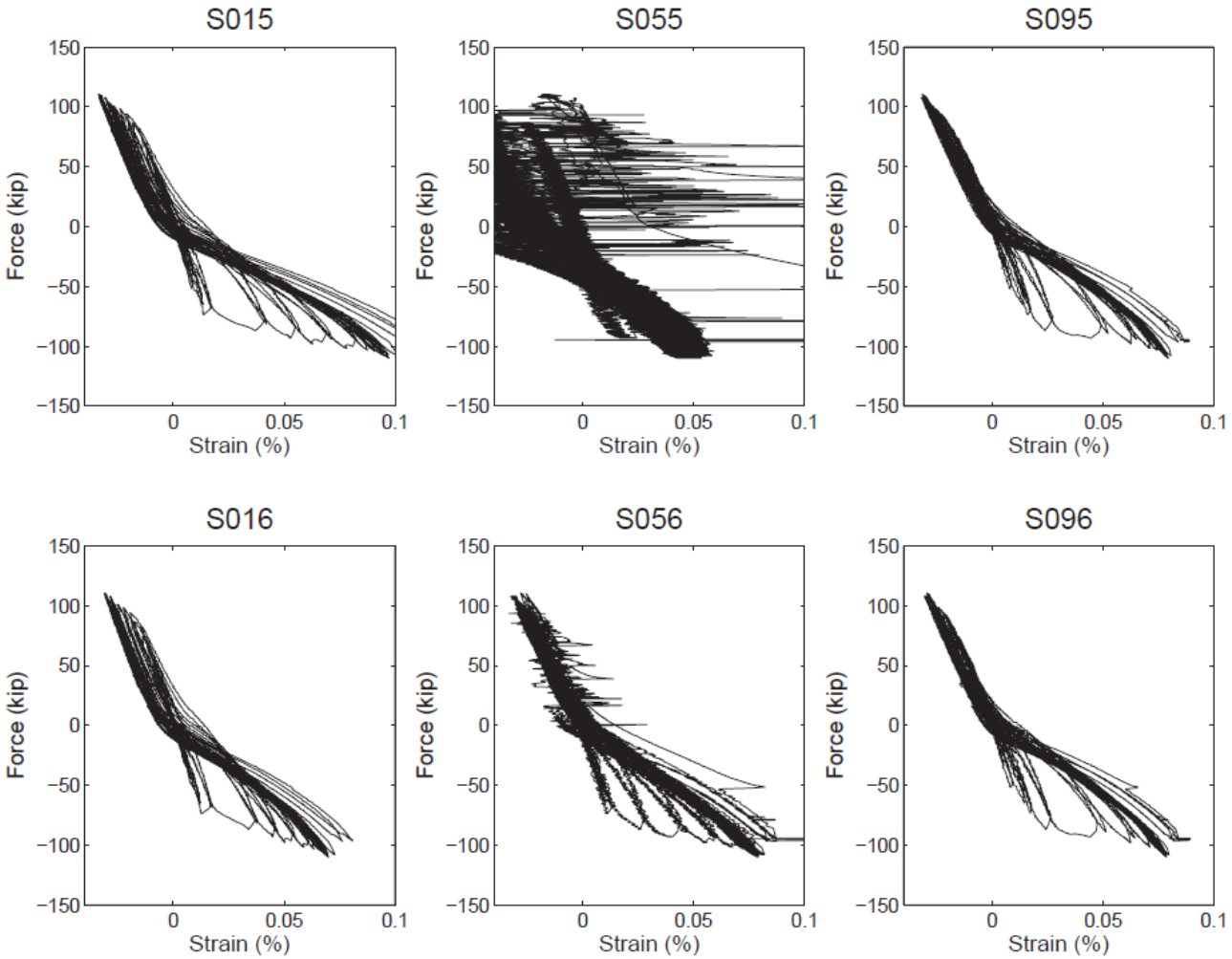

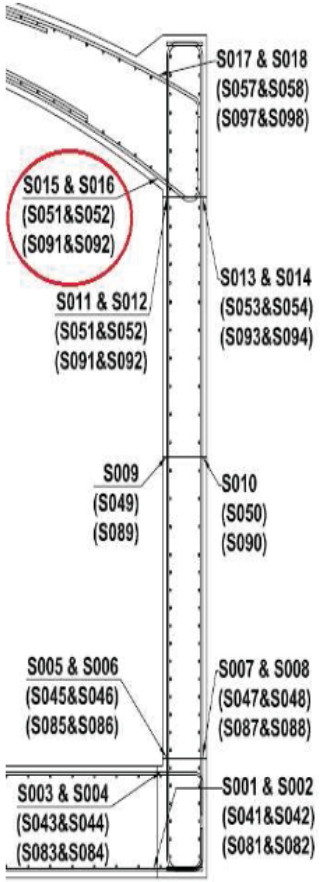

Figure D-9: Strains measured at bottom of the roof (North wall)

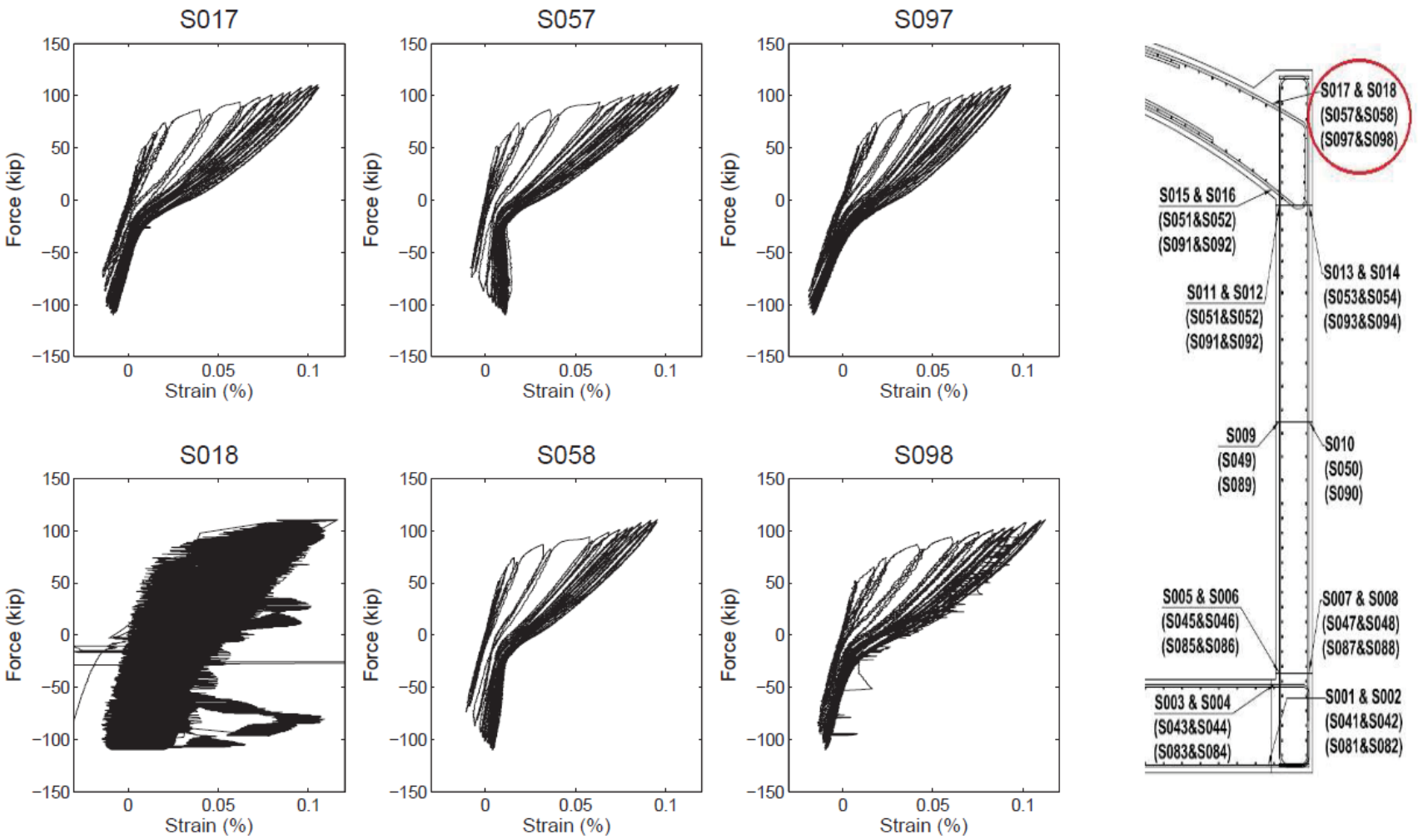

Figure D-10: Strains measured at top of the roof (North wall)

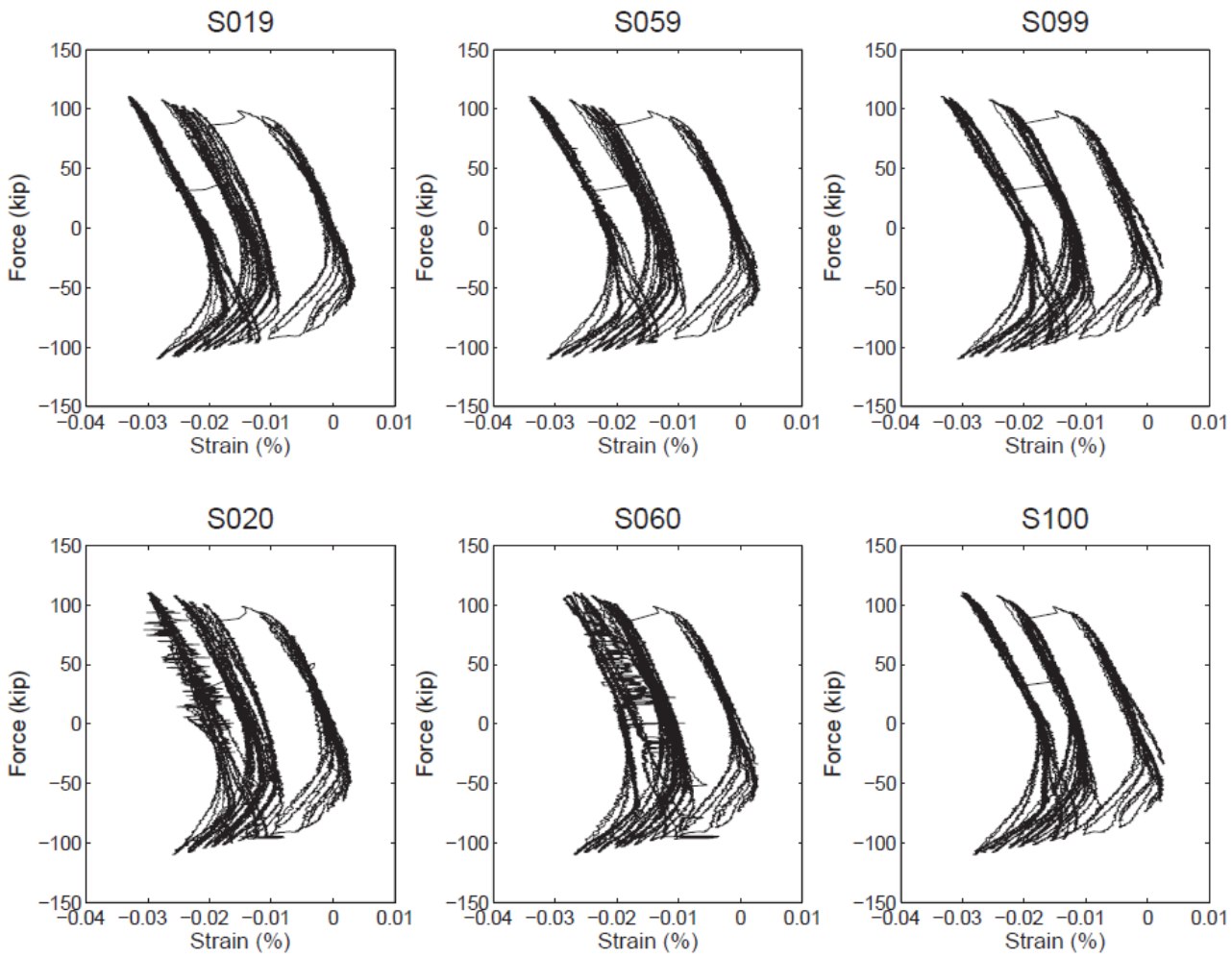

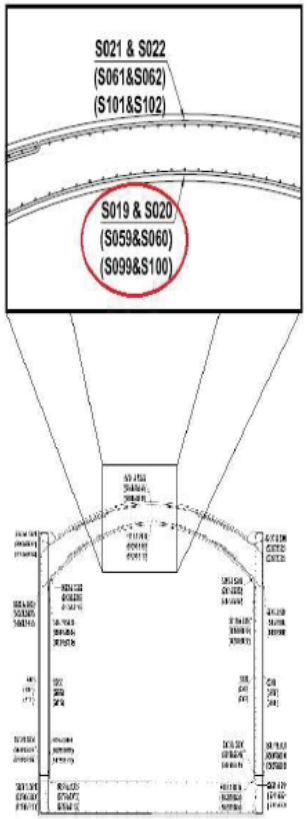

Figure D-11: Strains measured at middle of the roof (bottom)

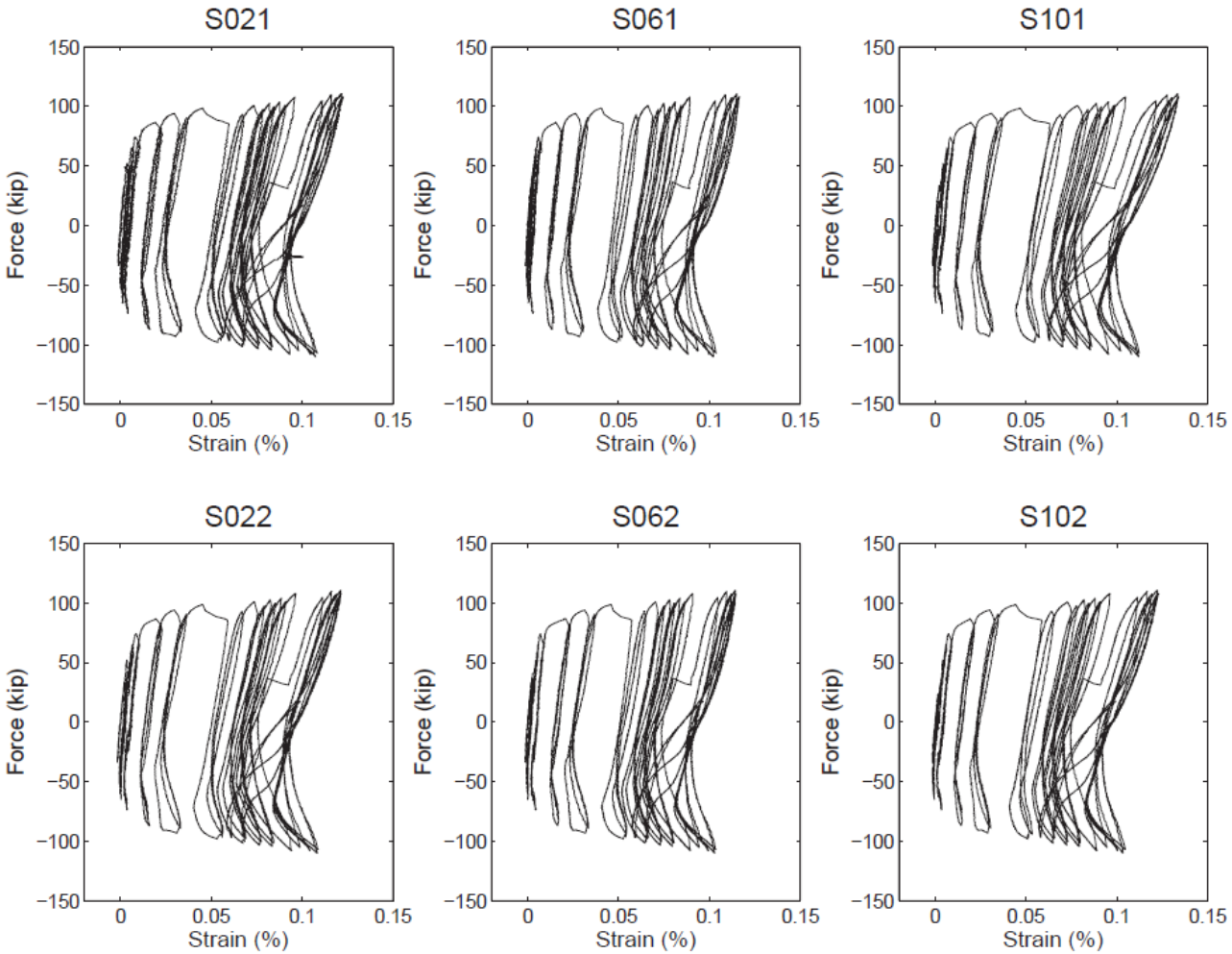

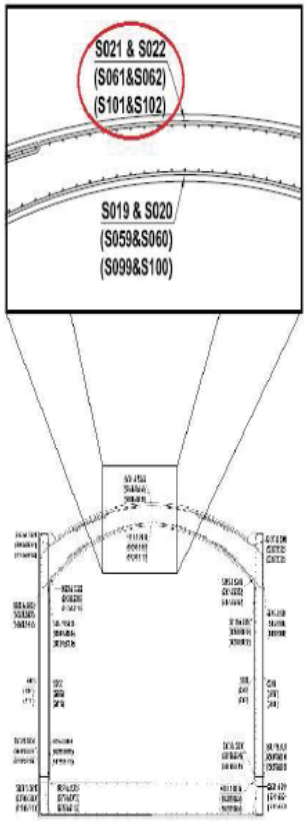

Figure D-12: Strains measured at middle of the roof (top)

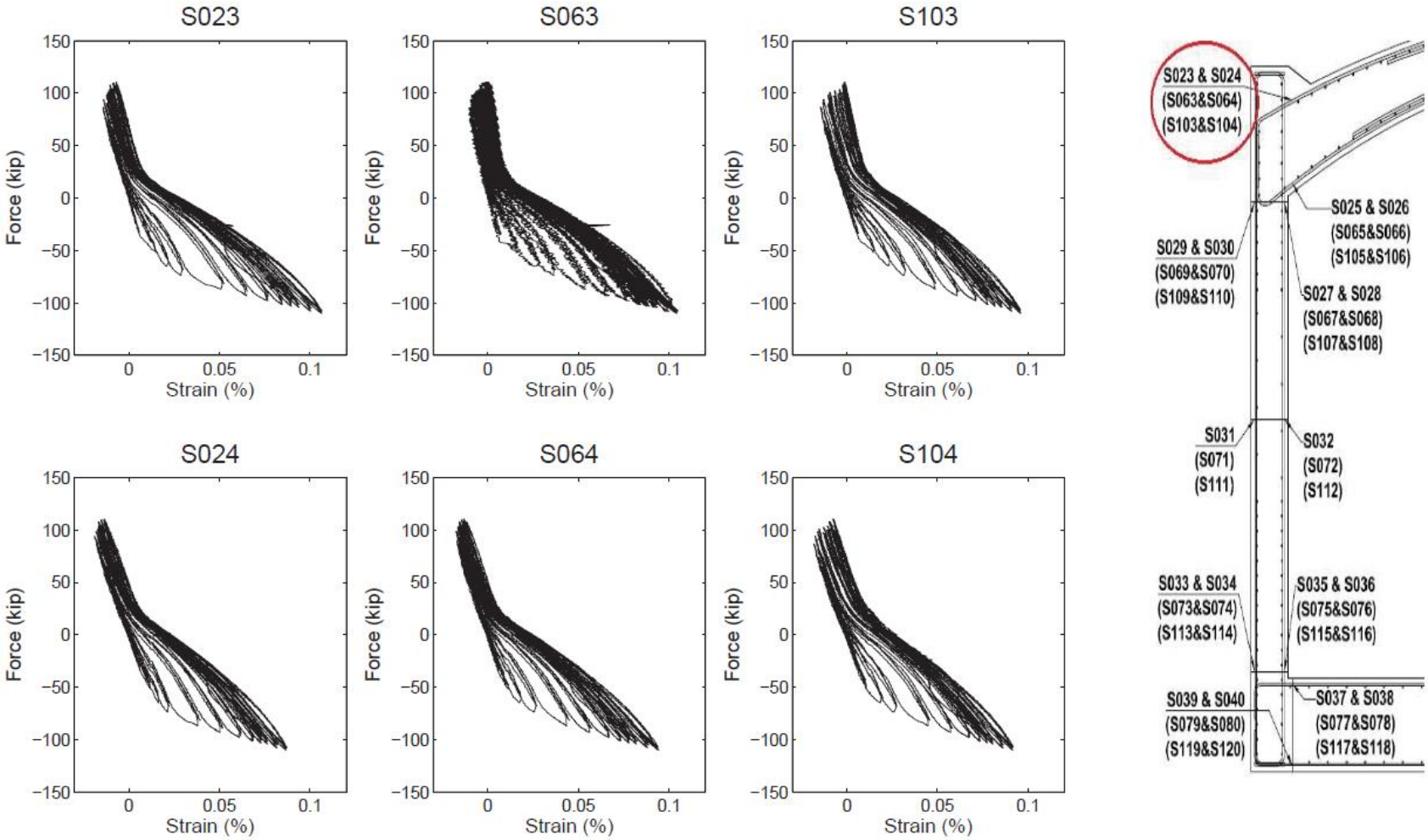

Figure D-13: Strains measured at top of the roof (South wall)

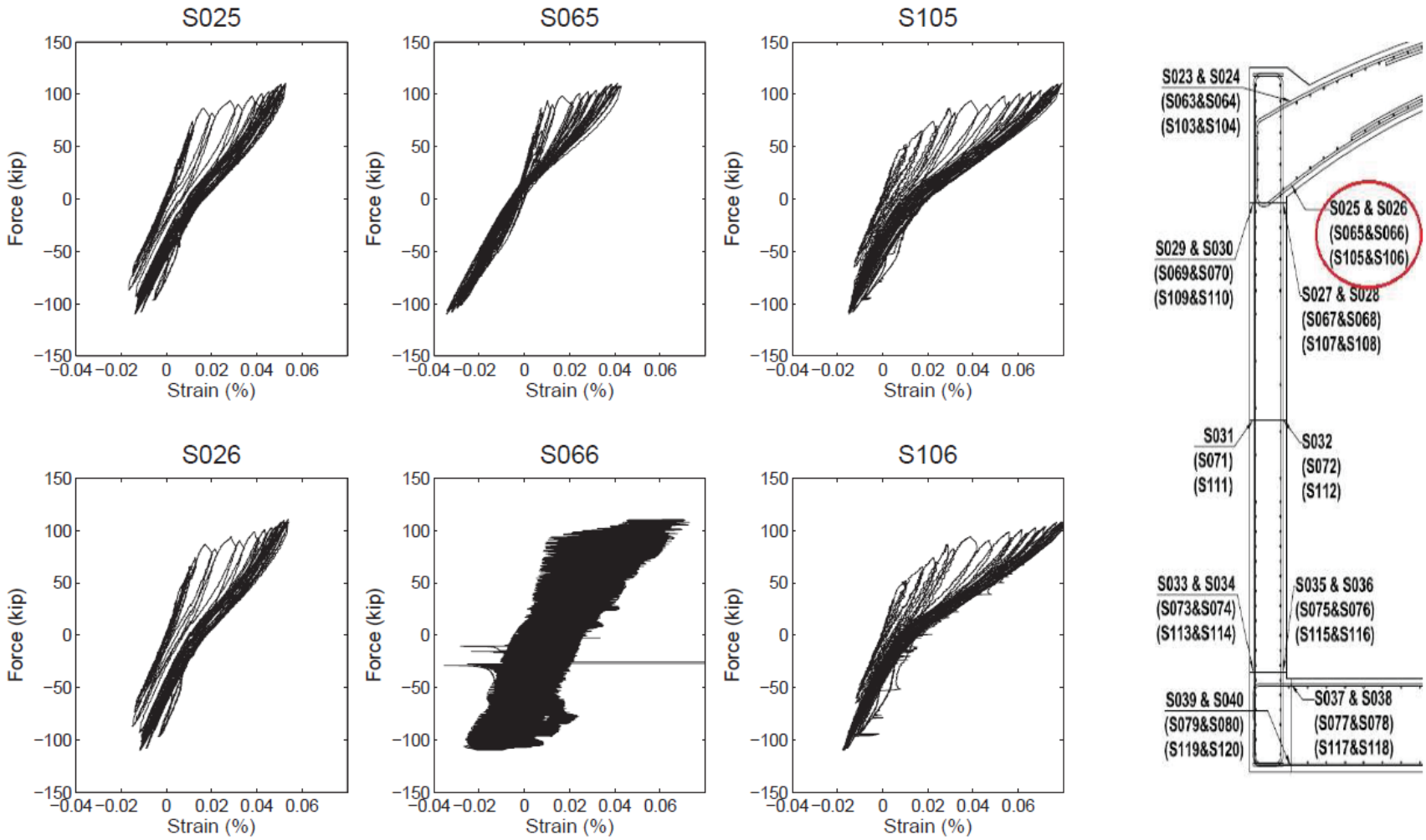

Figure D-14: Strains measured at bottom of the roof (South wall)

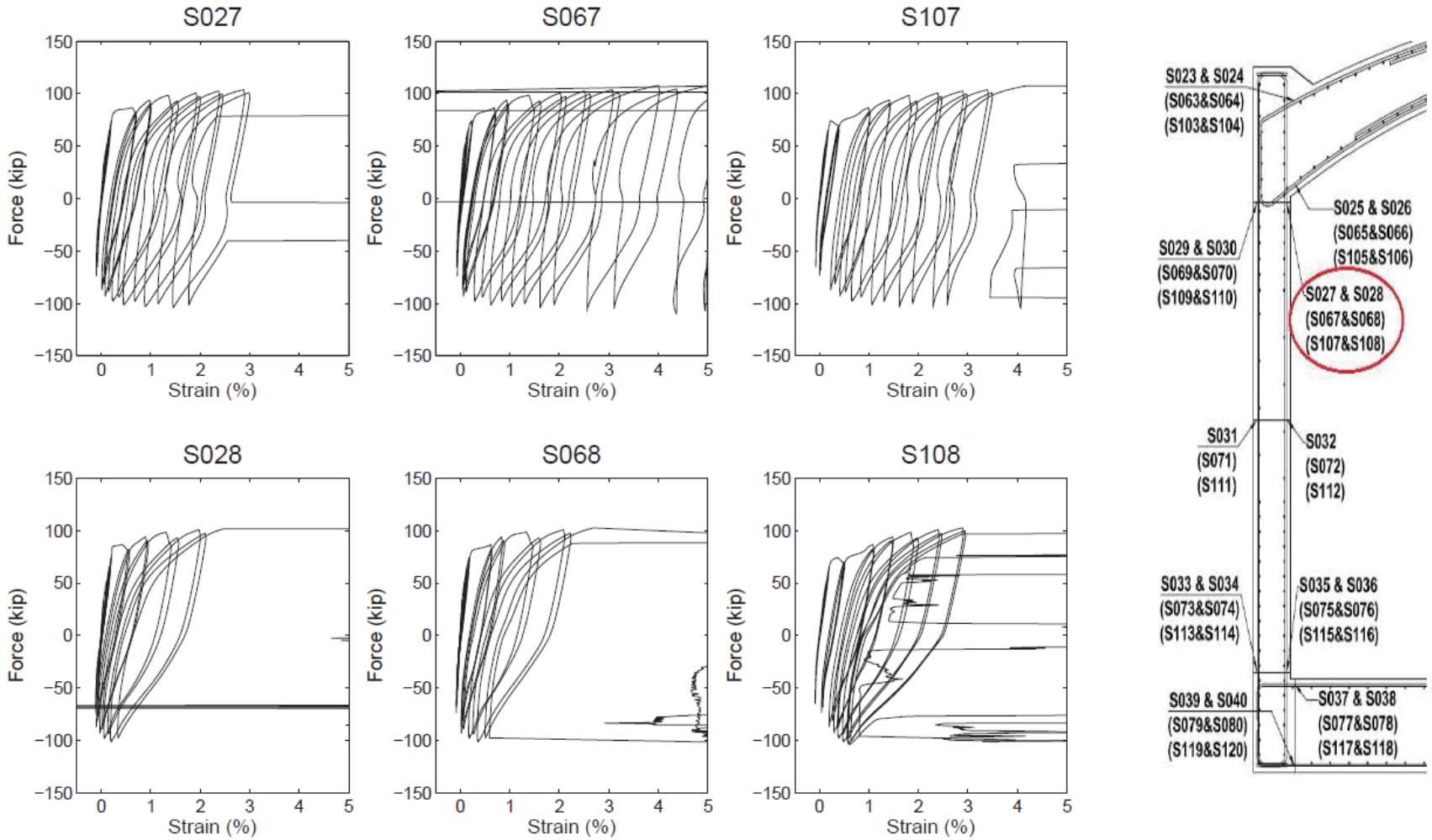

Figure D-15: Strains measured at top of the South wall (inside)

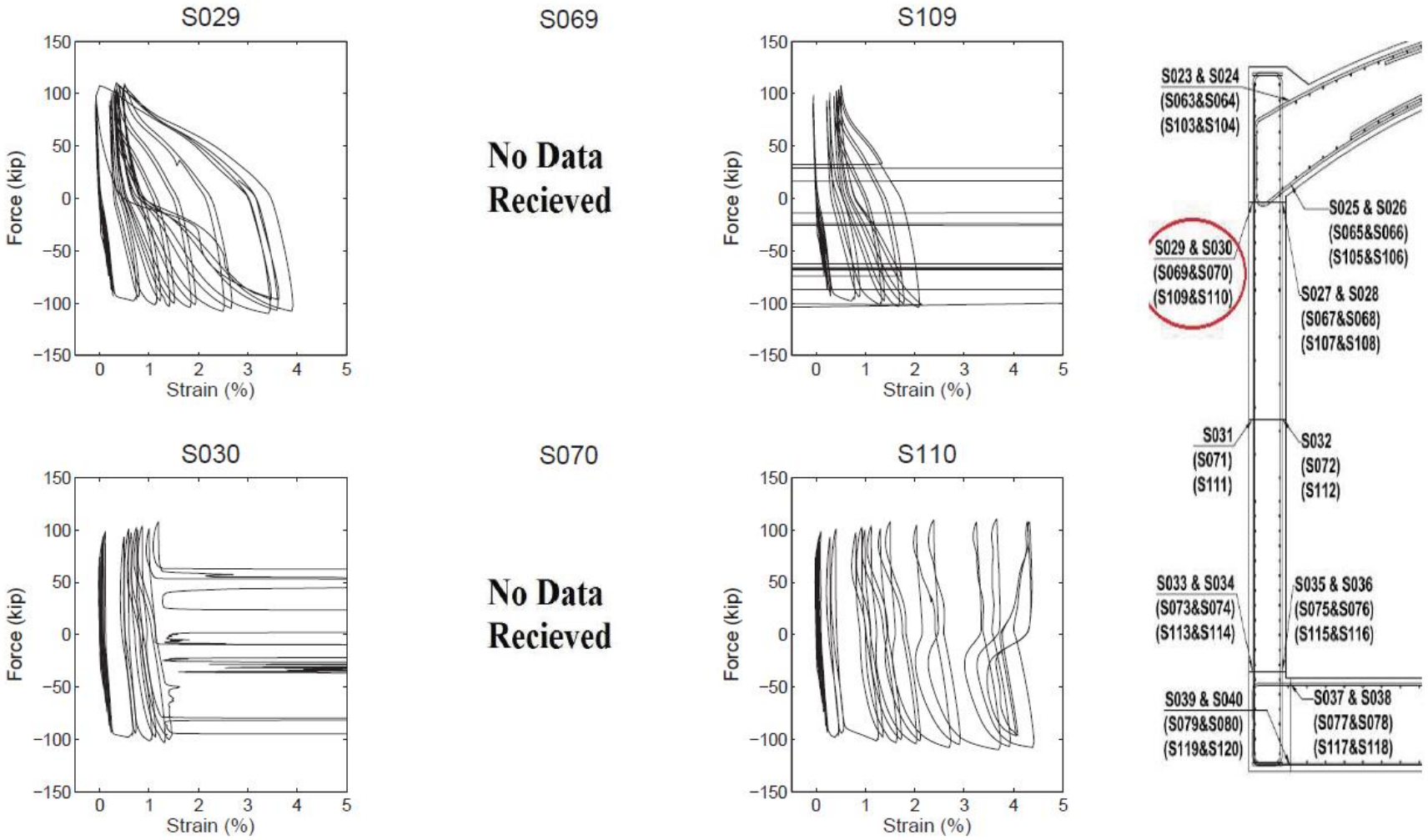

Figure D-16: Strains measured at top of the South wall (outside)

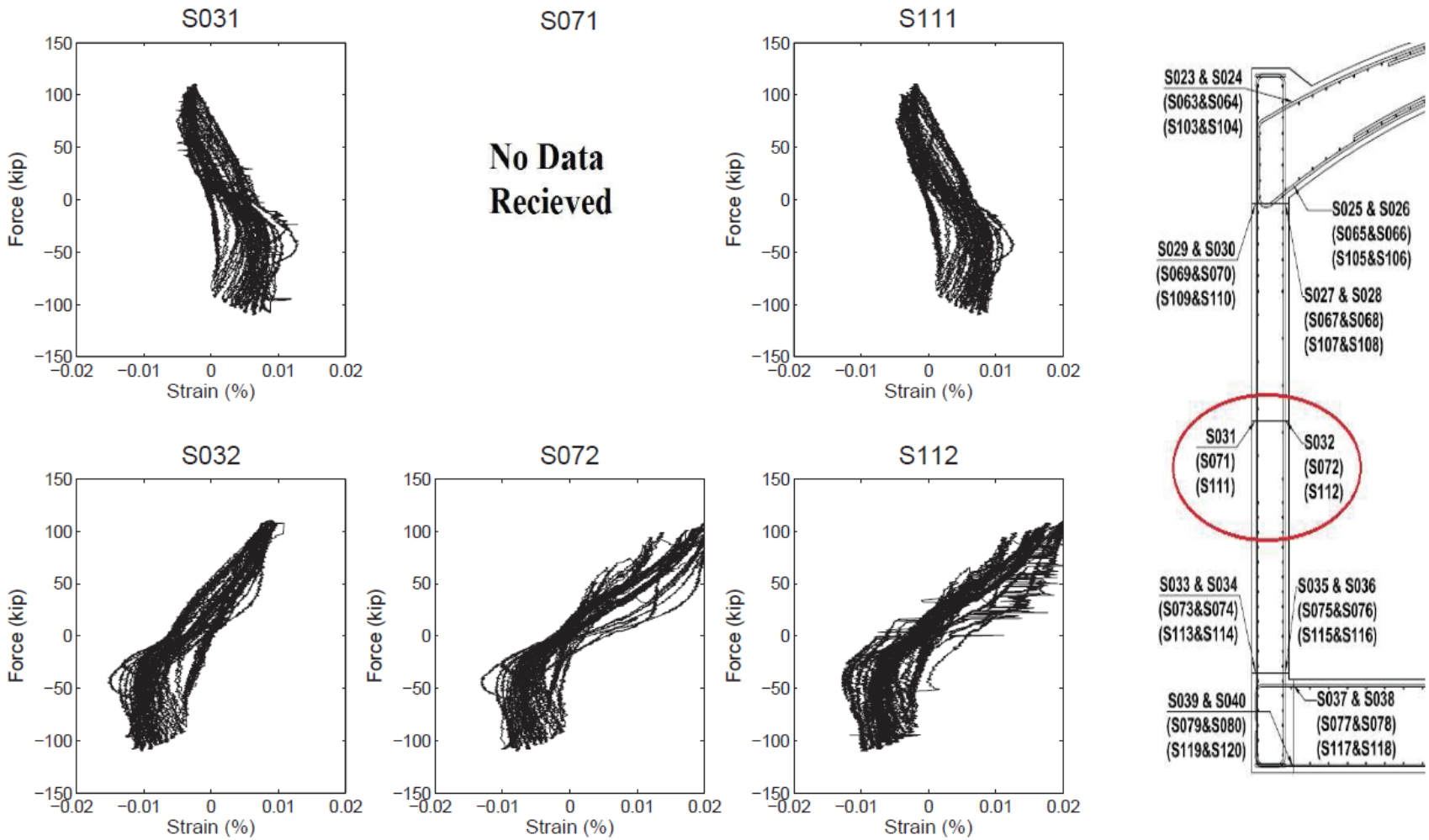

Figure D-17: Strains measured at middle of the South wall

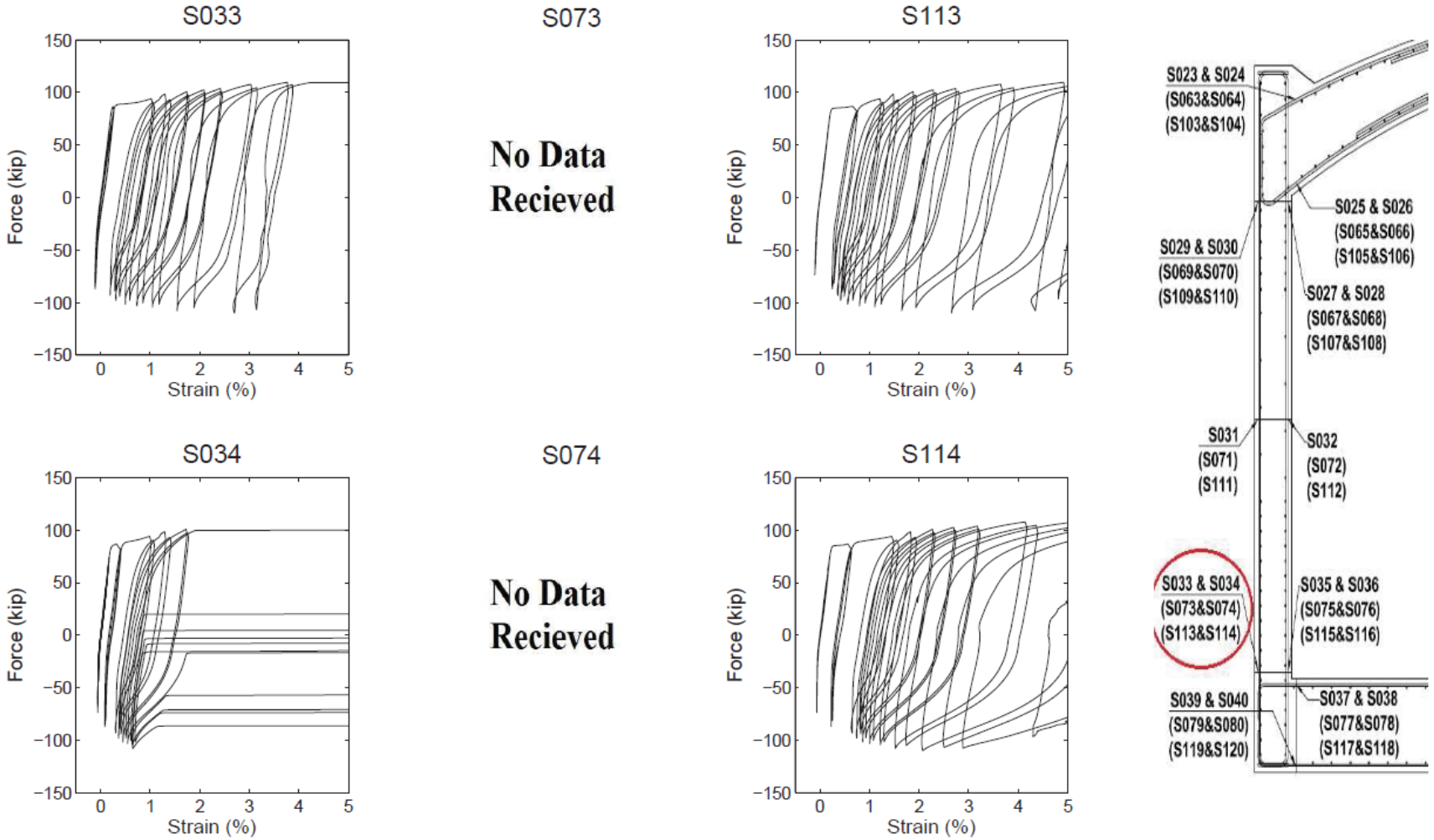

Figure D-18: Strains measured at bottom of the South wall (outside)

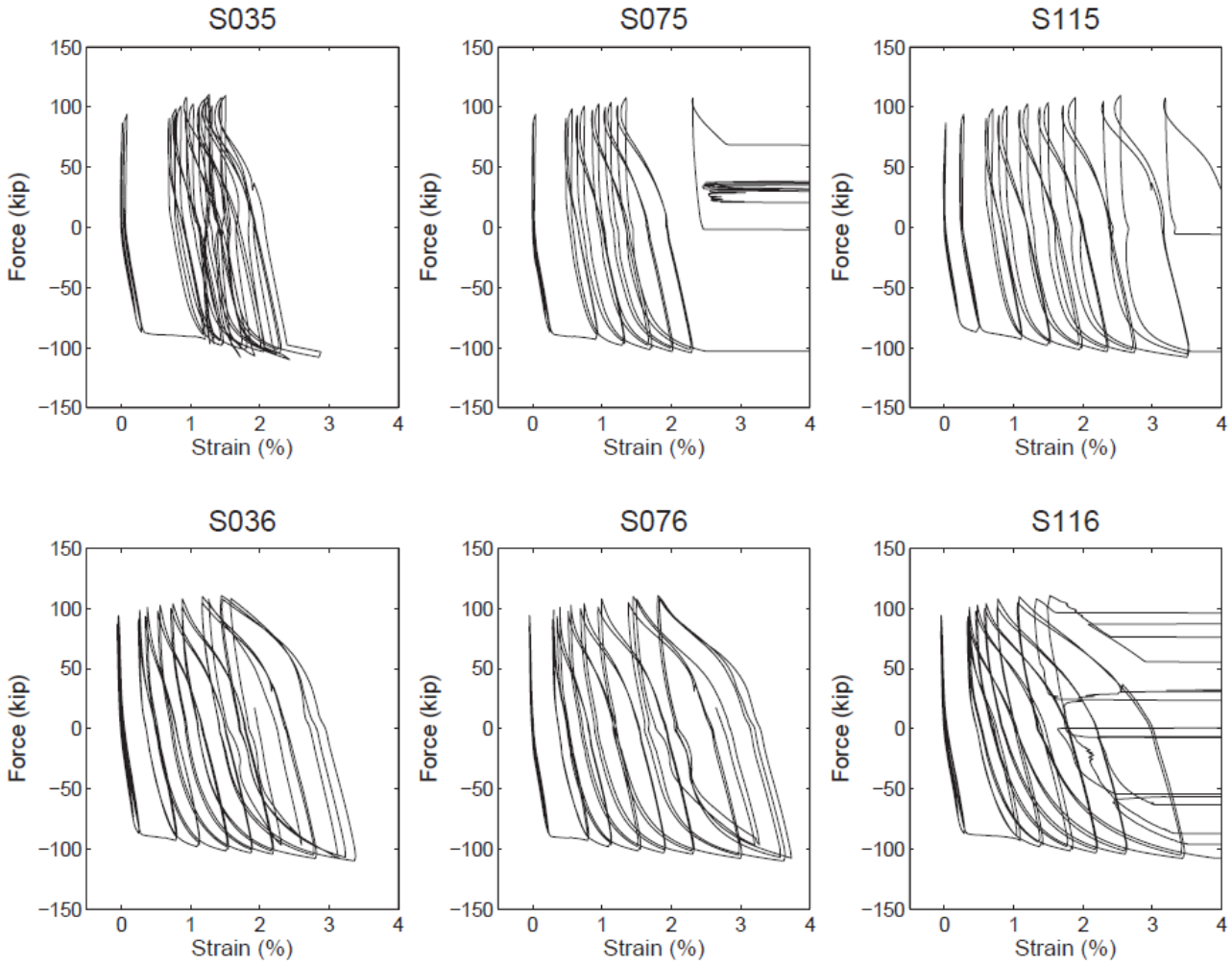

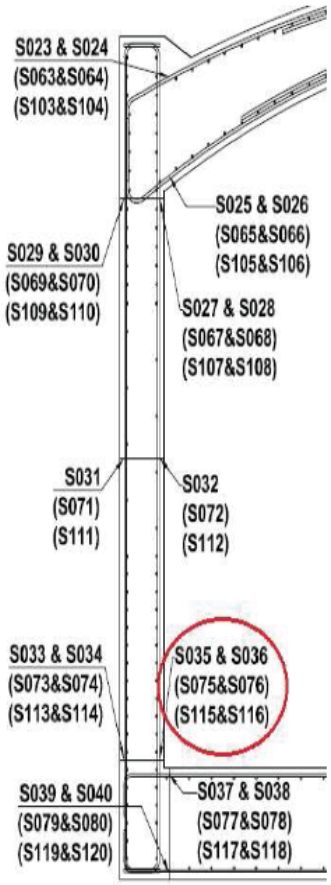

Figure D-19: Strains measured at bottom of the South wall (inside)

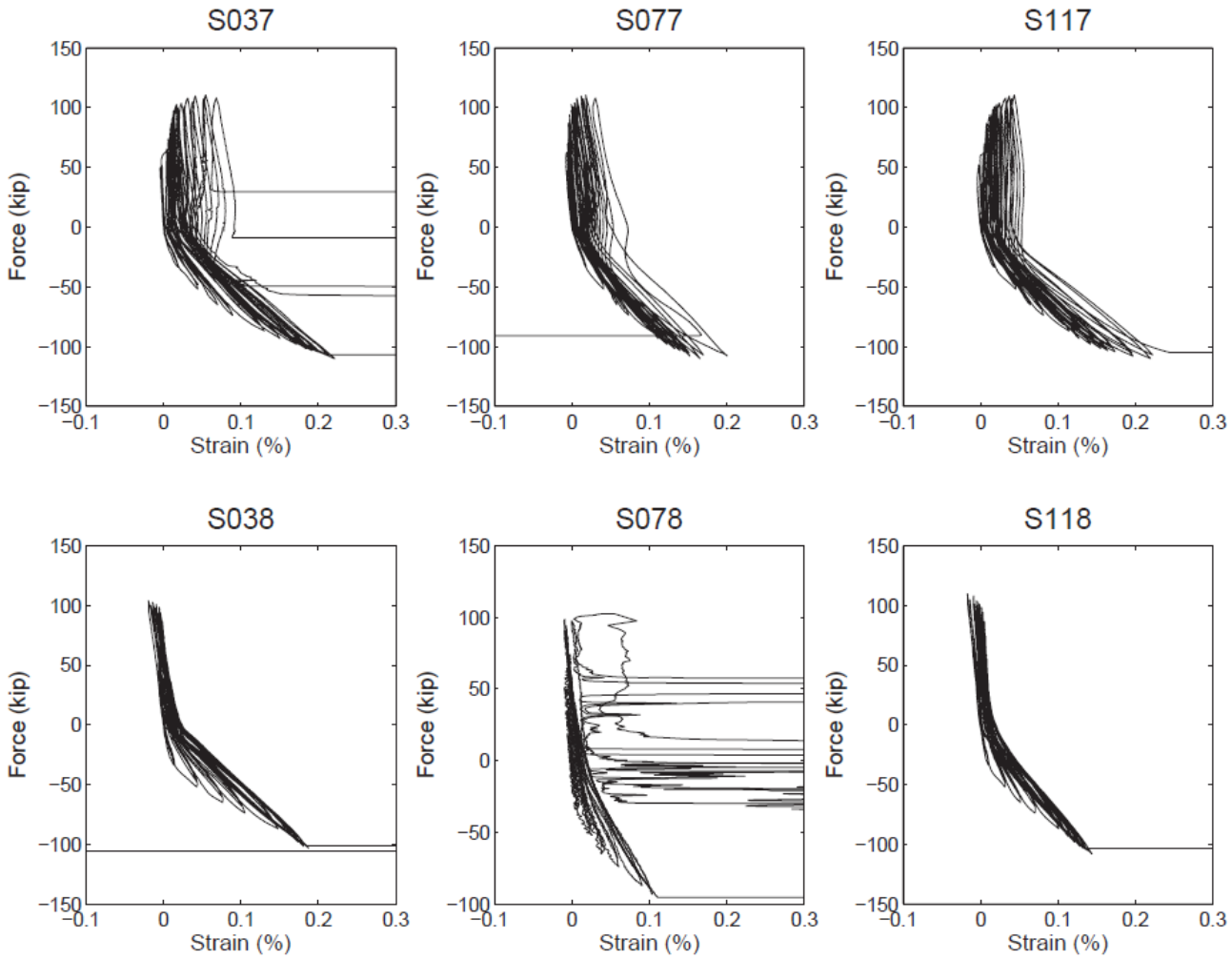

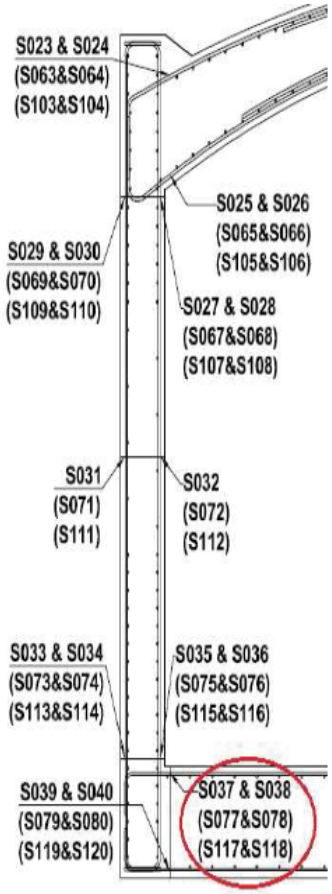

Figure D-20: Strains measured at top of the slab (South wall)

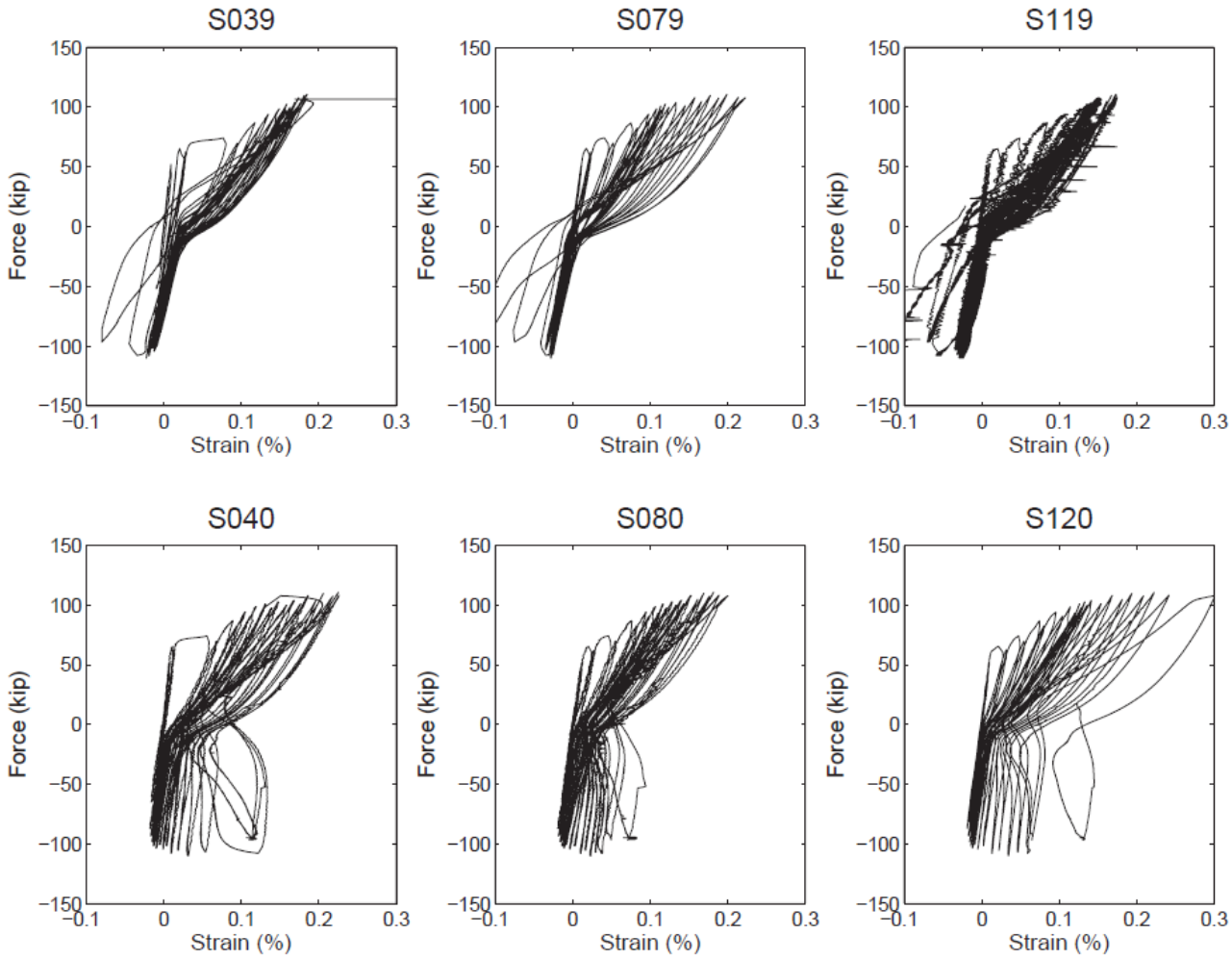

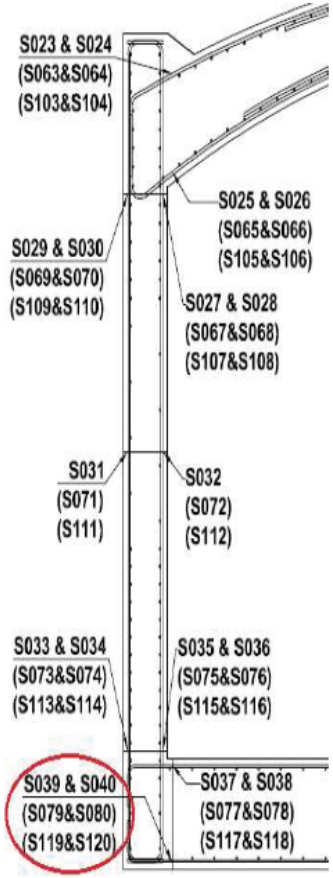

Figure D-21: Strains measured at bottom of the slab (South wall)

APPENDIX E: Displacement Transducer and Inclinometer Output

Displacements were measured from the displacement transducers and inclinometers (Figure E-1) during the quasi-static cyclic test presented in Chapter 3. The relationship of the displacement and the applied force (per unit width; 1ft) is shown in Figure E-2 through Figure E-10. The relationship of the rotation and the applied force (per unit width; 1ft) is shown Figure E-11 through Figure E-15.

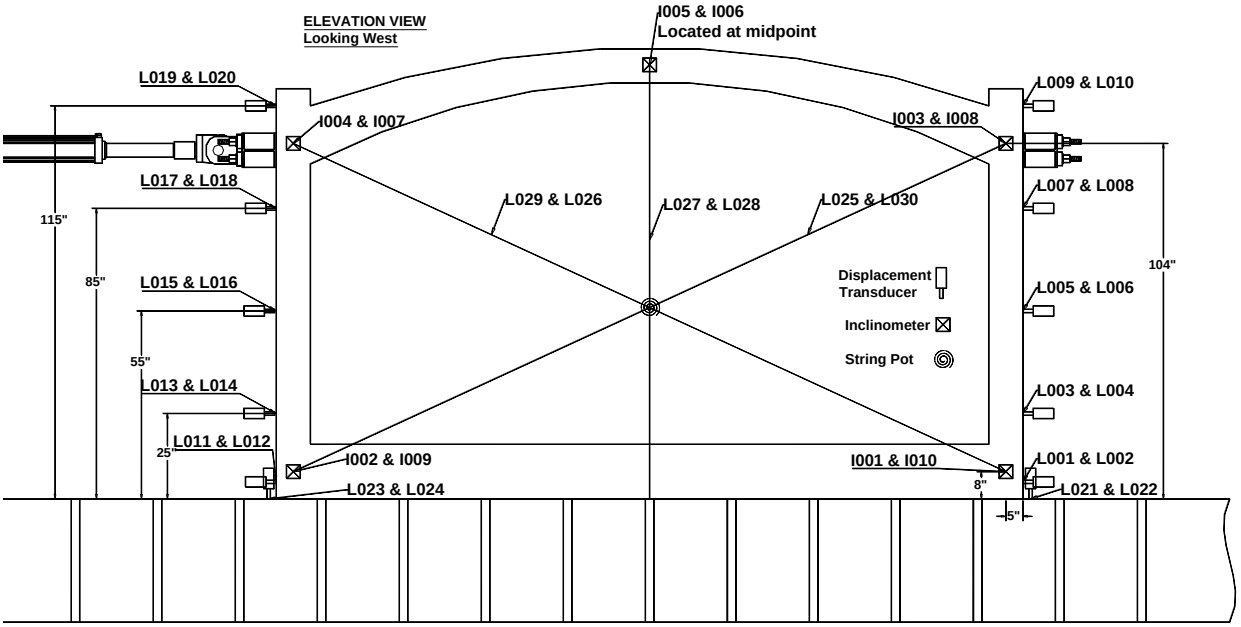

Figure E-1: Instrumentation layout of the displacement transducers and inclinometers

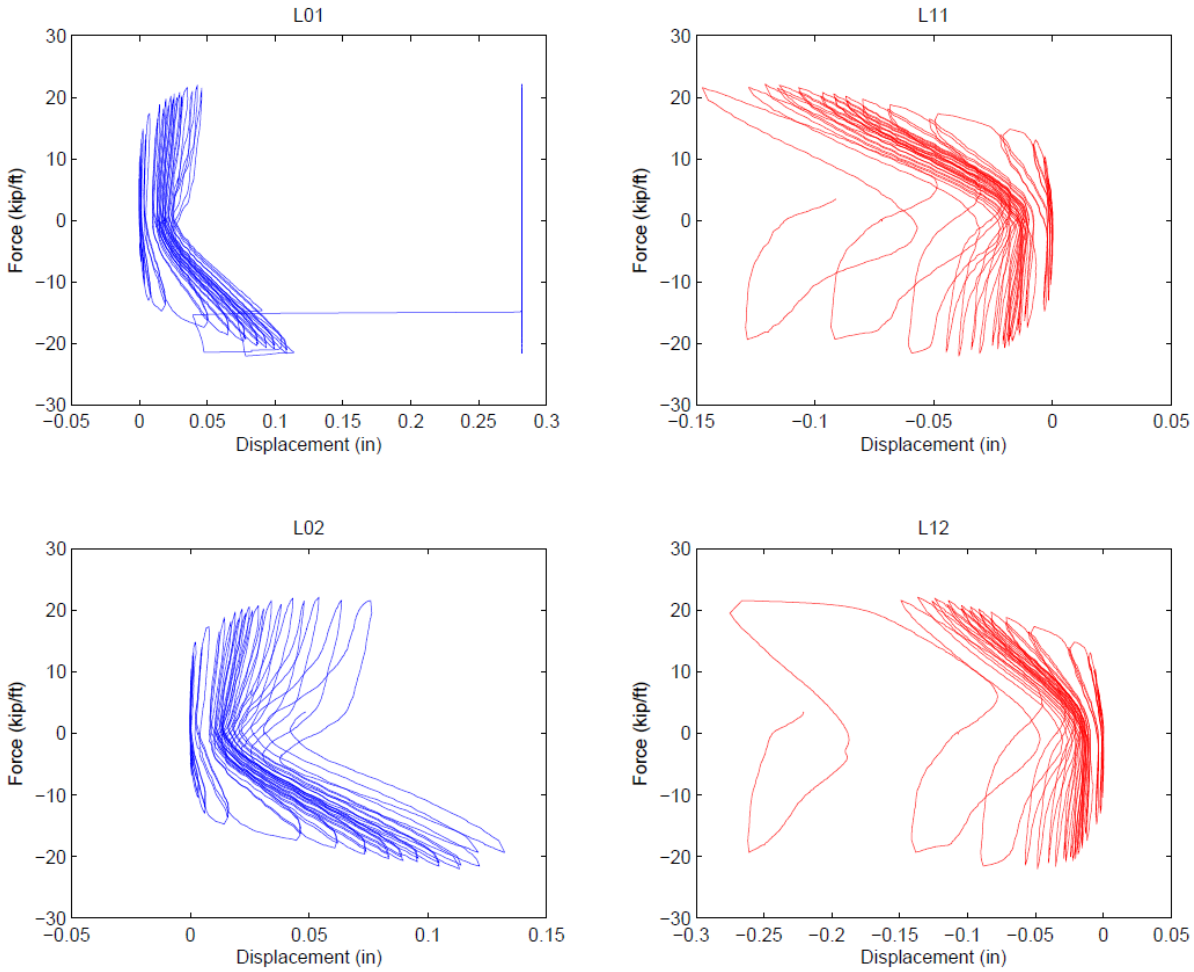

Figure E-2: Lateral displacements measured near base of the slab per unit width (1 ft)

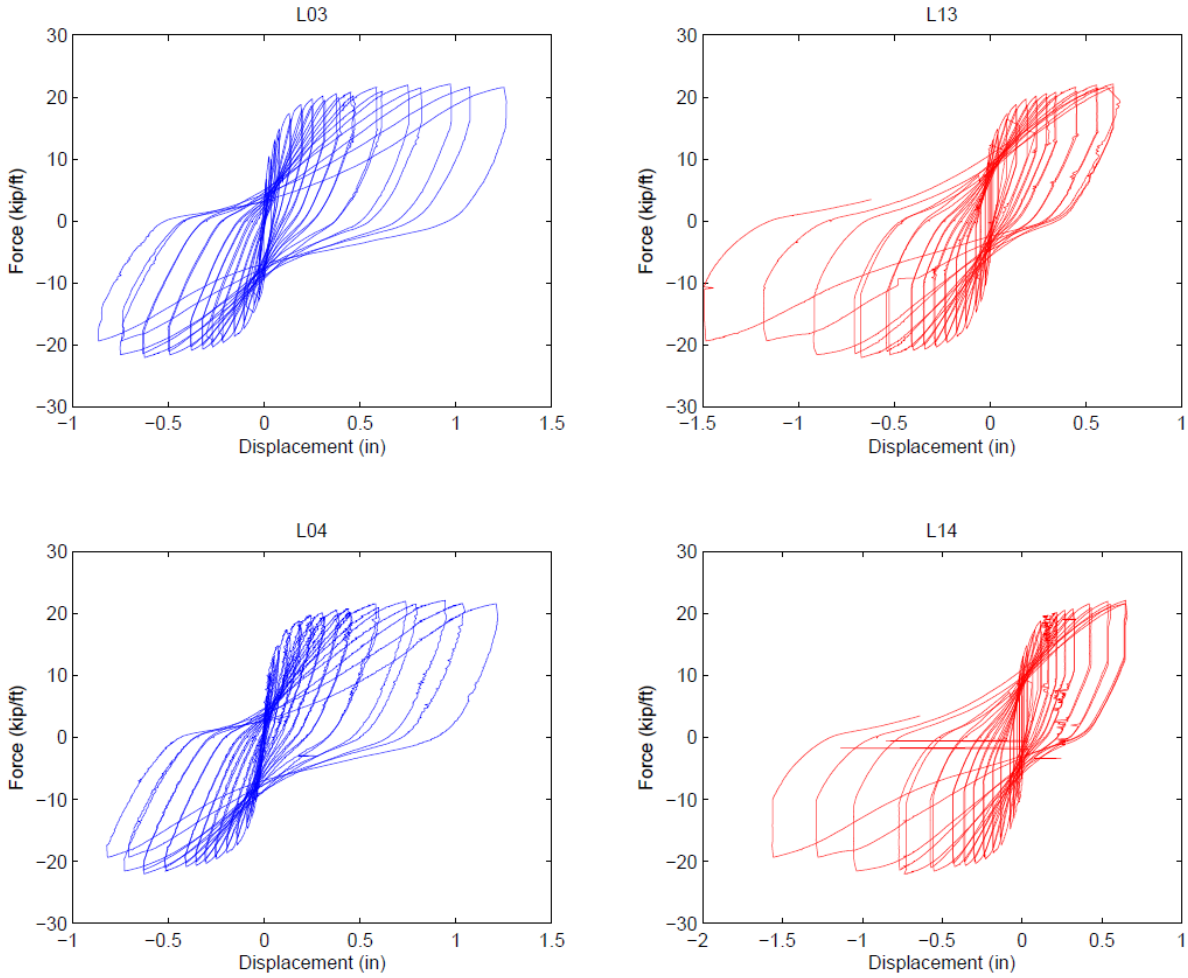

Figure E-3: Lateral displacements measured at the 25” height wall per unit width (1 ft)

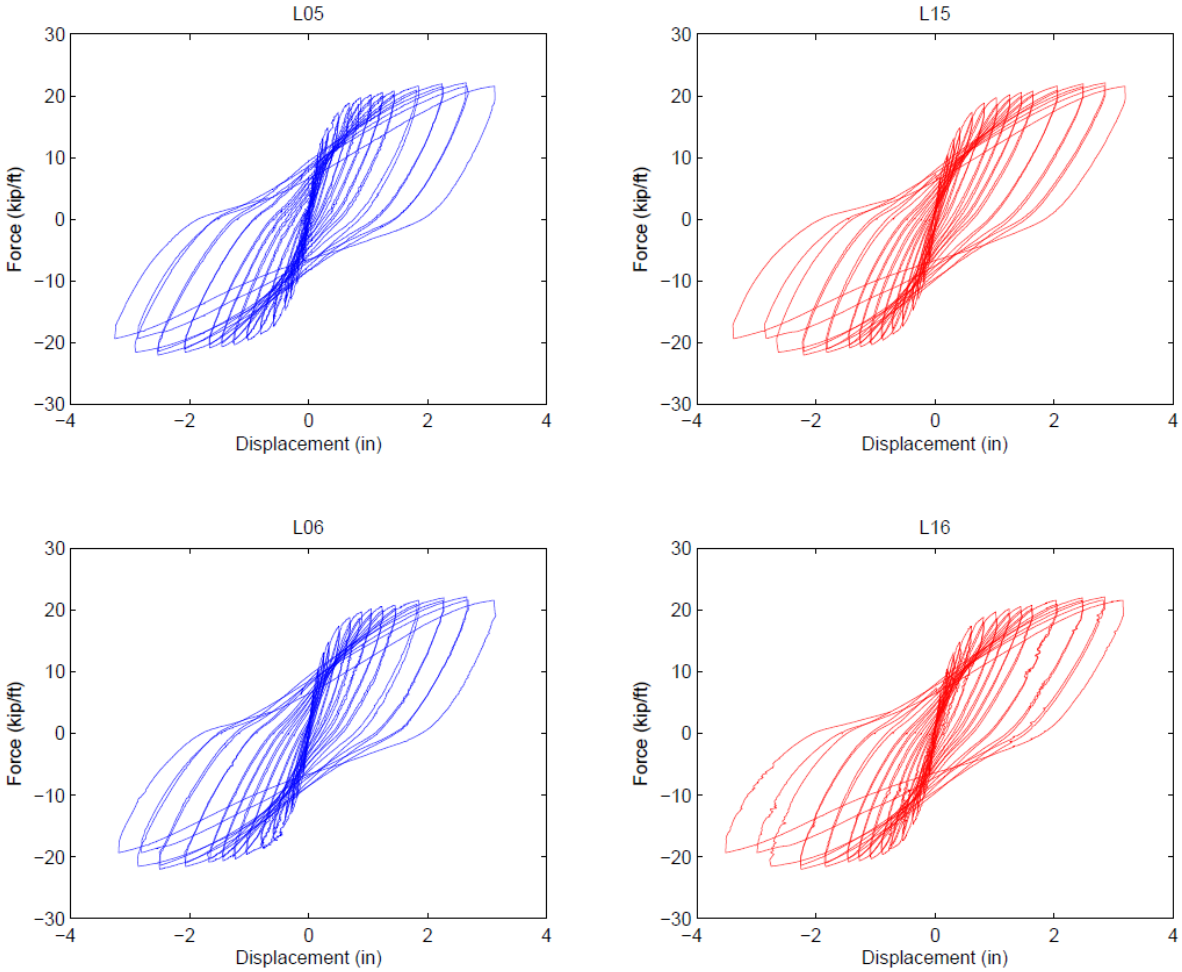

Figure E-4: Lateral displacements measured at the 55” height wall per unit width (1 ft)

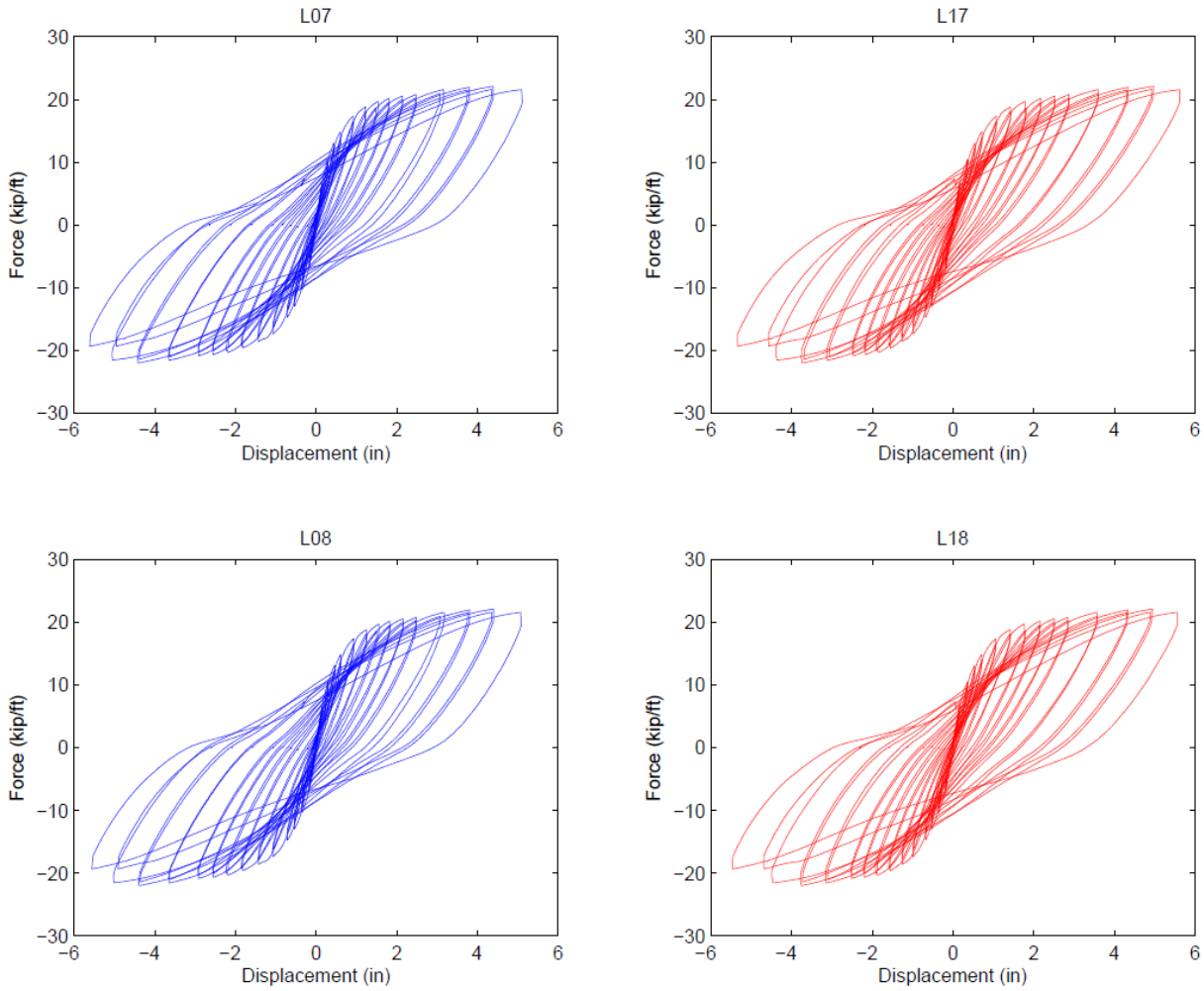

Figure E-5: Lateral displacements measured at the 85” height wall per unit width (1 ft)

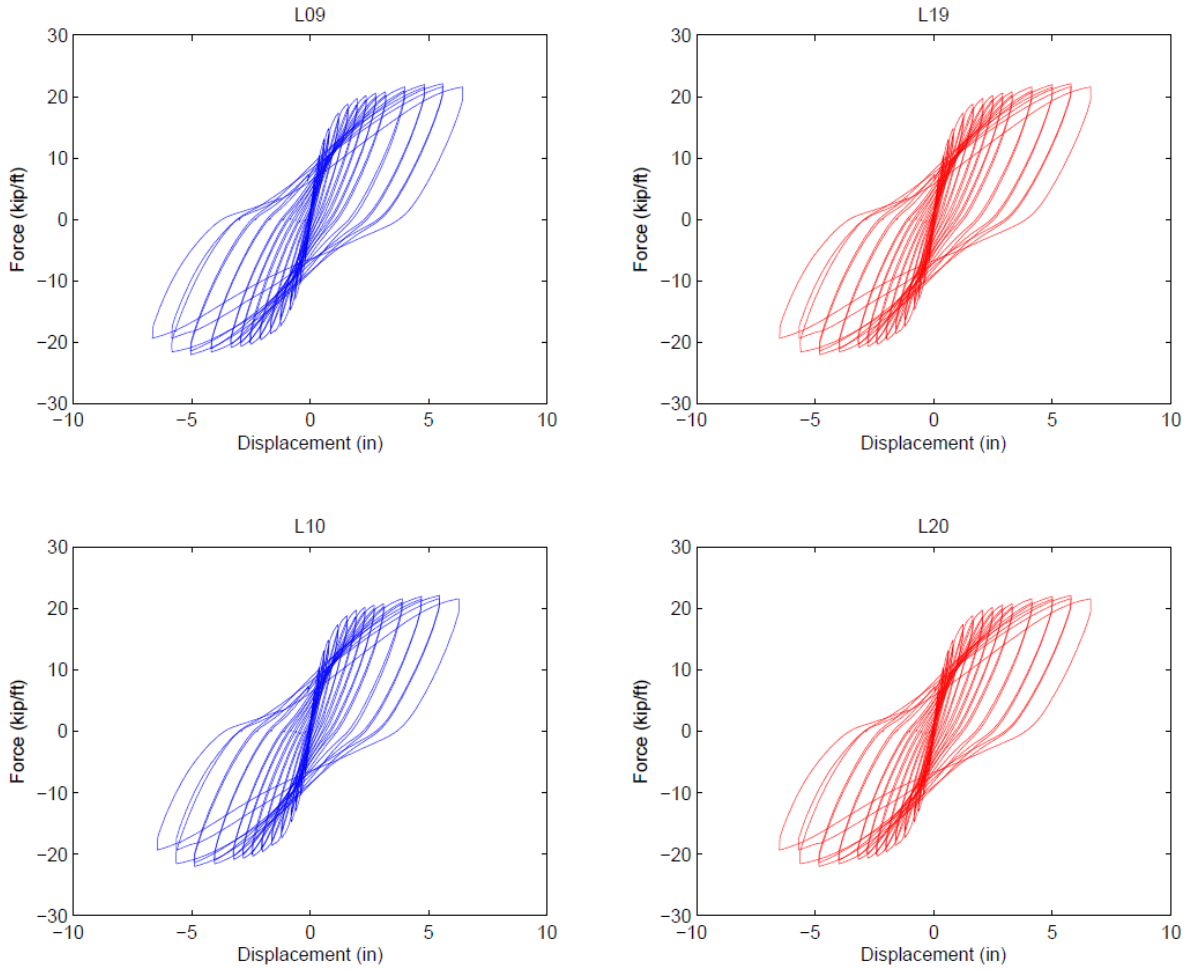

Figure E-6: Lateral displacements measured at the 115” height (top) wall per unit width (1 ft)

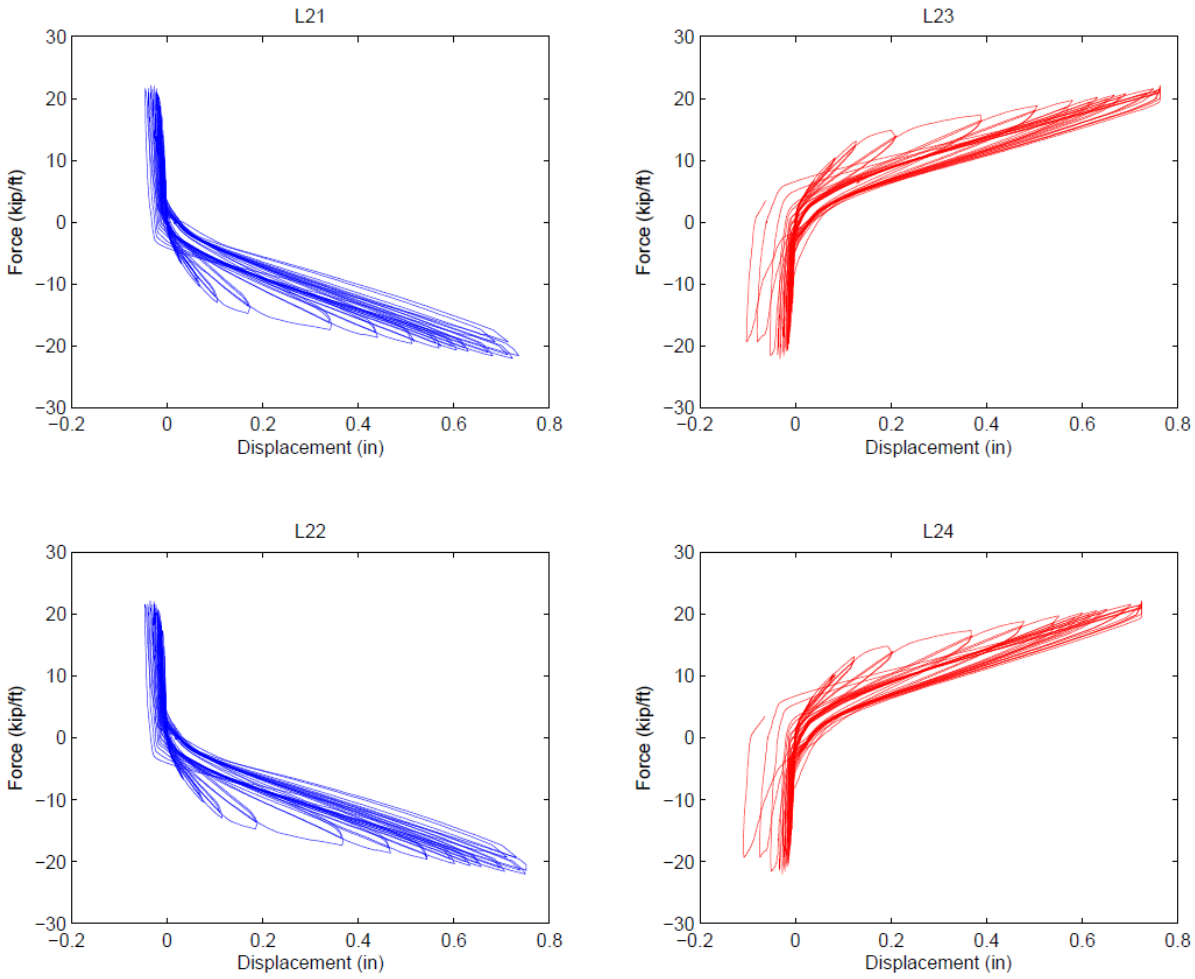

Figure E-7: Vertical displacements measured between lab floor and slab per unit width (1 ft)

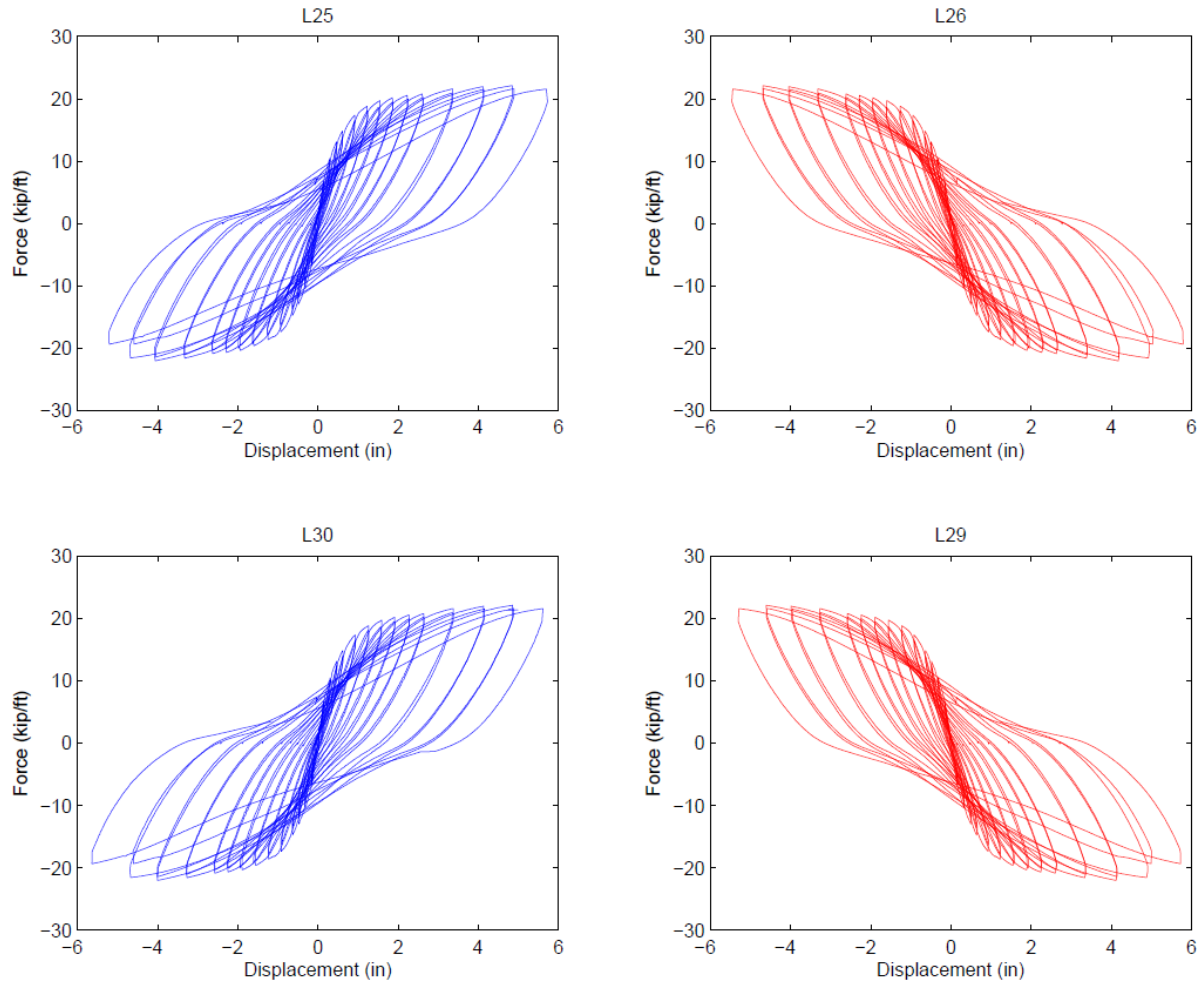

Figure E-8: Displacements measured from the transducer aligned in the diagonal direction (from slab to roof) per unit width (1 ft)

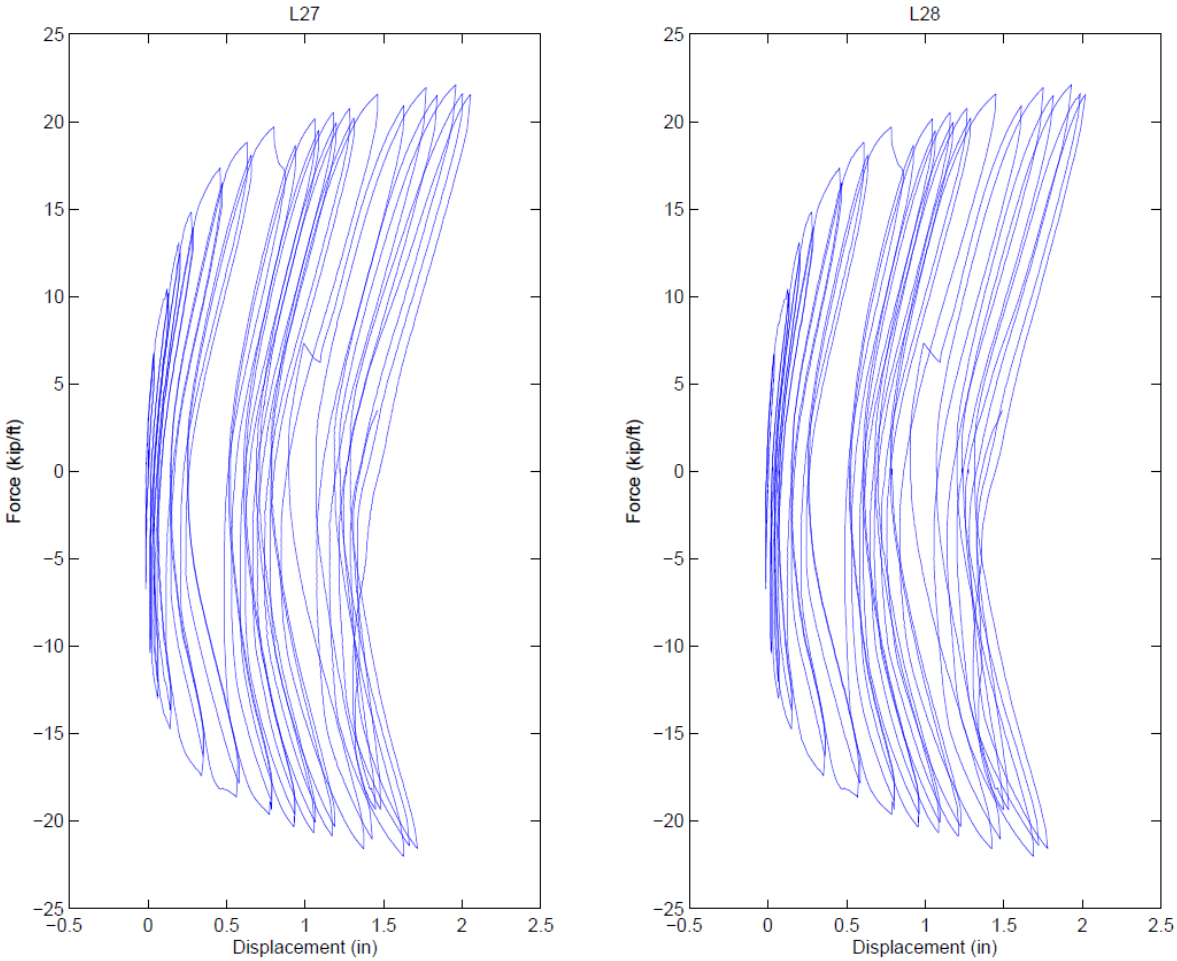

Figure E-9: Vertical displacements measured between center of slab and roof per unit width (1 ft)

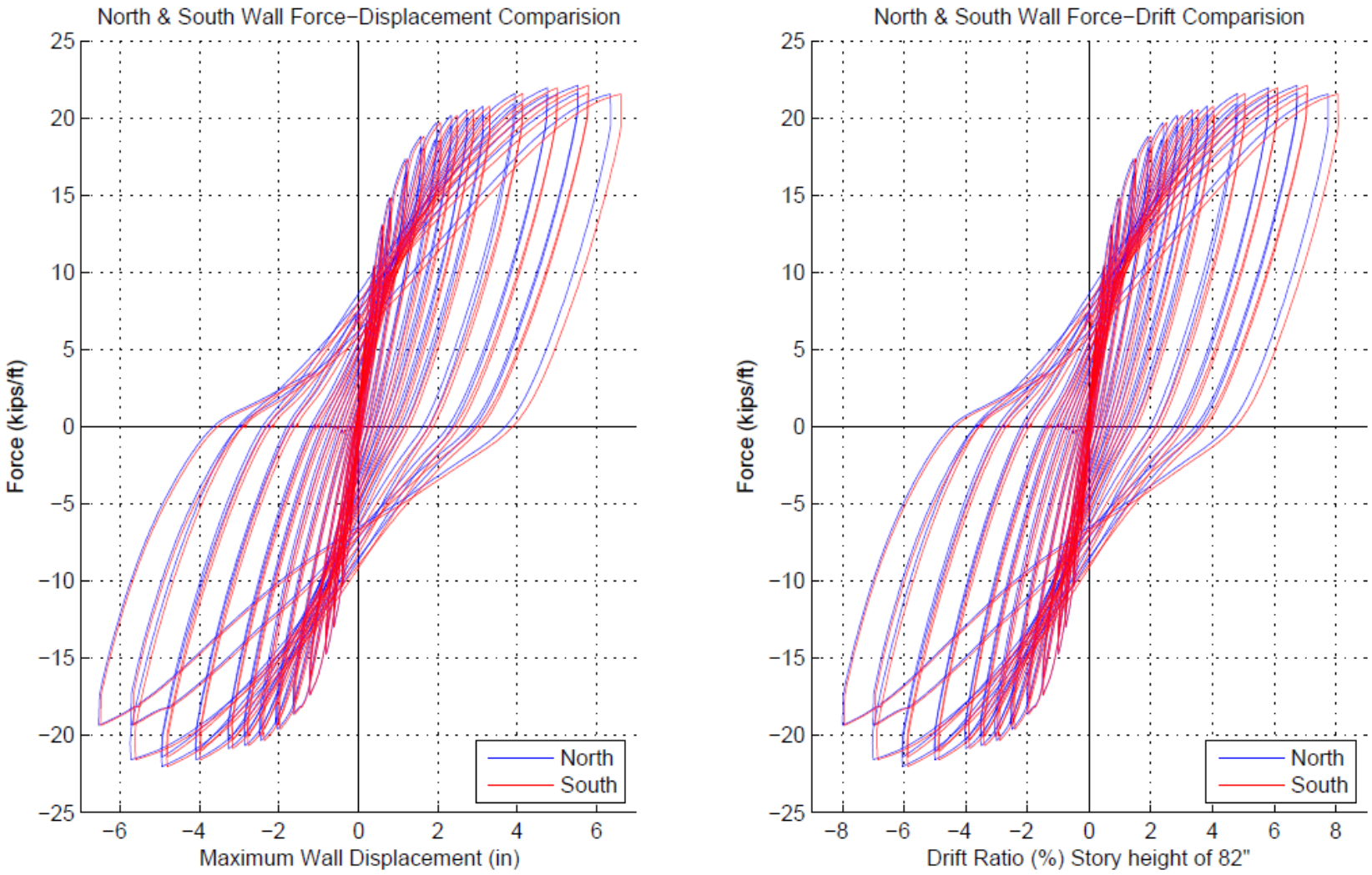

Figure E-10: Comparison of lateral displacement and drift ratio measured from top of South wall and North wall per unit width (1 ft)

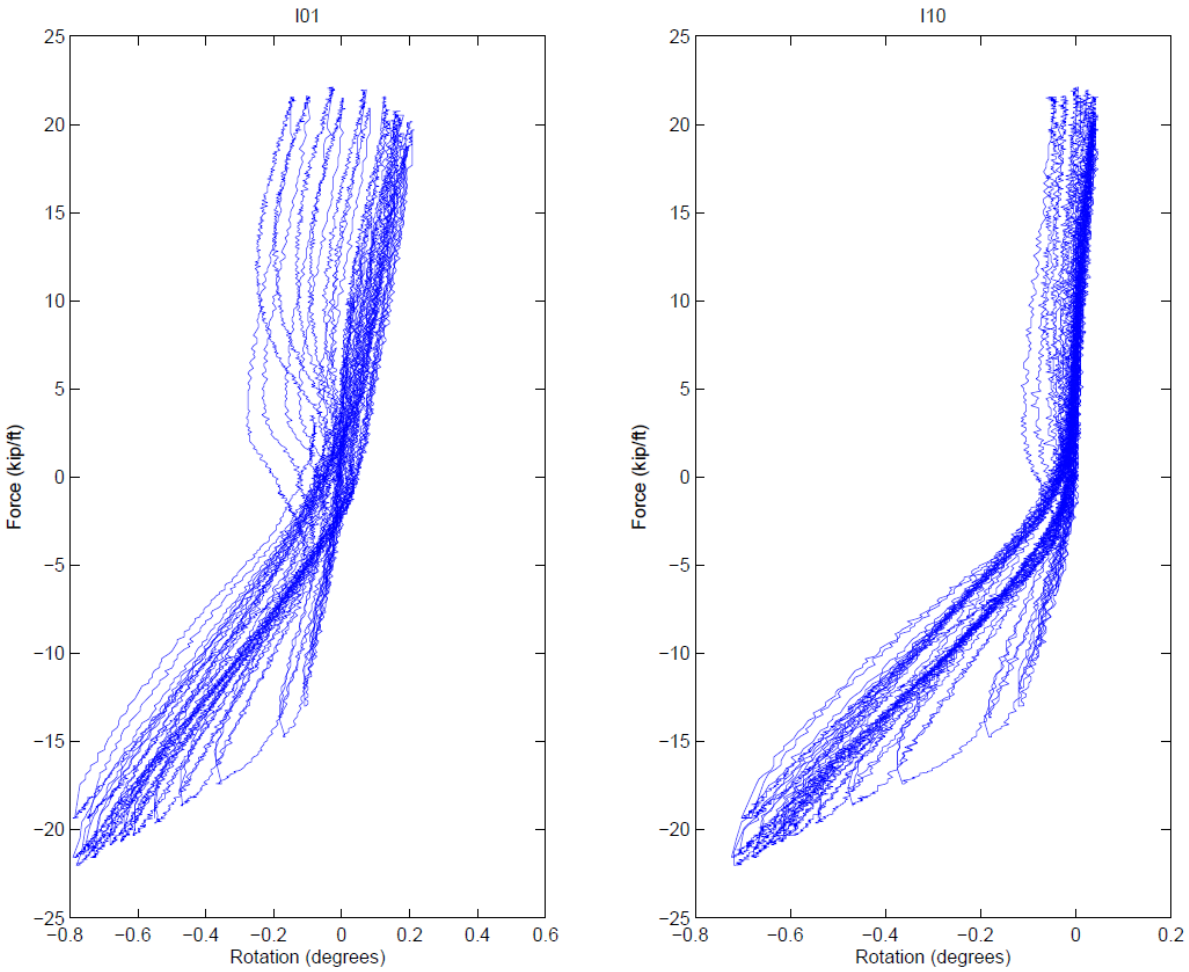

Figure E-11: Rotation (degrees) measured at the joint of slab and South wall

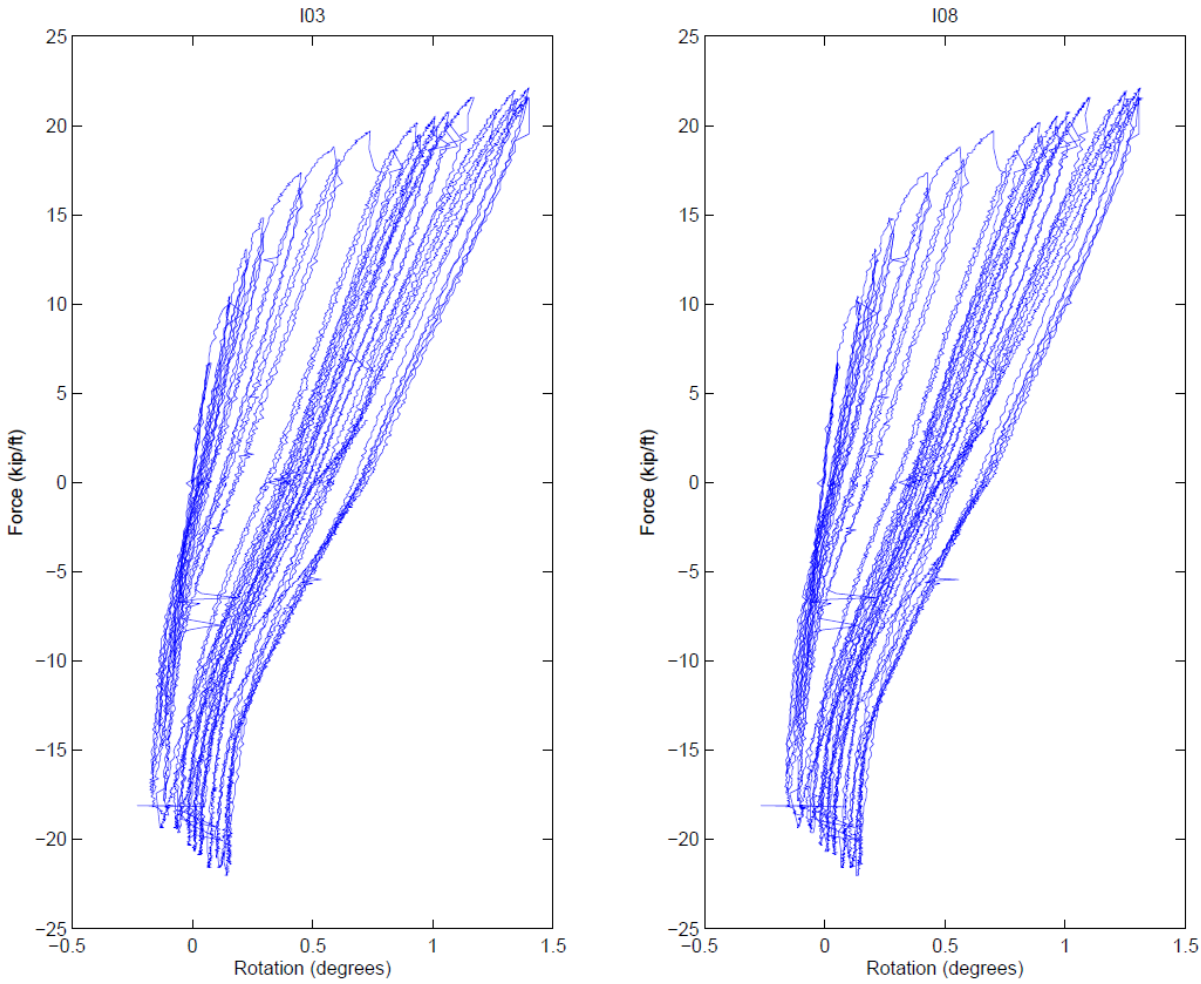

Figure E-12: Rotation (degrees) measured at the joint of roof and South wall

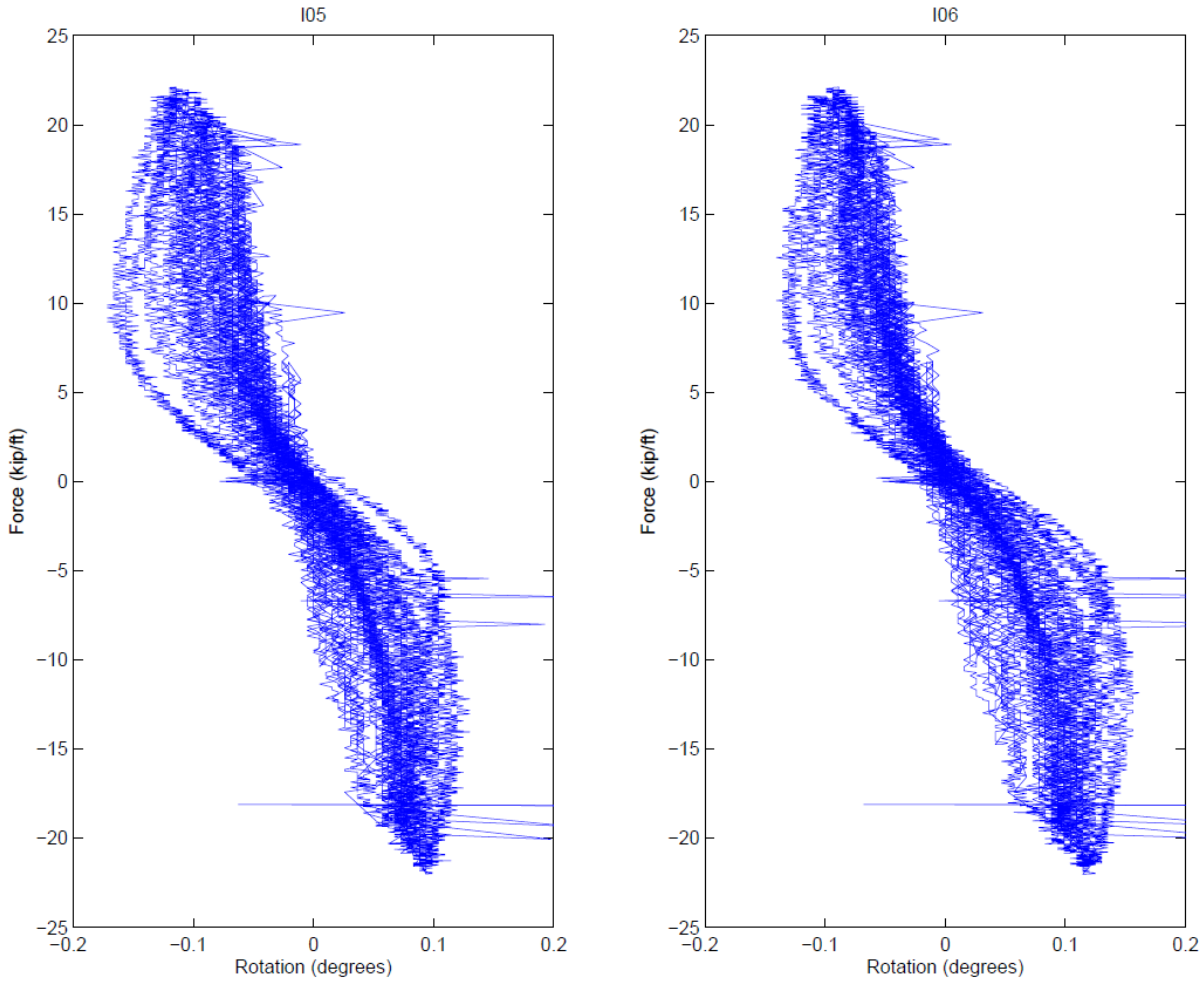

Figure E-13: Rotation (degrees) measured at middle of the roof

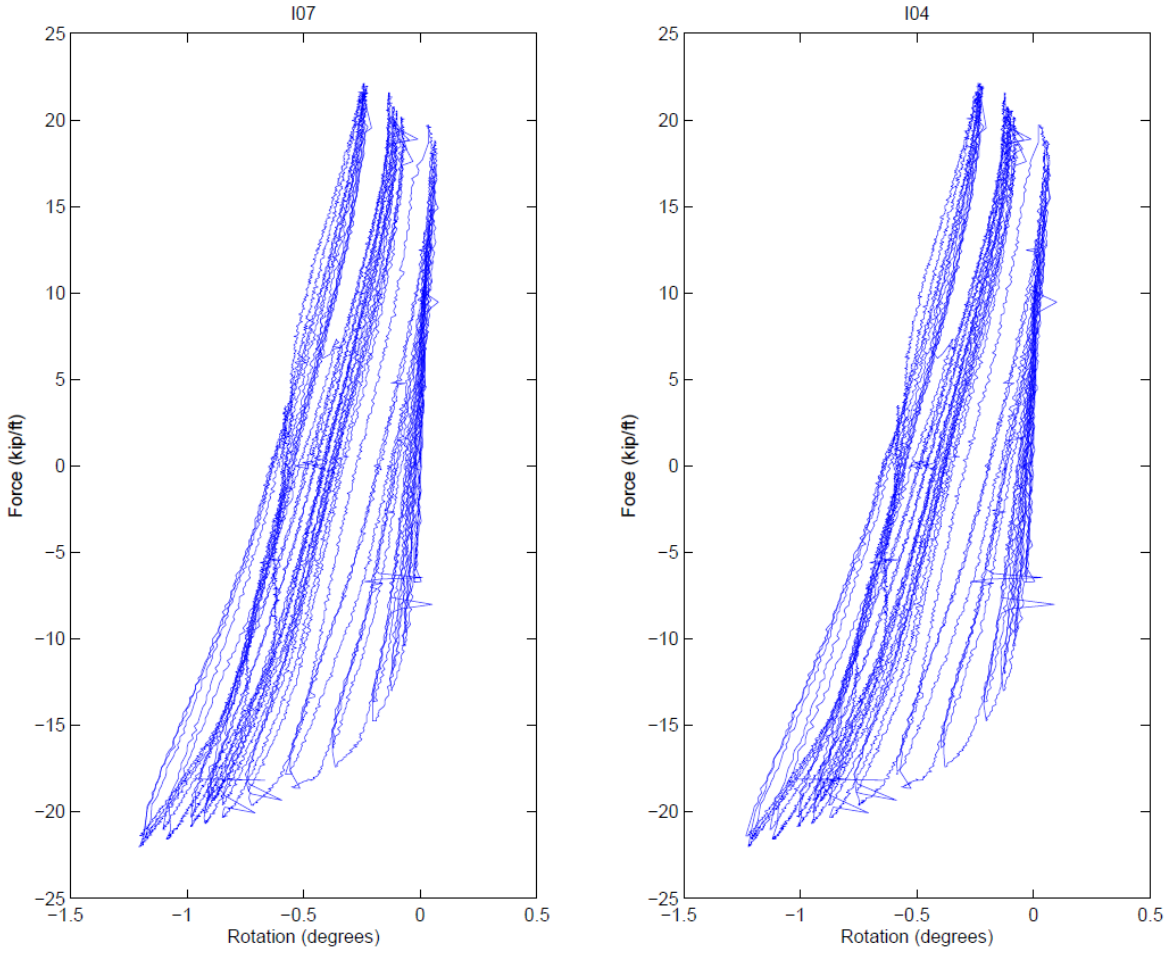

Figure E-14: Rotation (degrees) measured at the joint of roof and North wall

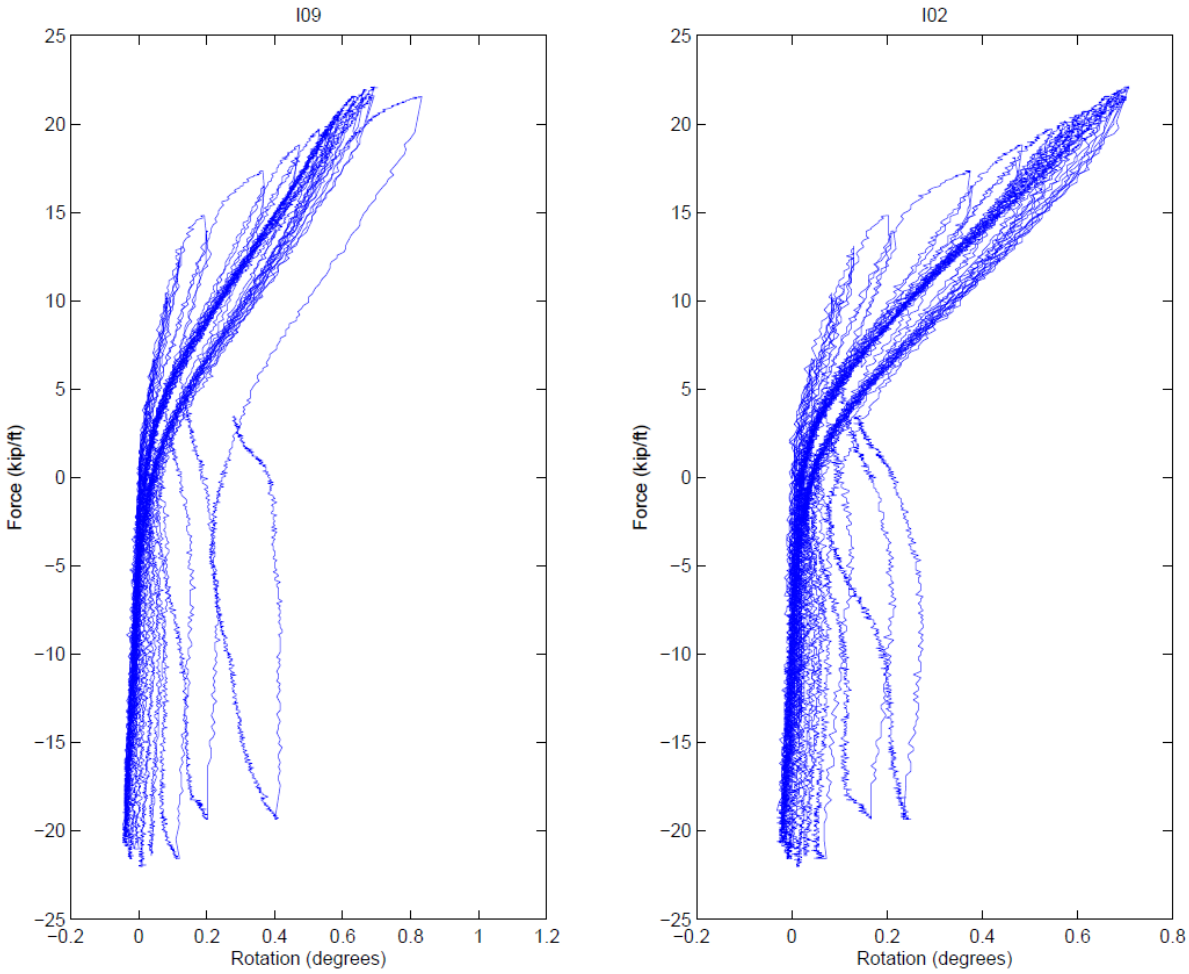

Figure E-15: Rotation (degrees) measured at the joint of slab and North wall

APPENDIX F: Construction Details

The construction sequence for the 1/9 scale laminar soil container test phase presented in Chapter 4 is presented.

Figure F-1: Photographs of the laminar soil container

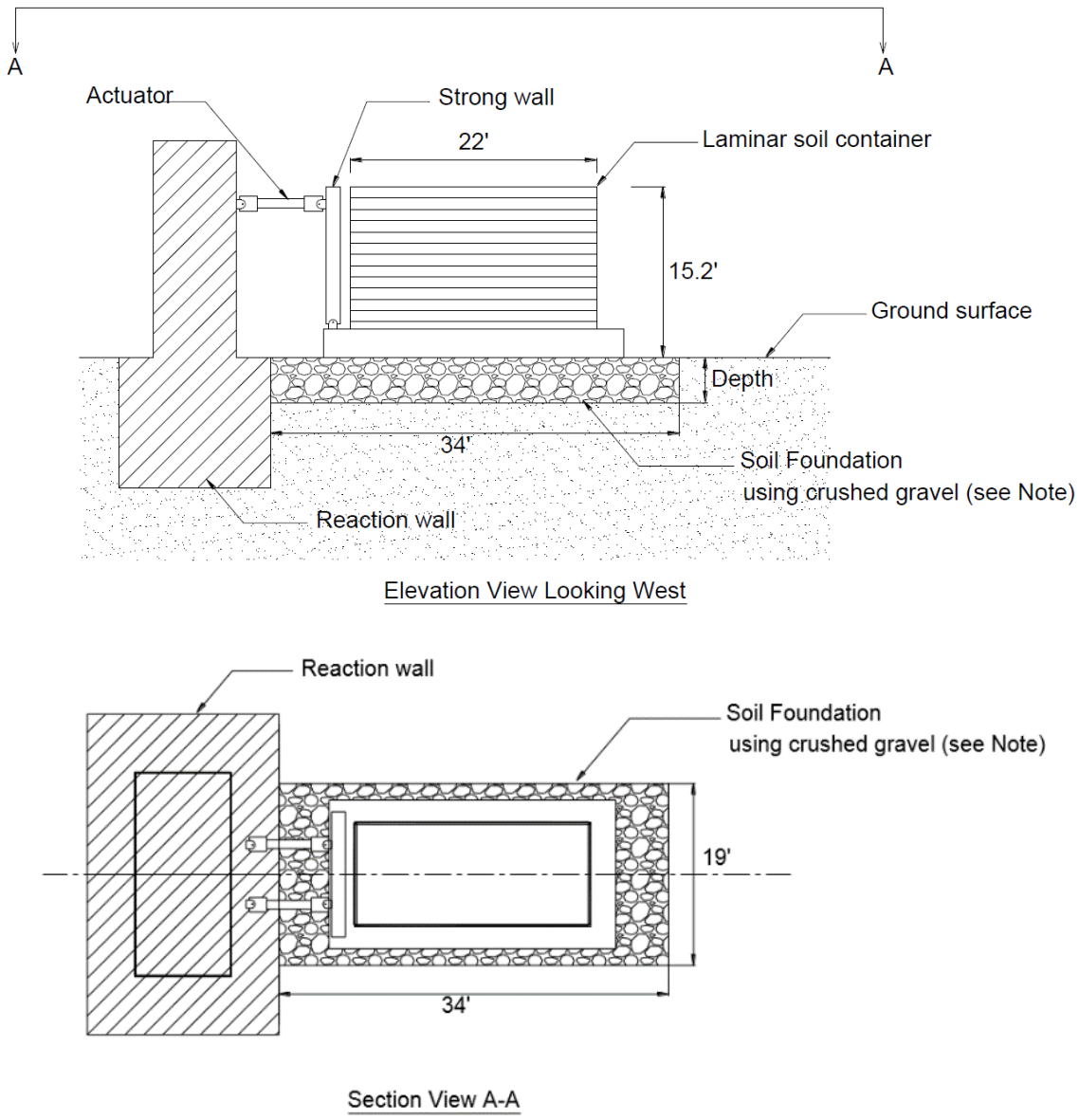

Figure F-2: Schematic elevation view of the foundation

Figure F-3: Photographs of the construction for the foundation

Figure F-4: Photographs of the transportation of the laminar soil box

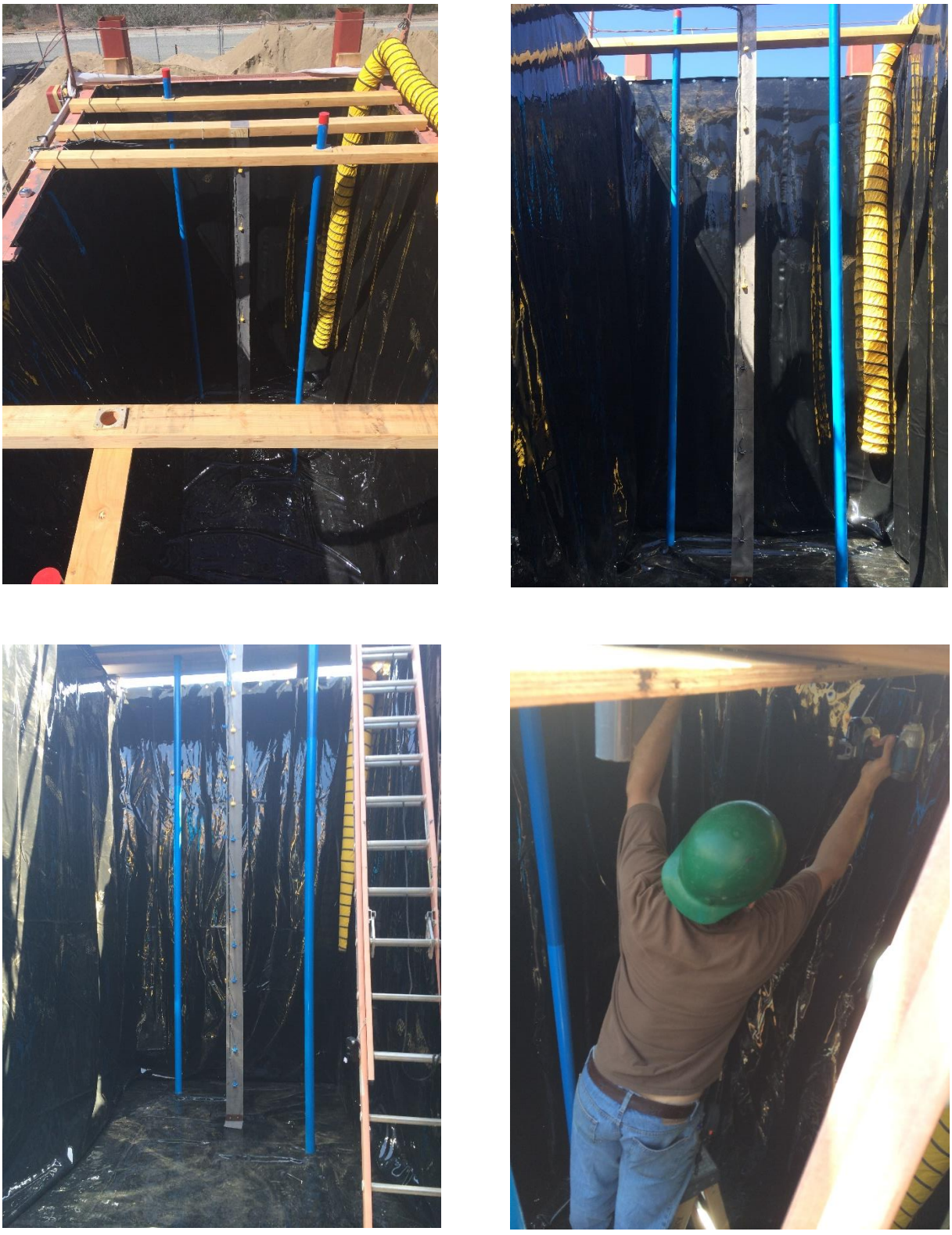

Figure F-5: Photographs of the installation of the liner

Figure F-6: Photographs of the installation and assembly of laminar container

Figure F-7: Photographs of the soil compaction

Figure F-7: Photographs of the tunnel replacement

APPENDIX G: Details of Instrumentation for Laminar Container Tunnel-Ground Test

Instrumentation layouts for the laminar container test phase presented in Chapter 4 are presented.

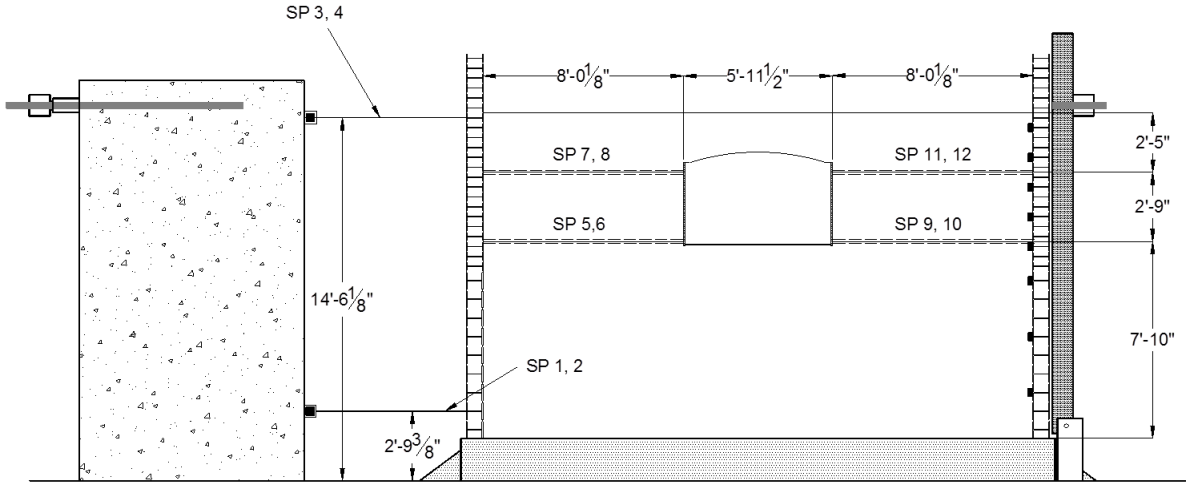

Figure G-1: Elevation view of the string potentiometer layout

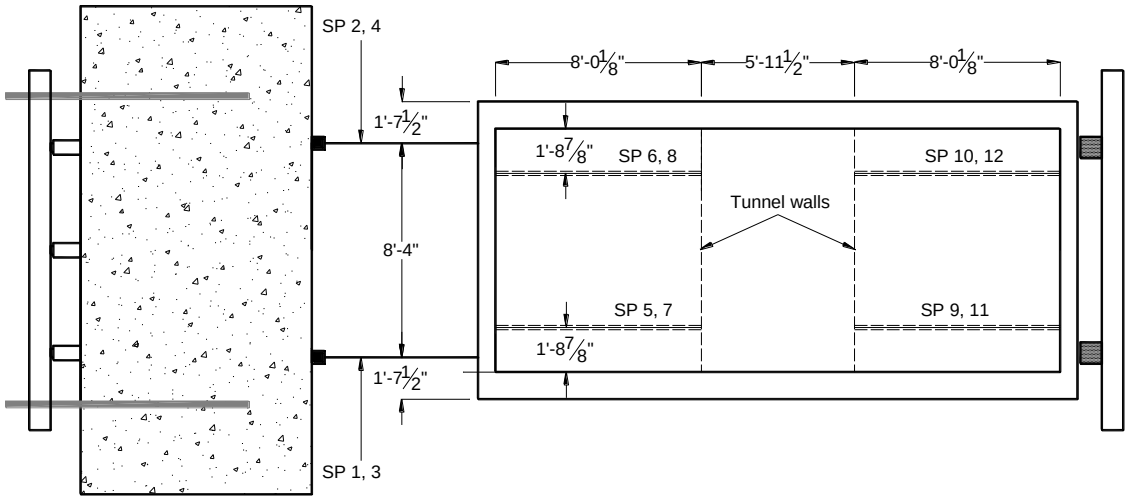

Figure G-2: Plan view of the string potentiometer layout

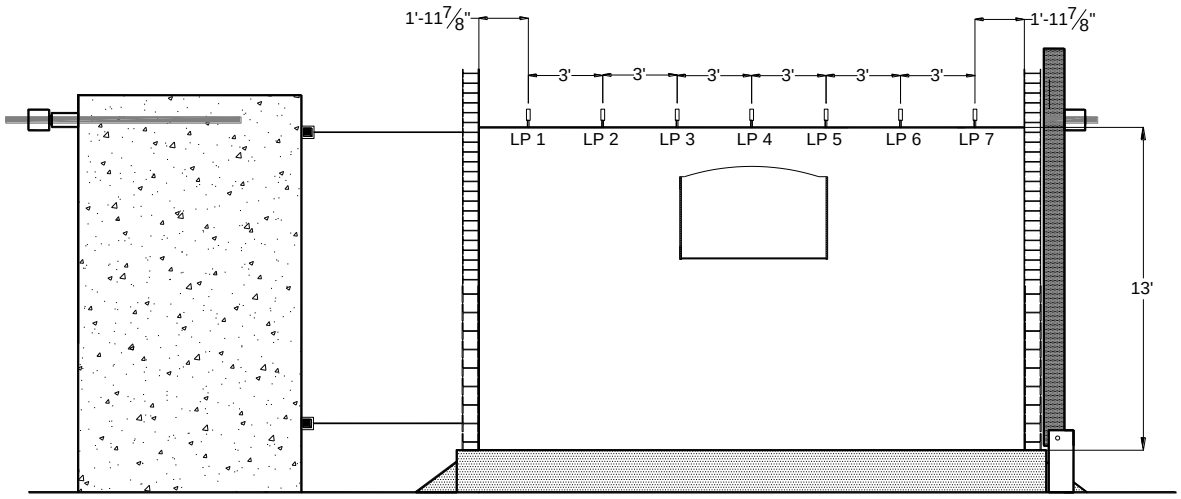

Figure G-3: Elevation view of the linear variable displacement transducer layout

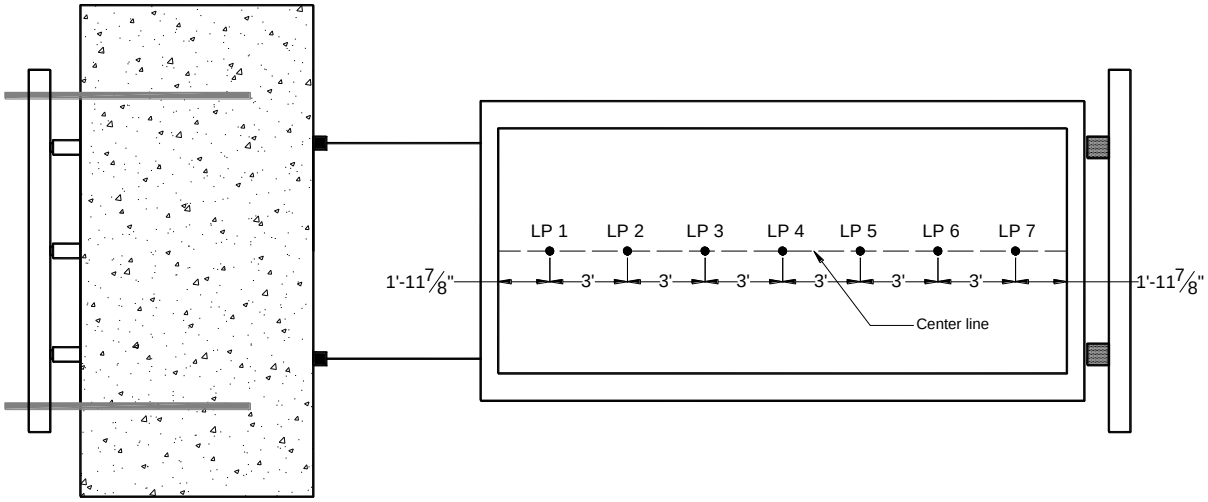

Figure G-4: Plan view of the linear variable displacement transducer layout

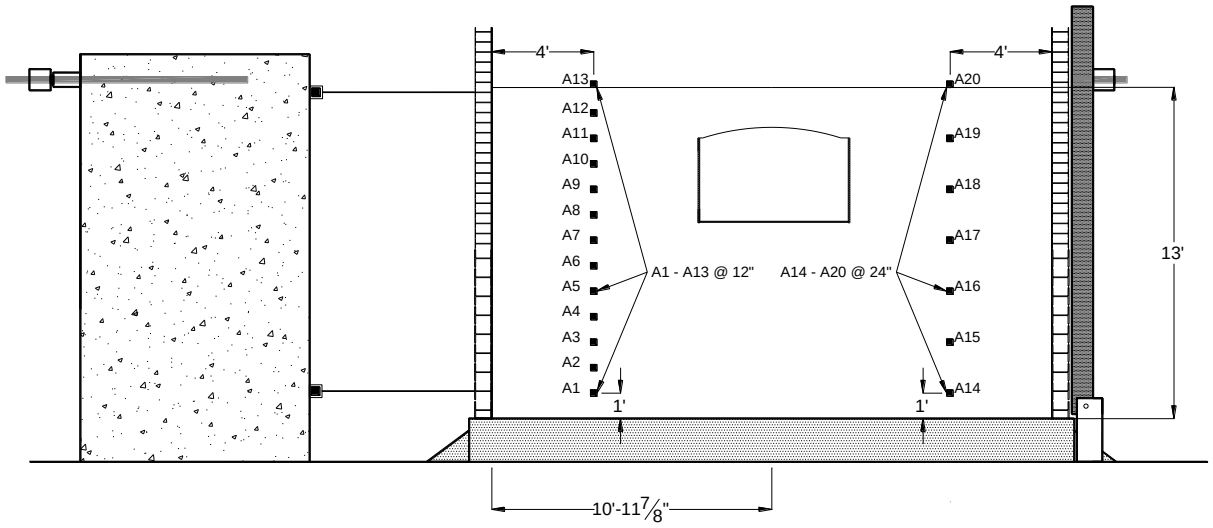

Figure G-5: Elevation view of the accelerometer layout

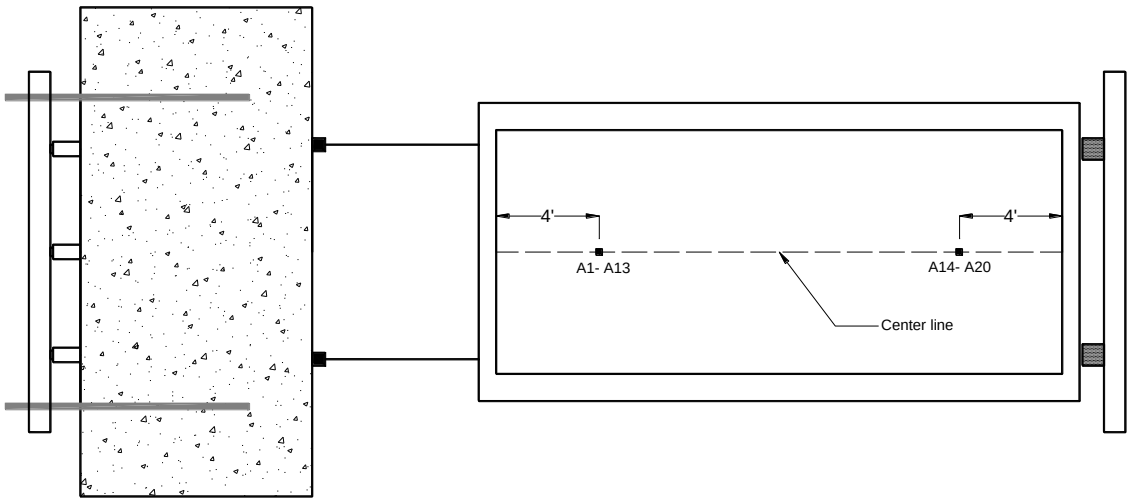

Figure G-6: Plan view of the linear variable displacement transducer layout

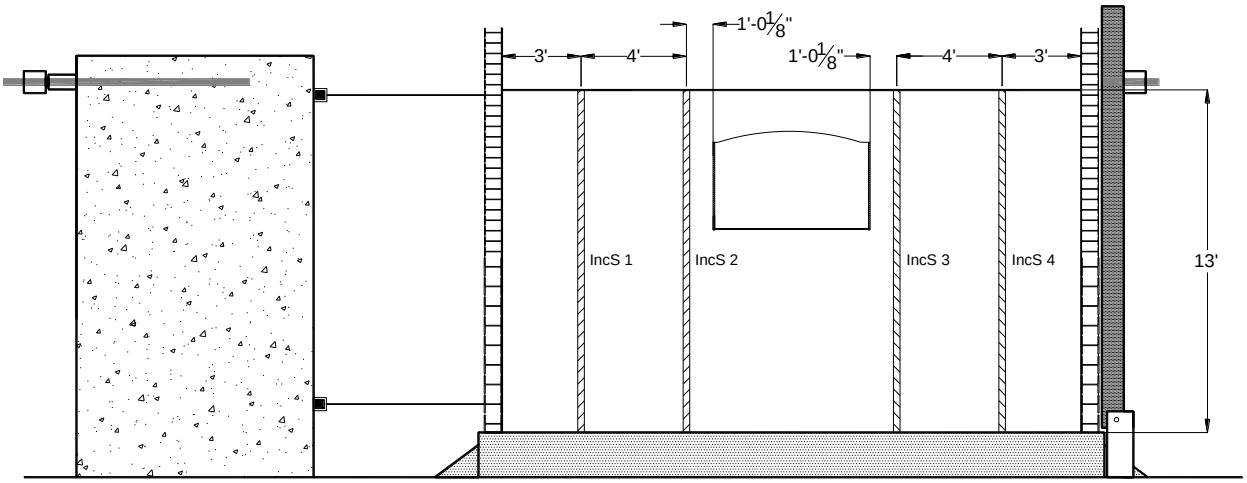

Figure G-7: Elevation view of the inclinometers layout

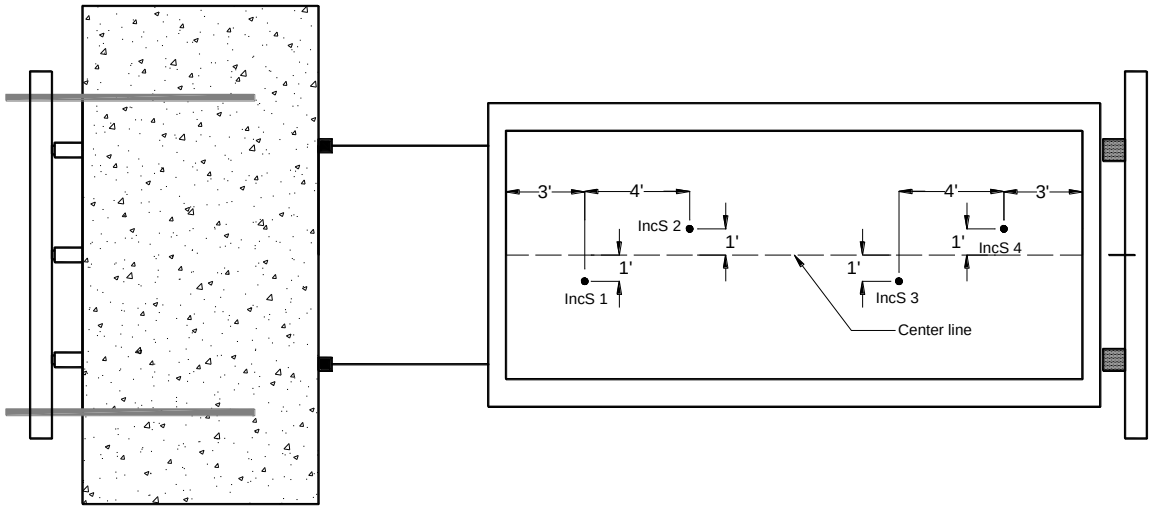

Figure G-8: Plan view of the inclinometers layout

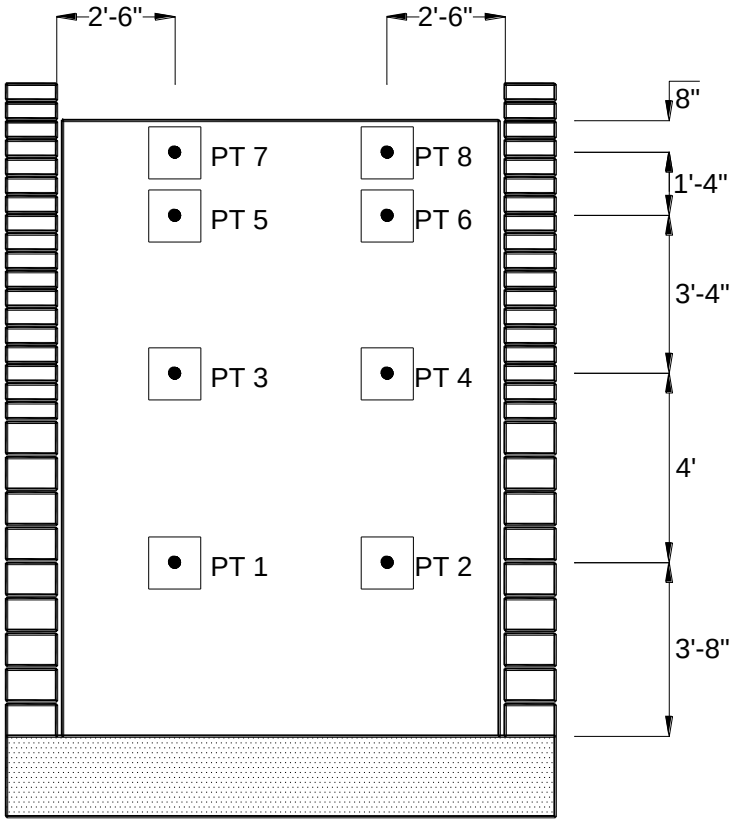

Figure G-9: Elevation view of the AfB pressure transducer layout

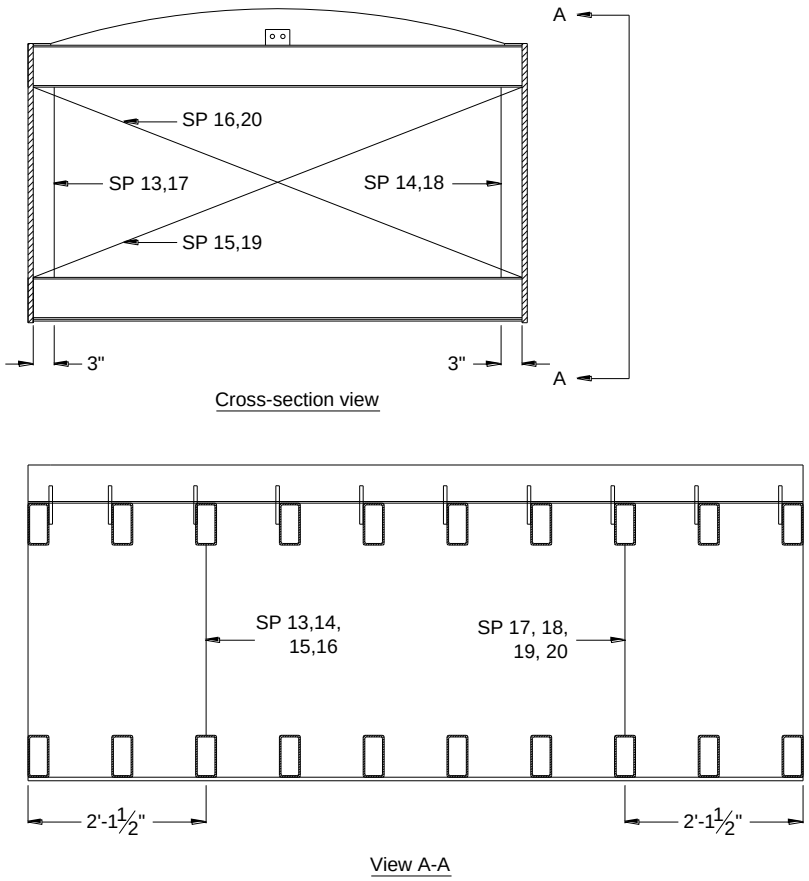

Figure G-10: Layout of string potentiometers inside the tunnel

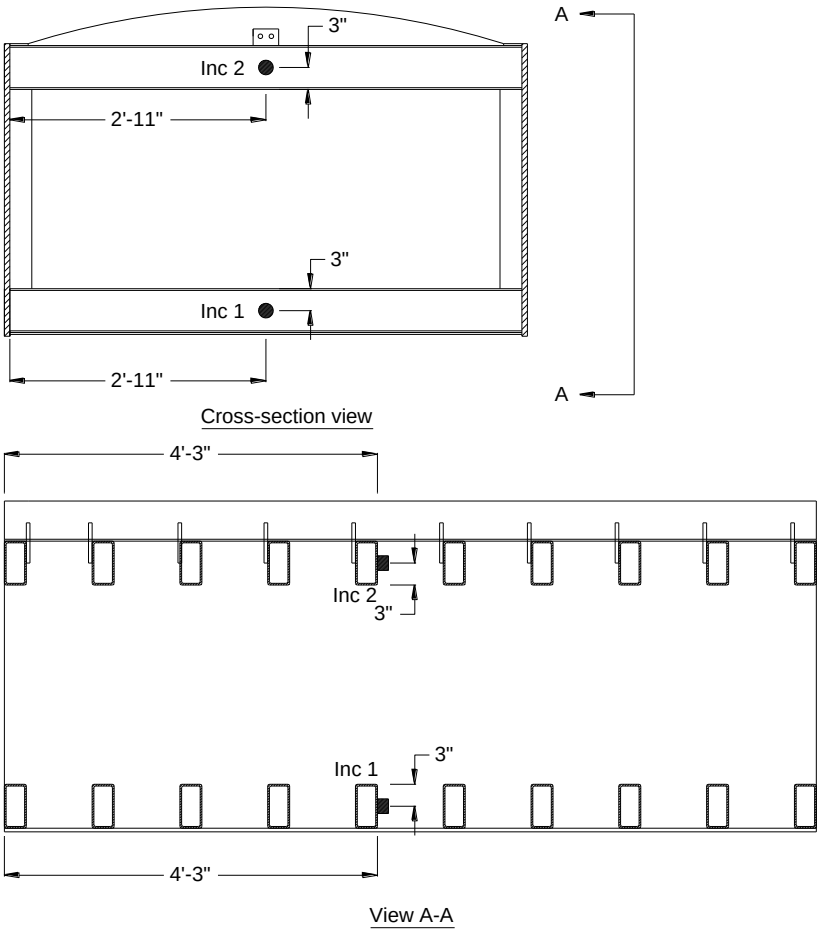

Figure G-11: Layout of inclinometer inside the tunnel

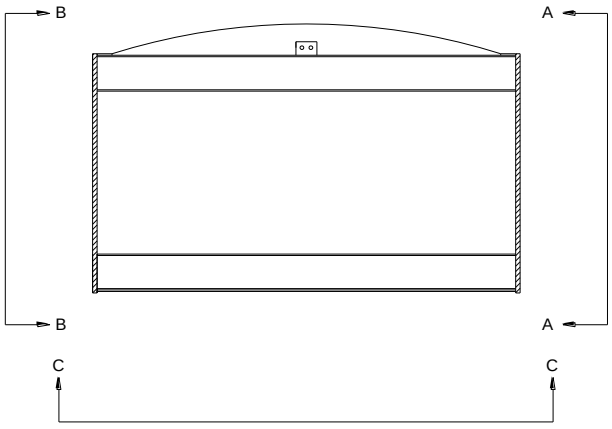

Figure G-12: Layout of strain gauges

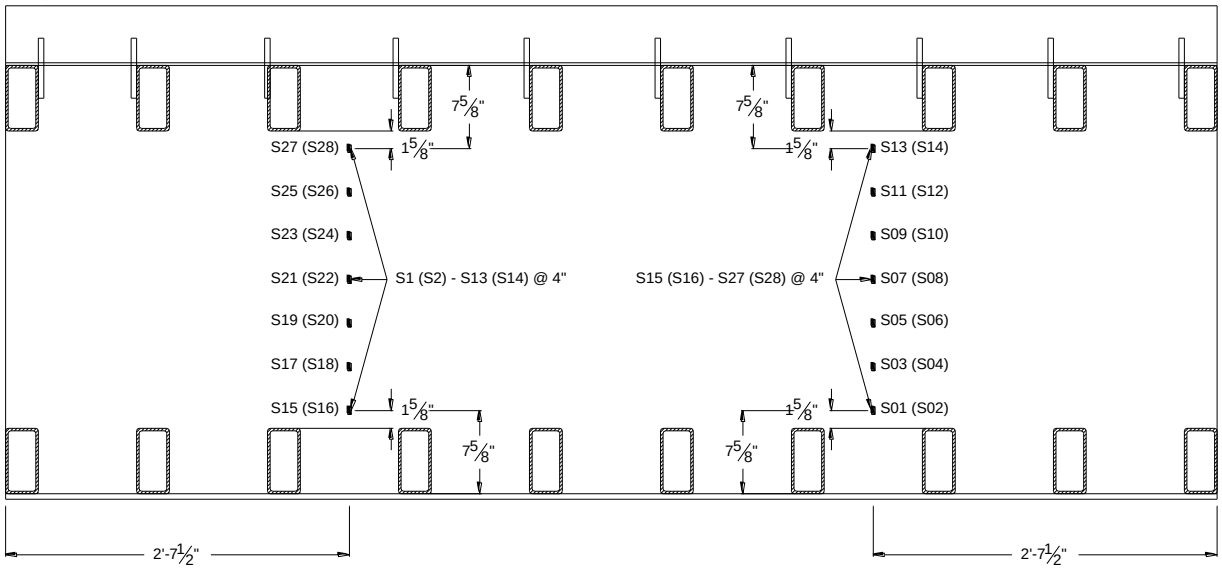

View A-A (North)

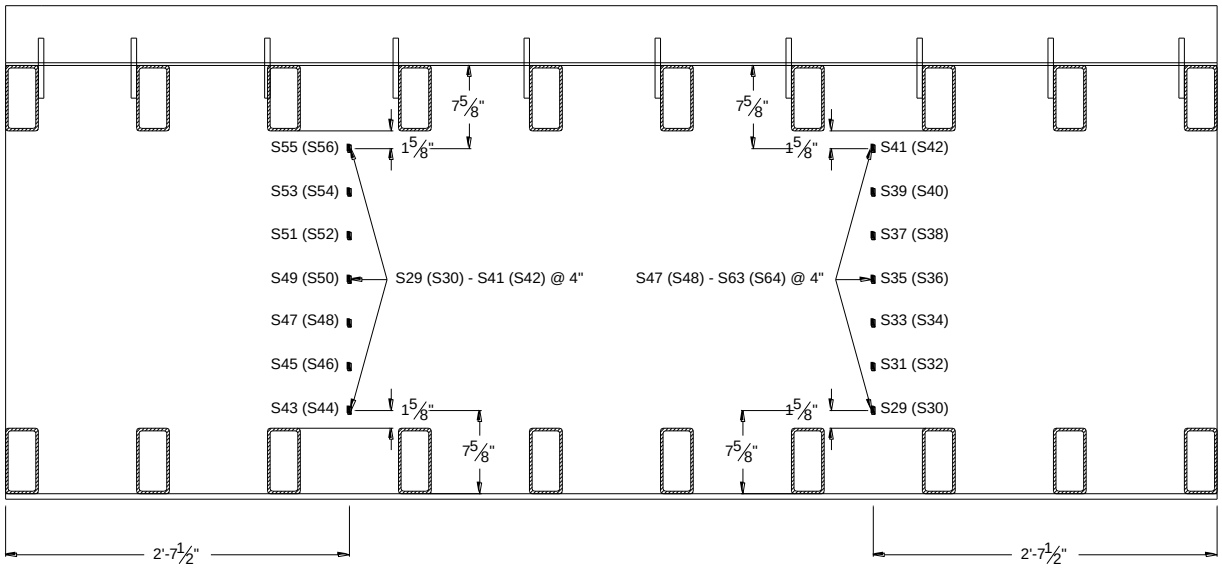

View B-B (South)

Figure G-12 (continued): Layout of strain gauges

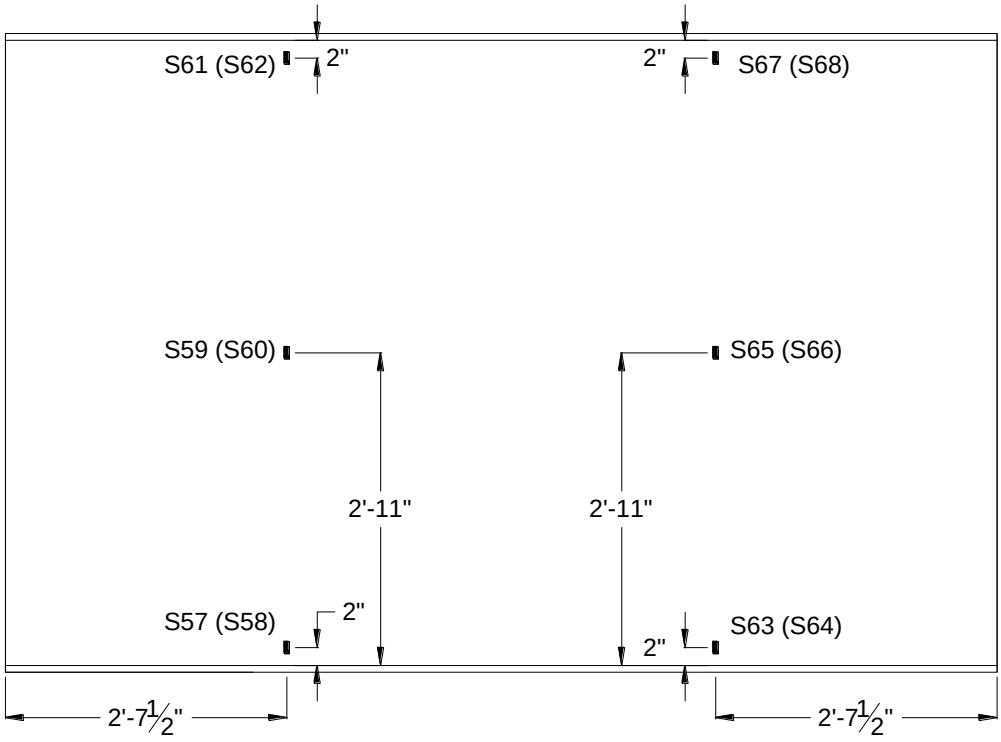

View C-C

Figure G-12 (continued): Layout of strain gauges

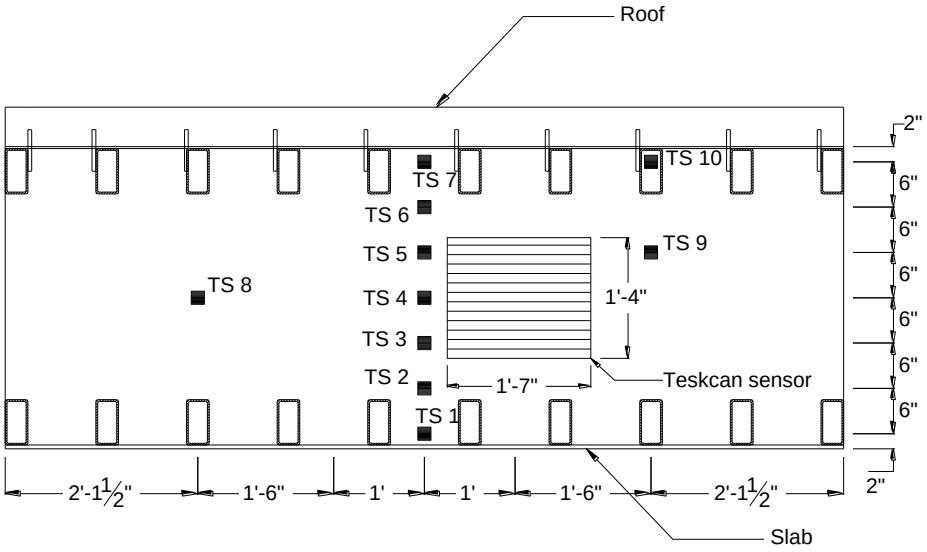

Wall (North)

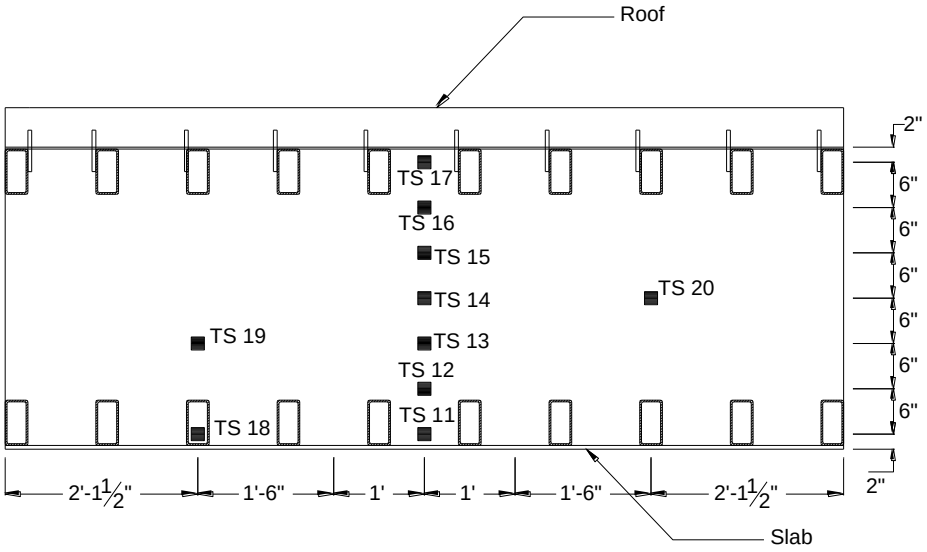

Wall (South)

Figure G-13: Layout of Tactilus sensors

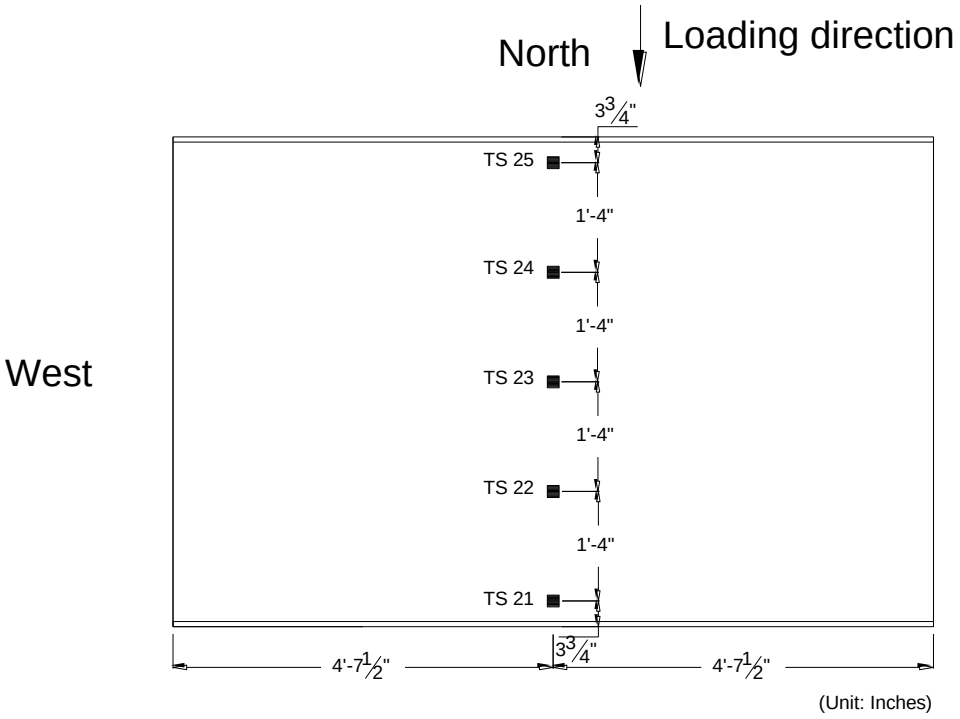

Slab

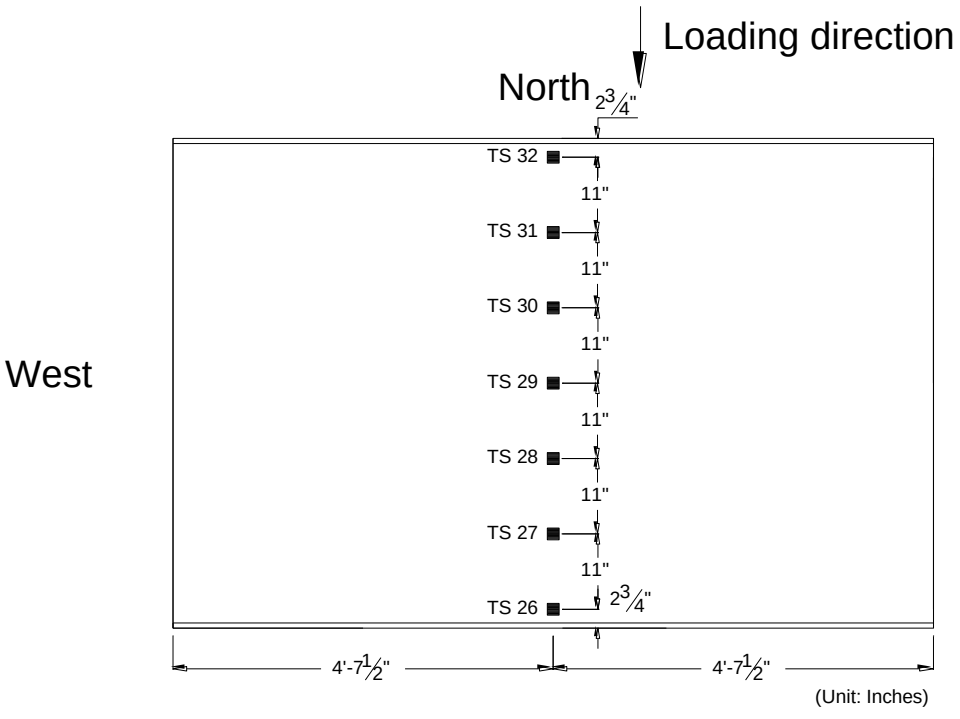

Roof

Figure G-13 (continued): Layout of Tactilus sensors

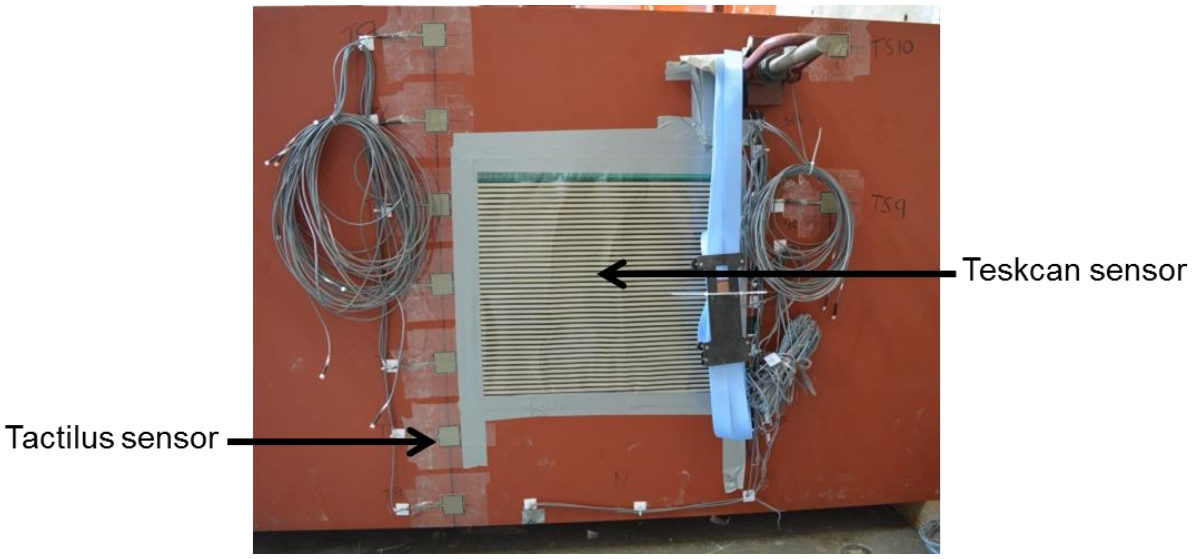

Figure G-14: Photograph of the Tekscan sensor

APPENDIX H: Additional Data from Laminar Container Tunnel-Ground Test

This appendix contains additional data for bending moment and curvature measured from strain gauges and for shear and compression wave velocities from accelerometers.

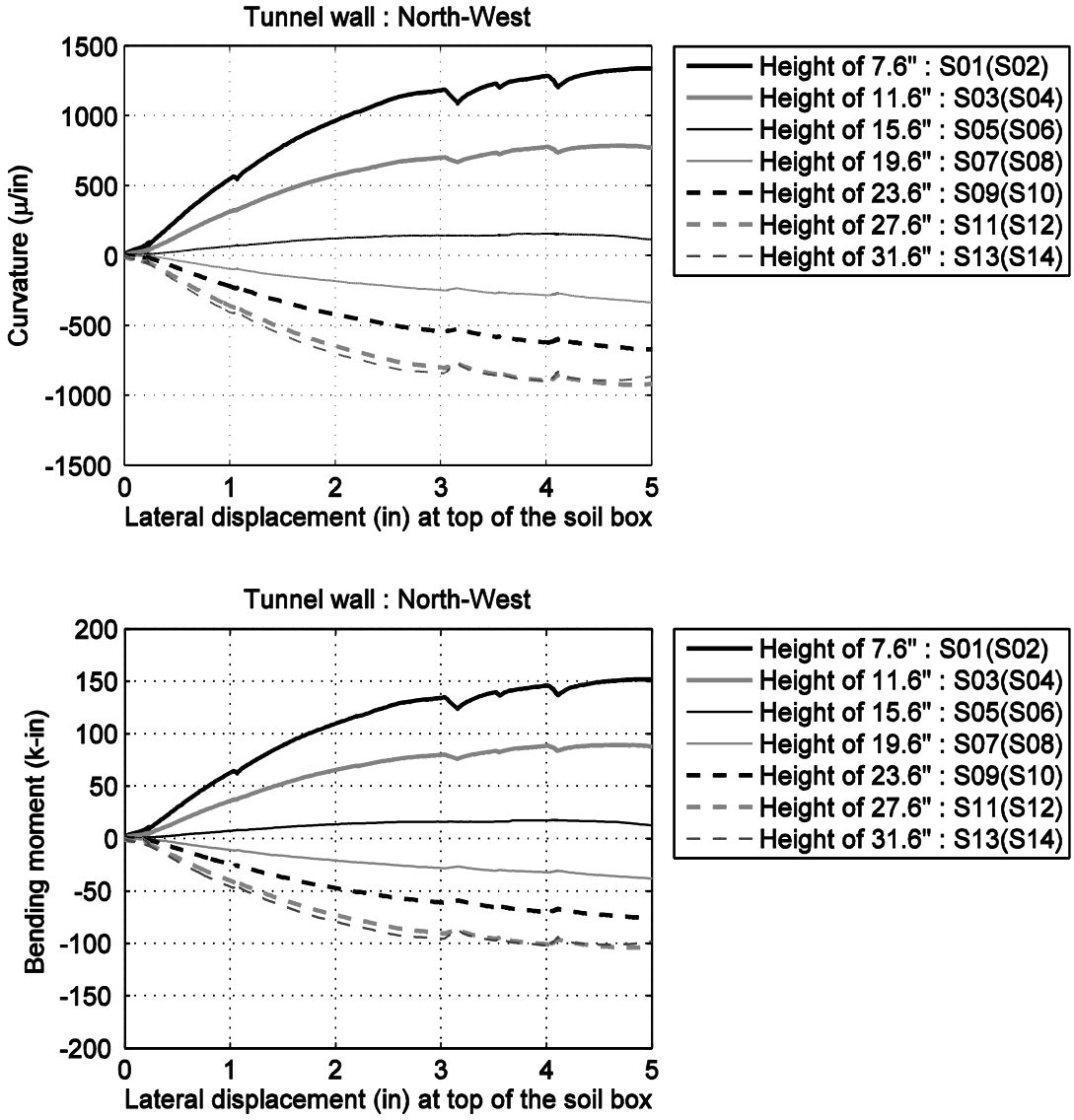

Figure H-1: Curvature and bending moment from strain gauges mounted on North-West side of tunnel wall

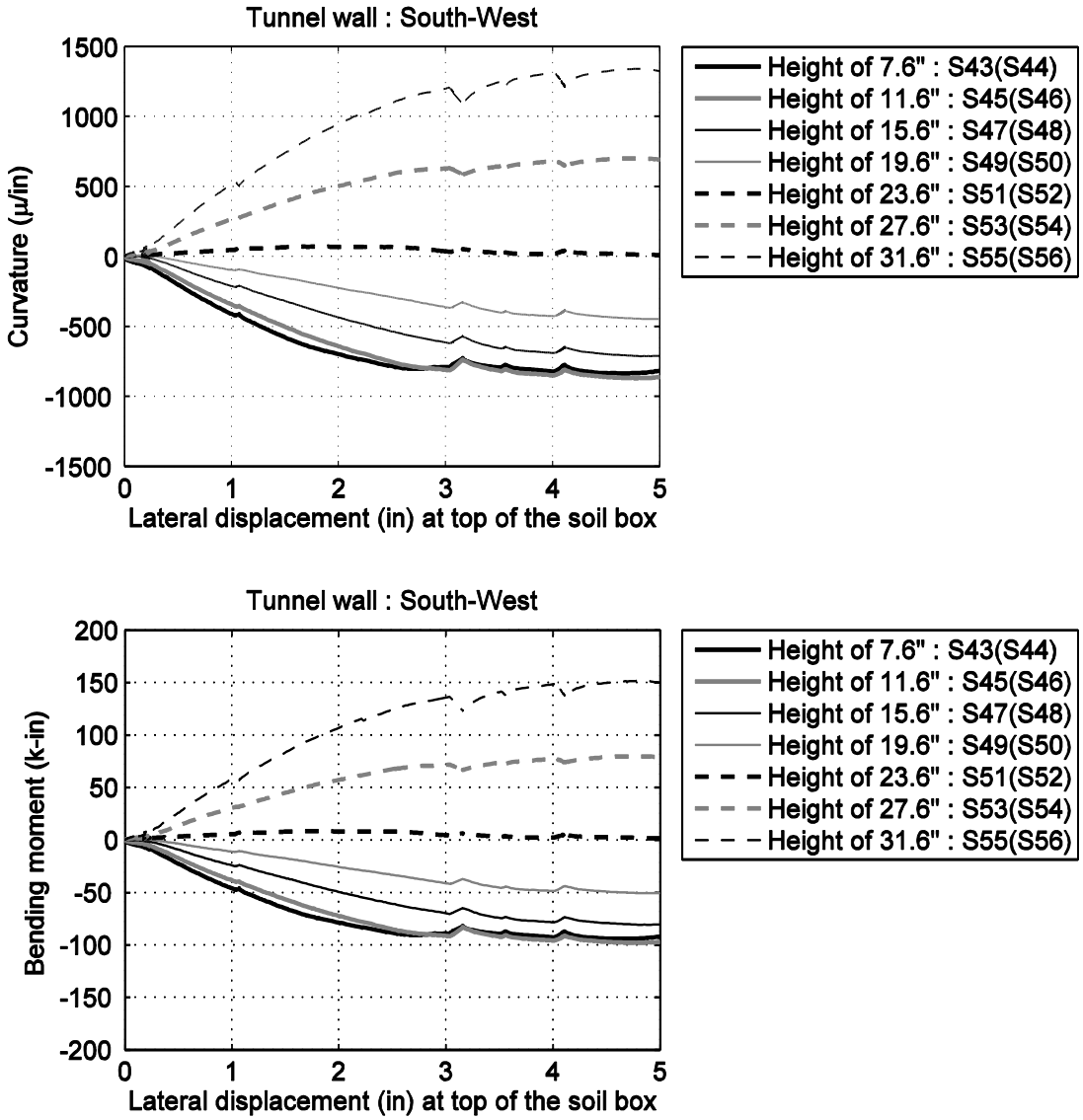

Figure H-2: Curvature and bending moment from strain gauges mounted on South-West side of tunnel wall

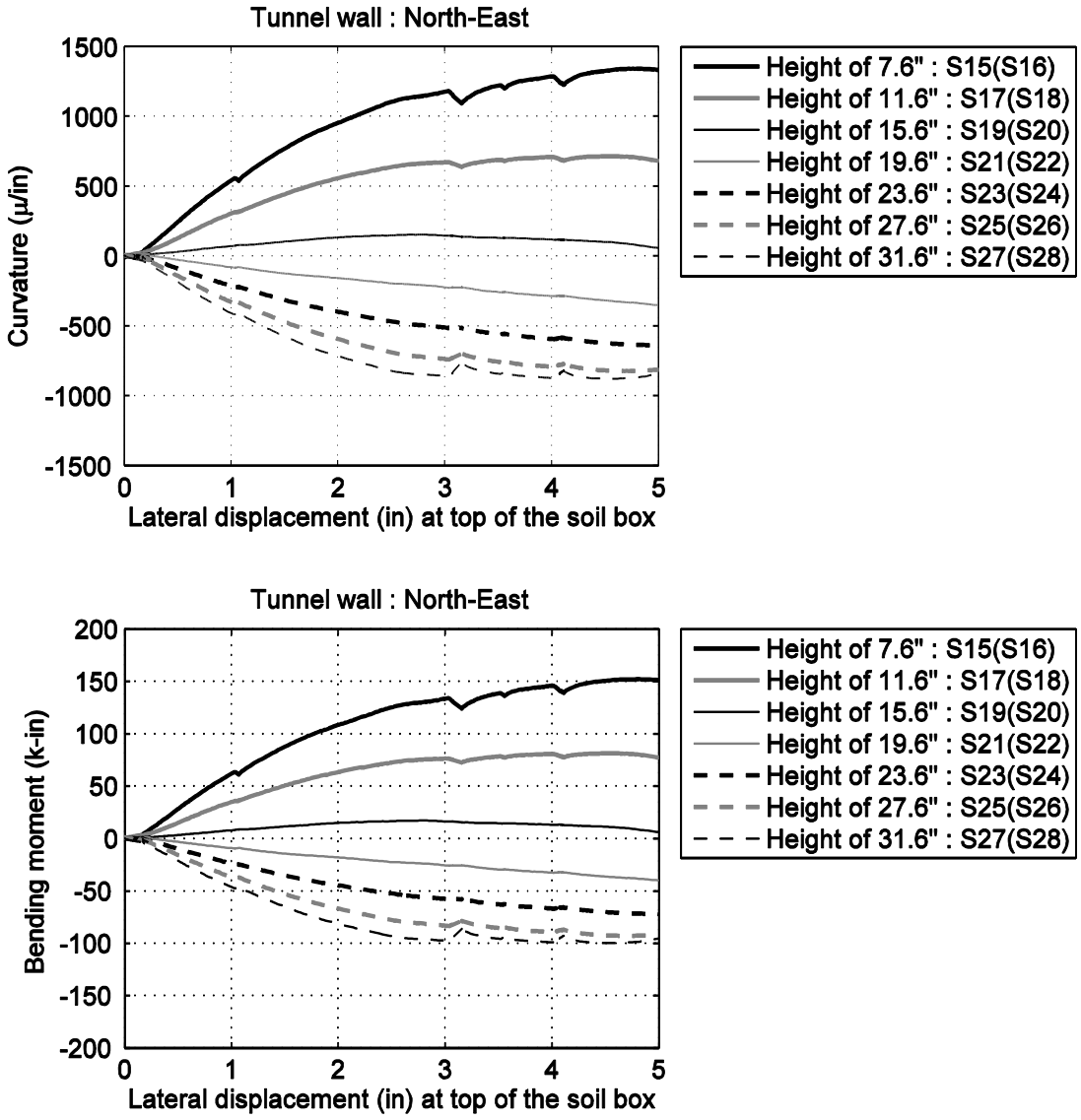

Figure H-3: Curvature and bending moment from strain gauges mounted on North-East side of tunnel wall

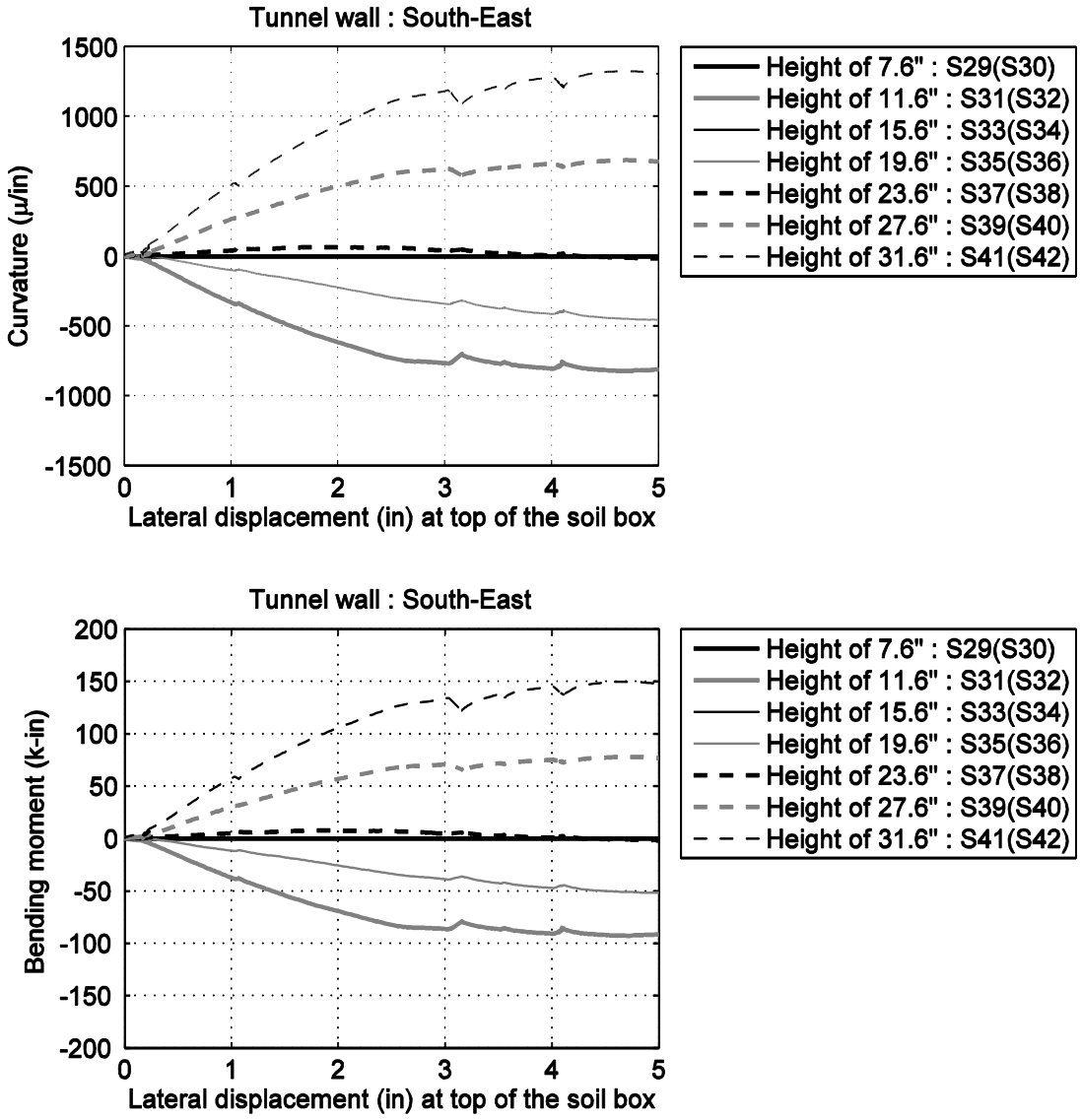

Figure H-4: Curvature and bending moment from strain gauges mounted on South-East side of tunnel wall

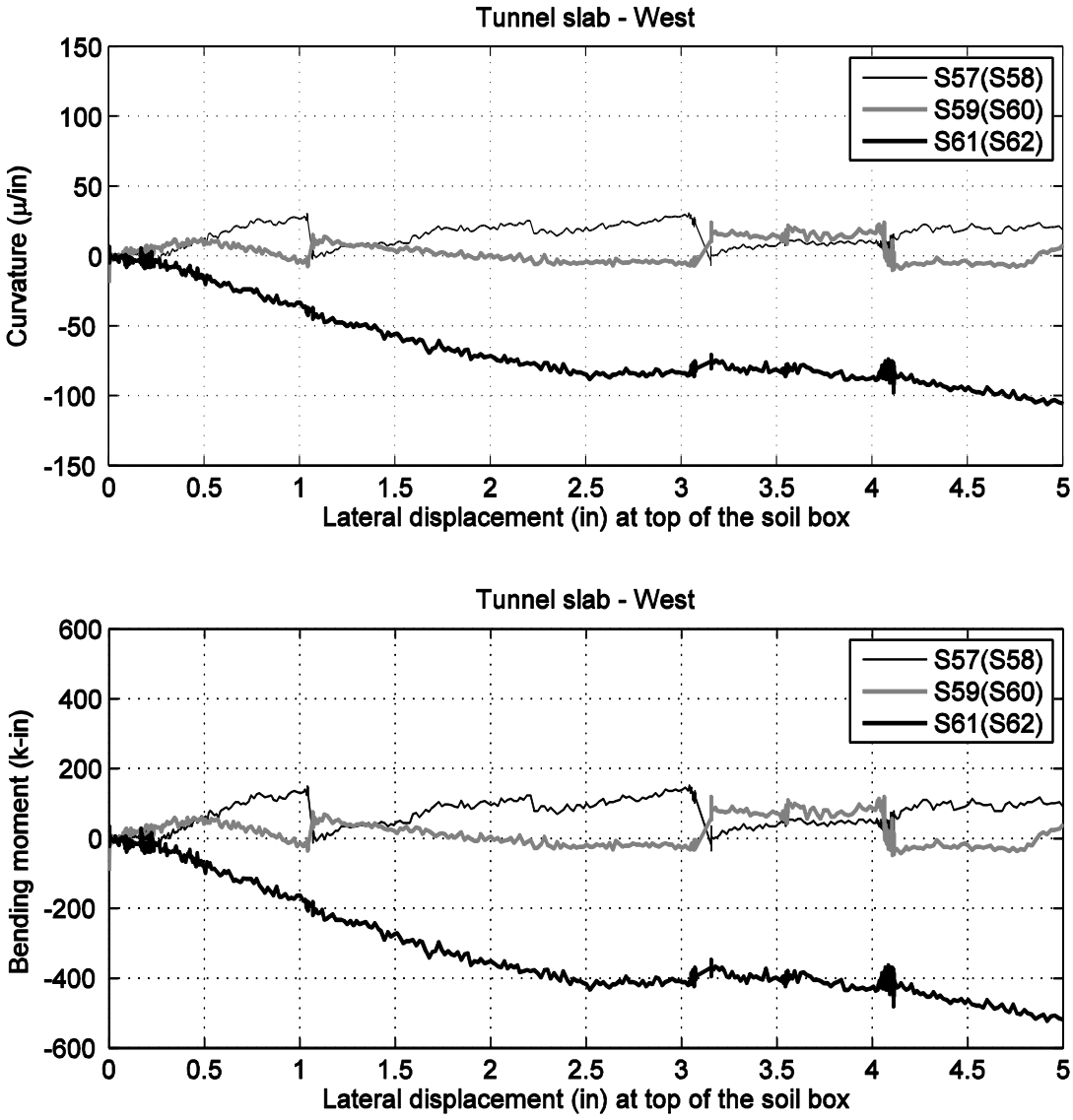

Figure H-5: Curvature and bending moment from strain gauges mounted on West side of tunnel slab

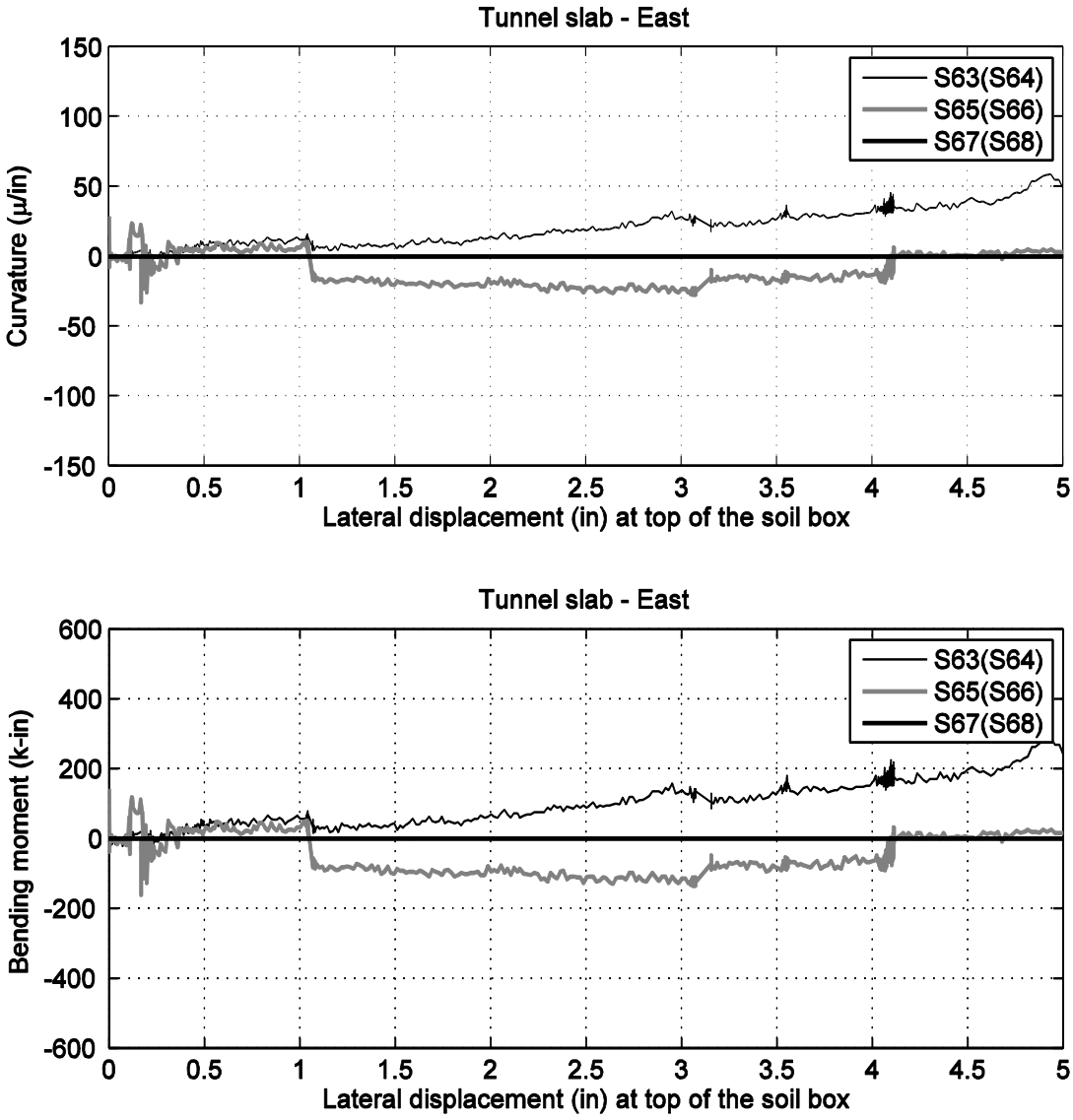

Figure H-6: Curvature and bending moment from strain gauges mounted on East side of tunnel wall

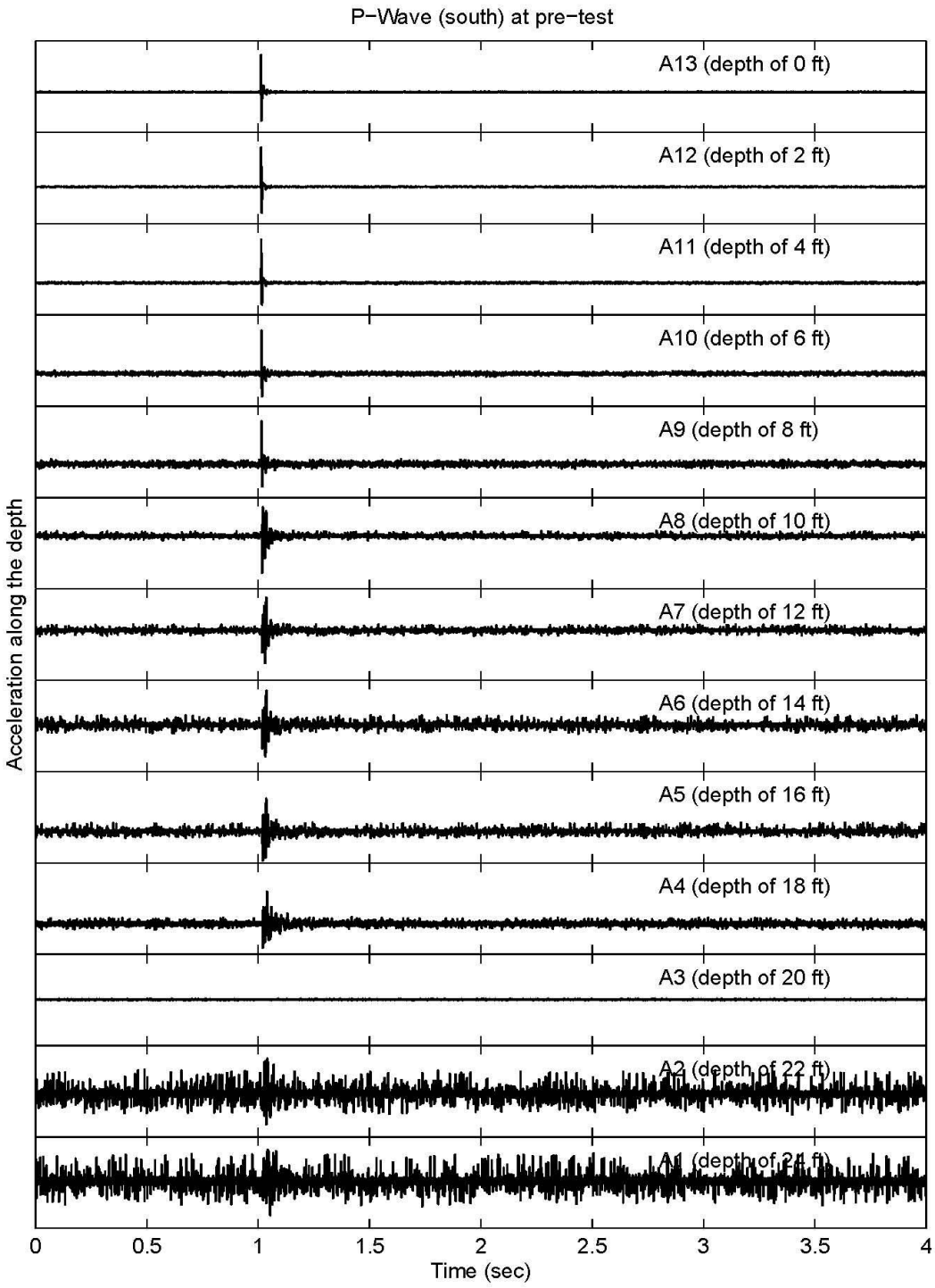

Figure H-7: Acceleration history at South side on soil surface for P-Wave velocity test

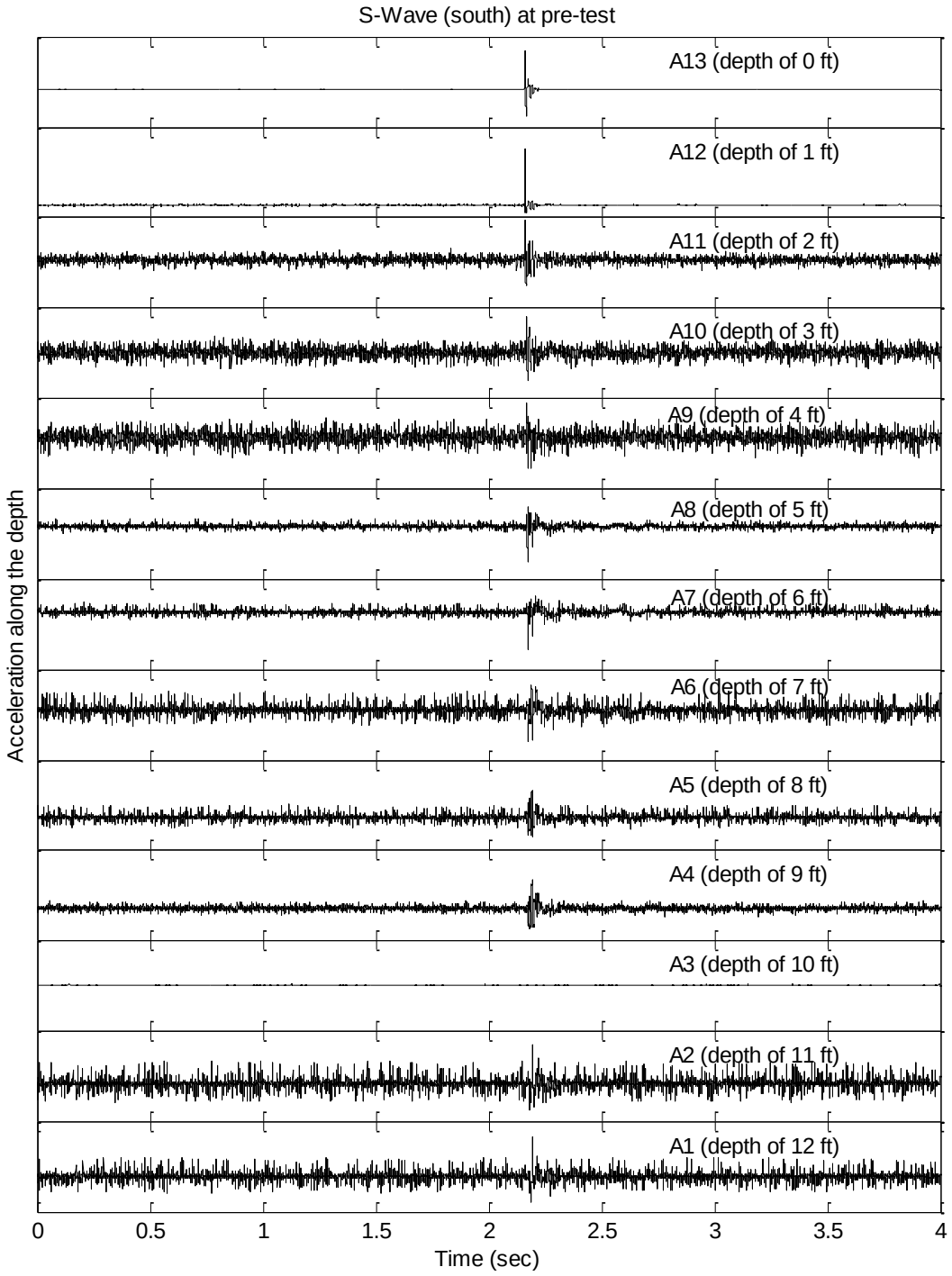

Figure H-8: Acceleration history at South side on soil surface for S-Wave velocity test before the test

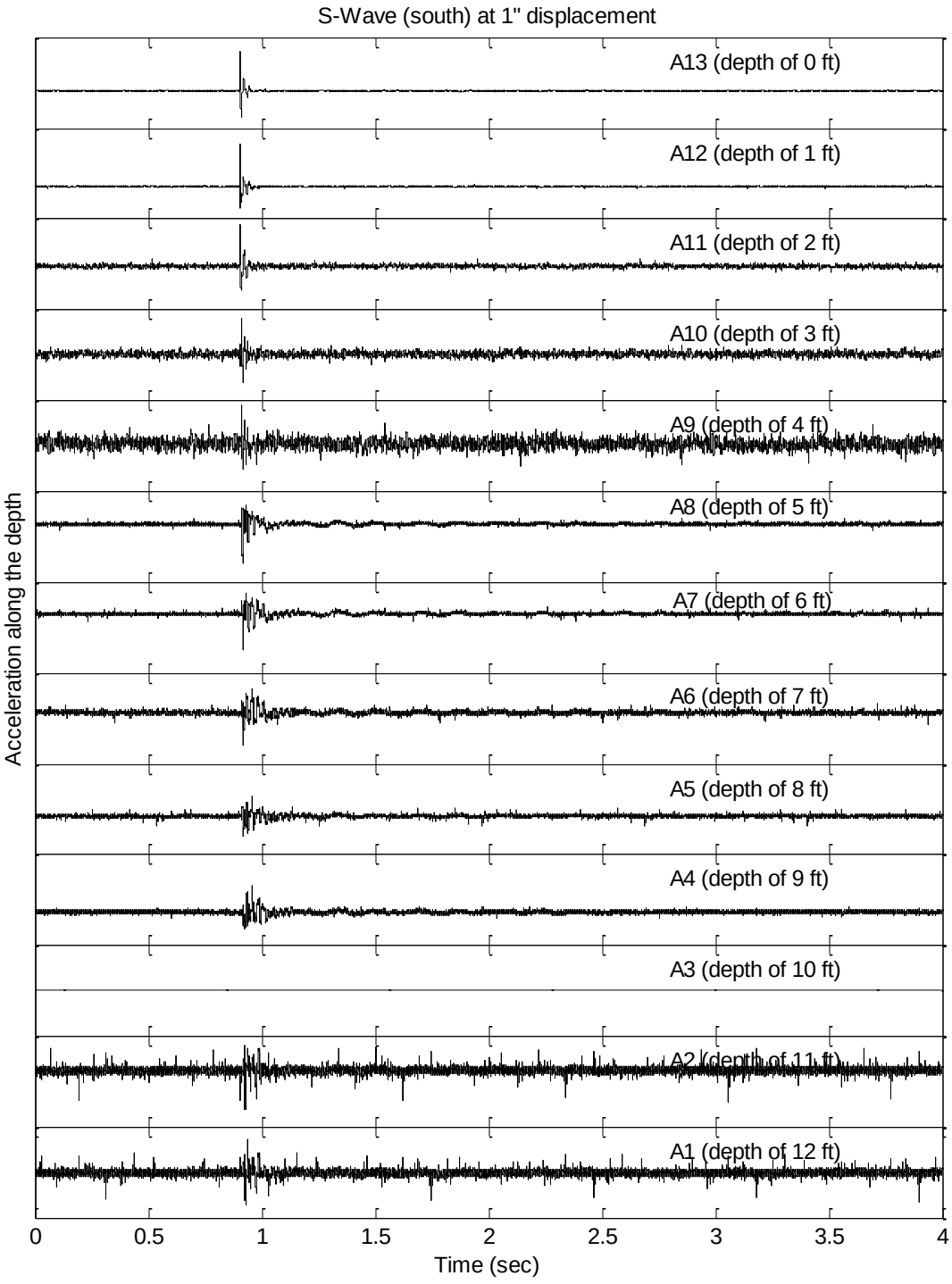

Figure H-9: Acceleration history at South side on soil surface for S-Wave velocity test at lateral displacement of 1 in

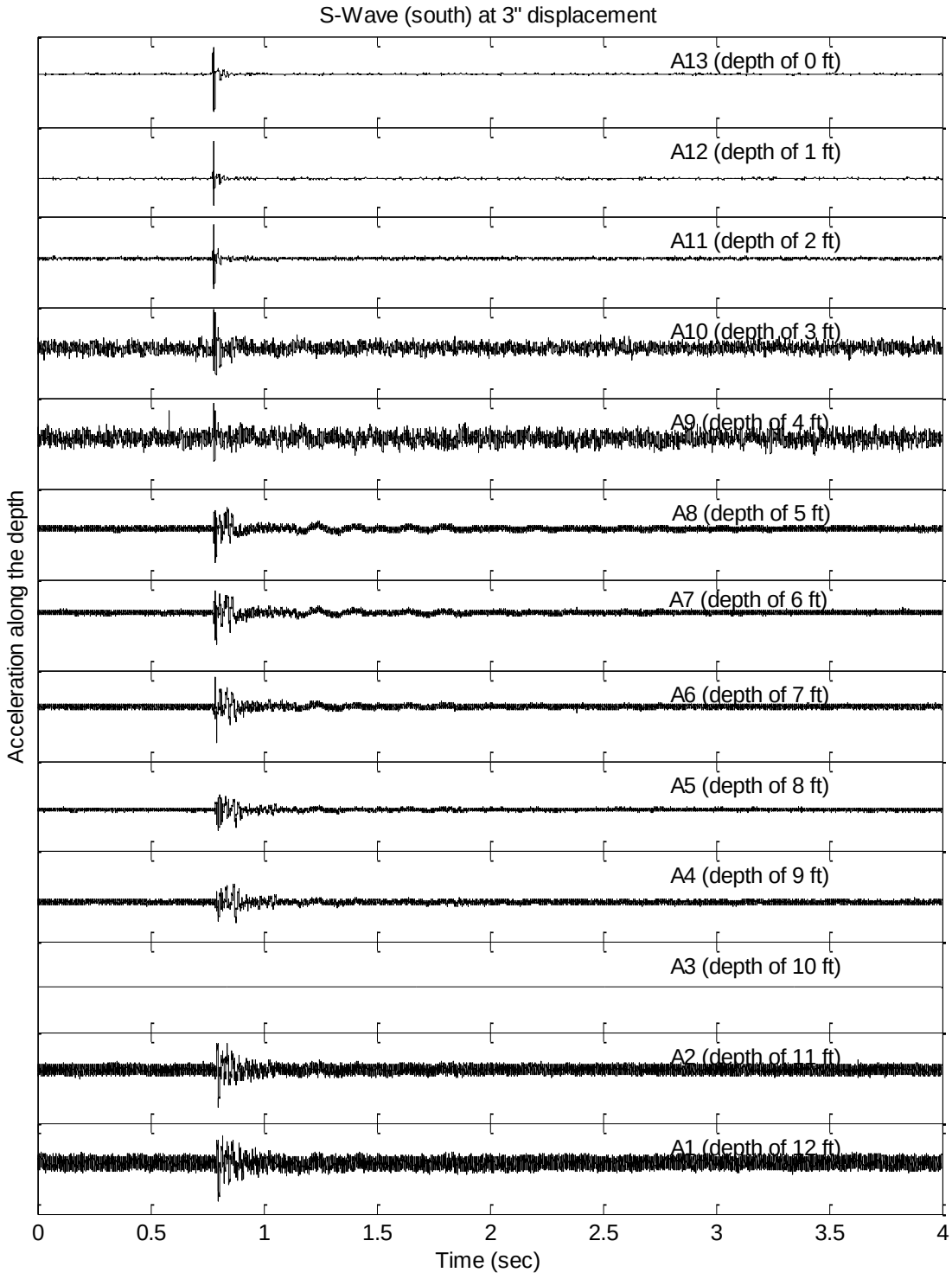

Figure H-10: Acceleration history at South side on soil surface for S-Wave velocity test at lateral displacement of 3 in

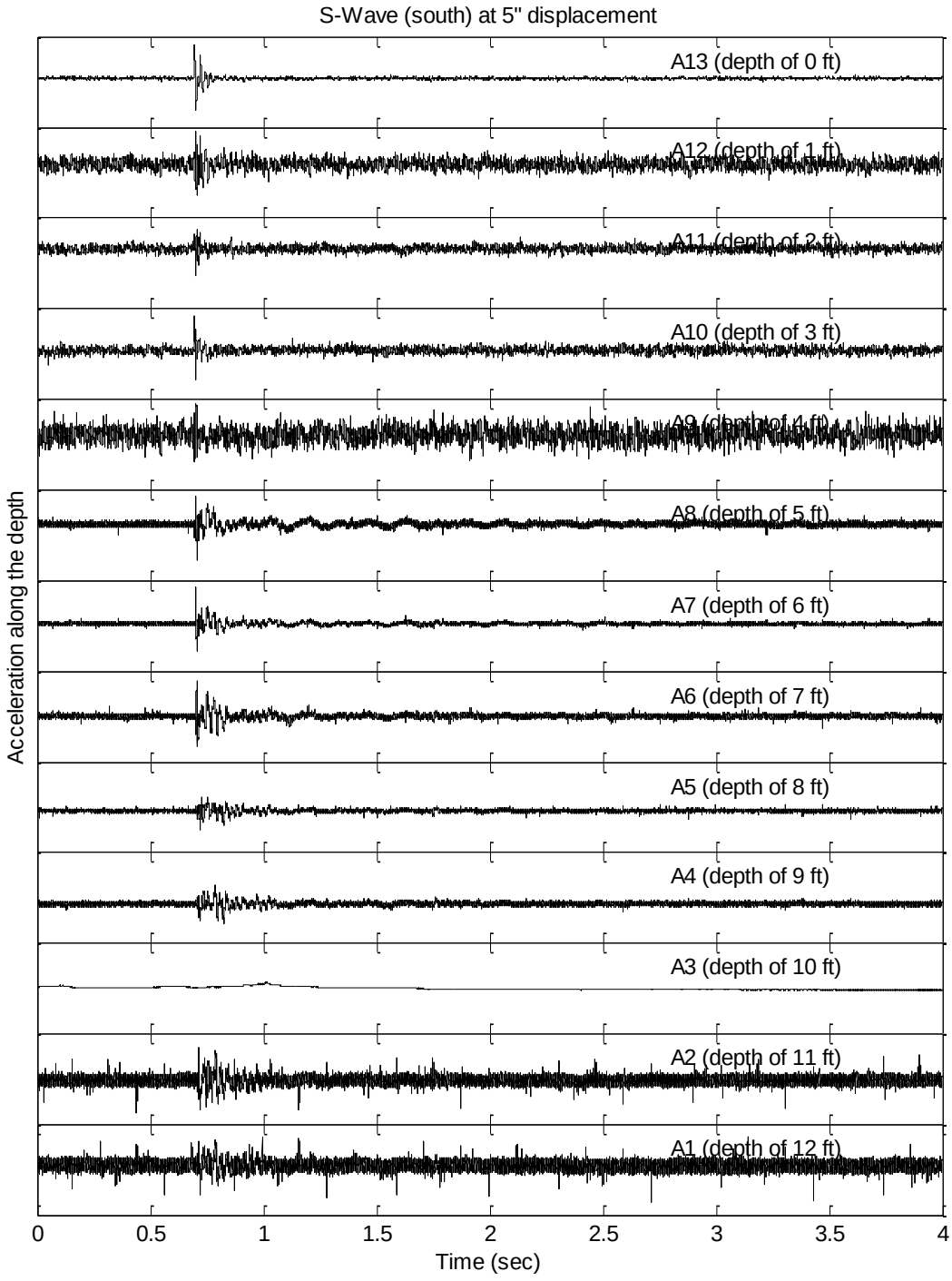

Figure H-11: Acceleration history at South side on soil surface for S-Wave velocity test at lateral displacement of 5 in

APPENDIX I: Earth Pressure Response from Laminar Container Test

This appendix contains data from the following pressure sensors:

1. Pressure cell sensor (AfB sensor): a total 8 sensors were installed along north side of the laminar container to measure lateral pressures developed on the container boundary from the pushover loading (Figure G-9 in Appendix G)
2. Tactilus sensor: total 32 sensors were installed along perimeter of the tunnel to measure normal earth pressures (Figure G-13 in Appendix G)
3. Tekscan sensor: one 16 in by 19 in sensor was installed on the north face of the tunnel (active earth pressure region; Figure G-13 in Appendix G)

I.1 Laminar Container Tunnel-Ground 1st Testing Phase

I.1.1 Lateral earth pressure along height of laminar container

Figure I-1 shows the lateral earth pressure from the AfB sensors on the container boundary during application of the loading. Figure I-2 shows the pressure profile along the depth, computed by average of two sensors at the same depth (except for PT4). It is noted that the results measured near the container base were significantly different from at-rest pressure. A triangular pressure distribution with a relatively high pressure at the tunnel roof was observed. Compared to the at-rest pressure of 20.5 psi at the roof level, a passive soil pressure was developed up to 400 psi as the lateral displacement reached 11.3 ft on soil surface (resulting in the tunnel drift ratio of 2.5%).

I.1.2 Normal earth pressure along tunnel

Tactilus sensors

Figure I-3 through Figure I-5 show the normal earth pressure along perimeter of the tunnel measured from the 32 Tactilus sensors. On north side of the wall, larger normal (active) pressures were developed above half of the tunnel height during the test (Figure I-6). A maximum pressure was developed at the roof level. After the tunnel drift ratio reached about 1%, a relatively steady gain of the pressure was exhibited. Compared to the initial pressure, the pressure increased about three times. On south side of the wall, the larger normal (passive) pressures were also developed above half of the tunnel height). The gain of the pressure also

appeared to be steady after the tunnel drift ratio reached about 1% as shown in the other side (Figure I-6).

Figure I-7 shows the normal pressure distribution along the roof and the slab. The normal pressure tended to decrease along the roof during the application of the static loading. Along the slab, normal pressure near the north side subjected to active earth pressures (Figure I-7).

Tekscan sensor

Figure I-8 shows a 2D pressure distribution measured from the Tekscan sensor (mounted on the center wall that was pushed). Figure I-9 shows average of the pressures along the wall. As the loading increased, relatively higher pressures were developed in the upper part of the sensor. Figure I-10 shows a comparison of the results to those from the Tactilus sensors

I.2. Laminar Container Tunnel-Ground 2nd Testing Phase

Normal earth pressure from Tactilus sensors

Figure I-11 through Figure I-13 show measured normal earth pressures on the tunnel from Tactilus sensors (no sensor on the roof). The larger active soil pressures were developed in the upper part of the north wall (Figure I-14). The pressure tended to decrease toward the roof. Figure I-15 shows the normal pressure profiles along the slab.

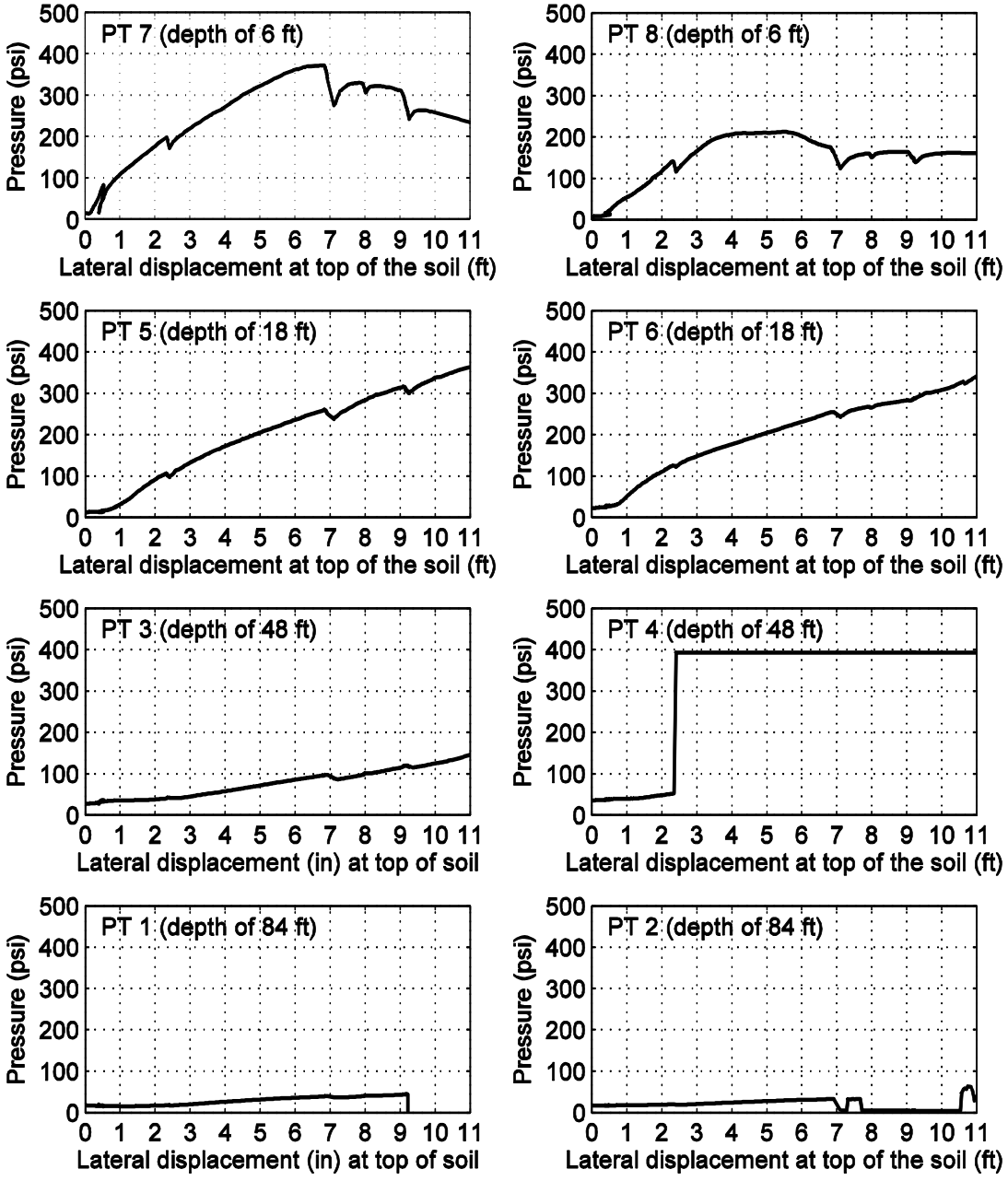

Figure I-1: Change of lateral pressure from AFB sensors mounted on north side of laminar container

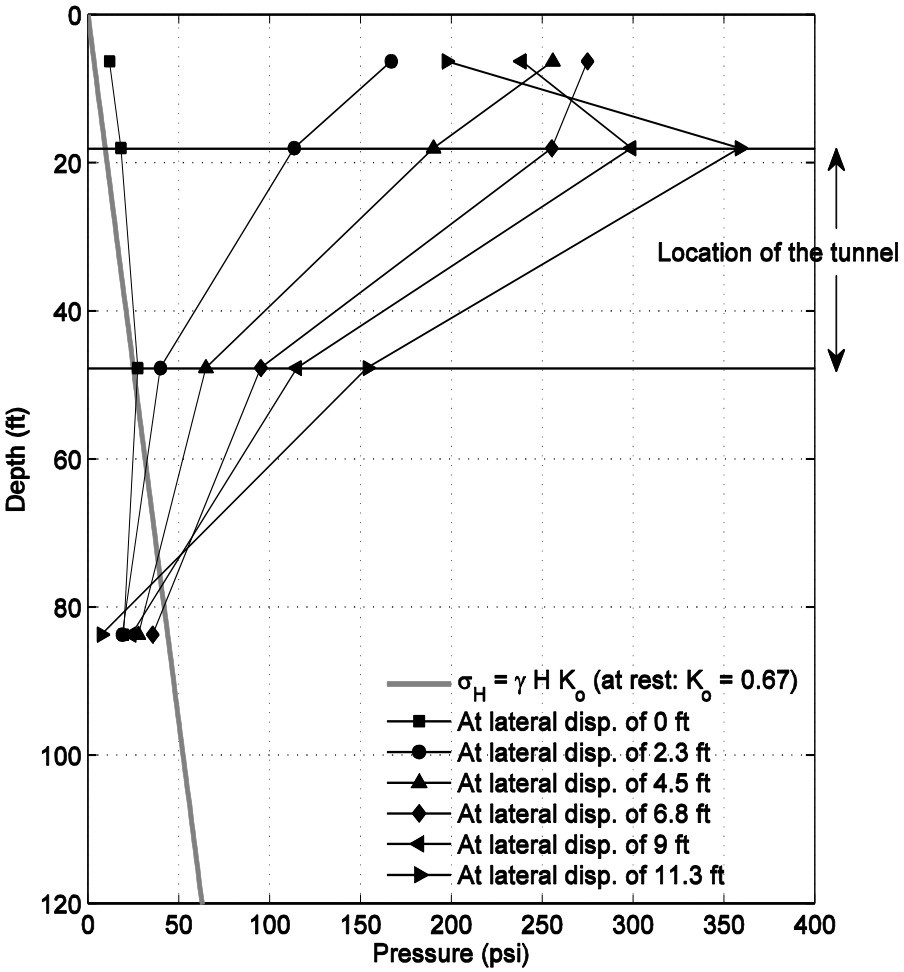

Figure I-2: Lateral pressure profile along the north side of laminar container

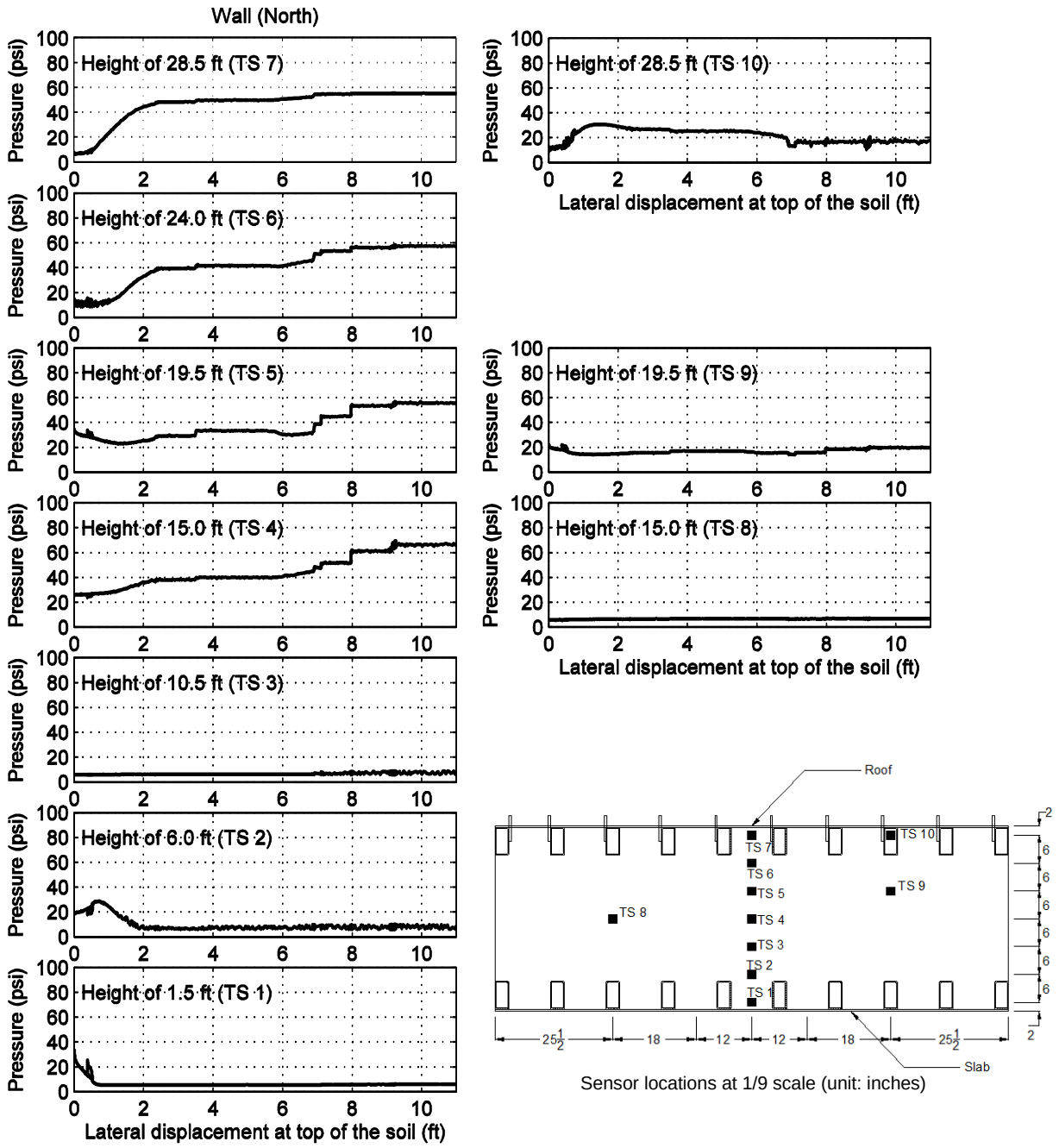

Figure I-3: Change of normal (lateral) pressure from Tactilus sensors mounted on north side of tunnel specimen

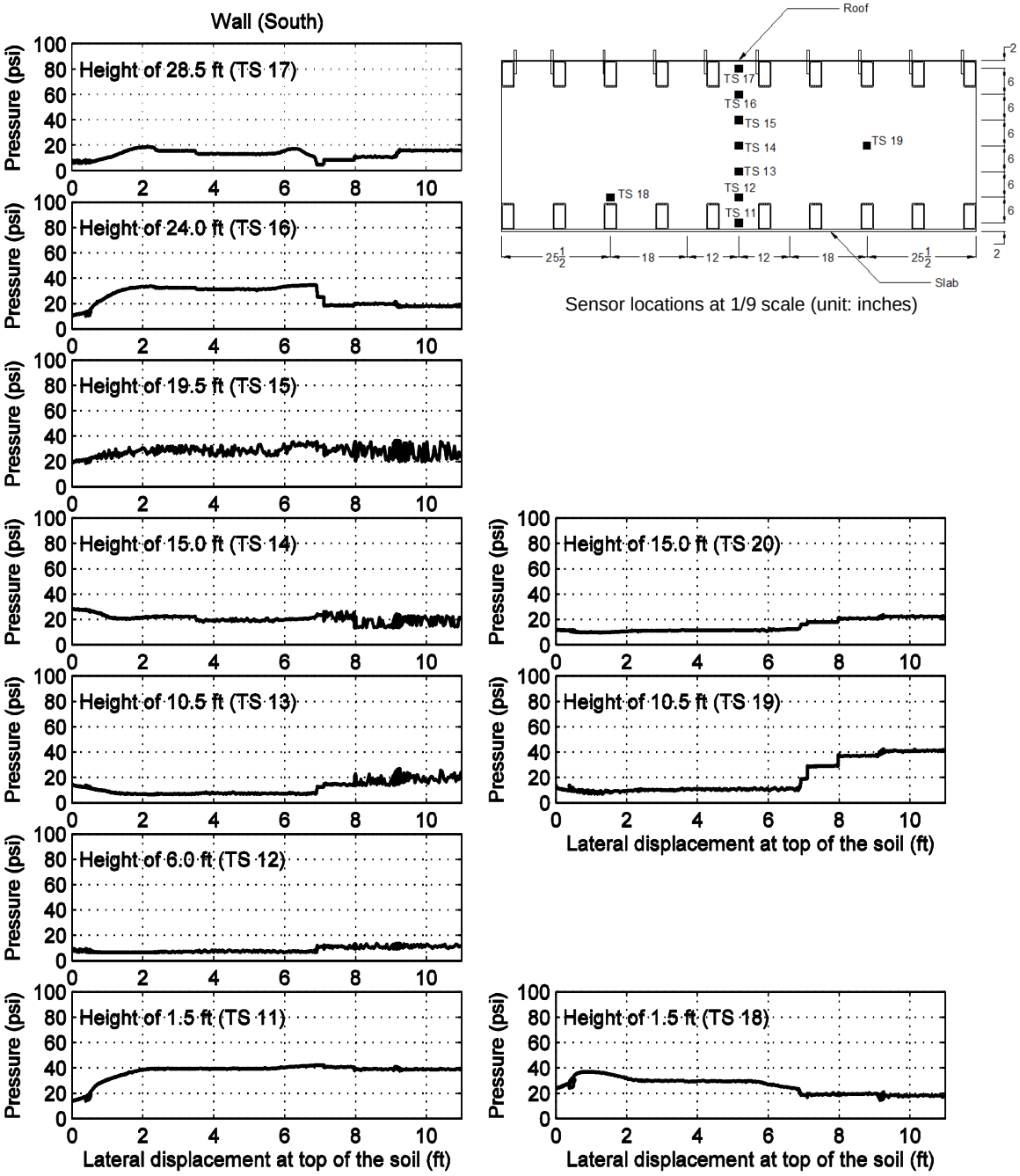

Figure I-4: Change of normal (lateral) pressure from Tactilus sensors mounted on south side of tunnel specimen

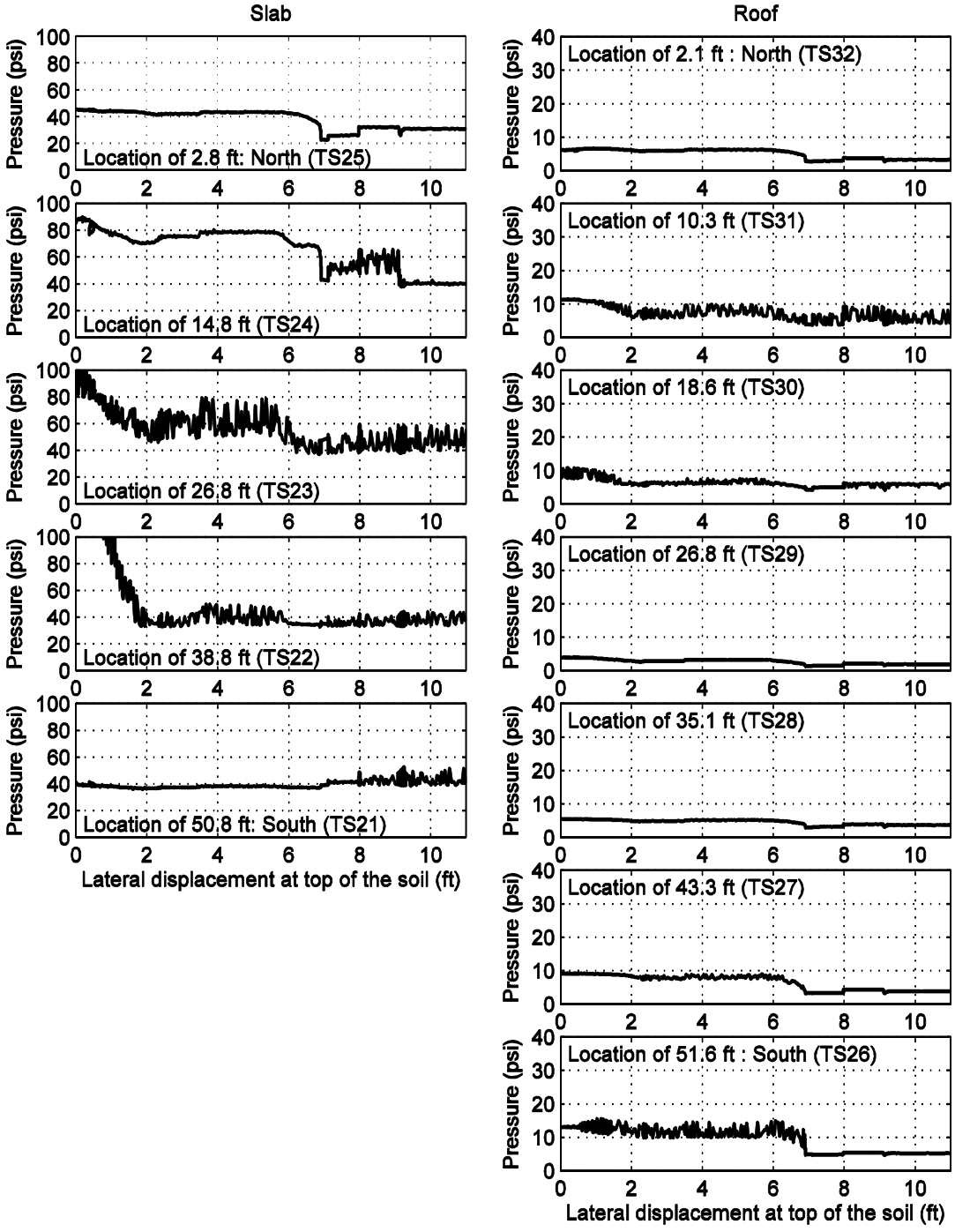

Figure I-5: Change of normal pressure from Tactilus sensors mounted on slab and roof

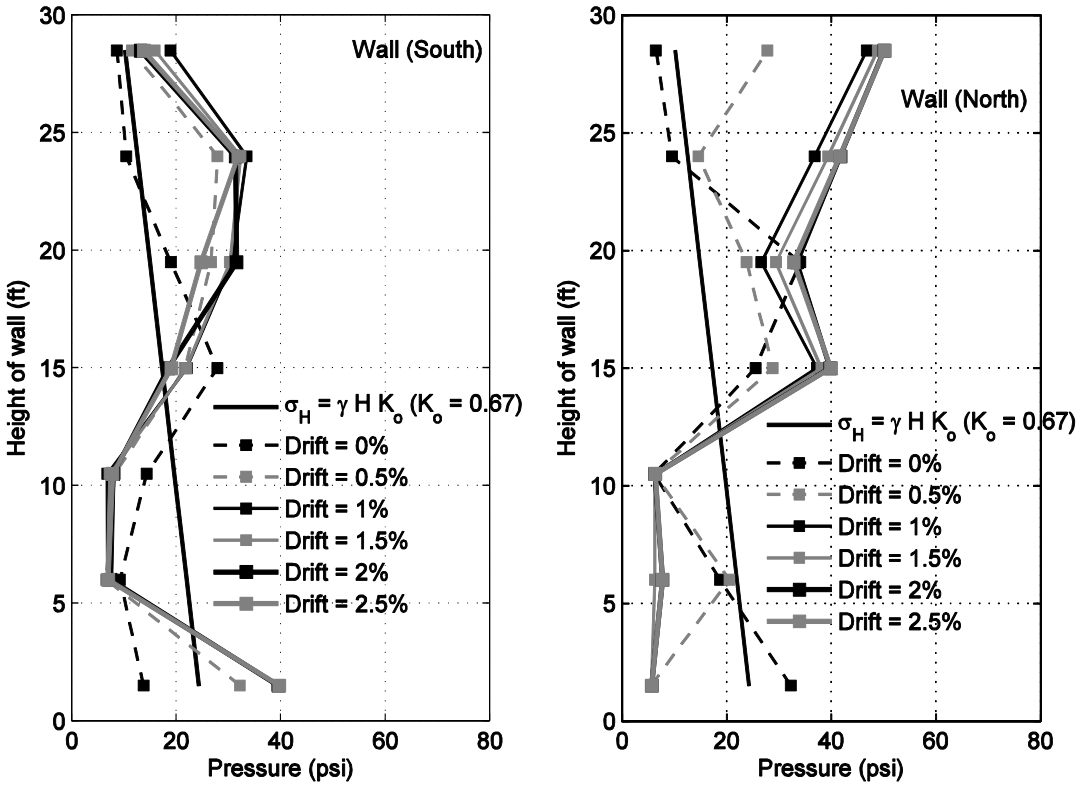

Figure I-6: Normal (lateral) pressure profile along wall of tunnel specimen

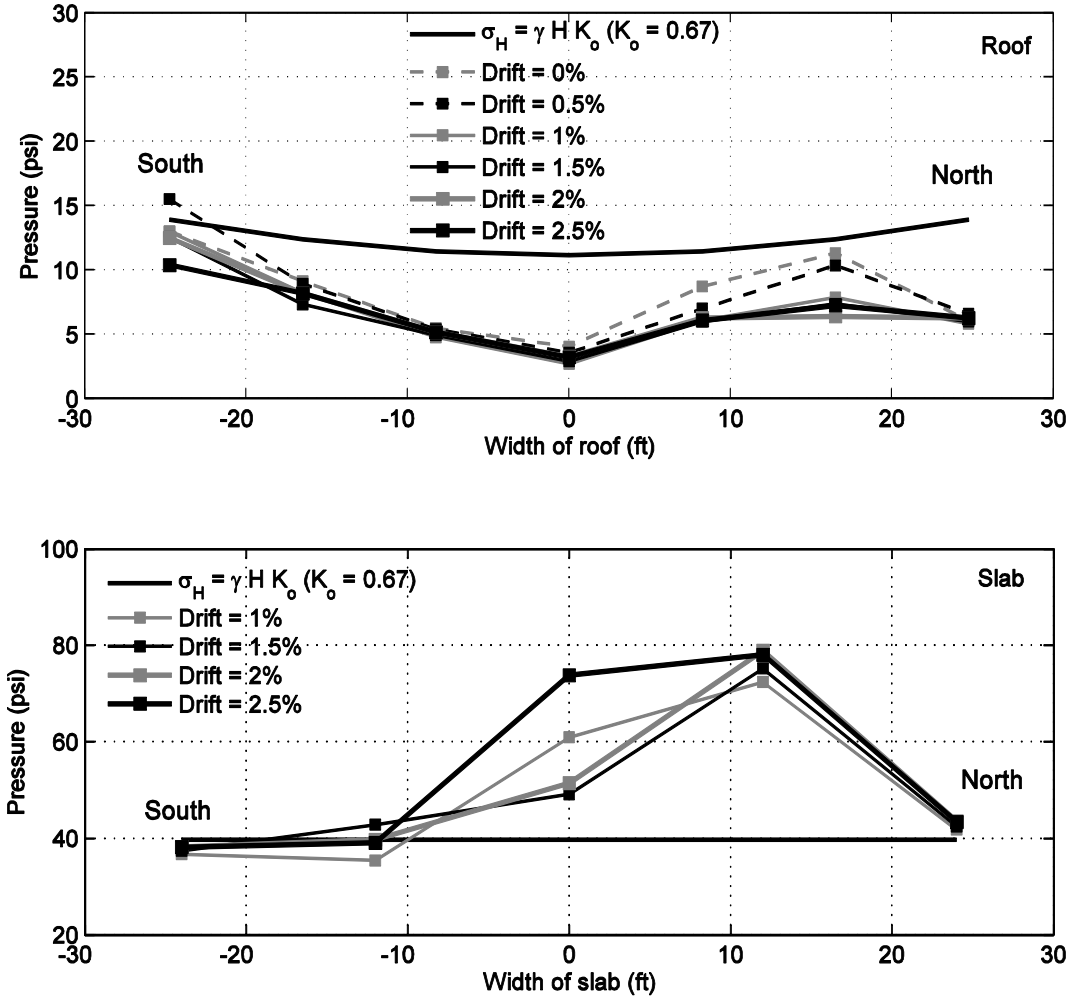

Figure I-7: Normal (vertical) pressure profile along width of slab and roof

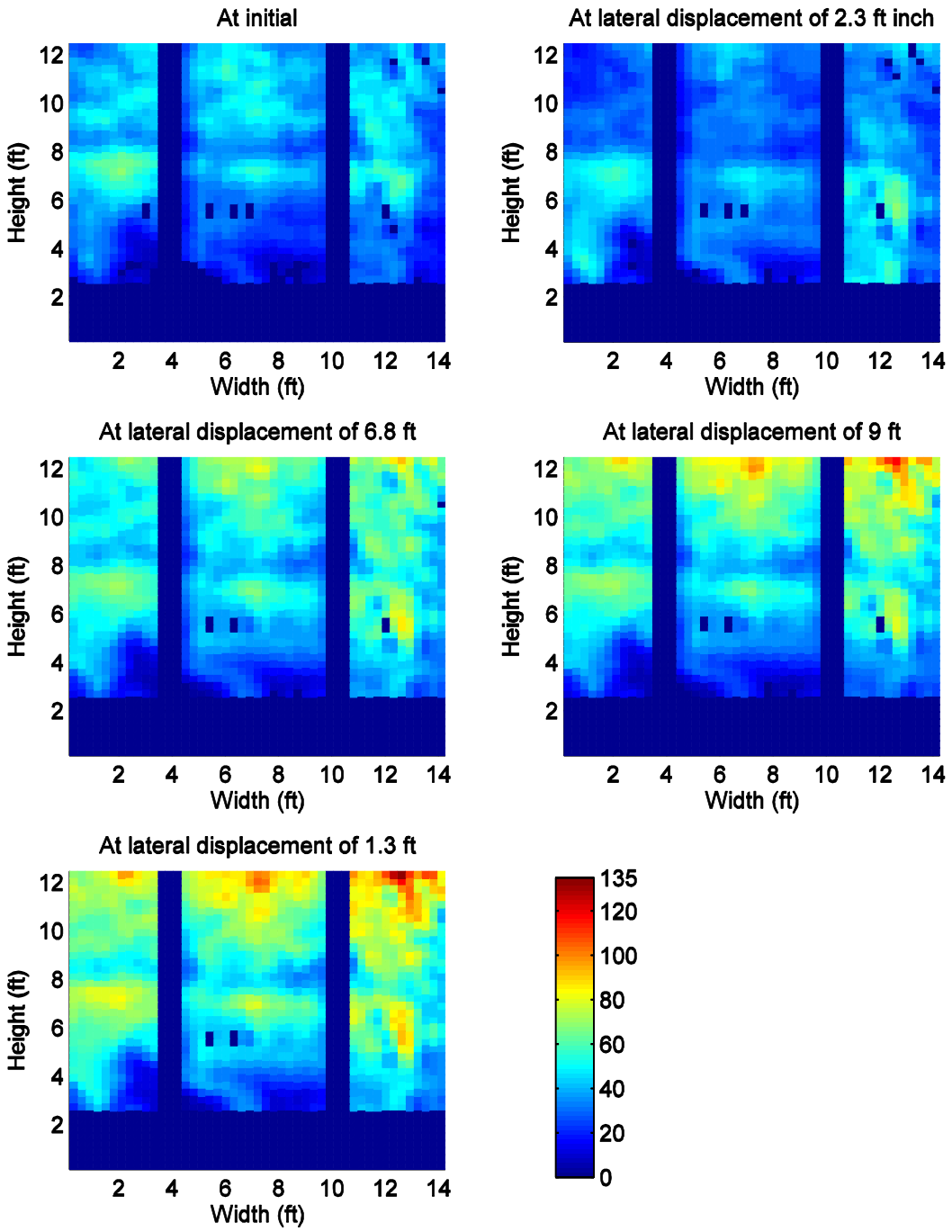

Figure I-8: Tekscan 2D pressure map at lateral displacement

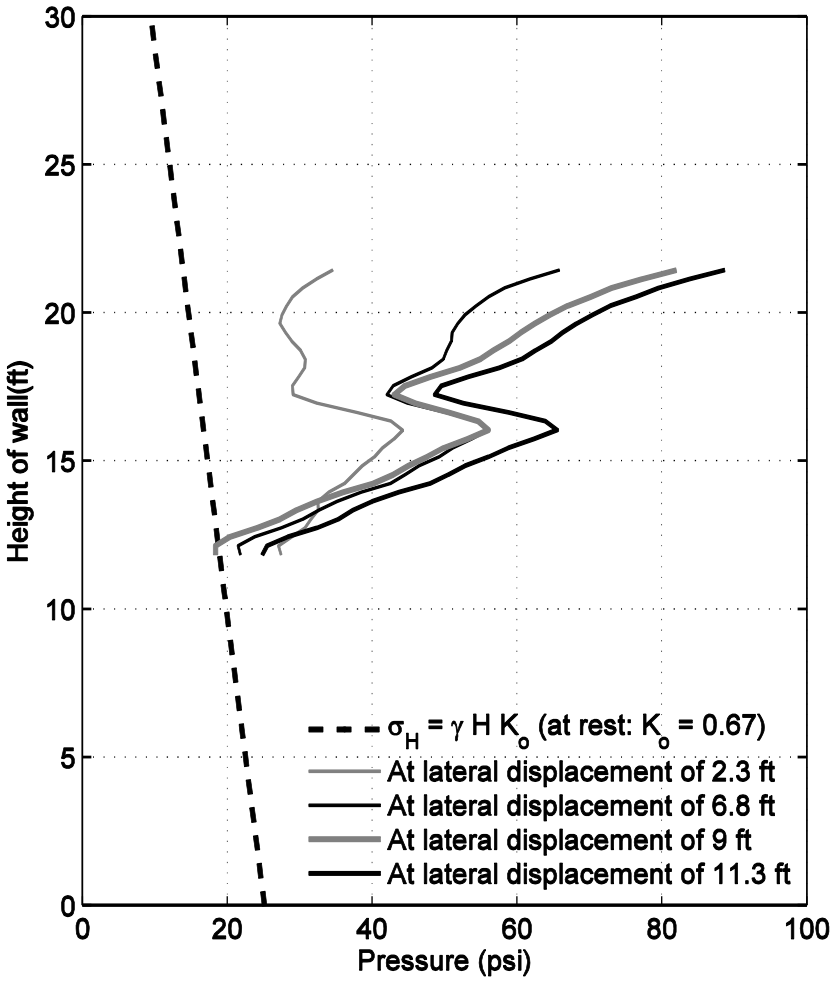

Figure I-9: Pressure vs. Distance histogram graph of average pressure across sensor rows from top to bottom (left to right x-axis on graph)

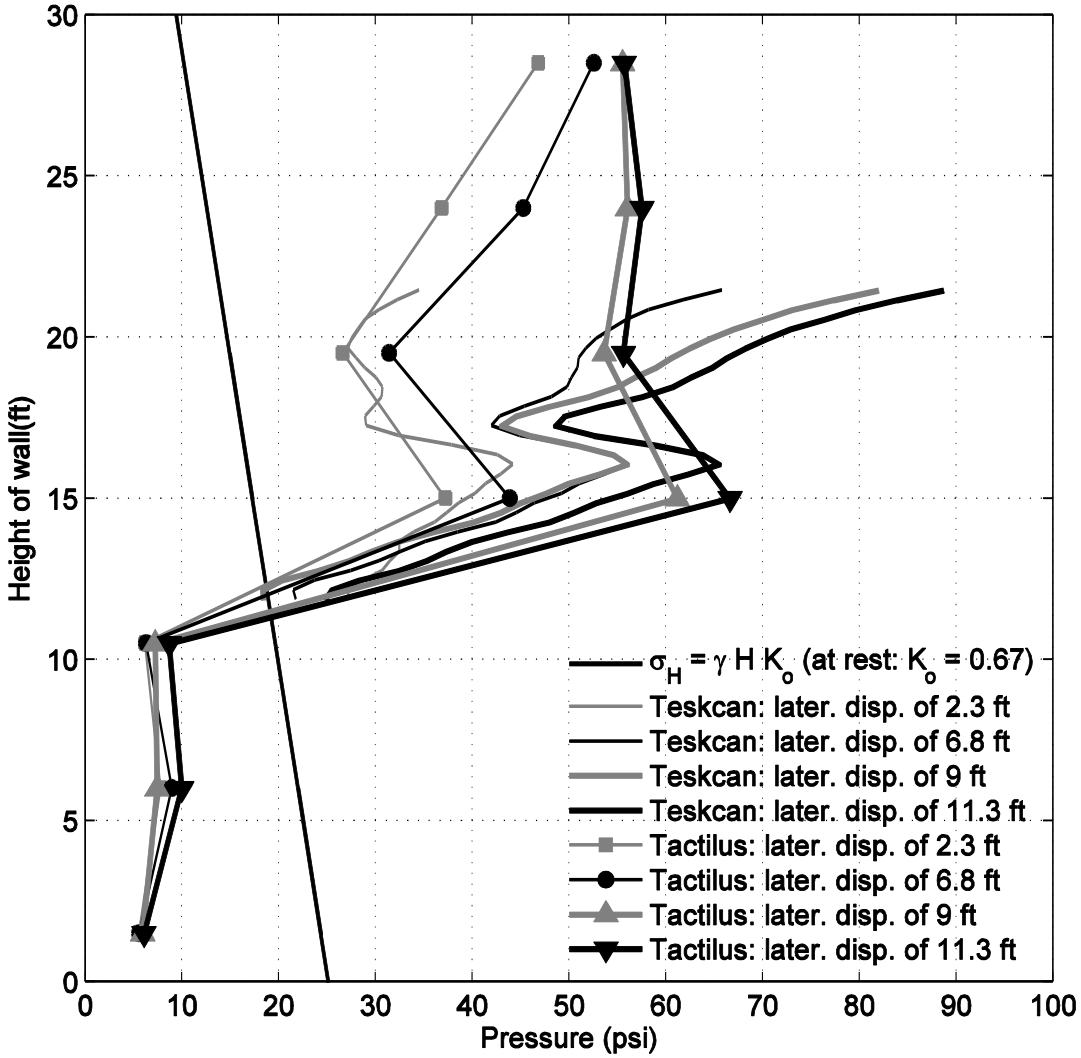

Figure I-10: Pressure vs. Distance histogram graph of average pressure across sensor rows from top to bottom (left to right x-axis on graph)

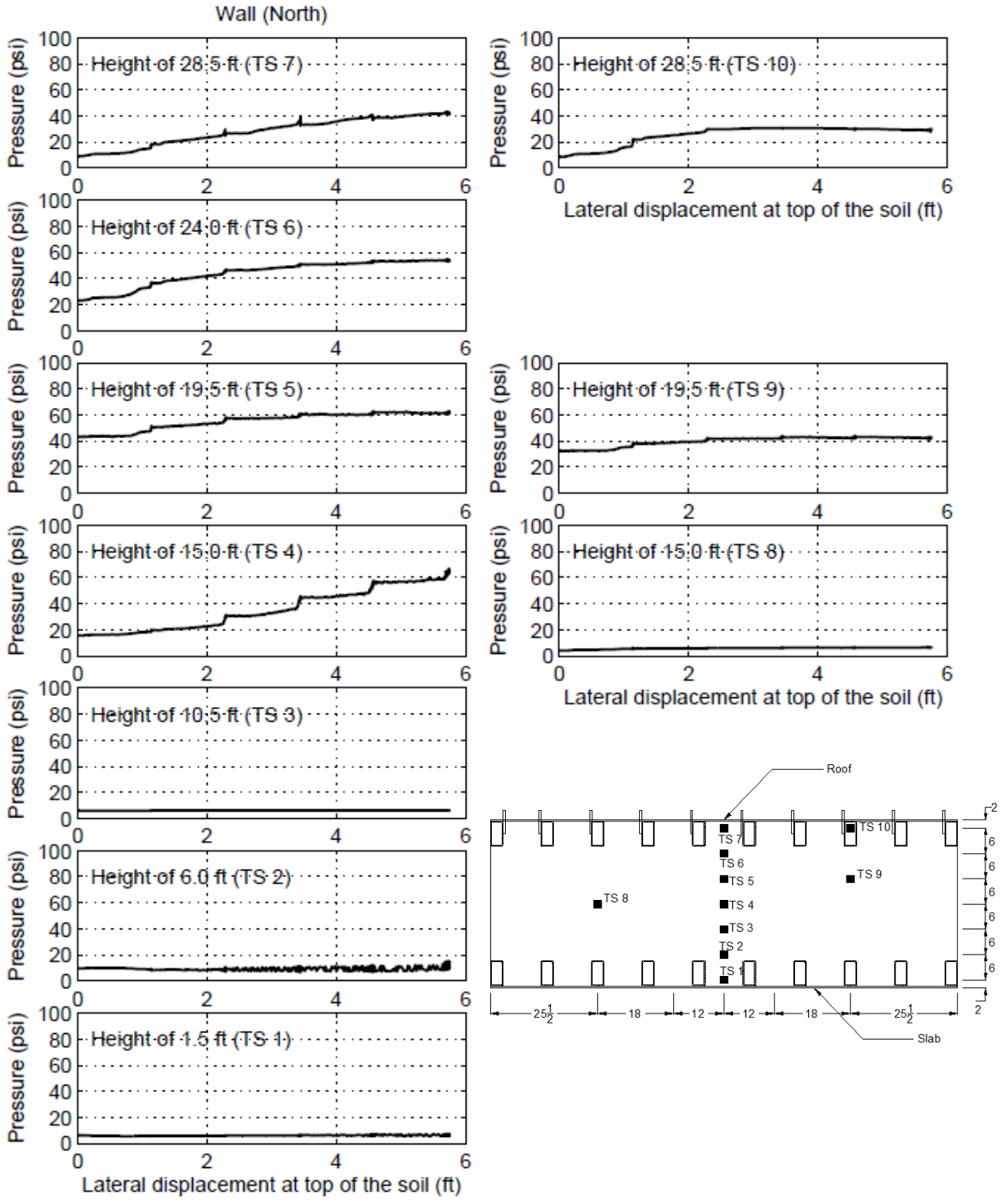

Figure I-11: Change of normal (lateral) pressure from Tactilus sensors mounted on north side of tunnel specimen in the 2nd test

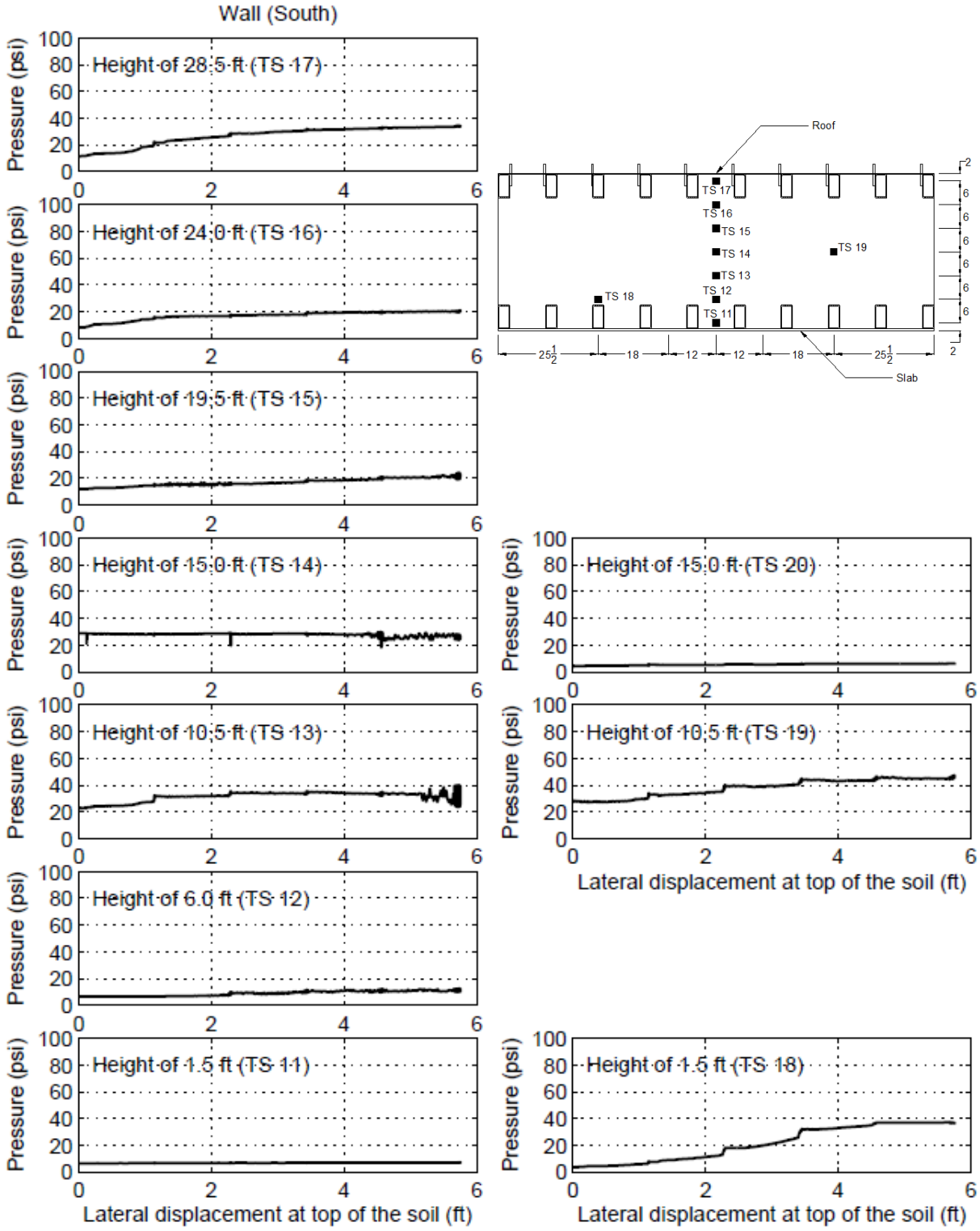

Figure I-12: Change of normal (lateral) pressure from Tactilus sensors mounted on south side of tunnel specimen in the 2nd test

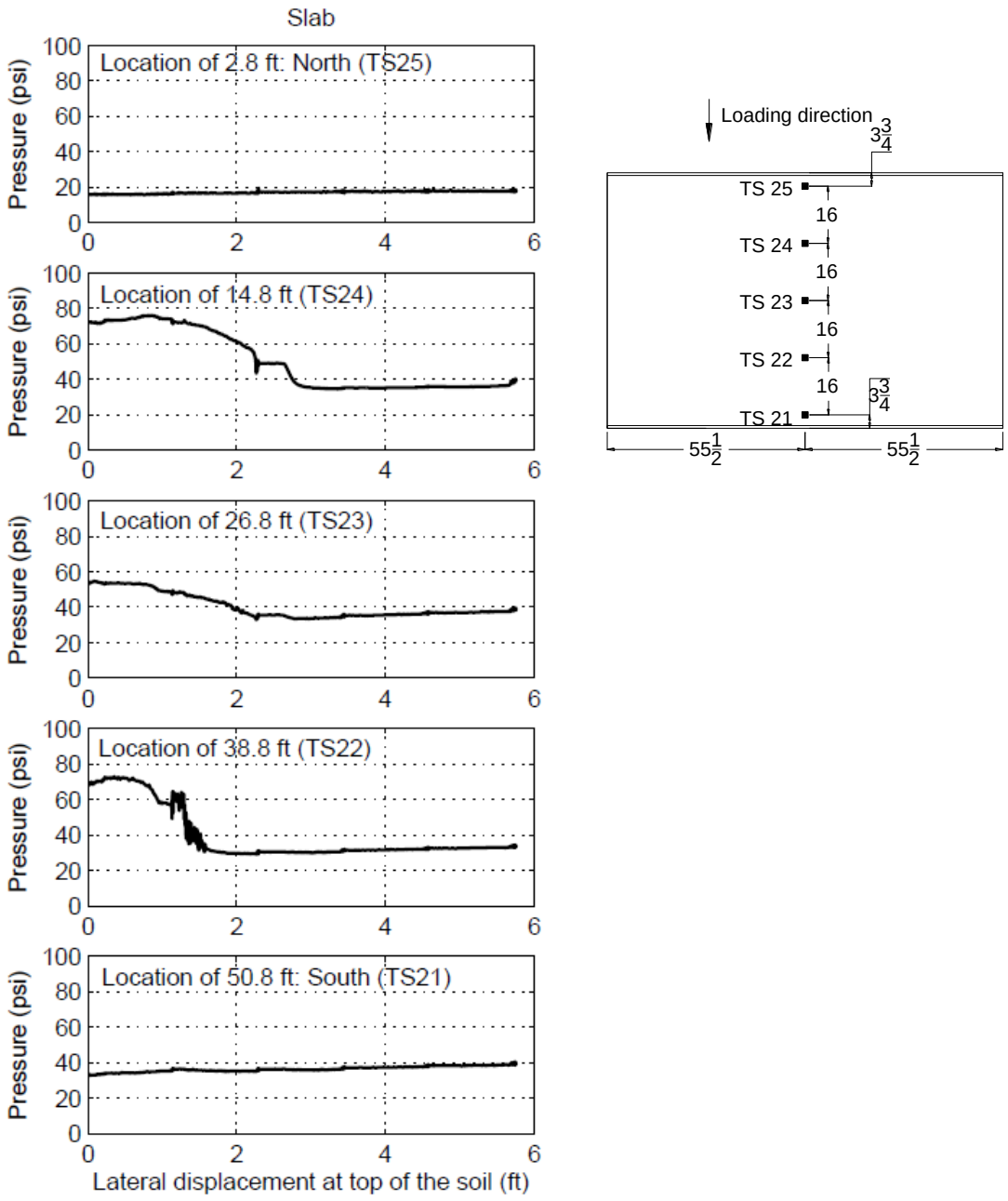

Figure I-13: Change of normal pressure from Tactilus sensors mounted on slab

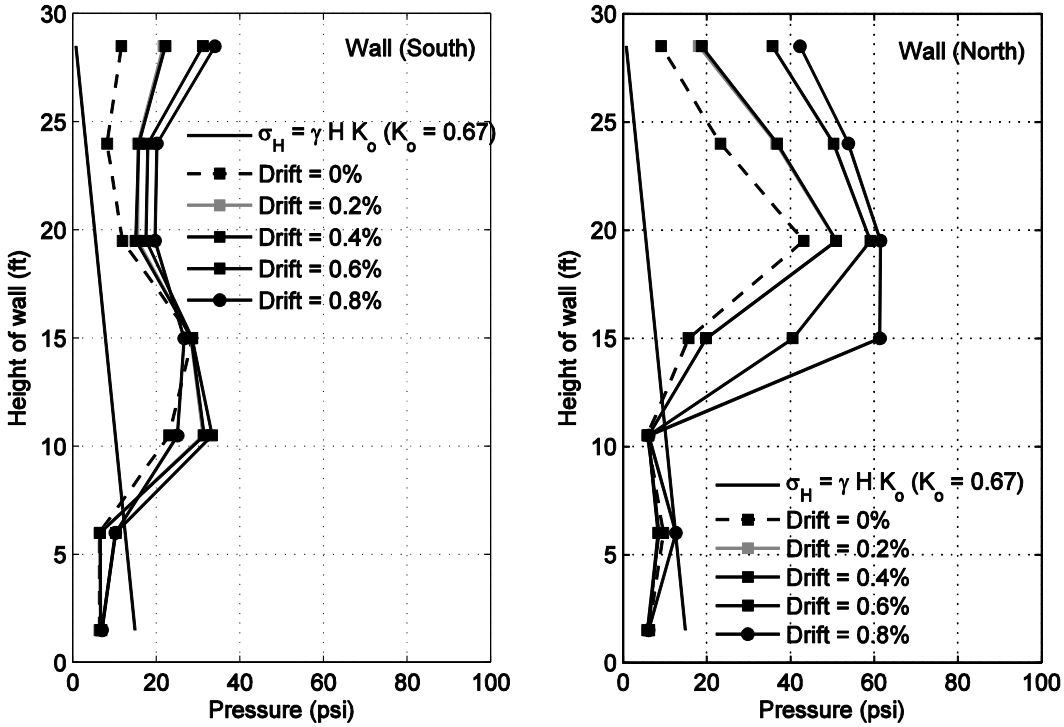

Figure I-14: Normal (lateral) pressure profile along wall of tunnel specimen

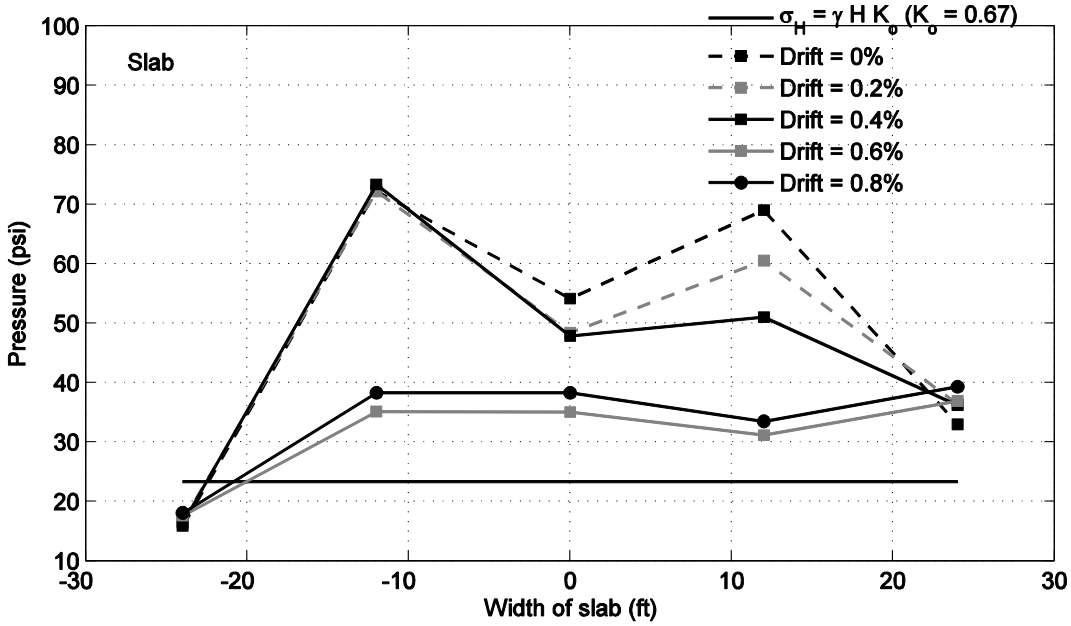

Figure I-15: Normal (lateral) pressure profile along width of slab

APPENDIX J: Dynamic FE SSI Analysis of Nonlinear Tunnel Model

This appendix presents a numerical analysis study using the nonlinear tunnel model ((in prototype scale) as discussed earlier in Section 3.7. Effort is directed towards: (1) inclusion of representative soil of stiffness/strength profiles that increase with depth, similar to the measured properties in the laminar container test (see Section 5.3); (2) investigation of nonlinear deformation of the tunnel under earthquake excitation; and (3) comparison of the resulting racking deformation to the FHWA (2009) procedure (see Section 2.2.2).

J.1 Finite Element Model

J.1.1 Soil and tunnel properties

For the soil mesh (Figure J-1), 4-node quadrilateral elements were used (total number of nodes and elements were 886 and 792, respectively). A total of 21 layers were specified along depth of 131 ft (Table J-1). Each layer was modeled as a nonlinear hysteretic material (Prevost 1978; Elgamal et al. 2008) with a Von Mises (J_2) multi-surface kinematic plasticity model (PressureIndependMultiYield, PIMY, model in OpenSees). Details of this material can be found in Section 7.2.

In each layer (total 21 layers), shear modulus at low strain ($< 10^{-6}$) was estimated (i.e. G_{max} in psf) using the following equation (Seed et al. 1986):

$$G_{max} = 20000\ (N_1)_{60}^{0.333}\ (\sigma_m')^{0.5} \qquad \text{(J-1)}$$

where σ_m' is confining pressure along depth, $(N_1)_{60}$ = the normalized blow count from the standard penetration test at an effective overburden pressure of 14.5 psi (100 kPa) and corrected to 60% of free fall energy.

In the conducted experiment, shear wave velocity (V_s) at level of the tunnel base was measured as V_s of 1044 ft/sec. see Section 5.3.1), corresponding to a low strain shear modulus G_{max} = 26.5 ksi (assuming a dry soil unit weight of 127 pcf). As such, an $(N_1)_{60}$ = 58 is derived from Equation J-1, that being representative of very dense sand (Skempton, 1986).

Soil shear strength (reached at a shear strain of 3 %) was defined by the friction angle (ϕ), with a hyperbolic backbone curve defining shear stress versus shear strain. The employed friction angle was obtained using the following equation (Sabatini et al. 2002):

$$\phi = \sqrt{15.4(N_1)_{60}} + 20 \quad \text{(J-2)}$$

On this basis, Table J-1 summarizes the model soil properties (with Poisson's ratio of 0.3 for all layers). Finally, the calibrated tunnel model properties (discussed earlier in Section 3.7) were multiplied by appropriate scaling factors (as discussed earlier in Section 3.7; see Table 3-1) to simulate the adopted tunnel cross section (Doyle Drive Battery Tunnel).

J.1.3 Boundary Conditions and Earthquake Input Motion

For the lateral boundaries, a shear beam condition was used to enforce identical translation in the horizontal and vertical directions. The lateral boundaries were located sufficiently far from the tunnel to minimize potential interaction effects. At the interface between the tunnel and the soil, no friction/separation was assumed.

Soil strata below the FE model base were replaced by the transmitting boundary of Lysmer and Kuhlemeyer (1969) to avoid spurious wave reflections. At each base node, one dashpot was activated in the horizontal (shear) direction. As such, incident seismic wave excitation was dictated by dynamic equivalent nodal forces. The coefficient of the dashpot tangential to the base boundary was defined as ρV_s, where ρ and V_s are the density and shear wave velocity of the soil base material (Table J-1). Further details of the dashpot boundary implementation can be found elsewhere (e.g., Zhang et al. 2008; Kim 2014).

As discussed earlier in Section 7.2.2, the 1994 Northridge earthquake ground motion recorded at CSMIP Station 24279 (Newhall-County Fire station; component 90 degrees) was selected. The incident motion derived by SHAKE 91 (Idriss and Sun 1992) was applied to the FE model base (Figure J-1). Further computational modeling details are discussed in Section 7.2.2.

On this basis, a parametric study was conducted, with base excitation scaled to various levels of PGA. In this effort, shear wave velocity and shear strength profile of the soil domain was changed systematically, where $(N_1)_{60}$ value was varied in the range of *2 - 58* with corresponding dry unit weight in the range of 93.4 pcf -127 pcf.

J.2 Simulation Results and comparison with the FHWA estimate

J.2.1 Selection of Racking Stiffness

To compare with racking estimated from the FHWA (2009) step-by-step procedure (Wang 1993), the flexibility ratio, F_r, is needed (see Eq. 2-1; and Section 2.2.2 for the step-by-step procedure). To develop this procedure, Wang (1993) performed dynamic soil-structure interaction FE analyses using linear elastic structural models. In computing the F_r, the racking stiffness (K_s) is computed, as indicated in FHWA (2009) stating that "the racking stiffness should be computed using the displacement of the roof subjected to a unit lateral force applied at the tunnel roof" in a structural frame analysis. It is recommended that "appropriate moment of inertia values taking into account the potential development of cracked section should be used". In this study, the racking stiffness of 2.6 ksi was computed on the basis of the cracked section of the walls ($0.35I_g$ for flexural beam members where I_g is gross moment of inertia; ACI 318-08). Thus, this constant racking stiffness was used for the entire parametric study as presented in this section. Figure J-2 To contrasts this FHWA (2009) 2.6 ksi stiffness with the employed FE tunnel stiffness as a function of drift ratio. Nevertheless, in the following section, the constant racking stiffness of 2.6 ksi was employed in the FHWA procedure, for comparison with the numerical parametric study outcomes.

J.2.2 Racking Response of Tunnel

Figures J-3 and J-4 present the results of this numerical parametric study, compared to the predictions of the FHWA (2009) procedure. The predicted drift ratio is shown as a function of PGA (Figure J-2) or alternatively PGV (Figure J-3), as either of these two quantities may be used to drive the FHWA (2009) peak soil shear strain estimate calculation. For instance, Table J-2 summarizes the FHWA procedure computation in the case of V_s of 1050 ft/s with PGA of 0.54g and PGV of 25 in/s. As shown in these Figures, the predicted tunnel drift ratio is presented for a wide range of soil stiffness values (reported in these Figures at the level of the tunnel base, essentially also equal to V_{s30} of these soil profiles). From these two figures, it may be concluded that (for this particular input excitation, nonlinear soil profile/properties, and tunnel model stiffness/geometric configuration):

1. For the PGA-based case:

1) The FHWA procedure overestimated the racking deformation (drift), compared to that from the numerical analysis. Racking deformation from the numerical results was lower by as much as 75%, compared to the FHWA estimate.
2) The extent of racking overestimation was partially a result of a higher simplified-procedure peak soil shear strain estimate.
3) The simplified method large soil peak shear strains resulted in considerably low flexibility (relative stiffness of soil to tunnel). As a consequence, large racking deformations were predicted by the simplified procedure (up to about 4% drift, noting that first yield occurs at 1% drift).

2. For the PGV case:
1) Similar outcomes are noted (Simplified procedure overestimates the peak soil shear strain and resulting tunnel racking estimate).
2) Overestimation is more pronounced at the higher levels of ground shaking, where PGV continues to increase, while PGA levels-off (eventually limited by the particular assumed soil shear strength profile)

Table J-1: Soil material properties

Layer	Thickness (ft)	Shear modulus (psi)	Shear strength (psi)
1	3.0	6225	0.7
2	3.0	10781	2.1
3	4.1	14442	3.8
4	4.1	17770	5.8
5	3.9	20493	7.7
6	3.4	22690	9.4
7	3.4	24565	11.0
8	3.4	26307	12.6
9	3.4	27939	14.3
10	3.4	29482	15.9
11	3.4	30948	17.5
12	3.6	32392	19.2
13	3.3	33749	20.8
14	10.7	36337	24.1
15	10.7	39975	29.2
16	10.7	43308	34.3
17	10.7	46403	39.3
18	10.7	49304	44.4
19	10.7	52043	49.5
20	10.7	54645	54.5
21	10.7	57129	59.6

Table J-2: FHWA step-by-step procedure for racking deformation on the basis of PGA and PGV (case of V_s = 1050 ft/s) and comparison with the OpenSees simulation results

i) On the basis of PGA		FHWA	OpenSees results
Step 1	PGA at soil surface	0.54 g	0.54 g
	$\sigma_v = \gamma_t$ (h+D)	35.3 psi	35.3 psi
	τ_{max} = (*PGA*/g) σ_v R_d	16.1 psi	14.8 psi
	Shear modulus, G_m	5.3 ksi	7.6 ksi
	$\gamma_{max} = \tau_{max} / G_m$	0.30%	0.196 %
	Free-field displacement, $\Delta_{free\text{-}field}$	0.89 in	0.57 in
Step 2	Racking stiffness, K_s	2.6 ksi	2.6 ksi
Step 3	Flexibility ratio, $F_{rec} = (G_m/K)\ (W/H)$	4.46	6.33
Step 4	Racking coefficient, $R_r = \frac{4(1-\nu_m)F_{rec}}{3-4\nu_m+F_{rec}}$ (for no slip)	1.99	2.18 (1.72 directly from $\Delta_s/\Delta_{free\text{-}field}$)
Step 5	Racking deformation, $\Delta_s = R_r\ \Delta_{free\text{-}field}$	1.76 in (0.7% drift)	1.0 in (0.4% drift)

ii) On the basis of PGV		FHWA	OpenSees results
Step 1	PGV at tunnel level	24.8 in/s	24.8 in/s
	C_{se}, effective shear wave propagation velocity	316 ft/s	531 ft/s
	$\gamma_{max} = PGV / C_{se}$	0.66%	0.196%
	Shear modulus, G_m	2.7 ksi	7.6 ksi
	Free-field displacement, $\Delta_{free\text{-}field}$	1.92 in	0.57 in
Step 2	Racking stiffness, K_s	2.6 ksi	2.6 ksi
Step 3	Flexibility ratio, $F_{rec} = (G_m/K)\ (W/H)$	2.34	6.33
Step 4	Racking coefficient, $R_r = \frac{4(1-\nu_m)F_{rec}}{3-4\nu_m+F_{rec}}$ (for no slip)	1.66	2.18 (1.72 directly from $\Delta_s/\Delta_{free\text{-}field}$)
Step 5	Racking deformation, $\Delta_s = R_r\ \Delta_{free\text{-}field}$	3.2 in (1.3% drift)	1.0 in (0.4% drift)

* H = height of the box structure (ft), W = width of the box structure (ft)

G_m = Effective strain-compatible shear modulus of ground surrounding tunnel (ksf)

τ_{max} = Maximum earthquake-induced shear stress (ksf)

σ_v = Total vertical soil overburden pressure at invert elevation of tunnel (ksf)

γ_t = Total soil unit weight (kcf)

h = Soil cover thickness measured from ground surface to tunnel crown (ft)

D = Height of tunnel (ft)

R_d = Depth dependent stress reduction factor; Rd = 1.0 – 0.00233z for z < 30 ft, 1.174-0.00814z for 30 ft < z < 75 ft; z = depth (ft) from ground surface to the invert elevation of the tunnel and is represented by z = $(h+D)$

K_s = racking stiffness taking into account the cracked section moment of inertia

C_{se} = effective shear wave propagation velocity (compatible with the level of the shear strain)

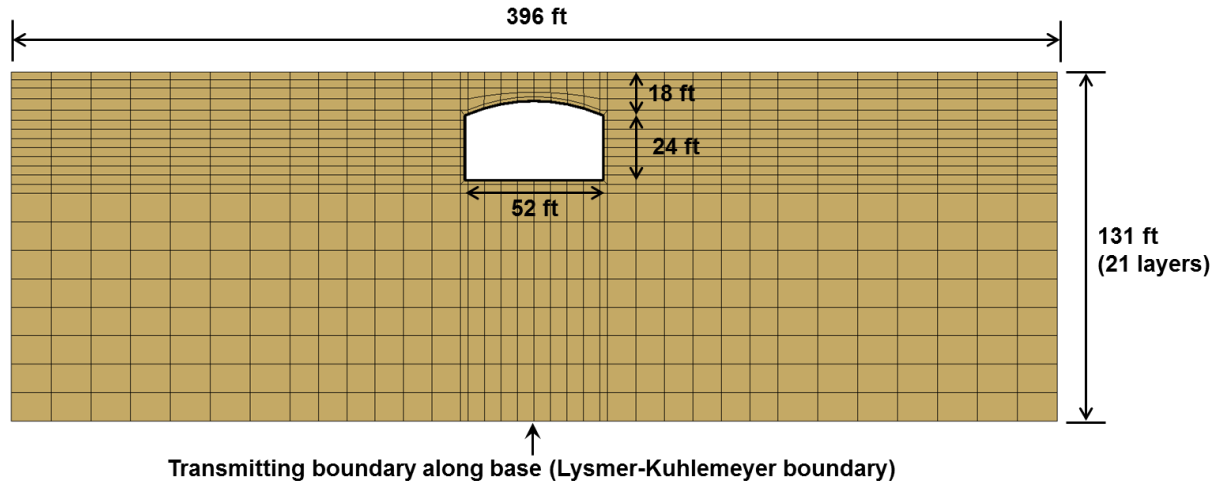

(a)

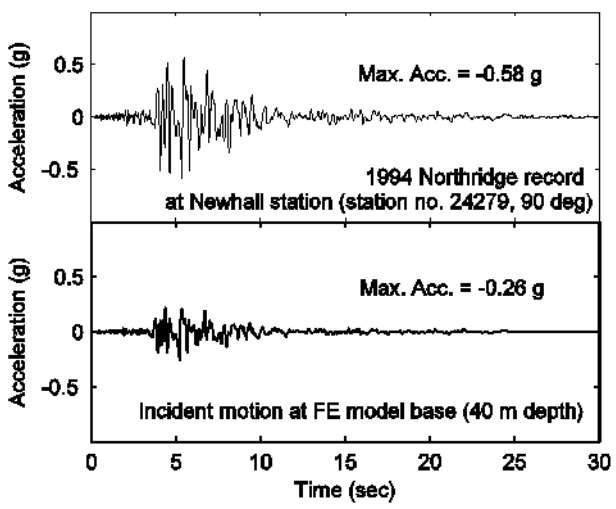

(b)

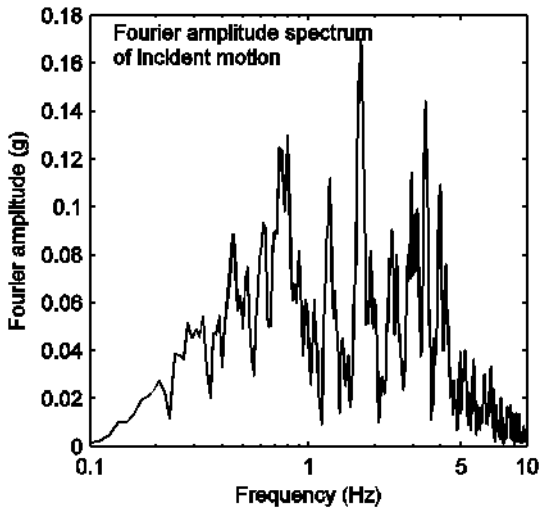

(c)

Figure J-1: Numerical model: (a) FE mesh of the tunnel-ground system; (b) Northridge earthquake record (Newhall station, CSMIP No. 24279, 90 degrees) and incident motion at FE model base from deconvolution

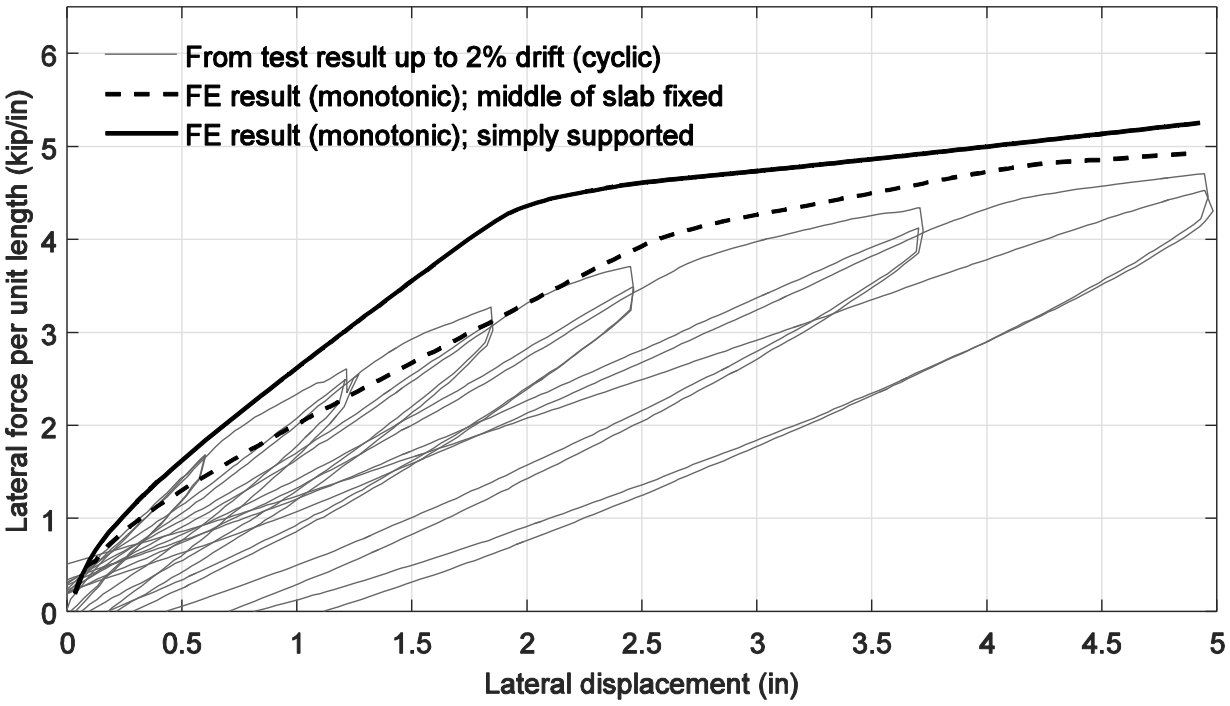

(a)

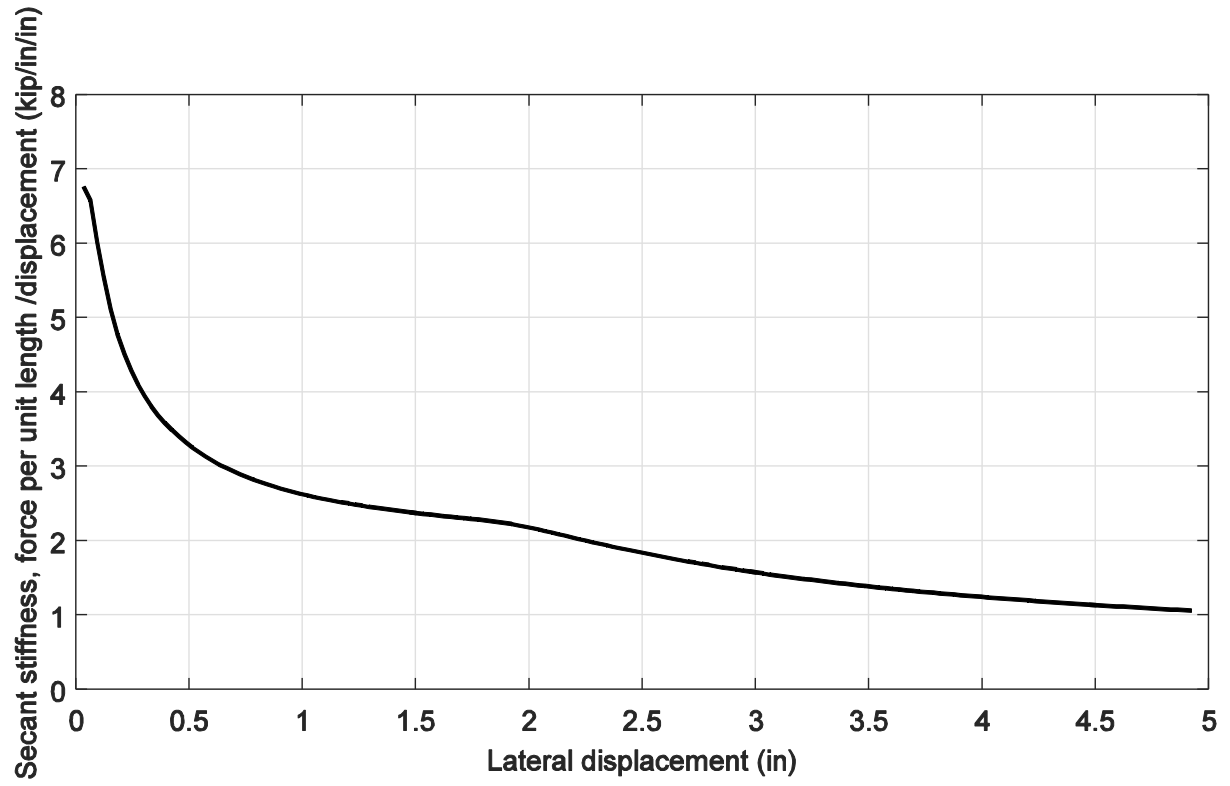

(b)

Figure J-2: Tunnel racking stiffness; (a) relationship of lateral force and displacement (up to 2% drift ratio) from the test result (in prototype scale) and the OpenSees tunnel model and (b) variation of tunnel racking stiffness associated with level of the deformation obtained from the numerical simulation (secant stiffness under the simply supported base condition)

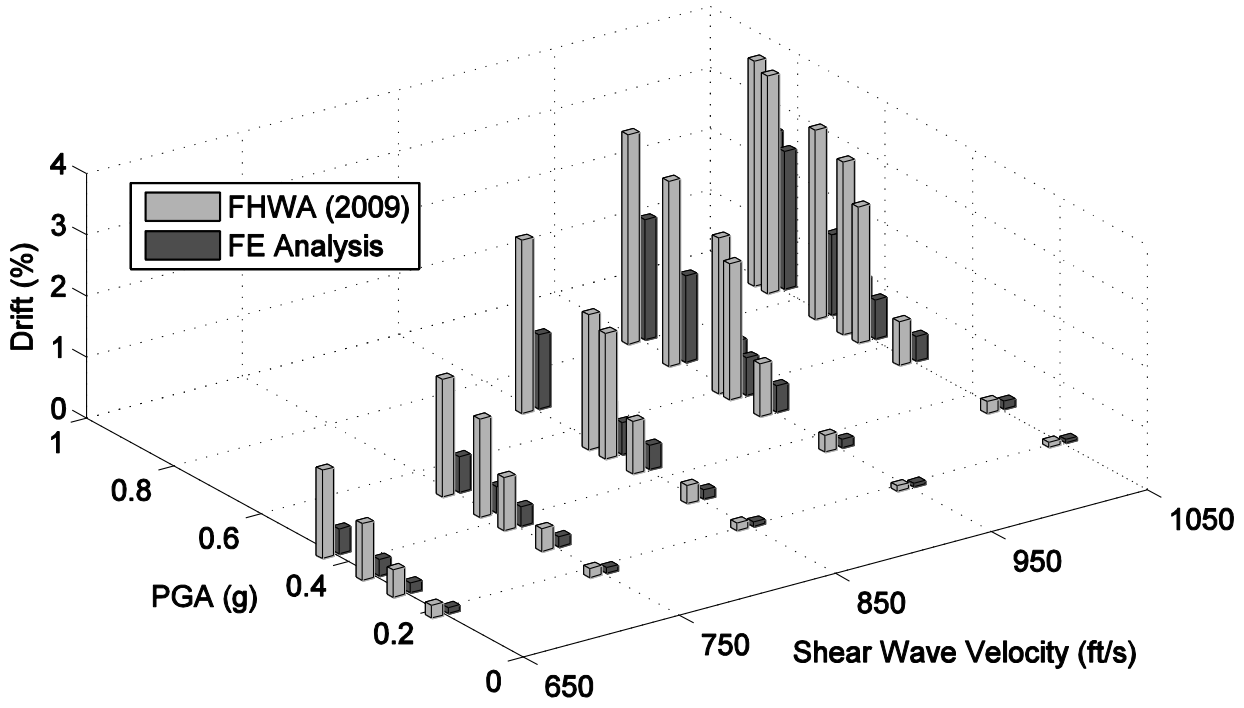

(a)

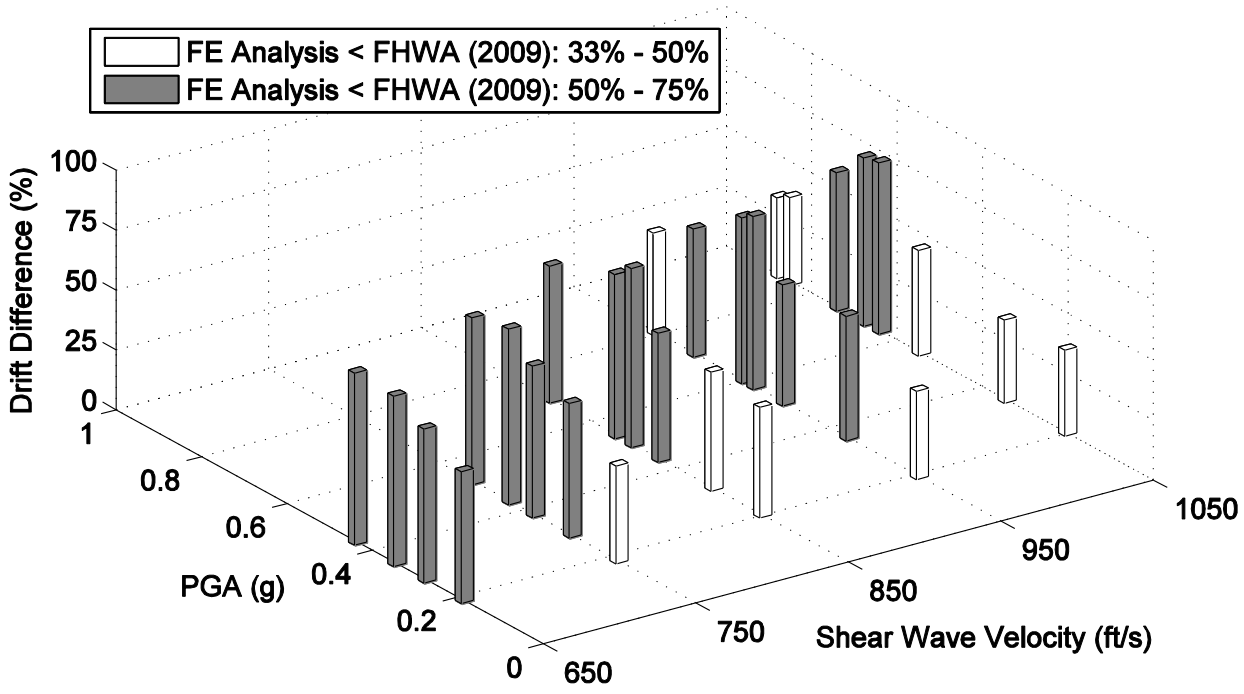

(b)

Figure J-3: On the basis of design PGA, comparison of FE results and FHWA (2009); (a) peak drift and (b) difference of peak drift from FHWA (2009) with respect to FE results

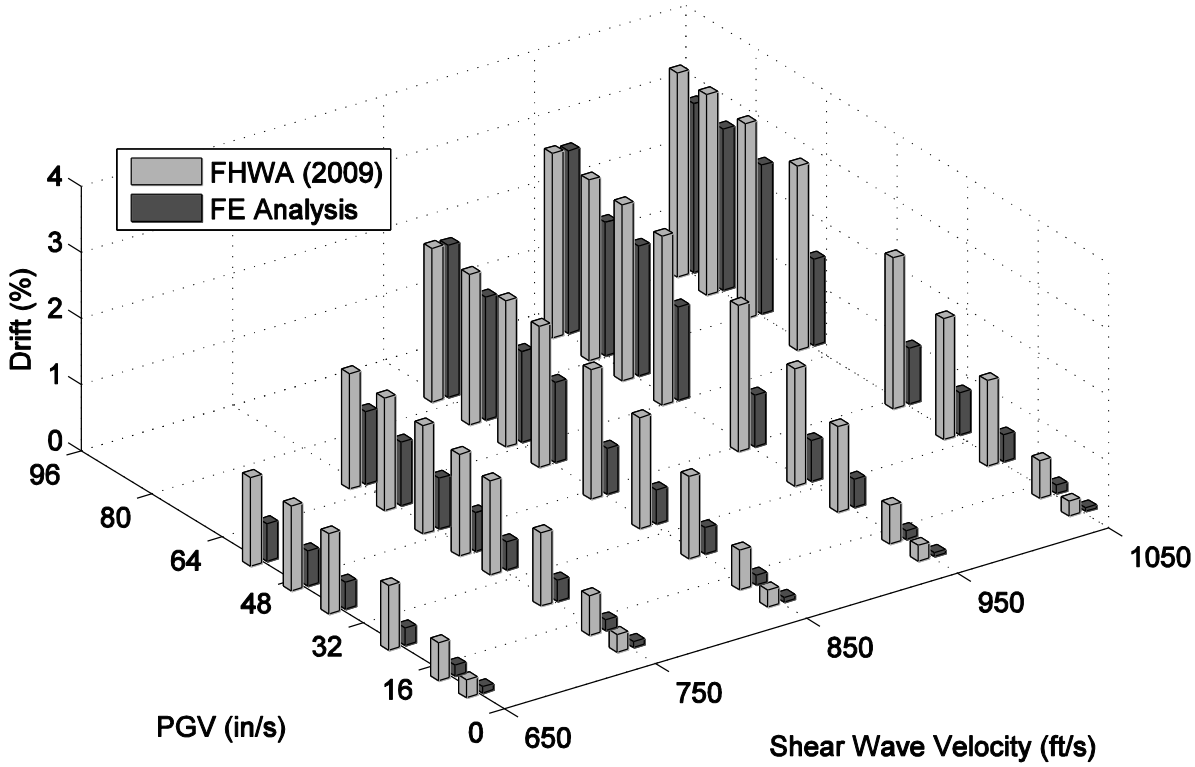

(a)

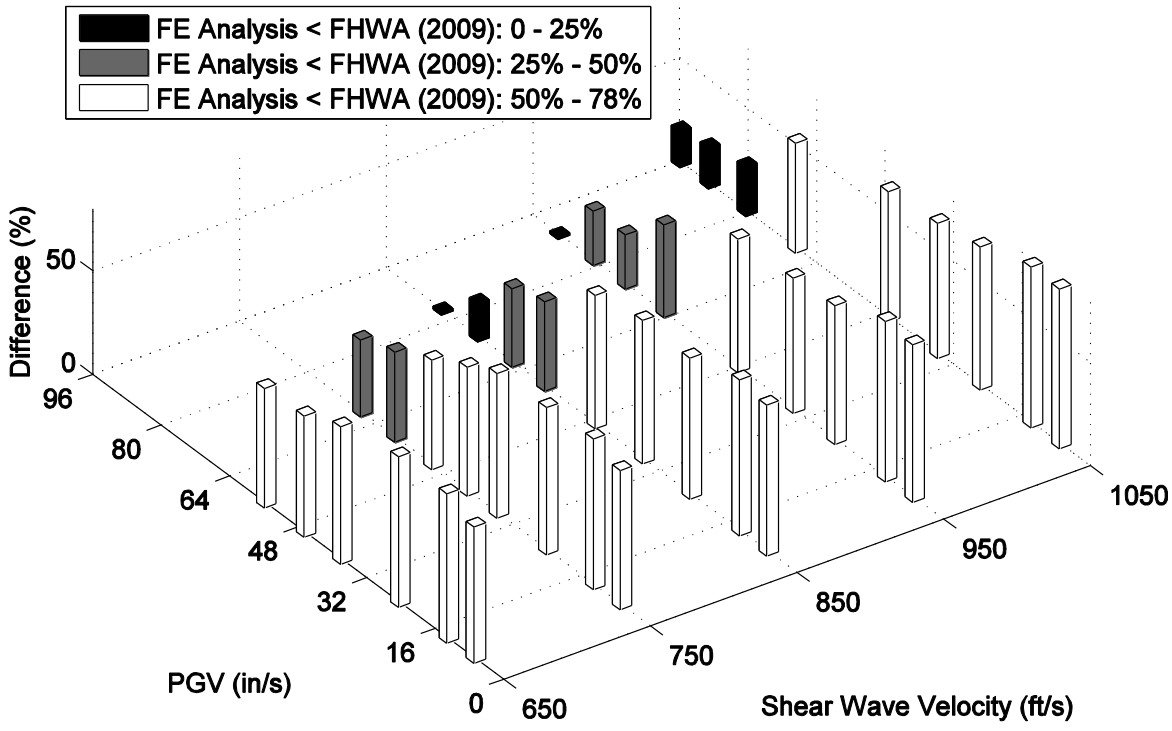

(b)

Figure J-4: On the basis of design PGV, comparison of FE results and FHWA (2009); (a) peak drift and (b) difference of peak drift from FHWA (2009) with respect to FE results